Biochemical and Biophysical Research Communications 420 (2012) 487–491

Contents lists available at SciVerse ScienceDirect

Biochemical and Biophysical Research Communications

journal homepage: www.elsevier.com/locate/ybbrc

The ASB2β Ubiquitin-interacting motif is involved in its monoubiquitination

Takehiro Nishiyama [a], Sakiko Kuroda [a], Eiko Takiguchi [a], Takaaki Nakamura [a], Keisuke Hashimoto [a], Kenta Tsuzuranuki [a], Takao Kawakami [b,c], Yasuhiko Masuho [a,*], Junya Kohroki [a,1]

[a] Faculty of Pharmaceutical Sciences, Tokyo University of Science, Chiba 278-8510, Japan
[b] Clinical Proteome Center, Tokyo Medical University, Tokyo 163-0217, Japan
[c] Medical ProteoScope Company, Tokyo 136-0071, Japan

ARTICLE INFO

Article history:
Received 6 February 2012
Available online 20 February 2012

Keywords:
ASB2
Ubiquitin
Ubiquitin-interacting motif
Monoubiquitination

ABSTRACT

ASB2 proteins are E3 ubiquitin (Ub) ligases that ubiquitinate filamins. There are two ASB2 splice variants, ASB2α and ASB2β. ASB2β has a ubiquitin-binding motif (UIM) at the N-terminal region but ASB2α does not. Here, we provide the first evidence that ASB2β but not ASB2α is monoubiquitinated and that this monoubiquitination involves the UIM. Myc-tagged ASB2β and hemagglutinin (HA)-tagged Ub were co-expressed in HEK293 cells using the pCMV expression vector. Immunoprecipitation with an anti-Myc antibody followed by immunoblotting with anti-Myc and anti-HA antibodies showed an additional ASB2β protein band that had both a Myc and a HA tag. The molecular weight of this protein was larger than that of ASB2β, and the difference in molecular weight between these two proteins corresponded to the molecular weight of monoubiquitin, strongly implying that monoubiquitinated ASB2β is produced in cells. ASB2β with mutations in the UIM motif; either Glu·Asp·Glu27–29Ala·Ala·Ala mutations (ASB2β M1) or a Ser38Ala mutation, (ASB2β M2) were not monoubiquitinated, suggesting the importance of the UIM for ASB2β monoubiquitination. Furthermore, an ASB2β mutant that lacked a SOCS box (ASB2β ΔC) and did not show E3 Ub ligase activity was monoubiquitinated to the same extent as the wild-type ASB2β. In contrast, an ASB2β mutant that lacked the UIM-containing domain (ASB2β ΔN) was not monoubiquitinated. These results suggest that ASB2β but not ASB2α might be monoubiquitinated and that the ASB2β UIM motif, but not its E3 Ub ligase activity, plays a pivotal role in this monoubiquitination.

1. Introduction

Ubiquitin (Ub) is a highly conserved 76 amino acid (aa) protein that is ubiquitously distributed in eukaryotic cells. Conjugation of Ub to proteins, known as ubiquitination, is involved in multiple cellular events such as proteasomal degradation, protein trafficking, endocytosis, and signal transduction [1,2]. In addition to single Ub conjugation (monoubiquitination), successive attachment of Ub to previously conjugated Ub (polyubiquitination) occurs in many kinds of proteins. Ubiquitination is mediated by the sequential catalytic actions of a Ub-activating enzyme (E1), a Ub-conjugating enzyme (E2), and a Ub ligase (E3) [3]. Since ubiquitination specificity and targeting of the ubiquitinated substrate for degradation are determined by the E3 Ub ligase, this enzyme is a key molecule in Ub-dependent cellular events [4].

The family of ankyrin repeat-and SOCS box-containing proteins (ASBs) has been shown to function as E3 Ub ligases. We detected a member of this ASB family, ASB2, in human myeloid leukemia cells stimulated with all-*trans* retinoic acid (ATRA) [5]. ASB2 exerts E3 Ub ligase activity when it forms a complex with Cullin 5 and Rbs2, which bind to the ASB2 SOCS box [6] and its substrates are filamins A and B [7]. A splice variant of ASB2 was found in muscle cells, and the hematopoietic-type and the muscle-type ASB2 proteins were designated ASB2α and ASB2β, respectively. ASB2β also exerts E3 Ub ligase activity towards filamin B [8].

ASB2β and ASB2α are composed of 635 and 587 aa, respectively, and the aa sequence of the residues 69–635 (567 aa) of ASB2β is identical to that of the residues 20–587 of ASB2α. The two variants differ at the N-terminal region, where a single Ubiquitin-interacting motif (UIM) is present in ASB2β but not in ASB2α [9]. A UIM is a Ub-binding domain (UBD) that consists of approximately 20–150 aa [10]. At least 16 different types of UBDs have been identified

Abbreviations: ASB2, ankyrin repeat-and SOCS box-containing protein 2; SOCS, suppressor of cytokine signaling; UIM, Ubiquitin-interacting motif; Ub, ubiquitin; polyUb-, polyubiquitinated; monoUb-, monoubiquitinated; amino acid, aa; UBD, ubiquitin-binding domain; SDS–PAGE, sodium dodecyl sulfate polyacrylamide-gel electrophoresis; IP, immunoprecipitation; IB, immunoblotting; HA-, hemagglutinin tagged; Myc-, myc-tagged; Ab, antibody; GST, glutathione S-transferase; HRP, horseradish peroxidase; PBS, phosphate-buffered saline.

* Corresponding author. Address: Faculty of Pharmaceutical Sciences, Tokyo University of Science, 2641, Yamazaki, Noda-shi, Chiba 278-0022, Japan. Fax: +81 4 7121 3614.
E-mail address: masuho@rs.noda.tus.ac.jp (Y. Masuho).
[1] Present address: Osaka Research Center, Dainippon Sumitomo Pharma Co. Ltd., 3-1-98 Kasugade-naka, Konohana-ku, Osaka 554-0022, Japan.

0006-291X/$ - see front matter © 2012 Published by Elsevier Inc.
doi:10.1016/j.bbrc.2012.02.070

to date and these UBDs are widely diverse in terms of structure and functions. UIMs have been found in numerous proteins, where they are involved in Ub metabolism and receptor endocytosis [11]. The chemically synthesized peptide corresponding to the aa sequence of the ASB2β-UIM strongly bound to polyubiquitinated-proteins, although little binding to free monoubiquitin was observed [9]. The biological role of the UIM in ASB2β remains to be elucidated.

A number of proteins that contain UBDs including a UIM have been shown to undergo auto-ubiquitination *in vivo* [10–12]. The activity of endocytic proteins such as Sts1, Sts2, Eps15 and Hrs, which contain UBDs, is regulated by monoubiquitination [12]. These proteins function in the transport of transmembrane proteins [13]. Although the biological roles of ASB2α and ASB2β are unknown, since these proteins differ by the presence or absence of a UIM, it is important to know if ASB2s are monoubiquitinated or not in order to elucidate their function.

In this study, we show that ASB2β, but not ASB2α, is monoubiquitinated *in vivo* and that this monoubiquitination involves its UIM but not its E3 Ub ligase activity.

2. Materials and methods

2.1. Reagents and antibodies

Reagents and antibodies were purchased from the following companies: *N*-ethyl maleimide (NEM) and protease inhibitor cocktail (PIC) from Sigma–Aldrich Co. LLC, St. Louis, MO; a glutathione Sepharose 4B column from Amersham Biosciences; protein G agarose beads from Santa Cruz Biotechnology and Na_3VO_4 from Wako Pure Chemical Industries, Ltd., Osaka; a mouse anti-Myc Ab (9E10) from Medical Biological Laboratories Co. Ltd., Nagoya; a mouse anti-hemagglutinin (HA) Ab (16B12) from Medical Biological Laboratories Co. Ltd.; horseradish peroxidase (HRP)-conjugated goat Abs to mouse Igs and HRP-conjugated porcine Abs to goat Igs from Biosource International Inc., Camarillo, CA; HRP-conjugated goat Abs to rabbit IgG from Rockland Immunochemicals, Inc., PA; and goat Abs to glutathione-S-transferase (GST) from Bethyl Laboratories, Montgomery, TX. Oligonucleotides were synthesized by Operon Biotechnologies, Tokyo.

2.2. Constructs

Human full-length cDNAs encoding ASB2α (GenBank accession No. NM_016150) and ASB2β (GenBank accession No. NM_001202429) were obtained as described previously [6,9].

The ASB2β truncation mutants; ASB2β ΔN, lacking residues 1–68, and ASB2β ΔC lacking residues 587–635, were amplified by PCR using ASB2β cDNA as the template. The amplified cDNAs encoding these mutants were inserted into pCMV-Myc N (TakaraBio, Inc., Tokyo) as described previously [6]. The ASB constructs containing mutations in the UIM motif, ASB2β M1, with the mutations Glu·Asp·Glu27–29Ala·Ala·Ala, and ASB2β M2 with the mutation Ser38Ala, were generated by site-directed mutagenesis using the wild-type ASB2β cDNA expression vector as the template. These mutants were inserted into the pCMV-Myc-N vector. Human ubiquitin was expressed using the pCMV-HA-N vector (TakaraBio, Inc.).

2.3. Monoubiquitination assay

HEK293 cells were cultured at a density of 6×10^6 cells/ml in Dulbecco's modified Eagle's medium (DMEM) containing 10% heat-inactivated fetal bovine serum, 100 units/ml penicillin and 0.1 mg/ml streptomycin under conditions of 37 °C and 5% CO_2. Plasmid DNA (5 μg) was mixed with 15 μl of TransFast (Promega Corporation, Wisconsin, WI) in 2 ml of DMEM at room temperature for 15 min. After washing the cells twice with PBS, the cells were cultured in medium containing plasmid DNA and TransFast at 37 °C and 5% CO_2 for 1 h. The plasmid DNAs used for transfection were pCMV-HA-Ub and/or pCMV-Myc-ASB2α, pCMV-Myc-ASB2β, pCMV-Myc-ASB2β M1, pCMV-Myc-ASB2β M2, pCMV-Myc-ASB2β ΔN and pCMV-Myc-ASB2β ΔC.

After culture for 1 h, the medium was removed and the cells were washed twice with PBS. The cells were lysed in 0.3 ml of Lysis Buffer (50 mM Tris–HCl at pH 7.5 containing 0.15 M NaCl, 1 mM EDTA, 0.5% Nonidet P-40, 10 mM NaF, 1 mM Na_3VO_4, 10 mM NEM and 1% PIC) and the cell suspensions were allowed to stand on ice for 30 min with gentle rotation every 10 min. The lysates were then centrifuged at 10,000×*g* and 4 °C for 30 min and the supernatants were used as the cell lysates.

Proteins in the cell lysates that were tagged with Myc were immunoprecipitated with an anti-Myc Ab by mixing with 1 μg (5 μl) of mouse anti-Myc Ab (9E10) and the mixture was gently rotated overnight at 4 °C. Protein G agarose beads (10 μl) were added to the solutions, and they were gently rotated at 4 °C for 1 h. The beads were washed twice with Lysis Buffer by centrifugation at 10,000×*g* and 4 °C. Sample Buffer (20 μl of 2× buffer) was added to the washed beads and the supernatants were heated at 95 °C for 5 min.

The proteins in immunecomplexes were separated by SDS–PAGE and analyzed by immunoblotting (IB) as described previously [9]. Briefly, proteins were transferred to polyvinylidene difluoride (PVDF) membranes. The membranes were blocked with 0.3% nonfat dry milk in 50 mM Tris–HCl at pH 7.5 containing 150 mM NaCl and 0.2% Tween 20 for 2 h at room temperature and were then probed with anti-Myc or anti-HA Abs for 2 h at room temperature. After washing with TBST, the membranes were probed with HRP-conjugated anti-mouse Igs Abs for 1 h at room temperature. The membranes were then treated with ECL Western blotting detection reagents and detected bands were exposed to an X-ray film.

2.4. In vivo ubiquitin ligase activity of ASB2β ΔC

The *in vivo* ubiquitin ligase activity of ASB2β and ASB2β ΔC was measured as previously described [6]. Briefly, HEK293 cells were transfected with pCMV-Myc-ASB2β or pCMV-Myc-ASB2β ΔC. Myc-ASB2β or Myc-ASB2β ΔC in the cell lysates were precipitated with 5 μg of anti-Myc Ab (9E10) and 10 μl of protein G agarose beads for 1 h at 4 °C. The beads were washed three times with 50 mM Tris–HCl at pH 7.5 containing 0.15 M NaCl, 1 mM EDTA, 0.5% Nonidet P-40 and 1 mM DTT and then twice with 40 mM HEPES buffer at pH 7.9 containing 60 mM CH_3COOK, 1 mM $MgCl_2$, 0.5 mM EDTA, 2 mM DTT and 10% glycerol. The resulting immunecomplexes were mixed with 500 ng of the E1 enzyme mouse Uba1 (Wako Pure Chemical Industries Ltd., Osaka, Japan), 1.5 μg of the His-tagged E2 enzyme 6× His-UbcH5a and 2.5 ng of GST-Ub in a total volume of 20 μl of 40 mM HEPES buffer at pH 7.9 containing 60 mM CH_3COOK, 5 mM $MgCl_2$, 1 mM DTT and 1.5 mM ATP. The reaction mixtures were incubated for 1 h at 37 °C, and the resulting protein products were separated by SDS–PAGE and subjected to immunoblotting using goat anti-GST Abs and HRP-conjugated porcine Abs to goat Igs.

3. Results

3.1. Monoubiquitination of ASB2β

To determine whetherASB2β is monoubiquitinated in cells, HEK293 cells were transiently co-transfected with Myc-ASB2β

and HA-Ub expression vectors. After incubation to allow protein expression, the cell lysates were immunoprecipitated with an anti-Myc Ab. Proteins in the precipitated immunecomplexes were separated by SDS–PAGE and analyzed by IB with anti-Myc and anti-HA Abs. The anti-Myc Ab blot showed a second, protein band in addition to that of ASB2β when the cells were co-transfected with both vectors (Fig. 1, lane 3). The molecular weight of this additional band was larger than ASB2β by 7–10 kDa. This protein band was not observed in cells that were transfected with HA-Ub alone or with Myc-ASB2β alone. When IB was performed with an anti-HA Ab, this additional protein band cross-reacted with the anti-HA Ab (lane 6), although the lower molecular weight ASB2β band did not. These data suggested that the additional protein band that was observed upon co-expression of ASB2β and Ub was composed of both ASB2β and Ub that were linked *via* a covalent bond. Moreover, since the molecular weight of this additional band was larger than that of ASB2β by the molecular weight of a single Ub molecule, these results imply that the higher molecular weight protein must be monoubiquitinated ASB2β (monoUb-ASB2β).

3.2. Examination of monoubiquitination of ASB2α

We next determined if the monoubiquitination of ASB2β was mediated by the UIM motif, by investigating if ASB2α, a splice variant of ASB2β that lacks the UIM motif (Fig. 2A), is also monoubiquitinated in cells. Myc-ASB2α or Myc-ASB2β was co-expressed with HA-Ub in HEK293 cells. The cell lysates were immunoprecipitated with an anti-Myc Ab, and the proteins in the immunecomplexes were separated by SDS–PAGE and analyzed by IB with anti-Myc and anti-HA Abs. Co-expression of Myc-ASB2α and HA-Ub resulted in no additional band following IB with the anti-Myc Ab and showed only a very faint band in IB with the anti-HA Ab, whereas Myc-ASB2β, as expected, showed an additional band that stained with both anti-Myc and anti-HA Abs (Fig. 2B). These data suggested that the N-terminal region of ASB2β is involved in, or is essential for its monoubiquitination.

3.3. Involvement of the UIM in ASB2β monoubiquitination

We next determined if the UIM motif within the ASB2β N-terminal region mediated ASB2β monoubiquitination". The residues Glu·Asp·Glu (EDE) 27–29 and Ser (S) 38 are highly conserved among the UIM sequences of different proteins. We therefore tested if mutation of these residues would abolish ubiquitin binding of ASB2β. As shown in Fig. 3A, two expression vectors were prepared to express such ASB2β mutants; EDE27–29AAA (ASB2β M1) or S38A (ASB2β M2). These different mutants were each co-expressed with HA-Ub in HEK293 cells. The cell lysates were subjected to IP with an anti-Myc Ab and proteins in the immunecomplexes were analyzed by IB with anti-Myc and anti-HA Abs. Neither the ASB2β M1 nor the ASB2β M2 mutant was monoubiquitinated, since no additional band that cross-reacted with both anti-Myc and anti-HA antibodies was observed, whereas ASB2β WT was monoubiquitinated under the same conditions (Fig. 3B). These results strongly suggest that the UIM motif is essential for the monoubiquitination of ASB2β.

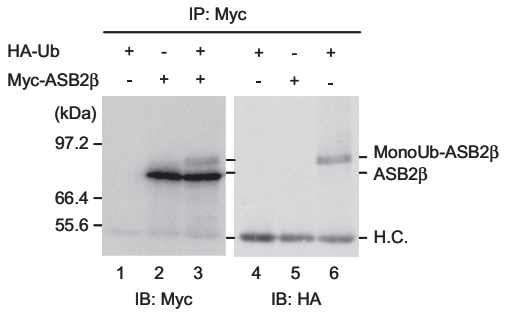

Fig. 1. Monoubiquitination of ASB2β. HA-Ub and/or Myc-ASB2β were co-expressed in HEK293 cells and the cell lysates were immunoprecipitated with an anti-Myc Ab. Proteins in the immunecomplexes were separated by SDS–PAGE and monoubiquitinated ASB2β (MonoUb-ASB2β) was analyzed by Western blotting using anti-Myc and anti-HA Abs. H.C.; a band that corresponds to the IgG heavy chain.

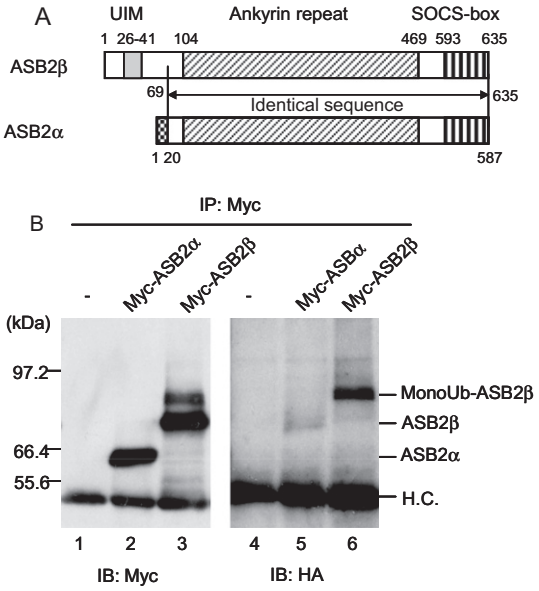

Fig. 2. Investigation of ASB2α monoubiquitination. (A) Schematic illustration of ASB2α and ASB2β protein domains. ASB2β is composed of three domains; the UIM (grey), the ankyrin repeat (slanted lines) and a SOCS box (vertical lines). The sequence of the 567 aa from aa 69 to aa 635 of ASB2β is identical to the sequence containing aa 21 to aa 587 of ASB2α. (B) Myc-ASB2α or Myc-ASB2β was co-expressed with HA-Ub in HEK293 cells, and the cell lysates were immunoprecipitated with an anti-Myc Ab. Proteins in the immunecomplexes were separated by SDS–PAGE and monoubiquitinated ASB (MonoUb-ASB2) proteins were analyzed by Western blotting using anti-Myc and anti-HA Abs.

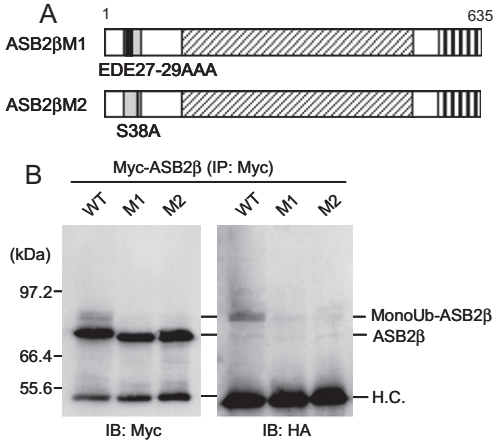

Fig. 3. The monoubiquitination of ASB2β is lost upon mutation of the UIM. (A) Schematic illustration of ASB2β UIM mutants. ASB2β was mutated at two different positions in the UIM: Glu·Asp·Glu27–29Ala·Ala·Ala (ASB2β M1) or Ser38Ala (ASB2β M2). (B) Myc-ASB2β, Myc-ASB2β M1 or Myc-ASB2β M2 was co-expressed with HA-Ub in HEK293 cells, and their monoubiquitination was analyzed by IP with an anti-Myc Ab followed by IB with anti-Myc and HA Abs.

3.4. ASB2β ΔC lacking Ub-ligase activity was monoubiquitinated

We next confirmed that the mono-ubiquitination of ASB2β required its N-terminal, UIM-containing domain, and we further

determined if ASB2β E3 ligase activity was required for its mono-ubiquitination. For these purposes, we determined the mono-ubiquitination of ASB2β that lacked the N-terminal domain, or that lacked the C-terminal domain, which is required for ASB2β E3 ligase activity. The ASB2β ΔN and ASB2β ΔC mutants were constructed as follows. ASB2β ΔN lacks the first 68 aa of the N-terminal domain of ASB2β, and ASB2β ΔC lacks 49 aa from aa 587 to the C-terminus (aa 635) (Fig. 4A). Myc-ASB2β WT, Myc-ASB2β ΔN or Myc-ASB2β ΔC was then co-expressed with HA-Ub in HEK293 cells, and the monoubiquitination of ASB2β WT, ASB2β ΔN and ASB2β ΔC in the cell lysates was analyzed by IB with anti-Myc and anti-HA Abs. Both mono-Ub-ASB2β WT and -ASB2β ΔC were detected by IB with both anti-Myc and anti-HA Abs (Fig. 4B, lanes 1, 3, 4, 6). However, mono-Ub-ASB2β ΔN was not detected by IB with the anti-Myc Ab and there were only a few faint bands detectable by IB with the anti-HA Ab (Fig. 4B, lanes 2, 5). Since ASB2β is itself an E3 Ub ligase, when Myc-ASB2β WT was precipitated from cell lysates, it could induce protein ubiquitination in association with added E1 and E2 enzymes (Fig. 4C, lane 5). However, ASB2β ΔC that lacks the SOCS box, which is contained within the C-terminal region and is required for E3 ligase activity, showed little protein ubiquitination under these conditions (lanes 4, 6). Since the ASB2β ΔC was monoubiquitinated, this result suggests that the E3 Ub ligase activity of ASB2β is probably not involved in ASB2β monoubiquitination and that some other Ub ligase monoubiquitinates ASB2β.

4. Discussion

The aim of this study was to determine whether ASB2α and/or ASB2β are monoubiquitinated *in vivo*. There were two important findings of this study. One finding was that ASB2β but not ASB2α is monoubiquitinated *in vivo*, and the second finding was that the UIM motif of ASB2β but not its E3 Ub ligase activity plays a pivotal role in this monoubiquitination.

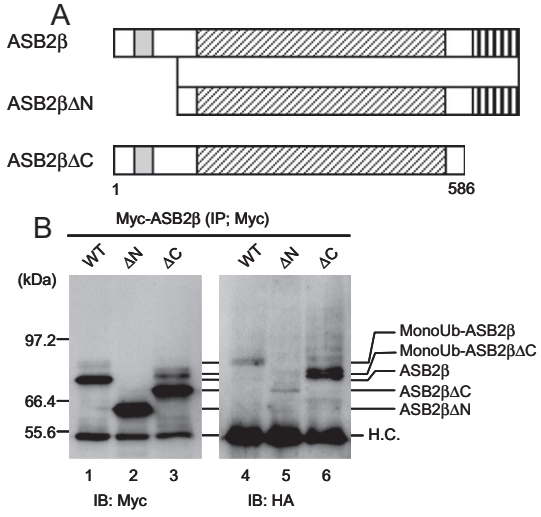

Fig. 4. Analysis of the monoubiquitination of ASB2β ΔN and ASB2β ΔC and of the E3 ligase activity of ASB2β ΔC. (A) Schematic illustration of ASB2β ΔN and ASB2β ΔC. ASB2β ΔN lacks the first 68 aa of ASB2β, and ASB2β ΔC lacks the last 49 aa of ASB2β (aa 587 to 635. (B) Myc-ASB2β WT, Myc-ASB2β ΔN or Myc-ASB2β ΔC was co-expressed with HA-Ub in HEK293 cells and monoubiquitinated (Mono-Ub)ASB2β WT, ASB2β ΔN and ASB2β ΔC in the cell lysates was analyzed following IP with an anti-Myc Ab and IB with anti-Myc and anti-HA Abs. (C) The Ub ligase activity of Myc-ASB2β ΔC was compared to that of Myc-ASB2β using GST-Ub, E1, E2 and HeLa cell lysates as its substrates. Following SDS–PAGE, polyubiquitinated-proteins were detected by Western blotting, using anti-GST antibodies.

A number of the experimental results support the fact that ASB2β is monoubiquitinated *in vivo*; (1) An additional ASB2β protein band was observed when cells were co-transfected with ASB2β and Ub expression vectors. The difference in molecular weight between this additional band and that of ASB2β corresponded to the molecular weight of a single Ub molecule (76 aa). (2) The higher molecular weight ASB2β protein included both ASB2β and Ub as assessed by Western blotting (Figs. 1, 2B, 3B and 4B). This result is in agreement with data regarding other UBD-containing proteins such as S5a, Vps9, Sts1, Hrs, which have also been shown to be monoubiquitinated. The biological activities of these other proteins were found to be modified upon monoubiquitination [11–16].

We showed that the monoubiquitination of ASB2β is dependent on the UIM sequence that is located at the N-terminal region of ASB2β. Thus, neither ASB2α, which lacks the UIM motif, nor ASB2β ΔN, an ASB2β mutant that lacks residues 1–68 that contain the UIM motif, were monoubiquitinated (Figs. 2B and 4B, respectively). In addition, the UIM motif has a highly conserved sequence, XeeeXϕXXAXXXSXXe, where e is a negatively charged residue, ϕ is a hydrophobic residue and X is any amino acid [11]. We showed that ASB2β constructs that had mutations within this domain: ASB2β M1 with the mutation EDE27–29AAA and ASB2β M2 with the mutation S38A, were not monoubiquitinated in cells when they were individually co-expressed with Ub.

Many proteins that are able to bind Ub through their UBD can themselves become monoubiquitinated [17–19]. Since a functional UBD is a prerequisite for this self-ubiquitination, the process is called "coupled monoubiquitination". ASB2β also undergoes coupled monoubiquitination. For other E3 Ub ligases that contain a UBD, coupled monoubiquitination inhibits their E3 Ub ligase activities [18–19]. It is therefore possible that the E3 Ub ligase activity of ASB2β might also be regulated by its monoubiquitination. We speculate that mono-Ub-ASB2β may lose its E3 Ub ligase activity and/or the Ub-binding activity of the UIM. Monoubiquitination may be important for differences in the function of ASB2β and ASB2α. The gene expression of these two ASB2 splice variants is very different with ASB2β being expressed in a variety of tissues and ASB2α being expressed in myeloid leukemia cells [5,8]. Although these two molecules are very similar in terms of aa sequence and substrate specificity, their gene expression is very different, as is their regulation by coupled monoubiquitination.

ASB2β ΔC was monoubiquitinated to the same or even to a greater extent than the wild-type ASB2β even though its E3 Ub ligase activity was totally inactivated by deletion of the C-terminal residues. ASB2β ΔC lacks the SOCS box domain of ASB2β, to which Cullin 5 and Rbs2 bind to form the E3 Ub ligase complex [6]. This result suggests that the E3 Ub ligase activity of ASB2β is not involved in ASB2β monoubiquitination. There are three possible mechanisms of ASB2β monoubiquitination: (1) monoubiquitination by an ASB2β-specific E3 ligase, (2) E3-independent monoubiquitination by a Ub-E2 [20], and (3) monoubiquitination by a number of different E3 Ub ligases [16]. Further study is necessary to determine the mechanism of ASB2β monoubiquitination.

Future studies will include analysis of the effect of monoubiquitination of ASB2β on its E3 Ub ligase activity and on ASB2β Ub-binding activity *via* the UIM motif. These studies will elucidate the mechanism of ASB2β-mediated ubiquitination and the regulation of its biological functions.

Acknowledgments

This study was supported by the Tokyo University of Science. We thank Professors Fumio Fukai and Shuji Kojima for their helpful discussions.

References

[1] A. Hershko, A. Ciechanover, The ubiquitin system, Ann. Rev. Biochem. 67 (1998) 425–479.
[2] K. Haglund, I. Dikic, Ubiquitylation and cell signaling, EMBO J. 24 (2005) 3353–3359.
[3] C.M. Pickart, Mechanisms underlying ubiquitination, Ann. Rev. Biochem. 70 (2001) 503–533.
[4] F.C. Guibal, C. Moog-Lutz, P. Smolewski, Y. Di Gioia, Z. Darzynkiewicz, P.G. Lutz, Y.E. Cayre, ASB-2 inhibits growth and promotes commitment in myeloid leukemia cells, J. Biol. Chem. 277 (2002) 218–224.
[5] J. Kohroki, S. Fujita, N. Itoh, Y. Yamada, H. Imai, N. Yumoto, T. Nakanishi, K. Tanaka, ATRA-regulated Asb-2 gene induced in differentiation of HL-60 leukemia cells, FEBS Lett. 505 (2001) 223–228.
[6] J. Kohroki, T. Nishiyama, T. Nakamura, Y. Masuho, ASB proteins interact with Cullin 5 and Rbx2 to form E3 ubiquitin ligase complexes, FEBS Lett. 579 (2005) 6796–6802.
[7] M.L. Heuze, I. Lamsoul, M. Baldassarre, Y. Lad, S. Leveque, Z. Razinia, C. Moog-Lutz, D.A. Calderwood, P.G. Lutz, ASB2 targets filamins A and B to proteasomal degradation, Blood 112 (2008) 5130–5140.
[8] N.F. Bello, I. Lamsoul, M.L. Heuzé, A. Métais, G. Moreaux, D.A. Calderwood, D. Duprez, C. Moog-Lutz, P.G. Lutz, The E3 ubiquitin ligase specificity subunit ASB2β is a novel regulator of muscle differentiation that targets filamin B to proteasomal degradation, Cell Death Differ. 16 (2009) 921–932.
[9] J. Kohroki, S. Kuroda, E. Takiguchi, T. Nakamura, T. Nishiyama, K. Tsuzuranuki, T. Kawakami, Y. Masuho, Comprehensive trapping of polyubiquitinated proteins using the UIM peptide of ASB2a, Biochem. Biophys. Res. Commun. 414 (2011) 292–297.
[10] J.H. Hurley, S. Lee, G. Prag, Ubiquitin-binding domains, Biochem. J. 399 (2006) 361–372.
[11] S.L. Miller, E. Malotky, J.P. O'Bryan, Analysis of the role of ubiquitin-interacting motifs in ubiquitin binding and ubiquitylation, J. Biol. Chem. 279 (2004) 33528–33537.
[12] D. Hoeller, N. Crosetto, B. Blagoev, C. Raiborg, R. Tikkanen, S. Wagner, K. Kowanetz, R. Breitling, M. Mann, H. Stenmark, I. Dikic, Regulation of ubiquitin-binding proteins by monoubiquitination, Nat. Cell Biol. 8 (2006) 163–169.
[13] Y. Mosesson, Y. Yarden, Monoubiquitylation: a recurrent theme in membrane protein transport, IMAJ 8 (2006) 233–237.
[14] D. Hoeller, I. Dikic, Regulation of ubiquitin receptors by coupled monoubiquitination, Subcell. Biochem. 54 (2010) 31–40.
[15] M. Isasa, E.J. Katz, W. Kim, V. Yugo, S. González, D.S. Kirkpatrick, T.M. Thomson, D. Finley, S.P. Gygi, B. Crosas, Monoubiquitination of RPN10 regulates substrate recruitment to the proteasome, Mol. cell 38 (2010) 733–745.
[16] D. Hoeller, C.M. Hecker, S. Wagner, V. Rogov, V. Dötsch, I. Dikic, E3-independent monoubiquitination of ubiquitin-binding proteins, Mol. Cell 26 (2007) 891–898.
[17] T. Woelk, B. Oldrini, E. Maspero, S. Confalonieri, E. Cavallaro, P.P. Di Fiore, S. Polo, Molecular mechanisms of coupled monoubiquitination, Nat. Cell Biol. 8 (2006) 1246–1254.
[18] Q. Yan, S. Dutt, R. Xu, K. Graves, P. Juszczynski, J.P. Manis, M.A. Shipp, BBAP monoubiquitylated histone H4 at lysine 91 and selectively modulates the damage response, Mol. Cell 36 (2009) 110–120.
[19] A.M. Ali, T.R. Singh, A.R. Meetei, FANCM-FAAP24 and FANCJ: FA proteins that metabolize DNA, Mutat. Res. 668 (2009) 20–26.
[20] K.C.M. Chew, N. Matsuda, K. Saisho, G.G.Y. Lim, C. Chai, H.-M. Tan, K. Tanaka, K.-L. Lim, Parkin mediates apparent E2-independent monoubiquitination in vitro and contains an intrinsic activity that catalyzes polyubiquitination, Plos One 6 (2011) e19720.

Biochemical and Biophysical Research Communications 420 (2012) 492–497

Contents lists available at SciVerse ScienceDirect

Biochemical and Biophysical Research Communications

journal homepage: www.elsevier.com/locate/ybbrc

KCC2 transport activity requires the highly conserved L_{675} in the C-terminal β1 strand

Annika Döding [1], Anna-Maria Hartmann, Timo Beyer, Hans Gerd Nothwang *

Abteilung Neurogenetik, Institut für Biologie und Umweltwissenschaften, Carl von Ossietzky Universität Oldenburg, Oldenburg, Deutschland

ARTICLE INFO

Article history:
Received 17 February 2012
Available online 3 March 2012

Keywords:
Chloride homeostasis
Inhibitory synapse
Regulation
HEK-293
Cation-chloride cotransporter
Evolution

ABSTRACT

The activity of the neuron-specific K^+, Cl^- co-transporter 2 (KCC2) is required for hyperpolarizing action of GABA and glycine. KCC2-mediated transport therefore plays a pivotal role in neuronal inhibition. Few analyses have addressed the amino acid requirements for transport-competent conformation. KCC2 consists of 12 transmembrane domains flanked by two intracellular termini. Structural analyses of a related archaeal protein have identified an evolutionary extremely conserved β1 strand, which links the transmembrane domain to a C-terminal dimerization interface. Here, we focused on the sequence requirement of this linker. We mutated four highly conserved amino acids of the β1 strand ($_{673}$QLLV$_{676}$) to alanine and analyzed the functional consequences in mammalian cells. Flux measurements demonstrated that L_{675A} significantly reduced KCC2 transport activity by 41%, whereas the other three mutants displayed normal activity. Immunocytochemistry and cell surface labeling revealed normal trafficking of all four mutants. Altogether, our results identify L_{675} as a critical residue for KCC2 transport activity. Furthermore, in view of its evolutionary conservation, the data suggest a remarkable tolerance of the KCC2 transport activity to amino acid substitutions in the β1 strand.

1. Introduction

Cation-chloride-cotransporters (CCCs) are electro neutral secondary-active transporters, which participate in essential physiological processes such as epithelial salt transport, osmotic regulation, and Cl^--homeostasis [1]. CCCs are divided into Na^+, K^+, Cl^- inward transporters (NKCC1-2, NCC), K^+, Cl^- extruders (KCC1-4), a polyamine transporter (CCC9), and the cotransporter-interacting protein CIP1 [1,2]. Among the KCCs, the neuron-specific KCC2 plays an outstanding role, as its activity is required for the hyperpolarizing action of the inhibitory neurotransmitters GABA and glycine [3–8]. In accord with this essential role, $KCC2^{-/-}$ mice die perinatally due to respiratory failure in the absence of synaptic inhibition [5], and knocking-down of the transporter leads to generalized seizure [9,10].

The structural organization of transport-active CCCs is highly conserved. The functional units are oligomers [11,12] and the individual genes encode polypeptides consisting of 12 transmembrane domains (TMD), a large extracellular loop (LEL), and intracellular termini [1]. Evolutionary sequence conservation is highest in the TMDs, followed by the C-terminus, whereas the N-terminus is poorly conserved [1,13]. Functional analyses of NKCCs revealed that TMD 2, 5 and 7 are necessary for the ion binding and transport [14–16]. The termini and the LEL are involved in allosteric or regulatory effects [16–18]. Concerning KCC2, several sites critical for its transport-active conformation have been identified. Mutation of the four cysteines in the LEL [18] or mutation of the C-terminal Y_{1087} to aspartate drastically reduced transport activity [19], whereas mutations that mimicked the dephosphorylated state of T_{906}/T_{1007} increased transport activity [20]. Finally, a KCC2-specific ISO domain was identified, which is involved in constitutive activity under isotonic conditions [21].

Recently, the X-ray structure of the C-terminus of a prokaryotic CCC (*Methanosaccrina acetovirans*, *ma*CCC) was determined [13]. This analysis revealed that the C-terminus is organized into two antiparallel subdomains, each composed of five parallel β-sheets, connected by α-helices. Notably, the highest evolutionary sequence conservation in the entire C-terminus was observed for the β1 strand [13]. To analyze the importance of this evolutionary conservation, we performed mutational analyses in the rat KCC2 (*rn*KCC2). Four highly conserved amino acids ($_{673}$QLLV$_{676}$) of the β1 strand were replaced by alanine and the functional consequences studied in mammalian cells.

* Corresponding author. Address: Abteilung Neurogenetik, Carl von Ossietzky Universität Oldenburg, D-26111 Oldenburg, Deutschland. Fax: +49 441 798 3250.
E-mail address: hans.g.nothwang@uni-oldenburg.de (H.G. Nothwang).
[1] Present address: Institut für Allgemeine Zoologie und Tierphysiologie, Universität Jena, Deutschland.

0006-291X/$ - see front matter © 2012 Elsevier Inc. All rights reserved.
doi:10.1016/j.bbrc.2012.02.147

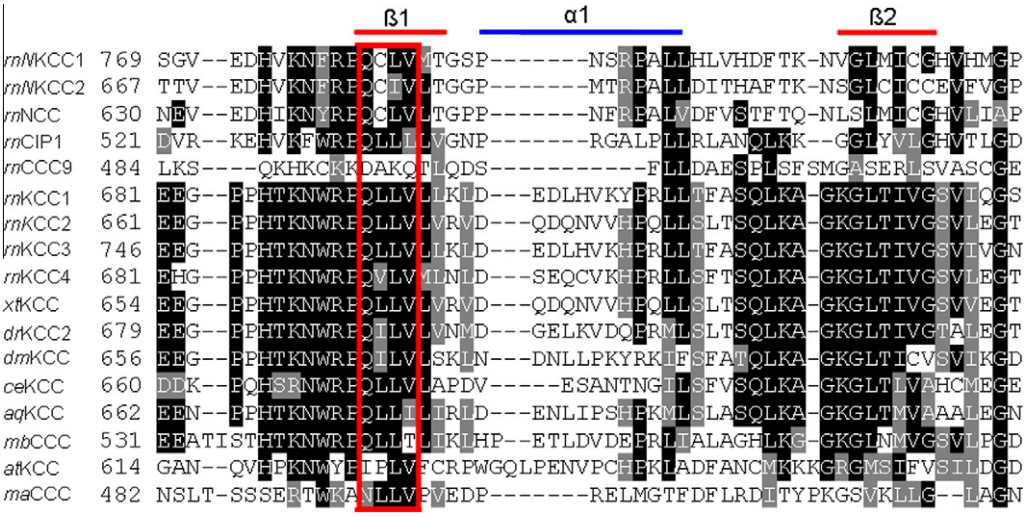

Fig. 1. QLLV residues are highly conserved in the β1 strand structure. A multiple sequence alignment of the C-terminal region of different CCC transporter was made with ClustalW [29]. Secondary structure data were derived from the crystal structure of the C-terminus of a CCC from *M. acetovirans* [13] and are shown above the alignment. QLLV residues are displayed in the box. The beginning of the C-terminus is indicated by an arrow. *Rn*, *rattus norvegicus*; *dm*, *drosophila melanogaster*; *aq*, *amphimedon queenslandica*; *mb*, *monosiga brevicollis*; *dr*, *daneo rerio*; *xt*, *xenopus tropicalis*; *ce*, *caenorhabtidis elegans*; *ma*, *methanosaccrina acetovirans*; *at*, *arabidopsis thaliana.* Amino acid sequences are: *rn*NKCC1 (GenBank ID: NP_113986.1), *rn*NKCC2 (GenBank ID: NP_062007.2), *rn*NCC (GenBank ID: NP_062218.3), *rn*KCC1 (GenBank ID: NP_062102.1), *rn*KCC2 (GenBank ID: NP_599190.1), *rn*KCC3 (GenBank ID: NP_001103100.1), *rn*KCC4 (GenBank ID: NP_001013162.2), *rn*CIP1 (GenBank ID: Q66HR0.1), *rn*CCC9 (GenBank ID: EDM11357.1), *xt*KCC (GenBank ID: NP_001072306.2), *dr*KCC (GenBank ID: XP_701000.4), *dm*KCC (GenBank ID: NP_726378.1), *ce*KCC (GenBank ID: ACN62948.1), *aq*KCC (GenBank ID: XP_003384645.1), *mb*KCC (GenBank ID: XP_001743661.1), *at*KCC (GenBank ID: AAF19744.1), and *ma*CCC (GenBank ID: NP_619366.1).

2. Materials and methods

2.1. Site-directed mutagenesis

Site directed mutagenesis was performed according to the Quick-Change mutagenesis system (Stratagene, Heidelberg, Germany), using a previously reported rat KCC2b (GenBank ID: NM_134363) expression clone [18]. Oligonucleotides for the generation of the mutations were as follows (only forward primers are given): $KCC2_{Q673A}$ 5′-CCAGCACCAGTAGCGCGGGCCTCCAGTTCT-3′, $KCC2_{L674A}$ 5′CTGGAGGCCCCAGGCACTGGTGCTGGTG-3′, $KCC2_{L675A}$ 5′TGGAGGCCCCAGCTAGCGGTGCTGGTGC-3′; $KCC2_{V676A}$ 5′-CCCCAG CTACTGGCGCTGGTGCGTGTG-3′. All generated clones used in this study were confirmed by sequencing.

2.2. Determination of K^+–Cl^- cotransport

Transport activity was determined by measuring Cl^--dependent uptake of $^{86}Rb^+$ (PerkinElmer Life Sciences Life Sciences) in HEK-293 cells [22]. Cells were cultured in DMEM (Invitrogen) and transfected using TurboFect (Fermentas, St. Leon-Roth, Germany). Cells were harvested 40 h after transfection and transferred into poly-L-lysine-coated wells of a six well culture dish and incubated for 3 h. After removal of the medium, cells were incubated in 1 ml preincubation buffer (100 mM N-methyl-D-glucamine-chloride, 5 mM KCl, 2 mM $CaCl_2$, 0.8 mM $MgSO_4$, 5 mM glucose, 5 mM HEPES, pH 7.4, 0.1 mM ouabain) for 15 min at room temperature. A 10 min uptake period in preincubation buffer supplemented with 1 μCi/ml $^{86}Rb^+$ at room temperature followed. At the end of the uptake period, cells were washed three times in 1 ml ice-cold preincubation buffer without ouabain to remove extracellular tracer. Cells were lysed in 500 μl 0.25 M NaOH for 1 h and then neutralized with 250 μl pure acetic acid. $^{86}Rb^+$ uptake was assayed by Cerenkov radiation, and the protein amount was determined by BCA (Thermo Fisher Scientific, Bonn, Germany).

In some experiments, non-radioactive flux measurements based on thallium (Tl^+)-mediated Fluozin-2 fluorescence were performed [18,23]. 24 h after transfection, HEK-293 cells were plated in poly-L-lysine-coated wells of a 96-well culture dish, black-walled with clear bottom (Greiner Bio-One) at a concentration of 100,000 cells/well. The next day, the medium was replaced by 80 μl of preincubation buffer (100 mM *N*-methyl-D-glucamine chloride, 5 mM KCl, 2 mM $CaCl_2$, 0.8 mM $MgSO_4$, 5 mM glucose, 5 mM HEPES, pH 7.4) containing 2 μM Flouzin-2 dye (Invitrogen) plus 0.2% (w/v) Pluronic F-127 (Invitrogen). Cells were incubated at room temperature for 48 min. Afterwards, the cells were washed three times with 80 μl of preincubation buffer and incubated for 15 min with 80 μl of preincubation buffer plus 0.1 mM ouabain. The cell plate was inserted into a fluorometer (Fluoroskan Accent, Thermo Scientific, Bremen, Germany), and the wells were injected with 40 μl of thallium stimulation buffer (12 mM Tl_2SO_4, 100 mM NMDG, 5 mM Hepes, 2 mM $CaSO_4$, 0.8 mM $MgSO_4$, 5 mM glucose, pH 7.4). The fluorescence was measured in a kinetic-dependent manner (excitation, 485 nm; emission, 538 nm; 1 frame in 5 s in a 200-s time span). The activity was calculated with the initial values of the slope of Tl^+-stimulated fluorescence increase by using linear regression.

In addition, expression of the respective construct was determined for each flux measurement by immunoblot analysis or immunocytochemistry. At least three biological and three technical replicas were performed for each experiment. Data are given as mean ± standard deviation. Significant differences between the groups were analyzed by a Student's *t*-test.

2.3. Immunocytochemistry

For immunocytochemistry, transfected cells were seeded on 0.1 mg/ml poly-L-lysine-coated coverslips. After 36 h, cells were fixed with 4% paraformaldehyde in 0.2 M phosphate buffer for 10 min. After fixation, cells were washed three times with phosphate-buffered saline (PBS) and incubated with blocking solution (0.3% Triton X-100, 3% bovine serum albumin, 11% goat serum in PBS) for 30 min at room temperature. Cells were then incubated with primary antibody N1/12 (NeuroMab, Davis, USA), diluted 1:500 in carrier solution (0.3% Triton X-100, 1% bovine serum albumin, 1% goat serum in PBS) for 1 h and washed three times with PBS for 5 min. After transfer in carrier solution, cells were treated

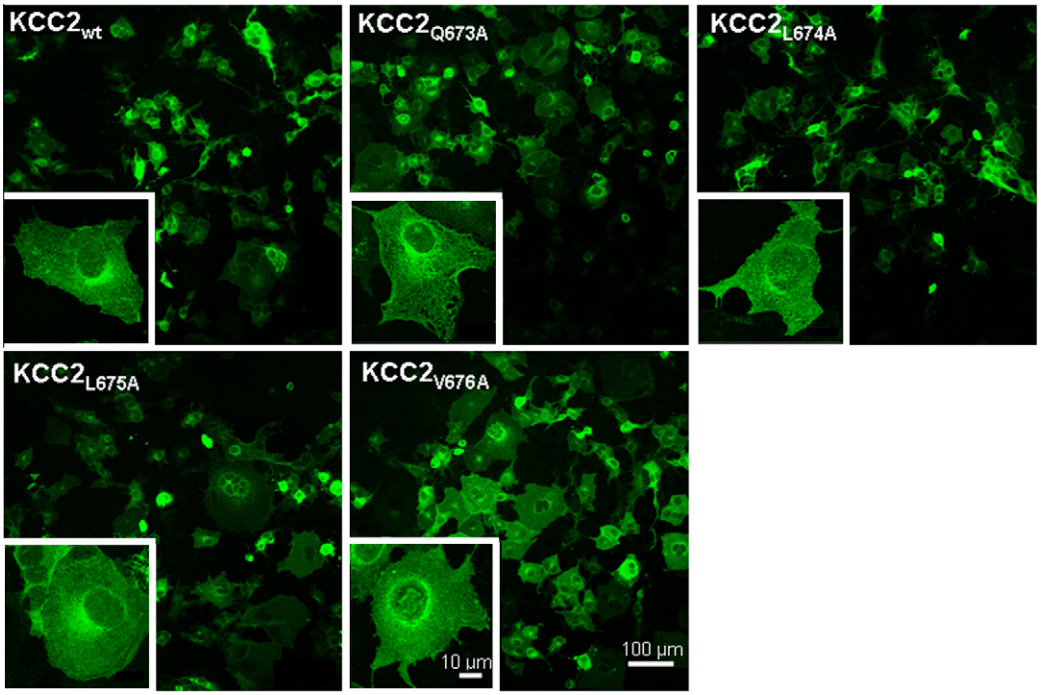

Fig. 2. Immuncytochemical labeling of KCC2 in COS-7 cells. COS-7 cells were transiently transfected with $KCC2_{wt}$ or KCC2 mutants ($KCC2_{Q673A}$, $KCC2_{L674A}$, $KCC2_{L675A}$ and $KCC2_{V676A}$). KCC2-ir revealed that all mutants were located at the plasma membrane and the perinuclear regions in a pattern indistinguishable from $KCC2_{wt}$. Photomicrographs were taken by confocal laser scanning microscopy with a 63x or a 20x objective (Leica TCS SP2).

with the secondary antibody (goat anti-rabbit conjugated to Alexa Fluor 488, diluted 1:1000, Invitrogen, Darmstadt, Germany). After washing, cells were mounted onto glass slides with Vectarshield Hard Set (Vector Laboratories, Burlingame, CA). Photomicrographs were taken by confocal laser scanning microscopy with a 63× and 20× objectives (Leica TCS SP2).

2.4. Cell-surface protein labeling

To detect cell surface expression of $KCC2_{wt}$ and $KCC2_{L675A}$, transfected cells were seeded on 0.1 mg/ml poly-L-lysine-coated coverslips. After 40 h, cells were incubated on ice and washed twice with ice-cold PBS. After incubation with 10 µg/ml Alexa 633-labeled wheat-germ agglutinin (WGA, Invitrogen) for 30 min on ice, cells were washed with ice-cold PBS. After fixation with 4% paraformaldehyde in 0.2 M phosphate buffer for 10 min, cells were incubated with primary and secondary antibody as described before. Colocalization between WGA-ir and KCC2-ir were analyzed with the software ImageJ and the plug-in OBCOL. At least 20 cells were analyzed for each construct. Data are given as mean ± standard deviation. Significant differences between the groups were analyzed by a Student's *t*-test.

3. Results

3.1. Evolutionary conservation of the $_{673}QLLV_{676}$ residues in the β1 strand of the C-terminus

The six amino acids of the β1 strand of KCC2 displayed the highest conservation in multiple sequence alignments of the C-terminus from mammalian CCCs, distantly related KCCs and *ma*CCC (Suppl. Fig. 1). The only exception was CCC9 where none of the amino acids was conserved (Fig. 1). The protein identity of the β1 strand was 4-fold increased (66.7%) between *rn*KCC2 and *ma*CCC compared to the entire C-terminus (16.5%). Within the β1 strand,

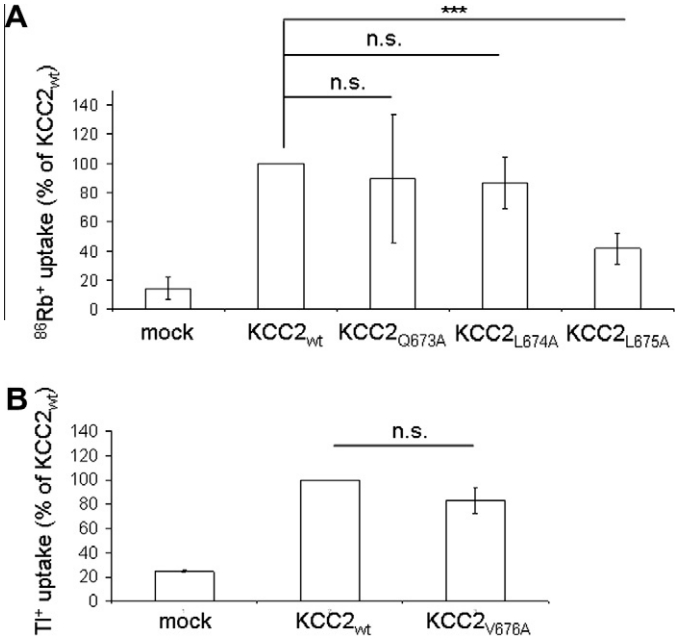

Fig. 3. Mutations in $_{673}QLLV_{676}$ differentially affect transport activity of KCC2. HEK-293 cells were transiently transfected 40 h prior flux measurements. An empty vector was used for mock transfection. Flux measurements were performed by $^{86}Rb^+$ uptake (A) and Tl^+ uptake (B). $KCC2_{Q673A}$, $KCC2_{L674A}$ and $KCC2_{V676A}$ exhibited normal transport activity. In contrast $KCC2_{L675A}$ displayed a 2.4-fold significant decrease of the transport activity (41.4 ± 10.6%, $p = 7.9 \times 10^{-7}$) compared to $KCC2_{wt}$. Values represent mean ± s.d. of at least 3 independent measurements. ns, none significant ($p > 0.05$); $^{***}p < 0.001$.

the first four residues (*rn*KCC2: $_{673}QLLV_{676}$) are the most highly conserved amino acids and three of them exist also in *ma*CCC. Evolutionary conservation was highest for $KCC2_{L675}$ (88.2%) followed by Q_{673} (82.4%), V_{676} (76.5%), and L_{674} (53%). The high conservation

of these residues across orthologs and paralogs in the structural β1 strand region of the C-terminus indicated a severe constraint on the sequence at this position.

3.2. Mutations of individual $_{673}$QLLV$_{676}$ residues differentially affect transport activity

To analyze the role of $_{673}$QLLV$_{676}$ residues for the transport activity of *rn*KCC2, we mutated them individually to alanine. This resulted in the four mutants KCC2$_{Q673A}$, KCC2$_{L674A}$, KCC2$_{L675A}$ and KCC2$_{V676A}$. To examine the functional consequences of the mutations, the constructs were transiently expressed in COS-7 cells and the expression was analyzed by immuncytochemistry. KCC2 immunoreactivity (KCC2-ir) of all mutants was detected at the plasma membrane and the perinuclear region (Fig. 2). The labeling pattern of the mutants was indistinguishable from KCC2 wild-type (KCC2$_{wt}$). These data indicate that single $_{673}$QLLV$_{676}$ mutations of KCC2 did not affect protein expression and localization.

Next, we determined the transport activity of KCC2 by $^{86}Rb^+$ or Tl^+ flux measurements in HEK-293 cells. To eliminate any uptake through endogenous NKCC1, the experiments were performed in Na^+-free solution with *N*-methyl-D-glucamine being the replacement cation (Gagnon 2006, Hartmann 2010). HEK-293 cells transiently transfected with KCC2$_{wt}$ exhibited a significant higher $^{86}Rb^+$ and Tl^+ uptake (100%) compared to mock-transfected control cells (14.3 ± 7.8% and 24.7 ± 0.85%) (Fig. 3). The mutant KCC2$_{L675A}$ displayed a 2.4-fold significant decrease of the transport activity (41.4 ± 10.6% residual activity, $p = 7.9 \times 10^{-7}$) compared to KCC2$_{wt}$ (Fig. 3A). The transport activities of KCC2$_{Q673A}$ (89.6 ± 44.23%, $p = 0.7$), KCC2$_{L674A}$ (86.4 ± 17.7%, $p = 0.17$) and KCC2$_{V676A}$ (83.4 ± 10.7%, $p = 0.13$) were not significantly different from KCC2$_{wt}$ (Fig. 3). Taken together, these results identify L$_{675}$ as a critical residue for KCC2 transport activity.

3.3. Cell surface expression of KCC2$_{L675A}$ is not altered

Of the four mutations, only KCC2$_{L675A}$ impaired transport activity. Our immunocytochemical analyses in COS-7 cells had indicated normal subcellular distribution (Fig. 2). To rule out that KCC2$_{L675A}$ behaved differentially between HEK-293 cells (flux measurements) and COS-7 cells (expression analysis), we performed immunocytochemical analysis in HEK-293 cells as well. Again, no difference was observed between KCC2$_{wt}$ and KCC2$_{L675A}$ (data not shown). To investigate surface expression of the mutant in more detail, WGA-surface labeling was performed (Solé et al. 2009) (Fig. 4). Quantitative pixel-by-pixel analysis revealed similar colocalization of KCC2$_{wt}$ (100 ± 23.4%) or KCC2$_{L675A}$ (98.6 ± 23.1%) with WGA in the plasma membrane. These data suggest that mutation of L$_{675}$ alters the conformation of KCC2 without affecting surface expression.

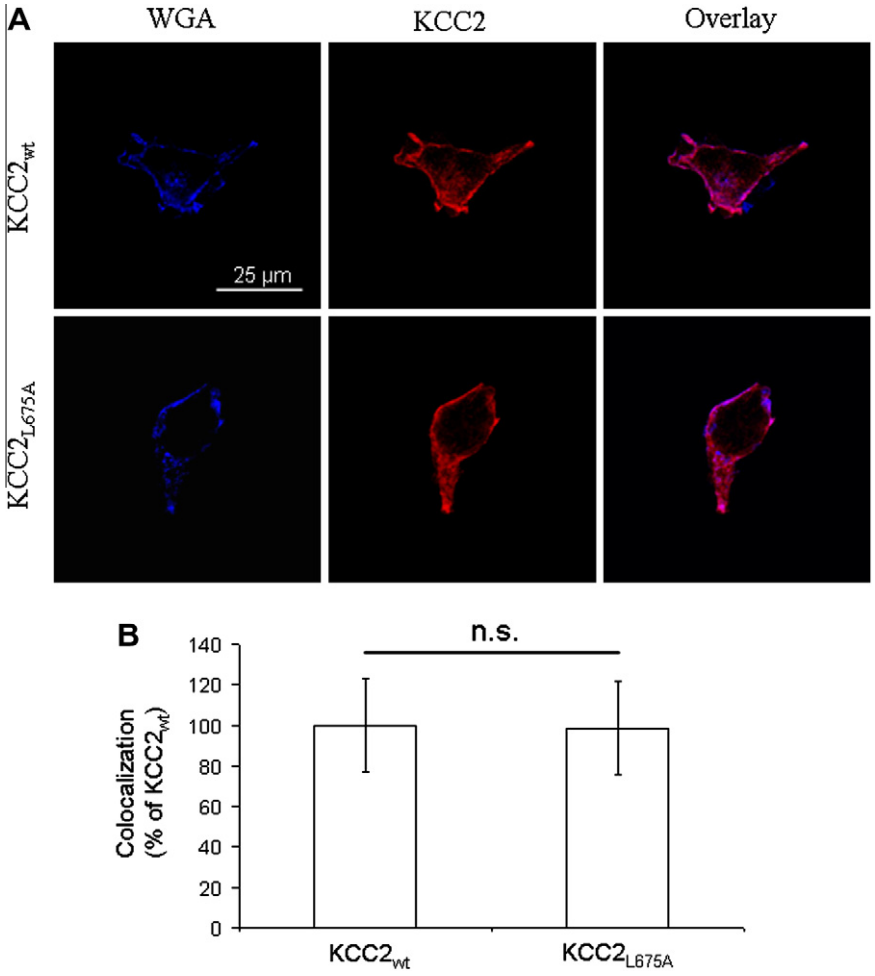

Fig. 4. Cell surface expression of KCC2$_{L675A}$ is not altered. HEK-293 cells were transiently transfected with KCC2$_{wt}$ and KCC2$_{L675A}$. Cell surface expression of KCC2 was analyzed through colocalization studies with WGA. Confocal images demonstrated a similar colocalization of KCC2$_{wt}$ and KCC2$_{L675A}$ with WGA (A). The relative cell surface expression of KCC2$_{wt}$ or KCC2$_{L675A}$ was analyzed by pixel-by-pixel intensities of confocal images using ImageJ software (B). Values represent mean ± s.d. of at least 20 cells. ns, none significant ($p > 0.05$).

4. Discussion

Here, we identified L_{675} within the C-terminal β1 strand as a critical amino acid residue for KCC2 transport activity. The β1 sequence is located between the TMDs and a presumed dimerization interface, consisting of the α helices 1 and 2 [13]. Both areas have been implicated in oligomerization of KCCs [11,13,24,25]. Thus, the high evolutionary sequence conservation of the β1 sequence was suggested to reflect the requirement of proper orientation of the α helices 1 and 2 with respect to the nearby TMDs. Mutation of L_{675} might therefore compromise dimerization, which is required for transport-activity [8,11]. Due to the formation of KCC2 aggregates in heterologous expression systems during biochemical purification [26,27], we were not able to investigate the oligomeric status of $KCC2_{L675A}$.

Other effects of the mutation might also be considered. The β1 sequence is at the surface of the molecule [13] and a binding site of the AP-2 complex is located in close proximity ($_{657}$LLXXEE$_{662}$) [28]. The β1 strand might therefore be involved in regulating endocytosis. We did, however, not observe any difference in the subcellular localization of $KCC2_{L675A}$ using immunocytochemistry and WGA surface labeling. These results argue against altered internalization. It is therefore most likely that mutation of L_{675} has an impact on the conformation of KCC2. This observation is in line with other point mutations that only impair transport activity without affecting surface expression of KCC2 [18,19].

Three out of four mutants displayed no change in transport activity, protein expression or localization. This was despite the fact that the mutations addressed extremely conserved amino acids. Several explanations might account for this observation. We substituted aliphatic (valine, leucine) or polar (glutamine) amino acid residues by the tiny amino acid alanine. This amino acid was chosen because of its absence in the analyzed positions in the *bona-fide* N(K)CC and KCC transporters. We cannot exclude that more severe amino acid replacements might have entailed functional consequences. Substitution of Y_{1087} by different amino acids, for instance, resulted in strikingly different phenotypes [19]. However, the phenotype of the L_{675} mutation to alanine indicates that our substitution strategy was well suited to identify sequence constraints. Previously, a different requirement of four evolutionary highly conserved cysteines in the LEL between the closely related KCC2 and KCC4 was reported [18]. Whereas loss of these cysteines abolished KCC2 transport activity, the same substitutions were well tolerated in KCC4. These data demonstrate a striking variability in sequence constraints even between closely related CCC members. It is therefore possible, that other CCC family members are more sensitive to mutations in these three amino acid residues in the β1 strand.

In summary, the identification of L_{675} as an important amino acid residue provides novel insights into the structural requirements of the C-terminus for KCC2 transport activity. In addition, our data indicate a surprisingly low sequence constraint in the β1 strand. Whether this is specific to KCC2, or holds true for other CCC family members as well will be an important topic for future studies to better understand the extreme evolutionary conservation of the β1 sequence. Finally, this study demonstrates the utility of structural information and evolutionary analysis to identify important amino acid residues in CCC members.

Acknowledgments

We thank Martina Reents for excellent technical support and Sina Lenski for help in generation of some constructs. This work was supported by grants from the Deutsche Forschungsgemeinschaft (No428/4-1 to H.G.N.).

Appendix A. Supplementary data

Supplementary data associated with this article can be found, in the online version, at doi:10.1016/j.bbrc.2012.02.147.

References

[1] G. Gamba, Molecular physiology and pathophysiology of electro neutral cation-chloride cotransporter, Physiology Review 85 (2005) 423–493.
[2] N.D. Daigle, G.A. Carpentier, R. Frenette-Cotton, M.G. Simard, M.-H. Lefoll, M. Noel, L. Caron, J. Noel, P. Isenring, Molecular characterization of a human cation-Cl^- cotransporter (SLC12A8A, CCC9A) that promotes polyamine and amino acid transport, Journal of Cellular Physiology 220 (2009) 680–689.
[3] C. Rivera, J. Voipo, J.A. Payne, E. Ruusuvuori, H. Lahtinen, K. Lamsa, U. Pirvola, M. Saarma, And Kaila, K, The K^+/Cl^- co-transporter KCC2 renders GABA hyperpolarizing during neuronal maturation, Nature 397 (1999) 251–255.
[4] W. Jarolimek, A. Lewen, U. Misgeld, A furosemide-sensitive K^+–Cl^- cotransporter counteracts intracellular Cl^- accumulation and depletion in cultured rat midbrain neurons, The Journal of Neuroscience 19 (1999) 4695–4704.
[5] C.A. Hübner, V. Stein, I. Hermans-Borgmeyer, T. Meyer, K. Ballanyi, T.J. Jentsch, Disruption of KCC2 reveals an essential role of K–Cl cotransport already in early synaptic inhibition, Neuron 30 (2001) 515–524.
[6] V. Balakrishnan, M. Becker, S. Löhrke, H.G. Nothwang, E. Güresir, E. Friauf, Expression and function of chloride transporters during development of inhibitory neurotransmission in the auditory brainstem, The Journal of Neuroscience 23 (2003) 4134–4145.
[7] A. Reynolds, E. Brustein, M. Liao, A. Mercado, E. Babilonia, D.B. Mount, P. Drapeau, Neurogenic role of the depolarizing chloride gradient revealed by global overexpression of KCC2 from the onset of development, The Journal of Neuroscience 28 (2008) 1588–1597.
[8] P. Blaesse, I. Guillemin, J. Schindler, M. Schweizer, E. Delpire, L. Khiroug, E. Friauf, H.G. Nothwang, Oligomerization of KCC2 correlates with development of inhibitory neurotransmission, The Journal of Neuroscience 26 (2006) 10407–10419.
[9] N.-S. Woo, J. Lu, R. England, R. McClellan, S. Dufour, D.B. Mount, A.Y. Deutch, D. Lovinger, E. Delpire, Hyperexcitability and epilepsy associated with disruption of the mouse neuronal-specific K–Cl cotransporter gene, Hippocampus 12 (2002) 258–268.
[10] J. Tornberg, V. Voikar, H. Savilahti, H. Rauvala, M.S. Airaksinen, Behavioural phenotypes of hypomorphic KCC2-deficient mice, European Journal of Neuroscience 21 (2005) 1327–1337.
[11] S. Casula, B.E. Shmukler, S. Wihelm, A.K. Stuart-Tilley, W. Su, M.N. Chernova, C. Brugnara, S.L. Alper, A dominant negative mutant of the KCC1 K–Cl cotransporter, The Journal of Biological Chemistry 276 (2001) 41870–41878.
[12] J.C. De Jong, P.H.G.M. Willems, F.J.M. Mooren, L.P.W.J. Van den Heuve, N.V.A.M. Knoers, R.J.M. Bindels, The structural unit of the Thiazide-sensitive NaCl cotransporter is a homodimer, The Journal of Biological Chemistry 278 (2003) 24302–24307.
[13] S. Warmuth, I. Zimmermann, R. Dutzler, X-ray structure of the C-terminal domain of a prokaryotic cation-chloride cotransporter, Structure 17 (2009) 538–546.
[14] P. Isenring, B. Forbush, Mutagenic mapping of the Na–K–Cl cotransporter for domains involved in ion transport and bumetanide binding, Journal of General Physiology. 112 (1998) 549–558.
[15] P. Isenring, S.C. Jacoby, B. Forbush, The role of transmembrane domain 2 in cation transport by the Na–K–Cl cotransporter, Proceedings of the National Academy of Sciences USA 95 (1998) 7179–7184.
[16] P. Isenring, B. Forbush, Ion transport and ligand binding by the Na–K–Cl cotranporter, structure-function studies, Comparative Biochemistry and Physiology Part A 130 (2001) 487–497.
[17] M.J. Bergeron, K.B.E. Gagnon, L. Caron, P. Isenring, Identification of Key functional domains in the C terminus of the K^+–Cl^- cotransporters, The Journal of Biological Chemistry 281 (2006) 15959–15969.
[18] A.-M. Hartmann, M. Wenz, A. Mercado, C. Störger, D.B. Mount, E. Friauf, H.G. Nothwang, Differences in the large extracellular loop between the K^+–Cl^- cotransporters KCC2 and KCC4, The Journal of Biological Chemistry 285 (2010) 23994–24002.
[19] K. Strange, T.D. Singer, R. Morrison, E. Delpire, Dependence of KCC2 K–Cl cotransporter activity on a conserved carboxy terminus tyrosine residue, American Journal of Physiology Cell Physiology 279 (2000) 860–867.
[20] J. Rinehart, Y.D. Maksimova, J.E. Tanis, K.L. Stone, C.A. Hodson, J. Zhang, M. Risinger, W. Pan, D. Wu, C.M. Colangelo, B. Forbush, C.H. Joiner, E.E. Gulcicek, P.G. Gallagher, R.P. Lifton, Sites of regulated phosphorylation that control K–Cl cotransporter activity, Cell 138 (2009) 525–536.
[21] A. Mercado, V. Broumand, K. Zandi-Nejad, A.H. Enck, D.B. Mount, A C-terminal domain in KCC2 confers constitutive K^+–Cl^- cotransporter, The Journal of Biological Chemistry 281 (2006) 1016–1026.
[22] A.-M. Hartmann, H.G. Nothwang, Opposite temperature effect on transport activity of KCC2/KCC4 and N(K)CCs in HEK-293 cells, BMC Research Notes 4 (2011) 526.
[23] E. Delpire, E. Days, L.M. Lewis, D. Mi, K. Kim, C.W. Lindsley, C.D. Weaver, Small-molecule screen identifies inhibitors of the neuronal K–Cl cotransporter KCC2, Proceedings of the National Academy of Sciences USA 106 (2009) 5383–5388.

[24] C.F. Simard, M.J. Bergeron, R. Frenette-Cotton, G.A. Carpentier, M.-E. Pelchat, L. Caron, P. Isenring, Homooligomeric and heterooligomeric associations between K+–Cl^- cotransporte isoforms and between K^+–Cl^- and Na^+–K^+–Cl^- cotransporter, The Journal of Biological Chemistry 282 (2007) 18083–18093.
[25] S. Casula, A.S. Zolotarev, A.K. Stuart-Tilley, S. Wilhelm, B.E. Shmukler, C. Brugnara, A.L. Alper, Chemical cross linking studies with the mouse KCC1 K–Cl cotransporter, Blood Cells, Molecules, and Diseases 42 (2009) 233–240.
[26] P. Uvarov, A. Ludwig, M. Markkanen, S. Soni, C.A. Hübner, C. Rivera, M.S. Airaksinen, Coexpression and heteromerization of two neuronal K–Cl cotransporter isoforms in neonatal brain, Journal of Biological Chemistry 284 (2009) 13696–13704.
[27] A.-M. Hartmann, P. Blaesse, T. Kranz, M. Wenz, A.F. Schinder, K. Kaila, E. Friauf, H.G. Nothwang, Opposite effect of membrane raft perturbation on transport activity of KCC2 and NKCC1, Journal of Neurochemistry 111 (2009) 321–331.
[28] B. Zhao, A.Y.C. Wong, A.M. Murshid, D. Bowie, J.F. Presley, F.K. Bedford, Identification of a novel di-leucine motif mediating K^+/Cl^- cotransporter KCC2 constitutive endocytosis, Cellular Signalling 20 (2008) 1769–1779.
[29] J.D. Thompson, D.G. Higgins, T.J. Gibson, Clustal W: improving the sensitivity of progressive multiple sequence alignment through sequence weighting, position-specific gap penalties and weight matrix choice, Nucleic Acid Research 22 (1994) 4673–4680.

Biochemical and Biophysical Research Communications 420 (2012) 498–504

Contents lists available at SciVerse ScienceDirect

Biochemical and Biophysical Research Communications

journal homepage: www.elsevier.com/locate/ybbrc

The effects of designed angiopoietin-1 variant on lipid droplet diameter, vascular endothelial cell density and metabolic parameters in diabetic db/db mice

Yu Jin Jung [a], Hyun Ju Choi [a], Jung Eun Lee [a], Ae Sin Lee [a], Kyung Pyo Kang [a,c], Sik Lee [a,c], Sung Kwang Park [a,c], Tae Sun Park [a,c], Heung Yong Jin [a,c], Sang Young Lee [b,c], Duk Hoon Kim [d], Won Kim [a,c,*]

[a] Department of Internal Medicine, Chonbuk National University Medical School, Jeonju, Republic of Korea
[b] Department of Diagnostic Radiology, Chonbuk National University Medical School, Jeonju, Republic of Korea
[c] Research Institute of Clinical Medicine of Chonbuk National University, Chonbuk National University Hospital, Jeonju, Republic of Korea
[d] Division of Forensic Medicine, National Forensic Service, Seoul, Republic of Korea

ARTICLE INFO

Article history:
Received 2 March 2012
Available online 10 March 2012

Keywords:
Angiopoietin-1
Fat droplet
Endothelial cells
Insulin resistance

ABSTRACT

Metabolic syndrome consists of metabolic abnormality with central obesity, hypertriglyceridemia, insulin resistance and hypertension. Adipose tissue has been known as a primary site of insulin resistance and its adipocyte size may be correlated with the degree of insulin resistance. A designed angiopoietin-1, COMP-Angiopoietin-1 (COMP-Ang1), mitigated high-fat diet-induced insulin resistance in skeletal muscle. In this study, we examined effects of COMP-Ang1 on adipocyte droplet size, vascular endothelial cell density in adipose tissue and metabolic parameters in db/db mice by administering COMP-Ang1 or LacZ (as a control) adenovirus. Administration of COMP-Ang1 decreased fat droplet diameter in epididymal and abdominal visceral adipocyte and visceral fat content in db/db mice. The density of vascular endothelial cell in adipose tissue was increased in db/db mice after treatment with COMP-Ang1. Serum resistin and tumor necrosis factor-α level was lower after treatment with COMP-Ang1 in db/db mice. COMP-Ang1 caused a restoration of fasting glycemic control in db/db mice and decreased serum insulin level and insulin resistance measured by HOMA index. These findings indicate that COMP-Ang1 regulates adipocyte fat droplet diameter, vascular endothelial cell density and metabolic parameters in db/db mice.

1. Introduction

Metabolic syndrome consists of metabolic abnormality with central obesity, hypertriglyceridemia, hyperglycemia and hypertension. Insulin resistance is a critical component in the pathogenesis of hyperglycemia and conveys an important role in metabolic abnormalities, such as dyslipidemia and obesity [1]. Obesity is an important factor of the metabolic syndrome in contributing a risk factor for cardiovascular disease, diabetes, and cancer.

Adipose tissue has been known as a primary site of insulin resistance [2]. Adipocytokines, such as tumor necrosis factor (TNF)-α and resistin, are associated with the underlying insulin resistance [3]. The function of adipocytes may differ depending on the size of adipocytes. Adipocyte size may determine activity of lipases such as adipose triglyceride lipase and hormone-sensitive lipase [4]. Larger adipocyte may release more pro-inflammatory adipokines than smaller adipocytes [5]. O'Connell et al. [6] have demonstrated that the mean omental adipocyte size in a metabolically healthy obese individual is significantly lower compared with metabolically unhealthy patients and that omental adipocyte size is correlated with the degree of insulin resistance. It has also been demonstrated that increased lipid content in the liver may be linked with increased visceral adiposity with increased adipocyte diameter [7]. Thus, adipocyte size can be a key target for metabolic syndrome.

Adipose tissue expansion is associated with compensatory increased vasculature. Relative decreased blood supply may lead to hypoxia and inflammation in person with obesity [8,9]. Chronic inflammation in adipose tissue may aggravate insulin resistance [10,11]. It has been suggested that increased adipose angiogenesis reduced adipose tissue hypoxia and fibrosis [12]. Therefore, increase of vascular endothelial cells in adipose tissue may mitigate the insulin resistance in obesity or diabetes.

Angiopoietin-1 is a growth factor and contributes to angiogenesis upon binding to Tie2 receptor [13,14]. Beside the angiogenic effect, angiopoietin-1 is involved in hematopoietic stem cell differentiation [15], cancer metastasis [16,17], antiapoptosis [18,19] and anti-inflammation [20]. COMP-Angiopoietin-1 (COMP-Ang1) is a designed variant of native angiopoietin-1 [21,22]. It is a soluble, stable, and more potent angiopoietin-1 variant in Tie2 phosphorylation in endothelial cells. COMP-Ang1 has been reported to exert

* Corresponding author. Address: Department of Internal Medicine, Chonbuk National University Medical School, 20, Geonjiro, Deokjin-gu, Jeonju-si, Jeollabuk-do 560-180, Republic of Korea. Fax: +82 63 254 1609.
E-mail address: kwon@jbnu.ac.kr (W. Kim).

0006-291X/$ - see front matter © 2012 Elsevier Inc. All rights reserved.
http://dx.doi.org/10.1016/j.bbrc.2012.03.019

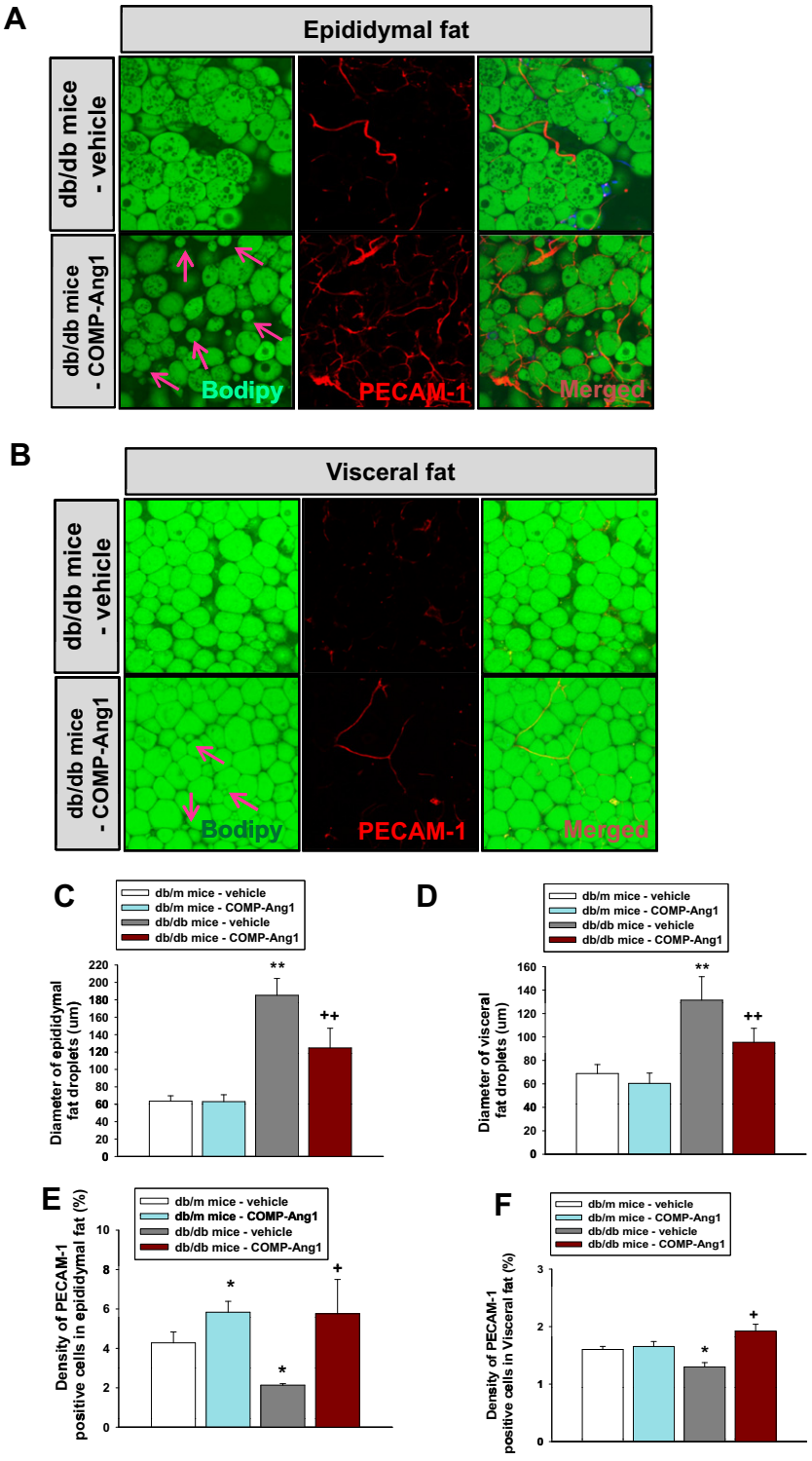

Fig. 1. Microscopic findings of abdominal epididymal and visceral adipocytes and PECAM-1-positive endothelial cells. (A) Microscopic findings of epididymal adipocytes. Arrows indicate decreased adipocyte fat droplets. (B) Microscopic findings of abdominal visceral adipocytes. Arrows indicate decreased adipocyte fat droplets. (C and D) Quantification of epididymal and abdominal visceral adipocytes fat droplets diameter. Visceral adipose tissue was harvested 7 d after COMP-Ang1 or vehicle treatment. Note that epididymal and visceral adipocyte fat droplet diameter was significantly decreased after treatment with COMP-Ang1 in db/db mice. (E) Quantification of PECAM-1-positive vascular endothelial cell area in epididymal adipose tissue. (F) Quantification of PECAM-1-positive vascular endothelial cell area in abdominal visceral adipose tissue. The values are the mean ± SD for five animals in each group. $^{*}P < 0.05$ vs. db/m mice treated with vehicle; $^{**}P < 0.01$ vs. db/m mice treated with vehicle; $^{+}P < 0.01$ vs. db/db mice treated with vehicle; $^{++}P < 0.01$ vs. db/db mice treated with vehicle.

an anti-inflammatory effect in vascular endothelial cell [20,23]. Recently, it has been reported that COMP-Ang1 increases skeletal muscle blood flow and may prevent high-fat diet-induced insulin resistance in skeletal muscle [24]. We have also shown that COMP-Ang1 has a renoprotective effect in diabetic nephropathy model [25]. However, effects of angiopoietin-1 on adipocyte size, vascular endothelial cell density in adipose tissue and metabolic parameters remain to be clarified.

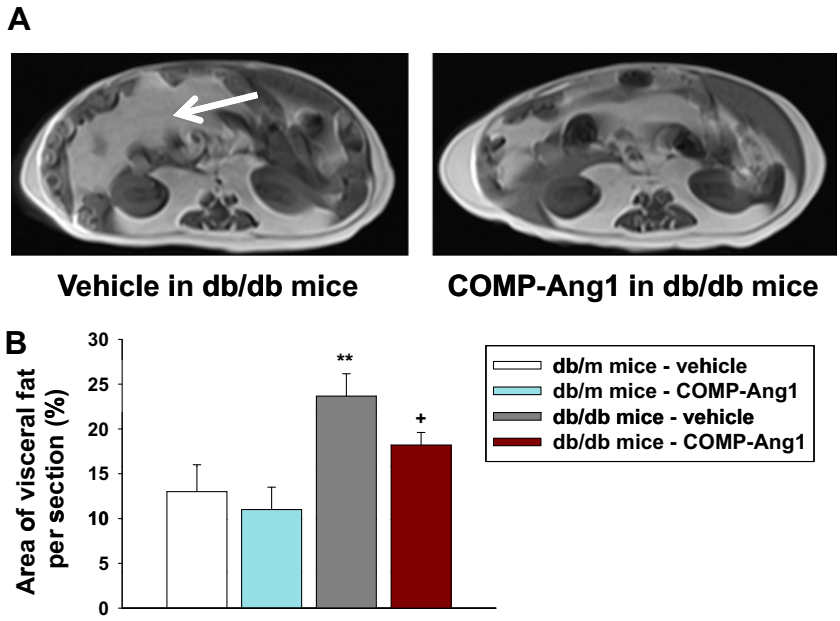

Fig. 2. MRI findings and quantification of abdominal visceral fat. Abdominal fat was measured 11 d after COMP-Ang1 or vehicle treatment by MRI. (A) The transverse T1-weighted MR images. Bright areas (arrow) represent abdominal visceral fat. (B) Quantification of abdominal visceral fat. This study used transverse magnetic resonance imaging to measure relative cross-sectional area of abdominal visceral fat at mid kidney level. Note that the area of visceral abdominal fat decreased in db/db mice treated with COMP-Ang1 compared to vehicle-treated db/db mice. The values are the mean ± SD for three animals in each group. $^{**}P < 0.01$ versus db/m treated with vehicle; $^{+}P < 0.05$ versus db/db treated with vehicle.

In this study, we explored effects of COMP-Ang1 on metabolic abnormalities and proinflammatory markers using db/db mice, evaluating the adipocyte lipid droplet diameter, the density of vascular endothelial cell in adipose tissue, serum levels of resistin and tumor mecrosis factor-α (TNF-α) and insulin and glucose lowering effects.

2. Materials and methods

2.1. Animals and experimental protocol

Male obese type 2 diabetic C57BL/KsJ db/db mice (db/db mice; Japan SLC, Inc., Shizuoka, Japan) and age matched non-diabetic C57BL/KsJ db/m control mice (db/m mice; Japan SLC, Inc., Shizuoka, Japan) were fed standard laboratory chow (Orient Bio Inc, Seoul, Republic of Korea) and given tap water ad libitum. Animals were housed in a temperature-controlled (20 ± 2 °C) and humidity-controlled (60%) room. All animal studies were reviewed and approved by the Institutional Animal Care and Use Committee of Chonbuk National University. The recombinant adenoviruses expressing COMP-Ang1 or LacZ as a vehicle were constructed using previously published methods [23]. In our previous experiments, circulating serum levels of COMP-Ang1 increased 3 d after treatment, peaked at 5 d, and declined thereafter [23]. Based on this study, we injected COMP-Ang1 or vehicle virus by intravenously through the tail vein every 2 weeks.db/db mice, which had already hyperglycemia (450–500 mg/dL in fasting glucose), were divided into four groups and injected (1) vehicle in db/m mice (2) COMP-Ang1 in db/m mice (3) vehicle in db/db mice (4) COMP-Ang1 in db/db mice. During treatment, we evaluated body weight, food and water intake, fasting glucose and insulin levels at 5 and 7 d after COMP-Ang1 injection. Fasting blood glucose was measured with an Accu-Check® Active (Roche Diagnostics GmbH, Mannheim, Germany) and was expressed as milligrams per deciliter [26]. After 1 week of the COMP-Ang1 or vehicle treatment, mice were anesthetized with ketamine (100 mg/kg) and xylazine (10 mg/kg), the blood and epididymal and abdominal visceral adipose tissue were sampled and serum samples were stored at −80 °C until use.

2.2. Immunofluoroscent staining

Mice were anesthetized by intramuscular injection of a combination of anesthetics (ketamine and xylazine). Epididymal and intra-abdominal visceral adipose tissues were fixed by vascular perfusion of 1% paraformaldehyde in phosphate buffered saline, removed, and whole-mounted. After blocking with 5% goat serum in PBST (0.3% Triton X-100 in PBS) for 1 h, the whole-mounted epididymal and intra-abdominal visceral adipose tissue were incubated overnight at 4 °C with hamster anti-PECAM-1 antibody (Chemicon International, Temecula, CA) for vascular endothelial cells and 4,6-diamidino-2-phenylindole (DAPI, Research Diagnostics) for nuclei. After washing in PBST, whole-mounted epididymal and intra-abdominal visceral adipose tissues were incubated for 1 h at room temperature with secondary antibody with Cy3- conjugated anti-hamster IgG antibody (Jackson ImmunoResearch Laboratories, Inc., West Grove, PA). For control experiments, the primary antibody was omitted or substituted with preimmune serum. Slides were viewed with a microscope equipped with a digital camera (Carl Zeiss, Goettingen, Germany).

2.3. BODIPY staining and visualization

Adipocytes are visualized by staining lipid droplets with the fluorescent dye, BODIPY® 493/503 (Invitrogen, Carlsbad, CA). A fresh solution of BODIPY 493/503 diluted in PBST was used for staining. For fixative staining, adipose tissues were incubated in 4% paraformaldehyde solution for 15 min. After paraformaldehyde solution was removed, adipose tissues were incubated in a volume of 500 μL of 1 μg/mL BODIPY 493/503 for 1 h at room temperature. Digital images were obtained with a LSM 510 META confocal laser scanning microscope (Carl Zeiss).

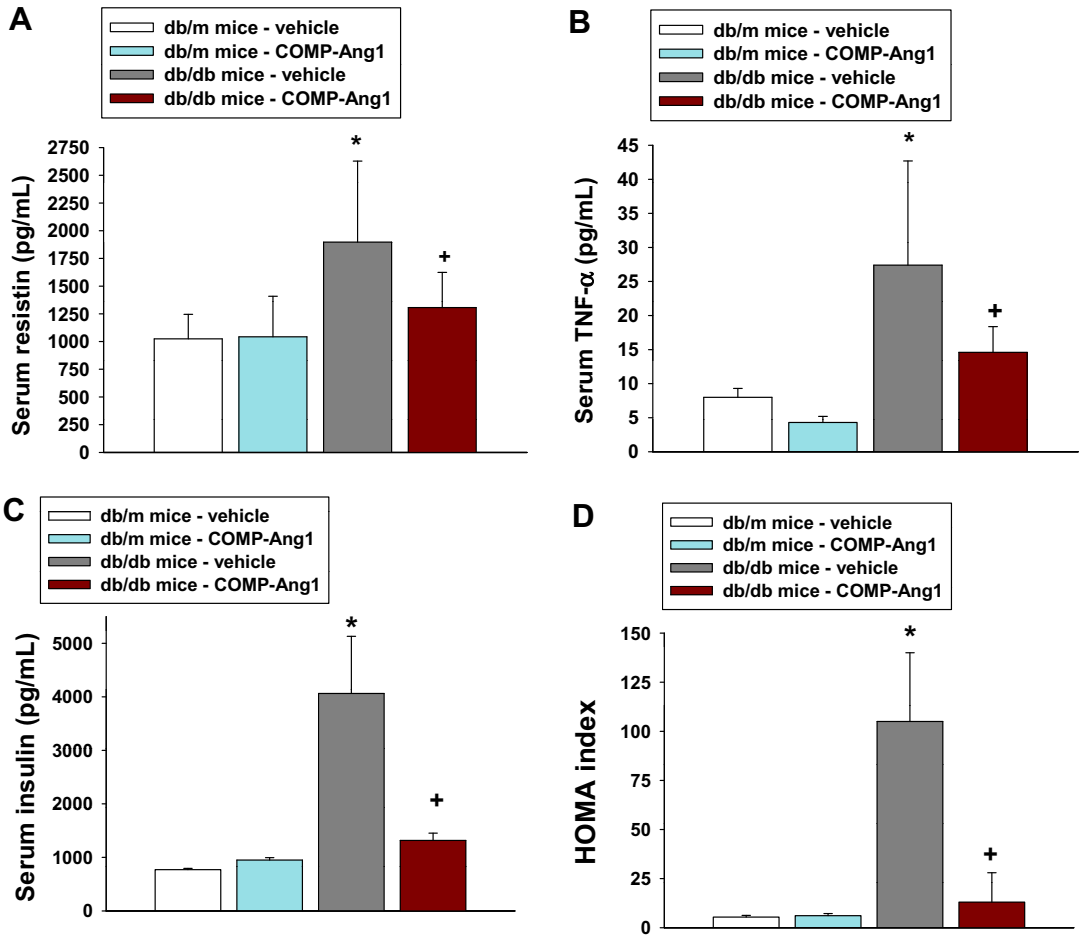

Fig. 3. Serum levels of resistin, TNF-α, insulin and insulin resistance calculation after COMP-Ang1 treatment. Serum resistin (A), TNF-α (B) and insulin (C) were determined 7 d after COMP-Ang1 or vehicle treatment. The values are the mean ± SD for four animals in each group. (D) HOMA index. HOMA index was calculated by multiplying fasting insulin (μmol/L) and fasting glucose (mmol/L), divided by 22.5. Data are means ± SD of seven mice (db/db mice treated with vehicle and db/db mice treated with COMP-Ang1) and five mice (db/m mice treated with vehicle and db/m mice treated with COMP-Ang1). $^{*}P < 0.05$ vs. db/m mice treated with vehicle; $^{+}P < 0.05$ vs. db/db mice treated with vehicle.

2.4. Determination of adipocyte fat droplet diameter

Diameter of fat droplets in epididymal and visceral adipocytes was measured according to the previous direct microscopic methods with some modifications [27,28]. Briefly, each adipose tissue was whole mount stained with bodipy, then 10 digital miages of every other nonoverlapping x 400 microscopic field were captured with a Zeiss LSM 510 confocal microscope (Carl Zeiss). The diameter of cells in each image was measured with software program (Strat LSM Image Browser, Carl Zeiss). With this method, we measured 300 cells in epididymal and visceral adipose tissue in each group.

2.5. Magnetic resonance imaging (MRI)

For MRI acquisition, anesthesia was induced by an intramuscular injection of ketamine (100 mg/kg) and xylazine (10 mg/kg). Mice were placed in a supine position and applied with a small flexible coil supplied by 1.5T MR machine (Symphony; Siemens Medical System, Erlangen, Germany). Transverse T1-wighted MR images (repetition time, 480 ms; echo time, 12 ms; field of view, 8 cm; matrix 192 × 256) were used to study the distribution of fat stores in db/db and db/m mice. Two transverse T1-weighted MR images were obtained at the level of mid-kidney. The area of visceral fat of the mice was calculated on T1-wighted MR image by using a digital image analysis program (AnalySIS, Soft Imaging System, Münster, Germany).

2.6. Resistin, TNF-α, insulin measurements and HOMA index calculation

Resistin and TNF-α were determined in mouse serum using an ELISA assay (Pierce Biotechnology, Rockford, IL). Insulin was measured using an ELISA kit (Shibayagi Co., Ltd, Gunma, Japan). Insulin resistance was determined by the homeostasis model assessment (HOMA) method by using the following equation: HOMA index = [fasting insulin (μU/mL) × fasting glucose (mmol/L)]/22.5 [29].

2.7. Statistical analysis

Data were presented as mean ± SD. Multiple comparisons were examined for using Student's unpaired *t* test. A statistical value of $p < 0.05$ was considered significant.

3. Results

3.1. COMP-Ang1 decreases fat droplet diameter and increase density of PECAM-1-positive cells

The epididymal and visceral adipocyte fat droplets diameter in db/db mice treated with vehicle were significantly increased 2.9-fold and 1.9-fold respectively, compared to that of control db/m

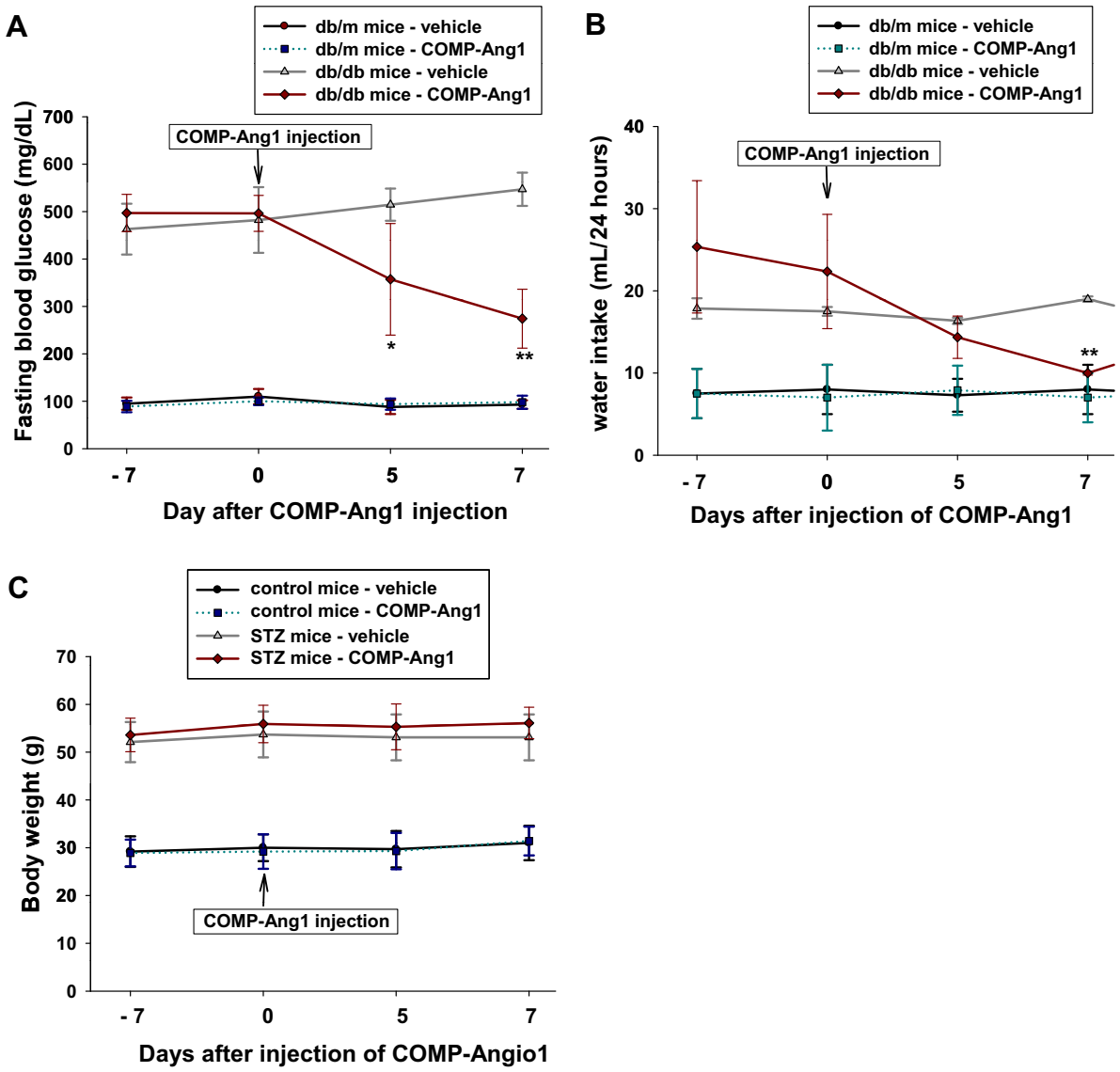

Fig. 4. Changes of fasting blood glucose, body weight and water intake. Fasting blood glucose (A), water intake (B) and body weight (C) were measured at 5 and 7 d after COMP-Ang1 injection in db/dm and db/db mice. The values are the mean ± SD (n = 7 in each group). $^{*}P < 0.05$ vs. db/m mice treated with vehicle in the same day, $^{**}P < 0.01$ db/m mice treated with vehicle in the same day.

mice (Fig. 1). Treatment with COMP-Ang1 significantly decreased the diameter of fat droplets in epididymal and visceral adipocyte of db/db mice by 32.6% and 27.4%, respectively (Fig. 1A–D). The density of PECAM-1-positive endothelial cell in epididymal and visceral adipose tissue was evaluated by immunofluorescent staining. Immunofluoroscent data showed that the density of PECAM-1-positive area in epididymal adipose tissue of vehicle-treated db/db mice was significantly decreased compared to that of control db/m mice (Fig. 1E). COMP-Ang1 treatment significantly increased the density of PECAM-1-positive area in epididymal and abdominal visceral adipose tissue of db/db mice (Fig. 1E and F). Treatment with COMP-Ang1 has no significant effect on the diameter of epididymal and visceral adipocyte fat droplets in db/m mice (Fig. 1C and D). The density of PECAM-1-positive area in visceral adipocyte was not significantly changed in db/m mice after treatment with COMP-Ang1 (Fig. 1F). However, the density of PECAM-1-positive area in epididymal adipocyte was increased in db/m mice after treatment with COMP-Ang1 (Fig. 1E).

3.2. COMP-Ang1 reduces abdominal visceral fat content

MRI in Fig. 2 is representative cross-sectional images. The area of bright signal intensity in the abdomen is the intra-abdominal fat, where as the outer band of bright signal intensity is the subcutaneous fat. The area of visceral abdominal fat in the COMP-Ang1-treated db/db mice was significantly decreased compared to vehicle-treated db/db mice at 11 d after administration of COMP-Ang1.

3.3. COMP-Ang1 suppresses serum resistin and TNF-α level

There was a significant increase in serum resistin levels in vehicle-treated db/db mice compared with control db/m mice (Fig. 3A). Administration of COMP-Ang1 resulted in a significant decrease in the level of serum resistin in db/db mice compared the level in vehicle-treated db/db mice. The level of serum TNF-α was significantly higher in db/db mice than the level in control db/m mice. Administration of COMP-Ang1 significantly blocked the increase in serum TNF-α in db/db mice (Fig. 3B). Treatment of db/m mice

with COMP-Ang1 has no significant effect on serum resistin and TNF-α level (Fig. 3A and B).

3.4. COMP-Ang1 ameliorates plasma insulin level and HOMA index

Effects of COMP-Ang1 on the plasma insulin levels in db/db mice were compared with those of the vehicle-treated db/db mice. The mean serum insulin level in vehicle-treated db/db mice was significantly increased compared to control db/m mice (Fig. 3C). However, the serum insulin level was markedly decreased in the COMP-Ang1-treated db/db mice (Fig. 3C). To evaluate insulin resistance, HOMA index was calculated using fasting glucose and insulin values. Vehicle-treated db/db mice showed a higher HOMA index than that of control db/m mice. COMP-Ang1 administration ameliorated the HOMA index in db/db mice (Fig. 3D). There was no significant change in the serum insulin level or HOMA index of db/m mice after treatment with COMP-Ang1. These data suggested that COMP-Ang1 improves insulin resistance in db/db mice.

3.5. Effect of COMP-Ang1 on plasma fasting blood glucose, water intake and body weight

Blood glucose level was significantly higher in the vehicle-treated db/db mice than in db/m mice (Fig. 4A). The blood glucose level in db/db mice was significantly reduced by treatment with COMP-Ang1 at d 5 and 7 (Fig. 4A). The water intake was significantly reduced after treatment with COMP-Ang1 compared with vehicle-treated db/db mice (Fig. 4B). Treatment with COMP-Ang1 did not result in a significant weight change for the db/db mice compared with the vehicle-treated db/db mice (Fig. 4C). Fasting plasma glucose, water intake and body weights for db/m control mice were little altered by COMP-Ang1 treatment (Fig. 4).

4. Discussion

This study has focused on the changes of adipocyte fat droplet diameter, angiogenesis in adipose tissue and metabolic parameters in db/db mice after injection of COMP-Ang1. Our data demonstrated that COMP-Ang1 decreased fat droplet diameter and visceral fat content in db/db mice. The density of PECAM-1-positive vascular endothelial cell in adipose tissue was increased after COMP-Ang1 treatment. COMP-Ang1 decreased serum resistin and TNF-α and improved insulin resistance measured by HOMA index. These results indicate that COMP-Ang1 may ameliorate metabolic parameters through regulation of fat droplet diameter and vascular endothelial cell density in type 2 diabetes.

Obesity is an important factor of the metabolic syndrome. Adipocytes are an important site in regulation of metabolic syndrome functioning as an endocrine organ with production of hormones or adipokines [30,31]. There is a growing body of evidence that adipocyte size is correlated with adipocyte function and insulin sensitivity in obesity or diabetes [32]. As the metabolic activity of mammalian adipocytes depends on their size, fat droplet size can be a one of important factors associated with insulin resistance in obesity or diabetes [32]. Therefore, we evaluated the changes of diameters of fat droplet in db/db mice. In line with previous data, our results demonstrated that COMP-Ang1 administration decreased epididymal and abdominal visceral adipocyte lipid droplet diameter and serum levels of resistin in db/db mice [5,32].

Insufficient angiogenesis in obesity may contribute to hypoxia and proinflammatory conditions in adipose tissue [33]. These hypoxia and inflammatory conditions may aggravate the signaling of insulin and insulin resistance [10,12]. Thus, appropriately increased vascular density in adipose tissue expansion is important in regulation of glucose. It was reported that capillary density in obese subjects was significantly lower than that of lean subjects [11]. Our immunofluoroscence data demonstrated that the density of PECAM-1-positive vascular endothelial cell in adipose tissue of db/db diabetic mice was lower than db/m mice (Fig. 1). This data suggests that decreased vascular endothelial cell density may be a contributing factor in insulin resistance in type 2 diabetes. Our data also demonstrated that COMP-Ang1 increased the PECAM-1-positive vascular endothelial cell density which was decreased in diabetic mice. These results indicate that COMP-Ang1-induced increase of vascular endothelial cell density may be a way to reverse the insulin resistance in diabetes or obesity.

One of the limitations of our study in the increasing effect of COMP-Ang1 on adipocyte fat droplet diameter is that there is no direct mechanism of COMP-Ang1 on adipocyte. Dallabrida et al. [34] have demonstrated that there is no protein expression of Tie2, a receptor of angiopoietin-1, in freshly isolated adipocyte from epididymal adipose tissue or pre-adipocytes (3T3-L1). Therefore, COMP-Ang1 does not directly act on adipocyte. Our immunofluoroscent data of PECAM-1 demonstrated that COMP-Ang1 increased angiogenesis in both epididymal and visceral adipose tissue (Fig. 1). In mechanism of COMP-Ang1 in adipocyte diameter, we suggest secondary effects with angiogenesis in adipose tissue of db/db mice.

We found that db/db mice showed a significant increase in insulin resistance (HOMA-IR) index and COMP-Ang1 significantly decreased HOMA-IR index of db/db mice (Fig. 3). It was already demonstrated that COMP-Ang1 increased muscle blood flow and decreased insulin resistance in obesity-induced diabetes models. All of these results suggest that administration of COMP-Ang1 decreased insulin resistance in both mice model. In this study, we also suggest that COMP-Ang1-induced decreased diameter of adipocyte fat droplet in epididymal and abdominal visceral adipose tissue can be an important factor in improvement of insulin resistance.

In summary, COMP-Ang1 may be a new therapeutic candidate for decreasing insulin resistance, diameter in adipocyte, visceral fat content, serum resistin and TNF-α level, insulin resistance and fasting high glucose and induce adipose tissue angiogenesis in db/db mice.

Acknowledgments

This study was supported by a grant of the Korea Healthcare technology R&D Project, Ministry for Health, Welfare & Family Affairs, Republic of Korea (A090268).

References

[1] B.J. Goldstein, Insulin resistance as the core defect in type 2 diabetes mellitus, Am. J. Cardiol. 90 (2002) 3G–10G.

[2] G.S. Hotamisligil, Molecular mechanisms of insulin resistance and the role of the adipocyte, Int. J. Obes. Relat. Metab. Disord. 24 (Suppl. 4) (2000) S23–S27.

[3] P. Arner, The adipocyte in insulin resistance: key molecules and the impact of the thiazolidinediones, Trends Endocrinol. Metab. 14 (2003) 137–145.

[4] H. Miyoshi, J.W. Perfield 2nd, M.S. Obin, A.S. Greenberg, Adipose triglyceride lipase regulates basal lipolysis and lipid droplet size in adipocytes, J. Cell. Biochem. 105 (2008) 1430–1436.

[5] T. Skurk, C. Alberti-Huber, C. Herder, H. Hauner, Relationship between adipocyte size and adipokine expression and secretion, J. Clin. Endocrinol. Metab. 92 (2007) 1023–1033.

[6] J. O'Connell, L. Lynch, T.J. Cawood, A. Kwasnik, N. Nolan, J. Geoghegan, A. McCormick, C. O'Farrelly, D. O'Shea, The relationship of omental and subcutaneous adipocyte size to metabolic disease in severe obesity, PLoS One 5 (2010) e9997.

[7] J. Koska, N. Stefan, P.A. Permana, C. Weyer, M. Sonoda, C. Bogardus, S.R. Smith, D.R. Joanisse, T. Funahashi, J. Krakoff, J.C. Bunt, Increased fat accumulation in liver may link insulin resistance with subcutaneous abdominal adipocyte enlargement, visceral adiposity, and hypoadiponectinemia in obese individuals, Am. J. Clin. Nutr. 87 (2008) 295–302.

[8] J. Yin, Z. Gao, Q. He, D. Zhou, Z. Guo, J. Ye, Role of hypoxia in obesity-induced disorders of glucose and lipid metabolism in adipose tissue, Am. J. Physiol. Endocrinol. Metab. 296 (2009) E333–E342.
[9] J. Ye, Emerging role of adipose tissue hypoxia in obesity and insulin resistance, Int. J. Obes. (Lond.) 33 (2009) 54–66.
[10] N. Hosogai, A. Fukuhara, K. Oshima, Y. Miyata, S. Tanaka, K. Segawa, S. Furukawa, Y. Tochino, R. Komuro, M. Matsuda, I. Shimomura, Adipose tissue hypoxia in obesity and its impact on adipocytokine dysregulation, Diabetes 56 (2007) 901–911.
[11] M. Pasarica, O.R. Sereda, L.M. Redman, D.C. Albarado, D.T. Hymel, L.E. Roan, J.C. Rood, D.H. Burk, S.R. Smith, Reduced adipose tissue oxygenation in human obesity: evidence for rarefaction, macrophage chemotaxis, and inflammation without an angiogenic response, Diabetes 58 (2009) 718–725.
[12] Z. Michailidou, S. Turban, E. Miller, X. Zou, J. Schrader, P.J. Ratcliffe, P.W. Hadoke, B.R. Walker, J.P. Iredale, N.M. Morton, J.R. Seckl, Increased angiogenesis protects against adipose hypoxia and fibrosis in metabolic disease-resistant 11beta-hydroxysteroid dehydrogenase type 1 (HSD1)-deficient mice, J. Biol. Chem. 287 (2012) 4188–4197.
[13] C. Suri, P.F. Jones, S. Patan, S. Bartunkova, P.C. Maisonpierre, S. Davis, T.N. Sato, G.D. Yancopoulos, Requisite role of angiopoietin-1, a ligand for the TIE2 receptor, during embryonic angiogenesis, Cell 87 (1996) 1171–1180.
[14] S. Davis, T.H. Aldrich, P.F. Jones, A. Acheson, D.L. Compton, V. Jain, T.E. Ryan, J. Bruno, C. Radziejewski, P.C. Maisonpierre, G.D. Yancopoulos, Isolation of angiopoietin-1, a ligand for the TIE2 receptor, by secretion-trap expression cloning, Cell 87 (1996) 1161–1169.
[15] F. Arai, A. Hirao, M. Ohmura, H. Sato, S. Matsuoka, K. Takubo, K. Ito, G.Y. Koh, T. Suda, Tie2/angiopoietin-1 signaling regulates hematopoietic stem cell quiescence in the bone marrow niche, Cell 118 (2004) 149–161.
[16] W.S. Moon, H.S. Park, K.H. Yu, K.Y. Jang, M.J. Kang, H. Park, A.S. Tarnawski, Expression of angiopoietin 1, 2 and their common receptor Tie2 in human gastric carcinoma: implication for angiogenesis, J. Korean Med. Sci. 21 (2006) 272–278.
[17] M. Saito, J. Watanabe, T. Fujisawa, Y. Kamata, Y. Nishimura, T. Arai, T. Miyamoto, A. Obokata, H. Kuramoto, Angiopoietin-1, 2 and Tie2 expressions in endometrial adenocarcinoma–The Ang2 dominant balance up-regulates tumor angiogenesis in the presence of VEGF, Eur. J. Gynaecol. Oncol. 27 (2006) 129–134.
[18] H.J. Kwak, S.J. Lee, Y.H. Lee, C.H. Ryu, K.N. Koh, H.Y. Choi, G.Y. Koh, Angiopoietin-1 inhibits irradiation- and mannitol-induced apoptosis in endothelial cells, Circulation 101 (2000) 2317–2324.
[19] H.J. Kwak, J.N. So, S.J. Lee, I. Kim, G.Y. Koh, Angiopoietin-1 is an apoptosis survival factor for endothelial cells, FEBS Lett. 448 (1999) 249–253.
[20] D.C. Simoes, T. Vassilakopoulos, D. Toumpanakis, K. Petrochilou, C. Roussos, A. Papapetropoulos, Angiopoietin-1 protects against airway inflammation and hyperreactivity in asthma, Am. J. Respir. Crit. Care Med. 177 (2008) 1314–1321.
[21] C.H. Cho, R.A. Kammerer, H.J. Lee, K. Yasunaga, K.T. Kim, H.H. Choi, W. Kim, S.H. Kim, S.K. Park, G.M. Lee, G.Y. Koh, Designed angiopoietin-1 variant, COMP-Ang1, protects against radiation-induced endothelial cell apoptosis, Proc. Natl. Acad. Sci. USA 101 (2004) 5553–5558.
[22] C.H. Cho, R.A. Kammerer, H.J. Lee, M.O. Steinmetz, Y.S. Ryu, S.H. Lee, K. Yasunaga, K.T. Kim, I. Kim, H.H. Choi, W. Kim, S.H. Kim, S.K. Park, G.M. Lee, G.Y. Koh, COMP-Ang1: a designed angiopoietin-1 variant with nonleaky angiogenic activity, Proc. Natl. Acad. Sci. USA 101 (2004) 5547–5552.
[23] W. Kim, S.O. Moon, S.Y. Lee, K.Y. Jang, C.H. Cho, G.Y. Koh, K.S. Choi, K.H. Yoon, M.J. Sung, D.H. Kim, S. Lee, K.P. Kang, S.K. Park, COMP-angiopoietin-1 ameliorates renal fibrosis in a unilateral ureteral obstruction model, J. Am. Soc. Nephrol. 17 (2006) 2474–2483.
[24] H.K. Sung, Y.W. Kim, S.J. Choi, J.Y. Kim, K.H. Jeune, K.C. Won, J.K. Kim, G.Y. Koh, S.Y. Park, COMP-angiopoietin-1 enhances skeletal muscle blood flow and insulin sensitivity in mice, Am. J. Physiol. Endocrinol. Metab. 297 (2009) E402–409.
[25] S. Lee, W. Kim, S.O. Moon, M.J. Sung, D.H. Kim, K.P. Kang, K.Y. Jang, S.Y. Lee, B.H. Park, G.Y. Koh, S.K. Park, Renoprotective effect of COMP-angiopoietin-1 in db/db mice with type 2 diabetes, Nephrol. Dial. Transplant. 22 (2007) 396–408.
[26] H.Y. Jin, K.A. Lee, S.K. Song, W.J. Liu, J.H. Choi, C.H. Song, H.S. Baek, T.S. Park, Sulodexide prevents peripheral nerve damage in streptozotocin induced diabetic rats, Eur. J. Pharmacol. 674 (2012) 217–226.
[27] L. Sjostrom, P. Bjorntorp, J. Vrana, Microscopic fat cell size measurements on frozen-cut adipose tissue in comparison with automatic determinations of osmium-fixed fat cells, J. Lipid Res. 12 (1971) 521–530.
[28] A. Ghorbani, M. Varedi, M.A. Hadjzadeh, G.H. Omrani, Type-1 diabetes induces depot-specific alterations in adipocyte diameter and mass of adipose tissues in the rat, Exp. Clin. Endocrinol. Diabetes 118 (2010) 442–448.
[29] D.R. Matthews, J.P. Hosker, A.S. Rudenski, B.A. Naylor, D.F. Treacher, R.C. Turner, Homeostasis model assessment: insulin resistance and beta-cell function from fasting plasma glucose and insulin concentrations in man, Diabetologia 28 (1985) 412–419.
[30] E.E. Kershaw, J.S. Flier, Adipose tissue as an endocrine organ, J. Clin. Endocrinol. Metab. 89 (2004) 2548–2556.
[31] P.E. Scherer, Adipose tissue: from lipid storage compartment to endocrine organ, Diabetes 55 (2006) 1537–1545.
[32] L.B. Salans, J.L. Knittle, J. Hirsch, The role of adipose cell size and adipose tissue insulin sensitivity in the carbohydrate intolerance of human obesity, J. Clin. Invest. 47 (1968) 153–165.
[33] F. Xu, D. Burk, Z. Gao, J. Yin, X. Zhang, J. Weng, J. Ye, Angiogenic deficiency and adipose tissue dysfunction are associated with macrophage malfunction in SIRT1-/- mice, Endocrinology (2012). http://dx.doi.org/10.1210en.2011-1667. [epub ahead of print]..
[34] S.M. Dallabrida, D. Zurakowski, S.C. Shih, L.E. Smith, J. Folkman, K.S. Moulton, M.A. Rupnick, Adipose tissue growth and regression are regulated by angiopoietin-1, Biochem. Biophys. Res. Commun. 311 (2003) 563–571.

Biochemical and Biophysical Research Communications 420 (2012) 505–510

Contents lists available at SciVerse ScienceDirect

Biochemical and Biophysical Research Communications

journal homepage: www.elsevier.com/locate/ybbrc

Chronic hypoxia in cultured human podocytes inhibits BK_{Ca} channels by upregulating its β4-subunit

Rui Zhang [a,1], Hui Sun [a,1], Chang Liao [a], He Yang [a], Bo Zhao [a], Jia Tian [a], Shuying Dong [a], Zhiren Zhang [b], Jundong Jiao [a,*]

[a] Department of Nephrology, The Second Affiliated Hospital, Harbin Medical University, PR China
[b] Department of Pharmacy, The Second Affiliated Hospital, Harbin Medical University, PR China

ARTICLE INFO

Article history:
Received 4 March 2012
Available online 13 March 2012

Keywords:
Hypoxia
Podocytes
BK_{Ca} channels

ABSTRACT

Accumulating evidence suggests that podocyte hypoxia is an alternative mechanism for the pathogenesis of renal diseases. Functional, large-conductance, calcium-activated potassium channels (BK_{Ca} channels) are expressed in podocytes as mechanosensitive channels; however, whether BK_{Ca} channels are involved in the podocyte response to chronic hypoxia and the possible underlying mechanisms remain unclear. Here, we use the patch clamp technique to show that the exposure of human podocytes to 2% O_2 for 24 h causes a significant reduction in BK_{Ca} channel currents. Molecular biology experiments showed that chronic hypoxia increased BK_{Ca} channel β4-subunit mRNA and protein expression, but not the expression of the BK_{Ca} pore-forming α- or β3-subunits. Furthermore, chronic hypoxia shifted the channel activation range toward more depolarized voltages and slowed its activation kinetics, which are similar to the properties conferred by the β4-subunit. We conclude that BK_{Ca} channels are involved in the response of podocytes to chronic hypoxia via the upregulation of the β4-subunit. These findings provide new insight into the mechanism underlying the cellular responses of podocytes to hypoxia.

1. Introduction

Chronic hypoxia is considered a common final pathway by which chronic kidney disease progresses to end stage renal disease (ESRD) [1]. However, most studies have focused on the tubulointerstitial space, with little attention paid to glomerular damage. Glomerular podocytes are critically required for the maintenance of the glomerular filtration barrier [2]. There is evidence that hypoxia and ischemia also compromise the structure and function of podocytes [3,4]. Hypoxia is an alternative mechanism for the pathogenesis of rapidly progressive glomerulonephritis [5]. It was recently shown that the glomerular expression levels of a majority of the genes regulated by hypoxia-inducible factors (HIFs) are significantly altered in human nephrosclerosis, suggesting that chronic hypoxia is involved in nephrosclerosis [6]. Although accumulating evidence indicates that hypoxia plays a critical role in the pathogenesis of renal disease, the mechanism underlying the cellular responses of podocytes to hypoxia is not clear.

Although O_2-sensitive tissues express a wide variety of channel types, the hypoxic suppression of large-conductance, calcium-activated K^+ channels (BK_{Ca} channels) is central to the cellular mechanism of O_2 sensing [7]. Indeed, the BK_{Ca} channel was one of the first native ion channels shown to be inhibited by hypoxia [8]. Subsequently, the hypoxic inhibition of BK_{Ca} channel activity was demonstrated in the carotid body [9], arteriolar smooth muscle [10], central neurons [11], and cardiac myocytes [12]. In these cells, the hypoxic inhibition of BK_{Ca} channels leads to their depolarization. Depolarization activates voltage-gated Ca^{2+} channels, and the subsequent influx of Ca^{2+} triggers cellular adaptive responses to hypoxic conditions [7–13]. However, some controversy still surrounds BK_{Ca} channel involvement in some cell types, such as vascular smooth muscle cells [14,15]. The mechanisms of the hypoxic inhibition of BK_{Ca} channel activity are unclear. The functional BK_{Ca} channels are composed of pore-forming α-subunits and accessory β-subunits [7]. It has been reported that the pore-forming α-subunits have an important role in the hypoxic inhibition of BK_{Ca} channel activity via the carbon monoxide pathway [16], a membrane-delimited mechanism [17] and the AMP-activated protein kinase (AMPK) pathway [18]. However, it has been proposed that β-subunits are involved in the hypoxia-induced inhibition of BK_{Ca} channel activity in cardiac myocytes [12] and arterial myocytes [10]. Functional BK_{Ca} channels were first reported in human podocytes [19] and were later described in mouse podocytes [20]. As BK_{Ca} channels have gating properties that are sensitive to the mechanical stretch of the plasma membrane [19], they may

* Corresponding author. Address: Xuefu Road 246, Harbin 150081, Heilongjiang Province, PR China. Fax: +86 451 86662640.
E-mail address: jiaojundong@yahoo.com.cn (J. Jiao).
[1] They contributed equally to the work.

0006-291X/$ - see front matter © 2012 Elsevier Inc. All rights reserved.
http://dx.doi.org/10.1016/j.bbrc.2012.03.021

contribute to mechanosensation in podocyte foot processes [21]. However, the relationship between the BK_{Ca} channels of podocytes and hypoxia has not yet been established.

We therefore hypothesized that BK_{Ca} channels are involved in the response of podocytes to chronic hypoxia. To test our hypothesis, we studied the effect of chronic hypoxia on the expression and function of BK_{Ca} channels in a cultured human podocyte cell line. We also examined the possible underlying mechanisms of the modulation of BK_{Ca} channels during chronic hypoxia.

2. Materials and methods

2.1. Cell culture and hypoxic treatments

A conditionally immortalized human podocyte cell line transfected with the temperature-sensitive SV40 gene construct was maintained in RPMI1640 medium (HyClone, USA) supplemented with ITS (insulin, transferrin, sodium selenate; Sigma–Aldrich, USA) and 10% FBS (HyClone, USA) at 33 °C. The cells were propagated at 33 °C, and their differentiation was induced by a shift to the nonpermissive temperature of 37 °C in the same medium for 11–14 days. Fully differentiated cells were placed into the normoxic (21% O_2) or hypoxic (2% O_2 r 10% O_2) environments.

2.2. Real-time PCR

Cells treated with hypoxia or drugs were isolated according to the manufacturer's protocol. Reverse transcription was performed using an RT system (Eppendorf Mastercycler, Hamburg, Germany) in a 10 μl reaction mixture. A total of 0.5 mg RNA was used in the reaction, and a High Capacity cDNA RT Kit (ABI Applied Biosystems, USA) was used for the initiation of cDNA synthesis. All real-time PCR experiments were performed with SYBR Green PCR Master Mix (ABI Applied Biosystems, UK) using an ABI PRISM 7500 (ABI Applied Biosystems, USA). Primer sequences for BK_{Ca} were as follows (5′–3′): KCNMA1 sense AACCCGCCCTATGAGTTTG and antisense GGATGGGATGGAGTGAACAG; KCNMB3 sense GAGAGGACCGAGCCGTGATG and antisense CACCACCTAGCAGAGTCAGTGAAG; KCNMB4 sense GCGTTCTCATTGTGGTCC and antisense TTCC-AGTTGTGCCTGTTTC. Amplification products were sequenced with ready-reaction mix from ABI using sense primer and read on an ABI Prism genetic analyzer.

2.3. Western blot

Fully differentiated podocytes were washed with ice-cold PBS, centrifuged at 3000 r/min for 10 min and then extracted in lysis buffer that contained 1% protease inhibitor solution. The cell lysates were subsequently incubated on ice for 15 min and centrifuged at 13,500 r/min for 15 min. The BCA Protein Assay Kit (Pierce, USA) was used to quantitate the total protein concentration. The samples were subjected to electrophoresis by 10% SDS–PAGE, and the separated proteins were then transferred to nitrocellulose membranes. After transfer, the nitrocellulose membranes were blocked in 5% non-fat milk for 2 h at room temperature and then incubated with the appropriate primary antibody: BK_{Ca} α-, β3- or β4-subunit antibodies (1:200; Abcam, England) or an actin antibody (1:500; Santa Cruz, USA). After washing, the membranes were incubated with fluorescence-conjugated goat anti-rabbit IgG or goat anti-mouse IgG secondary antibody (1:10,000; Invitrogen, USA). The band densities were quantified with the Odyssey infrared imaging system (Li-COR, Lincoln, NE, USA).

2.4. Electrophysiologic recordings

The BK_{Ca} currents were recorded in the whole-cell configuration. The fully differentiated cells were placed directly in the cell chamber, which was mounted on the stage of an inverted microscope (Nikon Eclipse Ti-S, Japan), and then washed with bath solution at a constant speed. Pipettes were drawn from borosilicate glass on a pipette puller P-97 (Sutter Instrument, USA) and had resistances of 2–5 MΩ when filled with electrolyte. Automatic series resistance compensation was performed routinely and monitored continuously. All experiments were performed at room temperature (20–22 °C). For whole-cell recordings, the internal solution contained 15 mM KCl, 130 mM K aspartate, 1 mM $MgCl_2$, 10 mM EGTA, 10 mM Hepes and 5.76 mM $CaCl_2$ (free Ca^{2+} concentration 200 nM); the pH was adjusted to 7.2 with KOH. The standard bath solution contained 145 mM NaCl, 4.5 mM KCl, 1 mM $MgCl_2$, 2 mM $CaCl_2$ and 10 mM Hepes; the pH was adjusted to 7.4 with NaOH. The podocytes in passages 5–15 were depolarized from a holding potential of −60 mV ranging from −80 mV to +80 mV in 20 mV steps for 700 ms for current recordings. Currents were amplified with the Axo-patch 200B (Axon Instruments, USA), low-pass filtered at 1 kHz, and recorded online via a Digidata 1440A interface (Axon Instruments, USA). Data acquisition and analysis was performed with pClamp 10.2 software (Axon Instruments, USA). Conductance data were expressed as G/Gmax and were fitted to the Boltzmann equation. All the reagents used in electrophysiologic recordings were purchased from the Sigma–Aldrich Company, USA.

2.5. Statistical analysis

Data are expressed as the mean ± SEM, with the number (n) of experiments indicated. Statistical analyses were performed using the unpaired t-test (SPSS 16.0), and graphs were prepared with Adobe Photoshop or plotted in Graphpad prism 5 (GraphPad Software, Inc.). A value of $p < 0.05$ was considered statistically significant.

3. Results

3.1. Chronic hypoxia inhibited BK_{Ca} channel currents

In initial experiments, the effects of chronic hypoxia on BK_{Ca} channel currents were examined by the patch clamp technique. In these experiments, the cells were dialyzed using a pipette solution containing a physiologic Ca^{2+} activity of 200 nM, and a substantial outward current was evoked (Fig. 1A). Fig. 1A shows that the reversal potential of channel currents was near −60 mV, which was similar to the equilibrium potential for K^+ (the concentration of K^+ outside and inside the cells was 145 mM and 4.5 mM, respectively). Furthermore, the currents at +80 mV were reduced to 41% by 5 mM TEA ($n = 5$, $p < 0.01$), a non-selective K^+ channel blocker, whereas 100 nM Penitrem A, a selective BK_{Ca} channel blocker [22], led to an irreversible 29% inhibition of the channel currents ($n = 4$, $p < 0.01$). Raising intracellular Ca^{2+} concentrations from 200 nM to 5 μM caused an increase in current amplitude, as shown in Fig. 1B. These data demonstrated that the outward currents evoked using this protocol were entirely attributable to BK_{Ca} channels, which is in agreement with a previous report by Morton et al. [19].

Fig. 1C shows that exposure of podocytes to 2% O_2 for 24 h caused a significant reduction in currents at +80 mV from 14.45 ± 2.06 pS to 4.78 ± 1.12 pS ($p < 0.01$). We confirmed that the cell viability of podocytes was not markedly changed during the

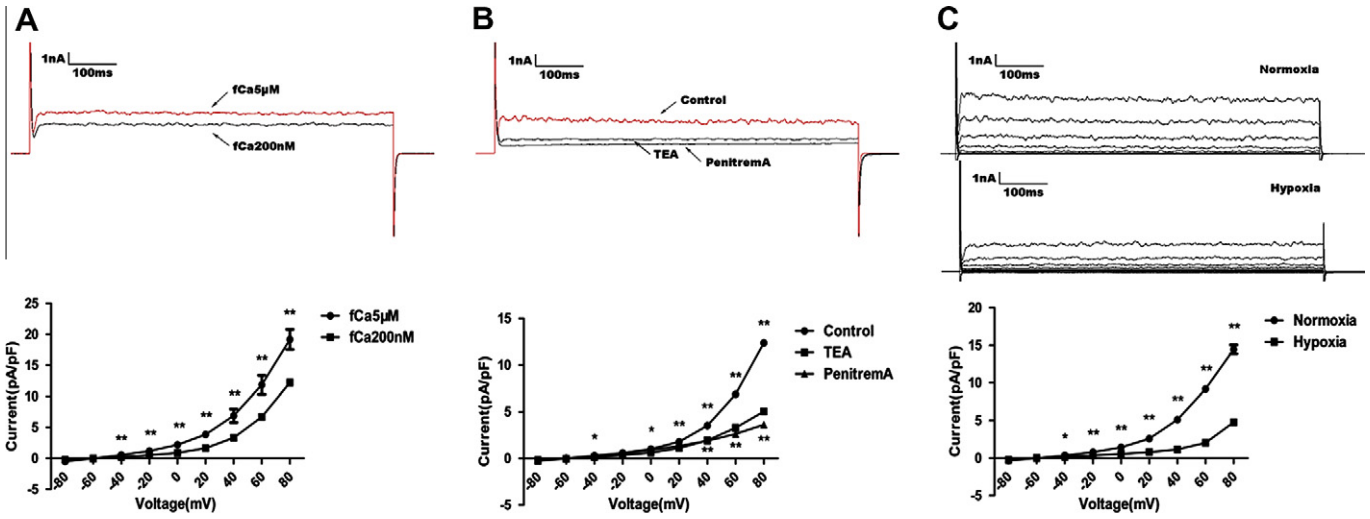

Fig. 1. Chronic hypoxia inhibits BK_{Ca} channel currents in human podocytes. (A) Representative whole-cell BK_{Ca} currents and mean *I–V* curves showed that raising the intracellular Ca^{2+} concentration from 200 nM ($n = 14$) to 5 μM ($n = 7$) caused an increase in current amplitude. (B) Representative currents and mean *I–V* relationship of BK_{Ca} channel blockage. Current amplitude reduced markedly after the addition of TEA ($n = 5$) or Penitrem A ($n = 4$) into the bath solution (extracellular) compared with the Control group ($n = 9$). (C) Representative currents and mean *I–V* relationship of BK_{Ca} channels recorded in podocytes cultured in normoxia (21% O_2) ($n = 12$) or hypoxia (2% O_2) ($n = 7$) for 24 h. The channel currents were notably suppressed in podocytes by oxygen deprivation. Data are reported as the mean ± SEM. Asterisks indicate the statistical significance ($^{*}p < 0.05$, $^{**}p < 0.01$).

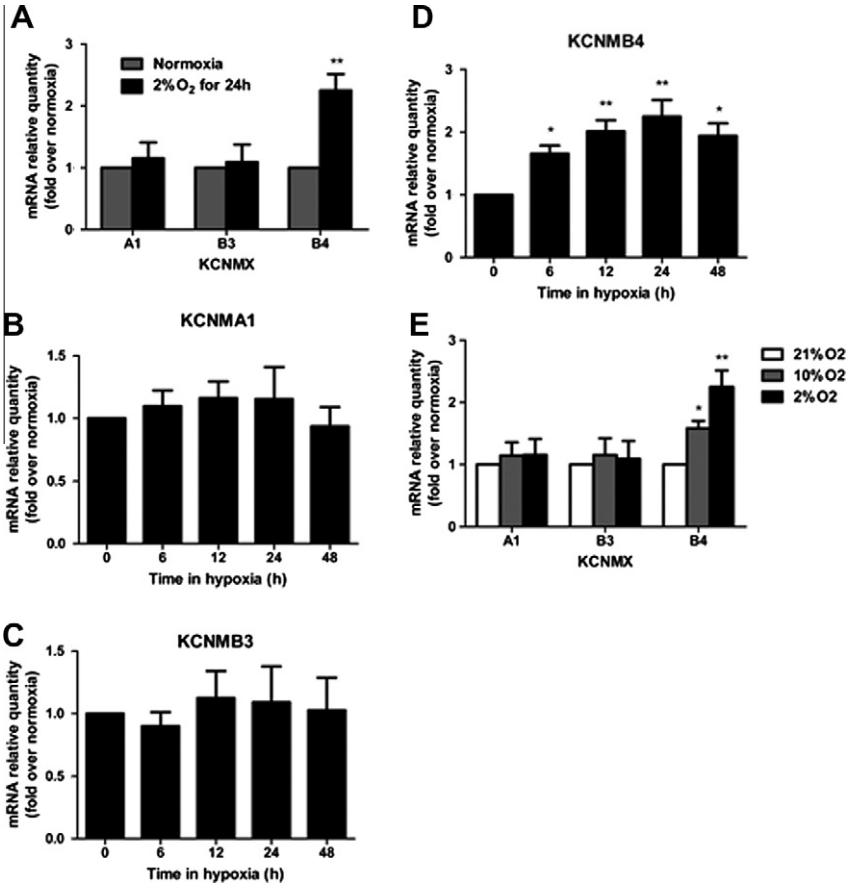

Fig. 2. The effects of chronic hypoxia on BK_{Ca} channel subunit mRNA expression. (A) Exposure of podocytes to 2% O_2 for 24 h caused a significant increase in only the β4-subunit mRNA level; neither the α-subunit nor the β3-subunit mRNA level increased. (B) The expression of BK_{Ca} channel α-subunit mRNA was not modified by the change in the time course of hypoxia from 6 h to 48 h. (C) Likewise, the β4-subunit mRNA level was also unaltered by the different hypoxia time course. (D) The upregulation of β4-subunit mRNA transcripts by chronic hypoxia was markedly time-dependent, showing an onset at 6 h, a peak at 12–24 h and reversion at 48 h. (E) The extent of β4-subunit mRNA upregulation was also dose-dependent, however, neither the α-subunit nor the β3-subunit mRNA level changed with varying oxygen concentration. Data are reported as the mean ± SEM of 3 experiments. Asterisks indicate the statistical significance ($^{*}p < 0.05$, $^{**}p < 0.01$) with respect to the values in normoxia.

course of these studies (data not shown). Additionally, the effect of chronic hypoxia on channel currents did not result from cell swelling or shrinkage because there was no change in mean membrane capacitance between the hypoxic and normoxic groups (151.50 ± 28.20 vs. 127.29 ± 38.72, $p > 0.1$), although a previous study has shown that BK_{Ca} channel activity is modulated by cell swelling in podocytes [19]. These data suggested that chronic hypoxia inhibited BK_{Ca} channel currents.

3.2. Chronic hypoxia selectively modulated BK_{Ca} channel subunit expression

Previous studies have demonstrated that the BK_{Ca} pore-forming α-subunit, which is encoded by the KCNMA1 gene, and two accessory β-subunits, the β3- and β4-subunits, which are encoded by the KCNMB3 and KCNMB4 genes, respectively, are expressed in native human podocytes and a human podocyte cell line [19]. The effects of chronic hypoxia on the expression of α- and β-subunit mRNAs were examined. Interestingly, exposure of podocytes to 2% O_2 for 24 h caused a significant increase in the β4-subunit mRNA level, but not the α- or β3-subunit mRNA levels, as shown in Fig. 2A. The expression of both α- and β3-subunit mRNA was unaltered by the changes in the time course of hypoxia from 6 h to 48 h, as shown in Fig.2B and C. However, Fig. 2D shows that the upregulation of β4-subunit mRNA transcripts by chronic hypoxia was markedly time-dependent, showing an onset at 6 h, a peak at 12–24 h and some reversion at 48 h. Furthermore, the extent of β4-subunit mRNA upregulation was dose-dependent, as shown in Fig. 2E.

Western blot experiments showed that chronic hypoxia induced by exposure to 2% O_2 for 24 h led to an increase in the protein levels of the β4-subunit but not the α-subunit or the β3-subunit (Fig.3). These experiments suggested that chronic hypoxia selectively upregulates the expression of the BK_{Ca} channel β4-subunit in podocytes.

3.3. Chronic hypoxia modified the voltage-dependence and activation kinetics of BK_{Ca} channels

It is well known that the β4-subunit of BK_{Ca} downregulates channel activity by shifting the activation range of BK_{Ca} toward more depolarized voltages and slowing its activation kinetics in both endogenous and exogenous systems [23,24]. Therefore, we examined the effects of chronic hypoxia on the voltage-dependence and activation kinetics of BK_{Ca} channels. Fig.4 shows that, as expected, the activation of the currents was significantly slower in the hypoxic cells than in the normoxic cells. Chronic hypoxia caused a marked increase in the time constant for activation (4.59 ± 1.67 vs. 25.16 ± 11.04, $p < 0.05$). In contrast to the activation kinetics, the deactivation kinetics of BK_{Ca} channels was not influenced by chronic hypoxia (Fig. 4C). Additionally, the voltage-dependence of steady-state activation was shifted to the right by chronic hypoxia (Fig. 4D). Our electrophysiologic data were in fair agreement with the molecular biologic data, suggesting that hypoxic inhibition of BK_{Ca} channels can be attributed to the upregulation of the β4-subunits of BK_{Ca} channels.

4. Discussion

Accumulating evidence has indicated that hypoxia in podocytes contributes to the pathogenesis and progression of glomerular disease [25]. In this study, we have obtained molecular and functional data indicating that BK_{Ca} channels are involved in the responses of podocytes to chronic hypoxia. We showed that in cultured human podocytes, chronic hypoxia causes an increase in the mRNA and protein expression levels of the β4-subunit, but not the

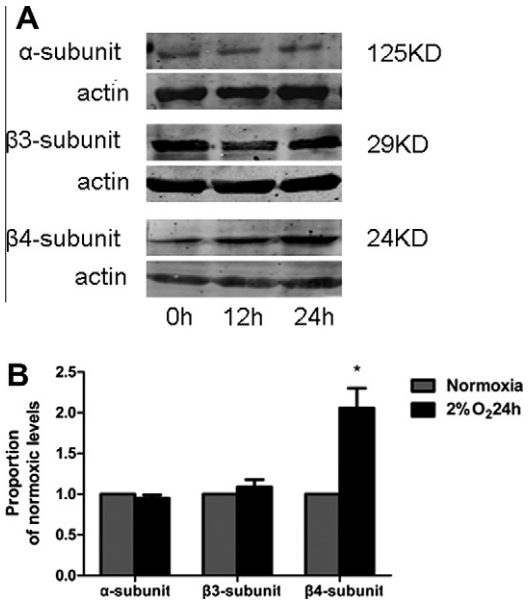

Fig. 3. The effects of chronic hypoxia on the expression of BK_{Ca} channel subunit proteins. (A) Western blot detection also showed augmented expression of BK_{Ca} channel β4-subunit and unchanged α- and β4-subunit protein levels in podocytes with hypoxic treatment. (B) Bars showed the quantitation of subunit expression level in podocytes cultured in 2% O_2 for 24 h vs. normoxic culture. Data are reported as the mean ± SEM of 3–4 experiments. Asterisks indicate the statistical significance ($^*p < 0.05$) with respect to the values calculated for normoxic conditions.

BK_{Ca} channel pore-forming α-subunit or β3-subunit. Functional evidence suggested that the exposure of podocytes to chronic hypoxia leads to a decrease in the activity of the BK_{Ca} channel. Our electrophysiologic data supports the results from the molecular biologic experiments that suggest that chronic hypoxia induces the selective upregulation of the β4-subunit of BK_{Ca} channels, as chronic hypoxia altered the electrophysiologic properties of BK_{Ca} channels conferred by the β4-subunit. These findings provide new insight into the mechanism underlying the cellular responses of podocytes to hypoxia.

BK_{Ca} channels have been identified as one of the key mediators of the response to hypoxia. Previous studies demonstrated that hypoxia inhibited BK_{Ca} channels in the carotid body [9], arteriolar smooth muscle [10], central neurons [11], and cardiac myocytes [12]. In contrast, BK_{Ca} channels are completely insensitive to hypoxia in some cells [14] and are even activated by hypoxia in other cells [15]. The responsiveness of native BK_{Ca} channels to changes in oxygen tension is as diverse as the tissues in which they are expressed [7]. In addition, the adaptive responses to hypoxia depend on prior and prevailing conditions, which may involve changes in BK_{Ca} channel expression, although the underlying mechanisms are essentially unknown [26]. The present study demonstrated that chronic hypoxia inhibited BK_{Ca} channel currents in human podocytes.

The mechanisms by which hypoxia regulates BK_{Ca} channel activity are unclear. BK_{Ca} channels are widely distributed channels activated by both voltage and intracellular Ca^{2+} [27]. The functional BK_{Ca} channels are composed of pore-forming α-subunits and accessory β-subunits. Heme seems to bind directly to BK_{Ca} channels through the C-terminus of α-subunits, which possess a conserved heme-binding sequence motif [28]. Additionally, the α-subunits of BK_{Ca} channels are physically associated with heme oxygenase-2 (HO-2) [16], which uses heme and electrons from NADPH cytochrome-P450 reductase to generate carbon monoxide in the presence of oxygen. Carbon monoxide was found to enhance BK_{Ca} channel activity directly in both native and recombinant

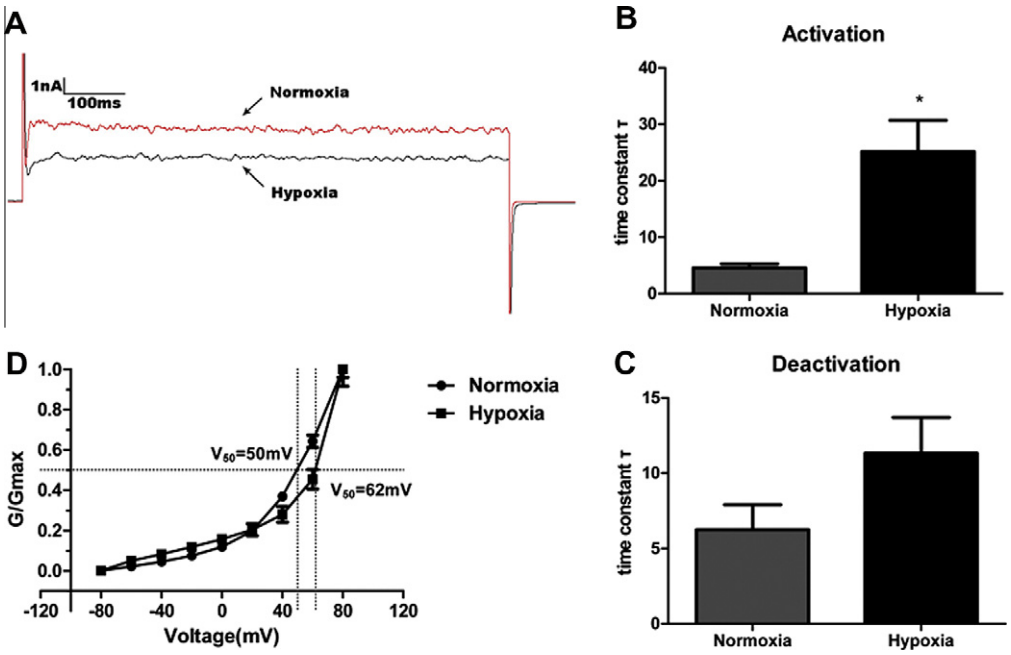

Fig. 4. The effects of chronic hypoxia on the voltage-dependence and activation kinetics of BK_{Ca} channels in human podocytes. (A) Normalized representative currents recorded at +80 mV from podocytes exposed to normoxia or hypoxia. (B) Activation kinetics: hypoxia intervention increased the activation time constant significantly ($n = 6$, $p < 0.05$). (C) Deactivation kinetics: hypoxia did not alter the deactivation time constant ($n = 6$, $p > 0.05$). (D) Exposure to hypoxia shifted the steady-state activation curve to the right, indicating that more depolarized voltages were required to open the channel. Data are reported as the mean ± SEM. Asterisks indicate the statistical significance ($^*p < 0.05$) with respect to the values for normoxic conditions.

systems [9–29]. Hypoxia reduces the availability of carbon monoxide which, in turn, results in channel closure. Thus, HO-2 is proposed to act as an enzyme-linked oxygen sensor of BK_{Ca} channels [7,16,30]. In contrast to the enzyme-linked mechanism, BK_{Ca} channels can also be activated by localized intracellular Ca^{2+} transients termed Ca^{2+} sparks, which generate the micromolar subsarcolemmal intracellular Ca^{2+} concentration elevation necessary for BK_{Ca} channel activation [31]. In cerebral artery smooth muscle cells [32] and HEK 293 cells stably co-expressing the α- and β-subunits of BK_{Ca} channels [33], patch clamp experiments showed that in inside-out membrane patches, and in the absence of any added enzyme substrates, BK_{Ca} channel activity is inhibited by hypoxia in an intracellular Ca^{2+}-dependent manner. These data indicate that hypoxia reduces BK_{Ca} channel activity through a membrane-delimited mechanism, leading to a decrease in the effective coupling of Ca^{2+} sparks to BK_{Ca} channels [32,33]. However, it has been proposed that the sensitivity of BK_{Ca} channels to hypoxia is conferred by a highly conserved motif within an alternatively spliced cysteine-rich insert, the stress-regulated exon (STREX), which is located within the intracellular C terminus of the channel [17].

In addition to the alternative splicing of α-subunits, β-subunits contribute to the molecular diversity of BK_{Ca} [27]. It has recently been reported that β-subunits are involved in the hypoxia-induced inhibition of BK_{Ca} channel activity in cardiac myocytes [12] and arterial myocytes [10]. At present, four BK_{Ca} channel β-subunits have been cloned in mammals (β1–β4, coded by the corresponding KCNMB1–4 genes) [27]. The β4-subunits are predominantly expressed in neurons as "downregulators of BK_{Ca} channels" due to shifts in their activation range toward more depolarized voltages, thereby slowing the activation kinetics of BK_{Ca} [23,24]. β4-subunits are also expressed in human podocytes [19] and act on the gating properties of BK_{Ca} channels similarly as in neural cells [20]. In the present study, our biologic evidence showing that chronic hypoxia exclusively modulated the mRNA expression and protein expression of the β4-subunits in podocytes was in agreement with the electrophysiologic evidence. Additionally, our data suggested that the influence of chronic hypoxia on the β4-subunits of BK_{Ca} channel in podocytes occurs at least at the transcriptional level. In almost every cell type, adaptation to chronic hypoxia (for hours to days) critically depends on transcriptional mechanisms that determine the level of expression of numerous genes [30]. However, we have not yet ruled out other mechanisms, such as subunit translation, trafficking, assembly, or a combination of these processes, which could provide a powerful stimulus for functional BK_{Ca} channel remodeling.

It has been proposed that the hypoxic-induced inhibition of BK_{Ca} channels contributes to the activation of voltage-gated Ca^{2+} channels through their depolarization in many cell types, such as the carotid body and central neurons [13]. However, podocytes do not express voltage-gated Ca^{2+} channels [34]. Available evidence suggests that TRPC6 channels represent a physiologicly important source of Ca^{2+} influx in podocytes [35]. It is speculated that in podocytes, BK_{Ca} channels that are colocalized with TRPC6 channels provide positive feedback for Ca^{2+} influx [21–36]. Owing to voltage-dependent pore blockage by Ca^{2+}, membrane hyperpolarization induced by BK_{Ca} channel activation causes TRPC6 channels to increase Ca^{2+} permeability, conversely, depolarization decreases Ca^{2+} influx through TRPC6 channels [37]. According to this view, the hypoxic inhibition of BK_{Ca} channels in podocytes may decrease Ca^{2+} permeability, leading to changes in intracellular calcium and Ca^{2+}-dependent signaling pathways. However, it has recently been proposed that there is an antagonistic relationship between TRPC5 and TPRC6 to coordinate Ca^{2+} signaling in podocytes [38]. The interaction between BK_{Ca} channels and TRPC5 channels has not yet been tested in podocytes. Future studies will be required to address these unresolved issues.

Acknowledgments

This work was supported by the National Nature Science Foundation of China (31071016), the Nature Science Foundation

of Heilongjiang Province (LC2009C03) and the Nature Science Foundation of Harbin city (2008RFLXS013).

References

[1] I. Mimura, M. Nangaku, The suffocating kidney: tubulointerstitial hypoxia in end-stage renal disease, Nat. Rev. Nephrol. 6 (2010) 667–678.
[2] G.I. Welsh, M.A. Saleem, The podocyte cytoskeleton-key to a functioning glomerulus in health and disease, Nat. Rev. Nephrol. 8 (2011) 14–21.
[3] M.C. Wagner, G. Rhodes, E. Wang, V. Pruthi, E. Arif, M.A. Saleem, S.E. Wean, P. Garg, R. Verma, L.B. Holzman, V. Gattone, B.A. Molitoris, D. Nihalani, Ischemic injury to kidney induces glomerular podocyte effacement and dissociation of slit diaphragm proteins Neph1 and ZO-1, J. Biol. Chem. 283 (2008) 35579–35589.
[4] L.C. Racusen, D.H. Prozialeck, K. Solez, Glomerular epithelial cell changes after ischemia or dehydration. Possible role of angiotensin II, Am. J. Pathol. 114 (1984) 157–163.
[5] M. Ding, S. Cui, C. Li, S. Jothy, V. Haase, B.M. Steer, P.A. Marsden, J. Pippin, S. Shankland, M.P. Rastaldi, C.D. Cohen, M. Kretzler, S.E. Quaggin, Loss of the tumor suppressor Vhlh leads to upregulation of Cxcr4 and rapidly progressive glomerulonephritis in mice, Nat. Med. 12 (2006) 1081–1087.
[6] M.A. Neusser, M.T. Lindenmeyer, A.G. Moll, S. Segerer, I. Edenhofer, K. Sen, D.P. Stiehl, M. Kretzler, H.J. Grone, D. Schlondorff, C.D. Cohen, Human nephrosclerosis triggers a hypoxia-related glomerulopathy, Am. J. Pathol. 176 (2010) 594–607.
[7] P.J. Kemp, V. Telezhkin, W.J. Wilkinson, R. Mears, S.B. Hanmer, H.C. Gadeberg, C.T. Muller, D. Riccardi, S.P. Brazier, Enzyme-linked oxygen sensing by potassium channels, Ann. NY Acad. Sci. 1177 (2009) 112–118.
[8] C. Peers, Hypoxic suppression of K+ currents in type I carotid body cells: selective effect on the Ca2(+)-activated K+ current, Neurosci. Lett. 119 (1990) 253–256.
[9] A.M. Riesco-Fagundo, M.T. Perez-Garcia, C. Gonzalez, J.R. Lopez-Lopez, O(2) modulates large-conductance Ca(2+)-dependent K(+) channels of rat chemoreceptor cells by a membrane-restricted and CO-sensitive mechanism, Circ. Res. 89 (2001) 430–436.
[10] J. Navarro-Antolin, K.L. Levitsky, E. Calderon, A. Ordonez, J. Lopez-Barneo, Decreased expression of maxi-K+ channel beta1-subunit and altered vasoregulation in hypoxia, Circulation 112 (2005) 1309–1315.
[11] H. Liu, E. Moczydlowski, G.G. Haddad, O(2) deprivation inhibits Ca(2+)-activated K(+) channels via cytosolic factors in mice neocortical neurons, J. Clin. Invest. 104 (1999) 577–588.
[12] L. Bautista, M.J. Castro, J. Lopez-Barneo, A. Castellano, Hypoxia inducible factor-2alpha stabilization and maxi-K+ channel beta1-subunit gene repression by hypoxia in cardiac myocytes: role in preconditioning, Circ. Res. 104 (2009) 1364–1372.
[13] C. Peers, C.N. Wyatt, The role of maxiK channels in carotid body chemotransduction, Respir. Physiol. Neurobiol. 157 (2007) 75–82.
[14] M.K. Park, S.H. Lee, S.J. Lee, W.K. Ho, Y.E. Earm, Different modulation of Ca-activated K channels by the intracellular redox potential in pulmonary and ear arterial smooth muscle cells of the rabbit, Pflugers Arch. 430 (1995) 308–314.
[15] D. Gebremedhin, P. Bonnet, A.S. Greene, S.K. England, N.J. Rusch, J.H. Lombard, D.R. Harder, Hypoxia increases the activity of Ca(2+)-sensitive K+ channels in cat cerebral arterial muscle cell membranes, Pflugers Arch. 428 (1994) 621–630.
[16] S.E. Williams, P. Wootton, H.S. Mason, J. Bould, D.E. Iles, D. Riccardi, C. Peers, P.J. Kemp, Hemoxygenase-2 is an oxygen sensor for a calcium-sensitive potassium channel, Science 306 (2004) 2093–2097.
[17] C.E. McCartney, H. McClafferty, J.M. Huibant, E.G. Rowan, M.J. Shipston, I.C. Rowe, A cysteine-rich motif confers hypoxia sensitivity to mammalian large conductance voltage- and Ca-activated K (BK) channel alpha-subunits, Proc. Natl. Acad. Sci. USA 102 (2005) 17870–17876.
[18] C.N. Wyatt, A.M. Evans, AMP-activated protein kinase and chemotransduction in the carotid body, Respir. Physiol. Neurobiol. 157 (2007) 22–29.
[19] M.J. Morton, K. Hutchinson, P.W. Mathieson, I.R. Witherden, M.A. Saleem, M. Hunter, Human podocytes possess a stretch-sensitive, Ca2+-activated K+ channel: potential implications for the control of glomerular filtration, J. Am. Soc. Nephrol. 15 (2004) 2981–2987.
[20] E.Y. Kim, K.J. Choi, S.E. Dryer, Nephrin binds to the COOH terminus of a large-conductance Ca2+-activated K+ channel isoform and regulates its expression on the cell surface, Am. J. Physiol. Renal Physiol. 295 (2008) F235–F246.
[21] S.E. Dryer, J. Reiser, TRPC6 channels and their binding partners in podocytes: role in glomerular filtration and pathophysiology, Am. J. Physiol. Renal Physiol. 299 (2010) F689–F701.
[22] H.G. Knaus, O.B. McManus, S.H. Lee, W.A. Schmalhofer, M. Garcia-Calvo, L.M. Helms, M. Sanchez, K. Giangiacomo, J.P. Reuben, A.B. Smith III, Tremorgenic indole alkaloids potently inhibit smooth muscle high-conductance calcium-activated potassium channels, Biochemistry 33 (1994) 5819–5828.
[23] T.M. Weiger, M.H. Holmqvist, I.B. Levitan, F.T. Clark, S. Sprague, W.J. Huang, P. Ge, C. Wang, D. Lawson, M.E. Jurman, M.A. Glucksmann, I. Silos-Santiago, P.S. DiStefano, R. Curtis, A novel nervous system beta subunit that downregulates human large conductance calcium-dependent potassium channels, J. Neurosci. 20 (2000) 3563–3570.
[24] B. Wang, B.S. Rothberg, R. Brenner, Mechanism of beta4 subunit modulation of BK channels, J. Gen. Physiol. 127 (2006) 449–465.
[25] K. Brukamp, B. Jim, M.J. Moeller, V.H. Haase, Hypoxia and podocyte-specific Vhlh deletion confer risk of glomerular disease, Am. J. Physiol. Renal Physiol. 293 (2007) F1397–F1407.
[26] M.E. Hartness, S.P. Brazier, C. Peers, A.N. Bateson, M.L. Ashford, P.J. Kemp, Post-transcriptional control of human maxiK potassium channel activity and acute oxygen sensitivity by chronic hypoxia, J. Biol. Chem. 278 (2003) 51422–51432.
[27] R. Lu, A. Alioua, Y. Kumar, M. Eghbali, E. Stefani, L. Toro, MaxiK channel partners: physiologic impact, J. Physiol. 570 (2006) 65–72.
[28] X.D. Tang, R. Xu, M.F. Reynolds, M.L. Garcia, S.H. Heinemann, T. Hoshi, Haem can bind to and inhibit mammalian calcium-dependent Slo1 BK channels, Nature 425 (2003) 531–535.
[29] S.E. Williams, S.P. Brazier, N. Baban, V. Telezhkin, C.T. Muller, D. Riccardi, P.J. Kemp, A structural motif in the C-terminal tail of slo1 confers carbon monoxide sensitivity to human BK Ca channels, Pflugers Arch. 456 (2008) 561–572.
[30] J. Lopez-Barneo, T.R. del, K.L. Levitsky, M.D. Chiara, P. Ortega-Saenz, Regulation of oxygen sensing by ion channels, J. Appl. Physiol. 96 (2004) 1187–1195.
[31] G.C. Wellman, M.T. Nelson, Signaling between SR and plasmalemma in smooth muscle: sparks and the activation of Ca2+-sensitive ion channels, Cell Calcium 34 (2003) 211–229.
[32] G. Zhao, A. Adebiyi, Q. Xi, J.H. Jaggar, Hypoxia reduces KCa channel activity by inducing Ca2+ spark uncoupling in cerebral artery smooth muscle cells, Am. J. Physiol. Cell Physiol. 292 (2007) C2122–C2128.
[33] A. Lewis, C. Peers, M.L. Ashford, P.J. Kemp, Hypoxia inhibits human recombinant large conductance, Ca(2+)-activated K(+) (maxi-K) channels by a mechanism which is membrane delimited and Ca(2+) sensitive, J. Physiol. 540 (2002) 771–780.
[34] T.B. Huber, J. Gloy, A. Henger, P. Schollmeyer, R. Greger, P. Mundel, H. Pavenstadt, Catecholamines modulate podocyte function, J. Am. Soc. Nephrol. 9 (1998) 335–345.
[35] H. Zhang, J. Ding, Q. Fan, S. Liu, TRPC6 up-regulation in Ang II-induced podocyte apoptosis might result from ERK activation and NF-kappaB translocation, Exp. Biol. Med. (Maywood) 234 (2009) 1029–1036.
[36] E.Y. Kim, C.P.varez-Baron, S.E. Dryer, Canonical transient receptor potential channel (TRPC)3 and TRPC6 associate with large-conductance Ca2+-activated K+ (BKCa) channels: role in BKCa trafficking to the surface of cultured podocytes, Mol. Pharmacol. 75 (2009) 466–477.
[37] M. Estacion, W.G. Sinkins, S.W. Jones, M.A. Applegate, W.P. Schilling, Human TRPC6 expressed in HEK 293 cells forms non-selective cation channels with limited Ca2+ permeability, J. Physiol. 572 (2006) 359–377.
[38] D. Tian, S.M. Jacobo, D. Billing, A. Rozkalne, S.D. Gage, T. Anagnostou, H. Pavenstaedt, H.H. Hsu, J. Schlondorff, A. Ramos, A. Greka, Antagonistic regulation of actin dynamics and cell motility by TRPC5 and TRPC6 channels, Sci. Signal. 3 (2010) ra77.

Biochemical and Biophysical Research Communications 420 (2012) 511–515

Contents lists available at SciVerse ScienceDirect

Biochemical and Biophysical Research Communications

journal homepage: www.elsevier.com/locate/ybbrc

UAP56 is a novel interacting partner of Bcr in regulating vascular smooth muscle cell DNA synthesis

Abha Sahni [b], Nadan Wang [c], Jeffrey D. Alexis [a,*]

[a] Aab Cardiovascular Research Institute, Department of Medicine, University of Rochester School of Medicine and Dentistry, Rochester, NY, USA
[b] Department of Pathology, University of Texas Medical Branch, Galveston, TX, USA
[c] Center for Translational Medicine, Department of Medicine, Thomas Jefferson University, Philadelphia, PA, USA

ARTICLE INFO

Article history:
Received 3 March 2012
Available online 13 March 2012

Keywords:
DNA synthesis
DExD/H box protein
RNA helicase

ABSTRACT

Bcr is a serine/threonine kinase that is a critical regulator of vascular smooth muscle cell inflammation and proliferation. We have previously demonstrated that Bcr acts in part via phosphorylation and inhibition of PPARγ. We have identified the RNA helicase UAP56 as another substrate of Bcr. In this report we demonstrate that knockdown of UAP56 blocks Bcr induced DNA synthesis in vascular smooth muscle cells (VSMC). We also found that over expression of Bcr increased the expression of cyclin E and decreased the expression of p27. Knockdown of UAP56 reversed the effect of Bcr on cyclin E and p27 expression. Furthermore, we found that Bcr binds to UAP56 and demonstrate that binding of UAP56 to Bcr is critical for Bcr induced DNA synthesis in VSMC. Our data identify UAP56 as an important binding partner of Bcr and a novel target for inhibiting vascular smooth muscle cell proliferation.

1. Introduction

Pathologic vascular smooth muscle cells (VSMC) proliferation occurs in many disease states including hypertension, atherosclerosis and restenosis after injury [1,2]. This proliferation is mediated by growth factors such as platelet-derived growth factor (PDGF) and vasoconstrictive hormones such as Angiotensin II (Ang II), which induces protein synthesis and DNA synthesis and enhances PDGF induced DNA synthesis [1,3,4]. We have recently reported that breakpoint cluster region (Bcr), a serine/threonine kinase is an important mediator of Ang II and PDGF mediated responses in VSMC [5]. We found that knockdown of Bcr inhibited Ang II mediated NF-κB activation in VSMC. Specifically, we found that over expression of Bcr inhibits PPARγ transcriptional activation via phosphorylation of PPARγ, resulting in enhancement of NF-κB transcriptional activation. In addition to PPARγ, we found evidence of UAP56 as another substrate for Bcr.

UAP56 is an RNA helicase that was first identified in an analysis of genes centromeric to HLA-B in the human major histocompatibility complex and was named BAT1 (HLA B associated transcript 1) [6]. BAT1 was rediscovered as an essential RNA splicing factor recruited to mRNA precursors (pre-mRNA) by the splicing factor $U2AF^{65}$ and was renamed UAP56 (56-kD U2AF associated protein) [7]. UAP56 is a member of the DExD/H box family of proteins (named after the amino acid sequence) and is an RNA dependent ATPase, hydrolyzing ATP into ADP [8,9]. UAP56 is part of the TREX (transcription/export) complex [10] which is recruited to activated genes during transcription and travels the length of the gene with RNA polymerase during transcription elongation [10]. UAP56 plays a major role in several steps of RNA biology including spliceosome assembly, mRNA export, and protein synthesis [11–14], and knockdown of UAP56 leads to down regulation of genes involved in the cell cycle, mitosis, cell division and DNA repair [15]. In the present study, we found that UAP56 is a key cell cycle regulator and is a novel interacting partner of Bcr in regulating VSMC DNA synthesis.

2. Materials and methods

2.1. Cell culture

Rat VSMC were isolated as previously described [5] and were maintained in DMEM. HeLa cells were grown in DMEM containing 10% fetal bovine serum.

2.2. Plasmids and adenoviruses

UAP56 wild-type (WT) plasmid was purchased from Origene. The single mutation of UAP56 was created with the QuikChange site-directed mutagenesis kit (Stratagene) as previously described [13]. Bcr WT plasmid was prepared as described previously [5]. For transient expression experiments, cells were transfected with Lipofectamine 2000 (Invitrogen) as previously described [13]. For siRNA experiments, VSMC were transfected with control

* Corresponding author. Address: Aab Cardiovascular Research Institute, University of Rochester School of Medicine and Dentistry, 601 Elmwood Ave., Box 679, Rochester, NY 14642, USA. Fax: +1 585 273 1129.
E-mail address: jeffrey_alexis@urmc.rochester.edu (J.D. Alexis).

0006-291X/$ - see front matter © 2012 Elsevier Inc. All rights reserved.
http://dx.doi.org/10.1016/j.bbrc.2012.03.022

or UAP56 siRNA oligonucleotides (Dharmacon) using Lipofectamine RNAiMAX reagent (Invitrogen). WT Bcr, WT UAP56, and UAP56 fragment 2 adenoviruses were generated using ViraPower Adenoviral Expression System (Invitrogen).

2.3. Immunoprecipitation and Western blot

After treatment with reagents (indicated in the legends), the cells were washed twice with PBS and harvested in 0.5 mL of lysis buffer as previously described [5]. For immunoprecipitation, cell lysates were incubated with mouse anti-UAP56 antibody (1–2 μg) overnight at 4 °C, and then protein A/G beads were added and further incubated for 2 h. The beads were then washed and boiled in 2X SDS sample buffer and western blotting was performed with primary antibodies as indicated in the legends followed by incubation with horseradish peroxidase-conjugated secondary antibody (Amersham Life Science).

2.4. [^{3}H] Thymidine incorporation assay

Cells were plated in 12 well plates and transfected with WT Bcr or WT UAP56 plasmids using Lipofectamine 2000 or were infected with adenoviruses. Cells were pulsed with [^{3}H] thymidine during the last 1-hour of incubation and DNA synthesis was measured as described before [5]. Briefly, cells were washed twice with cold PBS, then 500 μl of 10% ice-cold trichloroacetic acid was added to each well, and precipitates were collected on a micro-fiber filter using a manifold. Filters were washed twice with ice-cold 5% trichloroacetic acid, followed by 95% ethanol, allowed to air-dry, and then suspended in scintillation fluid. Acid precipitable counts were quantitated using a scintillation counter. Each experiment was performed at least three times, and triplicate wells were used in each experiment.

2.5. Mammalian two-hybrid assay

HeLa cells were transfected in Opti-MEM (Invitrogen) with Lipofectamine mixture containing the pG5-luc vector and various pBIND and pACT plasmids (Promega) for 4 h. The pBIND vector contains the yeast GAL4–DNA-binding domain upstream of a multiple cloning region, and the pACT vector contains the herpes simplex virus VP16 activation domain upstream of a multiple cloning region. Bcr and various UAP56 fragments/mutants were cloned into the pBIND and pACT vector, respectively. Because pBIND also contains the Renilla luciferase gene, the expression and transfection efficiencies were normalized with the Renilla luciferase activity. Cells were collected 48 h after transfection and the luciferase activity was assayed with the Dual-Luciferase kit (Promega) using a luminometer (TD-20/20; Turner Designs).

2.6. Statistics

Numerical data are expressed as mean ± SD. Statistical analysis was performed with the StatView 5.0 package (ABACUS Concepts, Berkeley, CA). Differences were analyzed with a one-way or a two way repeated–measure analysis of variance as appropriate, followed by Scheffé's correction for multiple comparisons. A probability value <0.05 was considered significant.

3. Results

3.1. UAP56 is a substrate for Bcr

In an in vitro kinase assay using rat VSMC, in which Bcr was immunoprecipitated with Bcr antibody, we previously demonstrated that Bcr phosphorylates PPARγ [5]. In these studies, we also identified a protein around 60 kDa which we believed to represent another Bcr substrate that coimmunoprecipitated with Bcr in VSMC (Fig. S1). We repeated these experiments (without P^{32}), cut out the band corresponding to the 60 kDa protein, and performed mass spectrometry. The highest hit was the protein UAP56 (BAT1) (Fig. S2).

3.2. Knockdown of UAP56 blocks Bcr induced DNA synthesis

We previously demonstrated that knockdown of Bcr inhibits DNA synthesis [5]. As UAP56 was identified as a substrate of Bcr, we assessed the importance of UAP56 in Bcr induced DNA synthesis. Using UAP56 siRNA and WT Bcr adenovirus (Ad-Bcr), we demonstrated that knock down of UAP56 blocks Bcr induced DNA synthesis in rat VSMC (Fig. 1A and B). Similarly, utilizing WT Bcr

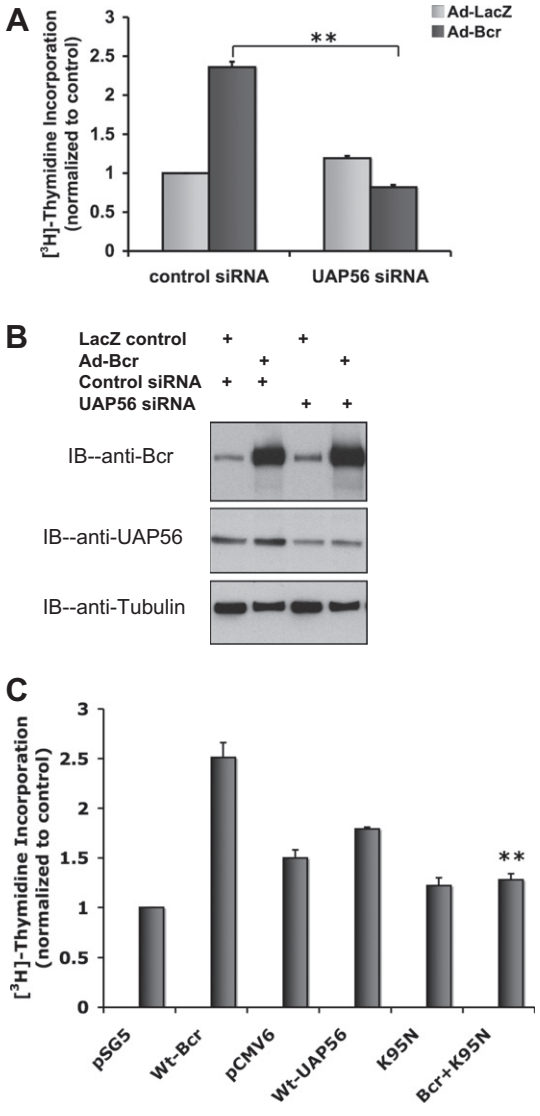

Fig. 1. Knockdown of UAP56 blocks Bcr induced DNA synthesis. (A) VSMC were transfected with UAP56 siRNA or control siRNA. 48 h later the cells were treated with 50 MOI of Ad-Bcr or Ad-LacZ for 24 h. During the last hour of incubation VSMC were pulse labeled with [^{3}H] thymidine and incorporation of [^{3}H] thymidine was measured. (**$p < 0.01$). (B) Western blots demonstrating Bcr and UAP56 expression in cells treated as in (A). (C) Following transfection with the indicated plasmids for 48 h, HeLa cells were pulse labeled with [^{3}H] thymidine for 1 h. Cells were then harvested and [^{3}H] thymidine incorporation was measured. (**$p < 0.01$ compared with Wt-Bcr). pSG5 and pCMV6 are control plasmids for WT-Bcr and WT-UAP56 respectively. Results are means ± SD. For all figures, the data are representative of triplicates using 2 or more different preparations of SMCs or HeLa cells.

and a dominant negative UAP56 mutant (K95N, [16]), we demonstrated that knockdown of UAP56 blocks Bcr induced DNA synthesis in HeLa cells (Fig. 1C).

3.3. UAP56 blocks cell cycle activation

DExD/H box proteins are thought to affect cell growth via cell cycle regulation [17,18]. For example, the RNA helicase p68 plays an important role in PDGF induced cell proliferation by up-regulating cyclin D1 expression [18]. We therefore assessed the effect of Bcr and UAP56 on the expression of several key cell cycle genes. Using WT Bcr adenovirus, we found that over expression of Bcr decreased the expression of the cyclin dependent kinase inhibitor p27 (Fig. 2), a negative regulator of the cell cycle G1/S transition [19,20]. This effect of WT Bcr was reversed by knockdown of UAP56 expression with UAP56 siRNA (Fig. 2). While the RNA helicase p68 acts in part via cyclin D1 expression, we previously saw no effect of Bcr expression on cyclin D expression (unpublished data). We did find however that over expression of Bcr increased the expression of cyclin E, a positive regulator of cell cycle G1/S transition [21,22], an effect that was reversed by knockdown of UAP56 expression with UAP56 siRNA (Fig. 2).

3.4. Bcr binds to UAP56

As our findings suggest an interaction between Bcr and UAP56 we next examined whether Bcr binds to UAP56. Immunoprecipitation/immunoblot studies demonstrated that Bcr does bind to UAP56 (Fig. 3A). We also demonstrated that Bcr binds to UAP56 using a mammalian-two hybrid assay (Fig. 3B). In addition to using full length UAP56, mammalian-two hybrid assay using UAP56 fragments (amino acids 1–100, 101–200, 201–300 and 301–428) demonstrated that fragment 2 (amino acids 101–200) of UAP56 binds to Bcr (Fig. 3B). In addition, immunoprecipitation/immunoblot studies demonstrated that over expression of UAP56 fragment 2 blocked the binding of UAP56 and Bcr in HeLa cells (Fig. 3C), further evidence of the importance of fragment 2 in Bcr/UAP56 binding.

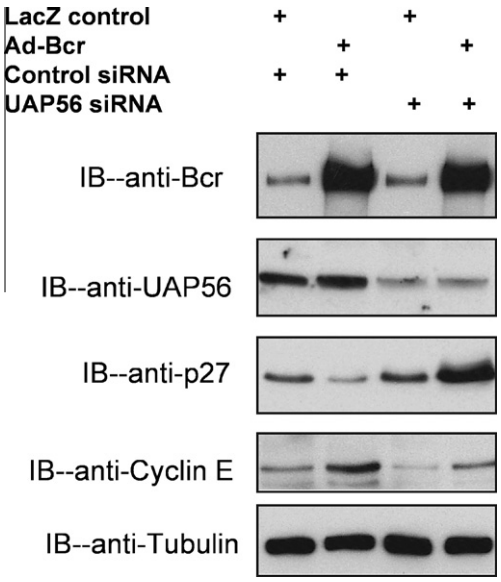

Fig. 2. Knockdown of UAP56 regulates expression of cyclin E and p27. VSMC were transfected with UAP56 siRNA or control siRNA. 48 h later the cells were treated with 50 MOI of Ad-Bcr or Ad-LacZ for 24 h. Cells were harvested and Western blot was done with antibodies as listed.

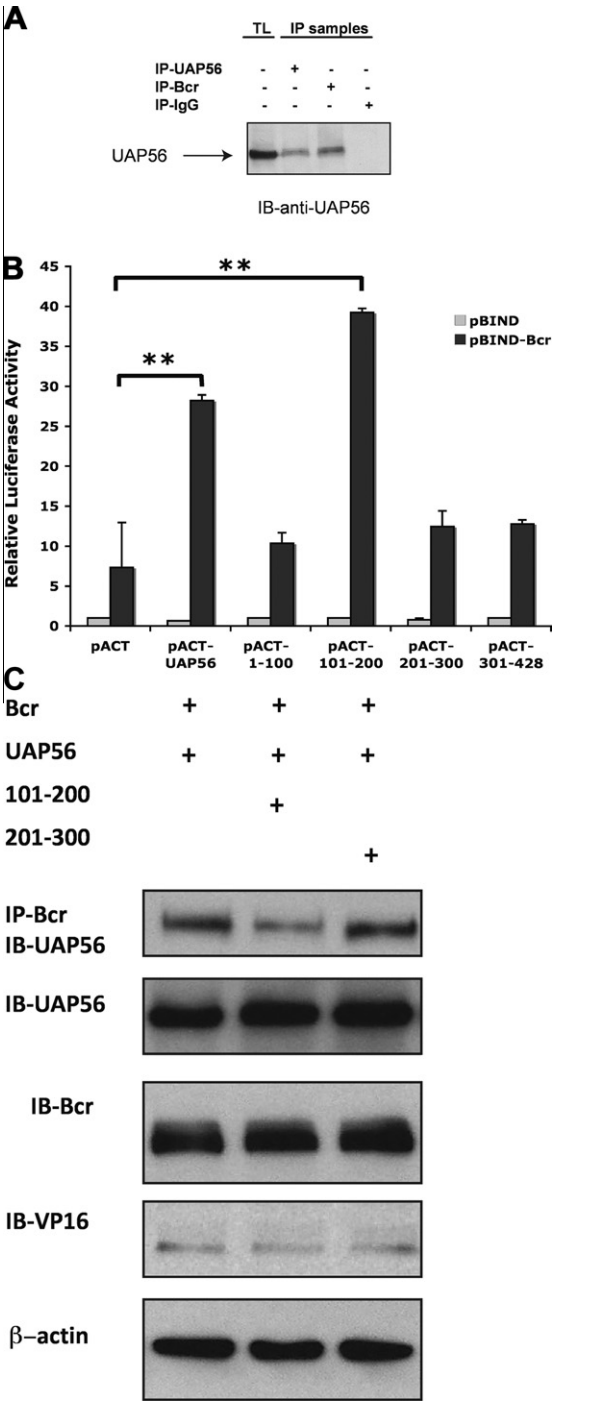

Fig. 3. Bcr binds to UAP56. (A) After over expressing Bcr and UAP56 in HeLa cells, total cell lysates (TL) were prepared and UAP56 and Bcr were immunoprecipitated using respective antibodies and Western blotting was performed with UAP56 antibody. (B) (Mammalian two-hybrid assay). HeLa cells were transfected with pBIND or pBIND-Bcr and pACT UAP56 full length or UAP56 fragments. Cells were harvested and luciferase assay performed. Full length UAP56 binds to Bcr as does UAP56 fragment 2 (amino acids 101–200). ($^{**}p < 0.01$). (C) HeLa cells were transfected with pBIND-Bcr and pACT UAP56 full length or UAP56 fragments as indicated (the pACT vector contains the herpes simplex virus VP16 activation domain). Bcr was immunoprecipitated with Bcr antibody and immunblot done with UAP56 antibody. Over expression of UAP56 fragment 2 [amino acids (aa) 101–200] blocked Bcr/UAP56 binding. Over expression of fragment 3 (aa 201–300) had no effect.

3.5. UAP56/Bcr interaction is critical for Bcr induced DNA synthesis

Having demonstrated that UAP56 binds to Bcr, we next examined whether the interaction between UAP56 and Bcr plays a role in Bcr

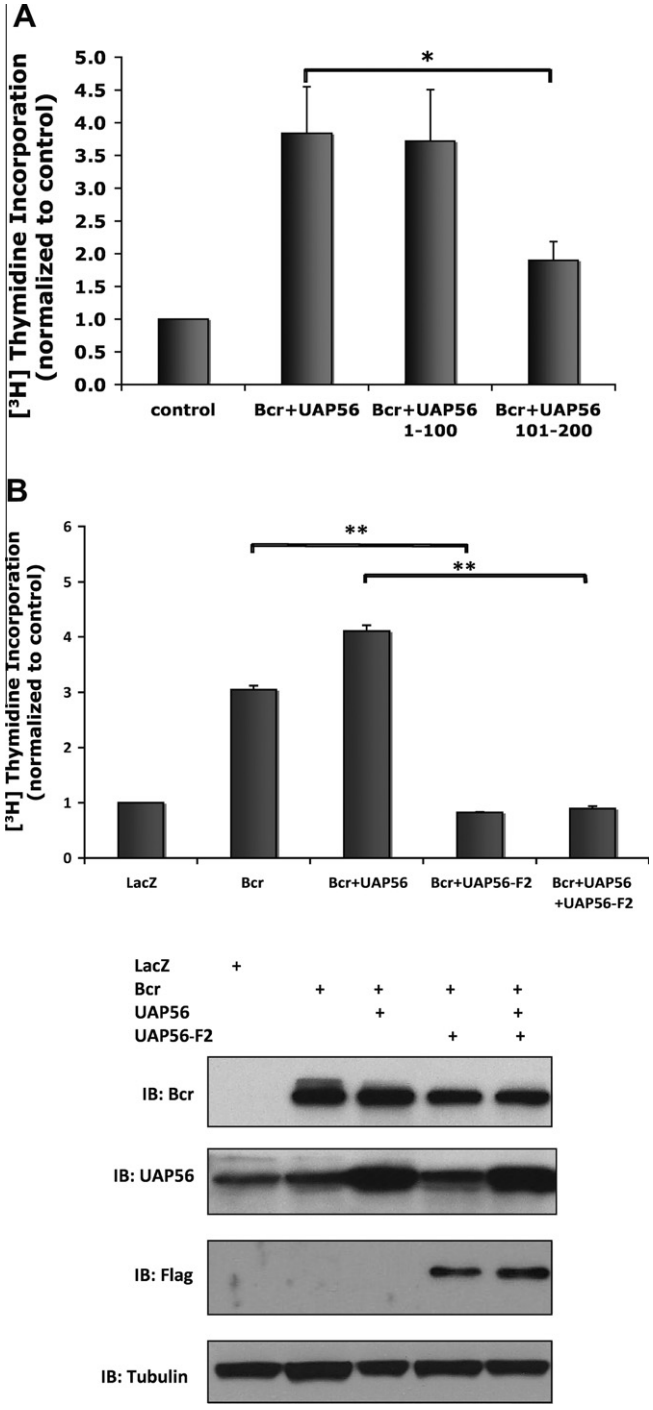

Fig. 4. Over expression of UAP56 fragment 2 inhibits Bcr induced DNA synthesis. (A) HeLa cells were transfected with control, Bcr, and UAP56 full length or UAP56 fragment plasmids as indicated. Cells were harvested and [^{3}H] thymidine incorporation was measured ($^*p < 0.05$). Over expression of fragment 1 (aa 1–100) had no effect. (B) VSMC were treated with Ad-Bcr, Ad-WT UAP56, or Ad-Fragment 2 UAP56 as indicated. Cells were harvested and [^{3}H] thymidine incorporation was measured. ($^{**}p < 0.01$). Western blots demonstrating protein expression of Bcr and UAP56 in VSMC treated with Bcr and UAP56 adenoviruses is shown below. Ad-Fragment 2 UAP56 contained a Flag tag.

induced DNA synthesis. Over expressing Bcr WT, UAP56 WT, UAP56 fragment 1 and UAP56 fragment 2 in HeLa cells, we found that over expression of UAP56 fragment 2 but not fragment 1, inhibited Bcr induced DNA synthesis (Fig. 4A). Similarly, using Bcr WT, UAP56 WT, and UAP56 fragment 2 adenoviruses, we demonstrated that over expression of UAP56 fragment 2 inhibits Bcr induced DNA synthesis in VSMC (Fig. 4B). These data demonstrate that UAP56/Bcr interaction is important for Bcr induced DNA synthesis.

4. Discussion

The major findings of this study are that UAP56 binds to Bcr and interaction between UAP56 and Bcr is critical for Bcr induced DNA synthesis. We previously demonstrated that Bcr is a major regulator of SMC proliferation and inflammation. We demonstrated that this effect was in part via inhibition of PPARγ transcriptional activation by Bcr. Our data now show that Bcr also acts via PPARγ independent signaling. While our initial studies of the interaction between Bcr and UAP56 were in HeLa cells, using Ad-Bcr and Ad-WT UAP56 we demonstrated the importance of this interaction in VSMC as well. These findings demonstrate an important role of UAP56 in VSMC proliferation and identify UAP56/Bcr interaction as a potential target for treatment of vascular proliferative disease.

UAP56 is known to play an important role in RNA splicing, mRNA export, and protein synthesis. Our study now demonstrates that UAP56 plays an important role in DNA synthesis as well, and further defines the role of UAP56 in cellular proliferation. Yamazaki et al. recently reported that knockdown of UAP56 in HeLa cells was associated with down regulation of genes affecting the cell cycle, mitosis, mRNA transport, DNA replication, DNA repair, and cell division, demonstrating the important role of UAP56 in cell growth [15]. Depletion of UAP56 causes mitotic delay and sister chromatid cohesion defects [15]. These findings suggest that UAP56 is a major control point for cell growth. UAP56 has a close homolog (URH49) which has 90% homology with UAP56 [12,15]. Like UAP56, URH49 is also a DExD/H box protein and an RNA helicase. The two helicases have different expression profiles in different tissues [12] but whether the two proteins have completely overlapping roles has been unknown. Using UAP56 and URH49 siRNA, Yamazaki et al. demonstrated that similar to UAP56, URH49 is important in mitotic progression, but unlike UAP56, depletion of URH49 causes chromosome arm resolution defects and failure of cytokinesis. These findings demonstrate that UAP56 is an important regulator of mitosis, distinct from URH49. Our data extend these findings demonstrating the role of UAP56 in VSMC DNA synthesis.

Our results also further define the role of DExD/H box proteins and RNA helicases in cellular proliferation. DExD/H box proteins have been thought to control cell growth through regulation of the cell cycle but the mechanism has been unknown [17]. Yang et al. demonstrated that the RNA helicase p68 regulates PDGF induced cell proliferation by upregulating cyclin D1 and c-myc expression [18]. We have now demonstrated that UAP56 is another DExD/H box protein that is an important regulator of the cell cycle and cell proliferation. DExD/H box proteins are important in abnormal proliferation in tumors [23] and may well play an important role in pathological SMC proliferation.

In conclusion, the data presented demonstrate that UAP56 is a novel partner of Bcr in regulating VSMC DNA synthesis. This effect may occur in part due to UAP56-dependent modulation of cell cycle progression. Bcr/UAP56 interaction may be a target for inhibiting pathological VSMC proliferation.

Sources of funding

This study was supported by a Grant from the National Institutes of Health to Dr. Alexis (HL80938).

Acknowledgment

The authors thank Dr. Alan Friedman for his assistance with mass spectrometry.

Appendix A. Supplementary data

Supplementary data associated with this article can be found, in the online version, at doi:10.1016/j.bbrc.2012.03.022.

References

[1] N. Fujita, Y. Furukawa, N. Itabashi, K. Okada, T. Saito, S. Ishibashi, Differences in E2F subunit expression in quiescent and proliferating vascular smooth muscle cells, Am. J. Physiol. Heart Circ. Physiol. 283 (2002) H204–H212.

[2] C.L. Jackson, S.M. Schwartz, Pharmacology of smooth muscle cell replication, Hypertension 20 (1992) 713–736.

[3] B. Bunkenburg, T. van Amelsvoort, H. Rogg, J.M. Wood, Receptor-mediated effects of angiotensin II on growth of vascular smooth muscle cells from spontaneously hypertensive rats, Hypertension 20 (1992) 746–754.

[4] A.J. Naftilan, R.E. Pratt, V.J. Dzau, Induction of platelet-derived growth factor A-chain and c-myc gene expressions by angiotensin II in cultured rat vascular smooth muscle cells, J. Clin. Invest. 83 (1989) 1419–1424.

[5] J.D. Alexis, N. Wang, W. Che, N. Lerner-Marmarosh, A. Sahni, V.A. Korshunov, Y. Zou, B. Ding, C. Yan, B.C. Berk, J. Abe, Bcr kinase activation by angiotensin II inhibits peroxisome-proliferator-activated receptor gamma transcriptional activity in vascular smooth muscle cells, Circ. Res. 104 (2009) 69–78.

[6] T. Spies, G. Blanck, M. Bresnahan, J. Sands, J.L. Strominger, A new cluster of genes within the human major histocompatibility complex, Science 243 (1989) 214–217.

[7] J. Fleckner, M. Zhang, J. Valcarcel, M.R. Green, U2AF65 recruits a novel human DEAD box protein required for the U2 snRNP-branchpoint interaction, Genes Dev. 11 (1997) 1864–1872.

[8] R.J. Allcock, J.H. Williams, P. Price, The central MHC gene, BAT1, may encode a protein that down-regulates cytokine production, Genes Cells 6 (2001) 487–494.

[9] J. Shen, L. Zhang, R. Zhao, Biochemical characterization of the ATPase and helicase activity of UAP56, an essential pre-mRNA splicing and mRNA export factor, J. Biol. Chem. 282 (2007) 22544–22550.

[10] K. Strasser, S. Masuda, P. Mason, J. Pfannstiel, M. Oppizzi, S. Rodriguez-Navarro, A.G. Rondon, A. Aguilera, K. Struhl, R. Reed, E. Hurt, TREX is a conserved complex coupling transcription with messenger RNA export, Nature 417 (2002) 304–308.

[11] D. Gatfield, H. Le Hir, C. Schmitt, I.C. Braun, T. Kocher, M. Wilm, E. Izaurralde, The DExH/D box protein HEL/UAP56 is essential for mRNA nuclear export in Drosophila, Curr. Biol. 11 (2001) 1716–1721.

[12] F. Kapadia, A. Pryor, T.H. Chang, L.F. Johnson, Nuclear localization of poly(A)+ mRNA following siRNA reduction of expression of the mammalian RNA helicases UAP56 and URH49, Gene 384 (2006) 37–44.

[13] A. Sahni, N. Wang, J.D. Alexis, UAP56 is an important regulator of protein synthesis and growth in cardiomyocytes, Biochem. Biophys. Res. Commun. 393 (2010) 106–110.

[14] H. Shen, X. Zheng, J. Shen, L. Zhang, R. Zhao, M.R. Green, Distinct activities of the DExD/H-box splicing factor hUAP56 facilitate stepwise assembly of the spliceosome, Genes Dev. 22 (2008) 1796–1803.

[15] T. Yamazaki, N. Fujiwara, H. Yukinaga, M. Ebisuya, T. Shiki, T. Kurihara, N. Kioka, T. Kambe, M. Nagao, E. Nishida, S. Masuda, The closely related RNA helicases, UAP56 and URH49, preferentially form distinct mRNA export machineries and coordinately regulate mitotic progression, Mol. Biol. Cell 21 (2010) 2953–2965.

[16] K.P. Kota, S.R. Wagner, E. Huerta, J.M. Underwood, J.A. Nickerson, Binding of ATP to UAP56 is necessary for mRNA export, J. Cell. Sci. 121 (2008) 1526–1537.

[17] F.V. Fuller-Pace, DExD/H box RNA helicases: multifunctional proteins with important roles in transcriptional regulation, Nucleic Acids Res. 34 (2006) 4206–4215.

[18] L. Yang, C. Lin, S. Zhao, H. Wang, Z.R. Liu, Phosphorylation of p68 RNA helicase plays a role in platelet-derived growth factor-induced cell proliferation by up-regulating cyclin D1 and c-Myc expression, J. Biol. Chem. 282 (2007) 16811–16819.

[19] C. Attwooll, E. Lazzerini Denchi, K. Helin, The E2F family: specific functions and overlapping interests, EMBO J. 23 (2004) 4709–4716.

[20] H.Z. Chen, S.Y. Tsai, G. Leone, Emerging roles of E2Fs in cancer: an exit from cell cycle control, Nat. Rev. Cancer 9 (2009) 785–797.

[21] H. Hochegger, S. Takeda, T. Hunt, Cyclin-dependent kinases and cell-cycle transitions: does one fit all?, Nat Rev. Mol. Cell Biol. 9 (2008) 910–916.

[22] M. Malumbres, M. Barbacid, Cell cycle, CDKs and cancer: a changing paradigm, Nat. Rev. Cancer 9 (2009) 153–166.

[23] L. Yang, C. Lin, Z.R. Liu, Phosphorylations of DEAD box p68 RNA helicase are associated with cancer development and cell proliferation, Mol. Cancer Res. 3 (2005) 355–363.

Biochemical and Biophysical Research Communications 420 (2012) 516–522

Contents lists available at SciVerse ScienceDirect

Biochemical and Biophysical Research Communications

journal homepage: www.elsevier.com/locate/ybbrc

Synthetic retinoid CD437 induces apoptosis and acts synergistically with TRAIL receptor-2 agonist in malignant melanoma

Gry Irene Magnussen [a], Anne Katrine Ree Rosnes [a], Susan Shahzidi [a], Hiep Phuc Dong [a], Elisabeth Emilsen [a], Birgit Engesæter [b], Vivi Ann Flørenes [a,*]

[a] Department of Pathology, Institute for Cancer Research, The Norwegian Radium Hospital, 0424 Oslo, Norway
[b] Department of Tumor Biology, Institute for Cancer Research, The Norwegian Radium Hospital, 0424 Oslo, Norway

ARTICLE INFO

Article history:
Received 5 March 2012
Available online 13 March 2012

Keywords:
CD437
Retinoids
TRAIL
Lexatumumab
Malignant melanoma
Apoptosis
Caspases

ABSTRACT

The novel synthetic retinoid, CD437, shows potent anti-tumor activity in a range of different cancer cell lines and now serves as a prototype for development of new retinoid related molecules (RRMs). The purpose of this study was to examine the effect and cellular targets of CD437 in the human metastatic melanoma cell lines FEMX-1 and WM239. We showed that treatment with CD437 led to cell cycle arrest and induced apoptosis through both the extrinsic- and intrinsic pathways (caspase 8, -9 and PARP cleavage) in both cell lines. Interestingly, apoptosis was induced independently of DNA-fragmentation in FEMX-1 cells, and appeared partially caspase-independent in the WM239 cells. Additionally, up-regulation of CHOP mRNA and cathepsin D protein expression, following retinoid treatment, suggests involvement of the endoplasmatic reticulum (ER) and lysosomes, respectively. Combination of suboptimal concentrations of CD437 and lexatumumab, a TRAIL death receptor-2 agonist, resulted in synergistic reduction of viable cells, along with increased PARP cleavage. These results indicate that CD437 has a strong anti-neoplastic effect alone and in combination with lexatumumab in melanoma cell lines.

1. Introduction

Malignant melanoma is one of the most increasing cancer forms, in addition to being the second most common cancer in young adults. Whereas the prognosis is good when detected early, there are no curative treatments once the cancer has spread to distant organs (stage IV) [1]. Thus, there is a desperate need for new and more effective treatment options.

Retinoids belong to a family of synthetic- and natural vitamin A derivatives and analogs, regulating growth, differentiation, metabolism, apoptosis, morphogenesis and homeostasis [2]. Several retinoids have been evaluated in clinical trials, such as all-trans retinoic acid (ATRA); now included in treatment of acute promyelocytic leukemia (>90% complete remission) [3]. Synthetic retinoid 6-[3-(1-adamantyl)-4-hydroxyphenyl]-2-naphthalene carboxylic acid (CD437/AHPN) has yielded promising results as an anti-tumor agent both *in vitro* and *in vivo* [4]. However, toxicity to normal cells have also been reported [5].

Although originally synthesized as a retinoid selective for the Retinoid-Acid-Receptor-γ, CD437 also induce apoptosis and growth arrest independently of retinoic receptors [6,7]. In prostate and lung cancers, CD437 has been shown to up-regulate the expression of death receptor 4 and 5 (DR4 and DR5) [8,9]. Furthermore, combination of CD437 and tumor necrosis factor-related apoptosis-inducing ligand (TRAIL) has been reported to enhance induction of apoptosis in lung cancer cells [10].

In the present study, we have demonstrated that treatment with CD437, alone and combined with lexatumumab (an agonistic TRAIL receptor-2 antibody), induce apoptosis and cell cycle arrest in the human malignant melanoma cell lines FEMX-1 and WM239.

2. Materials and methods

2.1. Cell lines and growth conditions

The human metastatic melanoma cell lines, FEMX-1 and WM239, were established as previously described [11,12] and cultivated in RPMI-1640 medium (LONZA, Verviers, Belgium) supplemented with 5% Fetal Calf Serum (Biochrom, KG, Berlin, Germany) and 2 mM L-glutamine (LONZA). CD437 [13] was from Sigma–Aldrich™ (St. Louis, MO) and diluted in DMSO (Sigma–Aldrich, stock concentration 10 mM) and further diluted in growth medium to desired final concentration prior to use. Z-VAD-fmk (50 μM), a pan-caspase inhibitor (Promega, Madison, WI), was

* Corresponding author. Address: Oslo University Hospital, The Norwegian Radium Hospital, Department of Pathology, N-0310 Oslo, Norway. Fax: +47 227 30 164.
E-mail address: Vivi.A.Flornes@rr-research.no (V.A. Flørenes).

0006-291X/$ - see front matter © 2012 Elsevier Inc. All rights reserved.
http://dx.doi.org/10.1016/j.bbrc.2012.03.023

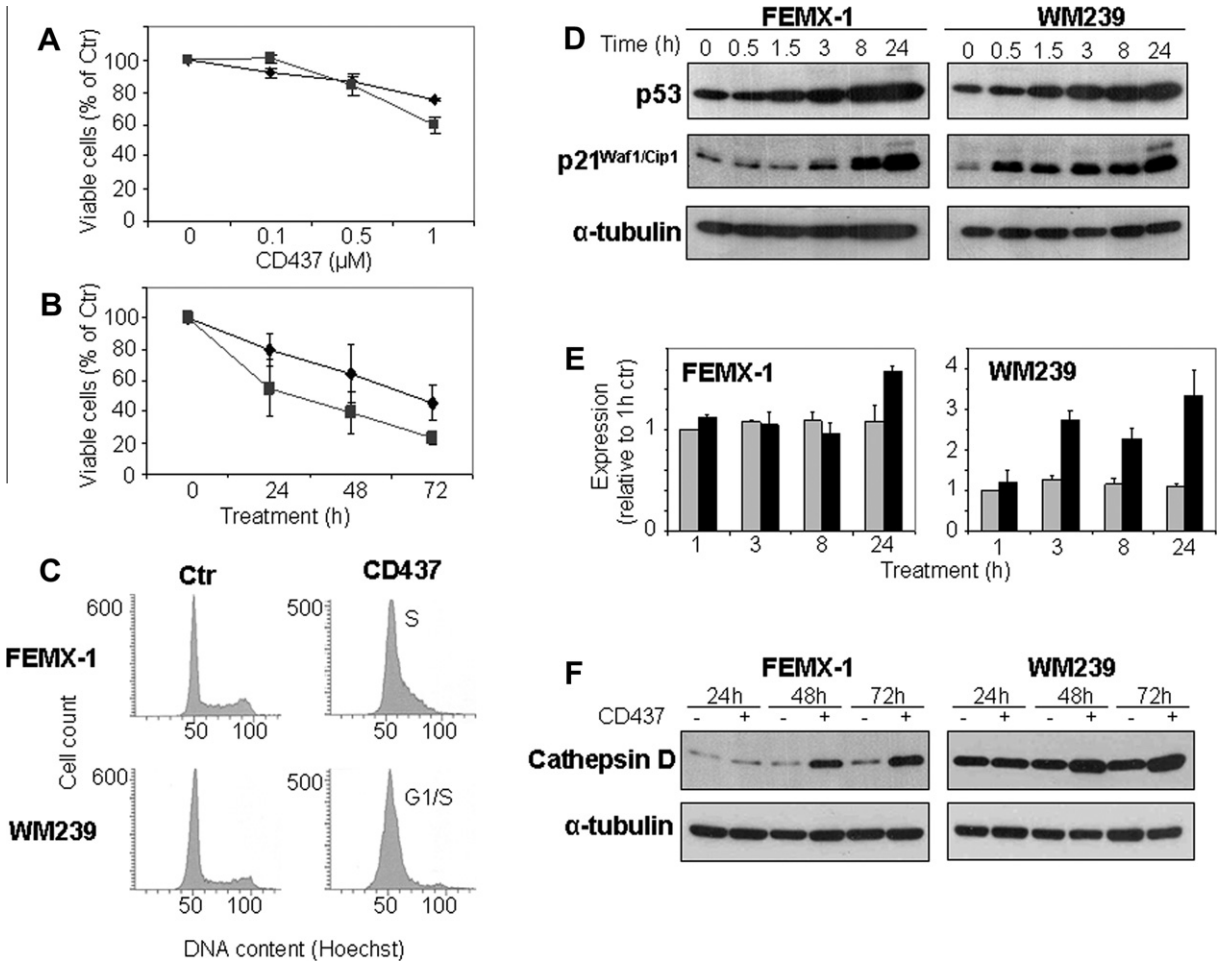

Fig. 1. CD437-induced changes to cell viability, cell cycle distribution, proteins and mRNA. Cell viability was determined by the MTS assay, and presented as percentage of control cells (squares: FEMX-1 cells and diamonds: WM239 cells). (A) Cells were treated with various doses of CD437 for 24 h. (B) Cells were treated with 1 μM CD437 for indicated time periods. (C) Cell cycle distribution was determined by the use of flow cytometry (24 h of treatment). (D) Western blot analysis was used to study the protein expression of p21 and p53 following treatment with 1 μM CD437 for the indicated time. (E) CHOP mRNA expression, relative the 1 h control, was studied by qRT-PCR. (F) Protein expression of cathepsin D was studied using western blot analysis. α-Tubulin has been used as loading control. Data are the mean or representative of at least three independent experiments.

added together with CD437. Lexatumumab (Human Genome Sciences, Rockville, MD, USA) was diluted in PBS with 0.1% HSA and added together with CD437. Control cells were treated with an isotype-matched mAb of irrelevant specificity (Human Genome Sciences).

2.2. MTS assay

Cells seeded in 96-wells plates (5000 cells/well) were left to attach overnight before addition of CD437 or vehicle as control. Cell viability was determined by the 3-(4.5-dimethylthiazol-2-yl)-5-(3-carboxymethoxyphenyl)-2-(4-sulfophenyl)-2H-tetrazolium) (MTS) viability assay (Promega). Absorbance was measured at 490 nm using ASYS UVM340 96-well plate reader (Fisher Scientific, Oslo, Norway).

2.3. Trypan blue dye exclusion test

Untreated- and CD437 treated cells were harvested using trypsin/EDTA (LONZA), along with medium containing floating cells. After centrifugation, the cell pellet was resuspended in PBS containing trypan blue (Merck, Stockholm, Sweden). Viable (dye excluding) and trypan blue stained dead cells were counted.

2.4. Fluorescence microscopy

For analysis of morphological changes to the nucleus, the medium was collected and the cells were harvested using EDTA (LONZA). Hoechst 33342 (4 μg/mL) (Sigma–Aldrich™) was added to each cell suspension, and cells were visualized using fluorescence microscopy (Nikon, Inter Instrument A/S, Baerum, Norway).

2.5. Cell death detection ELISA^{plus}

Determination of cytoplasmic histone-associated-DNA-fragments was assessed using a commercially available kit following the manufacturer's instructions (Roche Diagnostic, Mannheim, Germany). For detection of necrosis, occurrence of extracellular histone-associated-DNA-fragments in the medium was determined. The ELISA signal was quantified by measuring absorbance at 405 nm (reference 495 nm), using ASYS UVM340 96-well plate reader.

2.6. Flow cytometric analysis

Cells were harvested by trypsinization (cell cycle analysis) or EDTA-treatment (analysis of death receptors) and washed 1× in

PBS. Approximately 10^6 cells were re-suspended in 1 mL 70% ice-cold methanol and left to fixate for a minimum of 24 h. Fixated cells were washed 1× in PBS, and stained with 2 μg/mL Hoechst 33258 (Roche Diagnostics) in PBS. Flow cytometric analysis was performed using LSR II UV laser for cell cycle distribution (BD Biosciences, San Jose, CA) and analyzed with FlowJo software (Ashland, OR).

Relative expression of death receptors was determined as previously described [14], using PE-conjugated Anti-DR4 (Clone DJR1), anti-DR5 (clone DJR2-4) (Biolegend, San Diego, CA) and anti-CD95 (clone DX2) (BD Biosciences).

2.7. Western blot analysis

Procedure and reagents were as previously described [15]. Primary antibodies Caspase 3 (#9662/#9664 (even mix)), Caspase 8 (#9746), Caspase 9 (#9502), DFF45 (#9732), cleaved DFF45 (#9731), p21 (#2946) and PARP (#9532), were purchased from Cell Signaling (Beverly, MA). α-Tubulin (DMIB) was from Calbiochem (Nottingham, UK), whereas cathepsin D (sc-6486) and p53 (sc-126) were obtained from Santa Cruz (Santa Cruz, CA).

2.8. Quantitative real-time RT-PCR analysis

Procedure and reagents were as previously described [15]. The real-time PCR analyses were performed using TaqMan Fast Universal PCR Master Mix (2×) and TaqMan Gene Expression Assay (CHOP/DDIT3; Hs01123468_m1 and GUS; Hs99999908_m1, Applied Biosystems, CA, USA).

2.9. Calcusyn analysis

Synergy was determined by the Chou and Talalay Combination Index (CI) [16] for non-exclusive treatments (treatments affecting different targets or sites of the same target), and calculated by Calcusyn software (BioSoft, Feruson, MO, USA).

3. Results

3.1. Reduced cell viability following CD437 treatment of melanoma cell lines

To examine the effect of CD437 in melanomas, two human cell lines; FEMX-1 and WM239, were treated with various concentrations and for different time periods, and analyzed for cell viability using the MTS assay. As shown in Fig. 1A and B, a dose- and time-dependent reduction in viability was observed, indicating increased cell death and/or cell cycle arrest. Based on these results, and in accordance with previous studies [17], 1 μM CD437 was used in the following (unless otherwise stated). To discriminate between increased cell death and cell cycle arrest, the effect on cell cycle distribution was determined. As demonstrated in Fig. 1C, flow cytometric analysis revealed an S- and G_1/S-phase arrest in FEMX-1 and WM239 cells, respectively, after 24 h treatment. The arrests were accompanied by increased expression of the cell cycle regulators $p21^{Waf1/Cip1}$ and p53 (Fig. 1D).

To examine whether CD437 also induced cell death, the cells were treated for 24, 48 and 72 h, and percentage live and dead cells were estimated by the trypan blue exclusion assay. As shown in Fig. 2A, treatment for 72 h resulted in 45% (FEMX-1) and 37% (WM239) dead cells.

Since the trypan blue assay is not exclusively detecting apoptosis, the nature of cell death was examined in more detail. As seen in Fig. 3B, a profound augmentation of cytoplasmic histone-associated DNA-fragments (apoptotic index) was detected in WM239 cells after 48 h CD437 treatment, whilst only a very modest increase was seen in FEMX-1 cells. To further confirm apoptosis, morphological changes to the cell nucleus were studied by

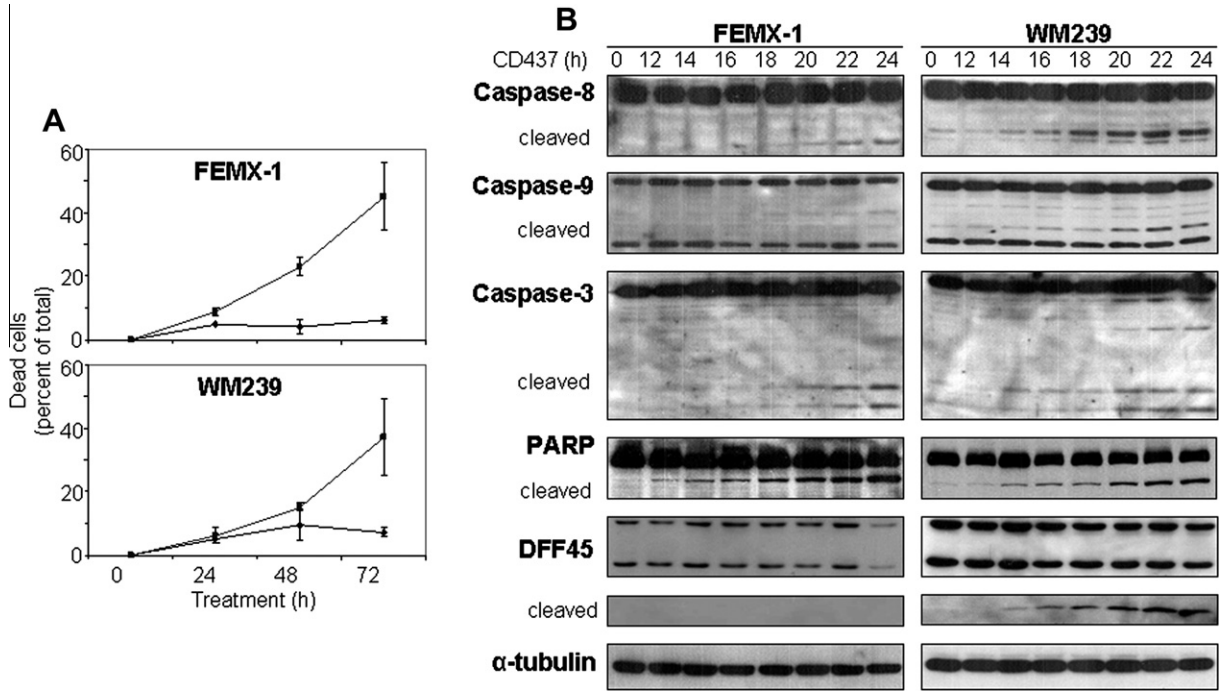

Fig. 2. Cell death induced by CD437. FEMX-1 and WM239 cells were treated with 1 μM CD437 and harvested after the indicated time. (A) Dead/dying cells were stained with trypan blue and both living and dead cells were counted. Dead cells are presented as percentage of total cell count (Diamonds: control cells and treated cells: squares). (B) Protein expressions of Caspase-8, -9, -3, PARP and DFF45 were examined by western blot analysis. α-Tubulin has been used as loading control. Data are the mean or representative of at least three independent experiments.

microscopy after Hoechst 33342 staining, and degree of caspase activation and PARP cleavage were examined by Western blot analysis. After 24 h, nuclear pycnosis and fragmentation (karyorrhexis) (Fig. 3D), as well as cleavage of pro-caspase-8, -9 (weakly in FEMX-1 cells), and -3 and Poly(ADP-ribose) polymerase (PARP) (Fig. 2B) were observed in both cell lines. Lastly, DNA fragmentation factor 45 (DFF45), a caspase target, was cleaved in WM239, but not in FEMX-1 cells.

3.2. CD437 mediated apoptosis is dependent and partially independent of caspases in FEMX-1 and WM239 cells, respectively

To elucidate whether CD437-mediated apoptosis was dependent on caspase-activation, the pan-caspase inhibitor Z-VAD-fmk was added along with CD437. Caspase-inhibition prevented cleavage of PARP, as well as nuclear morphological changes in FEMX-1, but not in WM239 cells (Fig. 3). Furthermore, Z-VAD-fmk slightly reduced DNA-fragmentation in WM239 cells, but not in FEMX-1. Together, our results suggest that CD437 mediates apoptosis in a caspase-dependent and in part-independent manner in FEMX-1 and WM239 cells, respectively.

Apoptotic cells grown *in vitro* die by a process of secondary necrosis [18]. In both FEMX-1 and WM239 cells treated with CD437, addition of Z-VAD-fmk reduced the amount of extracellular oligonucleosomes, indicative of necrosis (Fig. 3C). The reduced necrotic index may suggest that the process of cellular death is more time consuming. Thus it appears that caspase activity speeds up the process of CD437 mediated death in both melanoma cell lines.

3.3. CD437 mediated up-regulation of ER associated CHOP mRNA and lysosomal protein cathepsin D

Previous studies have shown that CD437 may initiate apoptosis through both the release of lysosomal proteases (such as cathepsin D) into cytosol and ER stress signaling [19–21,34]. In the present study we observed a marked increase in cathepsin D protein expression in both cell lines after 48 h of treatment (Fig. 1F). To determine whether CD437 also induced ER-stress, the mRNA level of C/EBP homologous protein (CHOP), a gene highly induced at the transcriptional level as one of the major regulators of ER-stress mediated apoptosis, was examined (Fig. 1E). In FEMX-1 cells a slight increase was detected after 24 h, whilst in WM239 cells a profound induction of CHOP was observed as early as 3 h after CD437 addition. Together, these results suggest that CD437 trigger responses from both the lysosomes and ER in melanoma cells.

3.4. CD437 up-regulates the death receptors DR5 and FAS and act synergistically with lexatumumab to induce apoptosis

Activation of the extrinsic apoptotic pathway, leading to caspase-8 activation, is initiated through binding of ligands to death receptors on the cell surface. This, and our findings demonstrating

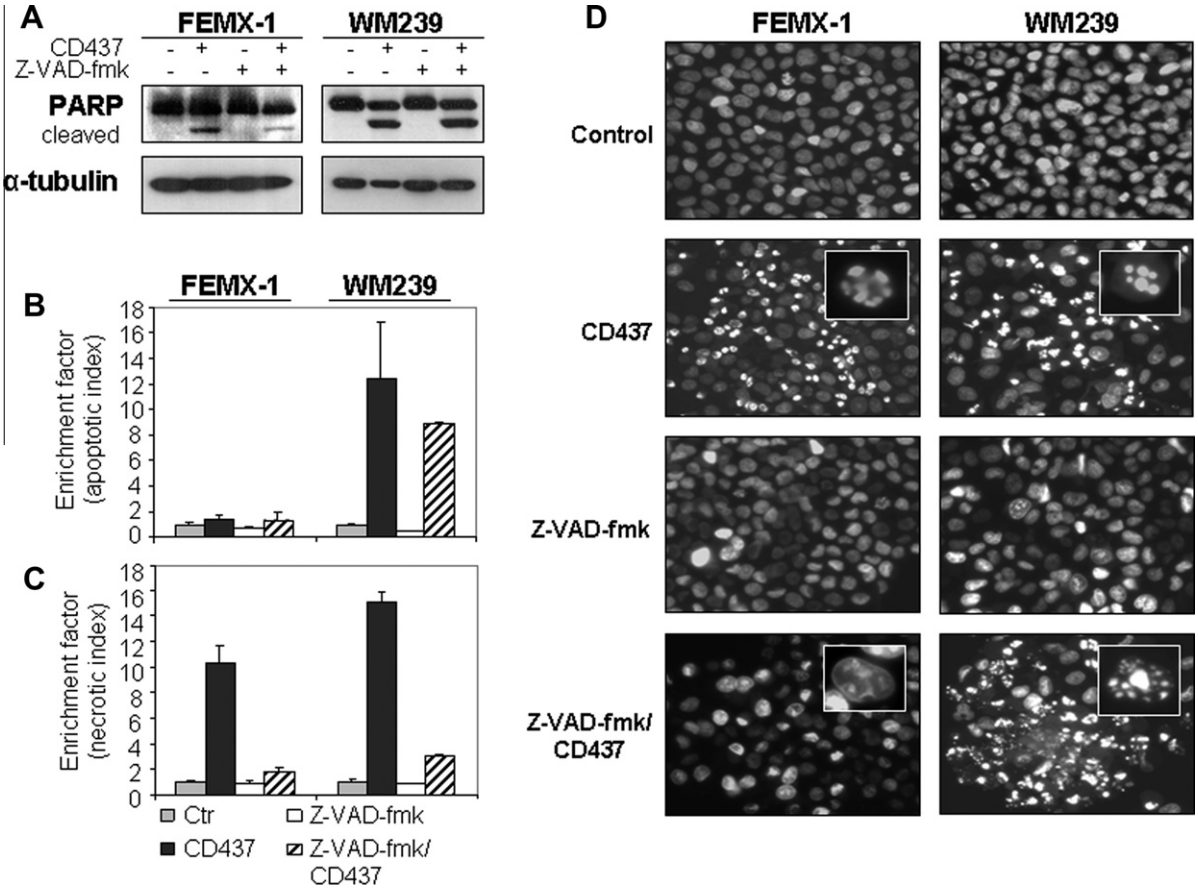

Fig. 3. Effects of caspase inhibition on CD437 mediated cell death. Cells were treated with CD437 (1 μM) for 48 h in the presence or absence of pan-Caspase inhibitor Z-VAD-fmk (50 μM, added simultaneously with CD437). (A) PARP-cleavage was determined by western blot analysis. α-Tubulin has been used as loading control. Relative amount of histone-associated-DNA-fragments (absorbance at 405nm relative the control; Enrichment factor), in the cytoplasm. (B) and in the extracellular fluid (C) were measured using a Cell death detection ELISA^{plus} kit. (D) Cell nuclei were stained with Hoechst 33342, and visualized by fluorescence microscopy. Insets show enlarged individual cell nuclei. Data are the mean or representative of at least three independent experiments.

caspase-8 cleavage following CD437 treatment, spurred us to examine if CD437 could up-regulate the expression of death receptors, thus sensitizing the cells to such signals. As shown in Fig. 4A, DR5 and FAS was constitutively expressed by both cell lines and were further induced by CD437. DR4, on the other hand, has previously been shown not to be expressed by WM239 and FEMX-1 cells [22], and CD437 did only vaguely induce its expression in FEMX-1, but not WM239 cells.

Based on these results, we next examined whether CD437 would sensitize the cells to treatment with agonistic TRAIL receptor-2 antibody (lexatumumab). All combination of the two drugs resulted in reduced cell viability, and had a clear synergistic effect, as demonstrated in both cell lines after 48 h (Fig. 4B and C). Furthermore, co-treatment resulted in increased PARP-cleavage, as well as enhanced activation of Caspase-3 and -8 in WM239 cells, compared to CD437 mono-treatment (Fig. 4D).

4. Discussion

In the present study, we demonstrated that CD437 caused cell cycle arrest and promoted apoptosis in the two melanoma cell lines FEMX-1 and WM239. The mechanisms leading to apoptosis differed, however, in regard to caspase-dependence and DNA-fragmentation. Furthermore, up-regulation of CHOP and cathepsin D suggests that ER and lysosomes, respectively, may play a role in CD437-mediated apoptosis. The diverse cellular targets of CD437 make it particularly eligible in terms of being a prototype for novel RRMs. Moreover, co-treatment with lexatumumab resulted in a synergistic reduction in cell viability, further highlighting the potential for combinational treatments.

In accordance with our findings showing S- and G1/S phase arrest in FEMX-1 and WM239 cells, respectively, numerous studies have demonstrated cell line specific cell cycle arrests following CD437 treatment [23–26]. The accompanying up-regulations of the cell cycle regulators p53 and $p21^{Waf1/Cip1}$, have also been found by others [27,25], and may account for the observed cell cycle arrests.

As has been reported also by others [4], CD437 induced apoptosis and caspase-cleavage in both cell lines. Caspase-mediated cleavage of endonuclease DFF45 causes release of DFF40, thus permitting its nuclear entry and generation of double-strand DNA-breaks [28]. However, although DNA-fragmentation is an indicator of apoptosis, this form of death may also occur in its absence [29]. In agreement with what has been reported by Risberg et al. [30],

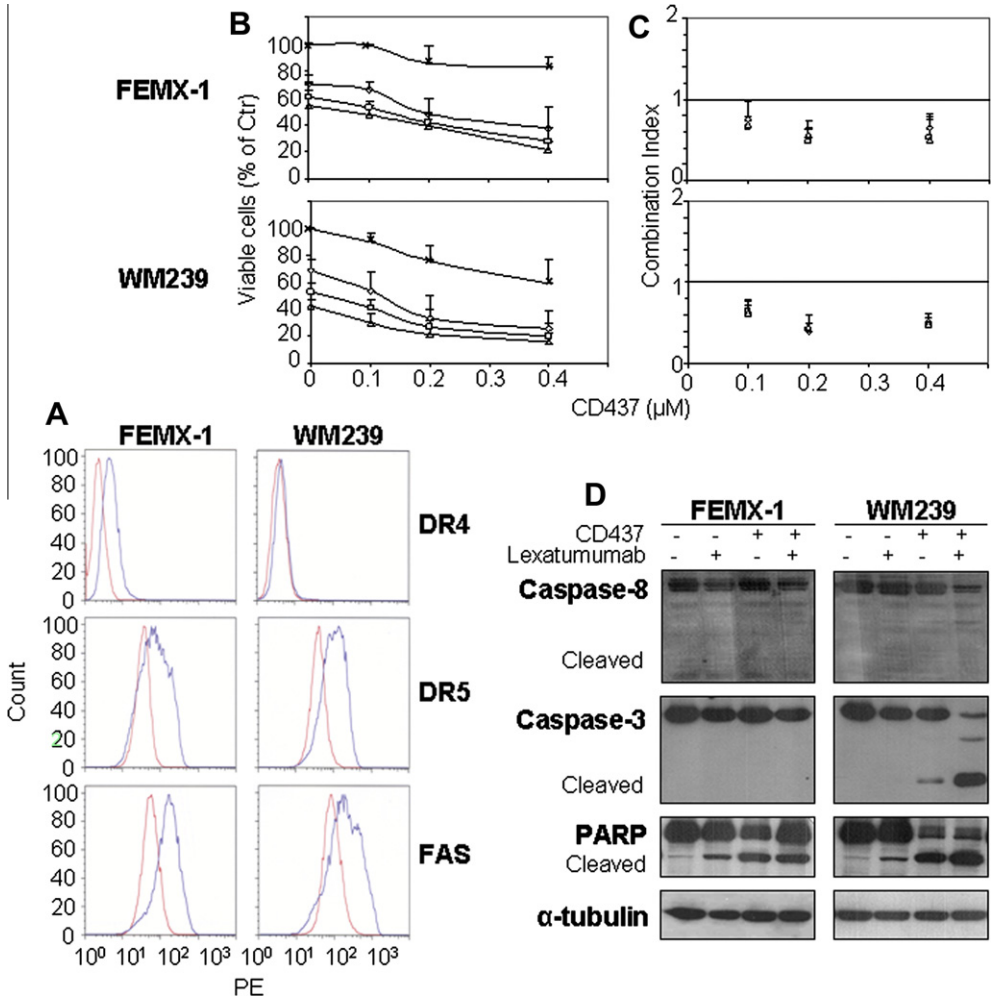

Fig. 4. CD437-induced increase of death receptors and combination with lexatumumab. (A) Death receptors DR4, DR5 and FAS were studied by flow cytometry. Blue lines indicate cells treated with CD437 for 24 h, and red lines represent control cells. (B) Cells were treated for 48 h with a combination of CD437 (indicated concentrations) and lexatumumab (crosses: 0.0 μg/mL, diamonds: 0.75 μg/mL, squares: 1.5 μg/mL and triangles: 3.0 μg/mL). Cell viability was measured by MTS assay, and presented with positive standard deviations. (C) The combination index was estimated by CalcuSyn, and indicates: <1 synergistic effect, 1 additive effect and >1 antagonistic effect. (D) Cells were treated with CD437 (0.2 μM) and/or lexatumumab (0.75 μg/mL) for 48 h. Protein cleavages of Caspase-8, Caspase-3 and PARP were assessed by western blotting. α-Tubulin has been used as loading control. Data are the mean or representative of at least three independent experiments. (For interpretation of the references to colour in this figure legend, the reader is referred to the web version of this article.)

apoptosis in FEMX-1 cells was not accompanied by DNA-fragmentation. In line with this, CD437 did not cleave DFF45 in this cell line.

Cleavage of pro-caspase-8, as seen in both cell lines, suggests that the extrinsic pathway of apoptosis has been activated. Similar results have been obtained by others [10,17]. Since CD437 itself has not been reported to activate extracellular receptors, we speculate whether retinoid-mediated up-regulation of DR5 and FAS may sensitize the cells to extracellular death signals thereby leading to activation of caspase-8. In support of this hypothesis, both cell lines exhibited increased expression of p53, an important transcription factor of the death receptors [31].

Despite caspase activation, inhibition by Z-VAD-fmk only partially reversed the apoptotic features imposed by CD437 in WM239 cells, suggesting a role of caspase-independent pathways. In contrast, CD437-mediated apoptosis appeared caspase-dependent in FEMX-1 cells. In accordance with our findings, Sun et al. [8] previously reported that CD437 could induce apoptosis both independently and dependently of caspases in human prostate carcinoma cells.

Whereas Z-VAD-fmk reversed the cleavage of PARP in FEMX-1, this was not the case in WM239 cells. In addition to caspases, cathepsins (B and D) may also cleave PARP into its apoptotic signature product of 89 kDa [32]. Cathepsin D is a lysosomal protease which upon lysosomal membrane permabilization is released into the cytoplasm and act as a key mediator of apoptosis [19]. Since CD437 increased cathepsin D protein expression in both cell lines, we speculate whether retinoid-mediated PARP cleavage in WM239 cells may primarily be performed by cathepsins. Emert-Sedlak et al. previously demonstrated that in VP-16 treated leukemia cells, cathepsin D was released into the cytosol independently of caspase inhibition, leading to apoptosis [33]. Furthermore, a lysosomal mediated apoptotic pathway involving cathepsin D has been suggested in leukemia cells treated with CD437 [34].

Moreover, two previous studies have shown that CD437 can initiate apoptosis through ER stress and subsequent increased expression of CHOP, a key protein involved in ER stress-mediated apoptosis and cell cycle arrest [20,35]. Increased expression of CHOP mRNA was found in both cell lines following treatment with CD437. Thus, it appears that CD437 activates apoptotic pathways through both lysosomes and ER in melanomas.

Co-treatment with suboptimal doses of CD437 and lexatumumab gave a synergistic reduction in viability in both cell lines. Similar results have been found by others [10]. The increased amount of DR5 following CD437 treatment may provide a rationale for this effect. Combinational treatment increased cleavage of PARP in WM239 cells, thus suggesting increased apoptosis. However, activation of caspase-8 was not detected in FEMX-1 at the concentrations used. It is thus possible that the observed synergistic effect may be the result of activation of caspase-10, another initiator caspase activated through the extrinsic pathway, or through other unknown mechanisms.

Together our results show that CD437 induces cell cycle arrest and apoptosis by targeting multiple cellular organelles, and appear to work at least partially independent of caspases in WM239 cells. When combined with lexatumumab a synergistic efficiency in terms of effect on viability was observed, suggesting a potential for targeted therapy. Knowledge of the molecular targets of CD437 may be of aid when designing more powerful and less toxic RRMs in the future, as well as for identifying rational combinations with other drugs.

Acknowledgments

This work was supported by grants from the South-Eastern Norway Regional Health Authority and The Norwegian Cancer Society. We also wish to acknowledge the technical assistance of G. Øy, Ø. Stakkestad and T. Stokke. Lexatumumab was kindly provided by Human Genome Sciences.

References

[1] G.M. Boyle, Therapy for metastatic melanoma: an overview and update, Expert Rev. Anticancer Ther. 11 (2011) 725–737.
[2] M. Pfahl, F.J. Piedrafita, Retinoid targets for apoptosis induction, Oncogene 22 (2003) 9058–9062.
[3] M.E. Huang, Y.C. Ye, S.R. Chen, J.R. Chai, J.X. Lu, L. Zhoa, et al., Use of all-trans retinoic acid in the treatment of acute promyelocytic leukemia, Blood 72 (1988) 567–572.
[4] J.A. Fontana, A.K. Rishi, Classical and novel retinoids: their targets in cancer therapy, Leukemia 16 (2002) 463–472.
[5] E. Garattini, M. Gianni, M. Terao, Retinoid related molecules an emerging class of apoptotic agents with promising therapeutic potential in oncology: pharmacological activity and mechanisms of action, Curr. Pharm. Des. 10 (2004) 433–448.
[6] C.A. Hsu, A.K. Rishi, X. Su-Li, T.M. Gerald, M.I. Dawson, C. Schiffer, et al., Retinoid induced apoptosis in leukemia cells through a retinoic acid nuclear receptor-independent pathway, Blood 89 (1997) 4470–4479.
[7] X. Zhao, K. Demary, L. Wong, C. Vaziri, A.B. McKenzie, T.J. Eberlein, et al., Retinoic acid receptor-independent mechanism of apoptosis of melanoma cells by the retinoid CD437 (AHPN), Cell Death Differ. 8 (2001) 878–886.
[8] S.Y. Sun, P. Yue, R. Lotan, Implication of multiple mechanisms in apoptosis induced by the synthetic retinoid CD437 in human prostate carcinoma cells, Oncogene 19 (2000) 4513–4522.
[9] S.Y. Sun, P. Yue, X. Chen, W.K. Hong, R. Lotan, The synthetic retinoid CD437 selectively induces apoptosis in human lung cancer cells while sparing normal human lung epithelial cells, Cancer Res. 62 (2002) 2430–2436.
[10] S.Y. Sun, P. Yue, W.K. Hong, R. Lotan, Augmentation of tumor necrosis factor-related apoptosis-inducing ligand (TRAIL)-induced apoptosis by the synthetic retinoid 6-[3-(1-adamantyl)-4-hydroxyphenyl]-2-naphthalene carboxylic acid (CD437) through up-regulation of TRAIL receptors in human lung cancer cells, Cancer Res. 60 (2000) 7149–7155.
[11] V.A. Florenes, C. Lu, N. Bhattacharya, J. Rak, C. Sheehan, J.M. Slingerland, et al., Interleukin-6 dependent induction of the cyclin dependent kinase inhibitor p21WAF1/CIP1 is lost during progression of human malignant melanoma, Oncogene 18 (1999) 1023–1032.
[12] O. Fodstad, I. Kjonniksen, S. Aamdal, J.M. Nesland, M.R. Boyd, A. Pihl, Extrapulmonary, tissue-specific metastasis formation in nude mice injected with FEMX-I human melanoma cells, Cancer Res. 48 (1988) 4382–4388.
[13] B.A. Bernard, J.M. Bernardon, C. Delescluse, B. Martin, M.C. Lenoir, J. Maignan, et al., Identification of synthetic retinoids with selectivity for human nuclear retinoic acid receptor gamma, Biochem. Biophys. Res. Commun. 186 (1992) 977–983.
[14] H.P. Dong, L. Kleinberg, I. Silins, V.A. Florenes, C.G. Trope, B. Risberg, et al., Death receptor expression is associated with poor response to chemotherapy and shorter survival in metastatic ovarian carcinoma, Cancer 112 (2008) 84–93.
[15] A. Slipicevic, K. Jorgensen, M. Skrede, A.K. Rosnes, G. Troen, B. Davidson, et al., The fatty acid binding protein 7 (FABP7) is involved in proliferation and invasion of melanoma cells, BMC Cancer 8 (2008) 276.
[16] T.C. Chou, Drug combination studies and their synergy quantification using the Chou–Talalay method, Cancer Res. 70 (2010) 440–446.
[17] E. Boisvieux-Ulrich, M. Sourdeval, F. Marano, CD437, a synthetic retinoid, induces apoptosis in human respiratory epithelial cells via caspase-independent mitochondrial and caspase-8-dependent pathways both up-regulated by JNK signaling pathway, Exp. Cell Res. 307 (2005) 76–90.
[18] M.T. Silva, V.A. Do, N.M. dos Santos, Secondary necrosis in multicellular animals: an outcome of apoptosis with pathogenic implications, Apoptosis 13 (2008) 463–482.
[19] S. Ivanova, U. Repnik, L. Bojic, A. Petelin, V. Turk, B. Turk, Lysosomes in apoptosis, Methods Enzymol. 442 (2008) 183–199.
[20] B. Liang, X. Song, G. Liu, R. Li, J. Xie, L. Xiao, et al., Involvement of TR3/Nur77 translocation to the endoplasmic reticulum in ER stress-induced apoptosis, Exp. Cell Res. 313 (2007) 2833–2844.
[21] Y. Watanabe, H. Tsuchiya, T. Sakabe, S. Matsuoka, Y. Akechi, Y. Fujimoto, et al., CD437 induces apoptosis in ovarian adenocarcinoma cells via ER stress signaling, Biochem. Biophys. Res. Commun. 366 (2008) 840–847.
[22] B.O. Engesaeter, M. Sathermugathevan, T. Hellenes, O. Engebraten, R. Holm, V.A. Florenes, et al., Targeting inhibitor of apoptosis proteins in combination with dacarbazine or TRAIL in melanoma cells, Cancer Biol. Ther. 12 (2011) 47–58.
[23] L. Farhana, M. Dawson, A.K. Rishi, Y. Zhang, B.E. Van, C. Trivedi, et al., Cyclin B and E2F–1 expression in prostate carcinoma cells treated with the novel retinoid CD437 are regulated by the ubiquitin-mediated pathway, Cancer Res. 62 (2002) 3842–3849.
[24] N. Hail Jr., R. Lotan, Synthetic retinoid CD437 promotes rapid apoptosis in malignant human epidermal keratinocytes and G1 arrest in their normal counterparts, J. Cell Physiol. 186 (2001) 24–34.

[25] Y. Li, B. Lin, A. Agadir, R. Liu, M.I. Dawson, J.C. Reed, et al., Molecular determinants of AHPN (CD437)-induced growth arrest and apoptosis in human lung cancer cell lines, Mol. Cell Biol. 18 (1998) 4719–4731.
[26] E. Parrella, M. Gianni, M. Fratelli, M.M. Barzago, I. Raska Jr., L. Diomede, et al., Antitumor activity of the retinoid-related molecules (E)-3-(4′-hydroxy-3′-adamantylbiphenyl-4-yl)acrylic acid (ST1926) and 6-[3-(1-adamantyl)-4-hydroxyphenyl]-2-naphthalene carboxylic acid (CD437) in F9 teratocarcinoma: Role of retinoic acid receptor gamma and retinoid-independent pathways, Mol. Pharmacol. 70 (2006) 909–924.
[27] S.Y. Sun, P. Yue, G.S. Wu, W.S. El-Deiry, B. Shroot, W.K. Hong, et al., Implication of p53 in growth arrest and apoptosis induced by the synthetic retinoid CD437 in human lung cancer cells, Cancer Res. 59 (1999) 2829–2833.
[28] P. Widlak, The DFF40/CAD endonuclease and its role in apoptosis, Acta Biochim. Pol. 47 (2000) 1037–1044.
[29] G. Kroemer, L. Galluzzi, P. Vandenabeele, J. Abrams, E.S. Alnemri, E.H. Baehrecke, et al., Classification of cell death: recommendations of the nomenclature committee on cell death 2009, Cell Death Differ. 16 (2009) 3–11.
[30] K. Risberg, O. Fodstad, Y. Andersson, The melanoma specific 9.2.27PE immunotoxin efficiently kills melanoma cells in vitro, Int. J. Cancer 125 (2009) 23–33.
[31] S. Haupt, M. Berger, Z. Goldberg, Y. Haupt, Apoptosis - the p53 network, J. Cell Sci. 116 (2003) 4077–4085.
[32] G.V. Chaitanya, A.J. Steven, P.P. Babu, PARP-1 cleavage fragments: signatures of cell-death proteases in neurodegeneration, Cell Commun. Signal. 8 (2010) 31.
[33] L. Emert-Sedlak, S. Shangary, A. Rabinovitz, M.B. Miranda, S.M. Delach, D.E. Johnson, Involvement of cathepsin D in chemotherapy-induced cytochrome c release, caspase activation, and cell death, Mol. Cancer Ther. 4 (2005) 733–742.
[34] Y. Zang, R.L. Beard, R.A. Chandraratna, J.X. Kang, Evidence of a lysosomal pathway for apoptosis induced by the synthetic retinoid CD437 in human leukemia HL-60 cells, Cell Death Differ. 8 (2001) 477–485.
[35] S. Oyadomari, M. Mori, Roles of CHOP/GADD153 in endoplasmic reticulum stress, Cell Death Differ. 11 (2004) 381–389.

Biochemical and Biophysical Research Communications 420 (2012) 523–529

Contents lists available at SciVerse ScienceDirect

Biochemical and Biophysical Research Communications

journal homepage: www.elsevier.com/locate/ybbrc

Chondroitin sulfate-E fine-tunes osteoblast differentiation via ERK1/2, Smad3 and Smad1/5/8 signaling by binding to N-cadherin and cadherin-11

Toshiyasu Koike [a], Tomomi Izumikawa [a], Jun-ichi Tamura [b], Hiroshi Kitagawa [a,*]

[a] Department of Biochemistry, Kobe Pharmaceutical University, Higashinada-ku, Kobe 658-8558, Japan
[b] Department of Regional Environment, Faculty of Regional Sciences, Tottori University, Tottori 680-8551, Japan

ARTICLE INFO

Article history:
Received 29 February 2012
Available online 13 March 2012

Keywords:
Cadherin
Chondroitin sulfate
Osteoblast differentiation
Proteoglycan
Signal transduction

ABSTRACT

Bone formation in the vertebrate skeleton occurs via the processes of endochondral and membranous ossification. Bone matrices contain chondroitin sulfate (CS) chains that regulate endochondral ossification. However, the function of CS in membranous ossification is unclear. Here, using preosteoblastic MC3T3-E1 cells we demonstrate that chondroitin sulfate-E (CS-E) promotes osteoblast differentiation by binding to both N-cadherin and cadherin-11. Differentiated MC3T3-E1 cells exhibited an increase in the total amount of CS and of E-disaccharide units of CS over time. In addition, CS-E polysaccharide, but not CS-A polysaccharide, bound to N-cadherin and cadherin-11 and enhanced osteoblast differentiation. In contrast, osteoblast differentiation was inhibited in chondroitinase ABC-digested MC3T3-E1 cells. Notably, CS-E polysaccharide and hexasaccharide activated intracellular signaling during osteoblast differentiation in non-contacting MC3T3-E1 cells, decreased ERK1/2 phosphorylation, and activated Smad3 and Smad1/5/8; these reactions were blocked by neutralizing antibodies against N-cadherin or cadherin-11, even though cell–cell adhesion is reported to be required for initiation of MC3T3-E1 cell differentiation. Furthermore, CS-E-unit overexpression in MC3T3-E1 cells increased adhesion of the cells to N-cadherin and cadherin-11, and promoted osteoblast differentiation. Collectively, these results suggest that CS-E is a selective ligand for the potential CS receptors, N-cadherin and cadherin-11, leading to osteoblast differentiation of MC3T3-E1 cells.

1. Introduction

Chondroitin sulfate (CS), a type of glycosaminoglycan, is present on the cell surface and in the extracellular matrix. CSs are attached to specific residues of core proteins and exist in the form of CS-proteoglycans. CS consists of the repeating disaccharide units of *N*-acetylgalactosamine (GalNAc) and glucuronic acid, and it has various structural modifications resulting from sulfation of different positions in the sugar residues [1–5]. It has recently become clear that bone disorders are caused by abnormal biosynthesis and sulfation of CS chains. For example, the cartilage of mice deficient in *CSGalNAcT1*, which is involved in CS synthesis [6,7], is significantly smaller than that of wild-type mice [8]. Type-II collagen fibers in the developing cartilage are abnormally aggregated and disarranged in the homozygous mutant mice. In addition, interference with chondroitin-4-*O*-sulfation causes spatial pathway-specific defects in the elaboration of morphogen signaling in the cartilage growth plate [4]. Moreover, deficiency in chondroitin-6-*O*-sulfation causes chondrodysplasia with major involvement of the spine [3]. Thus, the fine structure of CS chains plays important roles in bone development.

Bone formation in the vertebrate skeleton occurs via the processes of endochondral and membranous ossification. Bone matrices contain CS chains that regulate endochondral ossification. However, the mechanism underlying the involvement of CS in membranous ossification remains unclear. We therefore analyzed the function of CS chains in membranous ossification using cells of the mouse MC3T3-E1 osteoblastic cell line [9]. MC3T3-E1 cells produce increasing amounts of CS during differentiation into osteoblasts and depletion of CS delays differentiation [10]. The importance of cadherin-mediated cell–cell adhesion in such MC3T3-E1 cell differentiation is well established. Cadherin is a calcium-dependent cell adhesion molecule that is expressed in various types of tissues [11], and MC3T3-E1 cells express N-cadherin and cadherin-11, both of which regulate MC3T3-E1 differentiation [12,13]. We therefore hypothesized that the CS chains on the surface of MC3T3-E1 might bind to N-cadherin and/or cadherin-11 and modulate the differentiation of MC3T3-E1 cells. Here, we

Abbreviations: CS, chondroitin sulfate; ERK, extracellular signal-regulated kinase; CHase, protease-free chondroitinase ABC; ALP, alkaline phosphatase.

* Corresponding author. Address: 4-19-1 Motoyamakita-machi, Higashinada-ku, Kobe 658-8558, Japan. Fax: +81 78 4417571.
E-mail address: kitagawa@kobepharma-u.ac.jp (H. Kitagawa).

0006-291X/$ - see front matter © 2012 Elsevier Inc. All rights reserved.
http://dx.doi.org/10.1016/j.bbrc.2012.03.024

report that exogenous and endogenous CS-E do indeed promote osteoblast differentiation through control of ERK and Smad signaling pathways by binding to N-cadherin and cadherin-11.

2. Materials and methods

2.1. Materials

CS-A polysaccharide from whale cartilage, CS-E polysaccharide from squid cartilage, *Proteus vulgaris* chondroitinase ABC (EC 4.2.2.4), and protease-free *P. vulgaris* chondroitinase ABC (EC 4.2.2.20) were purchased from Seikagaku Corp. (Tokyo, Japan). The recombinant N-cadherin Fc chimera and the recombinant cadherin-11 Fc chimera were purchased from R&D Systems (Minneapolis, MN). The anti-N-cadherin antibody was purchased from Sigma. The anti-cadherin-11 antibody was purchased from Abcam. Antibodies against-extracellular signal-regulated kinase (ERK) 1/2, phospho-ERK1/2, Smad3, phospho-Smad3, Smad1, and phospho-Smad1/5/8 were purchased from Cell Signaling Technology (Boston, MA). CS-E hexasaccharide was chemically synthesized as described previously [14].

2.2. Cell culture

Mouse osteoblastic MC3T3-E1 cells were cultured in α-MEM containing 10% fetal bovine serum (FBS). For osteoblast differentiation, the cells were cultured in the presence of 100 mg/L ascorbic acid, 10 mM β-glycerophosphate and 10 nM dexamethasone.

2.3. Alkaline phosphatase (ALP) staining assays

Cultured cells were harvested on day 7. The culture medium was removed and the cells were washed with phosphate-buffered saline (PBS). The washed cells were incubated with 4% paraformaldehyde for 10 min on ice. The cells were then washed with PBS and incubated with ethanol/acetone (50:50 v/v) for 1 min at −20 °C. The stabilized cells were stained with 1-Step™ NBT/BCIP (Thermo Scientific) for 45 min at 37 °C and were observed under a fluorescence microscope.

2.4. Construction of the N-acetylgalactosamine 4-sulfate 6-O-sulfotransferase (GalNAc4S-6ST) expression vector, and establishment of cells stably expressing GalNAc4S-6ST

The cDNA fragment encoding *GalNAc4S-6ST* [15] was amplified using a 5′-primer (5′-ATAAGAATGCGGCCGCACTGGACTCCTCGAGG GCTG-3′) and a 3′-primer (5’-CCCAAGCTTTCCACGCTGTGGGTGAC AGT-3’) each containing a *Not*1 and a *Hind*III site. The polymerase chain reaction (PCR) was carried out with *KOD*-Plus DNA polymerase (TOYOBO, Osaka, Japan) for 30 cycles at 94 °C for 30 s, 56 °C for 30 s, and 68 °C for 90 s in 5% (v/v) DMSO. The PCR fragments were subcloned into the *Not*1 and *Hind*III sites of the pCMV expression vector (Invitrogen). The fidelity of the plasmid construct (pCMV-GalNAc4S-6ST) was confirmed by DNA sequencing. This expression plasmid (6 μg) was transfected into MC3T3-E1 cells on 100-mm plates using FuGENE 6 (Roche), according to the manufacturer's instructions. Transfectants were cultured in the presence of 800 μg/mL of G418. Transfected colonies were picked and propagated for experiments.

2.5. Quantitative real-time RT-PCR

Total RNA was extracted from MC3T3-E1 cells using TRIzolR reagent (Invitrogen). The cDNA was synthesized from 1 μg of total RNA using Moloney murine leukemia virus reverse transcriptase (Promega) and a random 9-mer primer (TaKaRa Bio Inc., Shiga, Japan). The primer sequences used were as follows: alkaline phosphatase, forward primer: 5′-CCTGACTGACCCTTCGC-3′ and reverse primer: 5′-GTCAAGGTGTCTTTCTGGGA-3′; GalNAc4S-6ST, forward primer: 5′-TATGACAACAGCACAGACGG-3′ and reverse primer: 5′-TGCAGATTTATTGGAACTTGCGAA-3′; and glyceraldehyde-3-phosphate dehydrogenase (GAPDH), forward primer: 5′-CATCTGAG GGCCCACTG-3′ and reverse primer: 5′-GAGGCCATGTAGGCCAT GA-3′. Quantitative real-time RT-PCR was performed using FastStart DNA Master plus SYBR Green I in a LightCycler ST300 (Roche). The expression levels of alkaline phosphatase and GalNAc4S-6ST mRNA were normalized to that of the GAPDH transcript.

2.6. Cell–cell adhesion assays

MC3T3-E1 and L cells were released from culture dishes by trypsin/EDTA digestion to obtain single cell suspensions, which were labeled with the membrane-permanent fluorescent dye PKH26 (2 mM). After washing in PBS to remove the excess dye, the labeled cells were laid on top of a confluent unlabeled monolayer of the same cell type in the presence of 3 mM $CaCl_2$ The labeled cells were allowed to settle for 30–60 min, nonadherent cells were gently washed away with PBS, and the number of fluorescent cells adherent to the cell substratum was counted from 10 microscope fields and was used as an index of cell–cell adhesion.

2.7. Cell-to-substrate adhesion assay

To assess the ability of MC3T3-E1 or L cells to bind to N-cadherin or cadherin-11, PKH26-labeled cells (1×10^4 cells/well) were plated in 4-well plates that had been coated with recombinant N-cadherin-Fc or cadherin-11-Fc (R&D Systems). Adhesion was allowed to continue for 30–60 min, after which non-adherent cells were gently washed away with PBS, and the number of fluorescent cells adherent to the substratum was counted from 10 microscope fields and was used as an index of cell–substrate adhesion.

2.8. Interaction analysis

The binding of CS-A or CS-E polysaccharide to N-cadherin or cadherin-11 was examined using the BIAcore J system (GE Healthcare), as described previously [16], with slight modifications. Briefly, recombinant N-cadherin-Fc or cadherin-11-Fc was immobilized on a CM5 sensor chip (GE Healthcare), according to the manufacturer's instructions. A series of CS-A or CS-E concentrations ranging from 20 to 400 nM in running buffer were applied to the flow cells, and changes in resonance units were recorded. Data were analyzed using BIAevaluation 3.0 software (GE Healthcare) using a 1:1 Langmuir binding model.

2.9. Protein extraction and western blot analysis

Cells were lysed with radioimmunoprecipitation buffer containing 0.5 mM phenylmethylsulfonyl fluoride, complete protease inhibitor mixture (Roche), 1% Triton X-100 and 1 mM sodium orthovanadate. Cell lysates were centrifuged at 12,000*g* for 20 min at 4 °C, and the supernatants were stored at −80 °C. Protein quantitate was performed using the bicinchoninic acid protein assay reagent (Pierce). Three micrograms of protein aliquots were denatured in SDS sample buffer and separated on 10% polyacrylamide–SDS gels. Proteins were transferred to polyvinylidene difluoride in 25 mM Tris, 192 mM glycine, and 20% methanol. Blots were blocked with 20 mM Tris–HCl (pH 7.6), 137 mM NaCl, 0.1% Tween 20 and 5% dried milk powder. The membranes were immunoblotted using primary antibodies against ERK1/2, Smad3, and Smad1/5/8. The antigen–antibody complexes were visualized

using the appropriate secondary antibodies (Sigma) and the enhanced chemiluminescence detection system as recommended by the manufacturer (GE Healthcare). The results depicted in Fig. 3 are representative of at least three separate cell preparations. Each experiment was repeated three times.

2.10. Disaccharide composition analysis of CS

CS from MC3T3-E1 cells was prepared as described previously [17]. The purified CS fraction was digested with chondroitinase ABC and the digests were then derivatized with 2-aminobenzamide and analyzed by HPLC as described previously [17].

3. Results and discussion

3.1. The E-unit of CS increases during MC3T3-E1 cell differentiation

To investigate the importance of CS chains for osteoblast differentiation, we analyzed CS disaccharide composition during the differentiation of MC3T3-E1 cells into osteoblasts. Differentiating MC3T3-E1 cells exhibited an increase in the total content of CS disaccharide over time (Fig. 1A). Additionally, the amount of ΔHexA-GalNAc(4-*O*-sulfate,6-*O*-sulfate) (CS-E-unit) markedly increased, that of ΔHexA-GalNAc and ΔHexA-GalNAc(4-*O*-sulfate) (CS-A-unit) decreased, and that of ΔHexA-GalNAc(6-*O*-sulfate) increased slightly as differentiation progressed (Fig. 1B and supplementary Table 1). These results suggest that CS-E chains may be important for MC3T3-E1 cell differentiation.

3.2. Endogenous CS chains and exogenous CS-E regulate osteoblast differentiation

To determine whether CS chains regulate osteoblast differentiation of MC3T3-E1 cells [10], the CS chains on the cell surface were removed using chondroitinase ABC (CHase) digestion and the extent of differentiation was then examined by analysis of ALP expression. Furthermore, since the CS-E-unit increases during MC3T3-E1 cell differentiation, MC3T3-E1 cell differentiation was analyzed after the addition of a CS-E polysaccharide that is E-unit-rich. ALP expression was significantly lower in MC3T3-E1 cells treated with CHase than in untreated cells (Fig. 1C, D). In contrast, addition of the CS-E polysaccharide elicited a marked increase in ALP expression compared to that of parental cells or to that of cells treated with CS-A polysaccharide (Fig. 1C, D), which is A-unit-rich and is the major disaccharide of MC3T3-E1 cells (Fig. 1B and Supplementary Table 1). These results suggest that CS chains on the MC3T3-E1 cell surface modulate osteoblast differentiation, and that exogenous CS-E can control this differentiation [10].

3.3. CS-E binds to N-cadherin and cadherin-11

It is well established that initiation of osteoblast differentiation in MC3T3-E1 cells is induced by adhesion between cells [9].

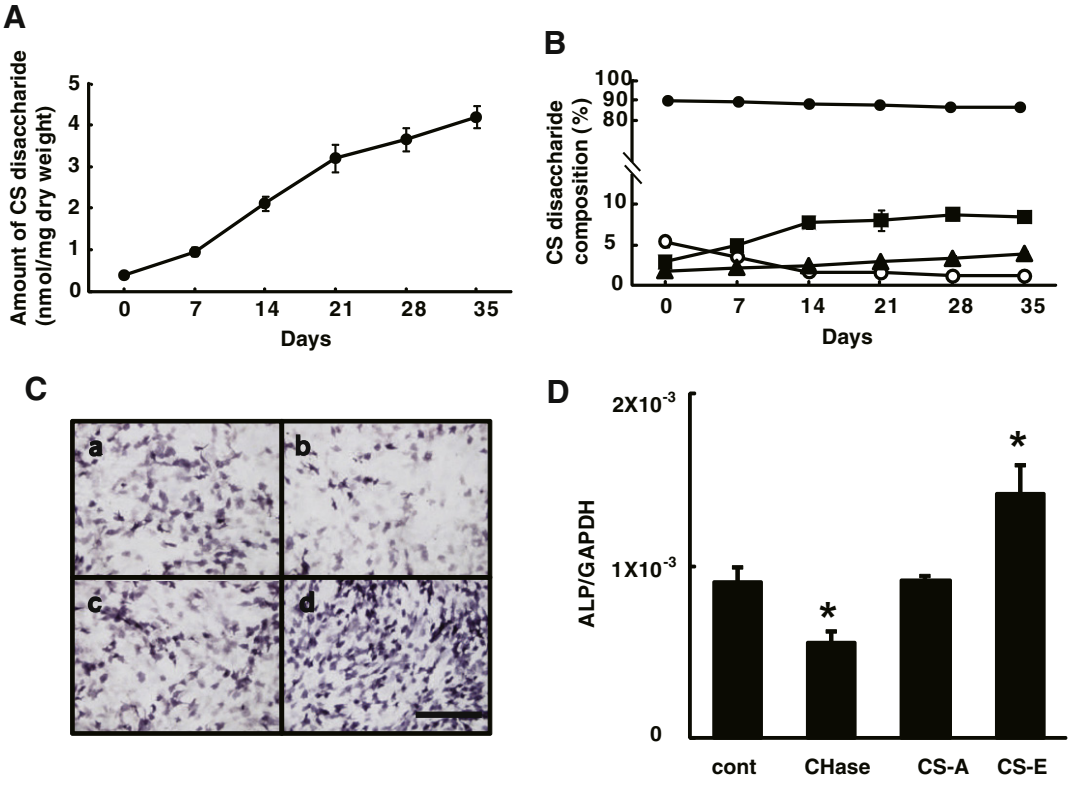

Fig. 1. Changes in CS in differentiating MC3T3-E1 cells and modulation of the differentiation by CSs. (A, B) MC3T3-E1 cells (4×10^5 cells/well) were cultured in growth medium in 10-cm plates. After 72 h, the medium was changed to fresh differentiation medium and the cells were cultured for a further 0–35 days. (A) Time course analysis of the total amount of CS disaccharides. Values are expressed as pmol of disaccharide per mg of dried cell homogenate. (B) Time course analysis of CS disaccharide composition. Values are expressed as mol% of dried cell homogenate. ΔHexA-GalNAc (open circles), ΔHexA-GalNAc(4S) (closed circles, CS-A-unit), ΔHexA-GalNAc(6S) (closed triangles), and ΔHexA-GalNAc(4S, 6S) (closed boxes, CS-E-unit) are shown. (C) MC3T3-E1 cells (5×10^4 cells/well) were cultured in growth medium in 6-well plates. After 48 h of culture, semi-confluent MC3T3-E1 cells were treated with one of the following agents for 24 h, and then the medium was changed to differentiation medium containing the same agent: (a) without or (b) with protease-free chondroitinase ABC (CHase, 30 mIU/mL), (c) with CS-A or (d) with CS-E (20 μg/mL each), and the cells were then stained for alkaline phosphatase (ALP) on day 7. *Scale bar* = 500 μm. (D) Cells treated as in (C) were analyzed for ALP mRNA expression using real-time RT-PCR and ALP-specific primers. Expression levels of ALP were normalized to those of GAPDH. Each *bar* represents the mean (+SE) of 3 determinations. $^*P < 0.05$ vs. control.

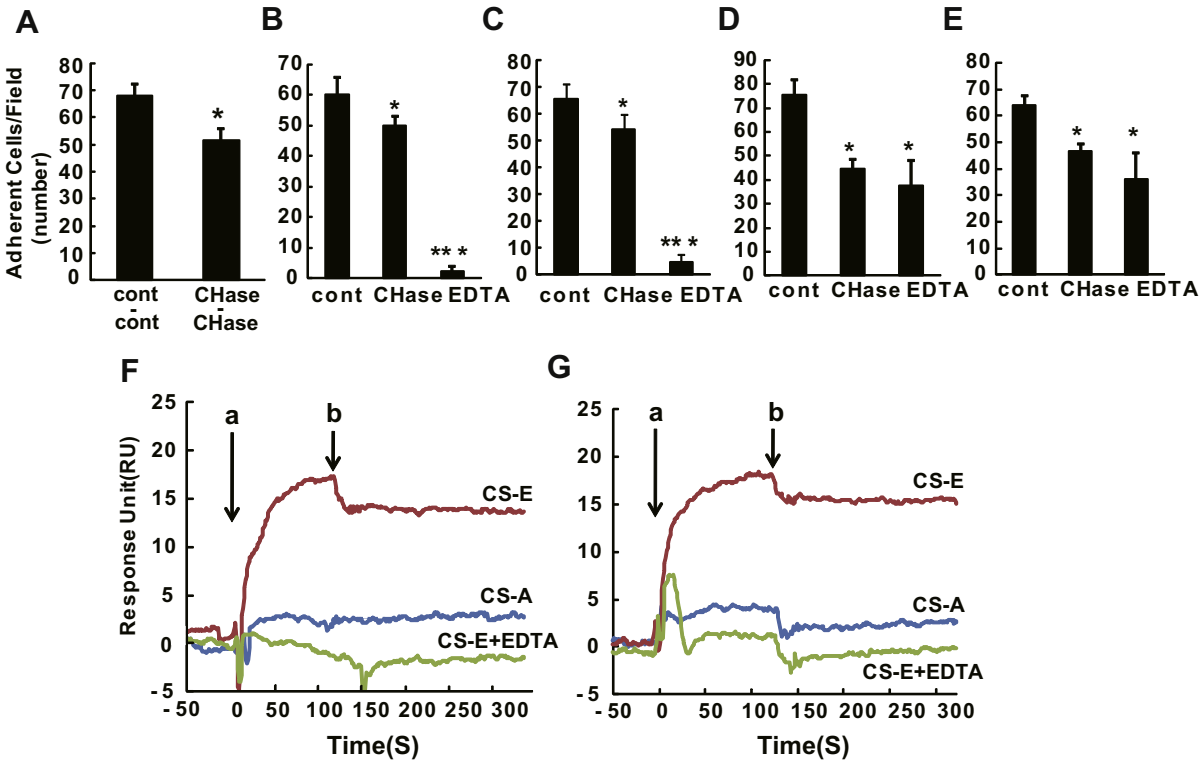

Fig. 2. CSs bind to N-cadherin and cadherin-11. (A) A suspension of fluorescence-labeled CHase-treated or control MC3T3-E1 cells was added to a monolayer of similarly treated cells. The number of cells adhering to the monolayer was assessed as a measure of cell–cell adhesion. (B–E) Adhesion of untreated (cont), CHase-digested, or EDTA-treated MC3T3-E1 cells (B, C) or L cells (lacking cadherins) (D, E) (1×10^4 cells/well) to recombinant N-cadherin-Fc (B and D, respectively) or cadherin-11-Fc (C and E, respectively). The number of MC3T3-E1 or L cells adherent to the substratum in 10 microscope fields was counted and was used as an index of cell–substrate adhesion. Each *bar* represents the mean (+SE) of 3 determinations. $^{*}P < 0.05$ vs. control, $^{***}P < 0.001$ vs. control. (F, G) CS-A polysaccharide and CS-E polysaccharide (400 nM) were individually injected over recombinant N-cadherin-Fc (F) or cadherin-11-Fc (G), which were immobilized on a sensor chip, in the presence of 3 mM $CaCl_2$ or 3 mM EDTA. The beginning of the association and dissociation phases is marked by the *arrows* a and b, respectively.

Therefore, the involvement of CS chains on the MC3T3-E1 cell surface in cell adhesion was investigated. We first analyzed the adhesion between untreated cells or CHase-digested cells. The adhesive ability of CHase-digested MC3T3-E1 cells was significantly lower than that of untreated cells (Fig. 2A), indicating that CS chains on the cell surface were involved in cell adhesion. Next, we sought to identify the proteins that bound to the CS chains on the MC3T3-E1 cell surface. The calcium-dependent cell–cell adhesion molecules N-cadherin and cadherin-11 are known to be involved in intercellular adhesion of MC3T3-E1 cells. We therefore analyzed the ability of untreated and CHase-treated MC3T3-E1 cells to bind to N-cadherin or cadherin-11. CHase-digested cells weakly bound to recombinant N-cadherin or cadherin-11, compared to untreated MC3T3-E1 cells (Fig. 2B, C). Furthermore, EDTA-treated MC3T3-E1 cells did not bind to N-cadherin or cadherin-11, suggesting that the interaction between CS chains on the surface of MC3T3-E1 cells and N-cadherin or cadherin-11 might be calcium-dependent (Fig. 2B, C). To further determine whether cell surface CS chains containing the E-unit do indeed bind to N-cadherin or cadherin-11, we took advantage of L cells, which lack N-cadherin and cadherin-11 expression [13] but which express CS-E-disaccharide units [18,19]. The adhesion of CHase-digested L cells to N-cadherin and cadherin-11 was significantly lower than that of untreated L cells (Fig. 2D, E). Furthermore, the binding of EDTA-treated L cells to N-cadherin and cadherin-11 was comparable to that of CHase-digested L cells (Fig. 2D, E). These results suggest that the CS chains on the cell surface are involved in cell–cell adhesion via interactions with N-cadherin and cadherin-11.

Next, to determine the type of CS involved in binding to N-cadherin and cadherin-11, we examined the interaction of CSs and cadherins using the surface plasmon resonance biosensor, BIAcore. CS-E polysaccharide bound strongly to N-cadherin (*Kd* = 25.6 nM) and to cadherin-11 (*Kd* = 50.0 nM) only in the presence of calcium (Fig. 2F, G, and Supplementary Fig. 1 and Table 2). In contrast, CS-A polysaccharide did not bind to N-cadherin or cadherin-11 in the presence of calcium. Thus, CS-E interacts with N-cadherin and cadherin-11 during calcium-dependent adhesion.

3.4. Endogenous CS chains activate intracellular signaling during cell–cell adhesion-induced MC3T3-E1 cell differentiation

The above results suggested that CS chains on the MC3T3-E1 cell surface controlled cell–cell adhesion. We therefore analyzed intracellular signaling to determine whether CS chains regulated osteoblast differentiation by binding to N-cadherin and cadherin-11. In MC3T3-E1 cells, the level of ERK1/2 phosphorylation decreases in response to N-cadherin-mediated adhesion [20]. Moreover, a reduction in ERK1/2 phosphorylation increases Smad3 activity [21]. Furthermore, phosphorylated Smad1/5/8 promotes the expression of osteoblastic differentiation markers such as alkaline phosphatase, by interacting with Smad3 [22]. Therefore, these intracellular signals were analyzed in untreated and CHase-digested MC3T3-E1 cells during cell adhesion. MC3T3-E1 cells treated with CHase exhibited an increase in ERK1/2 phosphorylation and a decrease in Smad3 and Smad1/5/8 phosphorylation compared to untreated MC3T3-E1 cells (Fig. 3A–C). Furthermore, ALP expression in CHase-treated MC3T3-E1 cells was lower than that in the untreated MC3T3-E1 cells (Fig. 3D). These results suggest that CS chains on MC3T3-E1 cells activate intracellular signaling during cell–cell adhesion-induced osteoblast differentiation.

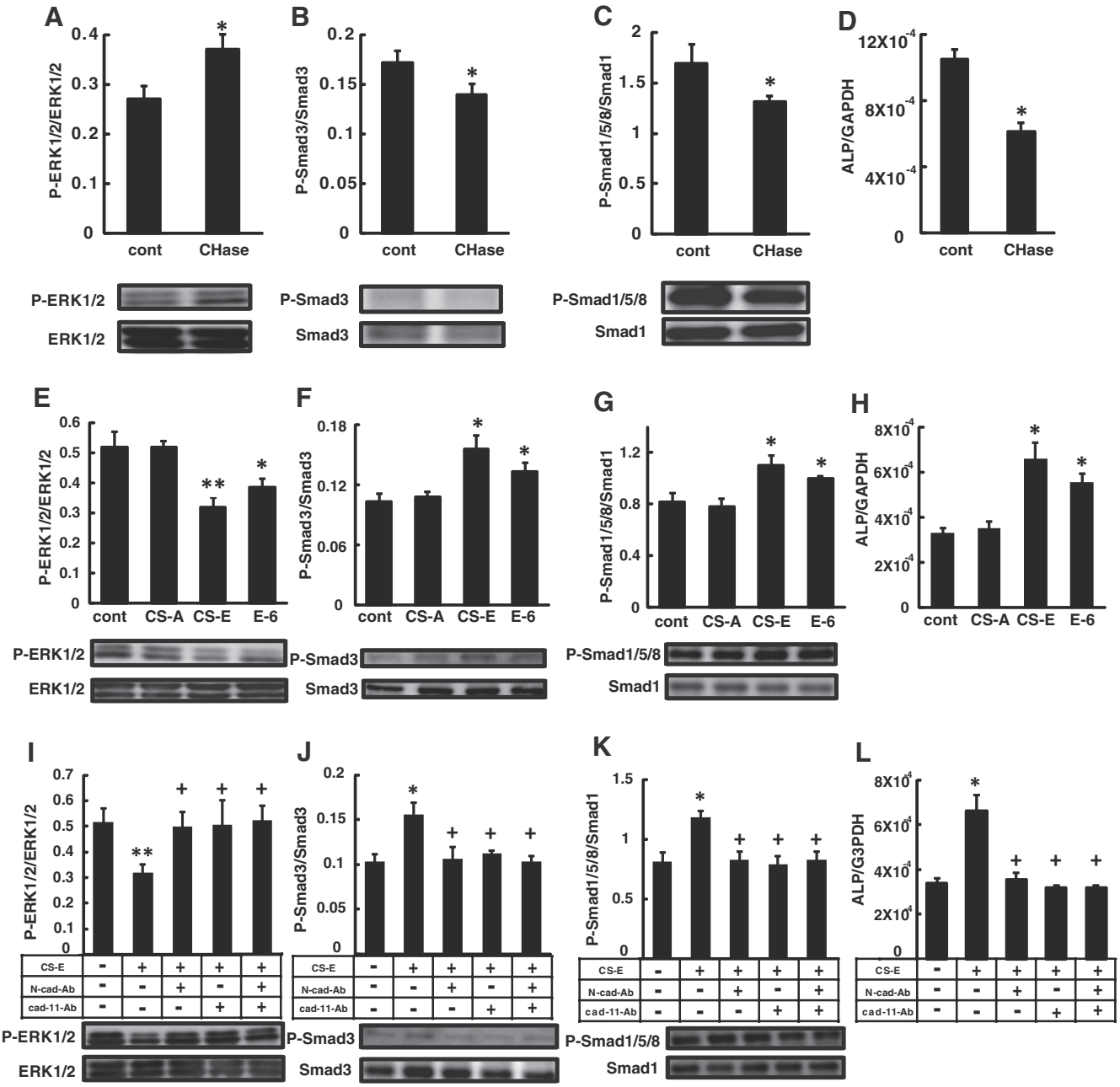

Fig. 3. CS-E modulates N-cadherin- and cadherin-11-mediated intracellular signaling (A–D) Semi-confluent MC3T3-E1 cells were treated with or without CHase and were cultured for 24 h until the cells attained confluence. (E–H) Semi-confluent MC3T3-E1 cells were treated with CS-A polysaccharide (CS-A), CS-E polysaccharide (CS-E) or CS-E hexasaccharide (E-6), and were cultured for 1 h. (I–L) Semi-confluent MC3T3-E1 cells were treated with or without anti-N-cadherin antibody and/or anti-cadherin-11 antibody for 1 h, followed by the addition of CS-E polysaccharide for 1 h. Proteins were extracted from the cells and analyzed by immunoblotting with anti-ERK1/2 and anti-phospho-ERK1/2 (A, E, I), anti-Smad3 and anti-phospho-Smad3 (B, F, J) or anti-Smad1 and anti-phospho-Smad1/5/8 (C, G, K) antibodies. (D, H, L) ALP mRNA expression was analyzed by real-time RT-PCR using ALP-specific primers and the mRNA levels were normalized to GAPDH mRNA. Each *bar* represents the mean (+SE) of 3 determinations. $^{*}P < 0.05$ vs. control or MC3T3-E1 cells without the addition of CS-E, $^{**}P < 0.01$ vs. control or MC3T3-E1 cells without the addition of CS-E, $^{+}P < 0.05$ vs. MC3T3-E1 cells treated with CS-E without the addition of any antibodies.

3.5. Exogenous CS-E activates intracellular signaling during osteoblast differentiation in non-contacting MC3T3-E1 cells by binding to N-cadherin and cadherin-11

Since it was clear from the above data that endogenous CS chains are involved in cell–cell adhesion and modulate osteoblast differentiation, we analyzed the regulation of cadherin adhesion-induced signaling by exogenous CS chains in non-contacting cells. Addition of CS-E polysaccharide or chemically synthesized CS-E hexasaccharide (E-6) to MC3T3-E1 cells decreased ERK1/2 phosphorylation and increased Smad3 and Smad1/5/8 phosphorylation and ALP expression (Fig. 3E–H and Supplementary Fig. 2). These effects are similar to the changes in signaling elicited by cell adhesion. In contrast, addition of CS-A polysaccharide did not alter intracellular signaling or ALP expression in MC3T3-E1 cells (Fig. 3E–H). These results indicate that exogenous CS-E activates intracellular signaling during osteoblast differentiation in non-contacting MC3T3-E1 cells.

We next analyzed whether the effect of exogenous CS-E on intracellular signaling during osteoblast differentiation was dependent on N-cadherin and cadherin-11, using neutralizing antibodies against N-cadherin and cadherin-11. In the presence of

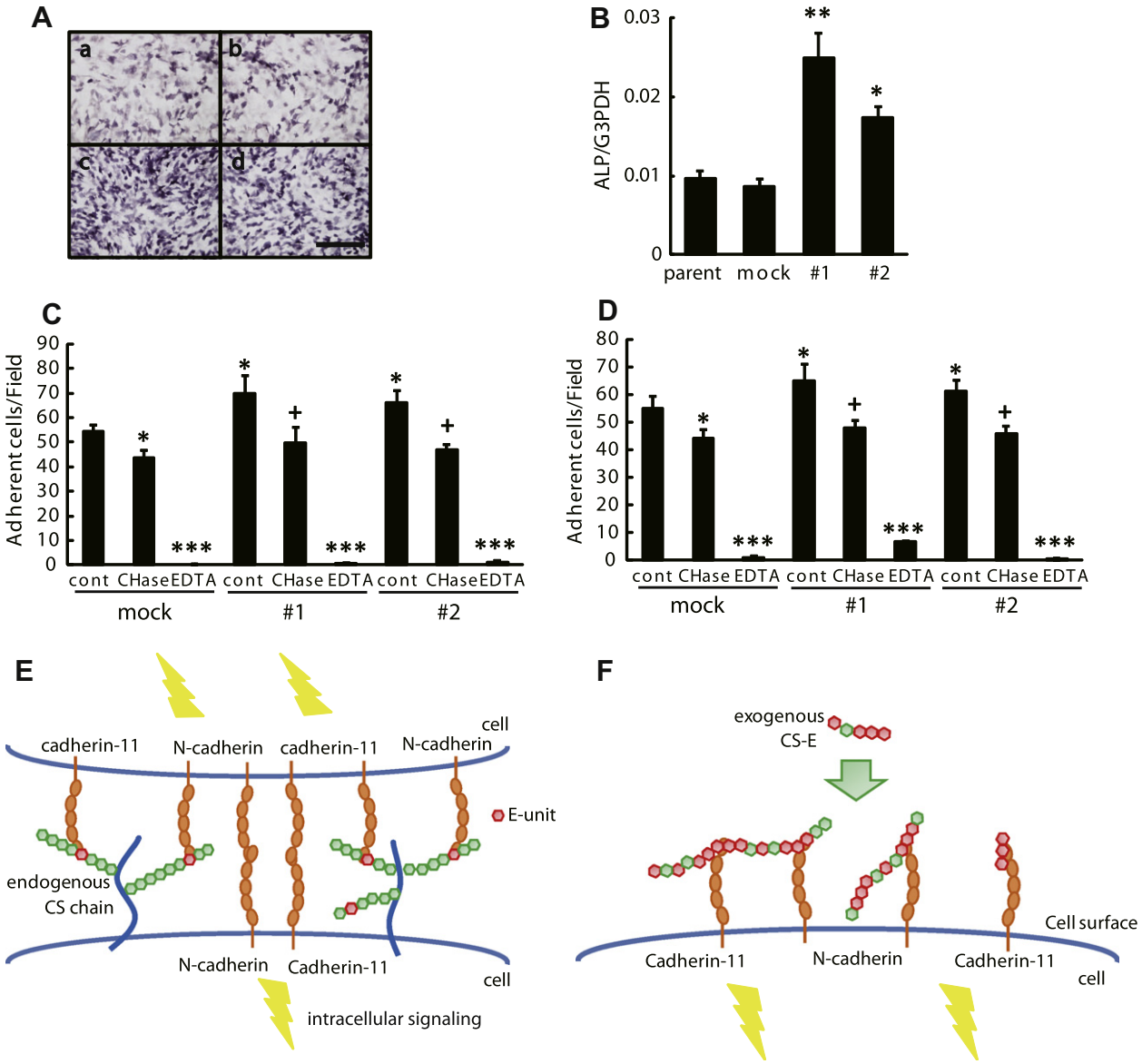

Fig. 4. The endogenous CS-E-unit regulates osteoblast differentiation in MC3T3-E1 cells. (A) Parental (a), mock (b), or *GalNAc4S-6ST*-overexpressing MC3T3-E1 cells (#1 and #2, c and (d) (5×10^4 cells/well) were cultured in growth medium in 6-well plates. After 72 h, the medium was changed to differentiation medium and the cells were stained for ALP on day 7. *Scale bar* = 500 μm. (B) ALP mRNA expression of the cells described in (A) was analyzed on day 7. The mRNA expression levels of ALP were normalized to those of GAPDH. (C, D) Adhesion of untreated (cont), CHase-digested, or EDTA-treated MC3T3-E1, #1, or #2 cells, or adhesion of mock-transfected cells (mock) to N-cadherin (C) or cadherin-11 (D). (E) Interaction between the endogenous E-unit of CS and N-cadherin and cadherin-11 on adjacent cells. (F) Interaction between the exogenous E-unit of CS and N-cadherin and cadherin-11 at the cell surface. The E-unit activates intracellular signaling during osteoblast differentiation by binding to both N-cadherin and cadherin-11. Each *bar* represents the mean (+SE) of 3 determinations. $^{*}P < 0.05$, $^{**}P < 0.01$, $^{***}P < 0.001$ vs. control MC3T3-E1 cells; $^{+}P < 0.05$ vs. control #1 or #2 cells.

anti-N-cadherin and/or anti-cadherin-11 neutralizing antibodies, exogenous CS-E polysaccharide did not alter intracellular signaling or ALP expression in MC3T3-E1 cells (Fig. 3I–L), suggesting that CS-E activates signaling and fine-tunes osteoblast differentiation by binding to both N-cadherin and cadherin-11.

3.6. The endogenous E-unit of CS regulates osteoblast differentiation

Finally, to confirm that the endogenous E-unit of CS chains was involved in osteoblast differentiation in MC3T3-E1 cells, we examined the extent of osteoblast differentiation in *GalNAc4S-6ST*-overexpressing MC3T3-E1 cells (#1 and #2) by analyzing ALP expression. GalNAc4S-6ST transfers sulfate to position 6 of the GalNAc(4-*O*-sulfate) residue, forming the E-unit. *GalNAc4S-6ST*-overexpressing MC3T3-E1 cells exhibited a 70–120% increase in GalNAc4S-6ST mRNA and a 44–77% increase in the amount of E-unit, ΔHexA-GalNAc(4-*O*-sulfate,6-*O*-sulfate), compared to parental or mock-transfected cells; the total amount of CS disaccharide was unchanged (Supplementary Table 3). Cell lines #1 and #2 exhibited increased ALP expression (Fig. 4A, B) and greater adhesion to N-cadherin and cadherin-11 compared to parental and mock-transfected cells (Fig. 4C, D). Furthermore, the adhesion of CHase-digested #1 and #2 cells to N-cadherin and cadherin-11 was almost equal to that of CHase-digested MC3T3-E1 cells. These results indicate that E-unit overexpression increases adhesion of MC3T3-E1 cells to N-cadherin and cadherin-11, and promotes osteoblast differentiation.

Osteoporosis, which is the most common bone disease, is a remodeling disease in which patients have a low bone mass with a high risk of fracture [23]. For every 10% of bone that is lost, the

risk of fracture doubles. This disease is caused by suppression of osteoblast activity. The results of the present study indicate that CS chains regulate osteoblast differentiation by binding to N-cadherin and cadherin-11 and that exogenous CS-E polysaccharide and hexasaccharides enhance osteoblast differentiation (Fig. 4E, F). Therefore, CS-E may act as an osteogenesis-promoting agent in patients with osteoporosis.

In conclusion, the findings from the present study not only elucidate a new mechanism of osteoblast differentiation, but may also prove useful in designing treatments for bone diseases such as osteoporosis.

Acknowledgments

This work was supported in part by a Grant-in-aid for Scientific Research-B #21390025 (to H.K.) from JSPS and for Scientific Research on Innovative Areas #23110003 (to H.K.) from MEXT, Japan.

Appendix A. Supplementary data

Supplementary data associated with this article can be found, in the online version, at http://dx.doi.org/10.1016/j.bbrc.2012.03.024.

References

[1] K. Sugahara, H. Kitagawa, Recently advances in the study of the biosynthesis and functions of sulfated glycosaminoglycans, Curr. Opin. Struct. Biol. 10 (2000) 518–527.
[2] H. Kitagawa, K. Tsutsumi, Y. Tone, K. Sugahara, Developmental regulation of the sulfation profile of chondroitin sulfate chains in the chicken embryo brain, J. Biol. Chem. 272 (1997) 31377–31381.
[3] H. Thiele, M. Sakano, H. Kitagawa, et al., Loss of chondroitin 6-*O*-sulfotransferase-1 function results in severe human chondrodysplasia with progressive spinal involvement, Proc. Natl. Acad. Sci. USA 101 (2004) 10155–10160.
[4] M. Klüppel, T.N. Wight, C. Chan, A. Hinek, J.L. Wrana, Maintenance of chondroitin sulfation balance by chondroitin-4-sulfotransferase 1 is required for chondrocyte development and growth factor signaling during cartilage morphogenesis, Development 132 (2005) 3989–4003.
[5] S. Miyata, Y. Komatsu, Y. Yoshimura, C. Taya, H. Kitagawa, Persistent cortical plasticity by upregulation of chondroitin 6-sulfation, Nat. Neurosci. 15 (2012) 414–422.
[6] T. Uyama, H. Kitagawa, J. Tamura, K. Sugahara, Molecular cloning and expression of human chondroitin *N*-acetylgalactosaminyltransferase: the key enzyme for chain initiation and elongation of chondroitin/dermatan sulfate on the protein linkage region tetrasaccharide shared by heparin/heparan sulfate, J. Biol. Chem. 277 (2002) 8841–8846.
[7] T. Izumikawa, T. Koike, H. Kitagawa, Chondroitin 4-*O*-sulfotransferase-2 regulates the number of chondroitin sulfate chains initiated by chondroitin *N*-acetylgalactosaminyltransferase-1, Biochem. J. 441 (2012) 697–705.
[8] Y. Watanabe, K. Takeuchi, S. Higa-Onaga, et al., Chondroitin sulfate *N*-acetylgalactosaminyltransferase-1 is required for normal cartilage development, Biochem. J. 432 (2010) 47–55.
[9] H. Sudo, H.A. Kodama, Y. Amagai, S. Yamamoto, S. Kasai, In vitro differentiation and calcification in a new clonal osteogenic cell line derived from newborn mouse calvaria, J. Cell. Biol. 96 (1983) 191–198.
[10] T. Miyazaki, S. Miyauchi, A. Tawada, et al., Oversulfated chondroitin sulfate-E binds to BMP-4 and enhances osteoblast differentiation, J. Cell. Physiol. 217 (2008) 769–777.
[11] M. Takeichi, Morphogenetic roles of classic cadherins, Curr. Opin. Cell. Biol. 7 (1995) 619–627.
[12] S.L. Cheng, C.S. Shin, D.A. Towler, R. Civitelli, A dominant negative cadherin inhibits osteoblast differentiation, J. Bone Miner. Res. 15 (2000) 2362–2370.
[13] I. Kii, N. Amizuka, J. Shimomura, Y. Saga, A. Kudo, Cell-cell interaction mediated by cadherin-11 directly regulates the differentiation of mesenchymal cells into the cells of the osteo-lineage and the chondro-lineage, J. Bone Miner. Res. 19 (2004) 1840–1849.
[14] J. Tamura, M. Tokuyoshi, Synthesis of chondroitin sulfate E hexasaccharide in the repeating region by an effective elongation strategy toward longer chondroitin oligosaccharide, Biosci. Biotechnol. Biochem. 68 (2004) 2436–2443.
[15] S. Ohtake, K. Kimata, O. Habuchi, A unique nonreducing terminal modification of chondroitin sulfate by *N*-acetylgalactosamine 4-sulfate 6-*O*-sulfotransferase, J. Biol. Chem. 278 (2003) 38443–38452.
[16] T. Mikami, D. Yasunaga, H. Kitagawa, Contactin-1 is a functional receptor for neuroregulatory chondroitin sulfate-E, J. Biol. Chem. 284 (2009) 4494–4499.
[17] T. Izumikawa, T. Koike, S. Shiozawa, K. Sugahara, J. Tamura, H. Kitagawa, Identification of chondroitin sulfate glucuronyltransferase as chondroitin synthase-3 involved in chondroitin polymerization: chondroitin polymerization is achieved by multiple enzyme complexes consisting of chondroitin synthase family members, J. Biol. Chem. 283 (2008) 27333–27343.
[18] S. Nadanaka, M. Ishida, M. Ikegami, H. Kitagawa, Chondroitin 4-*O*-sulfotransferase-1 modulates Wnt-3a signaling through control of E disaccharide expression of chondroitin sulfate, J. Biol. Chem. 283 (2008) 11396–11406.
[19] S. Nadanaka, H. Kinouchi, K. Taniguchi-Morita, J. Tamura, H. Kitagawa, Down-regulation of chondroitin 4-*O*-sulfotransferase-1 by Wnt signaling triggers diffusion of Wnt-3a, J. Biol. Chem. 286 (2011) 4199–4208.
[20] E. Haÿ, A. Nouraud, P.J. Marie, N-cadherin negatively regulates osteoblast proliferation and survival by antagonizing Wnt, ERK and PI3K/Akt signaling, PLoS One 4 (2009) e8284.
[21] H. Sowa, H. Kaji, T. Yamaguchi, T. Sugimoto, K. Chihara, Activations of ERK1/2 and JNK by transforming growth factor beta negatively regulate Smad3-induced alkaline phosphatase activity and mineralization in mouse osteoblastic cells, J. Biol. Chem. 277 (2002) 36024–36031.
[22] I. Hisa, Y. Inoue, G.N. Hendy, et al., Parathyroid hormone-responsive Smad3-related factor, Tmem119, promotes osteoblast differentiation and interacts with the bone morphogenetic protein-Runx2 pathway, J. Biol. Chem. 286 (2011) 9787–9796.
[23] G.A. Rodan, T.J. Martin, Therapeutic approaches to bone diseases, Science 289 (2000) 1508–1514.

Biochemical and Biophysical Research Communications 420 (2012) 530–535

Contents lists available at SciVerse ScienceDirect

Biochemical and Biophysical Research Communications

journal homepage: www.elsevier.com/locate/ybbrc

Evidence supporting the role of calpain in the α-processing of amyloid-β precursor protein

Huey T. Nguyen [a], Darrell R. Sawmiller [a], Qi Wu [a], Jerome J. Maleski [a], Ming Chen [a,b,*]

[a] Aging Research Laboratory, Bay Pines VA Medical Center, Bay Pines, FL 33744, USA
[b] Department of Molecular Pharmacology and Physiology, University of South Florida, Tampa, FL 33612, USA

ARTICLE INFO

Article history:
Received 28 February 2012
Available online 4 April 2012

Keywords:
Calpain
Aging
Amyloid
Calcium
Alzheimer's disease

ABSTRACT

Amyloid plaques are a hallmark of the aging and senile dementia brains, yet their mechanism of origins has remained elusive. A central issue is the regulatory mechanism and identity of α-secretase, a protease responsible for α-processing of amyloid-β precursor protein (APP). A remarkable feature of this enzyme is its high sensitivity to a wide range of cellular stimulators, many of which are agonists for Ca^{2+} signaling. This feature, together with previous work in our laboratory, has suggested that calpain, a Ca^{2+}-dependent protease, plays a key role in APP α-processing. In this study we report that overexpression of the μ-calpain gene in HEK293 cells resulted in a 2.7-fold increase of the protein levels. Measurements of intracellular calpain enzymatic activity revealed that the calpain overexpressing cells displayed a prominent elevation of the activity compared to wild-type cells. When the cells were stimulated by nicotine, glutamate or phorbol 12,13-dibutylester, the activity increase was even more remarkable and sensitive to calpeptin, a calpain inhibitor. Meanwhile, APP secretion from the calpain overexpressing cells was robustly increased under both resting and stimulated conditions over wild-type cells. Furthermore, cell surface biotinylation experiments showed that μ-calpain was clearly detected among the cell surface proteins. These data together support our view that calpain should be a reasonable candidate for α-secretase for further study. This model is discussed with an interesting fact that three other deposited proteins (tau, spectrin and crystalline) are also the known substrates of calpain. Finally we discuss some current misconceptions in senile dementia research.

Published by Elsevier Inc.

1. Introduction

Amyloid plaques and neurofibrillary tangles are the hallmarks of the aging as well as senile dementia brain, yet the mechanisms underlying their deposition have remained elusive. Amyloid plaques are made of amyloid-β peptide (Aβ), a proteolytic fragment of amyloid-β precursor protein (APP). In the young, APP is predominately processed by an α-processing pathway mediated by putative α-secretase, which generates the secreted form of APP (αAPPs or APPs) from the middle of the Aβ domain thus precluding the formation of Aβ. But in the aged brain, Aβ protein is somehow overly produced to form plaques. Thus it is of key importance to explain how such a shift of the processing pathways occur [1,2].

A number of studies have found that APP α-processing has declined during aging [3,4]. It has also been found that increase of APP α-processing through a wide variety of approaches is inevitably accompanied by a concomitant decrease of Aβ levels and *vice versa* [5–7], suggesting a reciprocal relationship between the two processing pathways which compete for the same APP pool. Based on these findings we have proposed that Aβ overproduction in the aged brain may result from an inefficient APP α-processing or decreased functionality of α-secretase, a model akin to the age-related cholesterol deposition resulting from an insufficient degradation of the lipids [8,9].

Along this line, the identity of α-secretase would be a central issue. Today, several proteases from a disintegrin and metalloprotease (ADAM) family, namely ADAM-9, ADAM-10 and ADAM-17 (TACE) are widely believed to be α-secretase [10–12] and have attracted most research interests. Nevertheless, apparent discrepancies exist among these proposals and they have not offered a systematic explanation for the mechanisms of plaque formation, e.g., how a metalloprotease activity could change during aging and how the change could lead to a selective deposition of Aβ, but not other substrates. It appears that further studies are required for resolving the issues and it may be important to keep an open mind for other models.

During the course of our studies, we have noticed that APP α-processing may be a Ca^{2+}-dependent process [8,9] and meanwhile work in our laboratory has found several lines of evidence to suggest that calpain, a Ca^{2+}-dependent protease, plays a key role in the process [13–15]. Calpain (EC 3.4.22.17) activity is regulated by Ca^{2+} and is widely thought to be involved in senile dementia but

* Corresponding author at: Department of Molecular Pharmacology and Physiology, University of South Florida, Tampa, FL 33612, USA.
E-mail address: ming.chen@va.gov (M. Chen).

0006-291X/$ - see front matter Published by Elsevier Inc.
http://dx.doi.org/10.1016/j.bbrc.2012.03.026

its precise roles there is unclear [16,17]. There are over a dozen isoforms in the calpain family, but only the two ubiquitous isoforms, μ- and *m*-calpains (calpain I and II), named by their sensitivity to the Ca^{2+} concentrations required for activation when tested *in vitro* [16], are most relevant to the ubiquitous APP processing.

2. Materials and methods

2.1. Materials

HEK293 and human skin fibroblast cells were purchased from ATCC (MD). Plasmid purification kit, ampicillin, geneticin, restriction enzymes Kpn I and Xho I were from QIAGEN (CA). Top 10 *Escherichia coli* strain, Lipofectamine 2000, agarose and precast SDS–PAGE gels were from Invitrogen (CA). Antibodies to N-terminus of APP, 22c11, the μ-calpain catalytic subunit, actin, integrin-α5, tau and fluorogenic cell-permeable calpain substrate (calpain substrate IV) were from EMD Millipore (CA). Dulbecco's modified Eagel's medium (DMEM), penicillin, streptomycin, nicotine, glutamate, phorbol 12,13-dibutylester (PDBu), calpeptin and other chemicals were all from Sigma–Aldrich (MO).

2.2. Methods

2.2.1. Construction of calpain I expression vector

The calpain expression vector pcDNA-CAPN I was generated by recombining pcDNA-DEST47 with pENTR-CAPN I following the manufacturer's instruction (Invitrogen, CA). The CAPN I gene was driven by a pCMV promoter. The resulting construct was introduced into Top 10 *E. coli* in the presence of 50 μg/ml ampicillin. The pcDNA-CAPN I construct-containing colonies were selected, amplified, and the construct was extracted, digested by Kpn I and Xho I and examined on 1.5% agarose gel.

2.2.2. Expressing μ-calpain gene in HEK293 cell

The pcDNA-calpain I construct was mixed with Lipofectamine 2000 (ratio: 0.8:2 μg/μg) for 20 min at RT. The construct was transfected into HEK293 at 50% confluence for 6 h. The calpain overexpressing cells were selected by incubating the cells in the presence of 400 μg/ml geneticin for 2 weeks. The stably-transfected colonies were allowed to propagate, the cells were harvested and lysed in a buffer (20 mM Tris, pH 7.2, 140 mM NaCl, 5 mM EGTA, 2 mM EDTA, 1× Sigma protease inhibitor cocktail and 1% Triton X-100). The cell lysates were analyzed by WB probed with an antibody to the μ-calpain catalytic subunit (EMD Millipore, CA).

2.2.3. Intracellular calpain activity assay

The calpain catalytic activity was measured *in situ* using a cell-permeable fluorogenic calpain substrate, (DABCYL)-TPLK∼SPPPS-PRE(EDANS)-RRRRRRR-NH_2 (calpain substrate IV, EMD, CA) [18]. Cells were subcultured in a 96-well cell culture plates (Corning, NY) in DMEM supplemented with 10% FBS, 1% penstrep and 400 μg/ml geneticin. At confluence, the medium was replaced with 100 μl Tyrodes buffer (140 mM NaCl, 4 mM KCl, 1 mM $MgCl_2$, 2 mM $CaCl_2$, 10 mM glucose, 10 mM HEPES, pH 7.4) and 10 μM calpain substrate IV was added. After preincubating for 20 min at 37 °C, the cells were treated with various reagents for 30 min at 37 °C, the fluorescence generated was measured in a BioTek FLX800 fluorescent plate reader using 360 nm excitation and 460 nm emission filters.

2.2.4. APP secretion assays

Cells were subcultured in the 12-well cell culture plates until confluence. The cells were preincubated in serum-free DMEM for 1 h and then incubated with various testing agents. After incubation for 2 h at 37 °C, 800 μl conditioned medium from each well was collected and cleared by centrifugation. Proteins in the conditioned medium were precipitated by the addition of 50 μl of 50% trichloroacetic acid containing 2 mg/ml bovine serum albumin. The samples were processed for WB utilizing a monoclonal antibody 22c11.

2.2.5. Biotinylation of cell surface calpain

The procedure used a surface protein biotinylation kit (Pierce, IL) according to the manufacturer's instruction. Cells were biotinylated with a cell-impermeable and cleavable bifunctional cross-linker (sulfo-NHS-SS-Biotin) and the labeled surface proteins were then affinity-purified. Cultured fibroblasts were cooled down to 4 °C and treated with 0.1 mM heparinase. The cells were incubated with sulfo-NHS-SS-Biotin for 30 min and lysed in the detergent-containing buffer (see above). The lysates were applied to a mini Avidin agarose column, washed 3× and eluted with a SDS–PAGE sample buffer containing 50 mM dithiothreitol. The flow-through and eluted fractions were collected separately, concentrated in a vacuum concentrator and analyzed by WB using antibodies to μ-calpain, integrin-α5 and tau, respectively.

2.2.6. SDS–PAGE and Western blotting

Precast SDS–polyacrylamide 4–20% gradient mini gels were used. Electrophoresis and Western blotting conditions were as described [19]. A near infrared dye-conjugated secondary antibody (Li-COR Biosci., NE) was used and the immunoreactive proteins were visualized with a Li-COR Odyssey Infrared Imaging System. The density of immunoreactive proteins was determined and values were calculated as band density multiplied by the area of the reactive proteins.

3. Results

3.1. Construction of calpain expression vector

The calpain expression vector pcDNA-CAPN I was generated by recombining pENTR-CAPN I and pcDNA-DEST47. The resulting construct was amplified, digested by restriction enzymes Kpn I and Xho I and examined on a 1.5% agarose gel. The construct after digestion appeared as a 2.6 kb band (Fig. 1A, arrow), which fits

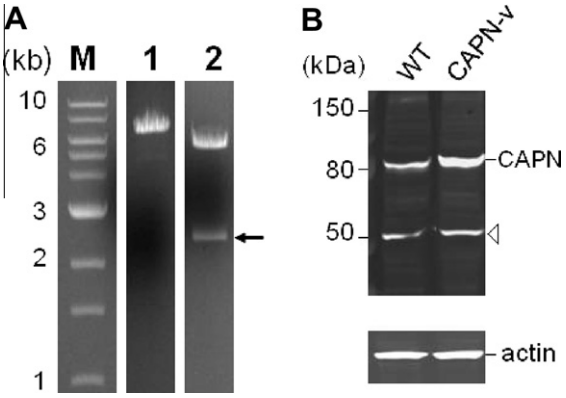

Fig. 1. Construction of the pcDNA-CAPN 1 vector and overexpression of μ-calpain. (A) The pcDNA-CAPN I construct was built by recombining pcDNA-DEST47 with pENTR-CAPN I. Lane M, 1 kb DNA ladder; lane 1, recombined pcDNA-CAPN I vector; lane 2, the pcDNA-CAPN I vector digested by Kpn I and Xho I; arrow, the calpain cDNA insert (2.6 kb). (B) Calpain overexpressing cells analyzed by WB with antibody to μ-calpain catalytic subunit. Lane 1, wild-type (WT) cells (empty vector); lane 2, pcDNA-CAPN I vector-transfected cells (CAPN-v). CAPN, μ-calpain (80 kDa); arrowhead, uncharacterized band (∼50 kDa). Lower panel, the filter probed with anti-actin antibody.

with the size of the calpain I catalytic subunit cDNA [16]. Expression of the construct in HEK293 cells resulted in a 2.7-fold increase of the μ-calpain band compared to the wild-type cells, as detected by Western blotting (Fig. 1B). Meanwhile, actin levels remained unchanged under the same conditions. The calpain overexpressing cells appeared to be stable for at least 6 months.

3.2. Measurement of calpain activity in situ

To confirm that calpain overexpressed in the HEK293 cells was functionally active, the enzymatic activity of calpain was measured *in situ* using a fluorogenic cell-permeable substrate. This peptide substrate is derived from the sequences of several calpain substrates and has an improved specificity to calpain [18]. The cells in the culture plate were allowed to react with the substrate for 30 min and the fluorescence generated was determined. Under the testing conditions, calpain activity in the overexpressing cells was remarkably increased over wild-type cells. As shown in Fig. 2, there was a 39.5% increase in the resting (basal) cells (compare bar 10 to 2). The increase of the enzyme activity was more prominent after the cells were stimulated with nicotine, glutamate and phorbol 12,13-dibutylester (PDBu), agents that are known for their intracellular Ca^{2+}-mobilizing effects [20–22]. These agents enhanced calpain activity to various degrees in wild-type cells (Fig. 2, WT), but exhibited much greater effects in the overexpressing cells (OE). As shown, nicotine (100 μM) increased calpain activity by 79.7% in these cells compared with wild-type cells (bars 11 to 3). At the same time glutamate (100 μM) and PDBu (1 μM) caused a 141.9% and 38.5% increase, respectively (compare bars 12 to 4, and 13 to 5). Thus, overexpressed μ-calpain appeared to be functionally active.

To confirm that the fluorescent signals measured in the assay were attributable to the activity of calpain, the cells were stimulated in the presence of calpeptin, a cell-permeable calpain inhibitor. Results showed that the stimulated enzyme activity by the reagents was blocked to various degrees by the inhibitor (Fig. 2, compare bars 6–8 to 3–5, and bars 14–16 to 11–13, respectively).

3.3. APPs secretion from the calpain overexpressing cells

To see if APPs secretion was affected in the calpain overexpressing cells, we determined APPs release from these cells in comparison with wild-type cells. Conditioned medium was collected after 2 h incubation and subjected to Western blotting analysis (Fig. 3A). Quantitative analysis of the APP bands revealed that APPs released from the overexpressing cells in the resting state was 65.9% greater than that from wild-type cells (Fig. 3B, compare bars 8 to 1). Upon stimulation with nicotine (100 μM), glutamate (100 μM) or PDBu (1 μM), which are also known for their APPs release-promoting effects [20–22], the overexpressing cells displayed an APPs increase of 85.3%, 53.3% and 34.4%, respectively, over wild-type cells (Fig. 3B, compare bars 9 to 2, 10 to 3, 11 to 4, respectively). Treatment of the cells with these agents in the presence of 50 μM calpeptin demonstrated that the stimulated APPs release from both cell types were partially or near-fully abolished (compare bars 5–7 to 2–4, and bars 12–14 to 9–11, respectively). Thus, APPs release from the calpain overexpressing cells was increased and sensitive to calpeptin.

3.4. Biotinylation of calpain at cell surface

Calpain is known as an intracellular protease active in the cytosol or at the inner site of the membranes [16]. To see if it can also be found at the cell surface where APP α-processing takes place, we biotinylated the cultured cells with a bifunctional cross-linker, which is cell-impermeable and labels only the cell surface proteins. The biotinylated proteins were then affinity-separated on an Avidin column and analyzed by Western blotting for calpain. As shown, μ-calpain was clearly detected in the eluted (bound) fraction after biotinylation (Fig. 4, left panel), but not in the same fraction of untreated cells (right panel), indicating that calpain was among the cell surface proteins. Notably, however, integrin-α5, a cell surface protein used as positive control, was also detected in the eluted faction, but tau, a cytosolic protein, was not (Fig. 4).

4. Discussion

4.1. The role of calpain in APP processing

In this study we demonstrated that overexpression of μ-calpain in HEK293 cells resulted in a pronounced increase of APPs secretion over wild-type cells, and that the effect is concurrent with an elevation of the enzymatic activity of calpain. Furthermore,

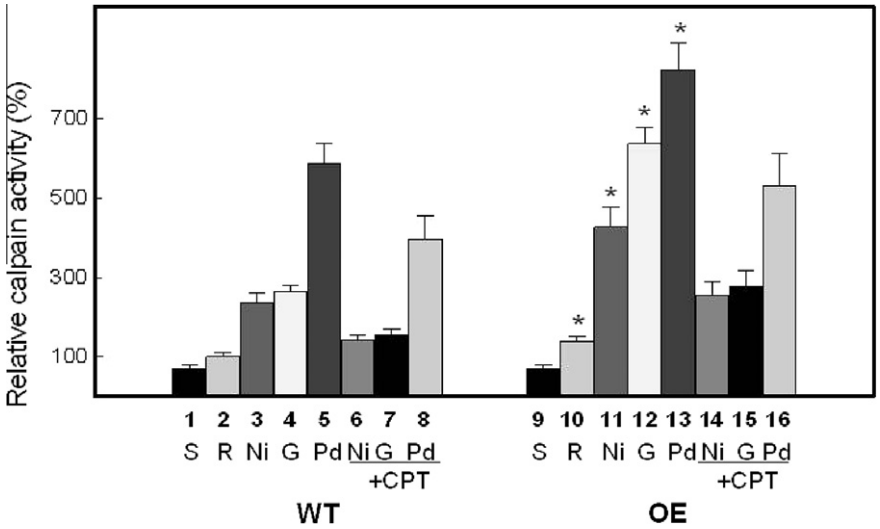

Fig. 2. Intracellular calpain activity in the calpain overexpressing and wild-type cells. Intracellular calpain activity was measured in wild-type (WT) and calpain overexpressing (OE) cells using a fluorogenic substrate. Cells were in the resting state (R) or stimulated by 100 μM nicotine (Ni), 100 μM glutamate (G) or 1 μM PDBu (Pd). The treatments with the agents in the presence of 50 μM calpeptin (CPT) were indicated. Values are percentage over control (means ± SE, $n \geqslant 3$); $^{*}p < 0.001$, versus corresponding data (bars 2–5) in the WT panel. Student's two-tailed *t*-test. S, substrate alone.

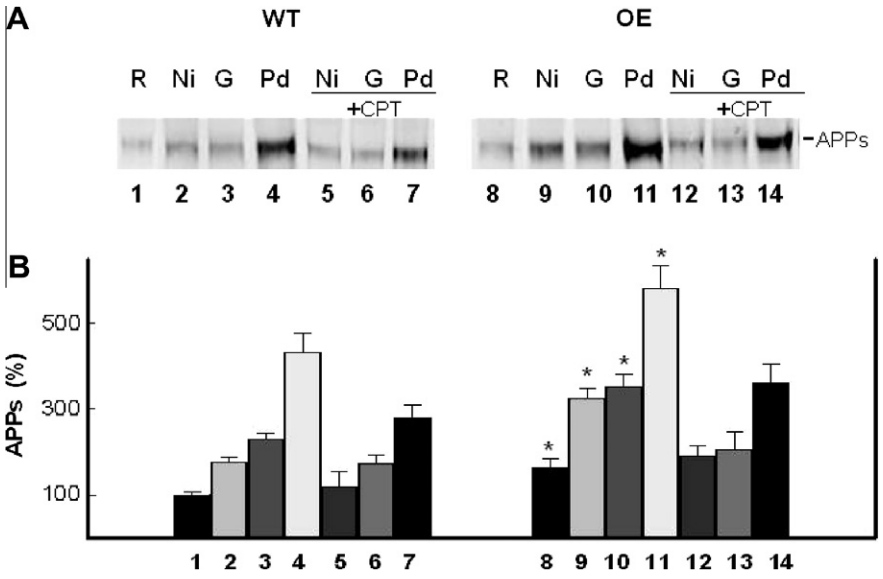

Fig. 3. APPs secretion from calpain overexpressing and wild-type cells. APPs released from wild-type (WT) or calpain overexpressing (OE) cells were analyzed by Western blotting with antibody to APPs. The cells were either in the resting state (R) or stimulated by 100 μM nicotine (Ni), 100 μM glutamate (G) or 1 μM PDBu (Pd). Experiments conducted in the presence of 50 μM calpeptin (CPT) were indicated. (B) Quantitative analysis of the scanning densitometry of the immunoreactive proteins in (A). Values are percentage changes (means ± SE, $n \geqslant 5$); $^{*}p < 0.05$, versus corresponding data (bars 1–4) in the WT panel. Student's two-tailed t-test.

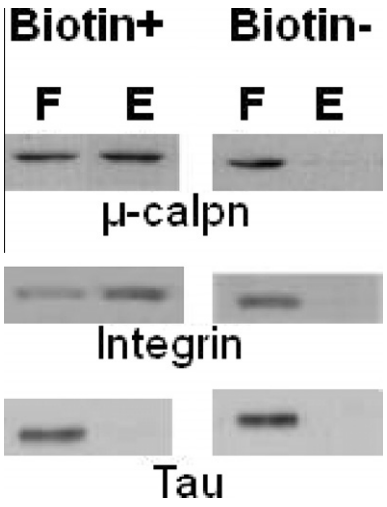

Fig. 4. Biotinylation of cell surface calpain. Cultured cells were first treated with heparinase and then biotinylated (Biotin+) or untreated (Biotin−). After treatment, the cells were dissolved with detergent and labeled proteins were affinity separated on an Avidin column. The flowthrough (F) and eluted (E) fractions were collected separately, then concentrated and analyzed by Western blotting with antibodies to μ-calpain (μ-calpain), integrin-α5 (integrin) and tau, respectively.

detection of μ-calpain at the cell surface by biotinylation suggests that calpain is not only active intracellularly, but also can be at least partially found at the plasma membrane surface of the cell, a finding that is consistent with several previous reports that calpain can be found at the platelet cell surface [23–25]. Taken together, these results provide additional support to our contention that calpain should be considered a reasonable candidate for α-secretase. Clearly, additional studies are required to validate this model, and such studies should determine whether calpain will meet all features of α-secretase [26].

Because other proteases have also been considered as α-secretase and each of them is supported by a substantial body of experimental evidence [10–12], this area of research remains controversial. At this point, however, a consideration from a broader background would perhaps be helpful.

4.2. The regulated nature of APP α-processing

APP α-processing is highly sensitive to a wide range of regulatory agents, most notably growth factors, excitatory neurotransmitters, muscarinic receptor agonists, IP_3, protein kinase C (PKC) activators, hormones and cytokines, and the processing activity is dose-dependent (see Refs. [8,9]). Such sensitivity to so many signal pathways would suggest that APP α-processing is a *regulated* process, or α-secretase a *regulated* protease, one whose catalytic activity *in vivo* fluctuates rapidly and dramatically in response to cellular signals. Since calpain is perhaps the only known protease that is truly regulated by a signal transduction cascade [16], it is plausible to think that this enzyme would receive particular research attention.

Further, upon a systematic analysis of the reported data, we noticed that many of the agents that promote APPs secretion also activate intracellular Ca^{2+}, whereas those which decrease APPs release also inhibit Ca^{2+} [8,9]. As Ca^{2+} appears to be a common denominator of the agents, these reports would be uniformly explained if APP α-processing is assumed to be a Ca^{2+}-dependent process, or α-secretase to be a Ca^{2+}-dependent protease [9,26].

The following findings further support this model. First, APP a-processing is sensitive to oxidative stress (Chen et al., unpublished data), a feature shared by calpain [27]. Second, APP α-processing is also energy-dependent [28], a feature consistent with that of the Ca^{2+} signaling system. Third, calpain isoforms have been implicated in the neuronal secretory process [29]. Fourth, the α-secretase-cleaving site on APP, i.e., the Lys-Leu bond at the 16–17 site of Aβ, is identical to an actual cleavage site on PKC, a known calpain substrate [30]. And fifth, infusion of a calpain inhibitor into rat brain has resulted in accumulation of Aβ or Aβ-containing fragments [31,32].

4.3. Why are calpain substrates selectively deposited?

Perhaps the most intriguing observation that corroborates our model comes from a remarkable but largely overlooked fact. That

is, three other proteins that are also deposited, namely tau, spectrin and β-crystalline (in cataracts) [33–35], are well-known substrates of calpain [16,33–35]. A challenging question is: why do calpain substrates selectively deposit during natural aging?

If this is not a coincidence and may not be explained by current models such as protein misfolding or autophagy, then it would be important to conceive that there may be some unique and as-yet-unidentified attributes in calpain that may hold a clue to this mind-boggling question. Along this line we propose a novel model for discussion.

Controlled by the Ca^{2+} signaling cascade in response to physiological demands, calpain's action would be unique in that it is not only specific, but also "exclusive" (meaning no other protease will act at the same sites of its substrates). This is because otherwise the signal transduction cascade would be disrupted (imagine what will happen if PKC is cleaved and activated by other proteases at the same site). For this reason, if calpain activity is diminished during aging, its substrates will not be attacked by other proteases and thus deposit – but other proteins will not.

This means that perhaps only calpain substrates (fragments) will deposit, and APP may be merely another one of them. And it also means that the functional state of α-secretase is the primary determinant, or rate-limiting factor, for the Aβ levels, to which other proteases play only secondary roles [9]. This is akin to cholesterol deposition being solely determined by the functional state of its normal degradation, i.e., there may not be a cholesterol "depository" pathway at all. While this challenging model awaits scrutiny and testing, it appears that thinking along this line may lead to a new frontier of study.

4.4. Misconceptions in senile dementia studies

As a matter of fact, APP α-processing has long been linked to Ca^{2+} by several research groups. For example, Baxbaum et al. have shown that a Ca^{2+} pathway is definitively involved in the α-processing of APP [36]. Wolf et al. have repeatedly reported that various muscarinic and glutamatergic agonists promote APPs release with concomitant Ca^{2+} activation [21,37]. Given such compelling evidence, together with many other supporting data [8,9 and references therein], one wonders: why has the regulatory mechanism of α-processing remained a conundrum today?

We think this may relate to the current "calcium overload/activation" hypothesis [38], a problematic theory that is based on measurements of Ca^{2+} "levels" rather than its *functionality* and on studies of "cell death" rather than the *natural aging* process, as we have scrutinized extensively [39]. Under this theory, Ca^{2+} and calpain, two indispensable factors for life and cognition, have been viewed as "destructive" and should be "blocked" in the elderly, like vicious pathogens. But due to its dominant status, other mechanisms would have to be found to explain APP α-processing (for review, see Ref. [12]) and the list is still growing. Such a *diverging* trend should be a concern to us since a healthy one is *converging* (approaching to a consensus). A synthesis of the data into a coherent theory is critically needed today.

But a fundamental question is: how can an unproven hypothesis become dominate for so long without being subject to the self-correcting mechanisms of science? We now think that the ultimate problem is the institutional definition of senile dementia as a curable disease (Alzheimer's disease) [40]. This politically correct definition has, among other things, excluded natural aging as its root cause, thereby allowing various "erroneous" pathway-based concepts such as "calcium overload/activation" hypothesis to prevail [40].

It thus appears that a paradigm shift is needed for understanding the true origins of the plaques during natural aging. In this regard, it is worth noting that our "Ca^{2+}/calpain functional deficits" model may coherently and mechanistically explain plaques, tangles and cognitive inefficiency, the three hallmarks of the aging brain that are related to senile dementia[9].

Acknowledgment

This work is supported by the U.S. Department of Veterans Affairs Administration.

References

[1] D.J. Selkoe, Cell biology of protein misfolding: the examples of Alzheimer's and Parkinson's diseases, Nat. Cell Biol. 6 (2004) 1054–1061.
[2] J. Kang, H.G. Lemaire, A. Unterbeck, et al., The precursor of Alzheimer's disease amyloid A4 protein resembles a cell-surface receptor, Nature 325 (1987) 733–736.
[3] M.R. Palmert, M. Usiak, R. Mayeux, et al., Soluble derivatives of the beta amyloid protein precursor in cerebrospinal fluid: alterations in normal aging and in Alzheimer's disease, Neurology 40 (1990) 1028–1034.
[4] L. Lannfelt, H. Basun, L.O. Wahlund, et al., Decreased alpha-secretase-cleaved amyloid precursor protein as a diagnostic marker for Alzheimer's disease, Nat. Med. 1 (1995) 829–832.
[5] M.J. Savage, S.P. Trusko, D.S. Howland, et al., Turnover of amyloid beta-protein in mouse brain and acute reduction of its level by phorbol ester, J. Neurosci. 18 (1998) 1743–1752.
[6] J.S. Jacobsen, M.A. Spruyt, A.M. Brown, et al., Sonnenberg-Reines, The release of Alzheimer's disease beta amyloid peptide is reduced by phorbol treatment, J. Biol. Chem. 269 (1994) 8376–8382.
[7] A.Y. Hung, D.J. Selkoe, Selective ectodomain phosphorylation and regulated cleavage of beta-amyloid precursor protein, EMBO J. 13 (1994) 534–542.
[8] M. Chen, Alzheimer's a-secretase may be a calcium-dependent protease, FEBS Lett. 417 (1997) 163–167.
[9] M. Chen, H.L. Fernandez, Where do Alzheimer's plaques and tangles come from? Aging-induced protein degradation inefficiency, Front. Biosci. 6 (2001) e1–e11.
[10] J.D. Buxbaum, K.N. Liu, J.L. Slack, et al., Evidence that tumor necrosis factor alpha converting enzyme is involved in regulated alpha-secretase cleavage of the Alzheimer amyloid protein precursor, J. Biol. Chem. 273 (1998) 27765–27767.
[11] S. Lammich, E. Kojro, R. Postina, et al., Constitutive and regulated alpha-secretase cleavage of Alzheimer's amyloid precursor protein by a disintegrin metalloprotease, Proc. Natl. Acad. Sci. USA 96 (1999) 3922–3927.
[12] S.F. Lichtenthaler, Alpha-secretase in Alzheimer's disease: molecular identity, regulation and therapeutic potential, J. Neurochem. 116 (2011) 10–21.
[13] M. Chen, J. Durr, H.L. Fernandez, Possible role of calpain in normal processing of Alzheimer's beta-amyloid precursor protein in human platelets, Biochem. Biophys. Res. Commun. 273 (2000) 170–175.
[14] M. Chen, H.L. Fernandez, Stimulation of beta-amyloid precursor protein alpha-processing by phorbol ester involves calcium and calpain activation, Biochem. Biophys. Res. Commun. 316 (2004) 332–340.
[15] M. Chen, H.L. Fernandez, μ-Calpain is functionally required for alpha-processing of Alzheimer's beta-amyloid precursor protein, Biochem. Biophys. Res. Commun. 330 (2005) 714–721.
[16] D.E. Goll, V.F. Thompson, H. Li, et al., The calpain system, Physiol. Rev. 83 (2003) 731–801.
[17] P.S. Vosler, C.S. Brennan, J. Chen, Calpain-mediated signaling mechanisms in neuronal injury and neurodegeneration, Mol. Neurobiol. 38 (2008) 78–100.
[18] Z. Bánóczi, A. Alexa, A. Farkas, et al., Novel cell-penetrating calpain substrate, Bioconjug. Chem. 19 (2008) 1375–1381.
[19] H. Towbin, T. Staehelin, J. Gordon, Electrophoretic transfer of proteins from polyacrylamide gels to nitrocellulose sheets: procedure and some applications, Proc. Natl. Acad. Sci. USA 76 (1979) 4350–4354.
[20] S.H. Kim, Y.K. Kim, S.J. Jeong, et al., Enhanced release of secreted form of Alzheimer's amyloid precursor protein from PC12 cells by nicotine, Mol. Pharmacol. 52 (1997) 430–436.
[21] C. Jolly-Tornetta, Z.Y. Gao, V.M. Lee, B.A. Wolf, Regulation of amyloid precursor protein secretion by glutamate receptors in human Ntera 2 neurons, J. Biol. Chem. 273 (1998) 14015–14021.
[22] N. Grandin, M. Charbonneau, Intracellular pH and intracellular free calcium responses to protein kinase C activators and inhibitors in *Xenopus* eggs, Development 112 (1991) 461–470.
[23] E.B. McGowan, K.T. Yeo, T.C. Detwiler, The action of calcium-dependent protease on platelet surface glycoproteins, Arch. Biochem. Biophys. 227 (1983) 287–301.
[24] A.H. Schmaier, H.N. Bradford, et al., Membrane expression of platelet calpain, Blood 75 (1990) 1273–1281.
[25] Q.X. Li, G. Evin, D.H. Small, G. Multhaup, K. Beyreuther, C.L. Masters, Proteolytic processing of Alzheimer's disease beta A4 amyloid precursor protein in human platelets, J. Biol. Chem. 270 (1995) 14140–14147.
[26] M. Chen, H.L. Fernandez, The Alzheimer's plaques, tangles and memory deficits may have a common origin. Part IV: can calpain act as α-secretase?, Front Biosci. 3 (1998) a66–a75.

[27] R.P. Guttmann, G.V. Johnson, Oxidative stress inhibits calpain activity in situ, J Biol Chem. 273 (1998) 13331–13338.
[28] D. Gabuzda, J. Busciglio, L.B. Chen, et al., Inhibition of energy metabolism alters the processing of amyloid precursor protein and induces a potentially amyloidogenic derivative, J. Biol. Chem. 269 (1994) 13623–13628.
[29] A. Kishimoto, K. Mikawa, K. Hashimoto, et al., Limited proteolysis of protein kinase C subspecies by calcium-dependent neutral protease (calpain), J. Biol. Chem. 264 (1989) 4088–4092.
[30] J.S. Evans, M.D. Turner, Emerging functions of the calpain superfamily of cysteine proteases in neuroendocrine secretory pathways, J. Neurochem 103 (2007) 849–859.
[31] I. Hajimohammadreza, V.E. Anderson, J.B. Cavanagh, et al., beta-Amyloid precursor protein fragments and lysosomal dense bodies are found in rat brain neurons after ventricular infusion of leupeptin, Brain Res. 640 (1994) 25–32.
[32] S.A. Frautschy, D.L. Horn, J.J. Sigel, et al., Protease inhibitor coinfusion with amyloid beta-protein results in enhanced deposition and toxicity in rat brain, J. Neurosci. (1998) 188311–188321.
[33] R.A. Nixon, Calcium-activated neutral proteinases as regulators of cellular function. Implications for Alzheimer's disease pathogenesis, Ann. N. Y. Acad. Sci. 568 (1989) 198–208.
[34] R.K. Sihag, A.M. Cataldo, Brain beta-spectrin is a component of senile plaques in Alzheimer's disease, Brain Res. 743 (1996) 249–257.
[35] L.L. David, T.R. Shearer, M. Shih, Sequence analysis of lens beta-crystallins suggests involvement of calpain in cataract formation, J. Biol. Chem. 268 (1993) 1937–1940.
[36] J.D. Buxbaum, A.A. Ruefli, C.A. Parker, et al., Calcium regulates processing of the Alzheimer amyloid protein precursor in a protein kinase C-independent manner, Proc. Natl. Acad. Sci. USA 91 (1994) 4489–4493.
[37] B.A. Wolf, A.M. Wertkin, Y.C. Jolly, et al., Muscarinic regulation of Alzheimer's disease amyloid precursor protein secretion and amyloid beta-protein production in human neuronal NT2N cells, J. Biol. Chem. 270 (1995) 4916–4922.
[38] Z.S. Khachaturian, Calcium hypothesis of Alzheimer's disease and brain ageing, Ann. N. Y. Acad. Sci. 747 (1994) 1–11.
[39] M. Chen, H.T. Nguyen, D.R. Sawmiller, What to look for beyond ''pathogenic'' factors in senile dementia? A functional deficiency of Ca^{2+} signaling, J. Alzheimer's Dis. 27 (2011) 3–10.
[40] M. Chen, J.J. Maleski, D.R. Sawmiller, Scientific truth or false hope? Understanding Alzheimer's disease from an aging perspective, J. Alzheimer's Dis. 24 (2011) 3–10.

Biochemical and Biophysical Research Communications 420 (2012) 536–541

Contents lists available at SciVerse ScienceDirect

Biochemical and Biophysical Research Communications

journal homepage: www.elsevier.com/locate/ybbrc

Monocyte–endothelial adhesion is modulated by Cx43-stimulated ATP release from monocytes

Dongdong Yuan [a,1], Qin Wang [a,1], Dengpan Wu [a,1], Meiling Yu [a], Suzhi Zhang [a], Li Li [a], Liang Tao [a,*], Andrew L. Harris [b]

[a] Department of Pharmacology, Zhongshan School of Medicine, Sun Yat-Sen University, Guangzhou, PR China
[b] Department of Pharmacology and Physiology (A.L.H.), New Jersey Medical School, Newark, NJ, USA

ARTICLE INFO

Article history:
Received 23 February 2012
Available online 13 March 2012

Keywords:
Connexin43
Monocyte–endothelial adhesion
Hemichannel
ATP release

ABSTRACT

Adhesion of circulating monocytes to vascular endothelial cells is a crucial event in development of vascular inflammatory conditions, including atherosclerosis. We investigated the roles of connexin43 (Cx43) and ATP release on monocyte–endothelial adhesion. Cx43 function and expression were manipulated by connexin channel inhibitors, overexpression and siRNA. Connexin channel inhibitors rapidly decreased ATP release from U937 monocytes and increased adhesion to human umbilical vein endothelial cells (HUVEC). Monocyte ATP release correlated with Cx43 expression, not with Cx37 expression. Exogenous adenosine (ADO) or ATP decreased adhesion, and inhibition of ATP conversion to ADO increased adhesion. We infer that monocyte Cx43 channel activity causes ATP release, likely via Cx43-containing hemichannels, and that ATP decreases adhesion via conversion to ADO. Inhibition of HUVEC connexin channel activity did not affect ATP release or adhesion. In contrast, expression of Cx43 protein in U937 cells enhanced adhesion. Thus, Cx43 channel function and expression have opposite effects: Cx43 channel function in monocytes, but not in HUVEC, rapidly decreases adhesion via ATP release and conversion to ADO, whereas Cx43 expression itself enhances adhesion. These studies suggest that local regulation of monocyte Cx43 activity within the vasculature can dynamically modulate the monocyte–endothelial adhesion that is an initiating event in vascular inflammatory pathologies, with the baseline adhesion set by Cx43 expression levels. This balance of rapid and tonic influences may be crucial in development of vascular pathologies.

1. Introduction

Under normal conditions, monocytes flowing in blood vessels interact minimally with vascular endothelial cells. However, circulating monocytes adhere to vascular endothelial cells that are inflamed, damaged or exposed to turbulent shear-stress [1]. This adhesion occurs at the initiating stages of inflammatory vascular processes. It is a pre-requisite for endothelial transmigration and extravasation, and is a primary initiator of atherogenesis [2]. For example, in atherosclerotic development, adherent monocytes transmigrate into the arterial intima where they propagate, mature and accumulate lipids. These intimal monocytes transform into macrophage foam cells, a hallmark of atherosclerotic pathology. Adherent monocytes also damage vascular endothelium, causing release of chemoattractants and inflammatory factors. Thus, self-reinforcing monocyte–endothelial cell adhesion not only initiates pathologic processes, but its consequences intensify their progression.

Monocytes transmigration to vascular intima that follows adhesion to endothelium is a major factor in other vascular pathologies, including acute coronary syndromes [3], vascular damage following cancer radiotherapy [4] and development of bacterial endocarditis [5]. Diapedesis following monocyte–endothelial adhesion plays a major role in monocytic infiltration in experimental autoimmune encephalomyelitis (an animal model of multiple sclerosis) [6] and in diabetic nephropathy [7].

For these reasons, it is important to understand the factors that initiate and modulate monocyte–endothelial adhesion. Many conditions enable or facilitate the initial adhesion, including haemodynamic turbulence, inflammatory factors secretion and endothelial dysfunction [8]. Recent studies indicated a role for hemichannels formed by connexin37 (Cx37) in modulation of monocyte–endothelial adhesion [9].

Connexins are a family of transmembrane proteins whose members are expressed in almost all human organs and tissues. They form gap junction channels that mediate intercellular movement of cytosolic signaling molecules [10]. The junctional channels are

* Corresponding author. Fax: +86 20 87332318.
E-mail address: taol@mail.sysu.edu.cn (L. Tao).
[1] The first three authors contributed equally to this study.

0006-291X/$ - see front matter © 2012 Elsevier Inc. All rights reserved.
http://dx.doi.org/10.1016/j.bbrc.2012.03.027

composed of two hemichannels, docked end-to-end. Hemichannels can also exist unapposed in plasma membranes, where they can serve a variety of functions, including release of ATP [11].

There are 21 human connexin isoforms. Vascular endothelial cells express Cx37, Cx40 and Cx43 [12]. As reported monocyte Cx37 promotes ATP release, which lessens monocyte adhesion to endothelial cells, thereby interfering with atherosclerotic development [9]. We show here that in addition to Cx37, the monocytic cell line U937 robustly expresses Cx43, which forms channels with much greater molecular permeability and which have been shown in many contexts to be permeable to ATP and to directly mediate ATP release [10].

The role of Cx43 in monocyte–endothelial adhesion has not been explored. Cx43 is the most widespread connexin in cardiovascular system, and is critically involved in normal physiology as well as many cardiovascular pathologies, including atherosclerosis [13]. Cx43 is upregulated in human atheromatous plaque and in animal models of atherosclerosis [14]. Neutrophil adhesion to endothelium has been shown to be modulated by ATP release via Cx43 hemichannels [15]. In present study, we show that inhibition of the function of Cx43 hemichannels in monocytes, but not in endothelial cells, increases monocyte–endothelial cell adhesion by decreasing ATP release. However, increased Cx43 expression per se by monocytes can increase monocyte–endothelial cell adhesion. This leads to the idea that, monocyte Cx43 function dynamically modulates vascular monocyte–endothelial adhesion around a baseline adhesion level set by Cx43 expression.

2. Materials and methods

2.1. Cell culture

HUVEC (human umbilical vein endothelial cells) were enzymatically isolated from fresh umbilical cord as previously described [16] and used up to passage 5. Human monocytic cells (U937) were purchased from American Type Culture Collection (ATCC). HUVEC were cultured with human endothelial SFM (Invitrogen) containing 15% fetal bovine serum (FBS; Invitrogen), 100 U/ml penicillin–streptomycin (Invitrogen), 100 μg/ml heparin (Sigma), and 150 μg/ml endothelial cell growth supplement (ECGS; BD). The study was approved by the local institutional Ethics Committee. U937 cells were cultured in RPMI1640 medium (Invitrogen) supplemented with 15% fetal bovine serum (FBS; Invitrogen), 100 U/ml penicillin–streptomycin (Invitrogen). HUVEC and U937 cells were cultured at 37 °C in a 5% CO_2 incubator at 90% humidity.

2.2. Adhesion assay

Adhesion of U937 to HUVEC was assessed as described: [17] briefly, U937 cells were labeled with 5 μM calcein-acetoxymethyl ester (calcein-AM; Invitrogen) for 30 min at 37 °C in a 5% CO_2 incubator at 90% humidity. U937 cells were then washed twice with PBS and resuspended in the medium without serum. U937 cells labeled with calcein-AM were added onto confluent monolayers of HUVEC that had been treated overnight with recombinant mouse tumor necrosis factor, TNF-α 20 ng/ml (Peprotech). After incubation for 1 h at 37 °C, the plates were rinsed twice with medium without serum. Adherent U937 cells remained on confluent monolayers of HUVEC and were counted using a fluorescence microscope. For each condition, 8 different 200× visual fields in the middle of the dish were chosen for analysis.

2.3. Cell treatments

HUVEC or U937 cells were pretreated with connexin channel inhibitors oleamide or 18-α-GA (Sigma), a Cx43 expression enhancer, retinoic acid (Sigma), a CD73 inhibitor, α,β-methylene ADP (APCP) (Sigma), exogenous ATP or adenosine (ADO) for indicated times before and during adhesion assays, then harvested for western blotting.

2.4. Overexpression of Cx43 and inhibition of Cx43 expression by siRNA transfection

Cx43 was expressed in U937 cells with a pcDNA3.1-Cx43 vector (gift of Ryan Jensen and Peter M. Glazer). Cells were transfected with siRNA targeting human Cx43 gene (CAGUCUGCCUUUCGUUGUA) or a nonspecific, control siRNA (NC in the figures). Transfection into U937 cells was carried out using Lipofectamine 2000 (Invitrogen) according to the manufacturer's instructions.

2.5. Western blotting

Western blotting protocols are described in previous studies [18]. Using anti-Cx43 (Sigma; 1:3000), the secondary antibody (Sigma) was 1:3000. Both anti-β-actin (Sigma) and the secondary antibody were at 1:10,000 dilution. All western blotting exposures were in the linear range of detection, and the intensities of the resulting bands were quantified by Quantity One software on a GS-800 densitometer (Bio-Rad Laboratories).

2.6. Extracellular ATP measurements

Cellular ATP release was determined with ATP bioluminescence assay kits (Sigma) according to the manufacturer's instructions. The supernatants of HUVEC and U937 cultures were collected on ice. Hundred microliters of supernatant was added to 100 μl ATP assay mix solution. The luminescence was read by a fluorospectrophotometer (Cary Eclipse, FL0811M005, Bio/Chemi-luminescence mode) in 96-well culture plates.

2.7. Statistical analysis

Data were statistically analyzed using unpaired Student's t test at a significance level of $P < 0.05$ using Sigma Plot (Jandel Scientific) and are presented as means ± SE.

3. Results

3.1. Effects of oleamide and retinoic acid on U937 Cx43 expression and U937-HUVEC adhesion

Previous studies have shown expression of Cx37 in monocytes [9]. We show that U937 cells, a widely used monocyte cell line, robustly express Cx43 as well (Fig. 1B and D) and investigate the role of monocyte Cx43 in adhesion to endothelial cells.

Treatment of U937 cells with oleamide (50 μM) caused a dramatic, rapid increase in adhesion (Fig. 1A). This rapid effect on adhesion is consistent with rapid inhibition of connexin channel activity by oleamide [19].

With continuous exposure to oleamide, the initial increase in adhesion decreased with time and was at near baseline levels at 24 h of treatment (Fig. 1A), which correlated with a decrease of Cx43 expression (Fig. 1B). Retinoic acid (25 μM) increased expression of Cx43 in U937 cells over a period of hours (Fig. 1D). Increased expression of Cx43 in U937 cells correlated with increased adhesion (Fig. 3C). Thus, in U937 cells, expression of Cx43 positively correlated with adhesion. Cx37 expression in U937 cells was unaltered by these treatments (Supplemental Fig. 1A and B).

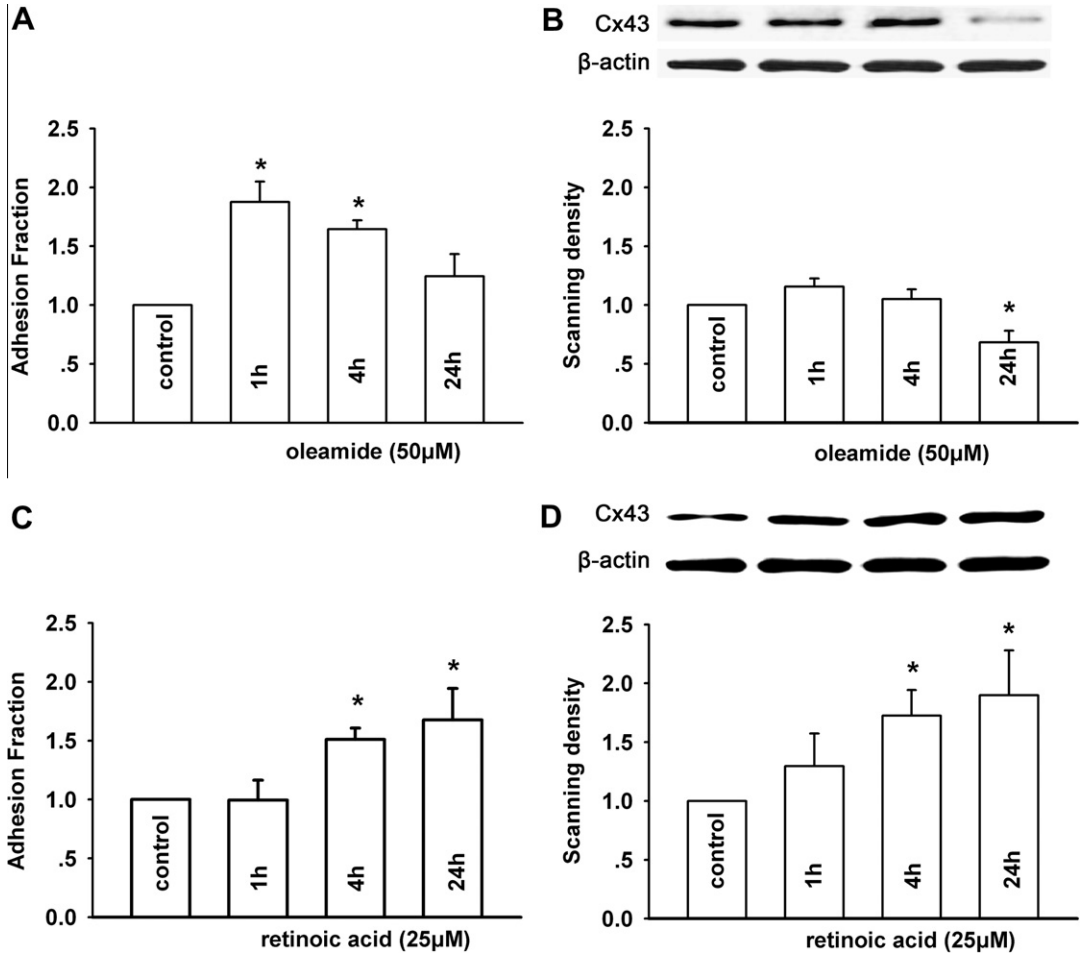

Fig. 1. Effects of U937 exposure to oleamide and retinoic acid on monocyte–endothelial cell adhesion and on expression of Cx43. (A, C) Effects on adhesion when U937 cells were treated with oleamide (50 μM) or retinoic acid (25 μM) for 1, 4, and 24 h ($n = 5$, $^*P < 0.05$). (B, D) Effects on Cx43 expression when U937 cells were treated with oleamide (50 μM) or retinoic acid (25 μM) for 1, 4 and 24 h ($n = 4–7$, $^*P < 0.05$).

3.2. Specific modulation of U937 Cx43 expression modulates U937-HUVEC adhesion

To more directly assess the role of U937 Cx43 expression on adhesion, we explored the effects of specific alteration of U937 Cx43 expression using two experiments: overexpression of Cx43 by transfection of pcDNA-Cx43 and knock-down of Cx43 expression with siRNA-Cx43. Fig. 2A and B shows that upregulation of U937 Cx43 expression by pcDNA-Cx43 enhanced adhesion. Conversely, knock-down of Cx43 expression with siRNA-Cx43 depressed adhesion (Fig. 2C and D). Cx37 expression was unchanged (Supplemental Fig. 1C and D). These experiments make clear that adhesion of U937 cells is a positive and specific function of Cx43 expression.

The data presented thus far suggest a differentiation between effects of Cx43 channel function and expression of Cx43: decreased Cx43 function in U937 cells increases adhesion to HUVEC, but when expression of Cx43 in U937 is increased by any of the manipulations, the adhesion also increases. Similarly, when Cx43 expression is decreased, the adhesion decreases. This suggests that expression of Cx43 per se increases adhesion, and that this is distinct from the effect of functional Cx43 channels to decrease adhesion. These dual and competing effects of Cx43 are reflected in the change in adhesion during oleamide treatment of U937 cells (Fig. 1A and B), which initially increased (due to block of connexin channel function) and later decreased to nearly control levels as Cx43 expression decreased. Thus it appears that the levels of Cx43 expression set a baseline level of adhesion, which can be rapidly modulated by monocyte Cx43 channel function.

3.3. Effect of U937 Cx43 activity on adhesion is mediated by ATP release

Previous studies showed that monocyte Cx37 correlated with ATP release and inhibition of monocyte–endothelial cell adhesion [9]. Cx37 is among the most size-restrictive of connexin channels, being impermeable to many of molecules that permeate other connexin channels. Cx43 channels are known to be permeable to ATP [10]. We therefore investigated the involvement of ATP release in modulation of adhesion by monocyte Cx43.

Cx43 is also expressed on HUVEC. In order to exclude the effect of ATP released from HUVEC, ATP release and U937-HUVEC adhesion was assessed with short-term exposure of each type of cell to oleamide or to a second inhibitor of connexin channel function, 18-α-GA [20], and with transfection with siRNA-Cx43. One hour exposure of HUVEC to oleamide or 18-α-GA had no effect on ATP release or adhesion (Fig. 3A and C). Importantly, knockdown of Cx43 expression in HUVEC also had no effect on ATP release (Fig. 3E; knockdown level shown in Supplemental Fig. 2), showing that Cx43 function does not regulate ATP release from HUVEC.

In contrast, 1 h treatment of U937 cells with oleamide or 18-α-GA dramatically decreased ATP release and increased adhesion

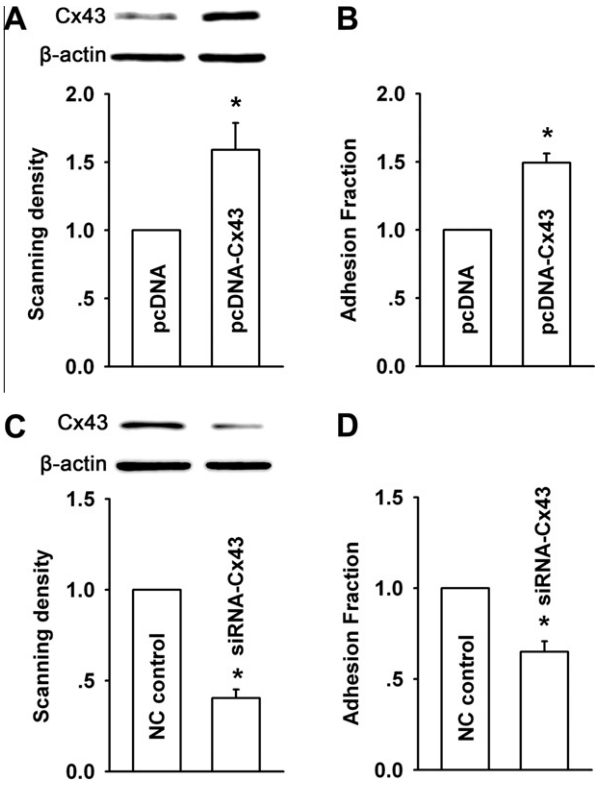

Fig. 2. Expression of Cx43 by U937 cells regulates monocyte–endothelial cell adhesion. (A) Expression of Cx43 in U937 cells following transfection by pcDNA-Cx43 ($n = 4$, $^*P < 0.05$). (B) Change of cell adhesion when Cx43 expression by U937 cells was increased ($n = 4$, $^*P < 0.05$). (C) Expression of Cx43 in U937 cells following treatment with siRNA-Cx43 ($n = 7$, $^*P < 0.05$). (D) Change of cell adhesion when U937 cells expression of Cx43 was knocked-down by siRNA-Cx43 ($n = 4$, $^*P < 0.05$).

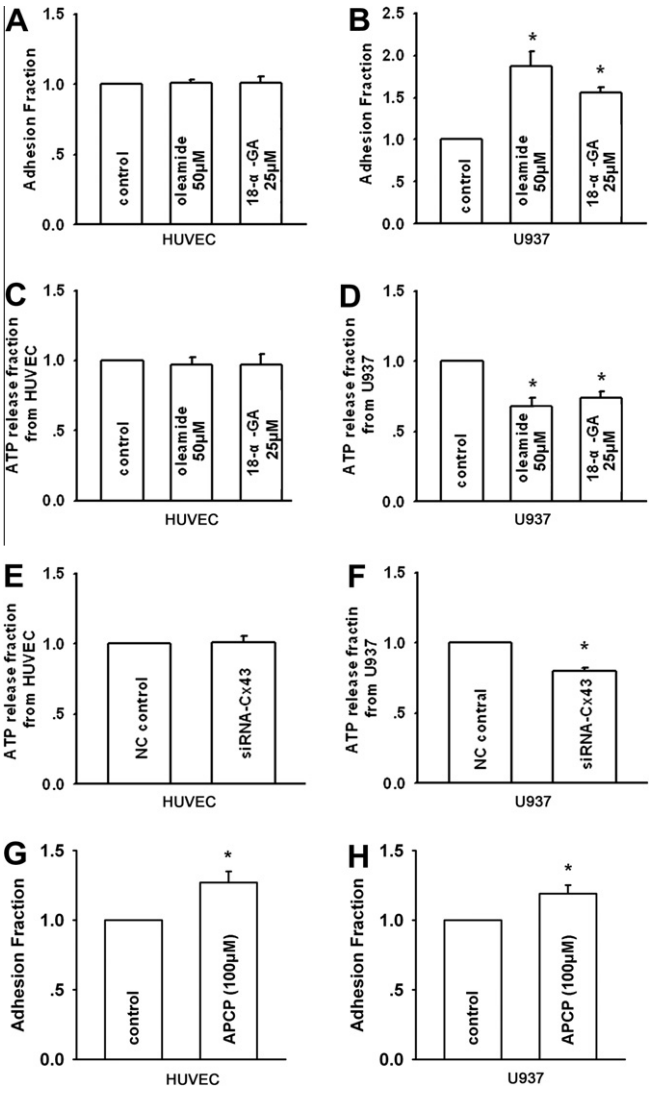

Fig. 3. Effects of oleamide and 18-α-GA on cell adhesion and ATP release from HUVEC and from U937 cells. (A, B) Effects of 1 h treatment of cells with oleamide and 18-α-GA on cell adhesion ($n = 5$, $^*P < 0.05$). (C, D) Effects of 1 h treatment of cells with oleamide and 18-α-GA on ATP release ($n = 5$, $^*P < 0.05$). (E, F) ATP release from HUVEC or U937 cells in which Cx43 expression was knocked-down by siRNA-Cx43 ($n = 3–5$, $^*P < 0.05$). (G, H) Effects of 1 h treatment of cells with APCP on cell adhesion.

(Fig. 3B and D). Knockdown of Cx43 expression also attenuated ATP release (knockdown level shown in Fig. 2C). These results make clear that Cx43 channel function in U937 cells decreases adhesion by enhancing ATP release. Thus, the effects of Cx43 functional modulation on U937-HUVEC adhesion are distinct and cell-specific. They also show that effect of decreased Cx43 expression in monocytes to decrease adhesion is not mediated by decreased ATP release (since decreased ATP release itself should have opposite effect; the adhesion enhancing effect of expression dominates).

ATP can be rapidly metabolized by extracellular enzymes to adenosine (ADO), which has well-known anti-inflammatory effects that decrease adhesion via A2B receptors [21]. The ecto-enzymes involved are CD39, converting ATP to AMP, and CD73, converting AMP to ADO. This pathway is robust in endothelial cells [22]. To reveal the role of ADO, we applied a competitive inhibitor of CD73, α,β-methylene ADP (APCP) [23], to inhibit ADO production from ATP. Application of APCP caused a significant increase in cell adhesion (Fig. 3G and H), strongly suggesting that ADO produced from endogenously released ATP has an anti-adhesive effect.

3.4. Exogenous ADO or ATP decrease adhesion

Experiments were conducted to determine whether (a) ADO could in fact decrease adhesion in this system, and (b) ADO could reverse the increased adhesion caused by treatment of U937 cells with connexin channel inhibitor oleamide. In both cell types, exogenous 100 μM ADO decreased the endogenous adhesion (Fig. 4A and C). Furthermore, ADO reversed the enhanced adhesion produced by oleamide treatment of U937 cells (i.e., by inhibition of endogenous ATP release; shown in Fig. 1) (Fig. 4B and D). These results confirm an anti-adhesive effect of ADO on these cells.

To determine whether exogenous ATP could substitute for endogenously released ATP, the same experiment was performed using 200 μM ATP. Exogenous ATP had a similar effect as exogenous ADO (Fig. 4E and G); exogenous ATP can reproduce the effect of exogenous ADO (though somewhat less effectively; compare Fig. 4E with Fig. 4A, and Fig. 4G with Fig. 4C). Like ADO, exogenous ATP also functionally reversed the increased adhesion that followed inhibition of ATP release from U937 cells by oleamide (Fig. 4F and H).

4. Discussion

4.1. Effects of Cx43 channel function

These studies show that functional Cx43-containing channels in monocytes are involved in purinergic signaling, via ATP release,

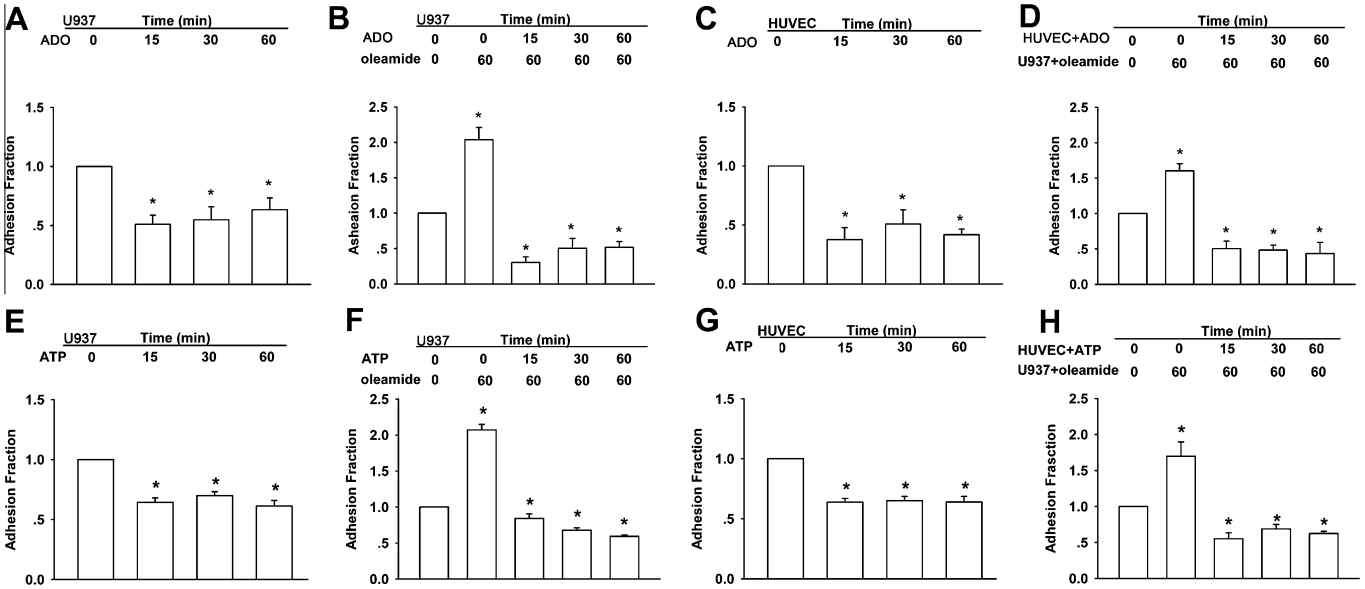

Fig. 4. Effects of exogenous ATP on monocyte–endothelial cell adhesion. (A, C) Effect on cell adhesion of U937 cells or HUVEC pretreatment with ADO (100 μM) for 15, 30 and 60 min ($n = 4$, $^*P < 0.05$). (B, D) Effect on cell adhesion when U937 cells were pretreated with oleamide (50 μM) for 60 min and U937 cells themselves or HUVEC were pretreated with exogenous ADO (100 μM) for 15, 30 and 60 min ($n = 3$, $^*P < 0.05$). (E, G) Effect on cell adhesion of U937 cells or HUVEC pretreatment with ATP (200 μM) for 15, 30 and 60 min ($n = 4$, $^*P < 0.05$). (F, H) Effect on cell adhesion when U937 cells were pretreated with oleamide (50 μM) for 60 min and U937 cells themselves or HUVEC were pretreated with exogenous ATP (200 μM) for 15, 30 and 60 min ($n = 4$, $^*P < 0.05$).

which modulates monocyte–endothelial adhesion. Inhibition of monocyte connexin channel function by connexin channel inhibitors oleamide or 18-α-GA causes a rapid decrease in ATP release and increase in adhesion to HUVEC, but similar treatment of HUVEC had no effect on either ATP release or adhesion. Downregulation of Cx43 in U937 cells reduces ATP release. There was no change in Cx37 expression, showing that ATP release is modulated by Cx43 rather than by Cx37. Inhibition of ecto-enzymatic pathway that generates ADO from ATP enhanced adhesion, and exogenous ADO or ATP could functionally substitute for ATP released by U937 cells. These studies show that Cx43-dependent ATP release is cell-specific, specifically correlates with Cx43 function and rapidly modulates monocyte–endothelial adhesion.

What is the pathway by which ATP is released from monocytes? Previous work suggested involvement of monocyte Cx37 channels [9,24]. We show that Cx43 is present and that ATP release correlates with changes in Cx43 function and expression, while Cx37 is unchanged. ATP permeability and release through Cx43 channels are well established [10]. Because homomeric Cx37 channels are among the most size restrictive among all connexin channels, being impermeable to 6-carboxyfluorescein, Lucifer yellow and Alexa 488, and only weakly permeable to the smaller molecules Alexa 350 and NBD-M-TMA [25,26], we favor the idea that ATP release from monocytes is via channels formed wholly and/or partially by Cx43 (homomeric Cx43 and/or heteromeric Cx43/Cx37 channels). Another potential pathway for ATP release is through pannexin1 (panx1) channels [27]. Panx1 has not been reported to be expressed in monocytes. However, 18-α-GA is without significant effect on panx1, particularly at the low concentration used here [28]. This, and the effects on ATP release by siRNA-Cx43, argue against ATP release via pannexin channels. No matter what the specific pathway, the data show that the pathway is rapidly and dynamically modulated by Cx43 channel function.

How does this ATP release from monocytes affect adhesion? ATP can be rapidly metabolized by extracellular enzymes to ADO, which has well-known anti-inflammatory effects via A2B receptors that decrease adhesion [22]. Released ATP is converted to ADO and exerts an anti-inflammatory effect. This pathway is supported by the demonstration that block of ADO production, using APCP, increased adhesion, and exogenous ADO decreased adhesion.

We show that exogenous ATP mimics the effect of cellular ATP release to decrease adhesion, presumably by metabolism to ADO. It is also possible that ATP itself could have an anti-adhesive effect on these cells, even though ATP is usually considered a pro-inflammatory agent. NCAM has an extracellular ATP binding site, occupancy of which can interfere with adhesion and downstream signaling [29]. Both monocytes and HUVEC express NCAM [30]. ATP can also interact with $P2Y_{11}$ receptors on HUVEC to reduce adhesion [31]. These interactions could contribute to the overall anti-adhesive effect of exogenous ATP, though metabolism to ADO is likely the dominant pathway.

ATP release through Cx43 channels is well-described [10]. It can be dynamically regulated by factors that include intracellular Ca^{2+}, ischemic stress, hypoxia, and important in the context of atherosclerosis, by cytokines [32]. Release of cytokines is a prominent feature of atherosclerosis. Cytokines including TNF-α, interleukin, IFN-γ and TGF-β inhibit the activity of Cx43 channels [33]. Therefore, cytokine release in early atherosclerotic development would attenuate ATP release from monocytes, enhancing adhesion in a positive-feedback inflammatory cycle.

4.2. Effects of Cx43 expression

Reduction of Cx43 expression in U937 decreased adhesion and upregulation of Cx43 expression enhanced adhesion. These effects on Cx43 expression are opposite to those of acute modulation of the connexin channel function. Manipulation of Cx43 levels had no effect on expression of Cx37 (Supplemental Fig. 1). This suggests lack of involvement of Cx37 in modulation of adhesion by changes in Cx43 expression.

The specific mechanism of the effect of Cx43 expression on adhesion is unclear, but may involve interactions between the carboxyl-terminal domain of Cx43 and elements of cellular signaling pathways, including cytoskeletal components, Src, PKA and PKC [34,35] which can have downstream effects on expression of cell adhesion molecules expressed on monocytes.

Our experiments focus on a crucial step in inflammatory vascular disease: monocyte adherence to endothelial cells. This adhesion is a required step in development of atherosclerosis and many inflammatory pathologies that involve leukocyte transmigration across endothelium. The results strongly suggest that adhesion is dynamically regulated by monocyte Cx43 hemichannel function, which will be responsive to the local environment of the circulating monocytes as they come into contact with vascular endothelium and exposed to local signaling molecules (e.g., due to local oscillatory shear stress). This local modulation is superimposed upon a baseline level of adhesivity set by the levels of Cx43 expression in monocytes. Thus, Cx43 seems to be a pivotal player – in unexpected ways – in defining how well and where monocytes will adhere to endothelial cells and thereby promote atherosclerotic development and progression of other vascular pathologies. The mechanisms described here may offer a basis for targeted intervention.

Acknowledgments

This work was supported by: 1. National Natural Science Foundation of China 30973434, 30901807; 2. Fundamental Research Funds for the Central Universities 10YKPY32 ; 3. Grant for Development of Important New Drugs from the Ministry of Health of China 2009ZX09303-007.

Appendix A. Supplementary data

Supplementary data associated with this article can be found, in the online version, at http://dx.doi.org/10.1016/j.bbrc.2012.03.027.

References

[1] R.A. Boon, A.J. Horrevoets, Key transcriptional regulators of the vasoprotective effects of shear stress, Hamostaseologie 29 (2009) 39–40, 41–33.
[2] C.J. Binder, M.K. Chang, P.X. Shaw, Y.I. Miller, K. Hartvigsen, A. Dewan, J.L. Witztum, Innate and acquired immunity in atherogenesis, Nat. Med. 8 (2002) 1218–1226.
[3] E. Shantsila, G.Y. Lip, Monocytes in acute coronary syndromes, Arterioscler. Thromb. Vasc. Biol. 29 (2009) 1433–1438.
[4] F.A. Stewart, S. Hoving, N.S. Russell, Vascular damage as an underlying mechanism of cardiac and cerebral toxicity in irradiated cancer patients, Radiat. Res. 174 (2010) 865–869.
[5] M.H. Veltrop, H. Beekhuizen, Monocytes maintain tissue factor activity after cytolysis of bacteria-infected endothelial cells in an in vitro model of bacterial endocarditis, J. Infect. Dis. 186 (2002) 1145–1154.
[6] L. Izikson, R.S. Klein, I.F. Charo, H.L. Weiner, A.D. Luster, Resistance to experimental autoimmune encephalomyelitis in mice lacking the CC chemokine receptor (CCR)2, J. Exp. Med. 192 (2000) 1075–1080.
[7] A.A. Elmarakby, J.C. Sullivan, Relationship between oxidative stress and inflammatory cytokines in diabetic nephropathy, Cardiovasc. Ther., 2010.
[8] I. Tzoulaki, G.D. Murray, J.F. Price, F.B. Smith, A.J. Lee, A. Rumley, G.D. Lowe, F.G. Fowkes, Hemostatic factors, inflammatory markers, and progressive peripheral atherosclerosis: the Edinburgh Artery Study, Am. J. Epidemiol. 163 (2006) 334–341.
[9] C.W. Wong, T. Christen, I. Roth, C.E. Chadjichristos, J.P. Derouette, B.F. Foglia, M. Chanson, D.A. Goodenough, B.R. Kwak, Connexin37 protects against atherosclerosis by regulating monocyte adhesion, Nat. Med. 12 (2006) 950–954.
[10] A.L. Harris, Connexin channel permeability to cytoplasmic molecules, Prog. Biophys. Mol. Biol. 94 (2007) 120–143.
[11] J.C. Saez, K.A. Schalper, M.A. Retamal, J.A. Orellana, K.F. Shoji, M.V. Bennett, Cell membrane permeabilization via connexin hemichannels in living and dying cells, Exp. Cell. Res. 316 (2010) 2377–2389.
[12] J.P. Derouette, C. Wong, L. Burnier, S. Morel, E. Sutter, K. Galan, A.C. Brisset, I. Roth, C.E. Chadjichristos, B.R. Kwak, Molecular role of Cx37 in advanced atherosclerosis: a micro-array study, Atherosclerosis 206 (2009) 69–76.
[13] L. Burnier, P. Fontana, A. Angelillo-Scherrer, B.R. Kwak, Intercellular communication in atherosclerosis, Physiology (Bethesda) 24 (2009) 36–44.
[14] J.E. Gabriels, D.L. Paul, Connexin43 is highly localized to sites of disturbed flow in rat aortic endothelium but connexin37 and connexin40 are more uniformly distributed, Circ. Res. 83 (1998) 636–643.
[15] H.K. Eltzschig, T. Eckle, A. Mager, N. Kuper, C. Karcher, T. Weissmuller, K. Boengler, R. Schulz, S.C. Robson, S.P. Colgan, ATP release from activated neutrophils occurs via connexin 43 and modulates adenosine-dependent endothelial cell function, Circ. Res. 99 (2006) 1100–1108.
[16] V. Azcutia, M. Abu-Taha, T. Romacho, M. Vazquez-Bella, N. Matesanz, F.W. Luscinskas, L. Rodriguez-Manas, M.J. Sanz, C.F. Sanchez-Ferrer, C. Peiro, Inflammation determines the pro-adhesive properties of high extracellular d-glucose in human endothelial cells in vitro and rat microvessels in vivo, PLoS One 5 (2010) e10091.
[17] C. Weber, W. Erl, A. Pietsch, P.C. Weber, Aspirin inhibits nuclear factor-kappa B mobilization and monocyte adhesion in stimulated human endothelial cells, Circulation 91 (1995) 1914–1917.
[18] Q. Wang, T. You, D. Yuan, X. Han, X. Hong, B. He, L. Wang, X. Tong, L. Tao, A.L. Harris, Cisplatin and oxaliplatin inhibit gap junctional communication by direct action and by reduction of connexin expression, thereby counteracting cytotoxic efficacy, J. Pharmacol. Exp. Ther. 333 (2010) 903–911.
[19] D.L. Boger, J.E. Patterson, X. Guan, B.F. Cravatt, R.A. Lerner, N.B. Gilula, Chemical requirements for inhibition of gap junction communication by the biologically active lipid oleamide, Proc. Natl. Acad. Sci. USA 95 (1998) 4810–4815.
[20] J.S. Davidson, I.M. Baumgarten, E.H. Harley, Reversible inhibition of intercellular junctional communication by glycyrrhetinic acid, Biochem. Biophys. Res. Commun. 134 (1986) 29–36.
[21] G.G. Yegutkin, Nucleotide- and nucleoside-converting ectoenzymes: important modulators of purinergic signalling cascade, Biochim. Biophys. Acta 1783 (2008) 673–694.
[22] H.K. Eltzschig, J.C. Ibla, G.T. Furuta, M.O. Leonard, K.A. Jacobson, K. Enjyoji, S.C. Robson, S.P. Colgan, Coordinated adenine nucleotide phosphohydrolysis and nucleoside signaling in posthypoxic endothelium: role of ectonucleotidases and adenosine A2B receptors, J. Exp. Med. 198 (2003) 783–796.
[23] A.R. Cappellari, G.J. Vasques, L. Bavaresco, E. Braganhol, A.M. Battastini, Involvement of ecto-5′-nucleotidase/CD73 in U138MG glioma cell adhesion, Mol. Cell. Biochem., 2011.
[24] J.P. Derouette, T. Desplantez, C.W. Wong, I. Roth, B.R. Kwak, R. Weingart, Functional differences between human Cx37 polymorphic hemichannels, J. Mol. Cell. Cardiol. 46 (2009) 499–507.
[25] P.A. Weber, H.C. Chang, K.E. Spaeth, J.M. Nitsche, B.J. Nicholson, The permeability of gap junction channels to probes of different size is dependent on connexin composition and permeant-pore affinities, Biophys. J. 87 (2004) 958–973.
[26] O. Kruger, J.L. Beny, F. Chabaud, O. Traub, M. Theis, K. Brix, S. Kirchhoff, K. Willecke, Altered dye diffusion and upregulation of connexin37 in mouse aortic endothelium deficient in connexin40, J. Vasc. Res. 39 (2002) 160–172.
[27] L. Bao, S. Locovei, G. Dahl, Pannexin membrane channels are mechanosensitive conduits for ATP, FEBS. Lett. 572 (2004) 65–68.
[28] F.B. Chekeni, M.R. Elliott, J.K. Sandilos, S.F. Walk, J.M. Kinchen, E.R. Lazarowski, A.J. Armstrong, S. Penuela, D.W. Laird, G.S. Salvesen, B.E. Isakson, D.A. Bayliss, K.S. Ravichandran, Pannexin 1 channels mediate 'find-me' signal release and membrane permeability during apoptosis, Nature 467 (2010) 863–867.
[29] G. Skladchikova, L.C. Ronn, V. Berezin, E. Bock, Extracellular adenosine triphosphate affects neural cell adhesion molecule (NCAM)-mediated cell adhesion and neurite outgrowth, J. Neurosci. Res. 57 (1999) 207–218.
[30] H.R. Lee, S.J. Cho, H.J. Park, K.H. Kim, D.K. Rhee, S. Pyo, The inhibitory effect of acrylamide on NCAM expression in human neuroblastoma cells: involvement of CK2/Ikaros signaling pathway, Toxicol. In Vitro 24 (2010) 1946–1952.
[31] A. Kaufmann, B. Musset, S.H. Limberg, V. Renigunta, R. Sus, A.H. Dalpke, K.M. Heeg, B. Robaye, P.J. Hanley, "Host tissue damage" signal ATP promotes non-directional migration and negatively regulates toll-like receptor signaling in human monocytes, J. Biol. Chem. 280 (2005) 32459–32467.
[32] F. Anselmi, V.H. Hernandez, G. Crispino, A. Seydel, S. Ortolano, S.D. Roper, N. Kessaris, W. Richardson, G. Rickheit, M.A. Filippov, H. Monyer, F. Mammano, ATP release through connexin hemichannels and gap junction transfer of second messengers propagate Ca2+ signals across the inner ear, Proc. Natl. Acad. Sci. USA 105 (2008) 18770–18775.
[33] M.C. Lim, G. Maubach, L. Zhuo, TGF-beta1 down-regulates connexin 43 expression and gap junction intercellular communication in rat hepatic stellate cells, Eur. J. Cell. Biol. 88 (2009) 719–730.
[34] B.N. Giepmans, Gap junctions and connexin-interacting proteins, Cardiovasc. Res. 62 (2004) 233–245.
[35] K. Smedlund, G. Vazquez, Involvement of native TRPC3 proteins in ATP-dependent expression of VCAM-1 and monocyte adherence in coronary artery endothelial cells, Arterioscler. Thromb. Vasc. Biol. 28 (2008) 2049–2055.

Biochemical and Biophysical Research Communications 420 (2012) 542–546

Contents lists available at SciVerse ScienceDirect

Biochemical and Biophysical Research Communications

journal homepage: www.elsevier.com/locate/ybbrc

Native expression and purification of hormone-sensitive lipase from *Psychrobacter* sp. TA144 enhances protein stability and activity

Giuseppina Ascione [a], Donatella de Pascale [b], Concetta De Santi [b], Carlo Pedone [a], Nina Alayne Dathan [a,*], Simona Maria Monti [a]

[a] Institute of Biostructures and Bioimaging, National Research Council, Via Mezzocannone 16, I-80134 Naples, Italy
[b] Institute of Protein Biochemistry, National Research Council, Via Pietro Castellino 111, I-80131 Naples, Italy

ARTICLE INFO

Article history:
Received 21 February 2012
Available online 13 March 2012

Keywords:
Lipase
Psychrophile
Trehalose
Benzyl alcohol
Molecular chaperones
Protein stability

ABSTRACT

Psychrobacter, a micro-organism originally isolated from Antarctic sea water, expresses an extremely active hormone-sensitive lipase (HSL) which catalyzes the hydrolysis of fatty acid esters at very low temperature and is therefore of great potential industrial and pharmaceutical interest. An insoluble form of the entire enzyme has previously been cloned and expressed in *Escherichia coli*, subsequently refolded and shown to be active, whilst a shorter but completely inactive version, lacking the N-terminal 98 amino acids has been expressed in soluble form. In this study the entire enzyme has been expressed as a fully soluble protein in *E. coli* in the presence of either the osmolyte trehalose, plus high salt concentration, or the membrane fluidizer benzyl alcohol. Trehalose promotes protein mono-dispersion by increasing the viscosity of the growth medium for bacterial cells, thereby helping circumvent protein aggregation, whilst the heat-shock inducer benzyl alcohol stimulates the production of a network of endogenous chaperones which actively prevent protein misfolding, whilst also converting recombinant aggregates to native, correctly folded proteins. The resultant recombinant protein proved to be more stable than its previously expressed counterpart, as shown by CD and enzymatic activity data which proved the enzyme to be more active at a higher temperature than its refolded counterpart. By light scattering analysis it was shown that the newly expressed protein was monomeric. The stability of the full length native protein will help in understanding the structure of *Psy*HSL and the role of its regulatory N-terminal for eventual application in a myriad of biotechnological processes.

1. Introduction

Lipases play a crucial role in lipid metabolism, catalyzing the hydrolysis of acylglycerides and a range of other fatty acid esters [1]. They are produced by organisms in a wide range of environments and are fully functional, often in an extreme range of conditions [2,3]. Due to their catalytic activities and adaptable nature they are potentially extremely useful enzymes for an ever growing number of industrial and pharmaceutical applications [4–6]. Cold-active enzymes produced by micro-organisms often show high catalytic efficiency at low temperatures, frequently associated with low stability at moderate and high temperatures. The specific activity of psychrophylic enzymes is higher than that of their mesophylic homologues at 0–30 °C. Over the past decade, the attention of many researchers has been focused on the biotechnological applications of these enzymes [5], thanks to the numerous economical and ecological advantages of enzymes that operate at lower temperatures.

The bacterial species TA144 of *Psychrobacter* is a micro-organism which has been isolated from Antarctic sea water, where it efficiently catalyzes the hydrolysis of acylglycerides and other fatty acid esters in the process of degradation of organic matter via its highly active hormone-sensitive lipase [7]. Cold-adapted micro-organisms normally grow very slowly, but with the aid of genetic engineering it has become possible to clone their highly catalytic genes in host strains such as *Escherichia coli* as has been the case for the *lip2* gene, normally expressed in *Psychrobacter* sp. TA144, hereafter referred to as recombinant *Psy*HSL [8]. As with other members of the HSL family *Psy*HSL contains a highly conserved sequence of His-Gly-Gly-Gly upstream of the catalytic site, shown to be homologous to the corresponding region of human HSL, Gly-Asp-Ser-Ala-Gly [9]. In fact *Psy*HSL shows a surprising degree of homology around the catalytic domain, displaying 42% identity and 60% similarity over a span of 87 amino acids, this region being proposed to be a common feature in triacylglycerol lipases and esterases [10].

* Corresponding author. Fax: +39 0812534574.
E-mail address: nina.dathan@unina.it (N.A. Dathan).

0006-291X/$ - see front matter © 2012 Elsevier Inc. All rights reserved.
http://dx.doi.org/10.1016/j.bbrc.2012.03.028

PsyHSL has previously been expressed in the bacterial vector pET22b, but proved to be highly insoluble. It has however been successfully refolded and shown to be catalytically active, although this activity does not confirm the true nature of the enzyme; all attempts to crystallize the refolded protein have proved unsuccessful [8]. However a deleted version of *Psy*HSL, lacking the initial 98 residues has been expressed in fully soluble form but not extensively characterized since this deleted version was completely inactive [8]; suggesting that the N-terminal region of HSL, like its human counterpart, could be considered as a regulative domain of the protein, rendering the attainment of the soluble full length protein to be of considerable potential interest [9].

The aim of this study was to find suitable expression conditions in order to provide us with a high level of native, soluble and fully active protein for extensive biochemical characterization and, eventually, crystallographic studies. For this purpose *PsyHSL* was initially re-cloned in two simple 6×His-tag (N-terminal and C-terminal) modified pET vectors pETM11 and pETM13 (EMBL, Heidelberg) via PCR using specific oligonucleotide primers and their soluble expression levels were confronted with that obtained from pET22b. Further to altering growth conditions two additives were also used to encourage correct folding of the recombinant protein expressed in *E. coli*. These were benzyl alcohol, a membrane fluidizer [11] known to artificially cause a heat-shock response in the modified membrane of bacterial cells, causing severe stress and inducing the expression of the cells own chaperone network, as well as the osmolyte trehalose which exerts an anti-aggregation effect on proteins in the presence of high salt concentration thereby encouraging uptake of the osmolyte into individual bacterial cells [12]. The addition of these compounds proved to be decisive in procuring a high expression level of stable, soluble, full length recombinant protein.

2. Materials and methods

2.1. Materials

Oligonucleotide primers for PCR were purchased from PRIMM srl (Milan), DNA extraction and purification kits were from Qiagen (Germany), Phusion polymerase (Finnzymes, Milan), expression vectors pETM11 and pETM13 were kindly provided by the Protein Expression and Purification Core Facility, EMBL (Heidelberg), restriction enzymes were from New England Biolabs (Milan), anti-His-HRP conjugated mouse monoclonal IgG from Santa Cruz (USA), HisTrapHP and Superdex 200 columns from GE Healthcare (Milan), Bio-Sep SEC3000 from Phenomenex (Germany). Bacterial expression strains were from Novagen, whilst the cloning strain TOP10F' was from Invitrogen (Milan). Benzyl alcohol, trehalose and other chemicals were from Sigma–Aldrich (Milan).

2.1.1. Construction of pETM11-HSL and pETM13-HSL

HSL ([8] GenBank X53868.1) cDNA was PCR-amplified from pET22b-HSL with Phusion polymerase using the site-specific oligonucleotide primers: HSL-F CGCGCGCCATGGGCATGCCTATTCTACCAGTACCGGC with HSL-11R CGCGCGCTCGAGTTACTACGCTCTGAGATTTGGCTTATCAC and again HSL-F with HSL-13R CGCGCGCTCGAGCGCTCTGAGATTTGGCTTATCAC and inserted in the appropriately cut expression vectors pETM11 and pETM13 before being transformed in TOP10F'. The resulting plasmids were named 11-HSL and 13-HSL, whilst the original was known as 22-HSL.

2.1.2. Expression screening of recombinant clones

Expression of recombinant HSL was screened in strains: BL21(DE3), BL21(DE3)pLysS, Rosetta(DE3), Rosetta(DE3)pLysS and Rosettagami2(DE3), using various bacterial growth media. Cultures were induced in exponential phase for 16 h at 20 °C with 0.2 mM IPTG. All pellets were lysed in B-PER (Pierce, Milan) to obtain soluble and insoluble fractions and loaded on 12% SDS/PAGE. Expression was confirmed by Western Blot with anti-His-HRP conjugated antibody before scaling-up optimized conditions.

2.1.3. Purification of recombinant HSL

Expression was scaled up under sequentially optimized conditions to 400 ml cultures grown in 1.8 L baffled shake flasks, with vigorous shaking, inducing HSL expression 16 h at 20 °C with 0.2 mM IPTG, before harvesting 15 min at 3000*g*, 4 °C. One gram pellets were resuspended in 10 ml of: 50 mM Tris–HCl, 40 mM imidazole, 0.1% Tween 20, 30 mM $MgCl_2$, 5 mM DTT, 1 mM PMSF, 10 μg/ml lysozyme, 5 μg/ml DNaseI, pH 8.0. The lysate was adjusted to 500 mM NaCl and sonicated gently on ice. The soluble fraction was recovered by centrifugation and loaded on a 1 ml HisTrapHP column, connected to an FPLC ÄKTA system, in the presence of 50 mM Tris–HCl, 500 mM NaCl, 40 mM imidazole, 2 mM DTT, 100 μM PMSF, pH 8.0. Peak fractions eluted at 100 mM and 250 mM imidazole, concentrated on Amicon 10 kDa MWCO and loaded on Superdex 200, Superose 6 or Bio-Sep SEC 3000 columns in 50 mM Tris–HCl, 150 mM NaCl, 2 mM DTT, pH 8.0.

2.1.4. Enzymatic activity of 13-HSL

13-HSL was tested for esterase activity as previously described [8].

2.1.5. Optimization of expression for correct protein folding

Recombinant HSL underwent growth and expression in the presence of additives to optimize the level of correct protein folding in bacteria. Either trehalose or benzyl alcohol were added at the initiation of the exponential stage of bacterial growth at various concentrations. Growth was continued and 13-HSL expression induced with IPTG. Lysates from 2 ml cultures were prepared in B-PER and 100 μg from each soluble fraction was subjected to 2 h digestion at 25 °C in the presence of 5 ng trypsin to determine optimal additive concentration.

Once optimized, growth was scaled up to 400 ml cultures as above and followed either to OD_{600} = 0.2 at 37 °C, before adding 50 mM trehalose and 400 mM NaCl, switching to 20 °C for 45 min before adding 0.2 mM IPTG and expressing 24 h at 16 °C; or to OD_{600} = 0.4 at 37 °C, before adding 20 mM benzyl alcohol, switching to 20 °C for 20 min before adding 0.2 mM IPTG and expressing 24 h at 16 °C. Pelleted cells were resuspended and treated as before, although following HisTrap purification, concentrated samples were further purified directly on Bio-Sep SEC 3000. Using this new purification procedure the protein yield was 1.6 mg/g cells, while refolding from inclusion bodies yielded 20 mg/g cells.

2.1.6. Circular dichroism

All CD spectra were recorded with a Jasco J-715 spectropolarimeter equipped with a Peltier temperature control system [Model PTC-423-S]. Molar ellipticity per mean residue, $[\theta]$ in deg $cm^2 \times dmol^{-1}$, was calculated from the equation: $[\theta] = [\theta]_{obs} \times mrw/10 \times l \times C$, where $[\theta]_{obs}$ is the ellipticity measured in degrees, mrw is the mean residue molecular mass, *C* is the protein concentration in mg × mL^{-1}, and l is the optical path length of the cell in cm. Far-UV measurements (183–250 nm) were carried out at 20 °C, at time constant of 4 s, 2 nm band width, scan rate of 10 nm min^{-1}, using a 0.1 cm optical path length cell and a protein concentration of 0.2 mg × mL^{-1} in 6.6 mM buffer phosphate pH 8.0. CD spectra were signal averaged over at least three scans, and the baseline was corrected by subtracting a buffer spectrum. Thermal unfolding curves were determined by recording the molar ellipticity at 222 nm, using a scanning rate of 1 °C/min.

2.1.7. Light scattering

The oligomeric form of recombinant HSL was determined by combining size exclusion chromatography with Light Scattering equipment; experiments were run at 0.5 ml/min in 50 mM Tris, 150 mM NaCl, 2 mM DTT, pH 8.0 buffer using a Bio-Sep SEC 3000 size exclusion column (Phenomenex) connected to an FPLC ÄKTA purifier system which in turn was connected to a Refractive index (Shodex RI 101) followed by a Mini Dawn Treos (Wyatt Technology, USA) Light Scattering instrument. All data collected were interpreted with an ASTRA V software package.

3. Results

11-HSL and 13-HSL were obtained by cloning PCR-amplified HSL cDNA in NcoI/XhoI cleaved pETM11 and pETM13. Resulting clones were verified by bidirectional sequencing.

Initial levels of expression were confronted with that of the original clone in pET22b [8] in various bacterial expression strains, being induced 16 h at 20 °C with 0.2 mM IPTG. The presence of recombinant HSL was checked by SDS/PAGE. Levels of expression were so low that the HSL could only be detected by Western blotting with an anti-His-HRP conjugated antibody. Expression levels were observed to be clearly higher in pETM13, despite there being a minimal difference between this vector and the commercial pET22b vector using the codon-optimized strain Rosetta(DE3) so all further optimization was carried out using this combination of vector/strain. Expression was further optimized by using enriched TB growth media [13], obtaining a visible expression level on Coomassie Blue stained SDS/PAGE.

Purification of 13-HSL on 1 ml HisTrap revealed two species of the 48 kDa protein, being eluted at 100 mM and 250 mM imidazole (Fig. 1). Both species were initially loaded on a Superdex G200 or Superose 6 column. In both cases 13-HSL eluted with the front, suggesting that the protein was highly aggregated, despite being run in reducing conditions to eliminate any covalent interactions. Although *Psy*HSL contains eight cysteine residues they are all predicted to be reduced (re. DiANNA 1.1 web server) so any aggregation is likely due to remaining non-covalent interactions brought about by incorrect folding of the protein at the expression level.

There are numerous alternatives available in attempting to reduce the level of misfolded protein expressed during bacterial growth [14–16] either by reducing the level of aggregated protein formed in the bacterial cells or by scavenging any misfolded proteins and converting them into a correctly folded species [17–20]. Lowering the induction temperature and optimizing the growth medium had minimal effects on the level of soluble recombinant *Psy*HSL expressed in *E. coli*. It was therefore decided to try two alternative approaches; firstly using the osmolyte trehalose [12] alone or in conjunction with a high salt concentration in the growth medium to encourage its uptake into the bacterial cells and create a more viscous environment, thereby helping stabilize cells under stress and improve protein stability overall [21–23]. The second approach was to use the membrane fluidizer benzyl alcohol [11] which alters the structure of the cytoplasmic membrane, creating stress and inducing the production of endogenous chaperones to prevent aggregation [24,25].

A series of concentrations of trehalose +/− NaCl and benzyl alcohol were added to the growth medium in early log phase. Optimal trehalose and benzyl alcohol concentrations were selected based on the results of trypsin digests of the supernatant collected from cell lysates: 5 ml cultures were treated initially with additive at the appropriate OD_{600} followed by 24 h induction in the presence of 0.2 mM IPTG. Trypsin treated lysates were loaded on 12% SDS/PAGE. The least digested full-length *PsyHSL* observed on SDS/PAGE were: 50 mM trehalose + 400 mM NaCl and 20 mM benzyl alcohol.

As before, trehalose and benzyl alcohol treated cultures were purified on 1 ml HisTrapHP and eluted at 100 and 250 mM imidazole. The four individual peak fractions were purified on Bio-Sep SEC 3000, together with untreated 100 mM and 250 mM imidazole fractions (Fig. 2). The 250 mM imidazole fractions were discarded, since they contained almost exclusively aggregated protein which eluted with the front (as verified by a standard calibration curve with proteins run in the same buffer, Fig. 2), but both the trehalose treated and benzyl alcohol treated 100 mM fractions showed a clear improvement over untreated cells since most of the protein eluted at the expected retention time for a 48 kDa protein, implying that the protein was correctly folded. Benzyl alcohol treatment provided a cleaner band, although trehalose + NaCl treatment also clearly improved the level of correctly folded protein.

3.1. Circular dichroism

Secondary structure of soluble HSL purified from benzyl alcohol treatment was investigated by means of CD in the far-UV region. The spectrum suggested that native HSL displays a high degree of secondary structure, showing a large negative band at 222 nm. Estimation of the secondary structure of native HSL performed on the basis of the CD spectrum, was carried out according to the Variable Selection Method (CDSSTR) using DICHROWEB and

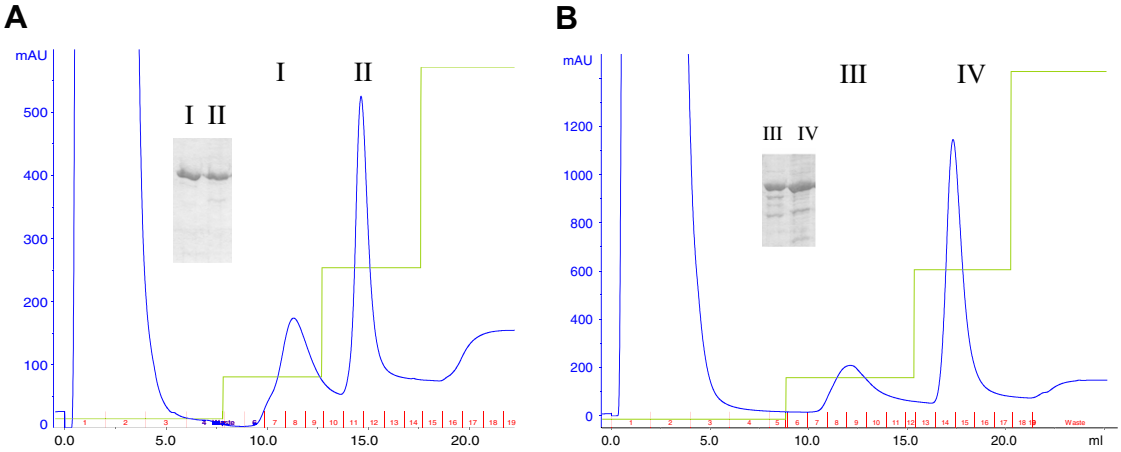

Fig. 1. Purification scheme of soluble 13-HSL. (A) 13-HSL HisTrap purification in the presence of 20 mM benzyl alcohol: I and II indicate 13-HSL fractions eluted with 100 mM and 250 mM imidazole respectively (B) 13-HSL HisTrap purification expression in the presence of 50 mM trehalose + 400 mM NaCl.: III and IV indicate 13-HSL fractions eluted with 100 mM and 250 mM imidazole respectively.

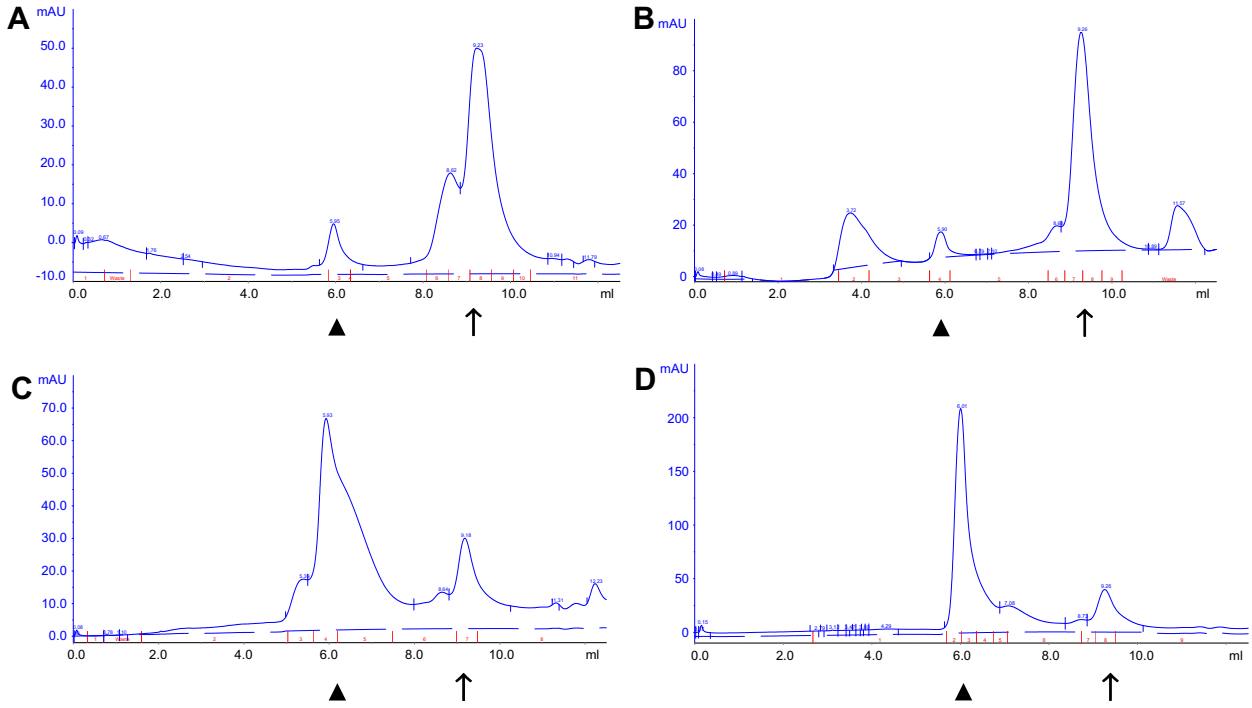

Fig. 2. Purification scheme of HisTrap purified 13-HSL on Bio-Sep SEC 3000. Panels on the left refer to 13-HSL expression in the presence of 20 mM benzyl alcohol; those on the right refer to 13-HSL expression in the presence of 50 mM trehalose + 400 mM NaCl. [A]–[B] 100 mM imidazole peak purification [C]–[D] 250 mM imidazole peak purification; [▲] represents aggregated protein; ↑ represents soluble protein.

revealed it to be comprised of 29% alpha helix and 18% beta sheet. The protein melted at 49 °C and was irreversible under the conditions used, likely due to cross-linking between the six cysteines present within the amino acidic sequence [26,27]. It is worth noting that the thermally denatured HSL at 75 °C still contains a substantial amount of secondary structure as calculated by DICHROWEB. The protein's transition curve is shown in Fig. S1. In order to investigate the influence of electrostatic interactions and solvent properties on the secondary structure of HSL, 1.0 and 1.5 M NaCl were added to HSL and thermal transition curves at 222 nm recorded. Because high concentrations of NaCl disrupt electrostatic interactions but stabilize hydrophobic interactions, they can be used as a method of testing which kind of interaction predominates [28]. In this case almost all secondary structure signals disappeared as temperature increased proving that residual secondary structure previously recorded was mainly due to electrostatic interactions. Also in this case the event was irreversible but the Tm registered was lower, being 43.5 °C indicating that the secondary structure is destabilized at high ionic strength [29].

3.2. Light scattering analysis

Size exclusion chromatography and light scattering analysis on native protein purified from benzyl alcohol treated cells clearly showed that HSL is monomeric in solution with a molar mass of 48 g/mol.

3.3. Enzymatic assays

The relationship between *Psy*HSL activity and temperature in the range 20–50 °C was investigated, using *p*NP-pentanoate as substrate. The apparent maximal activity was recorded at 35 °C, in good agreement with previous results [8]. *Psy*HSL thermal stability was evaluated in the range 35–45 °C (Fig. 3). Enzyme samples were incubated at any given temperature for up to 1 h and residual activity was measured. After 1 h incubation at 45 °C, the native protein still retained 10% of its enzymatic activity (Fig. 3), contrary to previous analyses of refolded *Psy*HSL which showed a dramatic drop in enzymatic activity after only 20 min incubation at 40 °C [8]. As far as specific activity of the enzyme is concerned, the recombinant native HSL showed a comparable specific activity of about 43 U/mg with those values obtained for the refolded *Psy*HSL (38 U/mg).

4. Discussion

Correct recombinant protein folding within the cell necessitates the presence, usually transient, of an array of molecular chaperones, either produced naturally or "induced" by the presence of additives which stimulate their endogenous production [21,24,30,31]. Cellular osmolytes act as chemical chaperones within the cell and are often produced naturally [11,21–23] to

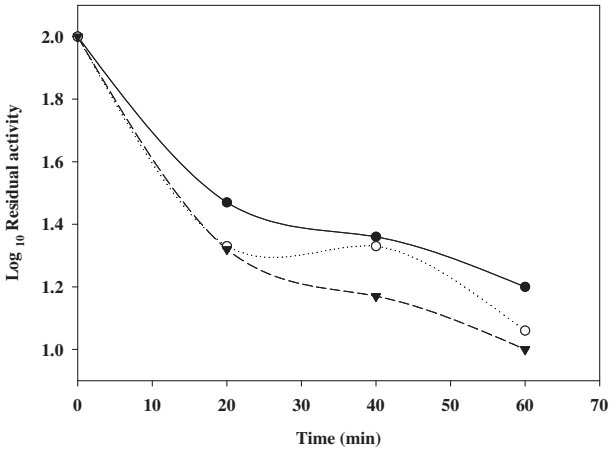

Fig. 3. Thermostability of *Psy*HSL at various temperatures: 35 °C [●], 40 °C [○], 45 °C [▼]. The enzyme was incubated in 0.1 M Tris–HCl pH 8.0 at the indicated temperatures for the times indicated. Residual activity was measured at 35 °C.

counteract a stressful environment, being composed of three classes of compounds. The first two classes include carbohydrates such as glycerol, sorbitol, trehalose and amino acids and derivatives such as alanine, taurine, γ-aminobutyric acid, which are compatible osmolytes and may accumulate in the cell at high concentration without affecting protein function. The third class is represented by methylamines such as betaine, trimethylamine N-oxide which are counteracting osmolytes which offset the adverse effects brought about by presence of inorganic ions such as urea. Normally the accumulation of cellular osmolytes is a relatively slow process, but interestingly it has been observed that the addition externally of a high concentration of NaCl leads to a rapid release of heat shock protein [11,21] and enhances the effect of using a cellular osmolyte alone, as observed here. In fact, in this study the use of additives to the bacterial growth media has had a determining effect in enabling us to produce enough full length *PsyHSL* native protein for extensive biochemical analyses. By comparison of CD spectra a significative shift of melting point was noted [8], highlighting the fact that in the conditions applied a more stable protein was produced. During thermal denaturation, secondary structure was disrupted only in the presence of high salt concentration, suggesting that solvent characteristics affect the conformational features of thermally treated HSL whilst residual secondary structure is influenced by electrostatic interactions [32].

Enzymatic assays performed at 40 °C revealed a more stable native *Psy*HSL, whilst the refolded protein lost its catalytic activity after only 20 min incubation at this temperature [8], despite the fact that the two forms of protein expressed had comparable specific activities. This may be due to the refolding process, leaving only a partially folded catalytically active enzyme unable to maintain its structure at higher temperature.

Catalytic activity was also tested at 45 °C, and unexpectedly the protein was at least 10% active after 1 h incubation confirming that the use of such chemical compounds represents an alternative strategy to obtain recombinant proteins in native form. The optimal temperature for native *Psy*HSL was 35 °C, the same as for the refolded enzyme, corroborating the psychrophilic character of *Psy*HSL.

In conclusion we have established a novel method for obtaining native HSL in *E. coli*. The native enzyme proved to be more stable during thermal denaturation compared to refolded inclusion bodies as shown by CD experiments and activity data.

Recent studies suggest that the relationship between enzymatic activity at low temperature and conformational stability is more complicated than that initially believed to be based on comparative activity and structural studies alone; in this case the native form of *Psy*HSL should allow us to better define its structure–function relationship especially with regard to its cold adaptation strategy, enabling it to be applied to a wide range of biotechnological processes.

Acknowledgments

This work was supported in part by italian PRIN grant 2008F5A3AF_001 (to G.A.).

Appendix A. Supplementary data

Supplementary data associated with this article can be found, in the online version, at doi:10.1016/j.bbrc.2012.03.028.

References

[1] I.J. Goldberg, Lipoprotein lipase and lipolysis: central roles in lipoprotein metabolism and atherogenesis, J. Lipid Res. 37 (1996) 693–707.
[2] D.W. Choo, T. Kurihara, T. Suzuki, K. Soda, N. Esaki, A cold-adapted lipase of an Alaskan psychrotroph, *Pseudomonas* sp. strain B11–1: gene cloning and enzyme purification and characterization, Appl. Environ. Microbiol. 64 (1998) 486–491.
[3] M. Royter, M. Schmidt, C. Elend, H. Höbenreich, T. Schäfer, U.T. Bornscheuer, G. Antranikian, Thermostable lipases from the extreme thermophilic anaerobic bacteria *Thermoanaerobacter thermohydrosulfuricus* SOL1 and *Caldanaerobacter subterraneus* subsp. *Tengcongensis*, Extremophiles 13 (2009) 769–783.
[4] P. Tirawongsaroj, R. Sriprang, P. Harnpicharnchai, T. Thongaram, V. Champreda, S. Tanapongpipat, K. Pootanakit, L. Eurwilaichitr, Novel thermophilic and thermostable lipolytic enzymes from a Thailand hot spring metagenomic library, J. Biotechnol. 133 (2008) 42–49.
[5] A. Houde, A. Kademi, D. Leblanc, Lipases and their industrial applications, an overview, Appl. Biochem. Biotechnol. 118 (2004) 155–170.
[6] F. Hasan, A.A. Shah, A. Hameed, Biotechnol. Adv. 27 (2009) 782–798.
[7] G. Feller, M. Thiry, J.L. Arpigny, C. Gerday, Cloning and expression in *Escherichia coli* of three lipase-encoding genes from the psychrotrophic antarctic strain *Moraxella TA144*, Gene 102 (1991) 111–115.
[8] C. De Santi, M.L. Tutino, L. Mandrich, M. Giuliani, E. Parrilli, P. Del Vecchio, D. de Pascale, The hormone-sensitive lipase from *Psychrobacter* sp. TA144: new insight in the structural/functional characterization, Biochimie 92 (2010) 949–957.
[9] D. Langin, H. Laurell, L.S. Holst, P. Belfrage, C. Holm, Gene organization and primary structure of human hormone-sensitive lipase: possible significance of a sequence homology with a lipase of *Moraxella TA144*, an antarctic bacterium, Proc. Natl. Acad. Sci. USA 90 (1993) 4897–4901.
[10] Z.S. Derewenda, U. Derewenda, Relationships among serine hydrolases: evidence for a common structural motif in triacylglyceride lipases and esterases, Biochem. Cell Biol. 69 (1991) 842–851.
[11] A. de Marco, L. Vigh, S. Diamant, P. Goloubinoff, Native folding of aggregation-prone recombinant proteins in *Escherichia coli* by osmolytes, plasmid- or benzyl alcohol-overexpressed molecular chaperones, Cell Stress Chap. 10 (2005) 329–339.
[12] T. Schultz, J. Liu, P. Capasso, A. de Marco, The solubility of recombinant proteins expressed in Escherichia coli is increased by *otsA* and *otsB* co-transformation, Biochem. Biophys. Res. Commun. 355 (2007) 234–239.
[13] J. Sambrook, E. F. Fritsch, T. Maniatis, Molecular cloning: a laboratory manual, 2nd ed. Cold Spring Harbor Laboratory, Cold Spring Harbor, New York, 1989.
[14] G. Georgiou, P. Valax, Expression of correctly folded proteins in *Escherichia coli*, Curr. Opin. Biotechnol. 7 (1996) 190–197.
[15] O. Kolaj, S. Spada, S. Robin, J.G. Wall, Use of folding modulators to improve heterologous protein production in *Escherichia coli*, Microb. Cell Fact. 8 (2009) 9.
[16] F. Baneyx, Recombinant protein expression in *Escherichia coli*, Curr. Opin. Biotechnol. 10 (1999) 411–421.
[17] A. Mogk, E. Deuerling, S. Vorderwülbecke, E. Vierling, B. Bukau, Small heat shock proteins, *ClpB* and the *DnaK* system form a functional triade in reversing protein aggregation, Mol. Microbiol. 50 (2003) 585–595.
[18] H.P. Sørensen, K.K. Mortensen, Soluble expression of recombinant proteins in the cytoplasm of *Escherichia coli*, Microb. Cell Fact. 4 (2005) 1.
[19] W.J. Welch, C.R. Brown, Influence of molecular and chemical chaperones on protein folding, Cell Stress Chap. 1 (1996) 109–115.
[20] A. Puig, H.F. Gilbert, Protein disulfide isomerase exhibits chaperone and anti-chaperone activity in the oxidative refolding of lysozyme, J. Biol. Chem. 269 (1994) 7764–7771.
[21] S. Diamant, D. Rosenthal, A. Azem, N. Eliahu, A.P. Ben-Zvi, P. Goloubinoff, Dicarboxylic amino acids and glycine-betaine regulate chaperone-mediated protein-disaggregation under stress, Mol. Microbiol. 49 (2003) 401–410.
[22] H.C. Tseng, D.J. Graves, Natural methylamine osmolytes, trimethylamine N-oxide and betaine, increase tau-induced polymerization of microtubules, Biochem. Biophys. Res. Commun. 250 (1998) 726–730.
[23] P.H. Yancey, Organic osmolytes as compatible, metabolic and counteracting cytoprotectants in high osmolarity and other stresses, J. Exp. Biol. 208 (2005) 2819–2830.
[24] D.H. Lee, M.D. Kim, W.H. Lee, D.H. Kweon, J.H. Seo, Consortium of fold-catalyzing proteins increases soluble expression of cyclohexanone monooxygenase in recombinant *Escherichia coli*, Appl. Microbiol. Biotechnol. 63 (2004) 549–552.
[25] K.S. Gunnarsen, E. Lunde, P.E. Kristiansen, B. Bogen, I. Sandlie, G.A. Løset, Periplasmic expression of soluble single chain T cell receptors is rescued by the chaperone *FkpA*, BMC Biotechnol. 10 (2010) 8.
[26] P. Del Vecchio, G. Graziano, G. Barone, L. Mandrich, M. Rossi, G. Manco, Temperature-induced denaturation of the Aes acetyl-esterase from *Escherichia coli*, Thermochimica Acta 441 (2006) 144–149.
[27] L. Tornatore, D. Marasco, N. Dathan, R.M. Vitale, E. Benedetti, S. Papa, G. Franzoso, M. Ruvo, S.M. Monti, Gadd45 beta forms a homodimeric complex that binds tightly to MKK7, J. Mol. Biol. 378 (2008) 97–111.
[28] S.H. Gerber, J. Rizo, T.C. Südhof, Role of electrostatic and hydrophobic interactions in Ca(2$^+$)-dependent phospholipid binding by the C(2)A-domain from synaptotagmin I, Diabetes 51 (2002) S12–18.
[29] K. Yamazaki, T. Iwura, R. Ishikawa, Y. Ozaki, Effects of ionic strength on the thermal unfolding process of granulocyte-colony stimulating factor, J. Biochem. 139 (2006) 41–49.
[30] A. de Marco, Strategies for successful recombinant expression of disulfide bond-dependent proteins in *Escherichia coli*, Microb. Cell Fact. 8 (2009) 26.
[31] F. Baneyx, M. Mujacic, Recombinant protein folding and misfolding in *Escherichia coli*, Nat. Biotechnol. 22 (2004) 1399–1408.
[32] B. Ibarra-Molero, J.A. Zitzewitz, C.R. Matthews, Salt-bridges can stabilize but do not accelerate the folding of the homodimeric coiled-coil peptide GCN4-p1, J. Mol. Biol. 336 (2004) 989–996.

Biochemical and Biophysical Research Communications 420 (2012) 547–551

Contents lists available at SciVerse ScienceDirect

Biochemical and Biophysical Research Communications

journal homepage: www.elsevier.com/locate/ybbrc

Destabilization of a bovine B_{12} trafficking chaperone protein by oxidized form of glutathione

Jihyun Park [1], Jinju Jeong [1], Jihoe Kim *

School of Biotechnology, Yeungnam University, Gyeongsan 712-749, Republic of Korea

ARTICLE INFO

Article history:
Received 18 February 2012
Available online 13 March 2012

Keywords:
Glutathione
Vitamin B_{12}
B_{12} trafficking chaperone
Thermostability

ABSTRACT

The protein, bCblCpro, is a bovine B_{12} trafficking chaperone involved in intracellular B_{12} metabolism. bCblCpro is highly thermolabile (T_m = ~42 °C) and the reduced form of glutathione, GSH, has been found to stabilize bCblCpro as a positive regulator. In this study, we discovered that the oxidized form of glutathione, GSSG, destabilizes bCblCpro, which is derived from changes in the conformation of the protein upon GSSG binding. The binding affinity for GSSG was determined to be similar with the affinity for GSH. The AC_{50} = 2.8 ± 0.4 mM of GSSG for destabilization of bCblCpro was consistently similar with the AC_{50} = 2.1 ± 0.5 mM of GSH for stabilization of the protein. These results suggest that GSSG is a negative regulator of bCblCpro and that the molar ratio of [GSH]/[GSSG] in cells may determine the stability of the B_{12} trafficking chaperone.

1. Introduction

B_{12} (vitamin B_{12} derivatives, cobalamins) is an essential micronutrient for mammals including humans. Since humans are incapable of de novo B_{12} synthesis, they must be supplemented with B_{12} from their diet. Malnutrition or malabsorption of B_{12} can result in its deficiency that is a cause of complex diseases such as megaloblastic anemia, neurological disease, cardiovascular disease and cognitive dysfunction. However, the pathological mechanism of B_{12} deficiency is not fully understood [1].

B_{12} is a complex organometallic enzyme cofactor and contains cobalt that is coordinated by four nitrogen atoms in the center of a tetrapyrrole (corrin) ring [2]. A dimethylbenzimidazole extended from the corrin ring forms the fifth ligand (α-ligand) of the cobalt. The sixth exogenous ligand (β-ligand) determines the biological activities of B_{12}. Adenosylcobalamin (coenzyme B_{12}, AdoCbl) and methylcobalamin (MeCbl) are active forms of B_{12} with a 5′-deoxyadenosyl and methyl β-ligand, respectively [3,4]. In humans, methylmalonyl-CoA mutase in mitochondria and methionine synthase in cytosol are dependent on AdoCbl and MeCbl, respectively. Hence, any other forms of B_{12} introduced into human cells should be converted to the enzyme cofactors.

Inherited disorders of intracellular B_{12} metabolism that causes B_{12} deficiency are classified into eight genetic complementation groups (*cblA-G* and *mut*) [3,4]. The majority of patients with genetic defects of the B_{12} metabolism belong to the *cblC* group [5]. The defective gene in the *cblC* group encodes the cytosolic protein MMACHC (methylmalonic aciduria and homocystinuria cblC type) [6]. This protein functions a B_{12} trafficking chaperone, which protects the highly reactive B_{12} from undesired reactions and transfers it to subsequent proteins for enzyme cofactor synthesis [7]. In addition, MMACHC catalyzes elimination of a cyanide β-ligand from vitamin B_{12} (cyanocobalamin, CNCbl) and alkyl β-ligands from alkylcobalamins yielding cob(II)- and cob(I)alamin, respectively. These can be common intermediates for subsequent enzyme cofactor synthesis [7–9]. MMACHC is extremely thermolabile with an in vitro melting temperature of T_m = 39.3 ± 1.0 °C that is very close to the human body temperature of 37 °C [10]. Binding of B_{12} stabilizes MMACHC and increases the T_m of the protein from 39.3 ± 1.0 °C to ~43–55 °C [10]. However, other cellular molecule(s) has been supposed to stabilize MMACHC, since B_{12} presents at low concentrations (0.03–0.6 μM) in normal cells [11].

B_{12} trafficking chaperone proteins are highly conserved in mammals and we previously identified bCblCpro, the bovine homolog of MMACHC [12]. bCblCpro was characterized to be also highly thermolabile with T_m = ~42 °C and stabilized by binding of the reduced form of glutathione GSH that is abundant (1–10 mM) in cells [13]. In addition, GSH-bound bCblCpro binds CNCbl with a higher affinity than apo-bCblCpro [14], indicating that GSH is a positive regulator of bCblCpro. The present study investigates the effect of the oxidized form of glutathione GSSG on the thermostability of bCblCpro. The half-life of bCblCpro decreased in the presence of GSSG, which is derived from conformational changes of the protein induced by

Abbreviations: B_{12}, vitamin B_{12} derivatives; bCblCpro, bovine CblC protein; GSH, reduced form of glutathione; GSSG, oxidized form of glutathione.

* Corresponding author. Fax: +82 53 810 4769.
E-mail address: kimjihoe@ynu.ac.kr (J. Kim).

[1] These authors are equally contributed to this study.

0006-291X/$ - see front matter © 2012 Elsevier Inc. All rights reserved.
http://dx.doi.org/10.1016/j.bbrc.2012.03.031

GSSG binding. The sensitivity of GSSG for destabilization of bCblCpro is similar with the sensitivity of GSH for stabilization of the protein. The binding affinity for GSSG was determined to be consistently similar with the affinity for GSH. Based on these results, the regulation of bCblCpro by glutathione is discussed.

2. Materials and methods

2.1. Materials and general methods

All chemicals used in this study were purchased from Sigma, unless otherwise stated. The recombinant bCblCpro protein was purified from *E. coli* by the over-expression of the encoding gene as previously described [12]. All experiments with CNCbl were carried out under dark conditions and concentration of CNCbl was determined using the reference extinction coefficient [15]. Protein concentrations were determined by Bradford assay [16].

2.2. Differential scanning fluorimetry (DSF)

DSF was conducted as previously described [13,17] with 0.2 mg/ml bCblCpro in 100 mM Hepes pH 8.0, 150 mM KCl and 5% glycerol containing 10× fluorescent reporter dye Sypro orange (Invitrogen). In the absence or presence of the indicated concentrations of the ligand(s), the protein was incubated with increasing temperatures from 4 °C to 75 °C at a rate of 1 °C/min using an ABI 7500 Real-Time PCR system (Applied Biosystem). The thermal unfolding of bCblCpro was monitored by following the fluorescence intensity of the Sypro orange that increases upon binding to the exposed hydrophobic regions of the unfolded protein. The melting temperature T_m was determined by fitting DSF data to a Boltzmann equation. The ligand concentration to achieve the half-maximal protein stabilization (AC_{50}) and the maximal change in T_m ($\Delta T_{m\ max}$) were estimated by fitting the plot of changes in T_m ($\Delta T_m = T_m$ in the presence of ligand $-T_m$ in the absence of ligand) vs. ligand concentrations ([L]) to the equation of $\Delta T_m = \Delta T_{m\,max} \times [L]/(AC_{50} + [L])$.

2.3. Isothermal denaturation (ITD)

ITD was conducted with bCblCpro prepared as described above by incubation at the constant temperature of 37 °C. bCblCpro unfolding rates (k_{ob}) were determined by fitting the fluorescence increase to a single exponential equation. AC_{50} of GSSG was estimated from the plot of changes in k_{ob} (Δk_{ob}) vs. GSSG concentrations ([GSSG]) that fits the equation of $\Delta k_{ob} = \Delta k_{ob\,max} \times [GSSG]/(AC_{50} + [GSSG])$, where the $\Delta k_{ob\ max}$ is the maximal change in k_{ob}.

2.4. Isothermal titration calorimetry (ITC)

ITC was carried out at 4 °C as previously described [14,18] using a VP-ITC microcalorimeter (1.44 ml cell volume) (Microcal Inc.). GSSG (2.0–4.5 mM) dissolved in 50 mM Hepes pH 8.0, 150 mM KCl and 5% glycerol was injected into 10–30 μM bCblC in the absence or presence of 100-fold molar excess CNCbl in the same buffer. The data was analyzed using a single-site binding model to determined K_d for GSSG.

2.5. Ligand binding titration by UV–vis spectroscopy

Binding of CNCbl to bCblCpro was titrated by UV–vis spectroscopy using the absorption difference at A550 nm between free CNCbl in the base-on state and bCblCpro-bound CNCbl in the base-off state [12]. bCblCpro was added in aliquots to 10–20 μM CNCbl in 50 mM Hepes pH 8.0, 150 mM KCl and 5% glycerol and UV–vis absorption spectrum was recorded at each addition of the protein following 10 min incubation at 20 °C to reach a binding equilibrium. The dissociation constant (K_d) for CNCbl was determined by fitting the plot of ΔA550 nm vs. protein concentration to a hyperbolic saturation equation, as previously described [12]. For the titration of CNCbl binding to GSSG-bound bCblCpro, 0.5 mM bCblCpro was pre-mixed with 5 mM GSSG and added to CNCbl in the presence of 5 mM GSSG as described above.

3. Results

3.1. Destabilization of bCblCpro by GSSG binding

Differential scanning fluorimetry (DSF) to examine the thermostability of bCblCpro showed the fluorescence increase in a sigmoidal shape, indicating two-state transition of the protein from the native to the unfolded state (Fig. 1A). The melting temperatures of bCblCpro were determined to be $T_m = 42.1 \pm 0.1$ °C that is close to the bovine body temperature of 39–40 °C [19]. The effect of glutathione was examined by DSF unfolding bCblCpro in the presence of 10 mM GSH or 10 mM GSSG. The unfolding curve obtained in the presence of 10 mM GSH shifted toward a higher temperature with a $T_m = 43.8 \pm 0.1$ °C, indicating stabilization of bCblCpro by GSH that is consistent with the previous report [13]. Whereas, in the presence of 10 mM GSSG, no significant change was observed in the unfolding curve with a $T_m = 42.0 \pm 0.2$ °C (Fig. 1A).

The effects of GSH and GSSG were investigated by using another method isothermal denaturation (ITD) that measures the kinetics of protein unfolding at a constant temperature [20,21]. ITD of bCblCpro at 37 °C showed a single exponential unfolding of the protein with a $k_{ob} = 0.19 \pm 0.01\ h^{-1}$ (Fig. 1B). The incubation of bCblCpro in the presence of 10 mM GSH showed no significant unfolding of the protein (Fig. 1B), consistently indicating stabilization of the protein by GSH. Whereas, in the presence of 10 mM GSSG, the unfolding of bCblCpro was significantly more rapid with a $k_{ob} = 0.54 \pm 0.01\ h^{-1}$. This result indicates destabilization of bCblCpro by GSSG that could not be detected by DSF likely due to the detection limit [21]. The bCblCpro destabilizing effect of GSSG was further investigated by ITD at various GSSG concentrations. bCblCpro unfolding rates were increased by increasing GSSG concentrations (Fig. 1C). The plot of Δk_{ob} vs. [GSSG] (Fig. 1C inset) clearly shows the hyperbolic relationship between the unfolding rate and the concentration of GSSG. This result indicates that the destabilization of bCblCpro is induced by binding of GSSG to the protein. The concentration of GSSG at half maximal destabilization for bCblCpro was estimated to be $AC_{50} = 2.8 \pm 0.4$ mM with the maximal k_{ob} of a $\Delta k_{ob\ max} = 0.49 \pm 0.03\ h^{-1}$.

The binding of GSSG to bCblCpro was confirmed by isothermal titration calorimetry (ITC). Analysis of the binding isotherm (Fig. 1D) revealed that bCblCpro binds GSSG stoichiometrically ($n = 0.9 \pm 0.1$) with a $K_d = 303 \pm 74$ μM that is significantly lower than the AC_{50} value obtained by ITD. This difference was supposed to be due to the lower experimental temperature of ITC at 4 °C than the temperature of ITD at 37 °C. However, the binding titration for GSSG at 37 °C was not possible because of the precipitation of bCblCpro.

3.2. GSSG binding-induced conformational changes of bCblCpro

It was shown that binding of CNCbl or GSH induces changes in the conformation of bCblCpro [13,14]. We assumed that binding of GSSG may also induce conformational changes of the protein. To prove this, limited proteolysis was conducted by treating bCblCpro with trypsin in the absence or presence of excess GSSG. Subsequent analysis by SDS–PAGE showed a significantly less cleavage of bCblCpro in the presence GSSG (Fig. 2), indicating that

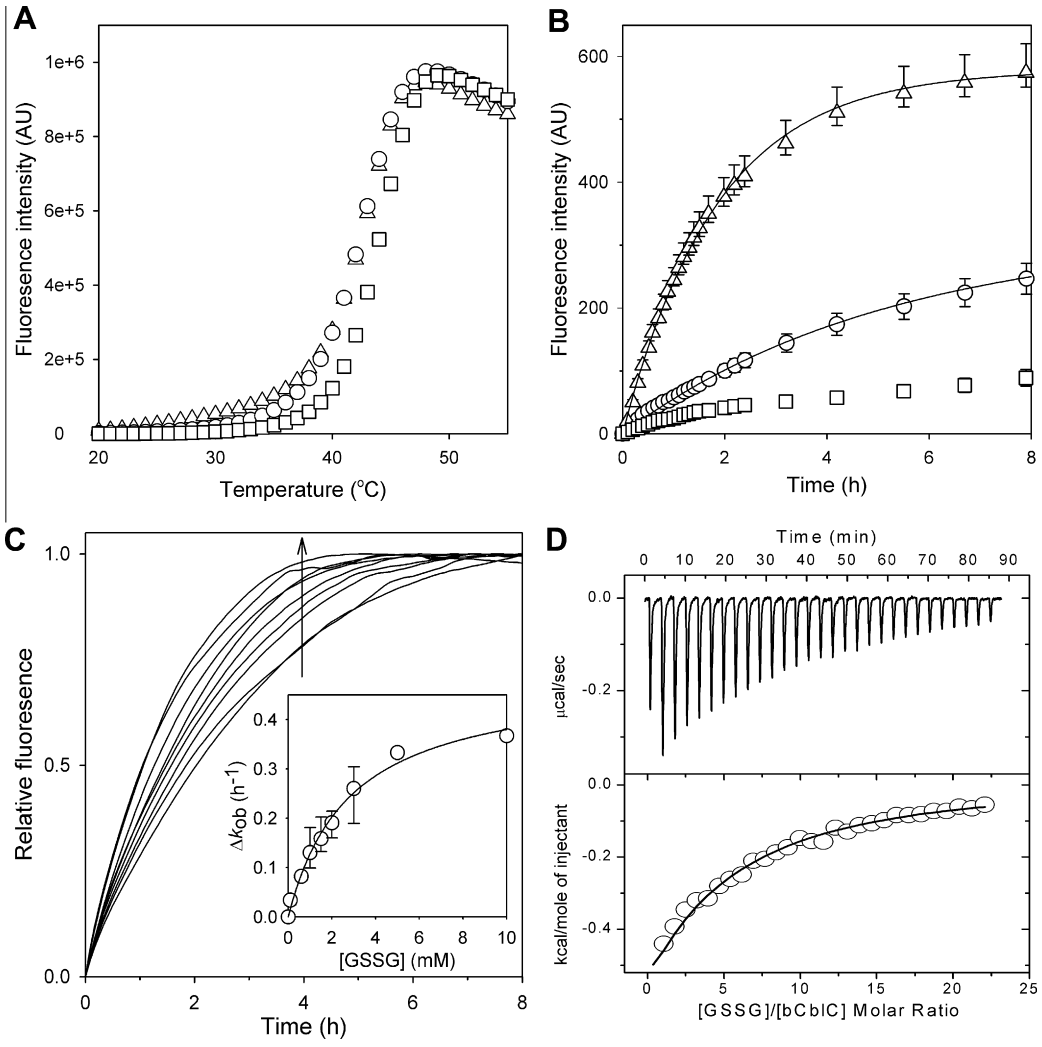

Fig. 1. Destabilization of bCblCpro by GSSG binding. DSF (A) and ITD at 37 °C (B and C) were conducted with 0.2 mg/ml bCblC in the absence (O) and presence of 10 mM GSSG (△) or 10 mM GSH (□). Each unfolding reaction is the average of $n = 6$ (error bars were omitted in A for clarity). Solid lines in B are fitting of the ITD data to a single exponential equation to determine protein unfolding rates (k_{ob} = 0.19 ± 0.01/h and 0.54 ± 0.01/h in the absence and presence of GSSG, respectively). GSSG concentration-dependent unfolding of bCblCpro was followed by ITD at the indicated GSSG concentrations (C). The arrow indicates the shift of unfolding curves by increasing GSSG concentrations. The inset shows a hyperbolic increase in Δk_{ob} (k_{ob} at the indicated [GSSG] $-k_{ob}$ in the absence of GSSG) dependent of GSSG concentrations ([GSSG]) and the solid line is fitting of the data as described in the materials and methods. A representative GSSG binding isotherm (D) was obtained by ITC as described in the materials and methods. Analysis of the data revealed that bCblCpro stoichiometrically binds GSSG (number of binding site = 0.9 ± 0.1) with a K_d = 303 ± 74 μM, which is the average of three independent determinations.

conformational changes of bCblCpro upon GSSG binding. In addition, bCblCpro in the presence of excess GSSG and CNCbl was more significantly resistant against trypsin proteolysis than in the presence of one of the ligands (Fig. 2). In addition, the cleavage patterns were also different from the patterns observed in the proteolysis of bCblCpro in presence of GSSG or CNCbl. These results suggest that one molecule of bCblCpro can bind both GSSG and CNCbl. Furthermore, the conformation of CNCbl-GSSG-bound bCblCpro may be different from the conformations of apo-bCblCpro and the protein bound with one of the ligands.

3.3. Binding of CNCbl to GSSG-bound bCblCpro

Binding of CNCbl to GSSG-bound bCblCpro was titrated by UV–vis spectroscopy as described in the materials and methods. The addition of GSSG-bound bCblCpro to CNCbl in the presence of excess GSSG induced changes in the absorption spectrum with the shifts of the γ-peak at 361 nm and the α/β-peak at 550–359 nm and 531 nm, respectively, (Fig. 3A). These spectral changes are characteristic for the base-off transition of CNCbl [12,14] and indicate binding of the ligand to GSSG-bound bCblCpro. The binding affinity of GSSG-bound bCblCpro for CNCbl was determined to be K_d = 12.7 ± 2.4 μM (Fig. 3A inset). Whereas, the binding affinity of apo-bCblCpro for CNCbl was determined to be lower with a K_d = 20.2 ± 3.4 μM (Fig. 3A inset).

The effect of CNCbl on the thermostability of apo-bCblCpro and GSSG-bound bCblCpro was examined by DSF unfolding bCblCpro in the absence or presence of excess GSSG and with various concentrations of CNCbl. Independent of the presence of GSSG, the obtained unfolding curves were shifted towards higher temperatures (Fig. 3B) with a hyperbolic increase in T_m by increasing the concentration of CNCbl (Fig. 3B inset). These results indicate that binding of CNCbl stabilizes not only apo-bCblCpro, but also GSSG-bound bCblpro. The concentration of CNCbl for half maximal stabilization of apo-bCblpro was estimated to be AC_{50} = 215 ± 25 μM that is similar with the previously reported result [13]. Interestingly, the sensitivity of CNCbl for stabilization of GSSG-bound bCblCpro was estimated to be higher with an AC_{50} = 60.7 ± 6.3 μM, consistently indicating that GSSG-bound bCblCpro binds CNCbl with a higher affinity than apo-bCblCpro. In addition, comparison of the estimated

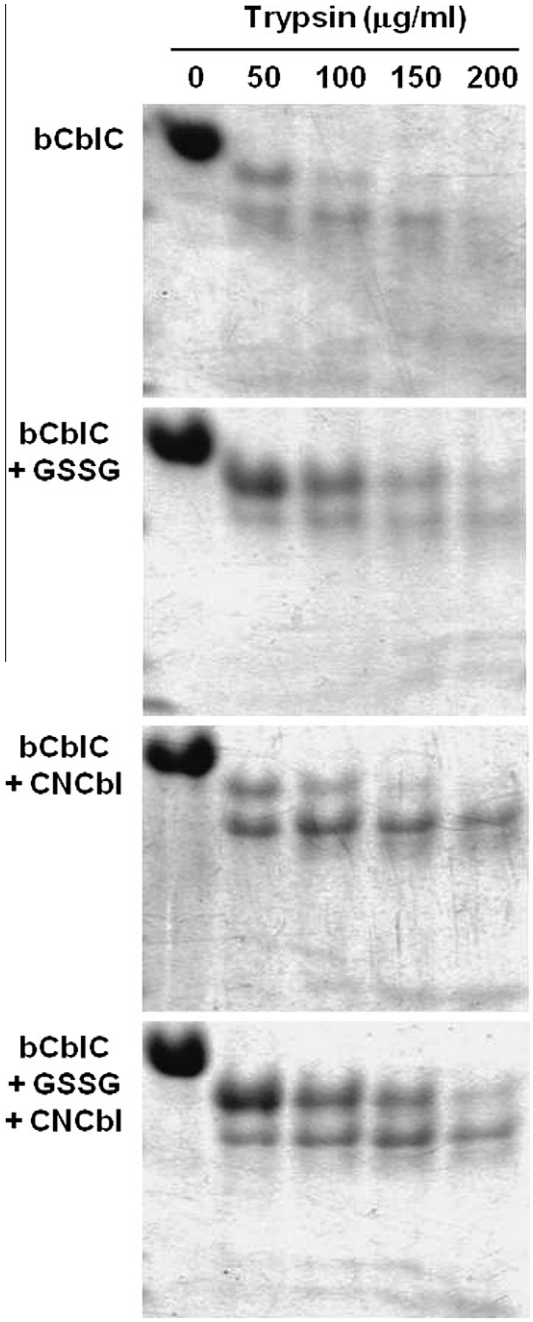

Fig. 2. Conformational changes of bCblCpro by ligand binding. bCblCpro (5 μg, 16 μM) was in 100 mM Hepes pH 8.0, 150 mM KCl and 5% glycerol in the absence or presence of 10 mM GSSG or/and 1 mM CNCbl. Limited proteolysis was initiated by addition of the indicated concentrations of trypsin and incubated at 15 °C for 30 min. The proteolysis was terminated by mixing with SDS–PAGE sample buffer and immediate boiling at 95 °C for 5 min. Proteolyzed proteins were separated by 12% SDS–PAGE and stained with coomassie brilliant blue.

$\Delta T_{m\ max}$ indicates that the stabilizing effect of CNCbl is greater for GSSG-bound bCblCpro ($\Delta T_{m\ max}$ = 7.0 ± 0.2 °C) than apo-bCblCpro ($\Delta T_{m\ max}$ = 4.5 ± 0.2 °C).

4. Discussion

The DSF method has been used to measure the stability of proteins owing to its experimental simplicity with small amount of proteins and a sensitive reporter dye for protein unfolding. Application of a Real-Time PCR system has improved DSF providing a high throughput assessment and greater accuracy [17]. Despite these advantages, small changes in protein stability are often undetectable by DSF due to its detection limit (usually ±1.0 °C) [21]. This limitation can be overcome by using ITD, which is a more sensitive method than DSF and measures the kinetics of protein unfolding at a constant temperature. The sensitivity of ITD is critically dependent on the temperature for protein unfolding, which is usually a few degrees below the T_m of proteins [20]. ITD of bCblCpro at the physiological temperature of 37 °C (~5 °C below the T_m = 42.1 ± 0.1 °C) clearly identify the destabilizing effect of GSSG (Fig. 1B). In addition, the GSSG concentration-dependent destabilization of bCblCpro (Fig. 1C) indicates binding of GSSG to the protein that has been confirmed by ITC (Fig. 1D). The binding affinity for GSSG (K_d = 303 ± 74 μM) appears to be similar to the previously reported affinity for GSH (355 ± 40 μM) (Table 1). The AC_{50} value of GSSG (2.8 ± 0.4 mM) for destabilization of bCblCpro as estimated by ITD is also similar to the previously reported AC_{50} of GSH (2.1 ± 0.5 mM) (Table 1) for stabilization of bCblCpro, which consistently indicates similar binding affinities for GSH and GSSG.

Previous work has shown that binding of GSH induces conformational changes of bCblCpro and stabilizes the protein [13,14]. The destabilization of bCblCpro by GSSG is also derived from conformational changes of the protein induced by GSSG binding as revealed by limited trypsin proteolysis (Fig. 2). Considering the crystal structure of the highly conserved human homolog of bCblCpro [22]; shares 88% amino acid sequence identity, bCblCpro would likely bind GSH and GSSG in the same site in close proximity to the B_{12} binding site. However, the difference in the stability of the ligand-bound proteins indicates that the thermodynamically different conformation of GSSG-bound bCblCpro, not only from apo-bCblCpro, but also from GSH-bound bCblCpro. GSSG-bound bCblC binds CNCbl with a higher affinity than apo-bCblCpro (Fig. 3A), but with a lower affinity than GSH-bound bCblC (Table 1). The AC_{50} of CNCbl for stabilization of GSSG-bound bCblCpro was consistently lower than the AC_{50} for stabilization of apo-bCblCpro (Fig. 3B), but higher than the AC_{50} for stabilization of GSH-bound bCblCpro (Table 1). It can thus be speculated that the conformation of both B_{12} binding sites of GSSG-bound and GSH-bound bCblCpro may be similar to those showing a favorable binding with CNCbl, although the stability determining regions of the ligand-bound proteins would be different. However, GSSG is bulkier than GSH and thus may hinder binding of CNCbl, which results in the significantly lower binding affinity of GSSG-bound bCblCpro for CNCbl than that found in GSH-bound bCblCpro (Table 1).

Glutathione is the most abundant non-protein thiol in mammalian cells and presents at high concentrations (1–10 mM) [23]. Cellular glutathione occurs predominantly in the reduced form GSH in normal cells and ~1% of total glutathione is in the oxidized disulfide form GSSG. GSH has numerous cellular functions, including that of an antioxidant defense against reactive oxygen species. Under oxidative stress, the GSSG level is elevated up to 50% of total glutathione [24]. Since the binding affinity of bCblCpro for GSSG and GSH appears to be similar (Table 1), the cellular fractions of GSH-bound and GSSG-bound bCblCpro may be determined by the molar ratio of [GSH]/[GSSG] in cells. Therefore, under oxidative stress, the cellular fraction of GSSG-bound bCblCpro would increase, which would result in defects in intracellular B_{12} metabolism. Our results in this and recent studies [13,14] may explain the previous observation that decreased GSH levels in rat tissues inhibit MeCbl-dependent methionine synthase due to the decreased ability to synthesize the enzyme cofactor from B_{12} derivatives [25].

To briefly summarize, we discovered that GSSG destabilizes the bovine B_{12} trafficking chaperone bCblCpro that is involved in intracellular B_{12} metabolism. The destabilizing effect of GSSG is derived from conformational changes of bCblCpro induced by GSSG binding.

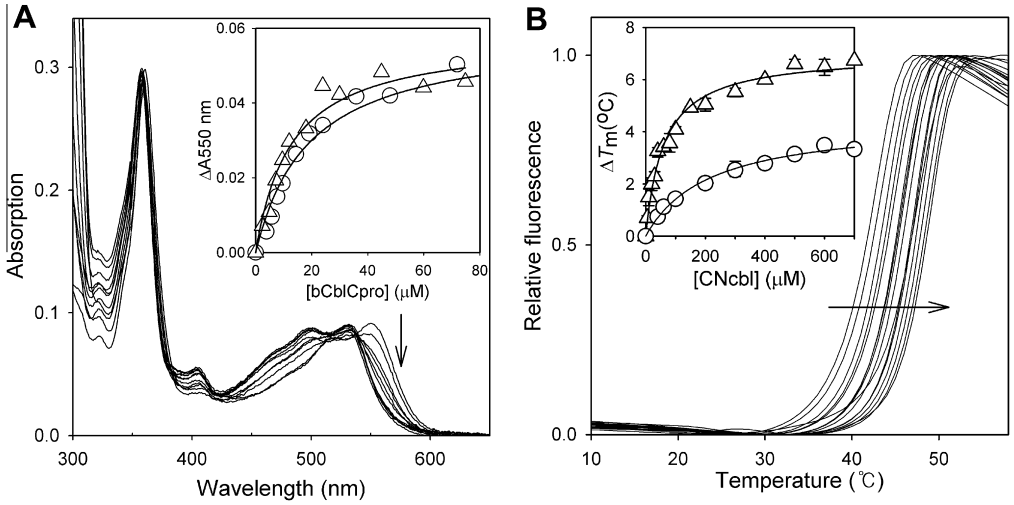

Fig. 3. Binding of CNCbl to GSSG-bound bCblCpro and the stabilizing effect of the ligand. UV–vis spectra (A) were recorded for binding of CNCbl to bCblC in the presence of 10 mM GSSG as described in the materials and methods. The arrow indicates the decrease of A550 nm by the addition of the protein in aliquots. The inset shows fitting (solid lines) of the data to a hyperbolic saturation equation and K_d for CNCbl were determined to be K_d = 20.2 ± 3.4 μM and 12.7 ± 2.4 μM in the absence (○) and presence of 10 mM GSSG (△), respectively. Unfolding of 0.2 mg/ml bCblC was monitored by DSF (B) in the presence of 10 mM GSSG with increasing CNCbl concentrations. The arrows indicate shifts of unfolding curves by increasing CNCbl concentrations. The inset shows a hyperbolic increase in ΔT_m (T_m at the indicated [CNCbl] – in the absence of CNCbl) dependent of CNCbl concentrations ([CNCbl]) in the absence (○) and presence of 10 mM GSSG (△). Solid lines are fitting of the data to a hyperbolic saturation equation as described in the materials and methods.

Table 1
Summary of dissociation constants (K_d) and the sensitivity of ligands (AC_{50}) for stabilization or destabilization of bCblCpro or ligand-bound bCblCpro.

Protein	Ligand	K_d (μM)	AC_{50} (μM)	References
Apo-bCblCpro	GSH	355 ± 40[a]	2100 ± 500[c]	[13,14]
Apo-bCblCpro	GSSG	303 ± 74[a]	2800 ± 400[c]	This study
Apo-bCblCpro	CNCbl	20.2 ± 3.4[b]	215 ± 25[d]	This study
GSH-bound bCblCpro	CNCbl	0.24 ± 0.09[a]	9.3 ± 1.6[d]	[13,14]
GSSG-bound bCblCpro	CNCbl	12.7 ± 2.4[b]	60.7 ± 6.3[d]	This study

The values are an average of the data from more than three independent experiments and represented ±SD. The K_d values were determined by isothermal titration calorimetry ([a]) or UV–vis spectroscopy ([b]). The AC_{50} values estimated by ITD ([c]) or DSF ([d]).

The decreased molar ratio of [GSH]/[GSSG] in cells under oxidative stress may cause defects in intracellular B_{12} metabolism by lowering the fraction of stable and functional B_{12} trafficking chaperones.

Acknowledgment

This research was supported by Basic Science Research Program through the National Research Foundation of Korea (NRF) funded by the Ministry of Education, Science and Technology (2010-0021596).

References

[1] R. Oh, D.L. Brown, Vitamin B_{12} deficiency, Am. Fam. Physician 67 (2003) 979–986.
[2] D.C. Hodgkin, J. Kamper, M. Mackay, J. Pickworth, K.N. Trueblood, J.G. White, Structure of vitamin B_{12}, Nature 178 (1956) 64–66.
[3] R. Banerjee, B_{12} trafficking in mammals: a for coenzyme escort service, ACS Chem. Biol. 1 (2006) 149–159.
[4] R. Banerjee, C. Gherasim, D. Padovani, The tinker, tailor, soldier in intracellular B12 trafficking, Curr. Opin. Chem. Biol. 13 (2009) 484–491.
[5] J.P. Lerner-Ellis, N. Anastasio, J. Liu, D. Coelho, T. Suormala, M. Stucki, A.D. Loewy, S. Gurd, E. Grundberg, C.F. Morel, D. Watkins, M.R. Baumgartner, T. Pastinen, D.S. Rosenblatt, B. Fowler, Spectrum of mutations in MMACHC, allelic expression, and evidence for genotype–phenotype correlations, Hum. Mutat. 30 (2009) 1072–1081.
[6] J.P. Lerner-Ellis, J.C. Tirone, P.D. Pawelek, C. Dore, J.L. Atkinson, D. Watkins, C.F. Morel, T.M. Fujiwara, E. Moras, A.R. Hosack, G.V. Dunbar, H. Antonicka, V. Forgetta, C.M. Dobson, D. Leclerc, R.A. Gravel, E.A. Shoubridge, J.W. Coulton, P. Lepage, J.M. Rommens, K. Morgan, D.S. Rosenblatt, Identification of the gene responsible for methylmalonic aciduria and homocystinuria, cblC type, Nat. Genet. 38 (2006) 93–100.
[7] J. Kim, C. Gherasim, R. Banerjee, Decyanation of vitamin B_{12} by a trafficking chaperone, Proc. Natl. Acad. Sci. USA 105 (2008) 14551–14554.
[8] L. Hannibal, J. Kim, N.E. Brasch, S. Wang, D.S. Rosenblatt, R. Banerjee, D.W. Jacobsen, Processing of alkylcobalamins in mammalian cells: a role for the MMACHC (cblC) gene product, Mol. Genet. Metab. 97 (2009) 260–266.
[9] J. Kim, L. Hannibal, C. Gherasim, D.W. Jacobsen, R. Banerjee, A human vitamin B_{12} trafficking protein uses glutathione transferase activity for processing alkylcobalamins, J. Biol. Chem. 284 (2009) 33418–33424.
[10] D.S. Froese, S. Healy, M. McDonald, G. Kochan, U. Oppermann, F.H. Niesen, R.A. Gravel, Thermolability of mutant MMACHC protein in the vitamin B_{12}-responsive cblC disorder, Mol. Genet. Metab. 100 (2010) 29–36.
[11] J.M. Hsu, B. Kawln, P. Minor, J.A. Mitchell, Vitamin B_{12} concentrations in human tissue, Nature 210 (1966) 1264–1265.
[12] J. Jeong, T.S. Ha, J. Kim, Protection of aquo/hydroxocobalamin from reduced glutathione by a B_{12} trafficking chaperone, BMB Rep. 44 (2011) 170–175.
[13] J. Park, J. Kim, Glutathione and vitamin B_{12} cooperate in stabilization of a B_{12} trafficking chaperone protein, Protein J. 31 (2012) 158–165.
[14] J. Jeong, J. Kim, Glutathione increases the binding affinity of a bovine B_{12} trafficking chaperone bCblC for vitamin B_{12}, Biochem. Biophys. Res. Commun. 412 (2011) 360–365.
[15] B.M. Babior, Cobalamin: Biochemistry and Pathophysiology, Wiley, New York, 1975.
[16] M.M. Bradford, A rapid and sensitive method for the quantitation of microgram quantities of protein utilizing the principle of protein-dye binding, Anal. Biochem. 72 (1976) 248–254.
[17] F.H. Niesen, H. Berglund, M. Vedadi, The use of differential scanning fluorimetry to detect ligand interactions that promote protein stability, Nat. Protoc. 2 (2007) 2212–2221.
[18] D. Padovani, T. Labunska, R. Banerjee, Energetics of interaction between the G-protein chaperone, MeaB, and B_{12}-dependent methylmalonyl-CoA mutase, J. Biol. Chem. 281 (2006) 17838–17844.
[19] G.C. Whittow, Comparative Physiology of Thermoregulation, Academic Press, New York, 1970.
[20] G.A. Senisterra, B. Soo Hong, H.W. Park, M. Vedadi, Application of high-throughput isothermal denaturation to assess protein stability and screen for ligands, J. Biomol. Screen. 13 (2008) 337–342.
[21] G.A. Senisterra, P.J. Finerty Jr., High throughput methods of assessing protein stability and aggregation, Mol. BioSyst. 5 (2009) 217–223.
[22] M. Koutmos, C. Gherasim, J.L. Smith, R. Banerjee, Structural basis of multifunctionality in a vitamin B_{12}-processing enzyme, J. Biol. Chem. 286 (2011) 29780–29787.
[23] N. Ballatori, S.M. Krance, S. Notenboom, S. Shi, K. Tieu, C.L. Hammond, Glutathione dysregulation and the etiology and progression of human diseases, Biol. Chem. 390 (2009) 191–214.
[24] R.E. Hansen, D. Roth, J.R. Winther, Quantifying the global cellular thiol-disulfide status, Proc. Natl. Acad. Sci. USA 106 (2009) 422–427.
[25] M.I. Waly, K.K. Kharbanda, R.C. Deth, Ethanol lowers glutathione in rat liver and brain and inhibits methionine synthase in a cobalamin-dependent manner, Alcohol Clin. Exp. Res. 35 (2011) 277–283.

Biochemical and Biophysical Research Communications 420 (2012) 552–557

Contents lists available at SciVerse ScienceDirect

Biochemical and Biophysical Research Communications

journal homepage: www.elsevier.com/locate/ybbrc

Systematic screen for genes involved in the regulation of oxidative stress in the nematode *Caenorhabditis elegans*

Shunsuke Ueno, Kiichi Yasutake, Daisuke Tohyama, Tsutomu Fujimori, Dai Ayusawa, Michihiko Fujii *

Graduate School of Nanobioscience, Yokohama City University, 22-2 Seto, Kanazawa-ku, Yokohama 236-0027, Japan

ARTICLE INFO

Article history:
Received 2 March 2012
Available online 16 March 2012

Keywords:
C. elegans
Reactive oxygen species
RNAi

ABSTRACT

Oxygen is essential for animals, but high concentrations of oxygen are toxic to them probably because of an increase in reactive oxygen species (ROS). Many genes are involved in the regulation of ROS, but they largely remain to be identified. To identify these genes, we employed the nematode *Caenorhabditis elegans* as a model organism, and systematically screened for genes that, when down-regulated by RNAi, lead to an increased sensitivity to ROS. We examined approximately 2400 genes on linkage group I and found that knock-down of 9 genes which participate in various cellular functions led to an increased sensitivity to ROS. This finding suggests an implication of a variety of cellular processes in the regulation of oxidative stress.

1. Introduction

Reactive oxygen species (ROS) are generated from oxygen as by-products in various metabolic pathways. Since ROS have the potential to damage cellular components such as proteins, DNA and lipids, animals have developed various defense mechanisms against ROS. However, ROS that escape from the defense mechanisms would cause cellular dysfunction that potentially accelerates diseases and aging. Superoxide dismutase (SOD), catalase, and glutathione peroxidase are well known to eradicate ROS, but many other genes are involved in the generation or the quenching of ROS.

To identify these genes, we employed the nematode *Caenorhabditis elegans* as a model organism. In *C. elegans*, several mutants have been shown to be hypersensitive to oxidative stress. For example, mutations in antioxidant proteins such as *sod-1, sod-2*, and *sod-3*, and a mutation in the stress response protein *skn-1* cause an increased sensitivity to oxidative stress [1–5]. In addition to the mutations in these cellular defense proteins, an increased sensitivity to oxidative stress is also caused by mutations in proteins such as MEV-1, GAS-1, OXY-4, OXY-5, and RAD-8, which are a subunit of the electron transport chain (complex II), a subunit of the electron transport chain (complex I), a protein for maturation of [Fe–S] proteins, a mitochondrial ribosomal protein, and a mitochondrial dehydrogenase/reductase, respectively [6–10]. The latter group of proteins would likely be involved in the reactions from which ROS are generated, rather than being involved in cellular defense against oxidative stress. Thereby, the sensitivity to oxidative stress is regulated, at least, both by the cellular defense proteins and by the proteins involved in the generation of ROS. Then, many proteins are involved in the regulation of oxidative stress; however, they are largely left unexplored even in the model organism such as *C. elegans*.

We employed an RNAi technique with the nematode *C. elegans* [11], and screened for genes whose down-regulation leads to an increased sensitivity to ROS. In this study, we knocked down approximately 2400 genes on linkage group I (LG I) in *C. elegans* by RNAi [12,13], and successfully identified 9 genes that, when knocked down by RNAi, caused an increased sensitivity to ROS. Identification of these genes suggests an implication of various cellular processes in the regulation of oxidative stress.

2. Materials and methods

2.1. Strains

The *C. elegans* strains used were obtained from the Caenorhabditis Genetics Center, USA. Worms were grown and maintained at 20 °C on NGM (Nematode growth medium) plates seeded with *Escherichia coli* as a food source [14]. In the RNAi experiments, the wild-type N2 and the RNAi-hypersensitive *rrf-3(pk1426)* strain were used.

2.2. RNAi bacteria

The bacterial RNAi library for LG I was purchased from Geneservice Ltd. The individual bacterial clones, which carry single gene sequences of *C. elegans*, were cultured on the NGM plates supplemented with 1 mM of IPTG and 50 μg/ml of ampicillin (referred to as "NGMI plates" hereafter) to induce the expression of the double-stranded RNAs for the genes of *C. elegans*.

* Corresponding author. Fax: +81 45 787 2213.
E-mail address: mifuji@yokohama-cu.ac.jp (M. Fujii).

0006-291X/$ - see front matter © 2012 Elsevier Inc. All rights reserved.
http://dx.doi.org/10.1016/j.bbrc.2012.03.032

2.3. Assay of the sensitivity to oxidative stress

Sensitivity to oxidative stress in *C. elegans* was determined as previously described [8,15]. L2–L3 larvae of N2 or *rrf-3* were placed on an NGMI plate seeded with a bacterial RNAi clone, and were allowed to grow to adulthood. The adult worms were then transferred to a fresh NGMI plate seeded with the identical bacterial clone, and were allowed to lay eggs for 4–6 h. After removal of the adult worms, the eggs left on the plate were cultured in the presence of various concentrations of oxygen gas for 4–5 days. The percentage of worms that reached adulthood was determined. Sensitivity to paraquat in *C. elegans* was similarly determined. Eggs were prepared from adult worms treated with RNAi, and were incubated on the NGMI plates supplemented with various concentrations of paraquat for 4–5 days. The percentage of worms that reached adulthood was determined.

2.4. Assay of the levels of carbonylated proteins

Eggs were cultured on NGMI plates seeded with bacterial RNAi clones in normal air for 3 days and subsequently in 60% oxygen overnight. The worms were collected in S-basal buffer, washed three times with the same buffer, and suspended in 100 μl of RIPA buffer (50 mM Tris–HCl pH 8.0, 150 mM NaCl, 1% Triton-X 100, 0.5% sodium deoxycholate, 0.1% SDS). Worms were sonicated and centrifuged at 15,000 rpm for 15 min, and the supernatants were used as protein samples, the concentrations of which were determined with a protein assay kit (Bio-Rad). Carbonylated proteins were detected with a detection kit according to the manufacturer's instruction (Protein carbonyls western blot detection kit, SHIMA Laboratories Ltd.). In brief, 30 μg of protein was run on an SDS–polyacrylamide gel and transferred onto a PVDF membrane. The membrane was processed with 2,4-dinitrophenylhydrazine, and incubated with a primary antibody against 2,4-dinitrophenyl and with a horseradish-peroxidase-labeled secondary antibody. The signals were detected and quantified with a chemiluminescence detection kit (ECL, GE Healthcare) and an image analyzer (Max, Bio-Rad).

3. Results

3.1. Screening for genes whose down-regulation leads to an increased sensitivity to oxygen

To gain a molecular insight into the mechanisms that regulate oxidative stress in cells, we aimed to identify genes whose down-regulation leads to an increased sensitivity to ROS. For this, we employed an RNAi technique with the nematode *C. elegans* [11], and systematically screened for genes that, when knocked down by RNAi, lead to an increased sensitivity to high concentrations of oxygen. In *C. elegans*, the target gene can be easily knocked down by simply feeding worms with bacteria that express double-stranded RNA for the target gene (feeding RNAi) [12]. We then systematically knocked down the genes on LG I in *C. elegans* by feeding RNAi with use of a bacterial RNAi library, which covers approximately 90% of the genes on LG I [13]. We placed L2–L3 larvae on plates seeded with individual bacterial RNAi clones, and allowed the worms to grow to adulthood and lay eggs. These eggs were then cultured in the presence of 21% oxygen (normal air) and 90% oxygen for 4 days, and the growth of the hatched worms was examined to determine the sensitivity to oxidative stress (Fig. 1A). Most of the hatched worms, when they possessed a normal sensitivity to oxygen, grew to adulthood in both 21% and 90% oxygen after incubation for 4 days, though they grew more slowly in 90% oxygen than in 21% oxygen. Then, the worms were judged

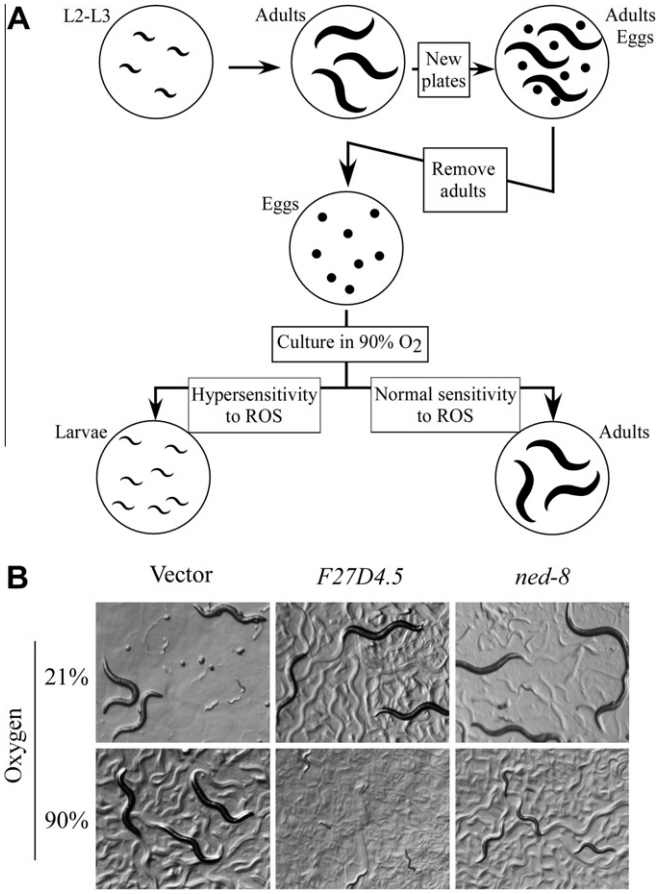

Fig. 1. RNAi screen. (A) The method for screening of the genes that, when knocked down by RNAi, cause an increased sensitivity to oxygen is illustrated. (B) Worms were fed with RNAi bacteria and examined for their growth in 21% and 90% oxygen. The growth of worms fed with bacteria carrying an empty vector, L4440 [12], is shown as a control.

to be hypersensitive to oxygen when they remained as larvae in 90% oxygen but grew to adulthood in 21% oxygen after incubation for 4 days. We selected the bacterial RNAi clones that caused an increased sensitivity to oxygen in worms; examples of the positive clones are shown in Fig. 1B. We next isolated the plasmids from these bacterial clones and re-introduced them into the *E. coli* HT115 strain to newly prepare the double-stranded RNA-expressing bacteria, with which we re-examined the sensitivity to oxygen in worms. The plasmids that reproducibly caused retarded growth in worms only in 90% oxygen were judged to contain the genes whose down-regulation causes an increased sensitivity to oxygen in *C. elegans*. Lastly, we examined the insert sequences in these plasmids by PCR or DNA sequencing to confirm that these plasmids carry the sequences indicated by the RNAi library (data not shown) [13]. Throughout the above screening, 9 genes which are involved in various cellular functions were identified (Table 1).

3.2. Assay of the sensitivity to oxidative stress in RNAi-treated worms

We determined the sensitivity to oxidative stress in the worms in which the identified genes were individually knocked down by RNAi. For this, N2 worms were treated with RNAi, and their eggs were cultured in the presence of various concentrations of oxygen. The sensitivity to oxygen was determined by examining the percentage of worms that grew to adulthood (Fig. 2A). Similarly, we also determined the sensitivity to paraquat, which generates superoxide anions in cells, by examining the percentage of worms

Table 1
Genes indentified in the RNAi screen.

Gene name	RNAi ID	Gene description	Molecular function	Biologic process
asd-2 (T21G5.5)	3I16	STAR protein	RNA binding, mRNA splicing	RNA processing
ctg-1 (H06O01.3)	3M22	CRAL/TRIO and GOLD domain-containing protein	Lipid metabolism, Vesicle transport	Golgi function
dbr-1 (C55B7.8)	3K07	Phosphodiesterase	RNA lariat debranching	RNA processing
F27D4.5	3H04	Branched chain keto acid dehydrogenase E1 β-subunit	Amino acid metabolism	Mitochondrial function
gsk-3 (Y18D10A.5)	7I15	Protein kinase	Protein kination	Protein modification, Signal transduction
ned-8 (F45H11.2)	5O03	NEDD8	Protein neddylation	Protein modification
uri-1 (C55B7.5)	3K01	Unconventional prefoldin RPB5 interactor	Molecular chaperone	Genome integrity, Gene expression
wwp-1 (Y65B4BR.4)	8A15	E3 ubiquitin ligase	Protein ubiquitination	Protein modification
wdr-23/xrep-1 (D2030.9)	3D06	WD40 repeat-containing protein	Protein ubiquitination	Protein modification

that grew to adulthood on the plates supplemented with various concentrations of paraquat (Fig. 2B). The results indicate that knock-down of these genes caused increased sensitivities to both oxygen and paraquat.

3.3. Measurement of carbonylated proteins

We examined whether knock-down of these genes caused increased oxidative damage in worms. We harvested proteins from worms treated with RNAi under hyperoxic conditions, and examined the levels of oxidized proteins by measuring carbonylated proteins by Western blot analysis (Fig. 3). These results indicate that knock-down of these genes caused increased oxidative damage in worms, which might lead to an increased sensitivity to ROS.

4. Discussion

A number of genes are involved in the generation or the quenching of ROS, but they are not fully identified. In this study, we employed the nematode *C. elegans* as a model organism, and identified 9 genes that, when knocked down by RNAi, led to increased sensitivities to oxygen and paraquat from the screening of the genes on LG I. These genes are involved in various cellular functions such as RNA processing, protein modification, signal transduction, genome integrity, mitochondrial function, and Golgi function. This result suggests that genes of diverse cellular functions would be involved in the regulation of oxidative stress.

wwp-1 and *wdr-23* are involved in the protein ubiquitination pathway and regulate the activity of their substrate proteins [16,17]. *wwp-1* encodes the HECT E3 ubiquitin ligase and regulates the nutrient-sensitive pathway in *C. elegans*: *wwp-1* is required for the extension of the life-span by dietary restriction [16]. Importantly, a mutation in *wwp-1* causes an increased sensitivity to paraquat [16], which finding is consistent with our result, though the molecular mechanisms by which *wwp-1* regulates longevity and oxidative stress are not understood well.

wdr-23, which encodes a WD40 repeat-containing protein, also participates in the protein ubiquitination pathway through interaction with the ubiquitin ligase complex, CUL-4/DDB-1 [17]. The protein complex CUL-4/DDB-1/WDR-23 regulates the function of SKN-1 through direct interaction with SKN-1 [17]. SKN-1 is a key transcription factor that induces the phase II detoxification enzymes to protect cells against stresses when cells are exposed to stresses [5]. *skn-1* is negatively regulated by *wdr-23* because a defect in *wdr-23* leads to an enhanced expression of the phase II detoxification enzymes in an *skn-1* dependent manner [17,18]. The protein complex CUL-4/DDB-1/WDR-23 probably ubiquitinates and degrades SKN-1 through the ubiquitin-proteasome system to prevent induction of the phase II detoxification enzymes under unstressed conditions [17,18]. The phase II detoxification enzyme genes in mammalian cells are regulated by the NF-E2-related factor, Nrf2, which shares sequence homology with *skn-1* of *C. elegans*. Interestingly, Nrf2 is also ubiquitinated by the Cul3/Keap1 E3 ubiquitin ligase complex and is degraded through the ubiquitin-proteasome system under unstressed conditions, but is stabilized and induces the phase II detoxification enzymes under stressed conditions [19–21]. Thus, the regulation of SKN-1 by CUL-4/WDR-23 in *C. elegans* is analogous to that of Nrf2 by Cul3/Keap1 in mammalian cells.

Since *wdr-23* negatively regulates *skn-1*, it seems to be reasonable that a defect in *wdr-23* causes increased resistance to stresses through constitutive activation of *skn-1*. Indeed, a defect in *wdr-23* is reported to cause increased resistance to ROS in *C. elegans* by Choe et al. [17]. Their result, however, appears to be inconsistent with our result that knock-down of *wdr-23* caused an increased sensitivity to ROS. The inconsistency may be attributable to the differences in the procedures for assaying the sensitivity to ROS. First, they used peroxide or juglone to impose oxidative stress [17], whereas we did high concentrations of oxygen gas or paraquat. Second, more importantly, they determined the sensitivity to oxidative stress by assaying the survival of young adult worms upon exposure to acute oxidative stress [17], whereas we did by assaying the growth of worms from larva to adult upon exposure to chronic oxidative stress. Then, a defect in *wdr-23* may cause hypersensitivity to ROS in larvae but resistance to ROS in adults. Additionally, it would be worthy to note that knock-out of *Keap1*, which leads to constitutive stabilization of NRF2, causes death at the weaning stage in mouse [22]. This result implies that constitutive stabilization of Nrf2 may cause toxicity through the mechanisms that are not yet identified. This might partly explain the reasons why the *wdr-23* mutant shows impaired growth in *C. elegans* [17], and why SKN-1 and Nrf2 are so strictly regulated through the ubiquitin-proteasome system that cells can activate them only when exposed to stresses.

gsk-3 encodes an evolutionarily conserved serine/threonine protein kinase involved in diverse cellular functions. Since *gsk-3* negatively regulates the function of *skn-1* through phosphorylation of SKN-1 in *C. elegans* [23], *gsk-3* might work in the same genetic pathway as does *wdr-23*.

ned-8 encodes the NEDD8 protein that is closely related to ubiquitin [24]. Like ubiquitin, NEDD8 is conjugated to its substrate proteins to regulate the functions of them [25]. Protein neddylation and protein ubiquitination appear to be closely coupled because the cullins, scaffold proteins for ubiquitin ligases, are regulated by protein neddylation in various organisms [25]. Indeed, both *ned-8* and an SCF (skp1/cullin/F-box) E3 ubiquitin ligase negatively regulate apoptosis mediated by *cep-1*, a homolog of p53, in germ cells upon genotoxic stresses in *C. elegans* [26]. Interestingly, the function of *p53* in human cells is negatively regulated by *NEDD8* and *WWP1*, a human homolog of *C. elegans wwp-1*, through neddylation and ubiquitination, respectively [27]. Then, these proteins might work together in *C. elegans* as well.

URI functions in a nutrient-sensitive transcriptional regulation pathway mediated by *TOR* (Target of rapamycin) in yeast and

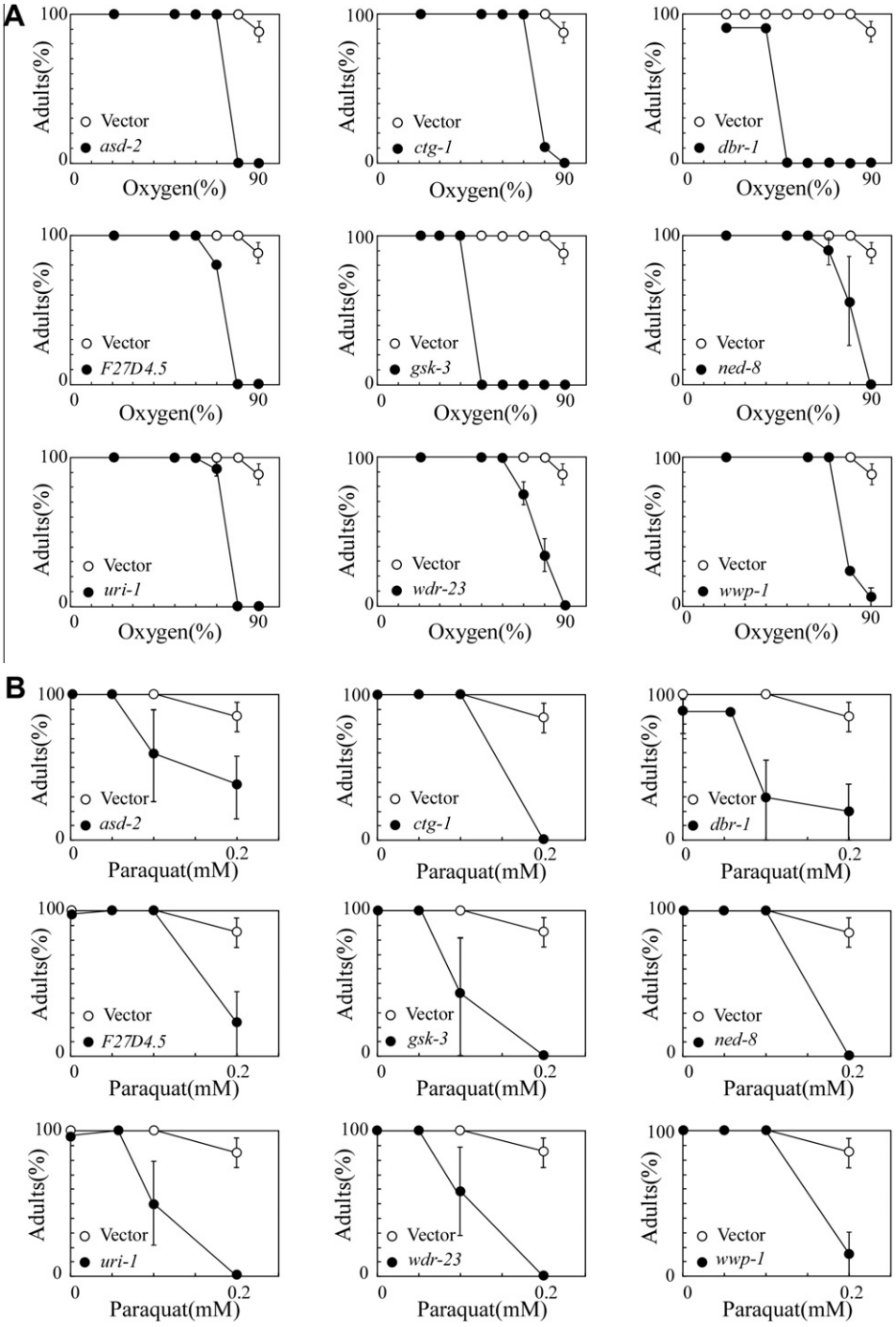

Fig. 2. Sensitivity to ROS. Worms were fed with RNAi bacteria indicated in the graphs, and were cultured in the presence of various concentrations of oxygen for 4 days (A), or in the presence of various concentrations of paraquat for 4 days (B). The percentage of worms that reached adulthood was determined. Error bars indicate SE.

human cells [28]. Loss of function of *URI* leads to a decrease in growing cells and an increase in apoptotic cells in human cells [29]. In *C. elegans*, a defect in *uri-1* causes decreased germ cells with increased apoptosis mediated by *cep-1*, and increased DNA breaks with loss of genome integrity [30]. Since ROS induce DNA damage, the increased DNA damage in *uri-1*-deficient cells would be further augmented by ROS. Thereby, increased DNA damage may, at least in part, account for the increased sensitivity to oxidative stress by knock-down of *uri-1*. On the other hand, since *URI* interacts with *SKP2*, a component of the SCF ubiquitin ligase complex [28], it would be interesting to speculate that *uri-1* also plays a role in the protein ubiquitination pathway to regulate the sensitivity to oxidative stress.

F27D4.5 encodes a possible homolog of a ß-subunit of branched-chain ∂-keto acid dehydrogenase/decarboxylase (BCKD) that is responsible for human maple syrup urine disease (MSUD) [31,32]. BCKD catalyzes oxidative decarboxylation of branched chain keto acids derived from transamination of branched chain amino acids such as leucine, isoleucine and valine [32,33]. The molecular mechanisms by which metabolic disorder of branched chain amino acids causes MSUD are not understood well, but BCKD functions in mitochondria, which are thought to be a major source

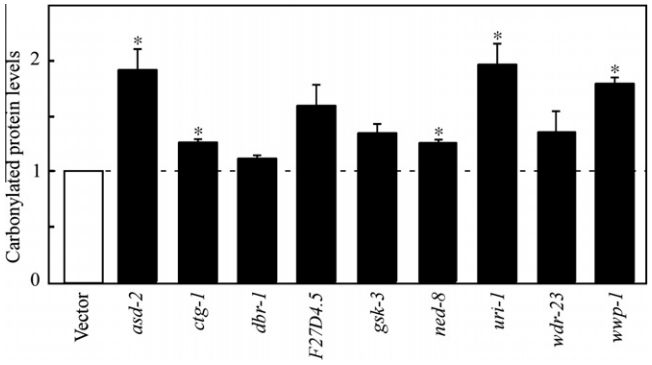

Fig. 3. Levels of carbonylated proteins. Protein samples were prepared from worms fed with RNAi bacteria, and were subjected to Western blot analysis to detect carbonylated proteins. The level of carbonylated proteins is expressed as a value relative to that of the protein sample from worms fed with bacteria carrying an empty vector, L4440 [12]. Error bars indicate SE. Statistical significance is indicated by asterisks ($^*P < 0.05$).

of ROS. Interestingly, increased oxidative damage is observed in MSUD patient cells and in normal cells treated with metabolites accumulated in MSUD patient cells [34,35]. In the previous study, we have shown that a mutation in another type of mitochondrial dehydrogenase/reductase causes mitochondrial dysfunction with increased generation of ROS and an increased sensitivity to ROS [9]. Thus, it may be possible to speculate that loss of function of BCKD may cause mitochondrial dysfunction that leads to an increased sensitivity to ROS as well.

ctg-1 encodes a protein similar to SEC14, which regulates phospholipid metabolism and vesicular transport from the Golgi apparatus in yeast [36]. *ctg-1* also possesses the GOLD domain which is involved in protein–protein interaction [37]. Although the SEC14-GOLD proteins are observed in diverse organisms, the functional roles of them are not understood well. However, it may be possible that *ctg-1* regulates oxidative stress through interaction with antioxidant proteins because *SFH2*, a SEC14-like protein in yeast, plays an important role in the regulation of oxidative stress through specific interaction with thioperoxidase II [38].

asd-2 encodes the STAR protein that plays crucial roles in RNA metabolism such as mRNA splicing, translation, localization, and regulation of mRNA stability. In *C. elegans*, *asd-2* regulates the developmental regulation of alternative splicing of the *let-2* gene [39]. *dbr-1* encodes a 2′-5′-phosphodiesterase that cleaves intron RNA lariat branch points after splicing to facilitate the turnover of introns, and then a defect in *dbr-1* causes accumulation of intron lariats [40]. Deficiencies in RNA processing by knock-down of these genes might lead to an increased sensitivity to ROS by causing aberrant expression of genes that regulate oxidative stress.

Finally, it is important to point out that we should have failed to identify a considerable number of genes involved in the regulation of oxidative stress in this screen. This is mainly due to a technical limitation of RNAi, by which the activity of the target gene is efficiently down-regulated but some residual activity remains in cells. The efficacy of RNAi to repress the expression of the target genes varies from gene to gene, and thus the repression levels of the target genes by RNAi are always crucial in the experiments with RNAi. That is, weak repression of genes by RNAi may not be sufficient to provide phenotypic changes; however, conversely, severe repression of genes by RNAi may lead to lethality when the target genes are essential for viability. This indicates that we were able to identify the genes involved in the regulation of oxidative stress in this screen only when their expression was repressed at the proper levels by RNAi. Despite of this technical limitation, there is no doubt that a systematic RNAi screen is a useful and powerful approach to identify responsible genes in various biologic phenomena, and we have successfully identified the genes involved in the regulation of oxidative stress. Further study of these genes would provide a better understanding of the molecular mechanisms underlying the regulation of oxidative stress.

Acknowledgments

Some nematode strains used in this work were provided by the Caenorhabditis Genetics Center, which is funded by the NIH National Center for Research Resources (NCRR). This work was supported in part by a grant-in-aid for Scientific Research from the Ministry of Education, Science and Culture of Japan.

References

[1] Y. Honda, M. Tanaka, S. Honda, Modulation of longevity and diapause by redox regulation mechanisms under the insulin-like signaling control in *Caenorhabditis elegans*, Exp. Gerontol. 43 (2008) 520–529.
[2] R. Doonan, J.J. McElwee, F. Matthijssens, G.A. Walker, K. Houthoofd, P. Back, A. Matscheski, J.R. Vanfleteren, D. Gems, Against the oxidative damage theory of aging: superoxide dismutases protect against oxidative stress but have little or no effect on life span in *Caenorhabditis elegans*, Genes Dev. 22 (2008) 3236–3241.
[3] J.M. Van Raamsdonk, S. Hekimi, Deletion of the mitochondrial superoxide dismutase sod-2 extends lifespan in *Caenorhabditis elegans*, PLoS Genet. 5 (2009) e1000361.
[4] S. Yanase, A. Onodera, P. Tedesco, T.E. Johnson, N. Ishii, SOD-1 deletions in *Caenorhabditis elegans* alter the localization of intracellular reactive oxygen species and show molecular compensation, J. Gerontol. A Biol. Sci. Med. Sci. 64 (2009) 530–539.
[5] J.H. An, T.K. Blackwell, SKN-1 links *C. elegans* mesendodermal specification to a conserved oxidative stress response, Genes Dev. 17 (2003) 1882–1893.
[6] N. Ishii, M. Fujii, P.S. Hartman, M. Tsuda, K. Yasuda, N. Senoo-Matsuda, S. Yanase, D. Ayusawa, K. Suzuki, A mutation in succinate dehydrogenase cytochrome b causes oxidative stress and ageing in nematodes, Nature 394 (1998) 694–697.
[7] P.S. Hartman, N. Ishii, E.B. Kayser, P.G. Morgan, M.M. Sedensky, Mitochondrial mutations differentially affect aging, mutability and anesthetic sensitivity in *Caenorhabditis elegans*, Mech. Ageing Dev. 122 (2001) 1187–1201.
[8] M. Fujii, N. Adachi, K. Shikatani, D. Ayusawa, [FeFe]-hydrogenase-like gene is involved in the regulation of sensitivity to oxygen in yeast and nematode, Genes Cells 14 (2009) 457–468.
[9] M. Fujii, K. Yasuda, P.S. Hartman, D. Ayusawa, N. Ishii, A mutation in a mitochondrial dehydrogenase/reductase gene causes an increased sensitivity to oxidative stress and mitochondrial defects in the nematode *Caenorhabditis elegans*, Genes Cells 16 (2011) 1022–1034.
[10] M. Fujii, K. Shikatani, K. Ogura, Y. Goshima, D. Ayusawa, Mutation in a mitochondrial ribosomal protein causes increased sensitivity to oxygen with decreased longevity in the nematode *Caenorhabditis elegans*, Genes Cells 16 (2011) 69–79.
[11] A. Fire, S. Xu, M.K. Montgomery, S.A. Kostas, S.E. Driver, C.C. Mello, Potent and specific genetic interference by double-stranded RNA in *Caenorhabditis elegans*, Nature 391 (1998) 806–811.
[12] L. Timmons, A. Fire, Specific interference by ingested dsRNA, Nature 395 (1998) 854.
[13] A.G. Fraser, R.S. Kamath, P. Zipperlen, M. Martinez-Campos, M. Sohrmann, J. Ahringer, Functional genomic analysis of *C. elegans* chromosome I by systematic RNA interference, Nature 408 (2000) 325–330.
[14] S. Brenner, The genetics of *Caenorhabditis elegans*, Genetics 77 (1974) 71–94.
[15] M. Fujii, Y. Matsumoto, N. Tanaka, K. Miki, T. Suzuki, N. Ishii, D. Ayusawa, Mutations in chemosensory cilia cause resistance to paraquat in nematode *Caenorhabditis elegans*, J. Biol. Chem. 279 (2004) 20277–20282.
[16] A.C. Carrano, Z. Liu, A. Dillin, T. Hunter, A conserved ubiquitination pathway determines longevity in response to diet restriction, Nature 460 (2009) 396–399.
[17] K.P. Choe, A.J. Przybysz, K. Strange, The WD40 repeat protein WDR-23 functions with the CUL4/DDB1 ubiquitin ligase to regulate nuclear abundance and activity of SKN-1 in *Caenorhabditis elegans*, Mol. Cell Biol. 29 (2009) 2704–2715.
[18] K. Hasegawa, J. Miwa, Genetic and cellular characterization of *Caenorhabditis elegans* mutants abnormal in the regulation of many phase II enzymes, PLoS One 5 (2010) e11194.
[19] K.R. Sekhar, X.X. Yan, M.L. Freeman, Nrf2 degradation by the ubiquitin proteasome pathway is inhibited by KIAA0132, the human homolog to INrf2, Oncogene 21 (2002) 6829–6834.
[20] M. McMahon, K. Itoh, M. Yamamoto, J.D. Hayes, Keap1-dependent proteasomal degradation of transcription factor Nrf2 contributes to the negative regulation of antioxidant response element-driven gene expression, J. Biol. Chem. 278 (2003) 21592–21600.

[21] K. Itoh, N. Wakabayashi, Y. Katoh, T. Ishii, T. O'Connor, M. Yamamoto, Keap1 regulates both cytoplasmic-nuclear shuttling and degradation of Nrf2 in response to electrophiles, Genes Cells 8 (2003) 379–391.
[22] N. Wakabayashi, K. Itoh, J. Wakabayashi, H. Motohashi, S. Noda, S. Takahashi, S. Imakado, T. Kotsuji, F. Otsuka, D.R. Roop, T. Harada, J.D. Engel, M. Yamamoto, Keap1-null mutation leads to postnatal lethality due to constitutive Nrf2 activation, Nat. Genet. 35 (2003) 238–245.
[23] J.H. An, K. Vranas, M. Lucke, H. Inoue, N. Hisamoto, K. Matsumoto, T.K. Blackwell, Regulation of the *Caenorhabditis elegans* oxidative stress defense protein SKN-1 by glycogen synthase kinase-3, Proc. Natl. Acad. Sci. USA 102 (2005) 16275–16280.
[24] D. Jones, E.P. Candido, The NED-8 conjugating system in *Caenorhabditis elegans* is required for embryogenesis and terminal differentiation of the hypodermis, Dev. Biol. 226 (2000) 152–165.
[25] G. Rabut, M. Peter, Function and regulation of protein neddylation. 'Protein modifications: beyond the usual suspects' review series, EMBO Rep. 9 (2008) 969–976.
[26] M.X. Gao, E.H. Liao, B. Yu, Y. Wang, M. Zhen, W.B. Derry, The SCF FSN-1 ubiquitin ligase controls germline apoptosis through CEP-1/p53 in *C. elegans*, Cell Death Differ. 15 (2008) 1054–1062.
[27] A. Hock, K.H. Vousden, Regulation of the p53 pathway by ubiquitin and related proteins, Int. J. Biochem. Cell Biol. 42 (2010) 1618–1621.
[28] M. Gstaiger, B. Luke, D. Hess, E.J. Oakeley, C. Wirbelauer, M. Blondel, M. Vigneron, M. Peter, W. Krek, Control of nutrient-sensitive transcription programs by the unconventional prefoldin URI, Science 302 (2003) 1208–1212.
[29] N. Djouder, S.C. Metzler, A. Schmidt, C. Wirbelauer, M. Gstaiger, R. Aebersold, D. Hess, W. Krek, S6K1-mediated disassembly of mitochondrial URI/PP1gamma complexes activates a negative feedback program that counters S6K1 survival signaling, Mol. Cell 28 (2007) 28–40.
[30] C.T. Parusel, E.A. Kritikou, M.O. Hengartner, W. Krek, M. Gotta, URI-1 is required for DNA stability in *C. elegans*, Development 133 (2006) 621–629.
[31] J.H. Menkes, P.L. Hurst, J.M. Craig, A new syndrome: progressive familial infantile cerebral dysfunction associated with an unusual urinary substance, Pediatrics 14 (1954) 462–467.
[32] D.T. Chuang, J.L. Chuang, R.M. Wynn, Lessons from genetic disorders of branched-chain amino acid metabolism, J. Nutr. 136 (2006) 243S–249S.
[33] F.H. Pettit, S.J. Yeaman, L.J. Reed, Purification and characterization of branched chain alpha-keto acid dehydrogenase complex of bovine kidney, Proc. Natl. Acad. Sci. USA 75 (1978) 4881–4885.
[34] R. Bridi, J. Araldi, M.B. Sgarbi, C.G. Testa, K. Durigon, M. Wajner, C.S. Dutra-Filho, Induction of oxidative stress in rat brain by the metabolites accumulating in maple sirup urine disease, Int. J. Dev. Neurosci. 21 (2003) 327–332.
[35] A.G. Barschak, A. Sitta, M. Deon, M.H. de Oliveira, A. Haeser, C.S. Dutra-Filho, M. Wajner, C.R. Vargas, Evidence that oxidative stress is increased in plasma from patients with maple sirup urine disease, Metab. Brain Dis. 21 (2006) 279–286.
[36] V.A. Bankaitis, J.R. Aitken, A.E. Cleves, W. Dowhan, An essential role for a phospholipid transfer protein in yeast Golgi function, Nature 347 (1990) 561–562.
[37] V. Anantharaman, L. Aravind, The GOLD domain, a novel protein module involved in Golgi function and secretion, Genome Biol. 3 (2002) research0023.
[38] M.K. Cha, S.K. Hong, Y.M. Oh, I.H. Kim, The protein interaction of *Saccharomyces cerevisiae* cytoplasmic thiol peroxidase II with SFH2p and its in vivo function, J. Biol. Chem. 278 (2003) 34952–34958.
[39] G. Ohno, M. Hagiwara, H. Kuroyanagi, STAR family RNA-binding protein ASD-2 regulates developmental switching of mutually exclusive alternative splicing in vivo, Genes Dev. 22 (2008) 360–374.
[40] K. Nam, G. Lee, J. Trambley, S.E. Devine, J.D. Boeke, Severe growth defect in a Schizosaccharomyces pombe mutant defective in intron lariat degradation, Mol. Cell Biol. 17 (1997) 809–818.

Biochemical and Biophysical Research Communications 420 (2012) 558–563

Contents lists available at SciVerse ScienceDirect

Biochemical and Biophysical Research Communications

journal homepage: www.elsevier.com/locate/ybbrc

AAV-mediated delivery of the transcription factor XBP1s into the striatum reduces mutant Huntingtin aggregation in a mouse model of Huntington's disease

Amparo Zuleta [a,b], Rene L. Vidal [a,e], Donna Armentano [c], Geoffrey Parsons [c], Claudio Hetz [a,b,d,e,*]

[a] Biomedical Neuroscience Institute, Faculty of Medicine, University of Chile, Santiago, Chile
[b] Center for Molecular Studies of the Cell, Institute of Biomedical Sciences, University of Chile, Santiago, Chile
[c] Department of Molecular Biology, Genzyme Corporation, 49 New York Avenue, Framingham, MA 01701, USA
[d] Department of Immunology and Infectious Diseases, Harvard School of Public Health, 651 Huntington Av., Boston, MA 02446, USA
[e] Neurounion Biomedical Foundation, Santiago, Chile

ARTICLE INFO

Article history:
Received 2 March 2012
Available online 16 March 2012

Keywords:
Huntington's disease
Unfolded protein response
Endoplasmic reticulum stress
XBP1
Htt aggregation
Gene therapy

ABSTRACT

Huntington's disease (HD) is caused by mutations that expand a polyglutamine region in the amino-terminal domain of Huntingtin (Htt), leading to the accumulation of intracellular inclusions and progressive neurodegeneration. Recent reports indicate the engagement of endoplasmic reticulum (ER) stress responses in human HD post mortem samples and animal models of the disease. Adaptation to ER stress is mediated by the activation of the unfolded protein response (UPR), an integrated signal transduction pathway that attenuates protein folding stress by controlling the expression of distinct transcription factors including X-Box binding protein 1 (XBP1). Here we targeted the expression of XBP1 on a novel viral-based model of HD. We delivered an active form of XBP1 locally into the striatum of adult mice using adeno-associated vectors (AAVs) and co-expressed this factor with a large fragment of mutant Htt as a fusion protein with RFP (Htt588^{Q95}-mRFP) to directly visualize the accumulation of Htt inclusions in the brain. Using this approach, we observed a significant reduction in the accumulation of Htt588^{Q95}-mRFP intracellular inclusion when XBP1 was co-expressed in the striatum. These results contrast with recent findings indicating a protective effect of XBP1 deficiency in neurodegeneration using knockout mice, and suggest a potential use of gene therapy strategies to manipulate the UPR in the context of HD.

1. Introduction

Huntington's disease (HD) is an autosomal dominant neurodegenerative disease characterized by motor abnormalities and onset of psychiatric symptoms and dementia in early- to mid-adult life. HD is caused by a CAG trinucleotide repeat expansion in the Huntingtin gene, generating an abnormal polyglutamine tract (polyQ) in the N-terminal region of Huntingtin (Htt) protein [1,2]. This mutation confers a neurotoxic activity to Htt protein, correlating with the progressive accumulation of mutant Htt (mHtt) as intracellular oligomers and inclusions that contribute to the selective loss of striatal neurons [3]. HD is part of a growing number of polyQ repeat diseases that cause region-specific neurodegeneration, including spinocerebellar ataxias, spinobulbar muscular atrophy, Machado–Joseph Disease, and many other diseases [1].

Although the molecular mechanisms involved in HD pathogenesis are still highly controversial, recent observations suggest the involvement of endoplasmic reticulum (ER) stress in the disease process (reviewed in [4,5]). ER stress is triggered by many pathological and physiological conditions that alter the protein folding status of the ER, resulting in the activation of the unfolded protein response (UPR). The UPR is a signal transduction pathway that increases the protein folding capacity and quality control of the ER to reduce the unfolded protein load [6]. However, chronic or prolonged ER stress triggers apoptosis to eliminate irreversibly damaged cells (reviewed in [7,8]). The UPR is initiated by the activation of three main stress sensors, including IRE1α (Inositol-requiring transmembrane kinase/endonuclease), ATF6 (activating transcription factor 6) and PERK (PKR-like ER kinase) [6,9]. IRE1α is a Ser/Thr protein kinase and endoribonuclease that upon activation mediates the processing of the mRNA encoding the transcriptional factor X-Box-binding protein 1 (XBP1), catalyzing the excision of a 26 nucleotide intron [10–12]. This non-conventional splicing event changes the coding reading frame of the protein, leading to the expression of a potent and stable transcription factor termed XBP1s (for the spliced form). XBP1s upregulates genes related to protein folding, ER protein entry, ER-mediated degradation (ERAD) and quality control mechanisms [13,14].

* Corresponding author at: University of Chile, P.O. Box 70086, Independencia 1027, Santiago, Chile.
E-mail addresses: chetz@med.uchile.cl, chetz@hsph.harvard.edu (C. Hetz).
URL: http://ecb-icbm.med.uchile.cl/Index.html (C. Hetz).

0006-291X/$ - see front matter © 2012 Elsevier Inc. All rights reserved.
http://dx.doi.org/10.1016/j.bbrc.2012.03.033

Markers of ER stress have been reported in human post-mortem HD brain samples [15–17]. In addition, we recently described the expression of XBP1s in HD brain [18]. Similarly, activation of the UPR was shown in different HD mouse models [15,16,19], whereas in other models there were no clear signs of ER stress [18,20]. Moreover, many different studies indicate that the expression of mutant Htt or expanded polyQ peptides triggers ER stress-mediated apoptosis in cellular models of HD [21–25]. At the molecular level, it has been proposed that expression of mHtt impairs ERAD function; resulting in chronic ER stress [22,26]. Other alternative mechanisms may also explain the occurrence of ER stress in HD including impairment of ATF6 activation [17] among other pathological effects (reviewed in [4]).

Although different studies suggest a possible involvement of ER stress in the pathogenesis of HD, the actual contribution of the UPR to the disease process *in vivo* is still poorly defined. We recently demonstrated that silencing XBP1 expression in an mHtt transgenic mouse reduces neuronal loss in the striatum and improves motor performance [18]. These protective effects were associated with enhanced mHtt degradation possibly due to the upregulation of autophagy levels a known pathway involved in mHtt clearance [27,28]. Similar observations were also described on a model of amyotrophic lateral sclerosis [29]. However, these studies were performed using a conditional knockout model of XBP1 where this UPR gene was deleted during embryogenesis, which may trigger compensatory mechanisms in the protein homeostasis network activating autophagy as a rescue pathway [30]. In contrast, two recent reports indicated that the overexpression of XBP1s locally in the brain of adult animals using viral-mediated gene delivery protects against experimental Parkinson's disease [31] and spinal cord injury [32]. To address the therapeutic potential of targeting the UPR in HD *in vivo*, here we have investigated the impact of expressing XBP1s in the striatum of a mouse model of HD using adeno-associated viruses (AAVs). This study reports the unexpected finding where XBP1s-gene transfer in adult animals decreases the accumulation of mHtt inclusions, suggesting a beneficial potential of developing gene therapy strategies or pharmacological approaches to upregulate the UPR in HD.

2. Methods

2.1. Plasmid constructs and AAV preparation

DNA sequence encoding the first 588 amino-acids of human Huntingtin fused to monomeric red fluorescent protein with a polyQ region of 95 glutamines (Htt588^{Q95}-mRFP) or 17 glutamines (Htt588^{Q17}-mRFP) were described before [33], and cloned into pAAV-CMV followed by confirmation by sequencing. We detected a difference in the length of polyQ compared with the initial characterization of the vector [33]. The XBP1s AAV construct was recently described [32]. The vector is bicistronic and carries an eGFP expression cassette that serves as a fluorescent marker for transduced cells. Recombinant AAV2 were produced by triple transfection of 293 cells using a rep/cap plasmid and pHelper (Stratagene, La Jolla CA, USA) and purified and quantified by column affinity chromatography and qCPR, as previously described [34,35]. Western blot and luciferase assays were performed as previously described [32]. The following antibodies and dilutions were used: EM48 (1:500, ON, 4 °C) (Millipore), anti-XBP1 (1:500, 2 h, RT), anti-Hsp90 (1:3000, ON, 4 °C) (Santa Cruz) and anti-tubulin (1:3000, ON, 4 °C) (Sigma).

2.2. Stereotaxic injection

Male mice C57BL/6j (10–12 weeks) were injected with 2 or 4 μl of virus AAV-Htt588^{Q95}-mRFP in the right striatum or were co-injected with 2 μl of each virus AAV-Htt588^{Q95}-mRFP and AAV-XBP1s-eGFP or AAV-Htt588^{Q95}-mRFP and AAV-eGFP in the left striatum (contralateral side). Stereotaxic coordinates with respect to the bregma used were: +0.5 mm anterior, +2 mm lateral and −3 mm depth, with a 1 μl/min infusion rate. Viral titters used were: AAV-Htt588Q95-mRFP: 1.37×10^{12} viral genomes/ml, AAV-XBP1s-eGFP: 1.13×10^{12} DRPs/ml, AAV-eGFP: 7.52×10^{7} viral genomes/ml. All experiments were performed under the animal experimental protocol approved by the Bioethics Comity of the Faculty of Medicine, University of Chile (protocol number CBA#0306 FMUCH).

2.3. Histological analysis

Mice were sacrificed 2, 4 or 8 weeks post-injection and mouse brains were perfused and fixed overnight with 4% paraformaldehyde. Serial-cut 30-μm sections of brain tissue between +2 and −0.2 mm lateral with respect to bregma were mounted onto Micro Slides Superfrost Plus (VWR International) and stained with anti-NeuN (1:500, ON, 4 °C) (Sigma) or anti-GFAP (1:500, ON, 4 °C) (Chemicon International), followed by AlexaFluor 488 secondary antibody (1:500, 2 h., RT) (Invitrogen) and Hoechst (1:1000, 10 min., RT) (Intergen). Images were captured with a fluorescent a BX61W1 microscope (Olympus). All RFP positive cells were counted in each series of brain sections between +2 and −0.2 mm lateral to bregma, distinguishing between RFP positive cells with small, large inclusions or without inclusions.

3. Results

3.1. Generation of a new HD mouse model

Several animal models have been developed for studying the pathogenesis of HD, classified into two main categories: transgenic mice and viral-mediated models [36]. Viral-mediated HD models develop characteristics associated with HD within 2 weeks post-transduction, including mHtt inclusion formation [37–39], allowing testing potential therapeutic strategies. However, most viral models of HD express a small fragment of mHtt (exon 1) that could lead to artifactual effects due to aggressive protein aggregation and acute toxicity even in brain regions that are not normally affected in HD [36]. To investigate the impact of targeting the UPR in mHtt aggregation, we developed a new HD model using AAVs to express a large N-terminal fragment of human Htt fused to the red fluorescent protein (RFP) for direct visualization of protein inclusions *in vivo* (Fig. 1A).

A DNA sequence encoding the first 588 amino acids of human Htt containing a polyQ region of 95 glutamines was fused to that of monomeric RFP (Htt588^{Q95}-mRFP) and cloned into a serotype 2 AAV vector. As a control, an Htt construct with 17 glutamines was generated (Htt588^{Q17}-mRFP). Expression of both fusion proteins was confirmed in N2A cells after transient transfection followed by Western Blot analysis (Fig. 1B) or fluorescent microscopy to visualize the generation of mHtt inclusions (Fig. 1C). AAV particles were injected into the striatum by stereotaxis. Histological analysis revealed the preferential expression of Htt588^{Q95}-mRFP in neurons as early as 2 weeks post-injection (Fig. 1D). In these experiments, we distinguished three different RFP-positive cell populations: cells presenting small mHtt inclusions, cells with large inclusions and cells showing a diffuse RFP pattern (Fig. 1E). Expression of Htt588^{Q17}-mRFP did not result in the accumulation of RFP-positive inclusions (Fig. 2B). Time course analysis of animals injected with AAVs expressing Htt588^{Q95}-mRFP after 2, 4 and 8 weeks post-surgery revealed a progressive accumulation of small Htt588^{Q95}-mRFP inclusions, reaching a maximum percentage of cells showing inclusions of 77.0 ± 4.6% using a viral

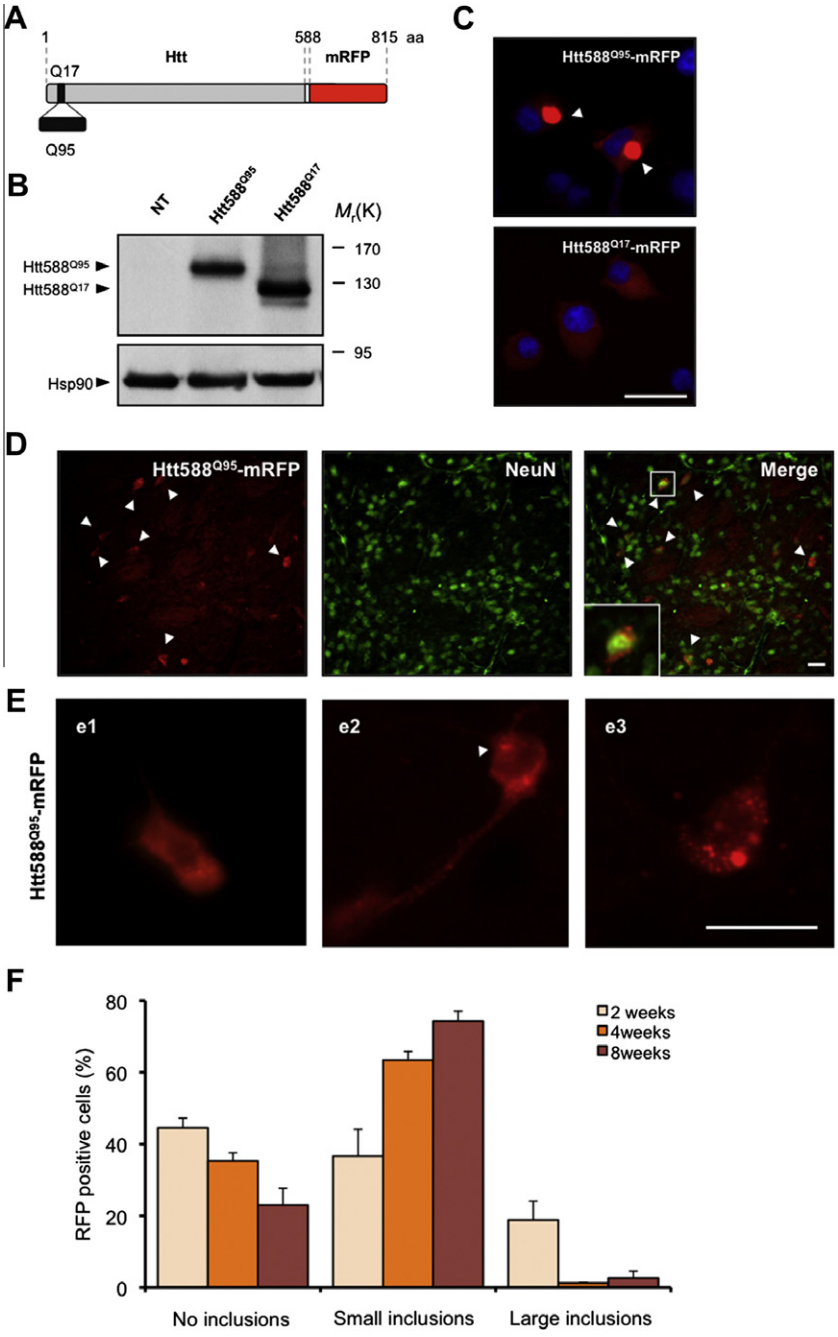

Fig. 1. Development of a new viral-mediated model of HD. (A) Schematic representation of two constructs of human mHtt fused with RFP (red) used in this study: Htt588^{Q17}-mRFP and Htt588^{Q95}-mRFP. Amino-terminal region of 588 amino acids carrying a polyQ fragment of 17 or 95 glutamines fused to the monomeric red fluorescent protein (RFP) gene were subcloned into an AAV expression vector for *in vivo* delivery. (B) N2A cells were transiently transfected with pAAV-Htt588^{Q17}-mRFP and pAAV-Htt588^{Q95}-mRFP plasmids, and Htt expression was evaluated after 48 h by Western blot analysis. Hsp90 protein levels were monitored as loading control. (C) In parallel, cells described in B were analyzed by fluorescent microscopy (red) to confirm the accumulation of mutant Htt inclusions (arrowheads). DNA was stained with Hoechst (blue). (D) Adult mice were injected by brain stereotaxis with AAV-Htt588^{Q95}-mRFP (2.47×10^9 viral genomes) viral particles into the striatum. Animals were then sacrificed 2 weeks post-injection and brain tissue was analyzed by histology to evaluate Htt588^{Q95}-mRFP expression by fluorescent microscopy (red). Co-staining with the neuronal marker NeuN (green) was performed. White triangles show examples of co-localization between transduced cells and the neuronal marker. (E) In experiments performed in D, three distinct cell populations were identified of cells expressing Htt588^{Q95}-mRFP: (e1) RFP positive cells without inclusions (diffuse RFP pattern), (e2) RFP positive cells with small inclusions, and (e3) RFP positive cell with large inclusions. (F) Htt588^{Q95}-mRFP distribution was evaluated in animals injected after 2, 4 and 8 weeks post-AVV transduction. Animals were sacrificed and brain tissue was analyzed by histology to quantytate the percentage of Htt588^{Q95}-mRFP aggregation distributed in cells that presented a diffuse pattern and small and large RFP-positive protein inclusions. The graphic represents mean and standard deviation between the analyses of 3 independent experiments. Scale bars: 10 μm. (For interpretation of the references to color in this figure legend, the reader is referred to the web version of this article.)

dose of 2.4×10^9 viral genomes (Fig. 1F). Among RFP positive cells, around 74% of neurons presented small inclusions and only 3% contained large intracellular mHtt inclusions (Fig. 1F). Using a viral dose of 5.5×10^9 viral genomes, the kinetics of Htt aggregation slightly differed, showing a maximum percentage of aggregation at 4 weeks post-transduction (Fig. S1A). Thus, we were able to develop a new viral-mediated model of HD that generates Htt inclusions in a few weeks post injection.

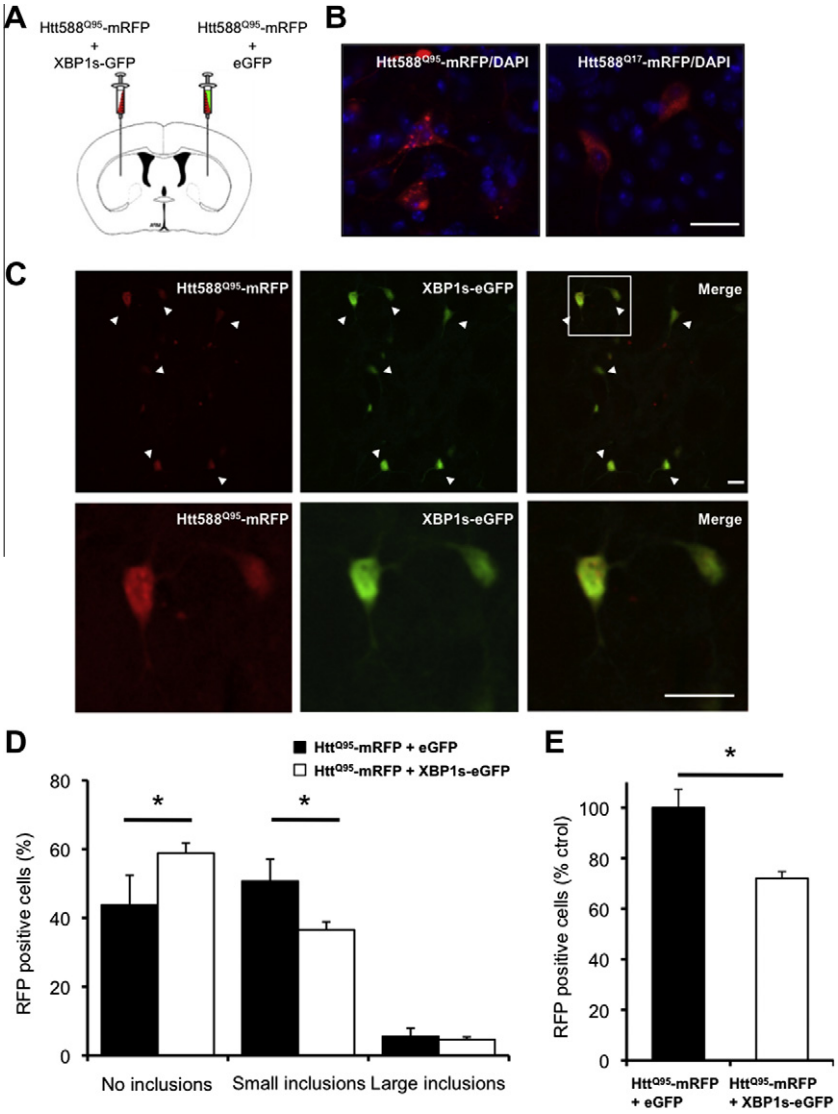

Fig. 2. Ectopic expression of XBP1s decreases mutant Huntingtin aggregation *in vivo*. (A) Experimental strategy to study the impact of XBP1s gene transfer on the generation of mutant Huntingtin inclusions. Adult mice were co-injected by stereotaxis into the striatum with a mix of AAVs encoding Htt588^{Q95}-mRFP (2.47×10^9 viral genomes) and XBP1s-eGFP (2.26×10^9 DRPs) in one brain hemisphere and with Htt588^{Q95}-mRFP and eGFP (1.50×10^8 viral genomes) in the opposite side. Animals were then sacrificed 4 weeks post-injection and brain tissue was analyzed by histology. (B) Adult mice were injected stereotaxically with viral vectors AAV-Htt588^{Q95}-mRFP (5.88×10^9 DRPs) and AAV-Htt588^{Q17}-mRFP (6.09×10^9 DRPs) into the striatum. Animals were sacrificed 4 weeks post-injection and brain tissue was prepared for histology to visualize the distribution of RFP. Expression of control Htt588^{Q17}-mRFP did not generate the accumulation of RFP-positive inclusions. (C) Representative image of brain tissue co-transduced with viral vectors AAV-Htt588^{Q95}-mRFP and AAV-XBP1s-eGFP in the striatum as described in A. White triangles show examples of RFP and GFP co-expressing cells. Lower panel's shows high magnification images from merge panel (white square). (D) The graph represents the mean and standard deviation from three independent experiments such as those presented in C. Data were analyzed with the Student *t* test ($^*p < 0.05$). Scale bars: 20 μm. (E) The percentage of aggregation in the number of cells containing small including in experiments presented in D is shown as a normalization with control cells transduced with AAV-eGFP viruses as 100%.

3.2. Effect of XBP1s on mutant Huntingtin aggregation in vivo

To test the impact of XBP1s in the aggregation of mHtt *in vivo* in adult animals, we developed viral vectors to express XBP1s using AAVs that expresses eGFP with a bicistronic promoter (AAV-XBP1s-eGFP) for visualization of transduced cells [32]. To verify the activity of the construct, N2A cells were transfected with the expression vector pAAV-XBP1s-eGFP and XBP1s expression was monitored by Western blot (Fig. S1B). The transcriptional activity of the expressed XBP1s was measured with a UPR-luciferase reporter assay (Fig. S1C) [13]. Then, adult mice were co-injected with AAV-Htt588^{Q95}-mRFP and AAV-XBP1s-eGFP viral vectors into the right striatum by stereotaxis. As control, we also injected the contralateral side of the same animals with AAV-Htt588^{Q95}-mRFP and AAV-eGFP (Fig. 2A). A high level of co-transduction was observed between both viral vectors used when GFP and RFP fluorescence was visualized after histological analysis of the brain (Fig. 2C). Analysis of the percentage of cells presenting Htt588^{Q95}-mRFP inclusions indicated that the ectopic expression of XBP1s led to a significant reduction in the number of cells presenting small RFP positive inclusions, without affecting the number of cells accumulating large Htt588^{Q95}-mRFP inclusions (Fig. 2D). Quantification and normalization revealed a decrease of 28% in the percentage of cells presenting small Htt588^{Q95}-mRFP inclusions cells after expression of XBP1s when compared with empty vector control AAV-eGFP (Fig. 2E).

4. Discussion

One of the main characteristics of most neurodegenerative diseases is the accumulation of abnormally folded proteins in the

brain. Although the pathological mechanisms of neurodegeneration in distinct diseases may drastically differ, accumulating evidence indicates that ER stress is a common response in several brain disorders (reviewed in [5]). To address the contribution of the UPR in mHtt pathogenesis *in vivo*, we tested the possible protective effect of a gene therapy approach to deliver an active form of XBP1s into the brain striatum of an HD model developed here. Our results suggest that this approach could significantly reduce the aggregation of mHtt. This observation contrasts with our recent report indicating that ablation of XBP1 using a conditional knockout system leads to mHtt degradation possibly due to the induction of macroautophagy [18]. Taken together, the current study suggests that strategies to manipulate the UPR locally in the adult brain may directly address the therapeutic implications of targeting the pathway in a disease context. Although informative, targeting the UPR during development using knockout mouse may trigger shift in the protein homeostasis network that could generate phenotypes that do not reflect the direct involvement of ER stress in HD. Therefore, such models may not be predictive when considering therapies that acutely modify the UPR. However, it is still possible to speculate that both XBP1 gain and lost of function may provide protection against degeneration through distinct mechanisms. XBP1 expression has been manipulated in several animal models of neurodegenerative diseases associated with protein misfolding [29,31,40–43]. For example, the overexpression of XBP1s in a pharmacological mouse model for Parkinson's disease and in a Drosophila transgenic model for Alzheimer's disease protects against neurodegeneration [31,40]. Conversely, the reduction of XBP1 expression in a Drosophila model for Retinitis Pigmentosa and Alzheimer's disease increases cell death [42,43]. We recently described that AAV-mediated delivery of XBP1s into the spinal cord led to enhanced motor recovery on a mouse model of spinal cord injury [32]. All these reports suggest that artificial engagement of XBP1-dependent responses may have therapeutic potential to treat neurodegenerative diseases including HD.

XBP1s controls the expression of a subset of UPR-target genes involved in protein folding and ERAD [44], which may explain the reduction in the number of cells containing small mHtt inclusions when XBP1s was ectopically expressed. The mechanism underlying the protective effects of the AAV-XBP1s gene therapy remains to be determined. Our results suggest that strategies to attenuate ER stress levels may have a beneficial effect to alleviate degeneration in HD.

Acknowledgments

We thank Dr. Ray Truant for kindly providing Htt1-588^{Q138}-mRFP and Htt1-588^{Q15}-mRFP vectors. This work was funded by CHDI Foundation Inc, FONDECYT No. 1100176, FONDAP Grant No. 15010006, Millennium Institute No. P09-015-F, Muscular Dystrophy Association, Alzheimer Association, North American Spine Society, ALS Therapy Allianze, and the Michael J. Fox Foundation for Parkinson research (to C.H.) and FONDECYT No. 3100039 (R.V.).

Appendix A. Supplementary data

Supplementary data associated with this article can be found, in the online version, at http://dx.doi.org/10.1016/j.bbrc.2012.03.033.

References

[1] A.J. Williams, H.L. Paulson, Polyglutamine neurodegeneration: protein misfolding revisited, Trends Neurosci. 31 (2008) 521–528.
[2] J.W. Longshore, J. Tarleton, Dynamic mutations in human genes: a review of trinucleotide repeat disease, J. Genetic 75 (1996) 193–217.
[3] C. Zuccato, M. Valenza, E. Cattaneo, Molecular mechanisms and potential therapeutical targets in Huntington's disease, Physiol. Rev. 90 (2010) 905–981.
[4] R. Vidal, B. Caballero, A. Couve, C. Hetz, Converging pathways in the occurrence of endoplasmic reticulum (ER) stress in Huntington's disease, Curr. Mol. Med. 11 (2011) 1–12.
[5] S. Matus, L.H. Glimcher, C. Hetz, Protein folding stress in neurodegenerative diseases: a glimpse into the ER, Curr. Opin. Cell Biol. 23 (2011) 239–252.
[6] C. Hetz, The Unfolded Protein Response: Controlling cell fate decisions under ER stress and beyond, Nat. Rev. Mol. Cell Biol. 13 (2012) 1–14.
[7] U. Woehlbier, C. Hetz, Modulating stress responses by the UPRosome: A matter of life and death, Trends Biochem. Sci. 36 (2011) 329–337.
[8] I. Tabas, D. Ron, Integrating the mechanisms of apoptosis induced by endoplasmic reticulum stress, Nat. Cell Biol. 13 (2011) 184–190.
[9] D. Ron, P. Walter, Signal integration in the endoplasmic reticulum unfolded protein response, Nat. Rev. Mol. Cell Biol. 8 (2007) 519–529.
[10] H. Yoshida, T. Matsui, A. Yamamoto, T. Okada, K. Mori, XBP1 mRNA is induced by ATF6 and spliced by IRE1 in response to ER stress to produce a highly active transcription factor, Cell 107 (2001) 881–891.
[11] K. Lee, W. Tirasophon, X. Shen, M. Michalak, R. Prywes, T. Okada, H. Yoshida, K. Mori, R.J. Kaufman, IRE1-mediated unconventional mRNA splicing and S2P-mediated ATF6 cleavage merge to regulate XBP1 in signaling the unfolded protein response, Genes Dev. 16 (2002) 452–466.
[12] M. Calfon, H. Zeng, F. Urano, J.H. Till, S.R. Hubbard, H.P. Harding, S.G. Clark, D. Ron, IRE1 couples endoplasmic reticulum load to secretory capacity by processing the XBP-1 mRNA, Nature 415 (2002) 92–96.
[13] A.H. Lee, N.N. Iwakoshi, L.H. Glimcher, XBP-1 regulates a subset of endoplasmic reticulum resident chaperone genes in the unfolded protein response, Mol. Cell Biol. 23 (2003) 7448–7459.
[14] D. Acosta-Alvear, Y. Zhou, A. Blais, M. Tsikitis, N.H. Lents, C. Arias, C.J. Lennon, Y. Kluger, B.D. Dynlacht, XBP1 controls diverse cell type- and condition-specific transcriptional regulatory networks, Mol. Cell 27 (2007) 53–66.
[15] A. Carnemolla, E. Fossale, E. Agostoni, S. Michelazzi, R. Calligaris, L. De Maso, G. Del Sal, M.E. MacDonald, F. Persichetti, Rrs1 is involved in endoplasmic reticulum stress response in Huntington disease, J. Biol. Chem. 284 (2009) 18167–18173.
[16] H. Lee, J.Y. Noh, Y. Oh, Y. Kim, J.W. Chang, C.W. Chung, S.T. Lee, M. Kim, H. Ryu, Y.K. Jung, IRE1 plays an essential role in ER stress-mediated aggregation of mutant Huntingtin via the inhibition of autophagy flux, Hum. Mol. Genet. 21 (2012) 101–114.
[17] M.R. Fernandez-Fernandez, I. Ferrer, J.J. Lucas, Impaired ATF6alpha processing, decreased Rheb and neuronal cell cycle re-entry in Huntington's disease, Neurobiol. Dis. 41 (2011) 23–32.
[18] [18] R. Vidal, A. Figueroa, F. Court, P. Thielen, C. Molina, C. Wirth, B. Caballero, R. Kiffin, J. Segura-Aguilar, A. Cuervo, L. Glimcher, C. Hetz, Targeting the UPR transcription factor XBP1 protects against Huntington's disease through the regulation of FoxO1 and autophagy, Hum Mol Genet (in press).
[19] K.J. Cho, B.I. Lee, S.Y. Cheon, H.W. Kim, H.J. Kim, G.W. Kim, Inhibition of apoptosis signal-regulating kinase 1 reduces endoplasmic reticulum stress and nuclear Huntingtin fragments in a mouse model of Huntington disease, Neuroscience 163 (2009) 1128–1134.
[20] P. Lajoie, E.L. Snapp, Changes in BiP availability reveal hypersensitivity to acute endoplasmic reticulum stress in cells expressing mutant Huntingtin, J. Cell Sci. 124 (2011) 3332–3343.
[21] Y. Kouroku, E. Fujita, A. Jimbo, T. Kikuchi, T. Yamagata, M.Y. Momoi, E. Kominami, K. Kuida, K. Sakamaki, S. Yonehara, T. Momoi, Polyglutamine aggregates stimulate ER stress signals and caspase-12 activation, Hum. Mol. Genet. 11 (2002) 1505–1515.
[22] M.L. Duennwald, S. Lindquist, Impaired ERAD and ER stress are early and specific events in polyglutamine toxicity, Genes Dev. 22 (2008) 3308–3319.
[23] H. Nishitoh, A. Matsuzawa, K. Tobiume, K. Saegusa, K. Takeda, K. Inoue, S. Hori, A. Kakizuka, H. Ichijo, ASK1 is essential for endoplasmic reticulum stress-induced neuronal cell death triggered by expanded polyglutamine repeats, Genes Dev. 16 (2002) 1345–1355.
[24] Y.C. Tsai, P.S. Fishman, N.V. Thakor, G.A. Oyler, Parkin facilitates the elimination of expanded polyglutamine proteins and leads to preservation of proteasome function, J. Biol. Chem. 278 (2003) 22044–22055.
[25] Y. Kouroku, E. Fujita, I. Tanida, T. Ueno, A. Isoai, H. Kumagai, S. Ogawa, R.J. Kaufman, E. Kominami, T. Momoi, ER stress (PERK/eIF2alpha phosphorylation) mediates the polyglutamine-induced LC3 conversion an essential step for autophagy formation, Cell Death Differ. 14 (2007) 230–239.
[26] H. Yang, C. Liu, Y. Zhong, S. Luo, M.J. Monteiro, S. Fang, Huntingtin interacts with the cue domain of gp78 and inhibits gp78 binding to ubiquitin and p97/VCP, PLoS One 5 (2010) e8905.
[27] S. Sarkar, E.O. Perlstein, S. Imarisio, S. Pineau, A. Cordenier, R.L. Maglathlin, J.A. Webster, T.A. Lewis, C.J. O'Kane, S.L. Schreiber, D.C. Rubinsztein, Small molecules enhance autophagy and reduce toxicity in Huntington's disease models, Nat. Chem. Biol. 3 (2007) 331–338.
[28] F.M. Menzies, K. Moreau, D.C. Rubinsztein, Protein misfolding disorders and macroautophagy, Curr. Opin. Cell Biol. 23 (2011) 190–197.
[29] C. Hetz, P. Thielen, S. Matus, M. Nassif, F. Court, R. Kiffin, G. Martinez, A.M. Cuervo, R.H. Brown, L.H. Glimcher, XBP-1 deficiency in the nervous system protects against amyotrophic lateral sclerosis by increasing autophagy, Genes Dev. 23 (2009) 2294–2306.
[30] S. Matus, M. Nassif, L.H. Glimcher, C. Hetz, XBP-1 deficiency in the nervous system reveals a homeostatic switch to activate autophagy, Autophagy 5 (2009) 1226–1228.
[31] M. Sado, Y. Yamasaki, T. Iwanaga, Y. Onaka, T. Ibuki, S. Nishihara, H. Mizuguchi, H. Momota, R. Kishibuchi, T. Hashimoto, D. Wada, H. Kitagawa, T.K. Watanabe,

Protective effect against Parkinson's disease-related insults through the activation of XBP1, Brain Res. 1257 (2009) 16–24.
[32] V. Valenzuela, E. Collyer, D. Armentano, G. Parsons, F. Court, H. C., Activation of the Unfolded Protein Response enhances motor recovery after spinal cord injury, Cell Death Disease, (in press).
[33] R.S. Atwal, J. Xia, D. Pinchev, J. Taylor, R.M. Epand, R. Truant, Huntingtin has a membrane association signal that can modulate Huntingtin aggregation nuclear entry and toxicity, Hum. Mol. Genet. 16 (2007) 2600–2615.
[34] J.C. Grieger, V.W. Choi, R.J. Samulski, Production and characterization of adeno-associated viral vectors, Nat. Protocl. 1 (2006) 1412–1428.
[35] U.P. Rohr, M.A. Wulf, S. Stahn, U. Steidl, R. Haas, R. Kronenwett, Fast and reliable titration of recombinant adeno-associated virus type-2 using quantitative real-time PCR, J. Virol. Methods 106 (2002) 81–88.
[36] M.Y. Heng, P.J. Detloff, R.L. Albin, Rodent genetic models of Huntington disease, Neurobiol. Dis. 32 (2008) 1–9.
[37] L.P. de Almeida, C.A. Ross, D. Zala, P. Aebischer, N. Deglon, Lentiviral-mediated delivery of mutant Huntingtin in the striatum of rats induces a selective neuropathology modulated by polyglutamine repeat size, Huntingtin expression levels, and protein length, J. Neurosci. 22 (2002) 3473–3483.
[38] M. DiFiglia, M. Sena-Esteves, K. Chase, E. Sapp, E. Pfister, M. Sass, J. Yoder, P. Reeves, R.K. Pandey, K.G. Rajeev, M. Manoharan, D.W. Sah, P.D. Zamore, N. Aronin, Therapeutic silencing of mutant Huntingtin with siRNA attenuates striatal and cortical neuropathology and behavioral deficits, Proc. Natl. Acad. Sci. USA 104 (2007) 17204–17209.
[39] N.R. Franich, H.L. Fitzsimons, D.M. Fong, M. Klugmann, M.J. During, D. Young, AAV vector-mediated RNAi of mutant Huntingtin expression is neuroprotective in a novel genetic rat model of Huntington's disease, Mol. Ther. 16 (2008) 947–956.
[40] S. Casas-Tinto, Y. Zhang, J. Sanchez-Garcia, M. Gomez-Velazquez, D.E. Rincon-Limas, P. Fernandez-Funez, The ER stress factor XBP1s prevents amyloid-{beta} neurotoxicity, Hum. Mol. Genet. 20 (2011) 2144–2160.
[41] C. Hetz, A.H. Lee, D. Gonzalez-Romero, P. Thielen, J. Castilla, C. Soto, L.H. Glimcher, Unfolded protein response transcription factor XBP-1 does not influence prion replication or pathogenesis, Proc. Natl. Acad. Sci. USA 105 (2008) 757–762.
[42] H.D. Ryoo, P.M. Domingos, M.J. Kang, H. Steller, Unfolded protein response in a Drosophila model for retinal degeneration, EMBO J. 26 (2007) 242–252.
[43] C.A. Loewen, M.B. Feany, The unfolded protein response protects from tau neurotoxicity in vivo, PLoS One 5 (2010).
[44] C. Hetz, L.H. Glimcher, Fine-tuning of the unfolded protein response: Assembling the IRE1alpha interactom, Mol. Cell 35 (2009) 551–561.

Biochemical and Biophysical Research Communications 420 (2012) 564–569

Contents lists available at SciVerse ScienceDirect

Biochemical and Biophysical Research Communications

journal homepage: www.elsevier.com/locate/ybbrc

A miRNA machinery component DDX20 controls NF-κB via microRNA-140 function

Akemi Takata, Motoyuki Otsuka *, Takeshi Yoshikawa, Takahiro Kishikawa, Yotaro Kudo, Tadashi Goto, Haruhiko Yoshida, Kazuhiko Koike

Department of Gastroenterology, Graduate School of Medicine, The University of Tokyo, Tokyo 113-8655, Japan

ARTICLE INFO

Article history:
Received 28 February 2012
Available online 16 March 2012

Keywords:
DDX20
NF-κB
MicroRNA

ABSTRACT

Hepatocellular carcinoma is the third leading cause of cancer mortality worldwide, but the molecular mechanisms in tumorigenesis remain largely unknown. Previously, a DEAD-box protein DDX20, a component of microRNA-containing ribonucleoprotein complexes, was identified as a liver tumor suppressor candidate in an oncogenomics-based *in vivo* RNAi screen. However, the molecular mechanisms were unknown. Here, we show that deficiency of DDX20 results in the enhancement of NF-κB activity, a crucial intracellular signaling pathway closely linked with hepatocarcinogenesis. While DDX20 normally suppresses NF-κB activity by regulating NF-κB-suppressing miRNA-140 function, this suppressive effect was lost in DDX20-deficient cells. The impairment of miRNA function due to DDX20 deficiency appears to be miRNA species-specific at the point of loading miRNAs into the RNA-induced silencing complex. These results indicate that DDX20 deficiency enhances NF-κB activity by impairing the NF-κB-suppressive action of microRNAs, and suggest that dysregulation of the microRNA machinery components may also be involved in pathogenesis in various human diseases.

1. Introduction

The incidence of hepatocellular carcinoma, the third most common cause of cancer-related mortality worldwide [1], is increasing in Western countries [2]. While numerous studies have investigated molecular abnormalities in hepatocarcinogenesis, the development of this disease cannot be attributed to any single oncogenic event. Thus, drugs targeting various molecular pathways must be evaluated in combination with, or in comparison with, the current therapeutic options [3]. Although recent findings on the effectiveness of sorafenib, a multi-kinase inhibitor, are promising, the survival benefit is only less than 3 months [4]. As no effective therapy currently exists, a better understanding of the exact mechanisms involved in hepatocarcinogenesis remains the fundamental foundation for developing new candidate drugs.

DDX20 (also known as Gemin3 or DP103) was originally isolated as a DEAD-box protein that associated with the Epstein–Barr virus nuclear proteins EBNA2 and EBNA3C [5]. This protein has also been isolated independently as an interactant of survival motor neuron protein (SMN) in the gems, and in cytoplasmic spliceosomal small nuclear ribonucleoprotein complexes (snRNPs) [6]. These results suggest that DDX20 is involved in both transcriptional regulation and RNA processing. More evidence has indicated that DDX20 acts as a transcriptional regulator [7–9]. Concurrently, DDX20 was identified as a major component of microRNA (miRNA)-containing ribonucleoprotein complexes (miRNPs) that also contain eIF2C2 (Argonaute 2; Ago2) [10,11], and which perform translational control in the miRNA pathway. In addition, attempts to create DDX20 knockout mice have resulted in embryonic lethality, suggesting that this protein has essential biologic roles [12].

Recently, an oncogenomics-based *in vivo* RNAi screen identified 13 new tumor-suppressor genes in murine liver cancers [13], one of which was DDX20. Because DDX20 has not been clearly linked to liver cancer previously, the molecular mechanisms by which the dysregulation of this gene causes hepatocellular carcinoma are unknown. To address these, we examined the deregulated intracellular signaling pathway caused by DDX20 deficiency and identified a previously unknown intracellular signaling pathway.

2. Methods

2.1. Cell culture

PLC/PRF/5, Huh7, and 293T cells were maintained in Dulbecco's modified Eagle's medium (DMEM) supplemented with 10% fetal bovine serum (FBS). Hep3B cells were cultured in DMEM supplemented with 10% nonessential amino acids and 10% FBS.

* Corresponding author. Address: Department of Gastroenterology, Graduate School of Medicine, The University of Tokyo, 7-3-1 Hongo, Bunkyo-ku, Tokyo 113-8655, Japan. Fax: +81 3 3814 0021.
E-mail address: otsukamo-tky@umin.ac.jp (M. Otsuka).

0006-291X/$ - see front matter © 2012 Elsevier Inc. All rights reserved.
http://dx.doi.org/10.1016/j.bbrc.2012.03.034

2.2. Plasmids

FLAG-tagged human DDX20-expressing plasmids were kindly provided by Dr. C. Glass and Dr. G. Dreyfuss [8,10]. FLAG-tagged human DDX20-expression plasmids used for generation of DDX20-overexpressing lentiviruses were constructed by inserting the PCR-amplified DDX20 cDNA at the NotI site of the pCDH vector (System Biosciences). Plasmids expressing microRNA precursors (miRNA-22 and miRNA-140 precursors) were purchased from System Biosciences (Mountain View, CA). Reporter plasmids to analyze miRNA function were constructed by inserting annealed synthetic primers containing two tandem sequences, complementary to each miRNA, into the 3′-UTR of the firefly luciferase gene, driven by the CMV promoter (pGL3-basic; Promega, Madison, WI), at the FseI site. Primers used for PCR amplification of DDX20 were: forward, 5′-GCG GCC GCG CCG CCA TGG ACT ACA AGG ACG ACG ACG ACA AGG ACT ACA AGG ACG ACG ACG ACA AGA TGG CGG CGG CAT TTG AAG C-3′ and reverse, 5′-GCG GCC GCT CAC TGG TTA CTA TGC ATC AT TTC-3′. The sequences of the primers used for reporter plasmid construction were as follows: miR-22, 5′-ACA GTT CTT CAA CTG GCA GCT TAA TTA CAG TTC TTC AAC TGG CAG CTT CTC GAG CCG G-3′; miRNA-140–3p, 5′-CCG TGG TTC TAC CCT GTG GTA AAT TCC GTG GTT CTA CCC TGT GGT ACT CGA GCC GG-3′; miRNA-140-5p, 5′-CTA CCA TAG GGT AAA ACC ACT GAA TTC TAC CAT AGG GTA AAA CCA CTG CTC GAG CCG G-3′.

2.3. Lentiviral production and transduction

Cells were transduced with DDX20 (Gemin3)-shRNA and control-shRNA lentiviral particles (Santa Cruz Biotechnology) and then selected on puromycin. To produce FLAG-tagged DDX20 expressing-lentiviruses, 293T cells were transfected with pPACKH1 Packaging Plasmid Mix (System Biosciences) and pCDH-FLAG-tagged DDX20 expressing-lentivector constructs. After 2 days, the supernatants were collected and the viruses were concentrated using PEG-it Virus Precipitation Solution (System Biosciences).

2.4. Transfection and luciferase assay

Transfection was performed using Fugene6 (Promega). Luciferase activities were measured by use of a Dual Luciferase Reporter Assay System (Promega) as described previously [14].

2.5. RNA isolation and reverse transcription

Total RNA was isolated using Trizol Reagent (Invitrogen, Carlsbad, CA). cDNA was synthesized from RNA using the SuperScript III First-Strand Synthesis System (Invitrogen).

2.6. Antibodies

The following antibodies were used: mouse anti-Gemin3 (Ddx20) (sc-57007), rabbit anti-TRADD (sc-7868), rabbit anti-RIP (sc-7881), mouse anti-IKKα (sc-7183), mouse anti-NF-κB p65 (sc-8008), and mouse anti-NF-κB p50 (sc-7188), all purchased from Santa Cruz Biotechnology (Santa Cruz, CA); mouse anti-β-actin (A5316), purchased from Sigma (St. Louis, MO); mouse anti-TRAF2 (#558890) and mouse anti-IKKγ (#559675), purchased from BD Pharmingen (San Diego, CA); rabbit anti-TAK1 (#4505) and rabbit anti-IKKβ (#2370), purchased from Cell Signaling Technology (Danvers, MA); mouse anti-IκBα (#610690), purchased from BD Transduction Laboratories (Lexington, KY); mouse anti-Ago2 (#015-22031) and mouse anti-DYKDDDDY (FLAG)-tag (#018-22381), purchased from Wako (Osaka, Japan).

2.7. Western blotting

Western blotting was performed as described previously [15].

2.8. Reporter plasmids for signal transduction

The following reporter plasmids were used to examine how DDX20 modulated intracellular signaling: pNF-κB-luc, pGAS (IFNγ-activated sequences)-luc, pSRE-luc, pAP-1-luc, and p53-luc were purchased from Stratagene (La Jolla, CA). IL-8-luc, and p3TP-luc (to determine TGFβ pathway activity), were described previously [16]. To construct a reporter plasmid containing mutated NF-κB binding sites, the NF-κB binding motifs, GGGAATTTCC, in pNF-κB-luc were mutated to ATCAATTTCA, as previously reported [17]. Synthetic oligonucleotides with four mutant binding sites (forward, 5′-CTA GCA TCA ATT TCA ATC AAT TTC AAT CAA TTT CAA TCA ATT TCA A-3′; reverse, 5′-GAT CTT GAA ATT GAT TGA AAT TGA TTG AAA TTG ATT GAA ATT GAT G-3′) were annealed and cloned into the NheI and BglII sites of pNF-κB-luc to replace the original NF-κB binding motifs. As positive controls, the following were used: transfection with pFC-MEKK, a MEKK-expressing plasmid, for NF-κB-luc, SRE-luc, and AP-1-luc; transfection with p53-expressing plasmid for p53-luc; incubation for 6 h with 5 ng/mL IFNγ (ProSpec-Tany TechnoGene, Rehovot, Israel) for GAS-luc, and with 5 ng/mL TGFβ (Peprotech, Rocky Hill, NJ) for p3TP-luc.

2.9. EMSA

Nuclear extracts were prepared as described previously [18]. Five micrograms of nuclear extract were incubated with a double-stranded biotin-labeled DNA probe containing NF-κB binding sites (5′-AGT TGA GGG GAC TTT CCC AGG C-3′) plus 1 μg of poly (dI-dC) in a binding buffer (50 mM Tris [pH 7.5], 250 mM NaCl, 2.5 mM DTT, 2.5 mM EDTA, 5 mM $MgCl_2$, and 20% glycerol) at 15 °C for 30 min. DNA–protein complexes were separated on a 6% non-denaturing polyacrylamide gel in 0.5x TBE, and then transferred to nylon membrane (Hybond-N^+; GE Healthcare Life Sciences). Oligonucleotides were visualized using the LightShift Chemiluminescent EMSA Kit (Thermo Scientific, Rockford, IL). DNA–protein complex specificity was tested by adding a 100-fold excess of unlabeled (cold) NF-κB probe. To confirm equal loading of nuclear-extracts, the amounts of TFIID, a nuclear protein, were examined by Western blotting using an anti-TFIID antibody (sc-273; Santa Cruz).

2.10. miRNA isolation and quantitation

To measure the amounts of different microRNAs in cells, a Mir-X miRNA qRT-PCR SYBR Kit (Clontech, Mountain View, CA) was used. The levels of U6 snRNA were used for the normalization of cellular miRNA levels. To purify miRNAs from Ago2-related RISCs and DDX20-associated miRNP complexes, microRNAs fractions were isolated using the Human Ago2 MicroRNA Isolation Kit (Wako, Osaka, Japan), which uses antibodies raised to Ago2 and DDX20 to precipitate miRNAs from Ago2-related RISCs and DDX20-associated miRNPs, respectively. The primers used in the quantitative PCR analysis for miRNAs were miRNA-140-5p, CAG TGG TTT TAC CCT ATG GTA G; miRNA-140-3p, TAC CAC AGG GTA GAA CCA CGG; miRNA-22, AAG CTG CCA GTT GAA GAA CTG T.

2.11. Quantitative PCR

Quantitative PCR was performed using the TaqMan Gene Expression system and SYBR Green (Applied Biosystems, Foster City, CA). All target gene expression values were normalized to the expression values for the housekeeping gene, GAPDH, and

relative expression levels were calculated by the $\Delta\Delta C_T$ method: $\Delta\Delta C_T = \Delta C_{Tsample} - \Delta C_{Tgapdh}$ The primers used included (5′–3′): IL-6 forward, CAC AGA CAG CCA CTC ACC TC; IL-6 reverse, TTT TCT GCC AGT GCC TCT TT; IL-8 forward, ATG ACT TCC AAG CTG GCC GTG GCT; IL-8 reverse, TCT CAG CCC TCT TCA AAA ACT TCT C; GAPDH forward, ATC AAC GAC CCC TTC ATT GAC C, and GAPDH reverse, CCA GTA GAC TCC ACG ACA TAC TCA GC.

2.12. Immunoprecipitation

For immunoprecipitation, 293T cells were transfected with FLAG-tagged DDX20-expressing plasmids. FLAG-tagged DDX20 protein was precipitated by incubation with anti-FLAG M2 agarose (Sigma) for 8 h. Cell extracts were prepared as described previously [16].

2.13. Statistical analysis

Statistically significant differences were determined using Student's *t*-test, when variances were equal. When variances were unequal, Welch's *t*-test was instead used.

3. Results

3.1. DDX20 modulates the NF-κB activity

Because it was reported that DDX20 regulates transcriptions [7–9,19], we first examined the effects of altered DDX20 levels on intracellular signaling pathways by a reporter assay (Fig. 1A). While SRE was repressed moderately by DDX20 overexpression consistent with a previous report (Fig. 1A) [8], NF-κB activity was also decreased significantly in our study (Fig. 1A). Thus, we next examined NF-κB activity in stable DDX20-knockdown PLC/PRF/5 cells (Fig. 1B). Whereas DDX20-knockdown cells showed slightly higher NF-κB activity than control cells (Fig. 1C), the response was significantly enhanced by TNFα, which induces NF-κB activity and is involved in the pathogenesis of hepatitis, leading to HCC [20–23] (Fig. 1C). DDX20-knockdown cells consistently showed significantly higher promoter activity for the interleukin (IL)-8 gene, a gene known to be induced by NF-κB [24] (Fig. 1D). To exclude the possibility of cell-specific effects, we established DDX20-knockdown Huh7 cells and observed a similar trend in these cell lines (Supplementary Fig. S1a, b, and c). To further confirm these findings in an overexpression model, we established FLAG-tagged DDX20-overexpressing stable cell lines (Supplementary Fig. S2a). Restoration of NF-κB activity and mRNA levels of IL-6 and IL-8 resulted from DDX20 overexpression, consistent with the results from DDX20-knockdown cells (Supplementary Fig. S2b and c). These results also suggest that DDX20 normally functions to suppress NF-κB activity and the resulting downstream effects of this pathway.

3.2. DDX20 does not modulate or interact with molecules in the NF-κB canonical pathway

To determine how DDX20 deficiency enhances NF-κB activity, we examined the DNA-binding activity of NF-κB, which was increased in DDX20-knockdown cells (Fig. 2A). Although we

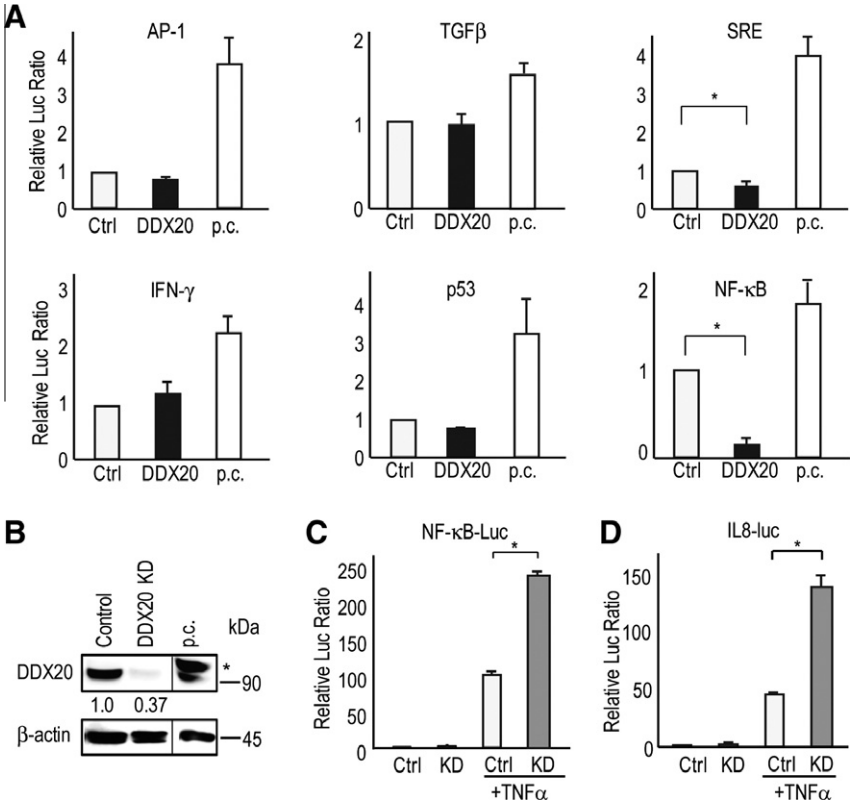

Fig. 1. Modulation of the NF-κB pathway by DDX20. (A) The effects of DDX20 on intracellular signaling pathways as assessed by a reporter assay. Huh7 cells were transiently transfected with a luciferase reporter plasmid and a DDX20-expressing (DDX20) or control plasmid (Ctrl). Luciferase values from control cells were set to 1. The data shown represent the means ± s.d. from at least four independent experiments. p.c.; positive control. (B) Establishment of stable DDX20-knockdown PLC/PRF/5 cells. *FLAG-tagged human DDX20 as a positive control (p.c.). (C, D) Reporter assay data showing that DDX20 deficiency enhances the TNFα-induced activity of NF-κB. Reporter plasmids for NF-κB (C) and its target gene, IL-8 (D), were transiently transfected into control (Ctrl) or DDX20-knockdown (KD) cells. The cells were treated with TNFα (5 ng/mL) or vehicle for 6 h before the reporter assay was performed. *$p < 0.05$. The data shown represent the means ± s.d. from three independent experimental trials. Similar results were obtained in DDX20-knockdown Huh7 cells.

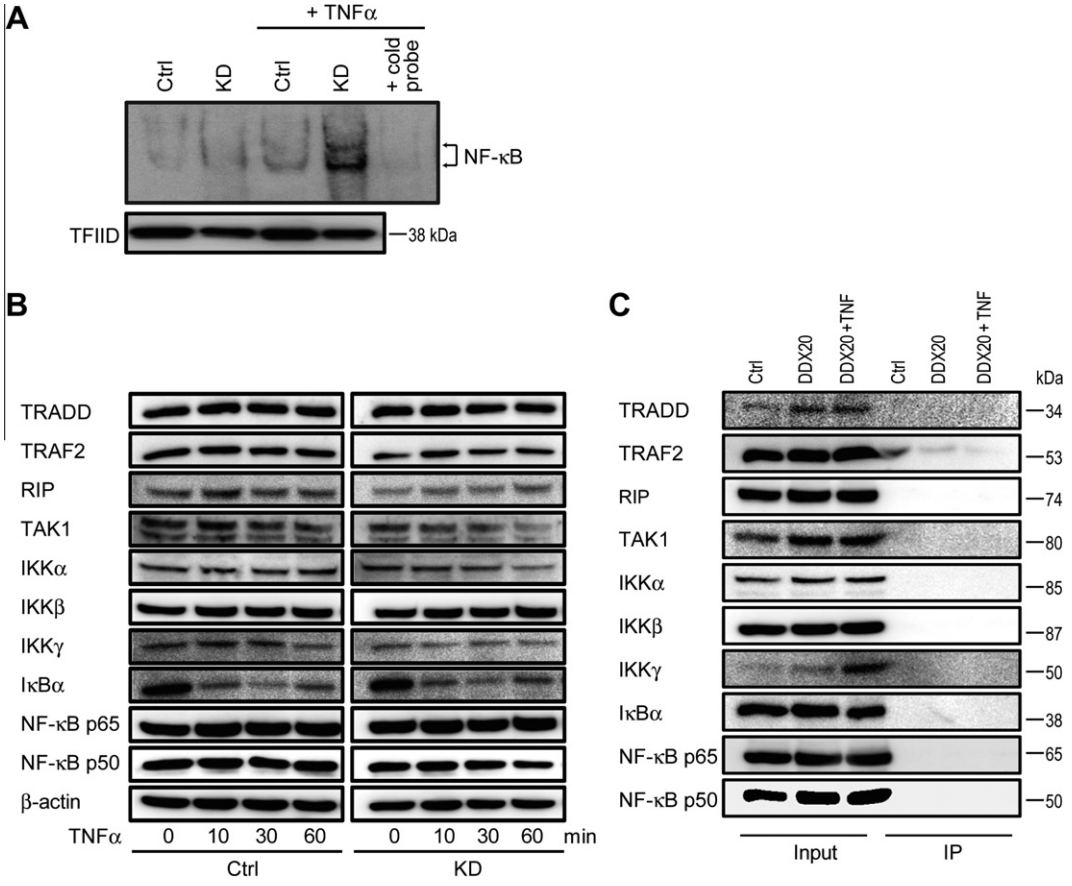

Fig. 2. NF-κB DNA binding is increased in DDX20 knockdown cells after TNFα stimulation. (A) Nuclear extracts from unstimulated and TNFα-stimulated control (Ctrl) and DDX20-knockdown (KD) PLC/PRF/5 cells were analyzed by electrophoretic mobility-shift assay. The specificity of the DNA–protein complex was tested by adding unlabeled NF-κB probe (cold probe) to the TNFα-stimulated KD nuclear extracts. TFIID amounts were examined to confirm equal nuclear extract loading. A representative result is shown from four independent experiments. Similar results were obtained using Huh7 cells. (B) Control (Ctrl) and DDX20-knockdown (KD) PLC/PRF/5 cells were stimulated with 5 ng/mL TNFα for the times indicated. Western blotting was performed using antibodies against the indicated proteins. A representative result is shown from two independent experiments. Similar results were obtained using Huh7 cells. (C) 293T cells (treated with or without 5 ng/mL TNFα for 6 h before the assay) were transfected with a control vector (Ctrl) or a FLAG-tagged DDX20-expressing (DDX20) plasmid. FLAG-tagged DDX20 was immunoprecipitated using anti-FLAG agarose. Co-precipitated proteins were blotted using antibodies against the indicated proteins. Five percent of the total cell lysates were loaded as an input control. Representative results from two independent experiments are shown.

observed IκB-α protein degradation after TNFα stimulation, as expected, the degree of degradation was similar in the control and DDX20-knockdown cells (Fig. 2B) and the levels of the other proteins examined were also similar (Fig. 2B). In addition, we were unable to detect any interactions between DDX20 and the NF-κB pathway-related molecules examined (Fig. 2C). These results suggest that it is unlikely that DDX20 modulates NF-κB activity either by interacting directly with these molecules or by altering their expression levels.

3.3. DDX20 deficiency enhances NF-κB activity by impairing miRNA-140-3p function

Because DDX20 interacts with Ago2 (Fig. 3A), which plays a central role in miRNA function [10,11], we hypothesized that DDX20 deficiency leads to impaired miRNA function and to subsequent activation of NF-κB. Because we previously identified by a comprehensive liver-expressing miRNA library screen that miRNA-22 and miRNA-140 are the critical suppressors of NF-κB activities [25], we hypothesized that DDX20 deficiency enhances NF-κB activity by impairing the NF-κB-suppressing miRNA function.

In DDX20-knockdown cells, the effects of miRNA-140-3p were reduced significantly (Fig. 3B). This impairment of miRNA function had miRNA species-specificity because the degree of functional impairment in DDX20-knockdown cells was much greater for miRNA-140-3p than for miRNA-140-5p and miRNA-22 (Fig. 3B).

While miRNA-22 and miRNA-140 suppressed NF-κB activity in the control cells as we previously reported [25] (Fig. 3C), the suppressive effects of miRNA-140 on NF-κB activity were reduced significantly in DDX20-knockdown cells (Fig. 3C). The reversal of the suppressive effect of miRNA-140 appeared to depend on miRNA-140-3p as miRNA-140-5p showed less functional impairment than did miRNA-140-3p when the corresponding reporter constructs were used as described above (Fig. 3B). The effect was NF-κB specific because no effects were observed for reporters with mutations in the NF-κB binding sites (Fig. 3D).

3.4. DDX20 preferentially interacts with miRNA-140-3p

To elucidate the mechanisms by which DDX20 preferentially impairs certain miRNA functions, we compared the levels of mature miRNAs (miR-22, 140-3p, and 140-5p) in control cells and in DDX20-knockdown cells and found them to be comparable (Fig. 4A). This suggests that DDX20 was not involved in miRNA maturation. We next considered the possibility that the preferential impairment of miRNA function in DDX20-knockdown cells was caused by preferential loading of miRNAs into the RNA-induced silencing complex (RISC). To test this, we immunoprecipitated

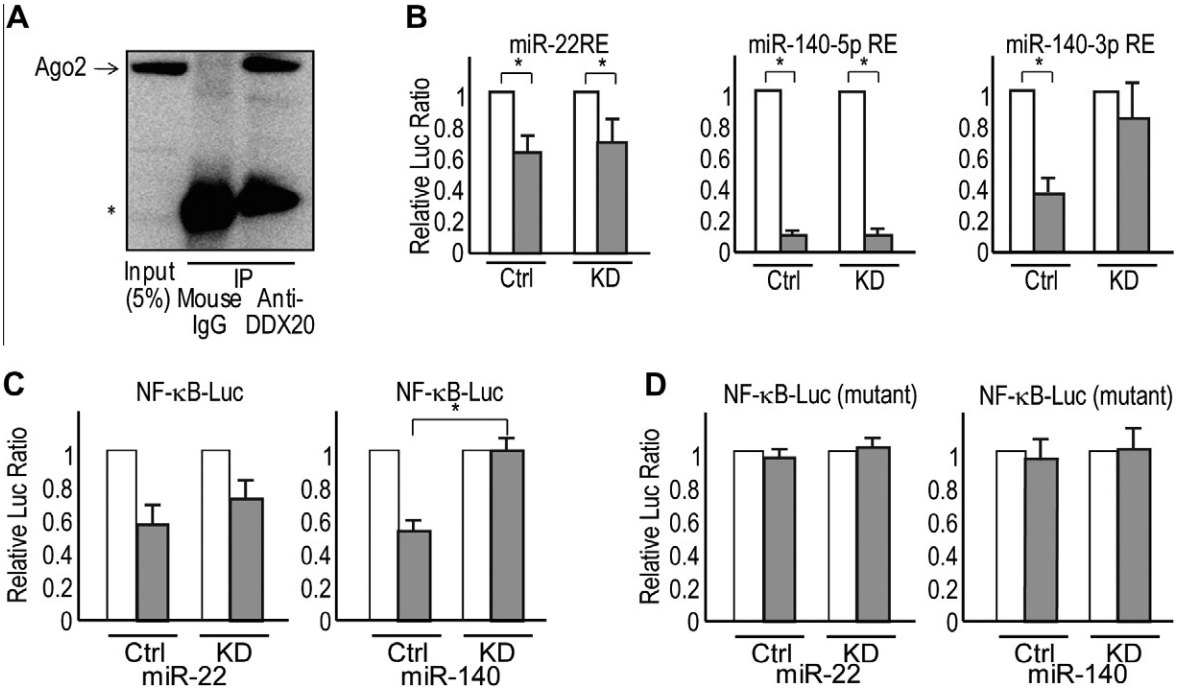

Fig. 3. DDX20 deficiency enhances NF-κB activity by impairing miRNA function. (A) DDX20 binds Ago2. 293T cells were transfected with a FLAG-tagged DDX20-expressing plasmid, and immunoprecipitated using monoclonal antibodies against FLAG-tag or non-immune mouse IgG. Precipitates were blotted with a human anti-Ago2 antibody. Five per cent of each cell lysate was used as an "input" to show the endogenous Ago2 protein. *Bands derived from immunoglobulin light-chain. (B) Overexpression of the miRNA precursors suppresses the activities of the corresponding promoter-reporter constructs in control cells (Ctrl), whereas DDX20 knockdown (DDX KD) reverses the suppressive effects of miRNA-140-3p in PLC/PRF/5 cells. The white and gray bars indicate results with the empty vector and with miRNA precursor overexpression, respectively. $^*p < 0.05$. (C) Expression of the miRNA-140 precursor suppresses NF-κB reporter activity in control cells (Ctrl), but this effect was attenuated in DDX20-knockdown PLC/PRF/5 cells (KD) as determined by NF-κB-Luc. The cells were treated with 5 ng/mL TNFα for 6 h. White and gray bars indicate empty vector and miRNA precursor overexpression, respectively. $^*p < 0.05$. (D) The suppressive effects by miR-22 and miR-140 were NF-κB-specific. Mutant NF-κB reporter plasmids were transfected with an empty vector (white bar) or the corresponding miRNA precursor-expression plasmids (black bar), into control (Ctrl) and DDX20-knockdown (KD) PLC/PRF/5 cells. Data were normalized and represent the mean ± s.d. of three independent experiments. Similar results were obtained using DDX20-knockdown Huh7 cells.

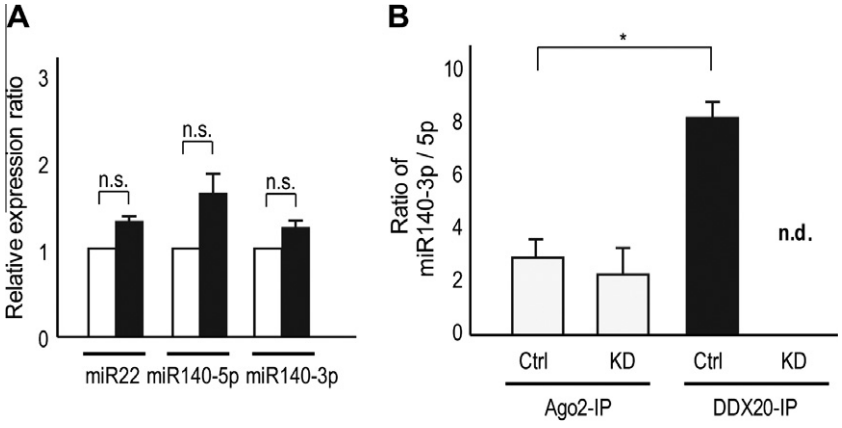

Fig. 4. DDX20 preferentially interacts with miRNA-140-3p. (A) Relative expression of indicated mature miRNAs in the total cellular RNA were measured and normalized to the level of U6 snRNA. The relative ratios of the miRNAs in control cells (white bars) and DDX20-knockdown cells (black bars) were calculated. The data represent the means ± s.d. of six independent experiments. n.s.; non significant. (B) The ratios of miRNA-140-3p to miRNA-140-5p in Ago2- and DDX20-associated RISCs as determined from anti-Ago2 or anti-DDX20 immunoprecipitates (IP) in PLC/PRF/5 control (Ctrl) and DDX20-knockdown (KD) cells. The ratios shown are the means ± s.d. of six independent experiments. Because DDX20-knockdown cells are deficient in DDX20, the anti-DDX20 miRNA ratio was not determined in these cells (n.d.).

Ago2-related RISCs and measured the amount of different miRNAs in the complexes. Because there are no standard small RNAs that can be used as a "house-keeping gene" to adjust for variation in sample loading, we compared miRNA140-5p:miRNA140-3p ratios (since both miRNAs are derived from a single precursor). This ratio in Ago2-related RISCs was approximately two in both control and DDX20-knockdown cells, suggesting that DDX20 was not involved in the preferential loading of specific miRNAs into Ago2-related RISCs (Fig. 4B). However, the ratio in the DDX20-associated miRNPs precipitated from control cells was approximately one to eight (Fig. 4B), indicating that DDX20 preferentially interacts with certain miRNAs, such as miRNA-140-3p, in DDX20-associated miRNPs. The results suggest that functional impairment of certain miRNAs in DDX20-knockdown cells might be caused by the preferential loading of certain miRNAs into DDX20-associated miRNPs. These results further suggest that DDX20 deficiency impairs the function of certain subsets of miRNAs and that this impairment could enhance NF-κB activity by deregulating the NF-κB-suppressive actions of miRNAs, especially miRNA-140-3p, in DDX20-deficient cells.

4. Discussion

Here we report that DDX20 deficiency may enhance NF-κB activities through impairing the NF-κB-suppressing miRNA-140 functions. It was reported that DDX20 is a possible liver tumor suppressor in mice [13]. NF-κB activation is a common feature of human HCCs, particularly those linked to hepatitis [26,27]. In fact, experiments using patient samples suggest that NF-κB activation in the liver leads to the development of HCC [28]. Taken together, these results suggest that the enhancement of NF-κB activity that occurs when DDX20 is deficient may play a role on hepatocarcinogenesis.

Our results indicate that, although DDX20 is one of the major components of Ago2-related RISCs, which play central roles in global miRNA functions [10], impairment of miRNA function due to DDX20 deficiency appears to be miRNA species-specific at the point of loading miRNAs into RISCs. While the precise mechanisms how DDX20 preferentially loads specific miRNAs into RISCs remain to be elucidated, because not all miRNPs have the same components, variation in RISC complexes may determine the properties or specificities of individual miRNAs [10].

Because DDX20 is a multifunctional protein, the miRNA functional impairment reported in the present study may not be the only consequence of DDX20 deficiency. In addition, because novel miRNAs are continually being discovered, other currently unknown miRNAs may also be involved in the biologic role of DDX20. Nonetheless, this study shows that DDX20 is involved in the function of specific miRNAs and the resulting control of NF-κB activity. These results suggest that it is important to investigate not only aberrant miRNA expression levels [29–32] but also deregulation of miRNP components with the subsequent impairment of miRNA function as a path of pathogenesis in human diseases.

Acknowledgments

We thank G. Dreyfuss, and C.K. Glass for providing materials. This work was supported by Grants-in-Aid from the Ministry of Education, Culture, Sports, Science and Technology, Japan (#22390058, #23590960, #17016016, and #20390204) (M. Otsuka, T.G., M. Omata, and K. Koike); by Health Sciences Research Grants from the Ministry of Health, Labor and Welfare of Japan (Research on Hepatitis) (to K. Koike).

Appendix A. Supplementary data

Supplementary data associated with this article can be found, in the online version, at http://dx.doi.org/10.1016/j.bbrc.2012.03.034.

References

[1] D. Parkin, F. Bray, J. Ferlay, P. Pisani, Global cancer statistics, 2002, CA Cancer. J. Clin. 55 (2005) 74–108.
[2] H. El-Serag, Epidemiology of hepatocellular carcinoma in USA, Hepatol. Res. 37 (Suppl.2) (2007) S88–94.
[3] J. Llovet, J. Bruix, Molecular targeted therapies in hepatocellular carcinoma, Hepatology 48 (2008) 1312–1327.
[4] J. Llovet, S. Ricci, V. Mazzaferro, P. Hilgard, E. Gane, J. Blanc, A. de Oliveira, A. Santoro, J. Raoul, A. Forner, M. Schwartz, C. Porta, S. Zeuzem, L. Bolondi, T. Greten, P. Galle, J. Seitz, I. Borbath, D. Häussinger, T. Giannaris, M. Shan, M. Moscovici, D. Voliotis, J. Bruix, S.I.S. Group, Sorafenib in advanced hepatocellular carcinoma, N. Engl. J. Med. 359 (2008) 378–390.
[5] M. Voss, A. Hille, S. Barth, A. Spurk, F. Hennrich, D. Holzer, N. Mueller-Lantzsch, E. Kremmer, F. Grässer, Functional cooperation of Epstein-Barr virus nuclear antigen 2 and the survival motor neuron protein in transactivation of the viral LMP1 promoter, J. Virol. 75 (2001) 11781–11790.
[6] B. Charroux, L. Pellizzoni, R. Perkinson, A. Shevchenko, M. Mann, G. Dreyfuss, Gemin3: a novel DEAD box protein that interacts with SMN, the spinal muscular atrophy gene product, and is a component of gems, J. Cell. Biol. 147 (1999) 1181–1194.
[7] Q. Ou, J. Mouillet, X. Yan, C. Dorn, P. Crawford, Y. Sadovsky, The DEAD box protein DP103 is a regulator of steroidogenic factor-1, Mol. Endocrinol. 15 (2001) 69–79.
[8] G. Klappacher, V. Lunyak, D. Sykes, D. Sawka-Verhelle, J. Sage, G. Brard, S. Ngo, D. Gangadharan, T. Jacks, M. Kamps, D. Rose, M. Rosenfeld, C. Glass, An induced Ets repressor complex regulates growth arrest during terminal macrophage differentiation, Cell 109 (2002) 169–180.
[9] A. Gillian, J. Svaren, The Ddx20/DP103 dead box protein represses transcriptional activation by Egr2/Krox-20, J. Biol. Chem. 279 (2004) 9056–9063.
[10] Z. Mourelatos, J. Dostie, S. Paushkin, A. Sharma, B. Charroux, L. Abel, J. Rappsilber, M. Mann, G. Dreyfuss, MiRNPs: a novel class of ribonucleoproteins containing numerous microRNAs, Genes Dev. 16 (2002) 720–728.
[11] G. Hutvágner, P. Zamore, A MicroRNA in a multiple-turnover RNAi enzyme complex, Science 297 (2002) 2056–2060.
[12] J. Mouillet, X. Yan, Q. Ou, L. Jin, L. Muglia, P. Crawford, Y. Sadovsky, DEAD-box protein-103 (DP103, Ddx20) is essential for early embryonic development and modulates ovarian morphology and function, Endocrinology 149 (2008) 2168–2175.
[13] L. Zender, W. Xue, J. Zuber, C. Semighini, A. Krasnitz, B. Ma, P. Zender, S. Kubicka, J. Luk, P. Schirmacher, W. McCombie, M. Wigler, J. Hicks, G. Hannon, S. Powers, S. Lowe, An oncogenomics-based in vivo RNAi screen identifies tumor suppressors in liver cancer, Cell 135 (2008) 852–864.
[14] M. Otsuka, Q. Jing, P. Georgel, L. New, J. Chen, J. Mols, Y.J. Kang, Z. Jiang, X. Du, R. Cook, S.C. Das, A.K. Pattnaik, B. Beutler, J. Han, Hypersusceptibility to vesicular stomatitis virus infection in Dicer1-deficient mice is due to impaired miR24 and miR93 expression, Immunity 27 (2007) 123–134.
[15] M. Otsuka, A. Takata, T. Yoshikawa, K. Kojima, T. Kishikawa, C. Shibata, M. Takekawa, H. Yoshida, M. Omata, K. Koike, Receptor for activated protein kinase C: requirement for efficient microRNA function and reduced expression in hepatocellular carcinoma, PLoS One 6 (2011) e24359.
[16] M. Otsuka, N. Kato, K. Lan, H. Yoshida, J. Kato, T. Goto, Y. Shiratori, M. Omata, Hepatitis C virus core protein enhances p53 function through augmentation of DNA binding affinity and transcriptional ability, J. Biol. Chem. 275 (2000) 34122–34130.
[17] J. Miyagawa, M. Muguruma, H. Aoto, I. Suetake, M. Nakamura, S. Tajima, Isolation of the novel cDNA of a gene of which expression is induced by a demethylating stimulus, Gene (1999) 289–295.
[18] E. Schreiber, P. Matthias, M. Müller, W. Schaffner, Rapid detection of octamer binding proteins with 'mini-extracts', prepared from a small number of cells, Nucleic Acids Res. 17 (1989) 6419.
[19] F. Fuller-Pace, A. Jacobs, S. Nicol, Modulation of transcriptional activity of the DEAD-box family of RNA helicases, p68 (Ddx5) and DP103 (Ddx20), by SUMO modification, Biochem. Soc. Trans. 35 (2007) 1427–1429.
[20] T. Luedde, R.F. Schwabe, NF-κB in the liver–linking injury, fibrosis and hepatocellular carcinoma, Nat. Rev. Gastroenterol. Hepatol. 8 (2011) 108–118.
[21] M. Arsura, L. Cavin, Nuclear factor-kappaB and liver carcinogenesis, Cancer Lett. 229 (2005) 157–169.
[22] E. Pikarsky, R. Porat, I. Stein, R. Abramovitch, S. Amit, S. Kasem, E. Gutkovich-Pyest, S. Urieli-Shoval, E. Galun, Y. Ben-Neriah, NF-kappaB functions as a tumour promoter in inflammation-associated cancer, Nature 431 (2004) 461–466.
[23] D. Tai, S. Tsai, Y. Chang, S. Huang, T. Chen, K. Chang, Y. Liaw, Constitutive activation of nuclear factor kappaB in hepatocellular carcinoma, Cancer 89 (2000) 2274–2281.
[24] N. Mukaida, Y. Mahe, K. Matsushima, Cooperative interaction of nuclear factor-kappa B- and cis-regulatory enhancer binding protein-like factor binding elements in activating the interleukin-8 gene by pro-inflammatory cytokines, J. Biol. Chem. 265 (1990) 21128–21133.
[25] A. Takata, M. Otsuka, K. Kojima, T. Yoshikawa, T. Kishikawa, H. Yoshida, K. Koike, MicroRNA-22 and microRNA-140 suppress NF-κB activity by regulating the expression of NF-κB coactivators, Biochem. Biophys. Res. Commun. 411 (2011) 826–831.
[26] T. Block, A. Mehta, C. Fimmel, R. Jordan, Molecular viral oncology of hepatocellular carcinoma, Oncogene 22 (2003) 5093–5107.
[27] M. Karin, Nuclear factor-kappaB in cancer development and progression, Nature 441 (2006) 431–436.
[28] J. Ji, J. Shi, A. Budhu, Z. Yu, M. Forgues, S. Roessler, S. Ambs, Y. Chen, P. Meltzer, C. Croce, L. Qin, K. Man, C. Lo, J. Lee, I. Ng, J. Fan, Z. Tang, H. Sun, X. Wang, MicroRNA expression, survival, and response to interferon in liver cancer, N. Engl. J. Med. 361 (2009) 1437–1447.
[29] K. Kojima, A. Takata, C. Vadnais, M. Otsuka, T. Yoshikawa, M. Akanuma, Y. Kondo, Y.J. Kang, T. Kishikawa, N. Kato, Z. Xie, W.J. Zhang, H. Yoshida, M. Omata, A. Nepveu, K. Koike, MicroRNA122 is a key regulator of α-fetoprotein expression and influences the aggressiveness of hepatocellular carcinoma, Nat. Commun. 2 (2011) 338.
[30] M.S. Kumar, J. Lu, K.L. Mercer, T.R. Golub, T. Jacks, Impaired microRNA processing enhances cellular transformation and tumorigenesis, Nat. Genet. 39 (2007) 673–677.
[31] J. Lu, G. Getz, E.A. Miska, E. Alvarez-Saavedra, J. Lamb, D. Peck, A. Sweet-Cordero, B.L. Ebert, R.H. Mak, A.A. Ferrando, J.R. Downing, T. Jacks, H.R. Horvitz, T.R. Golub, MicroRNA expression profiles classify human cancers, Nature 435 (2005) 834–838.
[32] G. Martello, A. Rosato, F. Ferrari, A. Manfrin, M. Cordenonsi, S. Dupont, E. Enzo, V. Guzzardo, M. Rondina, T. Spruce, A. Parenti, M. Daidone, S. Bicciato, S. Piccolo, A MicroRNA targeting dicer for metastasis control, Cell 141 (2010) 1195–1207.

Biochemical and Biophysical Research Communications 420 (2012) 570–575

Contents lists available at SciVerse ScienceDirect

Biochemical and Biophysical Research Communications

journal homepage: www.elsevier.com/locate/ybbrc

Glucocorticoid-induced loss of DNA methylation in non-neuronal cells and potential involvement of *DNMT1* in epigenetic regulation of *Fkbp5*

Xiaoju Yang [b], Erin R. Ewald [a], Yuqing Huo [a], Kellie L. Tamashiro [a], Roberto Salvatori [b], Akira Sawa [a,c], Gary S. Wand [a,b], Richard S. Lee [a,*]

[a] Department of Psychiatry and Behavioral Sciences, Johns Hopkins University School of Medicine, Baltimore, MD 21287, USA
[b] Department of Medicine, Division of Endocrinology, Johns Hopkins University School of Medicine, Baltimore, MD 21205, USA
[c] Department of Neuroscience, Johns Hopkins University School of Medicine, Baltimore, MD 21287, USA

ARTICLE INFO

Article history:
Received 29 February 2012
Available online 16 March 2012

Keywords:
Fkbp5
Dnmt1
Epigenetics
DNA methylation
AtT-20
Pituitary
Hippocampus
HPA-axis

ABSTRACT

Glucocorticoids may play a significant role in the etiology of neuropsychiatric illnesses. Abnormalities in plasma cortisol levels, glucocorticoid sensitivity, and HPA-axis function often accompany clinical symptoms of stress-related illnesses such as PTSD and depression. Of particular interest are genetic association studies that link single nucleotide polymorphisms of HPA-axis genes with illnesses only in the context of an early-life trauma exposure such as child abuse. These studies suggest that dysregulation of HPA-axis function can have lasting repercussions in shaping mood and anxiety, long after termination of the traumatic experience. As *persistent* glucocorticoid-induced loss of DNA methylation in FK506 binding protein 5 (*Fkbp5*) was previously observed in the hippocampus and blood and in the neuronal cell line HT-22, we asked whether these epigenetic alterations occur in non-neuronal, HPA-axis relevant cells. We used the pituitary adenoma cell line AtT-20 to demonstrate that the intronic enhancer region of *Fkbp5* undergoes loss of DNA methylation in response to dexamethasone treatment in a dose-dependent manner. We also focused on the mouse hippocampal dentate gyrus to test whether these changes would be enriched in a region implicated in the HPA-axis stress response, neurogenesis, and synaptic plasticity. We observed an increase in enrichment of DNA methylation loss in the dentate gyrus, as compared to whole hippocampal tissues that were similarly treated with glucocorticoids. We then asked whether DNA methyltransferase 1 (*Dnmt1*), a methyltransferase enzyme involved in maintaining DNA methylation following cell division, is involved in the observed epigenetic alterations. We found a dose-dependent decrease of *Dnmt1* expression in the AtT-20 cells following dexamethasone treatment, and a similar decrease in corticosterone-treated mouse hippocampus. Taken together, we provide evidence that these glucocorticoid-induced epigenetic alterations have a broader validity in non-neuronal cells and that they may involve the DNA methylation machinery.

1. Introduction

Glucocorticoids (GCs) may play a significant role in the etiology of several neuropsychiatric illnesses. A model for evaluating the role of GCs in mood disorders is Cushing's syndrome (CS), due to an endogenous increase in cortisol secretion, or secondary to iatrogenic GC treatment. Remarkably, up to 60–90% of patients with endogenous CS develop depression [1–3], and the depressive symptoms often disappear with resolution of hypercortisolemia [2,4]. In addition, non-CS patients suffering from major depressive disorder (MDD) often present with elevated levels of plasma cortisol and glucocorticoid resistance [5], further implicating glucocorticoids in mood disorder biology.

Effects of glucocorticoids are mediated in part by the glucocorticoid receptor (GR) and its associated chaperone protein complex consisting of FKBP5, HSP70, and HSP90. Upon activation by GC binding, GR dissociates from the chaperone complex, homodimerizes with other GR molecules, and translocates into the nucleus by interactions with FKBP4 and members of the dynein family of motor proteins [6]. In the nucleus, the GR dimer acts as a potent activator of transcription by binding glucocorticoid response elements (GREs) and recruiting transcription factors to gene promoters [7]. Importantly, FKBP5 is one of the immediate-early target genes of GC action, and GC induction of FKBP5 provides a short

Abbreviations: *Fkbp5*, FK506 binding protein 5; DNAm, DNA methylation; *Dnmt1*, DNA methyltransferase 1; HPA-axis, hypothalamic–pituitary–adrenal axis; CS, Cushing's syndrome; GC, glucocorticoid; DEX, dexamethasone.

* Corresponding author. Address: Meyer 4-136, 600N. Wolfe Street, Baltimore, MD 21287, USA. Fax: +1 410 502 0065.
E-mail address: rlee8@jhmi.edu (R.S. Lee).

0006-291X/$ - see front matter © 2012 Elsevier Inc. All rights reserved.
http://dx.doi.org/10.1016/j.bbrc.2012.03.035

intracellular negative feedback loop, where FKBP5 reduces its own transcription by impeding further translocation of the GR complex. As a result, FKBP5 has been shown to be a strong modulator of GC-signaling *in vitro*, as levels of FKBP5 reduce GR's affinity for GCs in a dose-dependent manner [6]. This event, along with GC-induced changes in levels of GR [8,9], forms the molecular basis for glucocorticoid resistance.

An animal model of hypercortisolemia and GC resistance provides additional *in vivo* support for FKBP5 as a key mediator of GC sensitivity. GC resistance in squirrel monkeys, New World primates of the genus *Saimiri*, has been attributed to elevated levels of FKBP5, and transfection assays implicate species- and sequence-specific FKBP5 as the key modulator of GC resistance in this primate [10,11]. In humans, several single nucleotide polymorphisms (SNPs) in *FKBP5* have been associated with depression, altered HPA-axis function, and rapid response to antidepressants. MDD patients that carry these SNPs exhibit symptoms of GC resistance in that they often fail to properly suppress their endogenous cortisol levels following dexamethasone suppression test [12–14]. Specifically, SNP rs1360780 confers decreased sensitivity to GCs by causing elevated FKBP5 protein levels [12], consistent with symptoms of GC resistance often comorbid with MDD.

Recently, results from several candidate gene association studies have linked *FKBP5* to MDD, suicide, or PTSD, *only* in the context of previous stressors such as early-life trauma or child abuse events, and have begun to highlight gene–environment interactions as crucial factors for disease development [15–19]. These studies suggest that the HPA-axis may become dysregulated during early-life traumatic events and that this alteration persists through many years, even decades, to help precipitate mental illnesses later in life. These findings also suggest that long-term consequences of these early-life traumatic events may be potentiated by DNA sequence-independent, non-mutational events that chronically alter function of HPA-axis genes. To comprehend the long-term consequences of GC exposure on the HPA-axis and mood disorder biology, an epigenetic approach may be useful.

During our efforts to identify GC-induced epigenetic alterations on candidate HPA-axis genes, we made several discoveries in *Fkbp5*: (i) GC administration decreases brain and blood DNA methylation (DNAm) in the *Fkbp5* gene; (ii) DNAm alterations in *Fkbp5* are associated with behavioral deficits in an animal model of Cushing's syndrome; and (iii) there is a persistence of GC-induced DNAm change in both blood and brain for up to 4 weeks following GC withdrawal [20,21].

To address whether the observed loss of DNAm is confined to cells of lymphocytic and neuronal origins, we chose the murine AtT-20 anterior pituitary corticotroph cells [22], as these cells synthesize adrenocorticotropic hormone (ACTH), and its transcription is suppressed by GCs [23]. We also tested this cell line for GC-induced changes in mRNA levels of DNA methyltransferase *Dnmt1*, hypothesizing that GCs would decrease *Dnmt1* expression.

2. Materials and methods

2.1. Animals

Four-week-old male C57BL/6 J mice (Jackson Laboratories, Bar Harbor, ME) were housed in a temperature- and humidity-controlled room. At five weeks of age, animals were given *ad libitum* access to solutions containing corticosterone (Sigma–Aldrich, St. Louis, MO; 100 μg/ml with 1% ethanol; "CORT" group) or 1% ethanol ("VEHICLE" group) in place of their normal drinking water, and this treatment continued for four weeks. Solutions were made fresh daily. On the morning of the last day of treatment, tail blood was collected (~20 μl) and centrifuged to separate plasma. Plasma was frozen and stored at −80 °C until assayed for corticosterone by radioimmunoassay (RIA). Following four weeks of treatment, the animals were euthanized, and their brains frozen on powdered dry ice and subsequently stored at −80 °C. All procedures were approved by the Institutional Animal Care and Use Committee at Johns Hopkins University School of Medicine and were performed in accordance with guidelines established in the National Research Council's Guide for the Care and Use of Laboratory Animals.

2.2. Brain dissections

Frozen brains were sectioned using a cryostat, and ~500 μm sections were mounted on plain glass slides. 19-Gauge needles (0.686 mm inner diameter and 1.086 mm outer diameter) were used to punch out the dentate gyrus from sections containing the hippocampus (bregma −0.98 mm through −1.5 mm and bregma −1.5 mm through −2.0 mm) [24]. Dissected samples were stored at −80 °C until processed for genomic DNA and mRNA.

2.3. Radioimmunoassay (RIA)

Plasma hormone levels were determined by commercially available RIA kits for corticosterone (MP Biomedicals, Costa Mesa, CA), according to manufacturer's instructions as previously described [25]. All samples were run in duplicate and comparisons were made within assay with a coefficient of variance of 3.9%.

2.4. Cell line

AtT-20 cell line (Atcc.org, Manassas, VA) derived from a mouse pituitary tumor was cultured using DMEM (Invitrogen, Carlsbad, CA) supplemented with 10% fetal bovine serum (Hyclone, Logan, UT) under standard conditions (5% CO_2, 37 °C). Cells were trypsinized and replated in six-well plates before treatment with dexamethasone (DEX; Sigma). Control samples were treated with an equal volume of EtOH as those treated with 1 μM DEX. Respective media were changed daily. Cells were split on the third day of treatment to maintain them in log phase of growth. After 5 days of treatment, cells were harvested for genomic DNA, and mRNA.

2.5. Gene expression

Messenger RNA from hippocampus and AtT-20 cell line was obtained using the RNeasy Lipid Tissue Mini (Qiagen, Valencia, CA). QuantiTect Reverse Transcription Kit (Qiagen) was used to generate cDNA for quantitative real-time PCR. Negative reverse transcriptase samples were used to ensure the absence of contaminating DNA. All reactions were carried out in triplicate using 1X Taqman master mix (Applied Biosystems, Foster City, CA), 1X Taqman probes for each gene [*Fkbp5*, *Dnmt1*, and *Actb* (ß-actin)], and 30 ng of cDNA in a total volume of 20 μl. Real-time reactions were performed on an Applied Biosystems 7900HT fast real-time PCR system with standard PCR conditions (50 °C for 2 min; 95 °C for 10 min; and 60 °C for 1 min for 40 cycles). To determine relative expression values, the −ΔΔCt method (Applied Biosystems) was used, where triplicate threshold cycle (Ct) values for each sample were averaged and subtracted from those derived from the housekeeping gene *Actb*. The Ct difference for a calibrator sample was subtracted from those of the test samples, and the resulting −ΔΔCt values were raised to a power of two to determine normalized relative expression.

2.6. DNA extraction and bisulfite conversion

Genomic DNA (gDNA) from mouse brain tissues and cell line was isolated with the Masterpure DNA Purification Kit, according

to manufacturer's instructions (Epicentre Biotechnologies, Madison, WI). Concentration of the gDNA was determined using a NanoDrop 1000 Spectrophotometer (Thermo Scientific, Rockford, IL), and 500 ng of the DNA was used for bisulfite conversion according to manufacturer's protocol (EZ DNA Methylation Gold Kit; Zymo Research, Irvine, CA).

2.7. Bisulfite PCR and pyrosequencing

We measured DNAm by pyrosequencing of the PCR products, which measures methylation variation at >90% precision [26]. Two sets of primers (outside: Forward 5′-GAAAAGTTTTTGAGAA TTAAGTTTAT-3′ and Reverse 5′-ATAACAAAACACCAAAAACCTCTA-3′; and nested: Forward 5′-TTGTTGTGGGTATGTATTGATGTT-3′ and Reverse 5′-CTCTCTCAACAATATAACTATAAA-3′) were designed to ultimately amplify a 206 bp intron 1 region of mouse *Fkbp5*. Another set of primers (outside: Forward 5′-GATGATTAG TTTTTTTTAGTAGTGATGT-3′ and Reverse 5′-CTTATTATTCTCTTAC-TACCCTAA-3′; and nested: Forward 5′-TAGTTTTTGGGGAAGAGTG TAGAGTTAT-3′ and Reverse 5′-ATTTTAAAAAACACAAAACACCCT-ATT-3′) were designed to amplify a 307 bp intron 5 region of mouse *Fkbp5*. 25 ng of bisulfite treated DNA was used for each PCR reaction. An additional nested PCR was performed with 2 μL of the outside PCR reaction and one biotinylated primer (other primer being unmodified). Amplification for both PCR steps consisted of 40 cycles (94 °C for 1 min, 53 °C for 30 s, 72 °C for 1 min). PCR products were confirmed on agarose gels. Pyro Gold reagents were used to prepare samples for pyrosequencing according to manufacturer's instructions (Qiagen). Percentage of methylation at each CpG as determined by pyrosequencing was compared between DNA from CORT- and VEHICLE-treated brain tissues, or DEX- and VEHICLE-treated cell line samples.

2.8. Statistical analysis

DNAm and relative gene expression measurements were analyzed by *t*-tests to compare CORT-treated and VEHICLE-treated groups (Microsoft Excel). A p-value <0.05 was considered statistically significant.

3. Results

3.1. Glucocorticoid-induced changes in Fkbp5 gene expression and DNA methylation in cell lines

We first attempted to establish whether the previously observed glucocorticoid-induced changes in gene expression and DNAm in brain and lymphocyte could also be observed in the AtT-20 cell line. Several concentrations of DEX (0, 10, 50, 100, 500, and 1000 nM) were used to treat the AtT-20 cells for five days. We observed a steady dose-dependent increase in relative *Fkbp5* mRNA expression (Fig. 1A). The highest expression occurred at 500 nM concentration of DEX, with a 257% ($p = 0.004$) increase over controls, suggesting that 500 nM may have saturated the glucocorticoid-signaling system. We then assessed the gDNA for any changes in DNAm in the two *Fkbp5* intronic regions previously characterized as glucocorticoid response elements (GREs, Supplementary Fig. S1) [27]. Using bisulfite pyrosequencing, we found subtle but significant dose-dependent decreases in DNAm at all four CpGs flanking the intron 5 GRE (Fig. 1B). The largest reduction was found at the second CpG position at 500 nM DEX, where we observed a 17.3% decrease in DNAm ($p = 0.002$). No further reduction was observed at 1000 nM DEX concentration (15.8%, $p = 0.01$), further supporting our speculation that GR-signaling has become saturated at 500 nM. In contrast, we failed to observe any significant differences between control and treated cells at any of the doses of DEX when we assessed for DNAm in the intron 1 GRE (Fig. 1C).

3.2. Corticosterone-induced changes in hippocampal Fkbp5 intronic DNA methylation

We have previously observed corticosterone-induced loss of *Fkbp5* DNA methylation in the whole hippocampus and hypothalamus. This time, we asked whether the epigenetic activity that we have also observed in AtT-20 cells would be enriched in the dentate gyrus, a region of the hippocampus that has been implicated in stress–response, neurogenesis, and antidepressant response [28–30]. Further, we were interested in whether focusing on a specific sub-region would allow us to observe glucocorticoid-induced DNAm differences in the intron 1 GRE. Mice were either treated with 1% EtOH vehicle-solution ("VEHICLE"; $N = 12$) or 100 μg/mL of corticosterone in their drinking water ("CORT"; $N = 12$) for 4 weeks. At the end of the treatment period, plasma corticosterone levels were 454.7 ± 78.3 ng/mL in corticosterone-treated animals and 22.9 ± 6.0 ng/mL in the vehicle-treated animals. We performed bisulfite pyrosequencing following gDNA extraction from the hippocampal punches. At intron 5, we observed a significant 14.0% decrease in DNAm ($p = 4.5 \times 10^{-6}$) at CpG position 4, and more subtle but still significant DNAm differences at CpG-1 (5.7%, $p = 0.03$), CpG-2 (2.9%, $p = 0.001$), and CpG-3 (7.6%, $p = 9.3 \times 10^{-5}$) (Fig. 2A). As in the AtT-20 cell line, we did not observe any significant differences in DNAm between VEHICLE-treated and CORT-treated mice at the intron 1 GRE, which suggested site-specific methylation changes both *in vitro* and *in vivo* (Fig. 2B).

3.3. Decrease in Dnmt1 expression in the AtT-20 cell line and mouse hippocampus

Given the crucial role played by DNA methyltransferase enzymes in maintaining status quo of DNAm in the cells, we asked whether the observed loss of DNAm could be explained by glucocorticoid-induced suppression of *Dnmt1* expression. We observed a dose-dependent decrease in *Dnmt1* expression with a maximum of 36.7% decrease ($p = 0.0002$) at 500 nM DEX concentration in AtT-20 cells. Interestingly, we observed no further decrease at the 1000 nM concentration, further supporting our previous observation with *Fkbp5* expression that GR-signaling may have become saturated at 500 nM DEX concentration (Fig. 3A). We also assessed for *Dnmt1* expression changes in the hippocampal tissue of mice treated with corticosterone. We found a 14.1% decrease in *Dnmt1* expression ($p = 0.02$), suggesting a similar effect of glucocorticoids in the brain as in the cell line (Fig. 3B).

4. Discussion

In this study, we explored two aspects of *FKBP5*'s role in mediating the stress–response, namely its glucocorticoid-induced DNAm loss in non-neuronal cells that participate in the HPA-axis system and a potential epigenetic mechanism that may underlie the observed loss in DNAm. We found GC-dependent transactivation and loss of DNAm of *Fkbp5* in the AtT-20 pituitary cell line that mirrored what were previously observed in other cells [20,21], suggesting a common mechanism of action. Our findings demonstrate that GC-induced loss of DNAm can be generalized to include such tissues and cells involved in the HPA-axis system.

Next, we examined whether focusing on a stress-relevant hippocampal region such as the dentate gyrus would allow us to observe a larger magnitude of epigenetic changes compared to

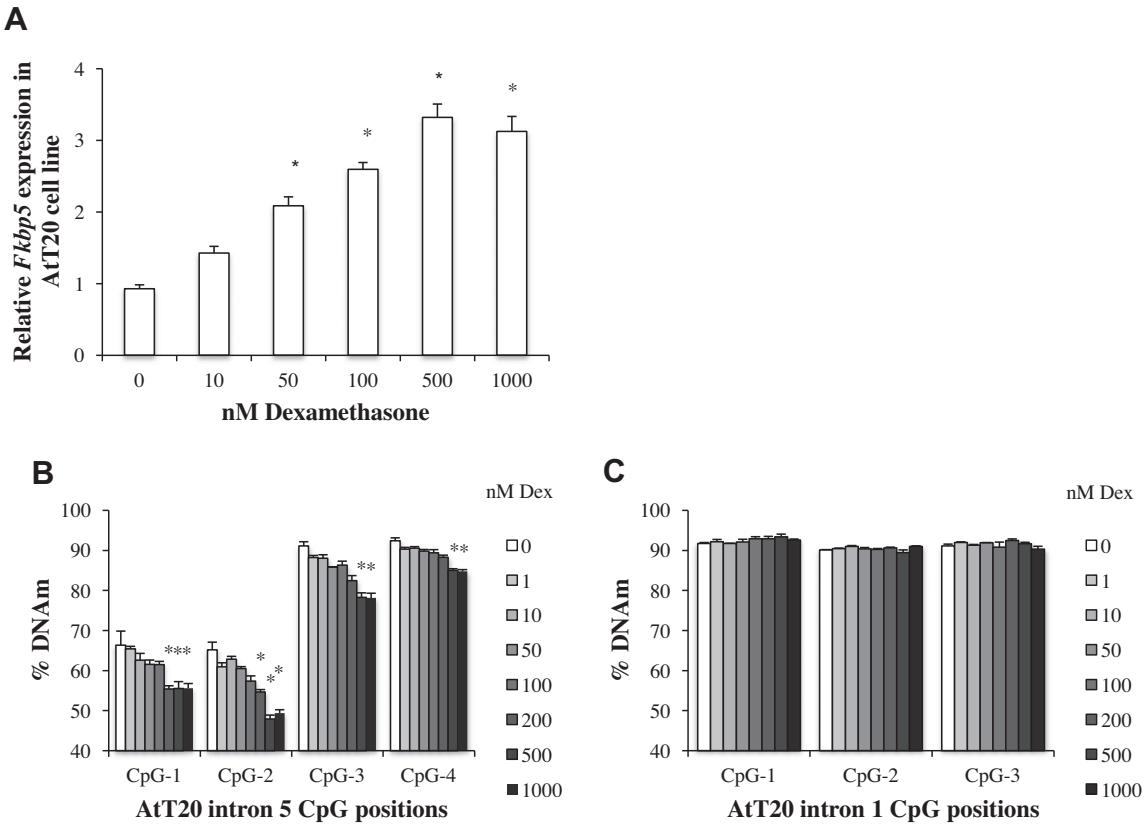

Fig. 1. Glucocorticoid-induced increase in *Fkbp5* gene expression and decrease in DNAm in the AtT-20 cell line. (A) *Fkbp5* gene expression increases with dexamethasone (DEX) treatment in a dose-dependent manner in the AtT-20 cell line. (B) Increase in gene expression was accompanied by statistically significant dose-dependent loss of DNAm of four CpG dinucleotides flanking the intron 5 GRE (glucocorticoid response element). (C) No dose-dependent change in DNAm was observed in the intron 1 GRE. Data are shown as mean ± SEM. $^{*}p \leqslant 0.05$: compared to 0 nM DEX-treated samples.

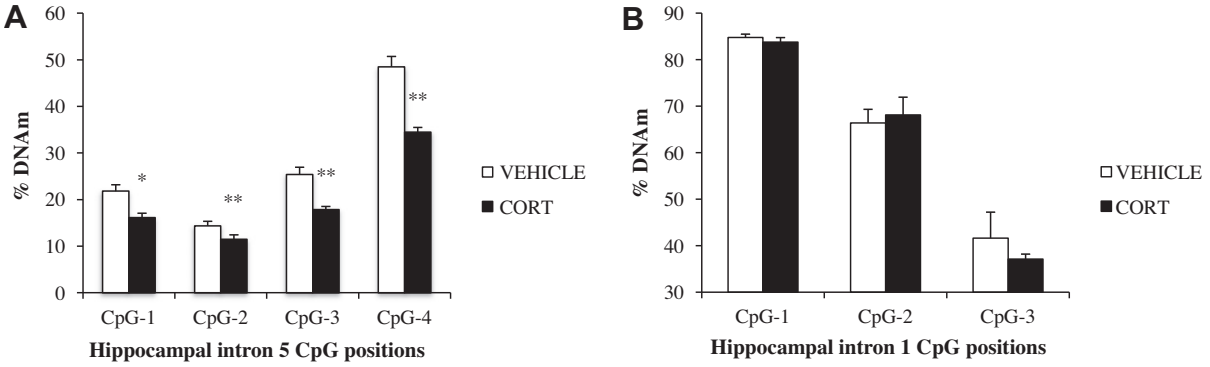

Fig. 2. Corticosterone-induced changes in hippocampal *Fkbp5* intronic DNAm (A) Loss of DNAm was found in the intron 5 GRE in the hippocampal tissue of mice treated with corticosterone ("CORT"; $N = 12$), compared to vehicle-solution treated controls ("VEHICLE"; $N = 12$). (B) No differences were observed in the intron 1 GRE. Data are shown as mean ± SEM. $^{**}p \leqslant 0.001$, $^{*}p \leqslant 0.05$.

bulk hippocampal tissues. In three of the four intron 5 CpGs tested, we observed a greater decrease in DNAm in this region compared to bulk hippocampal tissue. This phenomenon may be due to a larger ratio of granule neurons vs. glial cells that populate this region of the hippocampus, as we also observed greater corticosterone-induced DNAm changes in a homogenous neuronal cell line [20]. Recently, fluorescence activated cell sorting (FACS) was employed by Iwamoto et al. [31] to demonstrate that DNAm patterns from neurons were distinct from those of non-neurons and bulk tissues. In our experiments, we found that selective dissection of hippocampal tissue that enriched for granule neurons of the dentate gyrus preferentially represented the DNAm change that we initially observed in the AtT-20 cells. Since this DNAm change is shared by both granule neurons of the hippocampus and the pituitary cell line, additional experiments are needed to identify the common mechanism that governs this activity.

In an effort to identify one of the potential modulators of GC-dependent loss of DNAm, we assayed both the cell line and the dentate gyrus for expression levels of *Dnmt1*. We found that GCs caused a dose-dependent decrease in *Dnmt1*, providing a potential mechanism for the observed loss of DNAm. There is emerging evidence that active demethylation of 5-methylcytosines (5-mC) involves the formation of an intermediate 5-hydroxymethylcytosine (5-hmC), followed by a base-excision repair process that exchanges the 5-hmC with cytosine [32,33]. On the other hand, there's also evidence that nuclear hormone receptors employ a different mechanism of demethylation, particularly one involving methyl-CpG binding domain 4 protein MBD4, and DNA

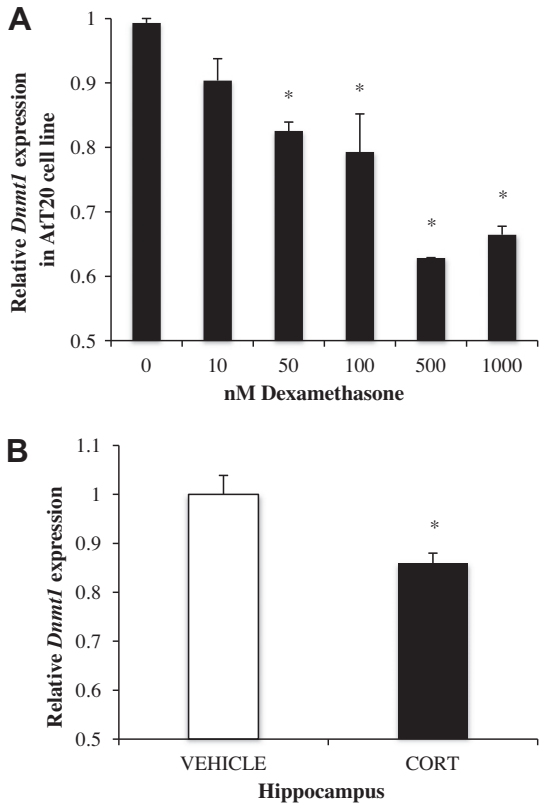

Fig. 3. Glucocorticoid-induced decrease in *Dnmt1* gene expression in the AtT-20 cell line and mouse hippocampus. (A) *Dnmt1* gene expression decreased with DEX treatment in a dose-dependent manner in the AtT-20 cell line. $^{*}p \leqslant 0.05$: compared to 0 nM DEX-treated samples. (B) Statistically significant decrease was also observed in the hippocampal tissue of mice treated with corticosterone ("CORT"; $N = 12$). Data are shown as mean ± SEM. $^{*}p < 0.05$.

methyltransferases DNMT1 and DNMT3B [34]. Since *Dnmt3b* is a *de novo* methyltransferase, and therefore unlikely to play a role in regions that are already methylated, we focused on the maintenance methyltransferase *Dnmt1* that methylates newly synthesized daughter strands following DNA replication. Given that cell lines and the dentate gyrus are capable of active cell proliferation [28,29], we propose a passive demethylation process that is mediated by reduction in *Dnmt1* expression coupled with cell replication that results in a failure to methylate the newly synthesized strand. It remains to be determined whether reduction in *Dnmt1* levels translates to global reduction of DNAm, and whether restoring its levels can rescue the loss of DNAm. Further, site-specific loss of DNAm in the intron 5 GRE, but not in the intron 1 GRE, suggests an interaction between the *GR* and *DNMT1* that may include mutually exclusive occupancy of the intron 5 GRE. Carefully designed chromatin immunoprecipitation (ChIP) experiments are necessary to confirm this relationship.

In this study, we have broadened the validity of GC-induced DNAm loss to include pituitary cells and have identified a potential epigenetic mediator of the stress response. A clearer understanding of GC target tissues and mechanism of gene function alterations are essential for the development of better therapeutic strategies for treatment of mood disorders and stress exposure.

Acknowledgments

This study was funded by NIH grants AA10158 (GSW), HD055030 (KLKT), and T32MH015330 (RSL), the Kenneth Lattman Foundation (GSW), a NARSAD Young Investigator Award (RSL), and the Dalio Family for Mood Disorders Research (RSL).

Appendix A. Supplementary data

Supplementary data associated with this article can be found, in the online version, at http://dx.doi.org/10.1016/j.bbrc.2012.03.035.

References

[1] S.I. Cohen, Cushing's syndrome: a psychiatric study of 29 patients, Br. J. Psychiatry 136 (1980) 120–124.
[2] L.D. Dorn, E.S. Burgess, T.C. Friedman, et al., The longitudinal course of psychopathology in Cushing's syndrome after correction of hypercortisolism, J. Clin. Endocrinol. Metab. 82 (1997) 912–919.
[3] J. Flitsch, S. Spitzner, D.K. Ludecke, Emotional disorders in patients with different types of pituitary adenomas and factors affecting the diagnostic process, Exp. Clin. Endocrinol. Diabetes 108 (2000) 480–485.
[4] M.N. Starkman, D.E. Schteingart, M.A. Schork, Cushing's syndrome after treatment: changes in cortisol ACTH levels and amelioration of the depressive syndrome, Psychiatry Res. 19 (1986) 177–188.
[5] R.T. Rubin, J.J. Phillips, J.T. McCracken, et al., Adrenal gland volume in major depression: relationship to basal and stimulated pituitary-adrenal cortical axis function, Biol. Psychiatry 40 (1996) 89–97.
[6] G.M. Wochnik, J. Ruegg, G.A. Abel, et al., FK506-binding proteins 51 and 52 differentially regulate dynein interaction and nuclear translocation of the glucocorticoid receptor in mammalian cells, J. Biol. Chem. 280 (2005) 4609–4616.
[7] V. Paakinaho, H. Makkonen, T. Jaaskelainen, et al., Glucocorticoid receptor activates poised FKBP51 locus through long-distance interactions, Mol. Endocrinol. 24 (2010) 511–525.
[8] H.M. Chao, L.Y. Ma, B.S. McEwen, et al., Regulation of glucocorticoid receptor and mineralocorticoid receptor messenger ribonucleic acids by selective agonists in the rat hippocampus, Endocrinology 139 (1998) 1810–1814.
[9] S. Makino, M.A. Smith, P.W. Gold, Increased expression of corticotropin-releasing hormone and vasopressin messenger ribonucleic acid (mRNA) in the hypothalamic paraventricular nucleus during repeated stress: association with reduction in glucocorticoid receptor mRNA levels, Endocrinology 136 (1995) 3299–3309.
[10] J.G. Scammell, W.B. Denny, D.L. Valentine, et al., Overexpression of the FK506-binding immunophilin FKBP51 is the common cause of glucocorticoid resistance in three New World primates, Gen. Comp. Endocrinol. 124 (2001) 152–165.
[11] W.B. Denny, D.L. Valentine, P.D. Reynolds, et al., Squirrel monkey immunophilin FKBP51 is a potent inhibitor of glucocorticoid receptor binding, Endocrinology 141 (2000) 4107–4113.
[12] E.B. Binder, D. Salyakina, P. Lichtner, et al., Polymorphisms in FKBP5 are associated with increased recurrence of depressive episodes and rapid response to antidepressant treatment, Nat. Genet. 36 (2004) 1319–1325.
[13] S. Horstmann, S. Lucae, A. Menke, et al., Polymorphisms in GRIK4, HTR2A, and FKBP5 show interactive effects in predicting remission to antidepressant treatment, Neuropsychopharmacology 35 (2010) 727–740.
[14] A. Zobel, A. Schuhmacher, F. Jessen, et al., DNA sequence variants of the FKBP5 gene are associated with unipolar depression, Int. J. Neuropsychopharmacol. 13 (2010) 649–660.
[15] E.B. Binder, R.G. Bradley, W. Liu, et al., Association of FKBP5 polymorphisms and childhood abuse with risk of posttraumatic stress disorder symptoms in adults, JAMA 299 (2008) 1291–1305.
[16] K.C. Koenen, M. Uddin, FKBP5 polymorphisms modify the effects of childhood trauma, Neuropsychopharmacology 35 (2010) 1623–1624.
[17] A. Roy, E. Gorodetsky, Q. Yuan, et al., Interaction of FKBP5, a stress-related gene, with childhood trauma increases the risk for attempting suicide, Neuropsychopharmacology 35 (2010) 1674–1683.
[18] P. Xie, H.R. Kranzler, J. Poling, et al., Interaction of FKBP5 with childhood adversity on risk for post-traumatic stress disorder, Neuropsychopharmacology 35 (2010) 1684–1692.
[19] K. Appel, C. Schwahn, J. Mahler, et al., Moderation of adult depression by a polymorphism in the FKBP5 gene and childhood physical abuse in the general population, Neuropsychopharmacology 36 (2011) 1982–1991.
[20] R.S. Lee, K.L. Tamashiro, X. Yang, et al., Chronic corticosterone exposure increases expression and decreases deoxyribonucleic acid methylation of Fkbp5 in mice, Endocrinology 151 (2010) 4332–4343.
[21] R.S. Lee, K.L. Tamashiro, X. Yang, et al., A measure of glucocorticoid load provided by DNA methylation of Fkbp5 in mice, Psychopharmacology (Berl.) 218 (2011) 303–312.
[22] R.W. Harrison, J. Yeakley, Corticosterone binding in AtT-20 pituitary tumor cell cytosol: evidence for one class of binding site for both natural and synthetic glucocorticoids, Biochim. Biophys. Acta 583 (1979) 360–369.
[23] J. Drouin, M.A. Trifiro, R.K. Plante, et al., Glucocorticoid receptor binding to a specific DNA sequence is required for hormone-dependent repression of pro-opiomelanocortin gene transcription, Mol. Cell. Biol. 9 (1989) 5305–5314.
[24] G. Paxinos, K.B.J. Franklin, The mouse brain in stereotaxic coordinates, second ed., Academic Press, San Diego, 2001.
[25] X. Yang, S. Wang, K.C. Rice, et al., Restraint stress and ethanol consumption in two mouse strains, Alcohol Clin. Exp. Res. 32 (2008) 840–852.

[26] S. Colella, L. Shen, K.A. Baggerly, et al., Sensitive and quantitative universal pyrosequencing methylation analysis of CpG sites, Biotechniques 35 (2003) 146–150.
[27] J.A. Magee, L.W. Chang, G.D. Stormo, et al., Direct, androgen receptor-mediated regulation of the FKBP5 gene via a distal enhancer element, Endocrinology 147 (2006) 590–598.
[28] H. van Praag, A.F. Schinder, B.R. Christie, et al., Functional neurogenesis in the adult hippocampus, Nature 415 (2002) 1030–1034.
[29] L. Santarelli, M. Saxe, C. Gross, et al., Requirement of hippocampal neurogenesis for the behavioral effects of antidepressants, Science 301 (2003) 805–809.
[30] J.S. Snyder, A. Soumier, M. Brewer, et al., Adult hippocampal neurogenesis buffers stress responses and depressive behaviour, Nature 476 (2011) 458–461.
[31] K. Iwamoto, M. Bundo, J. Ueda, et al., Neurons show distinctive DNA methylation profile and higher interindividual variations compared with non-neurons, Genome Res. 21 (2011) 688–696.
[32] K. Williams, J. Christensen, M.T. Pedersen, et al., TET1 and hydroxymethylcytosine in transcription and DNA methylation fidelity, Nature 473 (2011) 343–348.
[33] J.U. Guo, Y. Su, C. Zhong, et al., Hydroxylation of 5-methylcytosine by TET1 promotes active DNA demethylation in the adult brain, Cell 145 (2011) 423–434.
[34] M.S. Kim, T. Kondo, I. Takada, et al., DNA demethylation in hormone-induced transcriptional derepression, Nature 461 (2009) 1007–1012.

Biochemical and Biophysical Research Communications 420 (2012) 576–581

Contents lists available at SciVerse ScienceDirect

Biochemical and Biophysical Research Communications

journal homepage: www.elsevier.com/locate/ybbrc

Octaphlorethol A, a novel phenolic compound isolated from a brown alga, *Ishige foliacea*, increases glucose transporter 4-mediated glucose uptake in skeletal muscle cells

Seung-Hong Lee [a], Sung-Myung Kang [a], Seok-Chun Ko [a], Dae-Ho Lee [b], You-Jin Jeon [a,c,*]

[a] Department of Marine Life Science, Jeju National University, Jeju 690-756, Republic of Korea
[b] Department of Medicine, Jeju National University, Jeju 690-756, Republic of Korea
[c] Marine and Environmental Research Institute, Jeju National University, Jeju 695-814, Republic of Korea

ARTICLE INFO

Article history:
Received 6 March 2012
Available online 15 March 2012

Keywords:
Octaphlorethol A
Skeletal muscle cells
Glucose uptake
Glut4
Akt
AMPK

ABSTRACT

Skeletal muscle is the major site of glucose disposal. Promoting glucose uptake into this tissue may attenuate the insulin resistance that precedes type 2 diabetes. However, the anti-diabetic effect of marine algae on glucose uptake and metabolism in skeletal muscle remains poorly understood. Here, we report the glucose uptake effects of octaphlorethol A (OPA), a novel phenolic compound isolated from *Ishige foliacea*, on skeletal muscle cells. OPA increased glucose uptake in differentiated L6 rat myoblast cells in a dose-dependent manner relative to the control. In addition, we found that OPA increased glucose transporter 4 (Glut4) translocation to the plasma membrane. Furthermore, we also demonstrated these OPA effects essentially depended on the protein kinase B (Akt) and AMP-activated protein kinase (AMPK) activation. In summary, PI3-K/Akt and AMPK activation were involved in mediating the effects of OPA on glucose transport activation and insulin sensitivity. OPA can be further developed as a potential anti-diabetic therapy.

1. Introduction

Skeletal muscle is identified as the major tissue of glucose metabolism, accounting for nearly 75% of the entire body's insulin-stimulated glucose uptake [1]. Insulin-stimulated glucose uptake in skeletal muscle is critical for reducing blood glucose levels. In skeletal muscle, glucose uptake by glucose transporter 4 (Glut4) can be activated by at least two major mechanisms. The first is an insulin signaling pathway through phosphatidylinositol-3 kinase (PI3-K) and protein kinase B (Akt) activity. Activation of PI3-K and Akt promotes Glut4 translocation from an intracellular pool to the plasma membrane [2,3]. The other mechanism involves the heterotrimeric metabolite-sensing protein kinase, AMP-activated protein kinase (AMPK). AMPK plays a major role in energy homeostasis in ATP-depleting metabolic states such as ischemia, hypoxia, heart shock, and oxidative stress [4,5]. Once activated under such conditions, it accelerates the ATP-generating catabolic pathway involving glucose uptake and fatty acid oxidation through the direct regulation of key metabolic enzymes [6]. Skeletal muscle AMPK is activated by exercise and numerous compounds, including metformin [7] and thiazolidinediones [8], resulting in increased glucose uptake. The discovery of novel compounds that stimulate glucose uptake could provide new options for the treatment of insulin resistance and type 2 diabetes.

Interest in alternative therapies and therapeutic natural products for type 2 diabetes, particularly those derived from herbs is growing [9–11]. Marine algae yield an abundance of bioactive compounds with great pharmaceutical, nutritive, and biomedical potential. In particular, the brown algae contain a variety of biological compounds, including pigments, fucoidans, and phlorotannins [12]. Several studies have focused on the isolation of such compounds, and highlighted a variety of their biological activities, such as anti-oxidant, anti-tumor, anti-hypertensive, and anti-diabetic properties. However, the anti-diabetic effect of marine algae on glucose uptake and metabolism in skeletal muscle remains poorly understood.

Ishige foliacea (Phylum Phaeophyta, Class Isogeneratae, Order Ectocarpales, Family Ishigeaceae) is found throughout the temperate coastal zone of the Korean peninsula, generally forming highly persistent populations in clear waters [13]. It is abundant along the coast of Korea's Jeju Island, and is considered an edible brown alga; however, relatively few biological studies have been conducted it. Therefore, the present study focused on the isolation of a new anti-diabetic compound, octaphlorethol A (OPA) a type of phlorotannin, from *I. foliacea*. We examined whether OPA could stimulate glucose uptake in cultured L6 myotubes, and investigated the mechanism underlying this process.

* Corresponding author at: Department of Marine Life Science, Jeju National University, Jeju 690-756, Republic of Korea. Fax: +82 64 756 3493.
E-mail address: youjinj@jejunu.ac.kr (Y.-J. Jeon).

0006-291X/$ - see front matter © 2012 Elsevier Inc. All rights reserved.
http://dx.doi.org/10.1016/j.bbrc.2012.03.036

2. Materials and methods

2.1. Chemicals and reagents

Dulbecco's modified Eagle's medium (DMEM), wortmannin, and compound C were purchased from Sigma (St. Louis, MO, USA). Antibodies against insulin receptor substrate-1 (IRS-1), AMP-activated protein kinase (AMPK), phospho-AMPK (Thr 172), protein kinase B (Akt), phospho-Akt (Ser 473), and glucose transporter 4 (Glut4) were obtained from Cell Signaling Technology (Bedford, MA, USA). Phospho-IRS-1 (Tyr 612), and secondary IgG horseradish peroxidase-linked antibodies were from Santa Cruz Biotechnology (Santa Cruz, CA, USA). All other chemicals and reagents were of analytical grade.

2.2. Plant material

The brown alga *I. foliacea*, was collected along the coast of Jeju Island, Korea. The sample was washed three times with tap water to remove the salt, sand and epiphytes attached to its surface, then carefully rinsed with fresh water and maintained in a medical refrigerator at −20 °C. Thereafter, the frozen sample was lyophilized and homogenized with a grinder prior to extraction. A voucher specimen has been deposited in the author's laboratory, and Prof. Ki-Wan Lee at Jeju National University, Korea, performed taxonomic identification of *I. foliacea*.

2.3. Extraction and isolation

Dried *I. foliacea* powder was extracted three times with 80% methanol and filtered. The filtrate was evaporated at 40 °C to obtain the methanol extract, which was suspended in distilled water and partitioned with ethyl acetate. The ethyl acetate fraction was subjected to silica gel and Sephadex-LH 20 column chromatography. The active compound was purified by high-performance liquid chromatography, and the structure of the active compound (Fig. 1A) was identified the ^{1}H and ^{13}C NMR data, as well as the 2D NMR (HMBC) data.

2.3.1. Octaphlorethol A

^{1}H and ^{13}C DEPT and ESI-MS data revealed that the molecular formula was $C_{48}H_{34}O_{24}$ at *m/z* 992.19 $[M-2H]^{2-}$; the degree of unsaturation was 32 from 8 aromatic rings. The ^{1}H spectrum revealed two types of typical proton signals, representing aromatic and phenol protons. According to their coupling constants, all aromatic protons were designated as *meta* aromatic protons at 5.57 (1H, d, *J* = 2.8 Hz, H-4), 5.58 (1H, d, *J* = 2.8 Hz, H-6), 5.59 (1H, d, *J* = 2.8 Hz, H-9), 5.59 (1H, d, *J* = 2.8 Hz, H-11), 5.68 (1H, d, *J* = 1.8 Hz, H-15), 5.68 (1H, d, *J* = 1.8 Hz, H-17), 5.71 (1H, d, *J* = 1.8 Hz, H-21), 5.72 (1H, d, *J* = 1.8 Hz, H-23), 5.85 (1H, d, *J* = 1.6 Hz, H-26), 5.84 (1H, d, *J* = 1.8 Hz, H-30), 5.94 (1H, d, *J* = 1.8 Hz, H-32), 5.94 (1H, d, *J* = 1.8 Hz, H-36), 6.15 (1H, d, *J* = 1.8 Hz, H-38), 6.15 (1H, d, *J* = 1.8 Hz, H-42), 6.16 (1H, d, *J* = 1.6 Hz, H-44), 6.01 (1H, d, *J* = 1.6 Hz, H-46), and 6.16 (1H, d, *J* = 1.6 Hz, H-48), respectively. The other proton signals were characterized as phenol protons based on their chemical shifts at the lower filed, depicted as 9.02 (s, OH-1,3), 9.04 (s, OH-5,27,29,33,35), 8.98 (s, OH-8,12), 8.93 (s, OH-14, 18), 8.92 (s, OH-20,24), 9.06 (s, OH-39,41), and 9.07 (s, OH-45,47). The ^{13}C spectrum characterized the 48 carbon atoms as aromatic carbons, including 24 sp^2 quaternary carbon atoms at 153.0 (s, C-1), 153.0 (s, C-3), 156.1 (s, C-5), 152.9 (s, C-8), 151.1 (s, C-10), 152.9 (s, C-12), 151.1 (s, C-14), 154.5 (s, C-16), 151.1 (s, C-18), 151.1 (s, C-20), 151.1 (s, C-24), 154.1 (s, C-25), 154.1 (s, C-22), 151.1 (s, C-27), 151.1 (s, C-29), 154.0 (s, C-31), 150.8 (s, C-33), 150.8 (s, C-35), 156.2 (s, C-37), 152.7 (s, C-39), 152.7 (s, C-41), 161.0 (s, C-43), 158.6 (s, C-45), 161.0 (s, C-47); eight unsubstituted aromatic

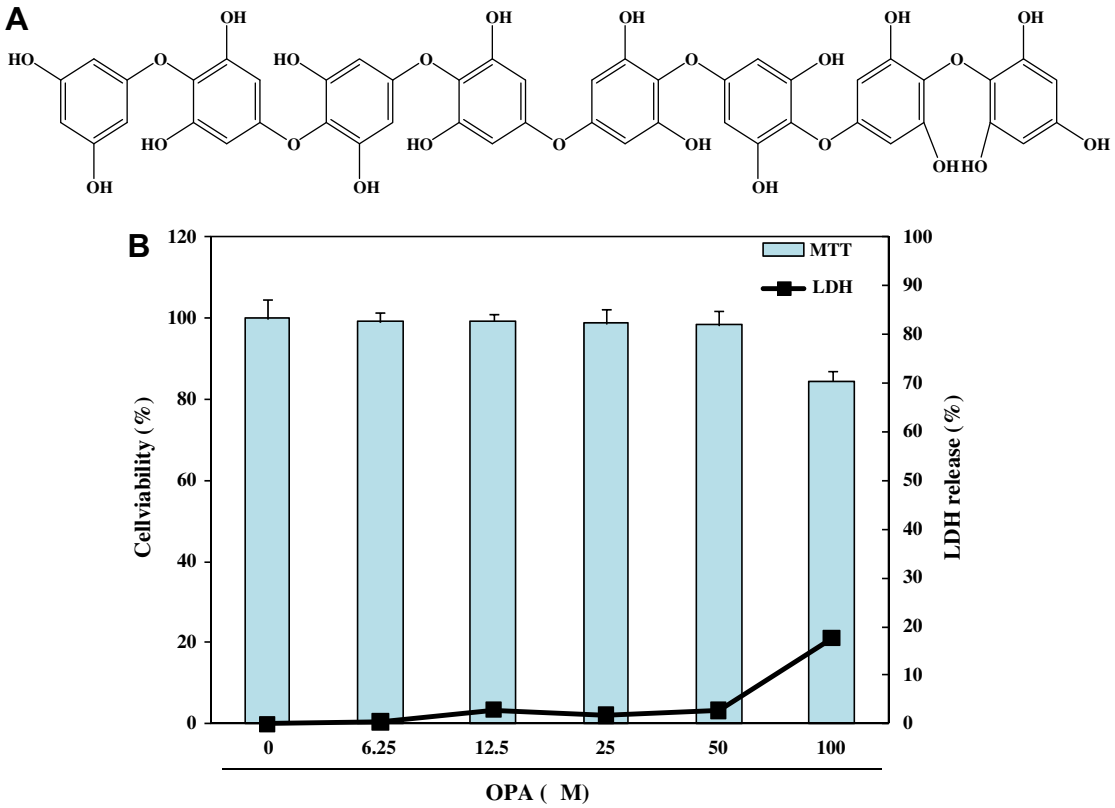

Fig. 1. (A) Chemical structure of octaphlorethol A (OPA) isolated from *Ishige foliacea* and (B) effect of OPA on cytotoxicity in differentiated L6 cells. Each value is expressed as the mean ± standard error of triplicate experiments.

carbons at 122.0 (s, C-2), 122.0 (s, C-7), 122.0 (s, C-9), 122.0 (s, C-13), 123.4 (s, C-19), 123.4 (s, C-28), 123.5 (s, C-34), 123.5 (s, C-40); and 16 phenol hydroxyl signals at 94.9 (d, C-6), 94.9 (d, C-4), 94.7 (d, C-11), 94.7 (d, C-15), 94.7 (d, C-17), 94.7 (d, C-21), 94.7 (d, C-23), 94.7 (d, C-26), 94.7 (d, C-30), 94.1 (d, C-32), 94.2 (d, C-36), 94.1 (d, C-38), 94.1 (d, C-42), 94.7 (d, C-44), 94.0 (d, C-46), and 94.7 (d, C-47). According to the chemical shifts and coupling constants in the ^{1}H and ^{13}C NMR data, these comprehensive analyses revealed that the active compounds were mainly polyphenols. The phenol hydroxyl signals were fully assigned based on the 2D NMR (HMBC) data. The major compound was determined to be a new compound after consulting the SCI finder database. The probable structure of the compound was deduced based on these spectral data and tentatively named octaphlorethol A (OPA).

2.4. Cell culture

The rat myoblast cell line L6 was purchased from the Korean Cell Line Bank (KCLB; Seoul, Korea). Rat myoblast L6 cells were maintained in high-glucose DMEM supplemented with 10% heat-inactivated fetal bovine serum, penicillin (100 U/ml) and streptomycin (100 μg/ml). Cultures were maintained at 37 °C in a 5% CO_2 incubator. For differentiation, the cells were seeded into appropriate culture plates; after reaching sub-confluence (~80% confluence), the medium was changed to DMEM containing 2% horse serum for 7 d, with subsequent media changes made daily. All experiments were performed in differentiated L6 myotubes after 7 d.

2.5. Cytotoxicity assay

The cytotoxicity of OPA against the L6 cells was determined by colorimetric MTT and LDH assays. Cells were seeded into a 24-well plate. After 24 h, the cells were treated with various concentrations (6.25, 12.5, 25, 50, and 100 μM) of OPA. The cells were incubated for an additional 24 h at 37 °C. MTT stock solution (100 μl; 2 mg/ml in PBS) was then added to each well. After incubating for 4 h, the plate was centrifuged at 500*g* for 10 min and the supernatant was aspirated. The formazan crystals in each well were dissolved in DMSO. The amount of purple formazan was determined by measuring the absorbance at 540 nm.

LDH activity in the medium was determined using an LDH cytotoxicity detection kit (Promega, Madison, WI, USA). Briefly, 100 μl of reaction mixture was added to each well, and the reaction was incubated for 30 min at room temperature in the dark. The absorbance of each well was measured at 490 nm using a UV spectrophotometer.

2.6. Glucose uptake assay

L6 cells were seeded into a 24-well plate. After differentiation, the cells were starved in serum-free low-glucose DMEM for 12 h, and then washed with PBS and incubated with fresh serum-free low-glucose DMEM. After that, the cells were treated with either insulin (100 nM) for 1 h, or the indicated concentrations of OPA (to determine the dose–response of L6 myotubes to OPA) for the

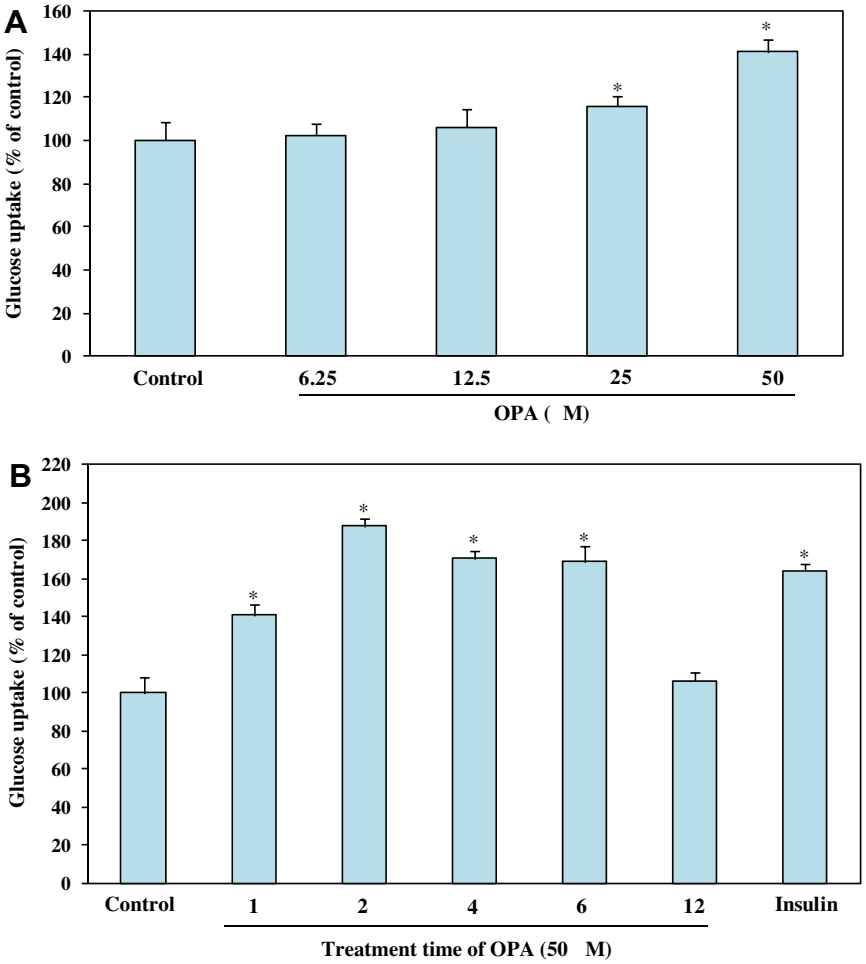

Fig. 2. OPA stimulates glucose uptake in L6 skeletal muscle cells in a dose and time-dependent manner. (A) Differentiated L6 cells were starved and then incubated for 1 h with the indicated concentrations of OPA. (B) Differentiated L6 cells were starved and then incubated for the indicated time with 50 μM OPA. Insulin (100 nM, for 1 h) was used as a positive control. Values are expressed as the mean ± standard error of triplicate experiments. $^{*}P < 0.05$, as compared with untreated control cultures.

specified times (to determine the time-response of L6 myotubes to OPA). After treatment, glucose uptake was measured by glucose concentration in the medium using a glucose assay kit (Asan Pharmaceutical Corp., Seoul, Korea). The glucose of the wells with cells was subtracted from the glucose of the blank wells to calculate the glucose uptake [14].

In some experiments, 100 nM of wortmannin (PI3-K inhibitor) and 10 μM of compound C (AMPK inhibitor) were added 30 min before the OPA treatment.

2.7. Western blot analysis

L6 myotubes were grown in 100-mm dishes and were starved in serum-free low-glucose DMEM for 12 h prior to treatment with the indicated agents. Following treatment the media were aspirated and the cells were washed twice in ice-cold PBS. The cells were lysed in NucBuster™ Protein Extraction Kit (Novagen, San Diego, CA, USA) for 10 min and then centrifuged at 13,000*g* for 5 min at 4 °C. The protein concentrations were determined with a BCA™ protein assay kit (Bio-Rad, CA, USA). The lysate, containing 50 μg of protein, was subjected to electrophoresis on 7.5% sodium dodecyl sulfate–polyacrylamide gel, and the gel was transferred onto nitrocellulose membranes. The membranes were blocked in 5% bovine serum albumin in TBST (25 mM Tris–HCl, 137 mM NaCl, 0.1% Tween 20, pH 7.4) for 2 h. The primary antibodies were used at a 1:500 dilution. The membranes were incubated with the primary antibodies at 4 °C overnight. The membranes were then washed with TBST and incubated with secondary antibodies at 1:2000 dilution. Signals were developed using an ECL western blot detection kit and exposed to X-ray films.

2.8. Plasma membrane fractionation and immunoblot analysis

L6 myotubes were treated with the indicated agents and harvested. The cell lysates were prepared with lysis buffer (RIPA, Millipore, Billerica, USA) and kept on ice for 20 min. The lysates were centrifuged at 13,000*g* for 5 min at 4 °C to obtain the supernatant. The supernatant was ultracentrifuged at 77,000*g* for 1 h at 4 °C and the resulting precipitate (the plasma membrane fraction) was collected. Immunoblot analyses of Glut4 are described in Section 2.7.

2.9. Statistical analysis

The data are presented as means ± standard error. Statistical comparisons were performed using the SPSS package for Windows (Version 14). *P*-values of less than 0.05 were considered significant.

3. Results

3.1. Cytotoxicity of OPA

The cytotoxicity of OPA in rat myoblast L6 cells was evaluated using the MTT and LDH assays at multiple OPA concentrations (6.25, 12.5, 25, 50, and 100 μM). OPA did not exhibit cytotoxicity at concentrations of up to 50 μM, as compared with control survival (Fig. 1B). Lower concentrations were therefore used in subsequent experiments.

3.2. OPA stimulates glucose uptake in a dose- and time-dependent manner

Differentiated rat myoblast L6 cells were used to determine the role of OPA in the glucose metabolism of muscle cells. As shown in Fig. 2A, OPA stimulated glucose uptake, compared with control conditions, in a dose-dependent manner (102%, 106%, 115%, and 140% at 6.25, 12.5, 25, and 50 μM of OPA, respectively). This indicates that OPA may produce metabolic effects in skeletal muscle cells. We next investigated the time dependency of the OPA effects in L6 skeletal muscle cells; the cells were maintained in serum-free media with 50 μM OPA for the indicated times. Uptake induced by OPA peaked after 2 h and then gradually decreased for the subsequent 10 h (Fig. 2B). A treatment time of 2 h resulted in a particularly significant increase in glucose uptake (187% of control uptake) relative to that induced by insulin (164% of control uptake). Subsequent OPA treatments were therefore performed using this time point and concentration.

3.3. Effect of OPA on Glut4 translocation to the plasma membrane

We examined the effect of OPA on the translocation of Glut4 to the plasma membrane, because this is an essential process for inducible glucose uptake into muscle cells. The translocation of Glut4 was observed after L6 myotubes were treated with OPA for 2 h. As seen in Fig. 3, Glut4 translocation to the plasma membrane of L6 myotubes was markedly increased by OPA treatment (1.5-fold relative to control). OPA also increased Glut4 translocation to the plasma membrane compared with the effect of insulin. These results suggest that OPA increases glucose uptake through Glut4 translocation to the plasma membrane.

3.4. OPA activates PI3-K/Akt pathway

Western blot analysis was performed to further investigate the role of the PI3-K/Akt pathway in OPA action. The phosphorylation levels of insulin receptor substrate 1 (IRS-1) and Akt were determined after L6 cells were treated with OPA for 2 h. Tyrosine phosphorylation of IRS-1 (at Tyr-612) was induced by insulin, and OPA treatment also significantly increased the level of phosphorylated IRS-1 (3.3- and 4.5-fold of control levels, respectively; Fig. 4A). In accordance with the activation of phosphorylated IRS-1, phosphorylated Akt (at Ser-473) also increased significantly after

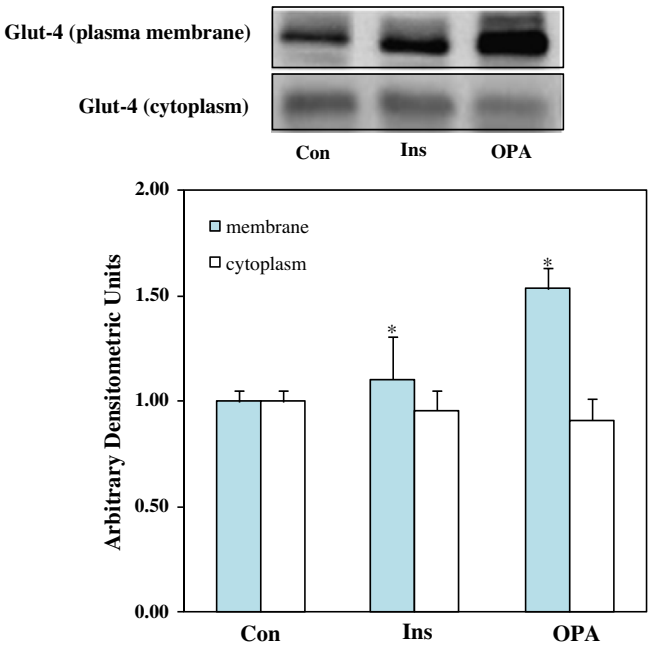

Fig. 3. Effect of OPA on Glut4 translocation to the plasma membrane. Starved differentiated L6 cells were treated with the indicated concentrations of OPA and insulin (INS) for 2 h and 10 min, respectively. Immunoblot figures are representative of 3 independent experiments, and each value is expressed as the mean ± standard error of 3 determinations. $^{*}P < 0.05$, as compared with untreated control cultures.

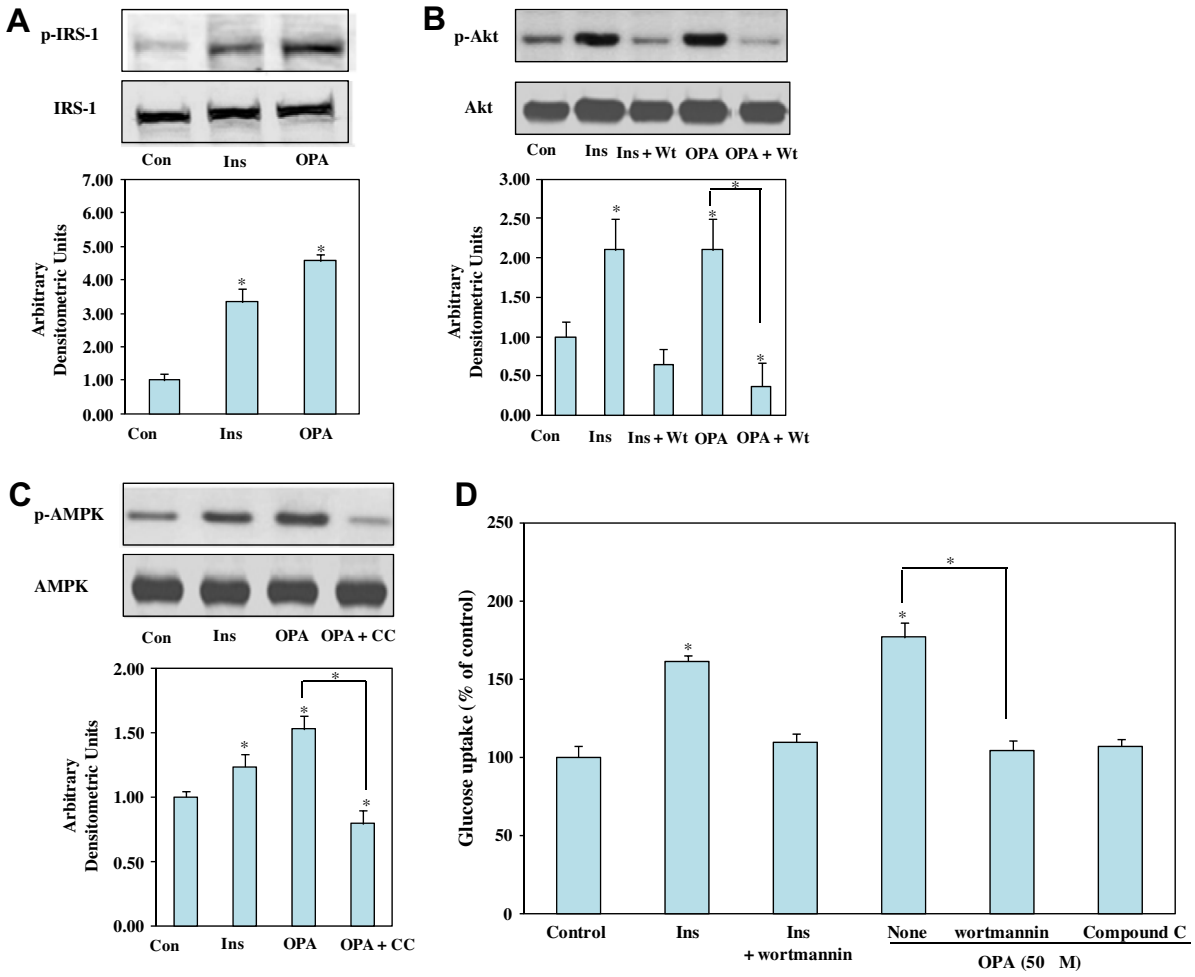

Fig. 4. Effects of OPA on (A) IRS-1, (B) Akt, and (C) AMPK phosphorylation in L6 cells and (D) OPA-induced increase of glucose uptake was reduced by wortmannin and compound C. Starved differentiated L6 cells were pretreated with or without 100 nM wortmannin or 10 μM compound C for 30 min, and then treated with 50 μM OPA or 100 nM insulin (INS) for 2 h and 10 min, respectively. Immunoblot figures are representative of 3 independent experiments, and each value is expressed as the mean ± standard error of 3 determinations. $^{*}P < 0.05$ vs. untreated control or between 2 conditions, as indicated.

OPA treatment (2.1-fold relative to control levels; Fig. 4B). As shown in Fig. 4B, pretreatment with wortmannin, a PI3-K inhibitor, inhibited the increase in the Akt phosphorylation. These results indicate that OPA strongly enhances insulin signaling, and the increase in phosphorylated IRS-1 and Akt may play an important role in this process.

3.5. OPA activates the AMPK pathway

We investigated the effects of OPA on AMPK activation in order to determine the role of OPA in the AMPK signaling pathway. We found that OPA treatment increased AMPK (Thr 172) phosphorylation in L6 cells (1.5-fold of control levels; Fig. 4C). However, the increase in AMPK phosphorylation was inhibited by pretreatment with compound C, a selective AMPK inhibitor, for 30 min prior to OPA treatment (Fig. 4C). This result, together with the above results, strongly indicates that OPA has a metabolic effect in skeletal muscle cells acting through the AMPK pathway.

3.6. OPA-induced increase in glucose uptake was dependent on both PI3-K/Akt and AMPK activation

To confirm the role of PI3-K/Akt and AMPK in OPA-stimulated glucose uptake, L6 cells were pretreated with wortmannin and compound C before OPA treatment. Wortmannin and compound C significantly decreased (by approximately 2-fold; Fig. 4D) the OPA-induced effect on glucose uptake. The results indicate that both the PI3-K/Akt and the AMPK signaling pathways are instrumental to the OPA-induced glucose uptake effect.

4. Discussion

Skeletal muscle plays a major role in the regulation of energy balance and is the primary tissue for glucose uptake and disposal [15]. It is therefore considered an important target tissue for type 2 diabetes [6]. Recent studies have investigated the effect of plant-derived compounds on glucose transport and metabolism in skeletal muscle cells for the treatment of insulin resistance and type 2 diabetes [10,11]. In the present study, we examined the effect of OPA, a novel phlorotannin compound isolated from *I. foliacea*, on glucose uptake as well as the underlying mechanism of action, in L6 muscle cells.

Results of the glucose uptake assay showed OPA-induced increases of glucose uptake in differentiated L6 cells that were both dose- and time-dependent, indicating its metabolic effects on skeletal muscle cells. In skeletal muscle, the stimulation of glucose uptake is mostly attributed to increased translocation of Glut4 to the plasma membrane, and this process becomes defective in insulin resistance [16]. In order to assess the potential activity of OPA in stimulating glucose uptake, we examined its effect on the

translocation of Glut4 to the plasma membrane. Glut4 translocation to the plasma membrane of L6 myotubes was markedly increased by treatment with OPA. These findings suggest that the effect of OPA in inducing glucose uptake occurs through the activation of Glut4 translocation to the plasma membrane.

In skeletal muscle, glucose uptake by Glut4 can be activated by at least two major mechanisms in skeletal muscle, such as the PI3-K/Akt and AMPK pathways. To determine which pathway mediates the effect of OPA on glucose uptake in L6 cells, we further examined several molecules involved in the PI3-K/Akt and AMPK signaling pathways. First, we examined the phosphorylation status of IRS-1 and Akt. Upon binding to insulin, the insulin receptor (IR) is activated, and this leads to the phosphorylation of the insulin receptor substrates IRS-1 and/or IRS-2 on tyrosine residues [17]. In particular, IRS-1 is primarily responsible for inducing glucose uptake in the skeletal muscle. IRS-1 activates PI3-K, which in turn promotes the phosphorylation of a central regulator of glucose uptake, the serine/threonine kinase Akt [18]. Our results indicated that insulin clearly increased IRS-1 and Akt phosphorylation. OPA also affected the phosphorylation status of the protein. PI3-K/Akt inhibitors such as wortmannin, inhibit insulin-stimulated Glut4 translocation from its basal compartment to the plasma membrane [19]. The stimulatory effect of OPA on Akt phosphorylation was completely abolished by wortmannin. This result suggests that the OPA effects on glucose uptake could be dependent on the PI3-K/Akt signaling pathway.

AMPK is a sensor that responds to changes in cellular energy balance [20]. Activation of AMPK leads to a stimulation of catabolism and an increase in glucose uptake in peripheral tissues through the stimulation of Glut4 translocation to the plasma membrane [21]. Therefore, AMPK is emerging as a potentially interesting target for the treatment of diabetes [22], particularly because it could play principal roles in the exercise-induced adaptation of the skeletal muscle [23], type 2 diabetes, obesity, and metabolic syndrome. Therefore, we have investigated the effect of OPA on the activation of AMPK. The present study confirmed that OPA could increase the phosphorylation of AMPK. Furthermore, the OPA-mediated activation of AMPK was abolished by compound C, highly-selective inhibitor. Our results suggest that the AMPK signaling pathway is likely responsible for the stimulation of Glut4 translocation by OPA.

Additionally, our study confirmed that wortmannin and compound C significantly decreased glucose uptake mediated by OPA. Thus, our results suggest that both Akt and AMPK may play crucial roles in OPA-stimulated glucose uptake. Recently, Kang et al. [24] reported that a polyphenol-rich extract of the brown alga *Ecklonia cava* activates both AMPK and PI3-K/Akt signaling in C_2C_{12} skeletal muscle cells. AMPK has been reported to stimulate Glut4 translocation independently of PI3-K/Akt [25]. However, it was also proposed that AMPK has a potential role in the regulation of insulin action [26], thus increasing the complexity of the interconnectivity of these two signaling pathways. Thus, the interaction between these two signaling pathways appears to be cell type-dependent and context-dependent. Further studies are required to elucidate the precise mechanisms of interconnection of these two signaling pathways.

In conclusion, we found that OPA, a new phenolic compound isolated from the brown alga, *I. foliacea*, increases Glut4-mediated glucose uptake by activating PI3-K/Akt and the AMPK signaling pathway in skeletal muscle cells, a novel target for the treatment of type 2 diabetes. Thus, we believe that OPA is a potential novel anti-diabetic compound.

Acknowledgments

This study was financially supported by the Ministry of Knowledge Economy and the Korea Institute for Advancement of Technology through the Research and Development for Regional Industry Program.

References

[1] R.A. Defronzo, E. Jacot, E. Jequier, E. Maeder, J. Wahren, J.P. Felber, The effect of insulin on the disposal of intravenous glucose. Results from indirect calorimetry and hepatic and femoral venous catheterization, Diabetes 30 (1981) 1000–1007.
[2] C.M. Taniguchi, B. Emanuelli, C.R. Kahn, Critical nodes in signaling pathways: insights into insulin action, Nat. Rev. Mol. Cell Biol. 7 (2006) 85–96.
[3] C.B. Dugani, V.K. Randhawa, A.W. Cheng, N. Patel, A. Klip, Selective regulation of the perinuclear distribution of glucose transport 4 (GLUT4) by insulin signals in muscle cells, Eur. J. Cell Biol. 87 (2008) 337–351.
[4] J. Harder, J. Bartels, E. Christophers, J.M. Schroder, Isolation and characterization of human β-defensin-3, a novel human inducible peptide antibiotic, J. Biol. Chem. 276 (2001) 5707–5713.
[5] P.A. Raj, A.R. Dentino, Current status of defensins and their role in innate and adaptive immunity, FEMS Microbiol. Lett. 206 (2002) 9–18.
[6] M.J. Sheetz, G.L. King, Molecular understanding of hyperglycemia's adverse effects for diabetic complications, JAMA 288 (2002) 2579–2588.
[7] M.H. Zou, S.S. Kirkpatrick, B.J. Davis, J.S. Nelson, W.G. Wiles 4th, U. Schlattner, D. Neumann, M. Brownlee, M.B. Freeman, M.H. Goldman, Activation of the AMP-activated protein kinase by the anti-diabetic drug metformin in vivo role of mitochondrial reactive nitrogen species, J. Biol. Chem. 279 (2004) 43940–43951.
[8] D. Konrad, A. Rudich, P.J. Bilan, N. Patel, C. Richardson, L.A. Witters, A. Klip, Troglitazone causes acute mitochondrial membrane depolarization and an AMPK-mediated increase in glucose phosphorylation in muscle cells, Diabetologia 48 (2005) 954–956.
[9] K. Zygmunt, B. Faubert, J. MacNeil, E. Tsiani, Naringenin, a citrus flavonoid, increases muscle cell glucose uptake via AMPK, Biochem. Biophys. Res. Commun. 398 (2010) 178–183.
[10] H.B. Li, Y.K. Ge, X.X. Zheng, L. Zhang, Salidroside stimulated glucose uptake in skeletal muscle cells by activating AMP-activated protein kinase, Eur. J. Pharmacol. 588 (2008) 165–169.
[11] A.K. Tamrakar, N. Jaiswal, P.P. Yadav, R. Maurya, A.K. Srivastava, Pongamol from *Pongamia pinnata* stimulates glucose uptake by increasing surface GLUT4 level in skeletal muscle cells, Mol. Cell. Endocrinol. 339 (2011) 98–104.
[12] B. Halliwell, J.M.C. Gutteridge, Antioxidants Defenses, Free Radicals in Biology and Medicine, third ed., Oxford Science Publications, Oxford, UK, 1999.
[13] I.K. Lee, J.W. Kang, A check list of marine algae in Korea, Algae 1 (1986) 311–325.
[14] J. Yin, R. Hu, M. Chen, J. Tang, F. Li, Y. Yang, J. Chen, Effects of berberine on glucose metabolism in vitro, Metabolism 51 (2002) 1439–1443.
[15] U. Ozcan, E. Yilmaz, L. Ozcan, M. Furuhashi, E. Vailancourt, R.O. Smith, C.Z. Gorgun, G.S. Hotamisligil, Chemical chaperones reduce ER stress and restore glucose homeostasis in a mouse model of type 2 diabetes, Science 313 (2006) 1137–1140.
[16] S. Huang, M.P. Czech, The GLUT4 glucose transporter, Cell. Metab. 5 (2007) 237–252.
[17] A. Virkamaki, K. Ueki, C.R. Kahn, Protein–protein interaction in insulin signaling and the molecular mechanisms of insulin resistance, J. Clin. Invest. 103 (1999) 931–943.
[18] Q. Wang, R. Somwar, P.J. Bilan, Z. Liu, J. Jin, J.R. Woodgett, A. Klip, Protein kinase B/Akt participates in GLUT4 translocation by insulin in L6 myoblasts, Mol. Cell. Biol. 19 (1999) 4008–4018.
[19] D. Malide, S.W. Cushman, Morphological effects of wortmannin on the endosomal system and GLUT4-containing compartments in rat adipose cells, J. Cell Sci. 110 (1997) 2795–2806.
[20] N. Musi, T. Hayashi, N. Fujii, M.F. Hirshman, L.A. Witters, L.J. Goodyear, AMP-activated protein kinase activity and glucose uptake in rat skeletal muscle, Am. J. Physiol. Endocrinol. Metab. 280 (2001) E677–E684.
[21] A. Krook, H. Wallberg-Henriksson, J.R. Zierath, Sending signal: molecular mechanisms regulating glucose uptake, Med. Sci. Sports Exerc. 36 (2004) 1212–1217.
[22] Y. Nakatani, H. Kaneto, D. Kawamori, K. Yoshiuchi, M. Hatazaki, T. Matsuoka, K. Ozawa, S. Ogawa, M. Hori, Y. Yamasaki, M. Matsuhisa, Involvement of endoplasmic reticulum stress in insulin resistance and diabetes, J. Biol. Chem. 280 (2005) 847–851.
[23] K. Ozawa, M. Miyazaki, M. Matsuhisa, K. Takano, Y. Nakatani, M. Hatazaki, T. Tamatani, K. Yamagata, J. Miyagawa, Y. Kitao, O. Hori, Y. Yamasaki, S. Ogawa, The endoplasmic reticulum chaperone improves insulin resistance in type 2 diabetes, Diabetes 54 (2005) 657–663.
[24] C. Kang, Y.B. Jin, H. Lee, M. Cha, E. Sohn, J. Moon, C. Park, S. Chun, E.S. Jung, J.S. Hong, S.B. Kim, J.S. Kim, E. Kim, Brown alga *Ecklonia cava* attenuates type 1 diabetes by activating AMPK and Akt signaling pathways, Food Chem. Toxicol. 48 (2010) 509–516.
[25] R.R. Russell III, R. Bergeron, G.I. Shulman, L.H. Young, Translocation of myocardial GLUT-4 and increased glucose uptake through activation of AMPK by AICAR, Am. J. Physiol. 277 (1999) H643–H649.
[26] J.S. Fisher, Potential role of the AMP-activated protein kinase in regulation of insulin action, Cellscience 28 (2006) 68–81.

Biochemical and Biophysical Research Communications 420 (2012) 582–587

Contents lists available at SciVerse ScienceDirect

Biochemical and Biophysical Research Communications

journal homepage: www.elsevier.com/locate/ybbrc

Characterization of the single transmembrane domain of human receptor activity-modifying protein 3 in adrenomedullin receptor internalization

Kenji Kuwasako [a,*], Kazuo Kitamura [b], Sayaka Nagata [b], Naomi Nozaki [a], Johji Kato [a]

[a] Frontier Science Research Center, University of Miyazaki, 5200 Kihara, Kiyotake, Miyazaki, Miyazaki 889-1692, Japan
[b] Division of Circulation and Body Fluid Regulation, Faculty of Medicine, University of Miyazaki, 5200 Kihara, Kiyotake, Miyazaki, Miyazaki 889-1692, Japan

ARTICLE INFO

Article history:
Received 6 March 2012
Available online 16 March 2012

Keywords:
Adrenomedullin
Calcitonin receptor-like receptor
Receptor activity-modifying protein
Transmembrane domain
Receptor chimeras
Receptor internalization

ABSTRACT

Two receptor activity-modifying proteins (RAMP2 and RAMP3) enable calcitonin receptor-like receptor (CLR) to function as two heterodimeric receptors (CLR/RAMP2 and CLR/RAMP3) for adrenomedullin (AM), a potent cardiovascular protective peptide. Following AM stimulation, both receptors undergo rapid internalization through a clathrin-dependent pathway, after which CLR/RAMP3, but not CLR/RAMP2, can be recycled to the cell surface for resensitization. However, human (h)RAMP3 mediates CLR internalization much less efficiently than does hRAMP2. Therefore, the molecular basis of the single transmembrane domain (TMD) and the intracellular domain of hRAMP3 during AM receptor internalization was investigated by transiently transfecting various RAMP chimeras and mutants into HEK-293 cells stably expressing hCLR. Flow cytometric analysis revealed that substituting the RAMP3 TMD with that of RAMP2 markedly enhanced AM-induced internalization of CLR. However, this replacement did not enhance the cell surface expression of CLR, [^{125}I]AM binding affinity or AM-induced cAMP response. More detailed analyses showed that substituting the Thr^{130}–Val^{131} sequence in the RAMP3 TMD with the corresponding sequence (Ile^{157}–Pro^{158}) from RAMP2 significantly enhanced AM-mediated CLR internalization. In contrast, substituting the RAMP3 target sequence with Ala^{130}–Ala^{131} did not significantly affect CLR internalization. Thus, the RAMP3 TMD participates in the negative regulation of CLR/RAMP3 internalization, and the aforementioned introduction of the Ile–Pro sequence into the RAMP3 TMD may be a strategy for promoting receptor internalization/resensitization.

1. Introduction

Adrenomedullin (AM), like calcitonin (CT) gene-related peptide (CGRP), is a potent vasodilator that belongs to the CT family of six regulatory peptides [1]. AM can also powerfully inhibit oxidative stress, inflammation, apoptosis and atherosclerosis as well as promote angiogenesis and lymphangiogenesis [2,3]. Therefore, AM is expected to become a new drug for various cardiovascular diseases such as hypertension, heart failure, myocardial infarction, arteriosclerosis obliterans and secondary lymph edema [2,3].

The discovery of two receptor activity-modifying proteins (RAMP2 and RAMP3) led to the identification of two AM receptors [4]. Both accessory proteins transport CT receptor-like receptor (CLR) to the cell surface as a 1:1 heterodimer (CLR/RAMP2 or CLR/RAMP3), whereas RAMP1 enables CLR to function as a CGRP receptor [4]. All three RAMPs each comprise approximately 160 amino acids, and all exhibit a common structure: a large extracellular domain (ECD), a single transmembrane domain (TMD) and a short cytoplasmic C-terminal tail (C-tail). Despite these similarities, the three isoforms share less than 30% sequence identity, even within their TMDs (Fig. 1B) [4,5]. Interestingly, the expression levels of the three RAMPs vary among tissues [4,5] and are differentially affected by pathological conditions [3]. Although no selective AM receptor antagonist has been found, the two AM receptors have been suggested to cooperatively or differentially protect against various cardiovascular disease states [3].

It has been long believed that each RAMP ECD mediates agonist binding to the CLR/RAMP heterodimer [6–8], which in turn mediates intracellular cAMP production and Ca^{2+} mobilization [4,9]. Very recently, crystal structural analysis revealed that human (h)RAMP1 ECD or hRAMP2 ECD forms an agonist-binding pocket together with hCLR ECD [10]. Upon binding of AM, recombinant or endogenous human CLR/RAMP2 and CLR/RAMP3 undergo rapid internalization via clathrin-coated vesicles [9,11,12], as is observed for many G protein-coupled receptors (GPCRs) [13]. Additionally, like many GPCRs [13], CLR/RAMP3 can be recycled back to the plasma membrane to promote the functional restoration of signal transduction, so-called "resensitization" [14], whereas CLR/RAMP2

Abbreviations: AM, adrenomedullin; CLR, calcitonin receptor-like receptor; eGFP, enhanced green fluorescent protein; RAMP, receptor activity-modifying protein; TMD, transmembrane domain; WT, wild type.

* Corresponding author. Fax: +81 985 85 9718.
E-mail address: kuwasako@fc.miyazaki-u.ac.jp (K. Kuwasako).

0006-291X/$ - see front matter © 2012 Elsevier Inc. All rights reserved.
http://dx.doi.org/10.1016/j.bbrc.2012.03.037

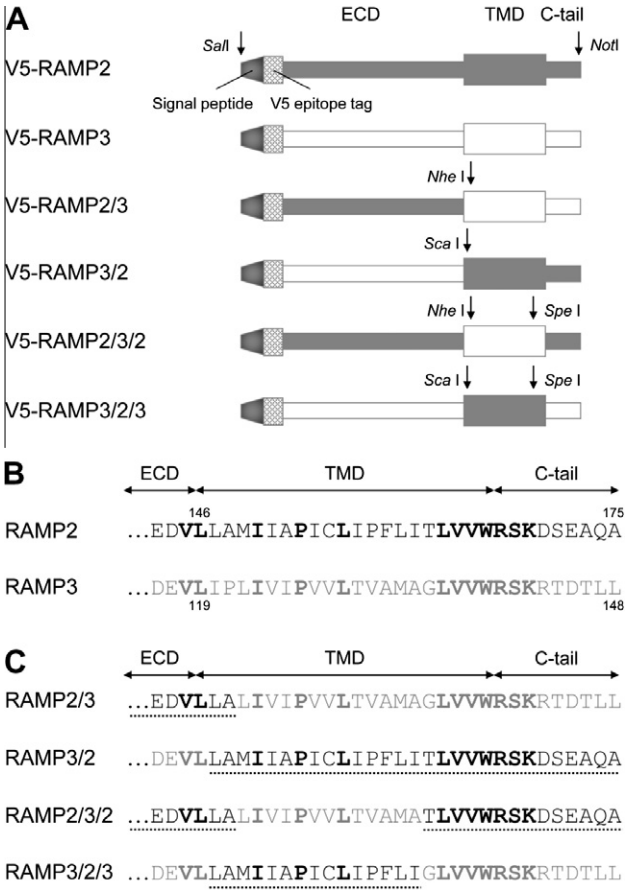

Fig. 1. (A) Schematic representation of the human RAMP domain swap constructs. *Gray boxes* are from RAMP2; *open boxes* are from RAMP3. V5 epitope-tagged RAMP chimeras were constructed using three restriction sites: *Nhe*I, *Sca*I and *Spe*I (see Section 2). ECD, extracellular domain or ectodomain; TMD, transmembrane domain; C-tail, cytoplasmic C-terminal tail. (B) Amino acid sequence alignment of the TMDs and C-tails of human RAMP2 and -3. The sequences are aligned for maximum homology; an alignment of all the sequences was presented by MacLatchie et al. [4]. The numbers indicate the amino acid positions in accordance with Sexton et al. [5]. Conserved amino acids are in bold. (C) Alignment of the four RAMP chimeras. The dotted underline indicates amino acid sequence of human RAMP2.

is targeted to lysosomes for degradation [9,11,12]. That is, receptor internalization is the primary mechanism of acute signal termination or desensitization of G protein signaling and is required for receptor resensitization [13]. It is noteworthy that hRAMP3 mediates hCLR internalization much less efficiently than does hRAMP2 [15]. Therefore, it is important to develop strategies to enhance the internalization of CLR/RAMP3 to promote receptor resensitization. However, little is known about the molecular basis of RAMP3 domains during CLR internalization. To address this issue, we constructed various chimeras targeting the TMDs and C-tails of hRAMP2 and hRAMP3 and characterized hRAMP3 domains during hCLR internalization by transiently transfecting their chimeric constructs into HEK-293 cells stably expressing hCLR.

2. Materials and methods

2.1. Materials

[^{125}I]hAM (specific activity 2 μCi/pmol) was produced in our laboratory [16]. Human AM was kindly donated by Shionogi & Co. (Osaka, Japan). Mouse anti-V5 antibody was purchased from Invitrogen (Carlsbad, CA). Fluorescein phycoerythrin (PE)-conjugated rabbit anti-mouse secondary antibody was from Exalpha Biologicals, Inc.

2.2. Expression constructs

Double V5 epitope-tagged RAMP2 and RAMP3 (V5-RAMP2 and V5-RAMP3, respectively) were prepared as described previously [17] and cloned into the mammalian expression pIRES1/Neo (Clontech, CA) using the 5′-*Sal*I and 3′-*Not*I sites (Fig. 1A), yielding pIRES-V5-RAMP2 and pIRES-V5-RAMP3.

Four hRAMP chimeras were constructed according to our previously described procedure [8,15,17,18]. To construct the TMD plus C-tail swap chimeras (V5-RAMP2/3 and V5-RAMP3/2) and TMD swap chimeras (V5-RAMP2/3/2 and V5-RAMP3/2/3) (Fig. 1A, C), *Nhe*I and *Sca*I restriction sites were introduced at the 5′ end of the TMDs of hRAMP2 and hRAMP3, respectively, and a *Spe*I site was introduced at the 3′ end of both RAMP ECDs. The individual DNA fragments were amplified by PCR using primers containing the restriction sites. The separate RAMP fragments were then ligated into the pIRES1/Neo expression vector.

Sequential substitution of the hRAMP3 TMD sequences with the corresponding sequence from hRAMP2 (Fig. 4A) to single and double amino acid substitutions (Fig. 4A) were carried out using a QuickChange kit (Stratagene, USA) according to the manufacturer's instructions, with pIRES-V5-RAMPs serving as the templates. For each mutation, two complementary 30- to 40-mer oligonucleotides (sense and antisense) were designed with the mutation in the middle.

The resulting chimeric and mutant constructs were all sequenced using an Applied Biosystems 310 Genetic Analyzer.

2.3. Cell culture and DNA transfection

HEK-293 cells stably expressing an hCLR–eGFP fusion protein [9] were maintained in Dulbecco's modified Eagle medium (DMEM) supplemented with 10% fetal bovine serum, 100 U/ml penicillin G, 100 μg/ml streptomycin, 0.25 μg/ml amphotericin B and 0.25 mg/ml G 418 at 37 °C under a humidified atmosphere of 95% air/5% CO_2. Transient transfection of the cells was accomplished using Lipofectamine™ with Plus™ reagent (Invitrogen, USA) according to the manufacturer's instructions. Briefly, the cells were seeded into 12- or 24-well plates and, upon reaching 70–80% confluence, were transiently transfected with the empty vector (pIRES1/Neo (*Mock*) or V5-tagged wild-type (WT)), pIRES-chimeric or pIRES-mutant construct; V5-RAMP2 and/or V5-RAMP3 were included in each transfection set. The DNA complex with transfection reagents was formed by incubating the cells for 4 h in OptiMEM 1 medium containing plasmid DNAs, Plus regent, and Lipofectamine reagent. All of the experiments were performed 36–48 h after transfection.

2.4. Flow cytometric analysis

Flow cytometry was used to assess the cell surface expression levels of V5-tagged receptor proteins. Following transient transfection of the indicated cDNAs for V5-RAMP WT, chimeras or mutants into CLR-eGFP-expressing HEK-293 cells in 12-well plates, the cells were washed once with ice-cold PBS and then non-enzymatically harvested with ice-cold FACS buffer [9]. After washing with the buffer, the cells were incubated for 60 min at 4 °C in the dark with anti-V5 monoclonal antibody (1:1000 dilution). Thereafter, the cells were incubated for 60 min at 4 °C in the dark with fluorescein PE-conjugated rabbit anti-mouse secondary antibody (1:400 dilution) and then washed twice with FACS buffer. The cells were then subjected to flow cytometry and analyzed as described previously [15].

2.5. Radioligand binding

To assess whole-cell radioligand binding, HEK-293 cells transfected in 24-well plates were incubated for 5 h at 4 °C with [^{125}I]AM (40 pM) in the absence (for total binding) or presence of different concentrations of unlabeled AM (1 μM) was used to define non-specific binding) in modified Krebs–Ringers–HEPES medium [9]. After washing once with ice-cold PBS, the cells were solubilized with 0.5 M NaOH, and the associated cellular radioactivity was measured in a γ-counter. Specific binding was defined as the difference between the total binding and non-specific binding.

2.6. Measurement of intracellular cAMP

cAMP assays were carried out as described previously [19]. The transfectants in 24-well plates were incubated for 15 min at 37 °C in Hanks' buffer containing 20 mM HEPES, 0.2% BSA, 0.5 mM 3-isobutyl-1-methylxanthine and the indicated concentrations of AM. The reactions were terminated by the addition of lysis buffer (GE Healthcare, Japan), after which the cAMP content was determined using a commercial enzyme immunoassay kit according to the manufacturer's instructions (GE Healthcare) for a non-acetylation protocol.

2.7. Flow cytometric analysis of receptor internalization

Following transfection of the indicated cDNA into HEK-293 cells stably expressing CLR–eGFP in 12-well plates, the cells were exposed to the selected concentrations of AM in prewarmed serum-free DMEM containing 20 mM HEPES and 0.2% BSA for the indicated periods (up to 2 h) at 37 °C. Receptor internalization was stopped by adding ice-cold PBS, after which the cells were harvested, resuspended in ice-cold FACS buffer and labeled with anti-V5 monoclonal antibody and fluorescein PE-conjugated rabbit anti-mouse secondary antibody. The cells were then subjected to flow cytometry and analyzed as described previously [15].

2.8. Data analysis and statistics

The results are expressed as the means ± SEM of at least three independent experiments. The data were analyzed using Prism 5.02 software (GraphPad Software Inc., USA). The binding and cAMP data were fitted to obtain pIC_{50} and pEC_{50} values, respectively. Differences among multiple groups were evaluated with one-way ANOVA as appropriate, where $p < 0.05$ were considered significant. Post hoc testing was via Dunnett's test for comparison with control.

3. Results

3.1. Characterization of RAMP TMD plus C-tail swap chimeras RAMP2/3 and RAMP3/2

In the present study, HEK-293 cells stably expressing CLR–eGFP were used because they are well suited for the evaluation of CLR/RAMP internalization when transiently transfected with RAMPs

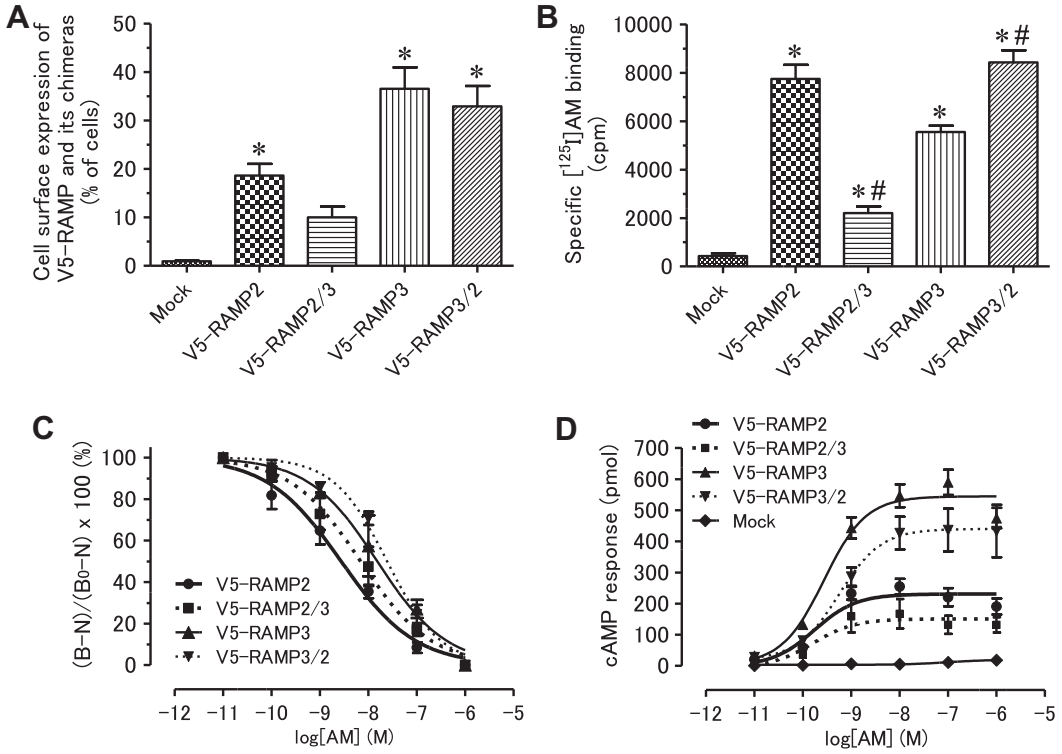

Fig. 2. Characterization of the RAMP TMD plus C-tail swap chimeras (RAMP2/3 and RAMP3/2). (A) Flow cytometric analysis of the cell surface expression of WT or chimeric V5-RAMP following transient transfection into HEK-293 cells stably expressing CLR–eGFP. Transfected cells were incubated with an anti-V5 monoclonal antibody and then with a fluorescein PE-conjugated rabbit anti-mouse secondary antibody. Samples incubated with only secondary antibody served as a control. Cell surface expression of each construct was estimated by flow cytometry. Data are shown as the means ± SEM of four separate experiments; $^{*}p < 0.05$ vs. control (*Mock*). (B) Specific binding of [^{125}I]AM. Transfected cells were incubated for 5 h at 4 °C with [^{125}I]AM (40 pM) in the presence or absence of 10^{-6} M unlabeled AM. Data are shown as the means ± SEM of three separate experiments; $^{*}p < 0.05$ vs. Mock; $^{\#}p < 0.05$ vs. corresponding V5-RAMP. (C) Displacement of [^{125}I]AM. Cells were transfected and incubated with [^{125}I]AM as in B. Data were normalized to the maximum specific binding in each experiment. Data are shown as the means ± SEM of three separate experiments. B, [^{125}I]AM bound; B_0, total binding in the absence of competing unlabeled AM; N, nonspecific binding (measured in the presence of 10^{-6} M AM). (D) AM-induced cAMP production. Cells expressing CLR–eGFP with WT or chimeric V5-RAMP were simultaneously exposed to the indicated concentrations of AM for 15 min at 37 °C and then lysed. The resultant lysates were analyzed for cAMP content. Data are shown as the means ± SEM of three separate experiments.

[15]. In addition, fusing eGFP to the C-terminus of CLR had no effect on the signaling and trafficking of the two AM receptors (CLR/RAMP2 and CLR/RAMP3) [9].

Fig. 2A shows the cell surface expression of WT and chimeric V5-RAMPs when transiently transfected into the CLR–eGFP-expressing HEK-293 cells. V5-RAMP2 significantly appeared at the cell surface of ~20% of cells, whereas the surface expression of V-RAMP2/3 was only half that of V5-RAMP2. In contrast, V5-RAMP3 was markedly increased at the cell surface; the surface expression was about twofold higher than that observed with V5-RAMP2. V5-RAMP3/2 appeared at the cell surface at levels that were nearly the same as those observed with V5-RAMP3.

The binding of [^{125}I]AM to cells co-expressing CLR–eGFP with WT or chimeric V5-RAMP is shown in Fig. 2B. When transfected with empty vector (*Mock*), the CLR–eGFP-expressing cells showed very low levels of specific [^{125}I]AM binding. In contrast, marked increases in specific [^{125}I]AM binding were observed with V5-RAMP2, V5-RAMP3 and V5-RAMP3/2 in the stable transfectants of CLR–eGFP. Notably, the specific binding of [^{125}I]AM to CLR–eGFP/V5-RAMP2/3 was markedly lower than that to CLR–eGFP/V5-RAMP2, while the specific binding of [^{125}I]AM to CLR–eGFP/V5-RAMP3/2 was significantly higher than that to CLR–eGFP/V5-RAMP3.

Fig. 2C shows a set of [^{125}]AM competition curves for receptors composed of CLR–eGFP and WT or chimeric V5-RAMP. The pIC_{50} value derived from the curve obtained when V5-RAMP2/3 was co-expressed with CLR–eGFP was 2.5-fold lower than that for V5-RAMP2 (8.16 and 8.56, respectively). In contrast, the pIC_{50} value obtained with co-expression of V5-RAMP3/2 was comparable to that observed with V5-RAMP3 (7.61 and 7.81, respectively).

For these WT and chimeric V5-RAMPs, their capacity to mediate AM-induced cAMP production was further characterized in the stable transfectants of CLR–eGFP (Fig. 2D). AM elicited little or no cAMP production in HEK-293 cells expressing CLR–eGFP alone, indicating that the stable transfectants used in this study endogenously expressed no functional RAMP proteins. In contrast, AM (pEC_{50} = 9.76) elicited marked increases in cAMP in cells co-transfected with CLR–eGFP and V5-RAMP2. This potency was equal to that of CLR–eGFP/RAMP2/3 (pEC_{50} = 9.79). However, there was no significant difference in their maximal responses (E_{max} values) (231.1 pmol for CLR–eGFP/V5-RAMP2; 150.9 pmol for CLR–eGFP/V5-RAMP2/3). On the other hand, in cells co-transfected with V5-RAMP3, AM also elicited significant increases in cAMP (pEC_{50} = 9.56). Very similar pEC_{50} values (pEC_{50} = 9.25) were obtained in cells co-transfected with V5-RAMP3/2. The E_{max} values for CLR–eGFP/V5-RAMP3/2 (440.1 pmol) were significantly lower than those for CLR–eGFP/V5-RAMP3 (544.8 pmol).

Fig. 3A shows the receptor internalization induced by 1 μM AM. Exposure to AM reduced the cell surface levels of CLR–eGFP/V5-RAMP2 and CLR–eGFP/V5-RAMP3 by approximately 80% and 40%, respectively, within 30 min, and this reduction persisted for at least 2 h. Most notably, the internalization of CLR–eGFP/V5-RAMP3/2 was markedly enhanced when compared to that of V5-RAMP3. In contrast, V5-RAMP2/3 promoted CLR–eGFP internalization by only 10%.

As shown in Fig. 3B, AM elicited the dose-dependent internalization of CLR–eGFP/V5-RAMP2, which was approximately 40% more efficient than V5-RAMP3-mediated internalization at high AM concentrations (100 nM and 1 μM). On the other hand, the V5-RAMP3/2-mediated internalization of CLR–eGFP was more

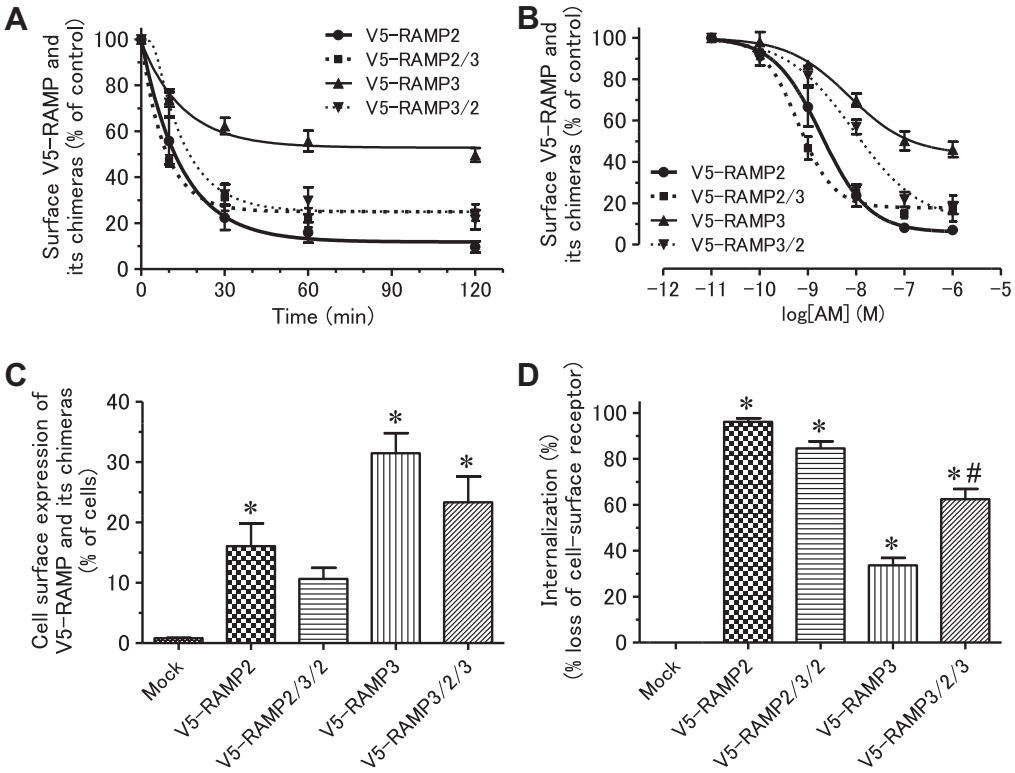

Fig. 3. Flow cytometric analysis of internalization of CLR coupled with RAMP TMD plus C-tail swap chimeras (RAMP2/3 and -3/2) or RAMP TMD swap chimeras (RAMP2/3/2 and -3/2/3). (A) Time-dependent loss of surface CLR/RAMP heterodimers. HEK-293 cells stably expressing CLR–eGFP were transiently transfected with V5-RAMP2, -3, -2/3 or -3/2 and then treated with 10^{-6} M AM for the indicated times. Cell surface expression of each construct was estimated by flow cytometry. Data are shown as the means ± SEM of three separate experiments. (B) Dose-dependent internalization of CLR with the indicated RAMPs. Each transfectant was incubated for 60 min with the indicated concentration of AM. Cell surface expression of each construct was estimated by flow cytometry. Data are shown as the means ± SEM of three separate independent experiments. (C, D) Cell surface expression (C) and internalization (D) of CLR and RAMP TMD chimeras. The indicated RAMP constructs were transiently transfected into CLR–eGFP-expressing HEK-293 cells. Surface expression of each construct was estimated by flow cytometry before and after exposing cells to 10^{-6} M AM for 60 min. Data are shown as the means ± SEM of three separate experiments; $^{*}p < 0.05$ vs. Mock; $^{\#}p < 0.05$ vs. corresponding V5-RAMP.

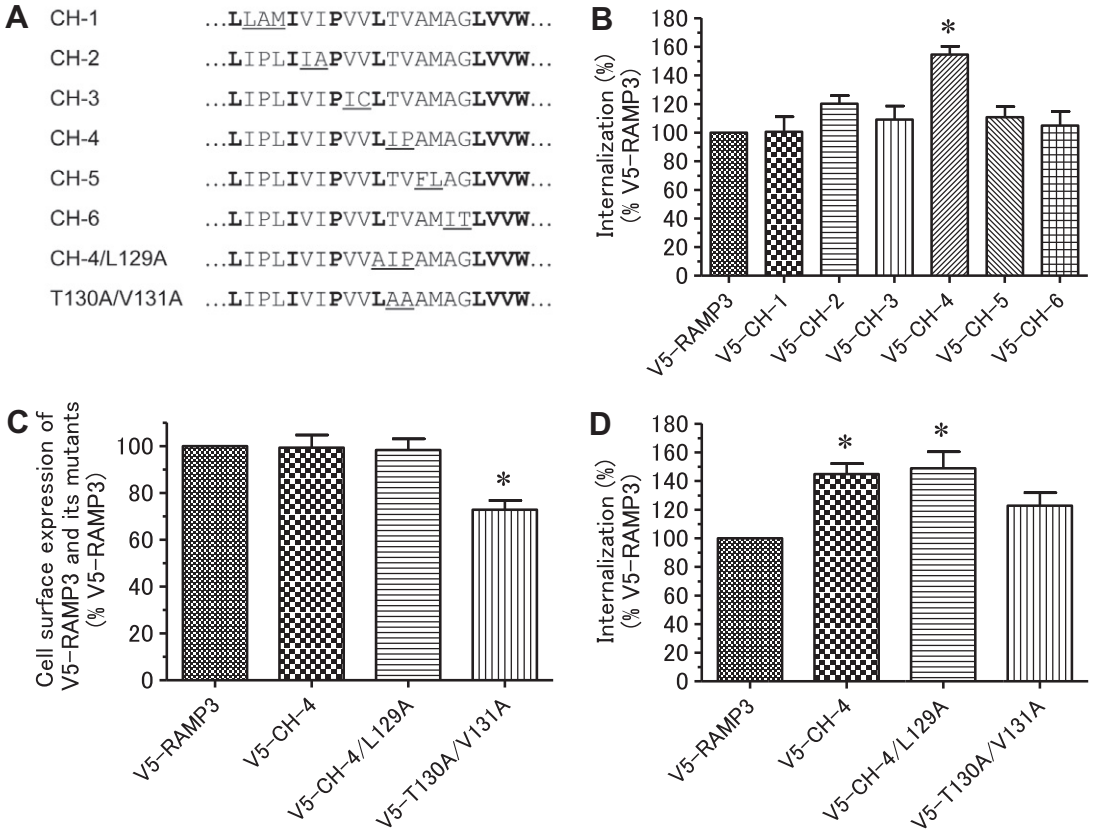

Fig. 4. Characterization of the RAMP3 TMD in AM receptor internalization. (A) Amino acid sequence alignment of the TMDs of the indicated chimeras and point mutants. The six chimeras (CH-1 to CH-6) were constructed by progressively substituting 2–3 amino acid residues of the RAMP3 TMD with the corresponding residues from the RAMP2 TMD. In addition, the two mutants CH-4/L129A and T130A/V131A were constructed. Bold letters indicate the conserved amino acid residues between RAMP2 and -3 TMDs. (B) Internalization of the indicated RAMP chimeras, along with CLR. Each of the indicated RAMP constructs was transiently transfected into CLR–eGFP transfectants, after which their surface expression was estimated by flow cytometry carried out before and after exposing cells to 10^{-6} M AM for 60 min. Data are shown as the means ± SEM of four separate independent experiments; $^{*}p < 0.05$ vs. V5–RAMP3. (C, D) Cell surface expression (C) and internalization (D) of the indicated RAMP3 mutants, along with CLR. Experimental procedures were carried out as in Fig. 3C and D. Data are shown as the means SEM of three separate experiments; $^{*}p < 0.05$ vs. V5-RAMP3.

efficient than that of V5-RAMP3, especially at high AM concentrations. However, such a marked enhancement of internalization was not observed in CLR–eGFP/V5-RAMP2/3.

3.2. Characterization of the RAMP TMD swap chimeras RAMP2/3/2 and RAMP3/2/3

To further examine the involvement of the RAMP2 TMD in AM receptor internalization, we constructed the V5-RAMP TMD swap chimeras shown in Fig. 1A, C (V5-RAMP2/3/2 and V5-RAMP3/2/3, respectively). As shown in Fig. 3C, the cell surface expression of these two RAMP TMD swap chimeras was lower than that of the corresponding V5-RAMP, which was very similar to that observed with the two RAMP TMD plus C-tail swap chimeras (Fig. 2A). Likewise, the effects of V5-RAMP2/3/2 and V5-RAMP3/2/3 on AM receptor internalization (Fig. 3D) were very similar to those of V5-RAMP2/3 and V5-RAMP3/2, respectively.

3.3. Progressive substitutions of RAMP3 TMD with RAMP2 TMD

To more precisely determine which residues within the RAMP2 TMD mediate the enhancement of CLR internalization, we used mutagenesis to construct six chimeras (CH-1 to CH-6) in which the RAMP3 TMD was progressively substituted with the corresponding residues from the RAMP2 TMD (Fig. 4A). The cell surface expression levels of these chimeras were all comparable to those observed with V5-RAMP3 (data not shown). Additionally, AM affinity (pIC_{50}) and potency (pEC_{50}) for CLR–eGFP and six chimeras did not differ from that for CLR–eGFP/V5-RAMP3 (data not shown). Nevertheless, the maximum CLR–eGFP internalization mediated by V5-CH-4 (or V5-RAMP3-T130I/V131P), in which Thr^{130}–Val^{131} in the RAMP3 TMD was substituted with the corresponding sequence (Ile^{157}–Pro^{158}) from RAMP2 TMD, was ~1.6-fold greater than that mediated by V5-RAMP3 (Fig. 4B). In contrast, co-expression of the remaining five chimeras had little effect on the internalization of CLR–eGFP (Fig. 4B).

3.4. Effect of point mutations in the RAMP3 TMD on receptor internalization

A CH-4 plus L129A mutant (CH-4/L129A) was also constructed because L129 of hRAMP3 is shared by hRAMP2, but not hRAMP1, which is seen for other animal species [20]. In addition, we introduced double point mutations into the Thr^{130}–Val^{131} sequence in the RAMP3 TMD (Fig. 4A). The L129A mutation did not change the cell surface expression and internalization of CLR–eGFP/V5-CH-4) (Fig. 4C, D). On the other hand, the RAMP3-T130A/V131A mutation significantly reduced the surface expression of CLR–eGFP but did not significantly affect CLR–eGFP internalization.

4. Discussion

In the present study, flow cytometric analysis showed that V5-RAMP3 mediates AM-induced CLR–eGFP internalization much less

efficiently than V5-RAMP2. However, simultaneous substitution of the RAMP3 TMD and C-tail with the corresponding RAMP2 domains enabled CLR–eGFP/V5-RAMP3/2 to be internalized to almost the same degree as CLR–eGFP/V5-RAMP2. This enhancement of internalization occurred with no significant alteration in the targeting of CLR–eGFP to the cell surface. In addition, no increase in AM affinity or potency was found in cells expressing CLR–eGFP/V5-RAMP3/2. Similarly, cells co-expressing CLR–eGFP with the V5-RAMP3/2/3 chimera in which the RAMP3 TMD was substituted with that from RAMP2 also exhibited significantly enhanced CLR–eGFP internalization with no change in AM signaling. Furthermore, previous studies showed that exchanging the C-tails between RAMP2 and RAMP3 did not affect CLR internalization [15]. Taken together, these findings suggested that within the structure of RAMP2, it is the RAMP TMD that primarily governs CLR internalization. To our knowledge, this report is the first showing that the TMD of accessory proteins, like RAMPs, coupled with GPCRs are critically involved in GPCR internalization and that the RAMP3 TMD participates in the negative regulation of AM receptor internalization.

More detailed analysis revealed that substituting Thr^{130}–Val^{131} within the RAMP3 TMD with the corresponding residues from RAMP2 (Ile^{157}–Pro^{158}) significantly enhanced AM-induced CLR–eGFP internalization. In this case, the surface expression and AM potency (not shown) of CLR–eGFP were very similar to those observed with the RAMP TMD swap chimera V5-RAMP3/2/3. In contrast, substituting the target sequence of RAMP3 with Ala–Ala had little effect on CLR–eGFP internalization, indicating that the presence of the Thr–Val sequence does not affect CLR/RAMP3 internalization. However, no marked reductions in internalization of V5-RAMP2/3 and V5-RAMP2/3/2 were observed in this study. Moreover, their surface expression levels were much lower than those observed with V5-RAMP3/2 and V5-RAMP3/2/3. In such cases, flow cytometric analysis is insufficient for accurately assessing receptor internalization [15]. Collectively, the transfer of the Ile–Pro sequence of RAMP2 to the corresponding sequence of RAMP3 contributed to a marked enhancement of CLR/RAMP3 internalization.

Internalization of GPCRs is often regulated by various proteins in the GPCR kinase family (GRK-1 to GRK-7), the β-arrestin family and others [13,21]. Upon agonist activation, GPCR C-tails are frequently phosphorylated by GRK(s), after which the phosphorylated sites associate with β-arrestin [13,21]. The receptor-β-arrestin complexes are then targeted to clathrin pits, leading to their internalization [13,21]. CLR/RAMP heterodimers are known to be internalized thorough these clathrin- and β-arrestin-dependent pathways [9,11]. Recently, GRK-2, GRK-3 and GRK-4 were shown to predominantly associate with a Ser/Thr-rich region in the C-tail of hCLR, significantly enhancing AM receptor internalization [22]. It is also well known that enhancing the binding of β-arrestins to some GPCR C-tails promotes bridge formation between β-arrestins and clathrin, which in turn enhances their internalization [23]. It thus seems likely that transfer of the Ile–Pro sequence of the RAMP2 TMD into the corresponding region of RAMP3 favors interaction of GRKs with the CLR C-tail, enhancing the binding of β-arrestins to the phosphorylated CLR.

In this study, we have shown that the hRAMP3 TMD is involved in the negative regulation of CLR/RAMP3 internalization and that substituting the Thr^{130}–Leu^{131}sequence of the RAMP3 TMD with the corresponding Ile–Pro sequence from the RAMP2 TMD enhances CLR/RAMP3 internalization. Furthermore, the binding of *N*-ethylmaleimide-sensitive factor to the PDZ domain (Thr–Leu–Leu) of the RAMP3 C-tail led to a slow recycling/resensitization of internalized human CLR/RAMP3 in HEK-293 cells [14]. Therefore, the aforementioned introduction of the Ile–Pro sequence into the RAMP3 TMD may be a strategy for promoting receptor resensitization.

Acknowledgments

This study was supported in part by grants-in-aid for Scientific Research from the Ministry of Education, Culture, Sports Science and Technology, Japan and by research grants from the Takeda Science Foundation.

References

[1] K. Kitamura, K. Kangawa, M. Kawamoto, et al., Adrenomedullin: a novel hypotensive peptide isolated from human pheochromocytoma, Biochem. Biophys. Res. Commun. 192 (1993) 553–560.
[2] T. Ishimitsu, H. Ono, J. Minami, et al., Pathophysiologic and therapeutic implications of adrenomedullin in cardiovascular disorders, Pharmacol. Ther. 111 (2006) 909–927.
[3] K. Kuwasako, K. Kitamura, S. Nagata, et al., Shared and separate functions of the RAMP-based adrenomedullin receptors, Peptides 32 (2011) 1540–1550.
[4] L.M. McLatchie, N.J. Fraser, M.J. Main, et al., RAMPs regulate the transport and ligand specificity of the calcitonin-receptor-like receptor, Nature 393 (1998) 333–339.
[5] P.M. Sexton, A. Albiston, M. Morfis, et al., Receptor activity modifying proteins, Cell. Signal. 13 (2001) 73–83.
[6] T. Qi, D.L. Hay, Structure-function relationships of the N-terminus of receptor activity-modifying proteins, Br. J. Pharmacol. 159 (2010) 1059–1068.
[7] K. Kuwasako, K. Kitamura, Y. Nagoshi, et al., Identification of the human receptor activity-modifying protein 1 domains responsible for agonist binding specificity, J. Biol. Chem. 278 (2003) 22623–22630.
[8] K. Kuwasako, K. Kitamura, K. Ito, et al., The seven amino acids of human RAMP2 (86) and RAMP3 (59) are critical for agonist binding to human adrenomedullin receptors, J. Biol. Chem. 276 (2001) 49459–49465.
[9] K. Kuwasako, Y. Shimekake, M. Masuda, et al., Visualization of the calcitonin receptor-like receptor and its receptor activity-modifying proteins during internalization and recycling, J. Biol. Chem. 275 (2000) 29602–29609.
[10] S. Kusano, M. Kukimoto-Niino, N. Hino, et al., Structural basis for extracellular interactions between calcitonin receptor-like receptor and receptor activity-modifying protein 2 for adrenomedullin-specific binding, Protein Science. A Publication of the Protein Society 21 (2012) 199–210.
[11] S. Hilairet, C. Belanger, J. Bertrand, et al., Agonist-promoted internalization of a ternary complex between calcitonin receptor-like receptor, receptor activity-modifying protein 1 (RAMP1), and beta-arrestin, J. Biol. Chem. 276 (2001) 42182–42190.
[12] L.L. Nikitenko, N. Blucher, S.B. Fox, et al., Adrenomedullin and CGRP interact with endogenous calcitonin-receptor-like receptor in endothelial cells and induce its desensitisation by different mechanisms, J. Cell Sci. 119 (2006) 910–922.
[13] F. Jean-Alphonse, A.C. Hanyaloglu, Regulation of GPCR signal networks via membrane trafficking, Mol. Cell. Endocrinol. 331 (2011) 205–214.
[14] J.M. Bomberger, N. Parameswaran, C.S. Hall, et al., Novel function for receptor activity-modifying proteins (RAMPs) in post-endocytic receptor trafficking, J. Biol. Chem. 280 (2005) 9297–9307.
[15] K. Kuwasako, Y.N. Cao, C.P. Chu, et al., Functions of the cytoplasmic tails of the human receptor activity-modifying protein components of calcitonin gene-related peptide and adrenomedullin receptors, J. Biol. Chem. 281 (2006) 7205–7213.
[16] K. Kitamura, Y. Ichiki, M. Tanaka, et al., Immunoreactive adrenomedullin in human plasma, FEBS Lett. 341 (1994) 288–290.
[17] K. Kuwasako, K. Kitamura, S. Nagata, et al., Flow cytometric analysis of the calcitonin receptor-like receptor domains responsible for cell-surface translocation of receptor activity-modifying proteins, Biochem. Biophys. Res. Commun. 384 (2009) 249–254.
[18] K. Kuwasako, D.L. Hay, S. Nagata, et al., The third extracellular loop of the human calcitonin receptor-like receptor is crucial for the activation of adrenomedullin signalling, Br. J. Pharmacol. (2011).
[19] K. Kuwasako, K. Kitamura, S. Nagata, et al., Structure-function analysis of helix 8 of human calcitonin receptor-like receptor within the adrenomedullin 1 receptor, Peptides 32 (2011) 144–149.
[20] D.L. Hay, D.R. Poyner, P.M. Sexton, GPCR modulation by RAMPs, Pharmacol. Ther. 109 (2006) 173–197.
[21] M.T. Drake, S.K. Shenoy, R.J. Lefkowitz, Trafficking of G protein-coupled receptors, Circ. Res. 99 (2006) 570–582.
[22] K. Kuwasako, K. Kitamura, S. Nagata, et al., Function of the cytoplasmic tail of human calcitonin receptor-like receptor in complex with receptor activity-modifying protein 2, Biochem. Biophys. Res. Commun. 392 (2010) 380–385.
[23] S.S. Ferguson, Evolving concepts in G protein-coupled receptor endocytosis: the role in receptor desensitization and signaling, Pharmacol. Rev. 53 (2001) 1–24.

Biochemical and Biophysical Research Communications 420 (2012) 588–593

Contents lists available at SciVerse ScienceDirect

Biochemical and Biophysical Research Communications

journal homepage: www.elsevier.com/locate/ybbrc

Long chain acyl CoA synthetase 1 and gelsolin are oppositely regulated in adipogenesis and lipogenesis

Rajib Mukherjee, Jong Won Yun *

Department of Biotechnology, Daegu University, Kyungsan, Kyungbuk 712-714, Republic of Korea

ARTICLE INFO

Article history:
Received 5 March 2012
Available online 16 March 2012

Keywords:
Gelsolin
Long chain acyl CoA synthetase 1
Knockdown
Lipogenesis
Obesity
3T3-L1

ABSTRACT

Our previous proteomics study revealed that long chain acyl CoA synthetase 1 (ACSL1) and gelsolin (GSN) are oppositely regulated in white adipose tissue of diet-induced obese rats. To firmly establish these proteins as mediators of adipogenic and/or lipogenic events, we efficiently knocked down the *Acsl1* and *Gsn* genes using siRNA in 3T3-L1 adipocyte cells. Expectedly, *Acsl1* knockdown stimulated expression of lipogenic genes. Interestingly, *Gsn* knockdown suppressed expression of lipogenic genes but strikingly increased that of *Tnfα* and *Il6*, which may have connections with lipolytic capacity of these genes. Conclusively, we provide clear evidence that ACSL1 and GSN are potential target proteins in the context of obesity.

1. Introduction

White adipose tissue (WAT) acts as an active endocrine organ that secretes signaling molecules termed as adipokines, which are involved in the regulation of food intake, energy homeostasis, and inflammatory conditions associated with several metabolic disorders [1–3]. Over the last decade, the 3T3-L1 mouse preadipocyte cell line has been used as an excellent *in vitro* model for the study of adiposity due to its similar characteristics to WAT upon reaching maturity [4].

Our previous proteomics study revealed that protein levels of long chain fatty acyl CoA synthetase 1 (ACSL1) are reduced in WAT of obese rats fed a high fat diet, whereas those of gelsolin (GSN) are increased, resulting in greater body weight gain [5].

ACSL1 is well documented for its role in complex fatty acid breakdown, fatty acid channeling, and transport of fatty acids to mitochondria for their oxidation [6–8]. ACSL1 also interacts with fatty acid transport protein to facilitate fatty acid uptake [9], and higher TG accumulation has been reported in heart-specific ACSL1 knockout mice [10]. In contrast, GSN is a Ca-binding actin filament protein and is reportedly linked with pathological conditions such as apoptosis and the lipid metabolic pathway [11,12]. *Gsn* knockout mice display attenuated platelet integrity, decreased wound-healing capability, and also increased incidence of lung injury [13,14]. To date, however, no evidence has linked GSN to lipogenesis.

As a follow-up to our proteomics experiment, the primary goal of this study was to investigate the lipogenic and pro-inflammatory responses in 3T3-L1 adipocyte cells. To this end, we knocked down *Acsl1* and *Gsn* and determined the effects on established lipogenic genes (*Pparγ*, *C/ebpα*, *Prkaa1*, *Acc1*, *Fasn*, *Fabp4*, and *6Pgd*) and two major pro-inflammatory genes (*Tnfα* and *Il6*).

2. Materials and methods

2.1. Cell culture and differentiation

3T3-L1 preadipocytes (ATCC, Manassas, VA, USA) were cultured in Dulbecco's Modified Eagle's Medium (DMEM, Thermo, Waltam, MA, USA) supplemented with 10% fetal bovine serum (FBS, PAA Laboratories, Pasching, Austria) and 100 μg/ml of penicillin–streptomycin (Invitrogen, Carlsbad, CA, USA) at 37 °C in a 5% CO_2 incubator. After the cells were sufficiently confluent, the medium was changed to differentiation induction medium containing 10 μg/ml of insulin (Sigma, St. Louis, MO, USA), 0.25 μM dexamethasone (Sigma) and 0.5 mM 3-isobutyl-1-methylxanthine (IBMX, Sigma) in DMEM. After 2 days, the differentiation medium was changed to DMEM supplemented with FBS and insulin, after which the cells were maintained in for 6–8 days

Abbreviations: *6Pgd*, 6 phosphogluconate dehydrogenase; *Acc1*, acyl CoA carboxylase 1; *Acsl1*, long chain acyl CoA synthetase 1; *C/ebpα*, CCAAT/ enhancer-binding protein α; *Fabp4*, fatty acid binding protein 4; *Fasn*, fatty acid synthase; *Gsn*, gelsolin; HFD, High fat diet; *Il6*, interleukin 6; *KD*, knockdown; *Pparγ*, peroxisome proliferator-activated receptor γ; *Prkaa1*, AMP-activated protein kinase alpha catalytic subunit 1; TG, triglyceride; *Tnfα*, tumor necrosis factor α; WAT, white adipose tissue.

* Corresponding author. Fax: +82 53 850 6559.
E-mail address: jwyun@daegu.ac.kr (J.W. Yun).

0006-291X/$ - see front matter © 2012 Elsevier Inc. All rights reserved.
http://dx.doi.org/10.1016/j.bbrc.2012.03.038

until maturation before further analysis. The medium was changed every 2 days.

2.2. Knockdown of Acsl1 and Gsn by siRNA

Commercially available siRNA specific for *Acsl1* and *Gsn* (a pool of three target-specific 20–25 nucleotide siRNAs designed to knockdown gene expression) from Santa Cruz Biotechnology Inc. (Santa Cruz, CA, USA) were used for gene silencing in 3T3-L1 cells. Post-confluent 3T3-L1 cells in six-well culture dishes were washed twice with transfection medium and overlaid by using a previously made mixture of siRNA and transfection reagent (Santa Cruz Biotechnology). The transfection process was continued for 5–7 h, after which differentiation medium was added. After 4–6 days, mature cells were collected for further experiments. Transfection efficiency was monitored by estimating the uptake of non-targeting fluorescein-labeled double-stranded RNA oligomers (BLOCK-iT, 150 nM per well, #2013, Invitrogen). Transcript levels of each gene were normalized to *β-actin* transcript levels. Finally, knockdown efficiency of transiently siRNA-expressing cells was determined as follows:

$$\% \text{ Knockdown} = (a - b)/b \times 100$$

a: Normalized expression levels of each gene in siRNA-transfected cells

b: Normalized expression levels of each gene in BLOCK-iT-transfected cells.

2.3. Oil Red-O staining

After knockdown of *Acsl1* or *Gsn*, cells matured for 4–6 days after induction of differentiation cells were washed with phosphate-buffered saline (PBS), fixed with 10% formalin for 1 h at room temperature, and then washed three times with deionized water. A mixture of Oil Red-O (0.6% Oil Red-O dye in isopropanol) and water at a 6:4 ratio was overlaid onto the cells for 10 min, washed three times with deionized water, and then photographed. Intracellular Oil Red-O stain was photometrically measured by dissolving the stain for 10 min in 60% isopropanol.

2.4. Quantification of triglycerides (TG)

Cells matured for 4–6 days were washed twice with PBS and harvested. Using RIPA buffer (Sigma), cell lysate was prepared and TG content was measured using a TG test kit (Asan Pharm. Co. Yeongcheon, Kyungbuk, Korea) according to the manufacturer's instructions. Absorbance was measured at 550 nm, and the TG content was normalized to the protein content by the Bradford method [15].

2.5. Quantitative real-time RT PCR

3T3-L1 cells matured for 6 days were harvested and total RNA was isolated using a total RNA isolation kit (RNA-spin, iNtRON Biotechnology, Seongnam, Gyeonggi, Korea), after which 1 μg of RNA was converted to cDNA using Maxime RT premix (iNtRON Biotechnology). Transcript levels of genes were quantitatively determined employing Power SYBR Green (Applied Biosystems, Warrington, UK) in real-time RT-PCR (Stratagene 246 mx 3000p QPCR System, Agilent Technologies, Santa Clara, CA, USA). Transcript levels of each gene were normalized to *β-actin* transcript levels. Sequences of primer sets used in this study are listed in Table 1.

2.6. Immunoblot analysis

Cell lysates were prepared by using RIPA buffer (Sigma), followed by homogenization and centrifugation at 12,000*g* for 20 min. The extract was diluted in 5× sample buffer (50 mM Tris of pH 6.8, 2% SDS, 10% glycerol, 5% β-mercaptoethanol, and 0.1% bromophenol blue) and then heated for 5 min at 95 °C before SDS–polyacrylamide gel electrophoresis (PAGE) using 8%, 10%, or 12% acrylamide gel. After electrophoresis, proteins were transferred to a polyvinylidene difluoride (PVDF, Santa Cruz Biotechnology) membrane and blocked for 1 h with TBS (Tris-buffered saline)-T buffer (10 mM Tris–HCl, 150 mM NaCl, 0.1% Tween 20 containing 5% skim milk). The membrane was rinsed with three changes of TBS-T buffer, followed by incubation for 1 h with a 1:1000 dilution of primary monoclonal antibody: anti-β-actin, anti-ACC, anti-pACC, anti-AMPK, anti-pAMPK, anti-PPARγ (Santa Cruz Biotechnology), and anti-FAS (Cell Signaling Technology, Beverly, MA, USA) in TBS-T buffer containing 1% skim milk. After three washes, the membrane was incubated for 1 h with horseradish peroxidase-conjugated anti-goat IgG or anti-rabbit IgG secondary antibody (1:1000, AB Frontier, Seoul, Korea) in TBS-T buffer containing 1% skim milk and developed using enhanced chemiluminescence (West Zol, iNtRON Biotechnology). Band intensities were quantified using ImageMaster (GE Healthcare).

Table 1
Sequences of the primers used for real-time RT-PCR.

Genes		Primer sequence (5′–3′)
Acsl1	F[a]	CAGAACATGTGGGTGTCCAG
	R[b]	CGGTGGAGATGTCACAGTTG
Gsn	F	GACTCTTTGCCTGCTCCAAC
	R	TTGCTGGATCTGTCTCGATG
Pparγ	F	GGTGAAACTCTGGAGATTC
	R	CAACCATTGGGTCAGCTCTT
C/ebpα	F	AGGTGCTGGAGTTGACCAGT
	R	CAGCCTAGAGATCCAGCGAC
Prkaa1	F	CAGGCCATAAAGTGCAGTTA
	R	AAAAGTCTGTCGGAGTGCTGA
Acc1	F	GAGAGGGGTCAAGTCCTTCC
	R	ACATCCACTTCCACACACGA
Fasn	F	CCTTAGAGGCAGTGCAGGAC
	R	TTGCTGCACTTCTTGGACAC
Fabp4	F	CACCTGGAAGACAGCTCCTC
	R	AATCCCCATTTACGCTGATG
6Pgd	F	TGAAGGGTCCTAAGGTGGTCC
	R	CCGCCATAATTGAGGGTCCAG
Tnfα	F	AGGCCTTGTGTTGTGTTTCCA
	R	TGGGGGACAGCTTCCTTCTT
Il6	F	ACAACCACGGCCTTCCCTACTT
	R	CACGATTTCCCAGAGAACATGTG
Internal control		
β-Actin	F	AGCCATGTACGTAGCCATCC
	R	CTCTCAGCTGTGGTGGTGAA

[a] F, sequence from sense strands.
[b] R, sequence from anti-sense strands.

2.7. Statistical analysis

All data expressed as the mean ± SD were compared by one-way analysis of variance (ANOVA) using the Statistical Package of Social Science (SPSS, version 14.0 K) program. Group means were considered significantly different at $p < 0.05$, as determined by the technique of protected least-significant difference (LSD) when ANOVA indicated an overall significant treatment effect ($p < 0.05$).

3. Results

3.1. Effects of knockdown of Acsl1 and Gsn on adipogenesis and lipogenesis in 3T3-L1cells

Current gene knockdown (KD) experiments were designed on the basis of our previous proteomic data on WAT, which showed that protein levels of ACSL1 decrease, whereas those of GSN

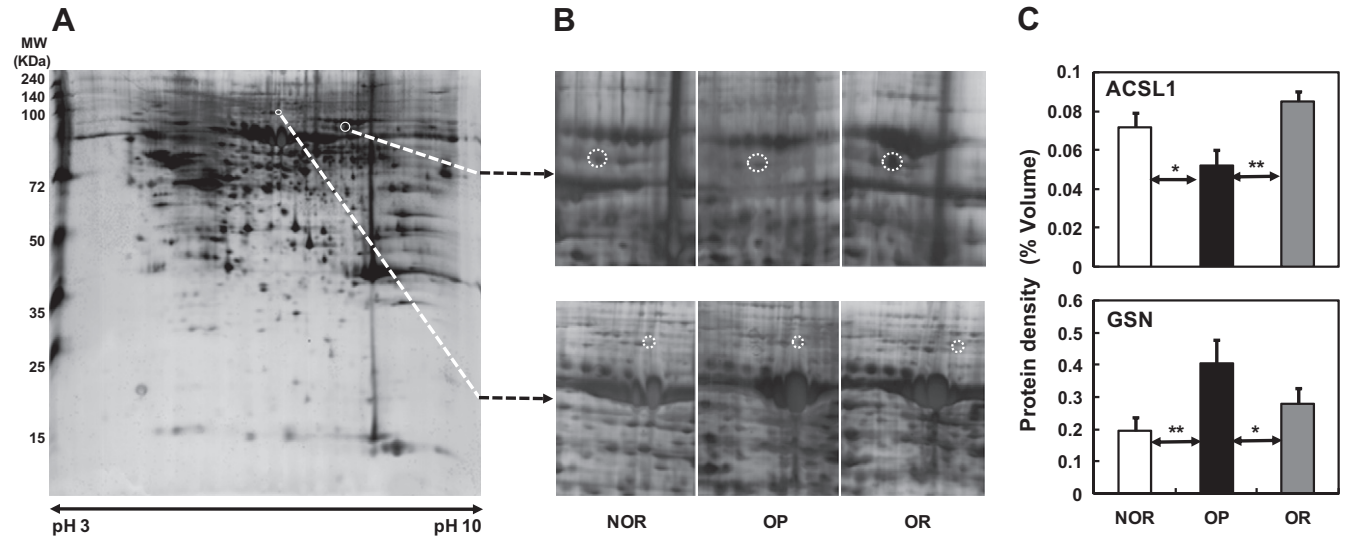

Fig. 1. Differentially expressed ACSL1 and GSN between obesity-prone (OP) and obesity-resistant (OR) rats fed a high fat diet compared to normal rats fed a standard diet (NOR). (A) A representative whole two-dimensional electrophoresis gel image of WAT of rat, (B) zoom-in-gel images of ACSL1 and GSN, (C) comparative protein density of ACSL1 and GSN. Data are exhibited as mean values ± SD of volume density (%) of the changed spot in three individual gels using WAT tissue. Statistical significance between each group was determined by ANOVA test, where p value is $^{*}p < 0.05$ and $^{**}p < 0.01$. These figures were redrawn using the data from our previous work [5].

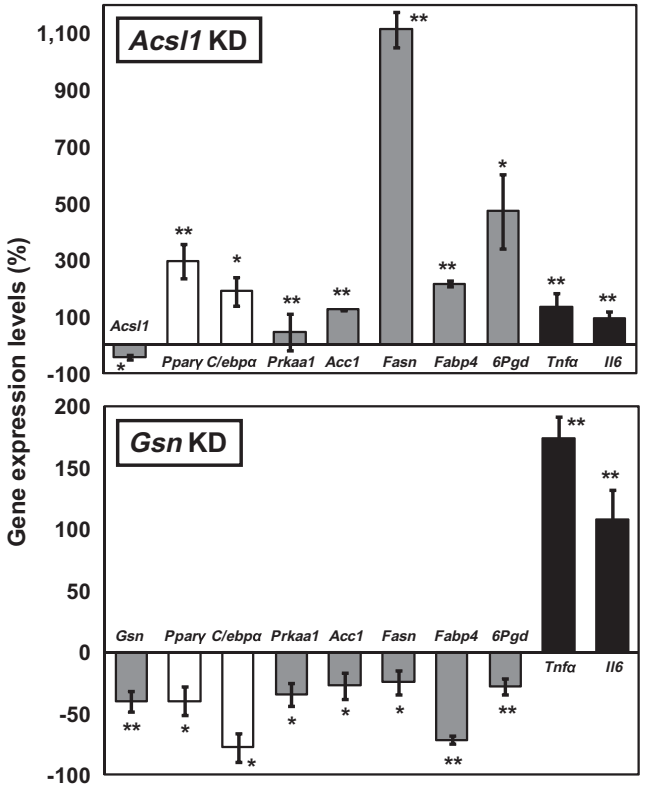

Fig. 2. Effects of *Acsl1* or *Gsn* knockdown on expression levels of adipogenic (white bars), lipogenic (gray bars), and pro-inflammatory (black) genes in 3T3-L1 cells. Transcript levels of each gene were normalized to *β-actin* transcript levels. Data are exhibited as mean values ± SD of % of differential gene expression level. Data are representative of three independent assays. Statistical significance between each group was determined by ANOVA test, where p value is $^{*}p < 0.05$ and $^{**}p < 0.01$.

increase, when rats consuming a high fat diet become obese (Fig. 1). To elucidate the roles of ACSL1 and GSN in both adipogenesis and lipogenesis, we specifically knocked down these two genes in 3T3-L1 adipocyte cells using commercially available siRNAs with no cytotoxicity on 3T3-L1 cells. We successfully knocked down these genes, resulting in reduction of gene expression by at least 50% compared to that of control cells (Fig. 2).

As the two types of 3T3-L1 KD cells showed opposite changes in TG content and since adipogenic transcription factors play profound roles in TG accumulation, we measured gene expression levels of the two adipogenic transcript factors (*Pparγ, C/ebpα*) and major lipogenic genes (*Prkaa1*, *Acc1*, *Fasn*, *Fabp4*, and *6Pgd*) in KD cells matured for 6 days. When *Acsl1* was knocked down, expression levels of adipogenic transcription factors and lipogenic genes were significantly greater compared to control cells. In particular, expression of *Fasn* in *Acsl1* KD cells was over 10-fold higher compared to control cells, suggesting that TG accumulation accelerated upon *Acsl1* KD (Fig. 2). Expectedly, two pro-inflammatory genes (*Tnfα* and *Il6*) were also overexpressed compared to control cells, reflecting their potential roles in obesity-induced inflammation. Conversely, in *Gsn* KD cells, all lipogenic genes together with adipogenic transcript factors exhibited significantly lower expression levels compared to control cells (Fig. 2). However, surprisingly, expression of *Tnfα* and *Il6* in *Gsn* KD cells was significantly greater compared to control cells, implying their differential roles in lipogenic events (Fig. 2). To firmly support these results, we next determined the contents of lipid droplets and accumulated TG in both KD cells compared to those in control cells. As shown in Fig. 3, after maintaining KD cells in differentiation and maturation medium for 6 days, the amount of visible oil droplets increased in *Acsl1* KD cells by 50–70% compared to control cells, whereas the amount decreased in *Gsn* KD cells by 40–60% (Fig. 3A and B). Accordingly, TG contents in 6-day-old mature *Acsl1* KD cells (80% increase) and *Gsn* KD cells (30% decrease) were in line with the results of oil droplet formation (Fig. 3C).

3.2. Effects of knockdown of Acsl1 and Gsn on regulation of adipogenic and lipogenic proteins in 3T3-L1 cells

We further confirmed the protein levels of several adipogenic and lipogenic proteins in 3T3-L1 cells by Western blot analysis before and after knockdown to test whether or not the differential expression patterns of genes ultimately confer their effects on protein levels. To this end, we measured the protein levels of

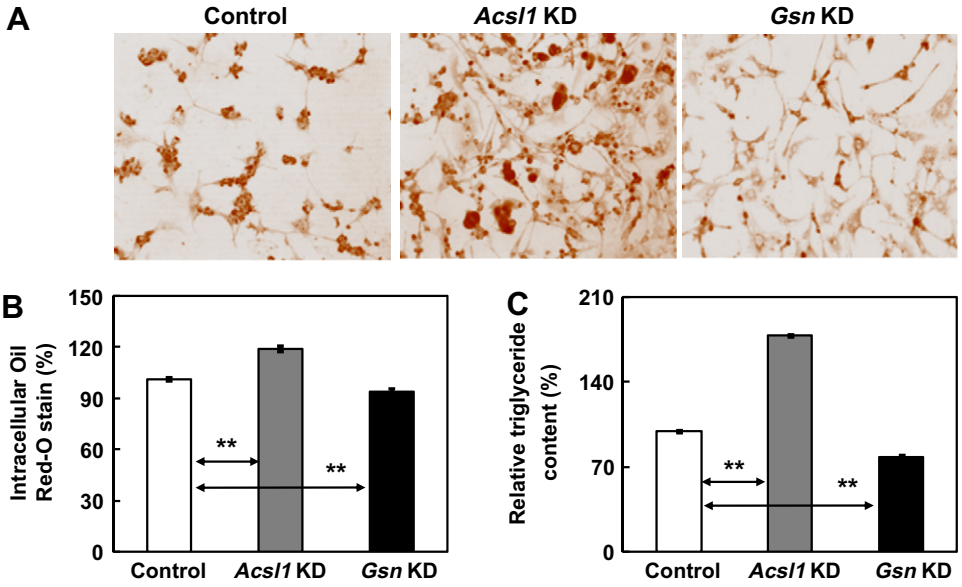

Fig. 3. Effects of *Acsl1* or *Gsn* knockdown on oil droplet accumulation and TG content in 3T3-L1 cells. (A) Oil Red-O staining of control, *Acsl1* KD, and *Gsn* KD cells; (B) quantification of intracellular Oil Red-O stain; (C) TG content assay. $^{**}p < 0.01$.

PPARγ, FAS, ACC, pACC, AMPK1, pAMPK1 in both types of 6-day-old mature KD cells. In *Acsl1* KD cells, all proteins except pACC and pAMPK1 exhibited elevated levels when compared to control cells, which may contribute to a higher rate of fatty acid synthesis *via* the ACC pathway. On the contrary, we observed attenuated expression levels of these lipogenic proteins in *Gsn* KD cells. Collectively, Western blot data support our hypothesis that *Acsl1* is an anti-lipogenic gene, whereas *Gsn* is a pro-lipogenic gene, in the context of obesity (Fig. 4).

4. Discussion

In our previous proteomic studies, we found numerous marker proteins determining the phenotype of obesity susceptibility and resistance in plasma and metabolic tissues of rats fed a high fat diet [5,16–18]. For better understanding of the molecular mechanism behind obesity susceptibility and resistance, the functional aspects and interrelationship between individual proteins or genes must be explored. In the present study, we tried to elucidate the physiological significance between ACSL1 and GSN protein with respect to obesity susceptibility and resistance. When exposed to a high fat diet, these two proteins were oppositely regulated in WAT of rats [5]. Thus, we attempted to knockdown *Acsl1* and *Gsn* encoding ACSL1 and GSN, respectively, in 3T3-L1 adipocyte cells.

ACSL family has a well established role in both the catabolism and anabolism of fatty acids [19]. ACSLs convert long chain fatty acids to acyl CoA products in an ATP-dependent pathway, facilitating their fate in TG formation, integration into the plasma membrane, as well as oxidation and differential partitioning [20]. Mammalian *Acsl* gene family contains five members, *Acsl1–Acsl5*, which differ in their tissue-specific localization and function [21]. Of these, *Acsl1* is primarily expressed in adipose tissue, and it is hypothesized to play an anabolic role in 3T3-L1 adipocyte cells as it is highly expressed during cell differentiation [22] in a *Pparγ*-controlled pattern [23]. However, our previous proteomic data showed that this protein is highly up-regulated in rat WAT, displaying obesity resistance [5]. Our current data also showed that *Acsl1* KD cells have a higher rate of oil droplet accumulation as well as a higher amount of TG compared to control cells, which suggests an anti-lipogenic role in adipocytes. Furthermore, in *Acsl1* KD cells, we detected higher expression of major lipogenic genes as well as *Pparγ* and *C/ebpα*, which are well established adipogenic activators [24,25]. We hypothesize that ample ACSL1 can also readily convert fatty acids to acyl CoA products, limiting the upregulation of *Pparγ* and/or *C/ebpα*. In *Acsl1* KD cells, a higher concentration of fatty acids may have efficiently up-regulated lipogenic transcription factors, ultimately stimulating lipogenic genes, including *Fabp4*, *6Pgd*, *Acc1*, and *Fasn*.

It is notable that lower levels of the active form of AMP-activated protein kinase (pAMPK1), which execute the fate of fatty acids in the catabolic or anabolic pathway by controlling ACC, have been observed in *Acsl1*-deficient cells [26]. Resembling a previous finding [27], our *Acsl1* KD cells exhibited reduced rate of AMPK1 conversion to pAMPK1, resulting in lower inactivation of ACC- and FAS-dependent lipogenesis. Conclusively, we anticipate that acyl CoA products not only induce expression of lipogenic genes *via* regulation of main lipogenic transcription factors but also regulate the upstream AMPK pathway, *via* inactivation of AMPK1. Thus, it is likely that inactivation of AMPK1 finally leads to lower inactivation of lipogenic enzymes such as ACC and FAS.

On the contrary, *Gsn* KD cells showed the opposite result as *Acsl1* KD cells. Gelsolin is an actin-binding protein located in the cytosol [28], and it plays a regulatory role in actin filament assembly–disassembly [29]. Further, gelsolin is a calcium-activated protein, and recently it has been linked with certain pathological conditions such as inflammation and cancer [11,12,30]. Gelsolin has been reported as a secreted factor during 3T3-L1 differentiation [31], and *Gsn* KD 3T3-L1 cells actually exhibit a lower rate of differentiation [32,33]. However, this is the first report to show an intense connection between *Gsn* and other lipogenic genes. Our previous proteomics study revealed that obesity-prone rats fed a high fat diet have a higher concentration of GSN in their WAT [5], which was clearly confirmed by the current gene KD study.

From the results of Oil Red-O staining as well as TG content determination, it is clear that *Gsn* KD cells have a diminished rate of lipid accumulation. To address this decrease in lipid accumulation, our data showed that *Gsn* KD cells exhibit attenuated expression of *Pparγ* and *C/ebpα*, suggesting lower adipogenesis [33]. As it

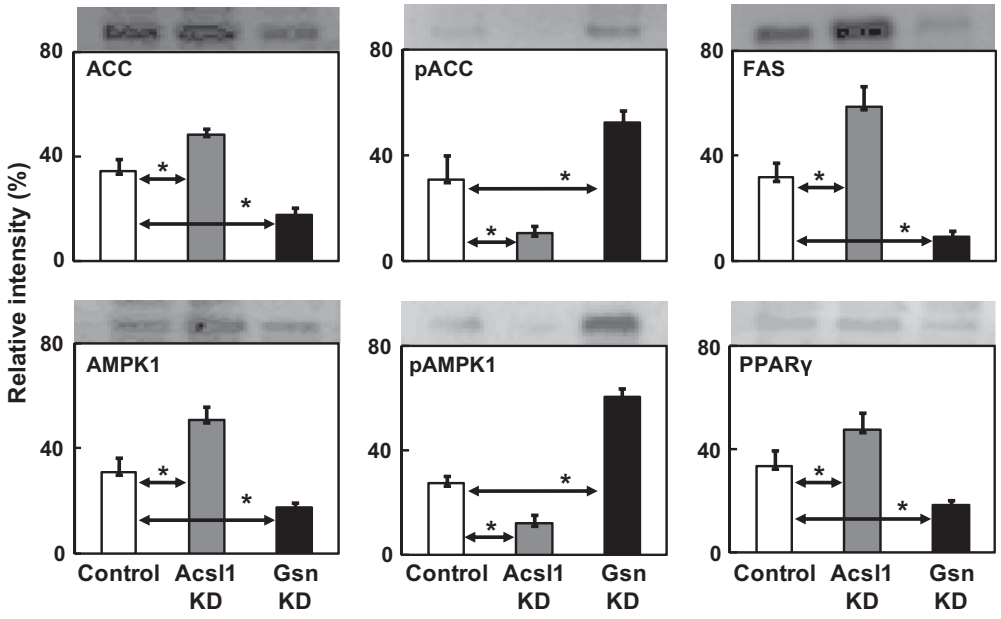

Fig. 4. Effects of *Acsl1* or *Gsn* knockdown on protein expression levels of selected lipogenic proteins in 3T3-L1 cells by immunoblot analysis. Band density was calculated by ImageMaster 2D software version 4.95, and relative intensity (%) demonstrated that values of proteins were normalized to those of β-actin. Data are shown representative of three independent experiments. $^{*}p < 0.05$.

is well established that *Pparγ* and *C/ebpα* are major lipogenic transcription factors, we postulate that down-regulation of the lipogenic genes examined in this study (e.g. *Fasn*, *Acc*, *Fabp4*, and *6Pgd*) is mediated by attenuation of these transcription factors. The results of our Western blot analysis also support this hypothesis, in those higher concentrations of the phosphorylated products of ACC and AMPK1 resulted in impaired lipogenesis. Taken together, we can conclude that GSN mediates attenuated effect on *Pparγ* and *C/ebpα* expression by regulating other nuclear receptors, thereby resulting in lower expression of lipogenic target genes. Consequently, a higher concentration of pAMPK1 to inactivate ACC into pACC resulted in lower TG synthesis and a higher chance of CPT1-mediated fat oxidation (Fig. 4).

Another important outcome of the current study was the establishment of a relationship between *Acsl1* and *Gsn* with the obesity-related pro-inflammatory genes *Tnfα* and *Il6* [34,35]. In earlier studies, it was found that *Tnfα* and *Il6* knockout mice display a reduced rate of development of obesity-induced insulin resistance [36,37]. In our *Acsl1* KD cells, these two pro-inflammatory cytokines were up-regulated, possibly due to a higher rate of lipid accumulation. However, to our surprise, this was not the case in *Gsn* KD cells. Significantly higher expression levels of *Tnfα* and *Il6* were observed even though adipogenesis and lipogenesis were suppressed. Considering earlier findings that *Tnfα* and *Il6* link to lipolytic capability in both *in vitro* and *in vivo* animal models [38–40], *Gsn* KD not only may be related to inhibition of lipogenesis but also to elevation of *Tnfα*- and *Il6*-mediated lipolysis, or a combined effect of these two phenomena, thereby resulting in lower TG content.

In conclusion, our current study reveals that *Acsl1* and *Gsn* are oppositely related with lipid metabolic and obesity-related inflammatory genes. It is likely that ACSL1 is a more important candidate protein due to its role not only in decreased lipogenesis but also in obesity-related inflammation. Attenuated expression of *Acsl1* can be considered as a key regulator in the development of obesity or other metabolic complications. In contrast, *Gsn* can be targeted only to reduce adipocity but not to attenuate obesity-induced inflammation in adipose tissue.

Acknowledgment

This study was supported by the Daegu University Research Grant 2011.

References

[1] E.D. Rosen, B.M. Spiegelman, Adipocytes as regulators of energy balance and glucose homeostasis, Nature 444 (2006) 847–853.
[2] H. Waki, P. Tontonoz, Endocrine functions of adipose tissue, Annu. Rev. Pathol. 2 (2007) 31–56.
[3] P.G. Kopelman, Obesity as a medical problem, Nature 404 (2000) 635–643.
[4] H. Green, M. Meuth, An established pre-adipose cell line and its differentiation in culture, Cell 3 (1974) 127–133.
[5] J.I. Joo, T.S. Oh, D.H. Kim, D.K. Choi, X. Wang, J.W. Choi, J.W. Yun, Differential expression of adipose tissue proteins between obesity-susceptible and -resistant rats fed a high-fat diet, Proteomics 11 (2011) 1429–1448.
[6] E. Soupene, F.A. Kuypers, Mammalian long-chain acyl-CoA synthetases, Exp. Biol. Med. (Maywood) 233 (2008) 507–521.
[7] L.O. Li, D.G. Mashek, J. An, S.D. Doughman, C.B. Newgard, R.A. Coleman, Overexpression of rat long chain acyl-coa synthetase 1 alters fatty acid metabolism in rat primary hepatocytes, J. Biol. Chem. 281 (2006) 37246–37255.
[8] D.G. Mashek, L.O. Li, R.A. Coleman, Rat long-chain acyl-CoA synthetase mRNA, protein, and activity vary in tissue distribution and in response to diet, J. Lipid Res. 47 (2006) 2004–2010.
[9] J.E. Schaffer, H.F. Lodish, Expression cloning and characterization of a novel adipocyte long chain fatty acid transport protein, Cell 79 (1994) 427–436.
[10] H.C. Chiu, A. Kovacs, D.A. Ford, F.F. Hsu, R. Garcia, P. Herrero, J.E. Saffitz, J.E. Schaffer, A novel mouse model of lipotoxic cardiomyopathy, J. Clin. Invest. 107 (2001) 813–822.
[11] D.J. Kwiatkowski, Functions of gelsolin: motility, signaling, apoptosis, cancer, Curr. Opin. Cell. Biol. 11 (1999) 103–108.
[12] M.J. DiNubile, Plasma gelsolin as a biomarker of inflammation, Arthritis Res. Ther. 10 (2008) 124.
[13] P.M. Becker, A.A. Kazi, R. Wadgaonkar, D.B. Pearse, D. Kwiatkowski, J.G. Garcia, Pulmonary vascular permeability and ischemic injury in gelsolin-deficient mice, Am. J. Respir. Cell. Mol. Biol. 28 (2003) 478–484.
[14] W. Witke, A.H. Sharpe, J.H. Hartwig, T. Azuma, T.P. Stossel, D.J. Kwiatkowski, Hemostatic, inflammatory, and fibroblast responses are blunted in mice lacking gelsolin, Cell 81 (1995) 41–51.
[15] M.M. Bradford, A rapid and sensitive method for the quantitation of microgram quantities of protein utilizing the principle of protein-dye binding, Anal. Biochem. 72 (1976) 248–254.
[16] X. Wang, J.W. Choi, J.I. Joo, D.H. Kim, T.S. Oh, D.K. Choi, J.W. Yun, Differential expression of liver proteins between obesity-prone and obesity-resistant rats in response to a high-fat diet, Br. J. Nutr. 106 (2011) 612–626.

[17] D.H. Kim, J.W. Choi, J.I. Joo, X. Wang, D.K. Choi, T.S. Oh, J.W. Yun, Changes in expression of skeletal muscle proteins between obesity-prone and obesity-resistant rats induced by a high-fat diet, J. Proteome Res. 10 (2011) 1281–1292.
[18] J.W. Choi, X. Wang, J.I. Joo, D.H. Kim, T.S. Oh, D.K. Choi, J.W. Yun, Plasma proteome analysis in diet-induced obesity-prone and obesity-resistant rats, Proteomics 10 (2010) 4386–4400.
[19] D.G. Mashek, L.O. Li, R.A. Coleman, Long-chain acyl-CoA synthetases and fatty acid channeling, Future Lipidol. 2 (2007) 465–476.
[20] Y.L. Wang, W. Guo, Y. Zang, G.C. Yaney, G. Vallega, L. Getty-Kaushik, P. Pilch, K. Kandror, B.E. Corkey, Acyl coenzyme a synthetase regulation: putative role in long-chain acyl coenzyme a partitioning, Obes. Res. 12 (2004) 1781–1788.
[21] D.G. Mashek, K.E. Bornfeldt, R.A. Coleman, J. Berger, D.A. Bernlohr, P. Black, C.C. DiRusso, S.A. Farber, W. Guo, N. Hashimoto, V. Khodiyar, F.A. Kuypers, L.J. Maltais, D.W. Nebert, A. Renieri, J.E. Schaffer, A. Stahl, P.A. Watkins, V. Vasiliou, T.T. Yamamoto, Revised nomenclature for the mammalian long-chain acyl-CoA synthetase gene family, J. Lipid Res. 45 (2004) 1958–1961.
[22] E. Oikawa, H. Iijima, T. Suzuki, H. Sasano, H. Sato, A. Kamataki, H. Nagura, M.J. Kang, T. Fujino, H. Suzuki, T.T. Yamamoto, A novel acyl-CoA synthetase, ACS5, expressed in intestinal epithelial cells and proliferating preadipocytes, J. Biochem. 124 (1998) 679–685.
[23] G. Martin, K. Schoonjans, A.M. Lefebvre, B. Staels, J. Auwerx, Coordinate regulation of the expression of the fatty acid transport protein and acyl-CoA synthetase genes by PPARalpha and PPARgamma activators, J. Biol. Chem. 272 (1997) 28210–28217.
[24] F.M. Gregoire, C.M. Smas, H.S. Sul, Understanding adipocyte differentiation, Physiol. Rev. 78 (1998) 783–809.
[25] L. Fajas, D. Auboeuf, E. Raspe, K. Schoonjans, A.M. Lefebvre, R. Saladin, J. Najib, M. Laville, J.C. Fruchart, S. Deeb, A. Vidal-Puig, J. Flier, M.R. Briggs, B. Staels, H. Vidal, J. Auwerx, The organization, promoter analysis, and expression of the human PPARgamma gene, J. Biol. Chem. 272 (1997) 18779–18789.
[26] D.G. Hardie, Regulation of fatty acid and cholesterol metabolism by the AMP-activated protein kinase, Biochim. Biophys. Acta 1123 (1992) 231–238.
[27] S. Lobo, B.M. Wiczer, D.A. Bernlohr, Functional analysis of long-chain acyl-CoA synthetase 1 in 3T3-L1 adipocytes, J. Biol. Chem. 284 (2009) 18347–18356.
[28] R.C. Koya, H. Fujita, S. Shimizu, M. Ohtsu, M. Takimoto, Y. Tsujimoto, N. Kuzumaki, Gelsolin inhibits apoptosis by blocking mitochondrial membrane potential loss and cytochrome c release, J. Biol. Chem. 275 (2000) 15343–15349.
[29] H.Q. Sun, M. Yamamoto, M. Mejillano, H.L. Yin, Gelsolin, a multifunctional actin regulatory protein, J. Biol. Chem. 274 (1999) 33179–33182.
[30] L. Spinardi, W. Witke, Gelsolin and diseases, Subcell. Biochem. 45 (2007) 55–69.
[31] I. Kratchmarova, D.E. Kalume, B. Blagoev, P.E. Scherer, A.V. Podtelejnikov, H. Molina, P.E. Bickel, J.S. Andersen, M.M. Fernandez, J. Bunkenborg, P. Roepstorff, K. Kristiansen, H.F. Lodish, M. Mann, A. Pandey, A proteomic approach for identification of secreted proteins during the differentiation of 3T3-L1 preadipocytes to adipocytes, Mol. Cell. Proteomics 1 (2002) 213–222.
[32] A. Kawaji, Y. Ohnaka, S. Osada, M. Nishizuka, M. Imagawa, Gelsolin, an actin regulatory protein, is required for differentiation of mouse 3T3-L1 cells into adipocytes, Biol. Pharm. Bull. 33 (2010) 773–779.
[33] K. Nishimura, H.J. Ting, Y. Harada, T. Tokizane, N. Nonomura, H.Y. Kang, H.C. Chang, S. Yeh, H. Miyamoto, M. Shin, K. Aozasa, A. Okuyama, C. Chang, Modulation of androgen receptor transactivation by gelsolin: a newly identified androgen receptor coregulator, Cancer Res. 63 (2003) 4888–4894.
[34] G.S. Hotamisligil, B.M. Spiegelman, Tumor necrosis factor alpha: a key component of the obesity-diabetes link, Diabetes 43 (1994) 1271–1278.
[35] Y.H. Lee, R.E. Pratley, The evolving role of inflammation in obesity and the metabolic syndrome, Curr. Diab. Rep. 5 (2005) 70–75.
[36] K.T. Uysal, S.M. Wiesbrock, M.W. Marino, G.S. Hotamisligil, Protection from obesity-induced insulin resistance in mice lacking TNF-alpha function, Nature 389 (1997) 610–614.
[37] G.B. Di Gregorio, L. Hensley, T. Lu, G. Ranganathan, P.A. Kern, Lipid and carbohydrate metabolism in mice with a targeted mutation in the IL-6 gene: absence of development of age-related obesity, Am. J. Physiol. Endocrinol. Metab. 287 (2004) E182–187.
[38] A. Green, S.B. Dobias, D.J. Walters, A.R. Brasier, Tumor necrosis factor increases the rate of lipolysis in primary cultures of adipocytes without altering levels of hormone-sensitive lipase, Endocrinology 134 (1994) 2581–2588.
[39] K.R. Feingold, W. Doerrler, C.A. Dinarello, W. Fiers, C. Grunfeld, Stimulation of lipolysis in cultured fat cells by tumor necrosis factor, interleukin-1, and the interferons is blocked by inhibition of prostaglandin synthesis, Endocrinology 130 (1992) 10–16.
[40] G. van Hall, A. Steensberg, M. Sacchetti, C. Fischer, C. Keller, P. Schjerling, N. Hiscock, K. Moller, B. Saltin, M.A. Febbraio, B.K. Pedersen, Interleukin-6 stimulates lipolysis and fat oxidation in humans, J. Clin. Endocrinol. Metab. 88 (2003) 3005–3010.

Biochemical and Biophysical Research Communications 420 (2012) 594–599

Contents lists available at SciVerse ScienceDirect

Biochemical and Biophysical Research Communications

journal homepage: www.elsevier.com/locate/ybbrc

nNOS downregulation attenuates neuronal apoptosis by inhibiting nNOS–GluR6 interaction and GluR6 nitrosylation in cerebral ischemic reperfusion

Jie-Hui Di [a,b,1], Chong Li [a,1], Hong-Min Yu [a], Jun-Nian Zheng [b], Guang-Yi Zhang [a,*]

[a] Jiangsu Key Laboratory of Brain Disease Bioinformation, Research Center of Biochemistry and Molecular Biology, Xuzhou Medical College, 84 West Huaihai Road, Xuzhou 221002, Jiangsu, China
[b] Jiangsu Key Laboratory of Biological Cancer Therapy, Xuzhou Medical College, 84 West Huaihai Road, Xuzhou 221002, Jiangsu, China

ARTICLE INFO

Article history:
Received 2 February 2012
Available online 16 March 2012

Keywords:
S-nitrosylation
GluR6
nNOS
Cerebral ischemia
Neuroprotection

ABSTRACT

Glutamate receptor 6 (GluR6) is well documented to play a pivotal role in ischemic brain injury, which is mediated by the GluR6·PSD95·MLK3 signaling module and subsequent c-Jun N-terminal kinase (JNK) activation. Our recent studies show that GluR6 is S-nitrosylated in the early stages of ischemia–reperfusion. NO (Nitric Oxide) is mainly generated from neuronal nitric oxide synthase (nNOS) in cerebral neurons during the early stages of reperfusion. Here, the effect of nNOS downregulation on GluR6 S-nitrosylation and GluR6-mediated signaling was investigated in cerebral ischemia and reperfusion. Administration of nNOS oligonucleotides confirmed that GluR6 nitrosylation is induced by nNOS-derived endogenous NO and further activates the GluR6·PSD95·MLK3 signaling module and JNK signaling pathway. Moreover, this study revealed for the first time that nNOS can bind with GluR6 during ischemic reperfusion, and PSD95 is involved in this interaction. In summary, our results suggest that nNOS binds with GluR6 via PSD95 and then produces endogenous NO to S-nitrosylate GluR6 in cerebral ischemia–reperfusion, which provides a new approach for stroke therapy.

1. Introduction

Kainate receptor subunit GluR6 is largely expressed in the hippocampus and plays an important role in brain ischemia/reperfusion-mediated neuronal cell death, which is mediated by the GluR6·PSD95·MLK3 signaling module and subsequent JNK activation [1–3]. Our previous studies demonstrate that treatment with Tat-GluR6-9c, GluR6 antisense oligonucleotides (AS-ODNs), or overexpression of C-terminal amino acids of GluR6 exerts a protective effect by depressing the assembly of GluR6·PSD95·MLK3 [2–5]. Our recent studies also demonstrate that GluR6 can be S-nitrosylated by endogenous NO in cerebral ischemia–reperfusion, which may be correlated with the NMDA receptor (NMDAR)·PSD95·nNOS signaling module, and further activates the GluR6·PSD95·MLK3 signaling module and JNK signaling pathway [6].

Protein S-nitrosylation is considered the principal post-translational modification by which nitric oxide exerts a myriad of biological effects. S-nitrosylation, the covalent attachment of an NO group to the thiol moiety of reactive cysteine residues, is postulated as a fundamental mechanism in cellular signal transduction [7,8]. The stability of proteins, cleavage of zymogens, and modification of active proteins can be controlled by this post-translational modification process [9,10]. NO is an important cellular signaling molecule that plays a vital role in many biological processes [11]. Nitric oxide signaling is mediated in mammals by the calcium/calmodulin-controlled isoenzymes endothelial NOS (eNOS) and neuronal NOS (nNOS). nNOS is expressed primarily in neurons, and NO is mainly generated from nNOS in cerebral neurons during the early stages of reperfusion [12,13].

In this study, to confirm that GluR6 S-nitrosylation is induced by nNOS-derived endogenous NO, we knocked down nNOS protein expression by administration of nNOS AS-ODNs and then measured changes in the level of GluR6 S-nitrosylation and GluR6 downstream JNK signaling. Moreover, we investigated how nNOS coupled with GluR6. Here, we report for the first time that nNOS could bind to GluR6 and that PSD95 was involved in this interaction, as well as further confirming that GluR6 S-nitrosylation was induced by nNOS-derived endogenous NO.

Abbreviations: AS-ODNs, antisense oligonucleotides; GluR6, glutamate receptor 6; IB, immunoblotting; IP, immunoprecipitation; JNK, c-Jun N-terminal kinase; MLK, mixed-lineage kinase; MS-ODNs, missense oligodeoxynucleotides; NMDA, *N*-methyl-D-aspartic acid; nNOS, neuronal nitric oxide synthase; NO, nitric oxide; SDS–PAGE, sodium dodecyl sulfate–polyacrylamide gel electrophoresis.

* Corresponding author. Fax: +86 516 8574 8486.
E-mail address: gyzhang@xzmc.edu.cn (G.-Y. Zhang).

[1] They contributed equally to this work.

0006-291X/$ - see front matter © 2012 Elsevier Inc. All rights reserved.
http://dx.doi.org/10.1016/j.bbrc.2012.03.039

2. Materials and methods

2.1. Antibodies and reagents

The following primary antibodies were used. Rabbit polyclonal anti-GluR6 (sc-7618), anti-nNOS (sc-648), anti-p-JNKs (sc-6254), and anti-p-c-jun (sc-16312) were obtained from Santa Cruz Biotechnology. Rabbit polyclonal anti-nNOS (#4234), anti-p-MLK3 (#2811), anti-MLK3 (#2817), anti-p-MKK7 (#4171), anti-MKK7 (#4172), and anti-c-jun (#9162) were acquired from Cell Signaling Biotechnology. Rabbit polyclonal anti-SNO-Cys (N5411), monoclonal anti-PSD95 (P-246), and the secondary anti-mouse IgG (A 1682) and anti-rabbit IgG (T 6778) were purchased from Sigma. Nitrocellulose filters were acquired from Amersham. BCIP and NBT were from Promega. The oligodeoxynucleotides were synthesized by Sangon Biotech Co. Ltd. All other chemicals were obtained from Sigma unless indicated otherwise.

2.2. Induction of ischemia

Adult male Sprague–Dawley rats weighing 200–250 g were used (Shanghai Experimental Animal Center, Chinese Academy of Science, Shanghai, China). Transient cerebral ischemia was induced by a four-vessel occlusion method as described previously [14]. Briefly, under chloral hydrate anesthesia (300 mg/kg, i.p.), vertebral arteries were electrocauterized, and carotid arteries were isolated. Rats were allowed to recover for 24 h, and ischemia (15 min) was induced by occluding the common arteries with aneurysm clips. Rats that lost their righting reflex within 30 s and whose pupils were dilated and unresponsive to light were selected for the experiments. Rectal temperature was maintained at 36.5–37.5 °C during ischemia. Sham control rats were treated using the same surgical procedures, except that the carotid arteries were not occluded.

2.3. Administration of drugs

Rats were administered 10 nmol nNOS, GluR6, or PSD95 AS-ODNs in 10 μl of TE buffer every 24 h for 3 days before ischemia. The same dose of missense oligodeoxynucleotides (MS-ODNs) or vehicle (TE buffer) was used as a control. The sequence of nNOS AS-ODNs was 5′-ACGTGTTCTCTTCCAT-3′, and that of MS-ODNs was 5′-TAAAGGGAGAACACGT-3′. The sequence for GluR6 AS-ODNs was 5′-CTTCATGATGTTTCCGTG-3′, and that for MS-ODNs was 5′-TCTAGCTTCTGAGTTCGT-3′. The sequence for PSD95 AS-ODNs was 5′-GAATGGGTCACCTCC-3′, and that for MS-ODNs was 5′-CCGC TCTATCGAGGA-3′.

2.4. Sample preparation

Rats were decapitated immediately after 6 h reperfusion, and then the hippocampal CA1 was isolated and quickly frozen in liquid nitrogen. Tissues were homogenized in ice-cold homogenization buffer. The homogenates were centrifuged at 800*g* for 10 min at 4 °C. Supernatants were collected, and protein concentration was determined by the method of Lowry et al. [15]. Samples were stored at −80 °C and were thawed only once just prior to use.

2.5. Determination of protein S-nitrosylation

Measurement of S-nitrosylated GluR6 was performed by immunoprecipitation with anti-GluR6 antibody, followed by separately immunoblotting with anti-SNO-Cys antibody.

2.6. Immunoprecipitation and immunoblotting

Tissue homogenates (400 μg protein) were incubated with 1 μg primary antibodies for 4 h or overnight at 4 °C. Protein A beads (15 μl) were then added to each immunoprecipitation (IP) reaction and allowed to incubate for an additional 1 h. After extensive washing with IP buffer, protein was then eluted from the beads by addition of 40 μl 2× SDS–PAGE loading buffer. Proteins were separated using polyacrylamide gels and then transferred onto nitrocellulose membrane for immunoblotting with the indicated antibodies. Membranes from at least three separate experiments were scanned, and the density of bands was analyzed with LabWorks image analysis software.

2.7. Immunohistochemistry and histology

Rats were perfusion-fixed with 4% paraformaldehyde in 0.1 M PBS under anesthesia at 6 h of reperfusion. Brains were fixed with the same fixation solution at 4 °C overnight and then embedded in paraffin. Coronal sections of 6-μm thickness were prepared using a microtome. Immunoreactivity was visualized by the avidin–biotin-peroxidase method. Briefly, sections were deparaffinized with xylene and rehydrated in a gradient of ethanol and distilled water. High-temperature antigen retrieval was then performed in 1 mM citrate buffer. To block endogenous peroxidase activity, the sections were incubated for 30 min in 1% H_2O_2. After blocking with 5% (v/v) normal goat serum in PBS for 1 h at 37 °C, sections were incubated with p-c-jun antibody (1:50) overnight at 4 °C. After washing three times in PBS, the sections were incubated for 2 h in biotinylated goat anti-rabbit secondary antibody (1:200) diluted in PBS containing 0.1% BSA, 0.3% Triton X-100, and 1% normal goat serum. The sections were then incubated with avidin-conjugated horseradish peroxidase for 1 h at 37 °C. Finally, sections were incubated with a 3,3′-diaminobenzidine peroxidase substrate kit and examined under a light microscope.

Histological analysis was determined by cresyl violet staining. Paraffin sections (6 μm) from rats perfusion-fixed as described above after 5 days of reperfusion following ischemia were prepared and stained with 0.1% (w/v) cresyl violet and then examined with a light microscope. The number of surviving hippocampal CA1 or CA3 pyramidal cells/mm was counted as the neuronal density.

2.8. Data analysis and statistics

Values are expressed as means ± SD. The statistical analysis of the results was carried out using the Student's *t*-test or one-way analysis of variance followed by the Duncan's new multiple range method or the Newman–Keuls test. *P* values <0.05 were considered significant.

3. Results

3.1. nNOS AS-ODNs significantly inhibit nNOS expression and the level of GluR6 S-nitrosylation

To confirm whether GluR6 could be S-nitrosylated by nNOS-derived endogenous NO, we initially abolished nNOS expression by administration of nNOS AS-ODNs or control MS-ODNs. As shown in Fig. 1A and B, nNOS AS-ODNs markedly reduced nNOS protein expression at 6 h reperfusion, whereas the MS-ODNs did not alter nNOS protein levels. We then examined the levels of GluR6 S-nitrosylation after treatment with nNOS oligonucleotides. As shown in Fig. 1C and D, GluR6 was S-nitrosylated at 6 h reperfusion, and the increase in GluR6 S-nitrosylation declined substantially in the nNOS AS-ODN group but not the vehicle or MS-ODN groups. These results confirmed that GluR6 S-nitrosylation is

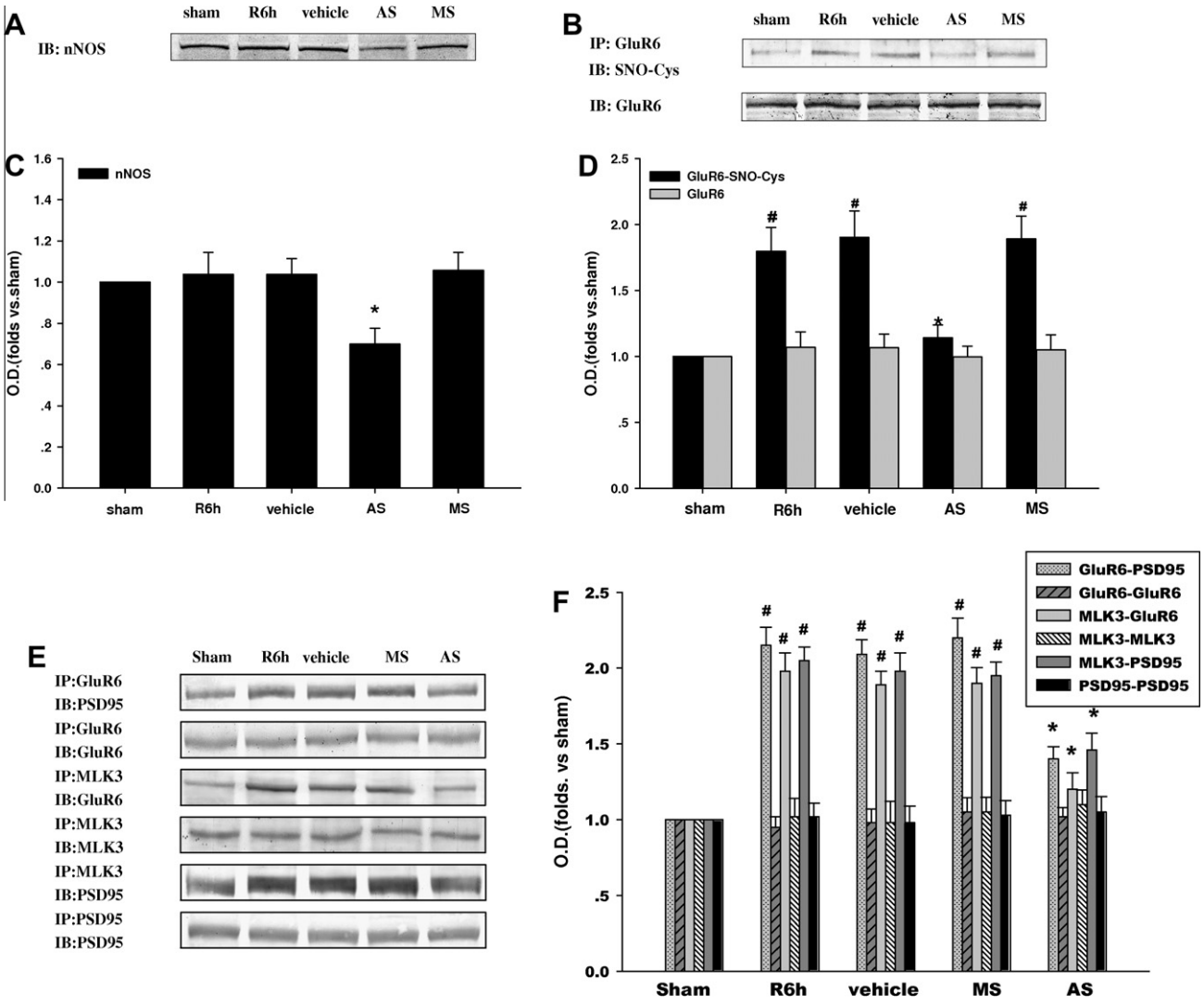

Fig. 1. Effect of nNOS AS-ODNs on S-nitrosylated GluR6 and assembly of GluR6, MLK3, and PSD95. (A, C) The effect of nNOS AS-ODNs on the expression of nNOS and S-nitrosylation of GluR6. To detect the expression of nNOS, samples were directly immunoblotted (IB) with anti-nNOS antibody. S-nitrosylation of GluR6 was determined by the biotin-switch assay: all of the S-nitrosylated proteins were immunoprecipitated (IP) with streptavidin–agarose, followed by immunoblot analysis with anti-GluR6 antibody to detect S-nitrosylation of GluR6. Immunoblotting directly with anti-GluR6 antibody was also performed. (E) Analysis of the effect of nNOS AS-ODNs on the assembly of GluR6 and MLK3 with PSD95 induced by transient brain ischemia followed by 6 h reperfusion in hippocampal CA1. Sample proteins were examined by immunoprecipitation with anti-GluR6, anti-PSD95, or anti-MLK3 antibody followed by immunoblotting separately with anti-GluR6, anti-PSD95, and anti-MLK3 antibodies. (B, D, F) Bands were scanned, and their intensities were represented as fold change versus sham treatment. Data are expressed as mean ± SD from four independent experiments ($n = 4$). (B) $^{*}P < 0.05$ versus sham. (D) $^{*}P < 0.05$ versus vehicle; $^{\#}P < 0.05$ versus sham.

mediated mainly by nNOS-derived endogenous NO during cerebral ischemia–reperfusion.

3.2. nNOS knockdown inhibits the increased assembly of the GluR6·PSD95·MLK3 signaling module by suppressing the increased S-nitrosylation of GluR6 during ischemia–reperfusion

As shown in Fig. 1C and D, knockdown of nNOS reduced the increased S-nitrosylation of GluR6 that was induced by cerebral ischemia–reperfusion. Previous studies indicate that regulation of GluR6 could further influence the assembly of GluR6 and MLK3 with PSD95. We then analyzed the effects of nNOS knockdown on the assembly of the GluR6·PSD95·MLK3 signaling module. As illustrated in Fig. 1E and F, treatment with nNOS AS-ODNs diminished the combination of GluR6 and MLK3 as well as PSD95, but no significant change was observed in the vehicle or MS-ODN treatment groups. These results indicate that knockdown of nNOS attenuates the combination of GluR6 and MLK3 with PSD95 by downregulating S-nitrosylation of GluR6 and further suggest that S-nitrosylation of GluR6 regulates the assembly of the GluR6·PSD95·MLK3 signaling module.

3.3. nNOS knockdown inhibits the increased activation of the MLK3·MKK7·JNK signaling module by suppressing the increased S-nitrosylation of GluR6 during ischemia–reperfusion

To further confirm whether GluR6 downstream proteins were also affected by S-nitrosylation of GluR6, nNOS oligonucleotides were injected, and the variation of phosphorylated downstream proteins was observed. As shown in Fig. 2A and B, the nNOS AS-ODN group, but not the vehicle or MS-ODN groups, demonstrated a large decline in the increased phosphorylation of MLK3 and MKK7, while the protein levels of MLK3 and MKK7 were not changed. Downregulation of endogenous nNOS was also accompanied by a significant decrease in JNK3 activation at its peak level 3 days following ischemia–reperfusion (Fig. 2C and D). These results suggest that S-nitrosylation of GluR6 affected the phosphorylation and activation of its downstream protein targets.

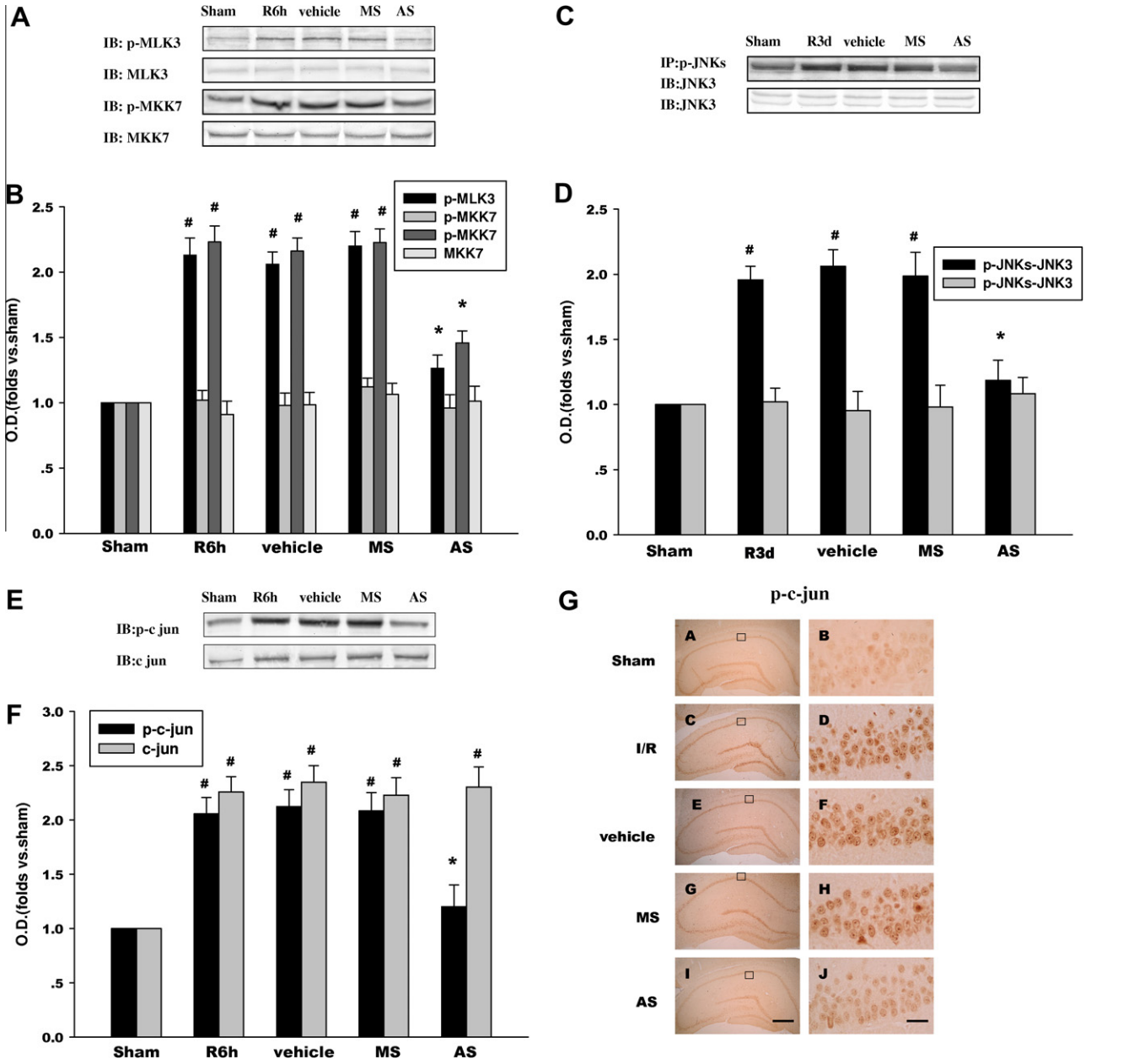

Fig. 2. Effect of nNOS AS-ODNs on GluR6-mediated downstream signaling. (A, C) Rats were treated with nNOS AS-ODNs to observe their effect on the assembly of the MLK3-MKK7-JNK signaling module induced by transient brain ischemia followed by 6 h (R6h) or 1 day (R3d) of reperfusion in hippocampal CA1. (A) Homogenized samples of the hippocampal CA1 region were examined by immunoblotting (IB) separately with anti-p-MLK3, anti-p-MKK7, anti-MLK3, and anti-MKK7 antibodies. (C) Sample proteins were examined by immunoprecipitation (IP) with anti-p-JNK antibody followed by immunoblotting with anti-JNK3 antibody, or directly immunoblotting with anti-JNK3 antibody. (E) Rats were treated with nNOS AS-ODNs to observe their effect on JNK downstream proteins of the nuclear signaling pathway induced by transient brain ischemia followed by 6 h reperfusion in hippocampal CA1. Protein samples were examined by immunoblotting separately with anti-p-c-jun and anti-c-jun antibodies. (B, D, F) Bands were scanned, and the intensities were represented as fold change versus sham control. Data are expressed as mean ± SD from four independent experiments ($n = 4$). $^{*}P < 0.05$ versus vehicle; $^{\#}P < 0.05$ versus sham. (G) Immunohistochemical analysis of the expression and subcellular localization of p-c-jun after different treatments. Representative images of immunohistochemical staining of hippocampal sections from sham-operated rats (A, B), rats subjected to 15 min ischemia followed by 6 h reperfusion (I/R; C, D), and rats subjected to 15 min ischemia followed by 6 h reperfusion with administration of vehicle (E, F), MS-ODNs (MS; G, H), or AS-ODNs (AS; I, J). Boxed areas in the left column are shown at higher magnification in the right column. Magnification is ×40 in the left panels; scale bar = 200 μm; Magnification is ×400 in the right panels; scale bar = 10 μm.

3.4. nNOS AS-ODNs attenuate the elevation of c-Jun phosphorylation in the hippocampal CA1 by suppressing the increased S-nitrosylation of GluR6

To further investigate whether JNK downstream proteins were also influenced by S-nitrosylation of GluR6, we examined the phosphorylation of JNK downstream protein c-Jun after administration of nNOS oligonucleotides. The nuclear fraction from hippocampal CA1 was analyzed for levels of p-c-Jun, an indicator of c-Jun activation. As shown in Fig. 2E and F, p-c-jun was suppressed by treatment with nNOS AS-ODNs, but no change was observed with nNOS MS-ODN or vehicle treatment. Similar results were observed via immunohistochemistry. As shown in Fig. 2G, these results confirmed that administration of nNOS AS-ODNs markedly decreased p-c-jun immunoreactivity in the nuclei of hippocampal CA1 pyramidal neurons compared to the 6-h reperfusion group, whereas

the nNOS MS-ODN and vehicle treatment groups did not demonstrate a marked change in immunoreactivity compared to the 6-h reperfusion group.

3.5. nNOS knockdown exerts a neuroprotective effect against cerebral ischemia–reperfusion injury

To assess the role of nNOS oligonucleotides in ischemia-evoked neuronal apoptosis, cresyl violet staining was used to assess the survival of hippocampal CA1 pyramidal neurons 5 days after ischemia. Cells with round, pale-stained nuclei were counted as normal cells, whereas shrunken cells with pyknotic nuclei were regarded as dead. As shown in Fig. 3A, 15 min ischemia followed by 5 days of reperfusion led to severe cell death (Fig. 3A (c,d)). Administration of nNOS AS-ODNs dramatically decreased neuronal degeneration (Fig. 3A (i,j)), but vehicle and nNOS MS-ODN control treatment did not show any protective effect against the degeneration induced by ischemia and 5 days of reperfusion (Fig. 3A (e–h)). The numbers of surviving pyramidal cells in the CA1 region in the sham operation group, ischemia insult group, vehicle treatment group, nNOS MS-ODN treatment group, and nNOS AS-ODN treatment group were 202.4 ± 9.8, 27.2 ± 8.5, 31.4 ± 7.7, 22.3 ± 5.6, and 150.3 ± 7.6, respectively (Fig. 3B).

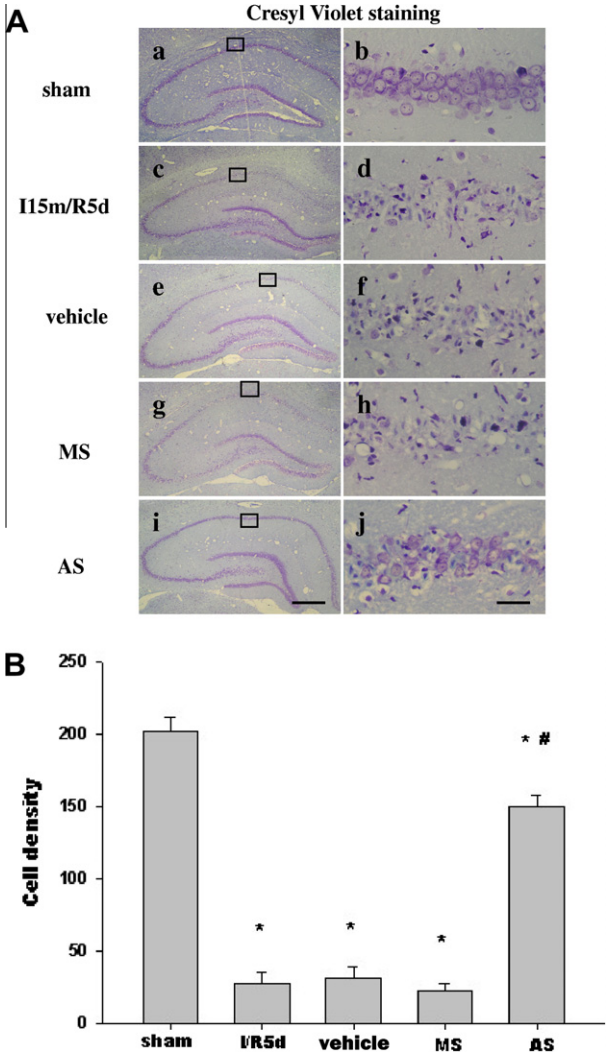

Fig. 3. Effect of nNOS AS-ODNs on the survival of CA1 pyramidal neuron. (A) Cresyl violet staining was performed on hippocampal sections from sham-operated rats (a, b), rats subjected to 5 days of reperfusion after global ischemia (I15 m/R5d; c, d), and rats subjected to 5 days of reperfusion after global ischemia with administration of vehicle (e, f), MS-ODNs (MS; g, h), or AS-ODNs (AS; i, j) before or after ischemia. Cresyl violet staining data were obtained from six independent animals, and a typical experiment is presented. (B) Cell density was expressed as the number of cells per 1 mm length of the CA1 pyramidal cell layer counted under a light microscope. Data are expressed as mean ± SD ($n = 6$). Scale bars = 200 μm (left panel); 10 μm (right panel). $^{*}P < 0.05$ versus vehicle; $^{\#}P < 0.05$ versus sham.

3.6. nNOS can bind with GluR6, and PSD95 knockdown can suppress the interaction of nNOS and GluR6

To further investigate the coupling mechanism of GluR6 and nNOS, we first examined the interaction of nNOS with GluR6 at 6 h reperfusion after transient global cerebral ischemia using endogenous immunoprecipitation. As shown in Fig. 4A, the interaction of nNOS with GluR6 was clearly detected in the 6-h reperfusion group, but no interaction was detected in the IgG and preserum (serum pretreatment) control groups. As shown in Fig. 4B–E, administration of nNOS or GluR6 AS-ODNs attenuated the enhancement of the interaction between nNOS and GluR6 after ischemia and 6 h reperfusion; however, no significant change was detected in the vehicle and MS-ODN treatment groups. PSD95 is a principal scaffolding component of the postsynaptic density. To investigate whether PSD95 mediates the binding of nNOS with GluR6, we observed the effect of PSD95 AS-ODN administration on the interaction between nNOS and GluR6. The same dose of PSD95 MS-ODNs and vehicle were used as control. As shown in Fig. 4F and G, immunoblotting analyses indicated that PSD95 AS-ODNs significantly decreased PSD95 protein expression and attenuated the enhancement of the interaction between nNOS and GluR6 6 h after ischemia; however, no significant change was detected in the vehicle and MS-ODN treatment groups. These results suggest that nNOS can bind with GluR6, and PSD95 may be involved in this binding.

4. Discussion

In the present study, we confirmed that GluR6 S-nitrosylation is induced by nNOS-derived endogenous NO and can further influence the assembly of the GluR6·PSD95·MLK3 signaling module and downstream JNK signaling pathway. Furthermore, we demonstrated for the first time that nNOS can bind with GluR6, and that PSD95 may be involved in this binding. A possible molecular mechanism underlying this phenomenon is that during the early stages of brain ischemia–reperfusion, nNOS binds with GluR6, and this binding "delivers" nNOS-derived NO to GluR6 to elicit its S-nitrosylation. S-nitrosylation further upregulates the increased assembly of the GluR6·PSD95·MLK3 signaling module, leading to subsequent activation of the JNK signaling pathway. nNOS AS-ODNS exerted a neuroprotective role against cerebral ischemia–reperfusion injury by suppressing nNOS to decrease GluR6 S-nitrosylation.

Substantial evidence indicates that brain ischemia–reperfusion promotes the assembly of NMDAR and nNOS with PSD95, as well as promoting the assembly of the GluR6·PSD95·MLK3 signaling module [2,16,17]. Our previous study demonstrated that S-nitrosylation of GluR6 was suppressed by treatment with an NMDAR antagonist, which suggests that the NMDAR·PSD95·nNOS signaling module is likely involved in GluR6 S-nitrosylation. GluR6 S-nitrosylation can further influence the assembly of the GluR6·PSD95·MLK3 signaling module and downstream JNK signaling pathway [6]. In this study, we demonstrated that nNOS can bind with GluR6 at 6 h reperfusion after transient global cerebral ischemia using endogenous immunoprecipitation. Compared with the vehicle and MS-ODN groups, treatment with nNOS or GluR6 AS-ODNs attenuated the enhancement of the interaction between nNOS and GluR6 6 h after ischemia.

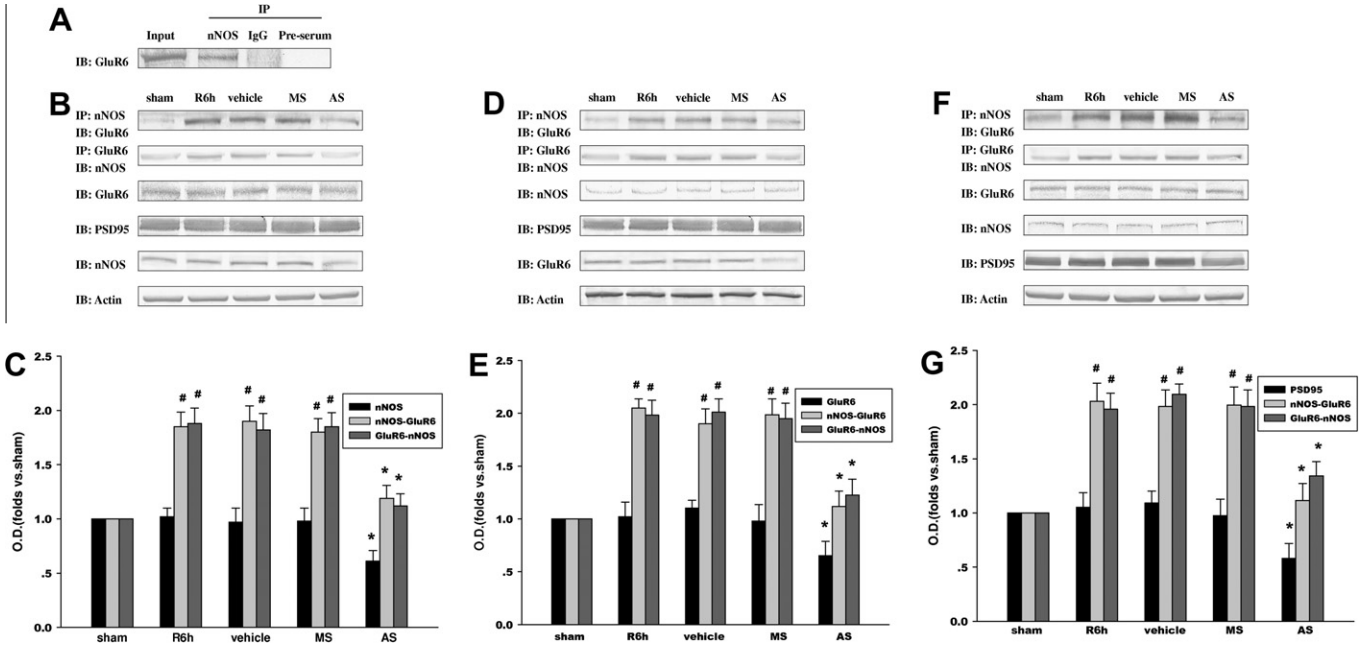

Fig. 4. Effect of nNOS AS-ODNs, GluR6 AS-ODNs, and PSD95 AS-ODNs on the combination of GluR6 with nNOS. (A) The same protein sample was examined by immunoprecipitation (IP) with anti-nNOS, anti-IgG antibody, and pre-serum, followed by immunoblotting (IB) with anti-GluR6 antibody. The same sample was also subjected to standard immunoblotting to detect the expression of GluR6 as a control. (B, D, F) Analysis of the effect of nNOS AS-ODNs, GluR6 AS-ODNs, and PSD95 AS-ODNs on the assembly of GluR6 with nNOS induced by transient brain ischemia followed by 6 h reperfusion in hippocampal CA1. Sample proteins were examined by immunoprecipitation with anti-GluR6 or anti-nNOS antibody followed by immunoblotting separately with anti-GluR6, anti-nNOS, and anti-PSD95 antibodies. (C, E, G) Corresponding bands were scanned, and their optical density (O.D.) was represented as fold change versus sham control. Data are expressed as mean ± SD ($n = 4$). $^{*}P < 0.05$ versus vehicle; $^{\#}P < 0.05$ versus sham.

More interestingly, administration of PSD95 AS-ODNs also attenuated the enhancement of the interaction between nNOS and GluR6. PSD95 is able to interact with a large number of proteins through its multiple protein interaction domains and can also multimerize to form an extended scaffold [18]. This finding therefore suggests that nNOS may bind with GluR6 through PSD95 to assemble a nNOS·PSD95·GluR6 signaling module. Further studies are needed to prove the assembly of a nNOS·PSD95·GluR6 signaling module and to determine what domain of nNOS or GluR6 mediates this binding.

Acknowledgments

This work was supported by grants from the National Natural Science Foundation of China (30870543; 31000360), the Natural Science Funds of Jiangsu Province (BK2010171; BK2010176), the Education Departmental Nature Science Funds of Jiangsu Province (09KJB310015, 10KJA310053), the Science and Technology Bureau of Xuzhou (XF10C077), the Priority Academic Program Development of Jiangsu Higher Education Institutions (PAPD), and the Qing Lan Project. Dr. Chong Li was supported by "333 Projects" and "Six Talent Peaks Program" of Jiangsu Province.

References

[1] A. Savinainen, E.P. Garcia, D. Dorow, J. Marshall, Y.F. Liu, Kainate receptor activation induces mixed lineage kinase-mediated cellular signaling cascades via post-synaptic density protein 95, J. Biol. Chem. 276 (2001) 11382–11386.
[2] D.S. Pei, X.T. Wang, Y. Liu, Y.F. Sun, Q.H. Guan, W. Wang, J.Z. Yan, Y.Y. Zong, T.L. Xu, G.Y. Zhang, Neuroprotection against ischaemic brain injury by a GluR6-9c peptide containing the TAT protein transduction sequence, Brain 129 (2006) 465–479.
[3] H. Tian, Q.G. Zhang, G.X. Zhu, D.S. Pei, Q.H. Guan, G.Y. Zhang, Activation of c-Jun NH2-terminal kinase 3 is mediated by the GluR6.PSD-95.MLK3 signaling module following cerebral ischemia in rat hippocampus, Brain Res. 1061 (2005) 57–66.
[4] D.S. Pei, Q.H. Guan, Y.F. Sun, Q.X. Zhang, T.L. Xu, G.Y. Zhang, Neuroprotective effects of GluR6 antisense oligodeoxynucleotides on transient brain ischemia/reperfusion-induced neuronal death in rat hippocampal CA1 region, J. Neurosci. Res. 82 (2005) 642–649.
[5] T. Li, H.M. Yu, Y.F. Sun, Y.J. Song, G.Y. Zhang, D.S. Pei, Inhibition of cerebral ischemia/reperfusion-induced injury by adenovirus expressed C-terminal amino acids of GluR6, Brain Res. 1300 (2009) 169–176.
[6] H.M. Yu, J. Xu, C. Li, C. Zhou, F. Zhang, D. Han, G.Y. Zhang, Coupling between neuronal nitric oxide synthase and glutamate receptor 6-mediated c-Jun N-terminal kinase signaling pathway via S-nitrosylation contributes to ischemia neuronal death, Neuroscience 155 (2008) 1120–1132.
[7] J.S. Stamler, D.I. Simon, J.A. Osborne, M.E. Mullins, O. Jaraki, T. Michel, D.J. Singel, J. Loscalzo, S-nitrosylation of proteins with nitric oxide: synthesis and characterization of biologically active compounds, Proc. Natl. Acad. Sci. USA 89 (1992) 444–448.
[8] S.R. Jaffrey, H. Erdjument-Bromage, C.D. Ferris, P. Tempst, S.H. Snyder, Protein S-nitrosylation: a physiological signal for neuronal nitric oxide, Nat. Cell. Biol. 3 (2001) 193–197.
[9] D.T. Hess, A. Matsumoto, S.O. Kim, H.E. Marshall, J.S. Stamler, Protein S-nitrosylation: purview and parameters, Nat. Rev. Mol. Cell Biol. 6 (2005) 150–166.
[10] S.R. Tannenbaum, J.E. Kim, Controlled S-nitrosylation, Nat. Chem. Biol. 1 (2005) 126–127.
[11] J.R. Steinert, T. Chernova, I.D. Forsythe, Nitric oxide signaling in brain function, dysfunction, and dementia, Neuroscientist 16 (2010) 435–452.
[12] A.F. Samdani, T.M. Dawson, V.L. Dawson, Nitric oxide synthase in models of focal ischemia, Stroke 28 (1997) 1283–1288.
[13] R.G. Keynes, J. Garthwaite, Nitric oxide and its role in ischaemic brain injury, Curr. Mol. Med. 4 (2004) 179–191.
[14] W.A. Pulsinelli, J.B. Brierley, A new model of bilateral hemispheric ischemia in the unanesthetized rat, Stroke 10 (1979) 267–272.
[15] O.H. Lowry, N.J. Rosebrough, A.L. Farr, R.J. Randall, Protein measurement with the Folin phenol reagent, J. Biol. Chem. 193 (1951) 265–275.
[16] J.E. Brenman, D.S. Chao, S.H. Gee, A.W. McGee, S.E. Craven, D.R. Santillano, Z. Wu, F. Huang, H. Xia, M.F. Peters, S.C. Froehner, D.S. Bredt, Interaction of nitric oxide synthase with the postsynaptic density protein PSD-95 and alpha1-syntrophin mediated by PDZ domains, Cell 84 (1996) 757–767.
[17] K.S. Christopherson, B.J. Hillier, W.A. Lim, D.S. Bredt, PSD-95 assembles a ternary complex with the N-methyl-D-aspartic acid receptor and a bivalent neuronal NO synthase PDZ domain, J. Biol. Chem. 274 (1999) 27467–27473.
[18] E. Kim, M. Sheng, PDZ domain proteins of synapses, Nat. Rev. Neurosci. 5 (2004) 771–781.

Biochemical and Biophysical Research Communications 420 (2012) 600–604

Contents lists available at SciVerse ScienceDirect

Biochemical and Biophysical Research Communications

journal homepage: www.elsevier.com/locate/ybbrc

Low-affinity copper transporter *CTR2* is regulated by copper-sensing transcription factor Mac1p in *Saccharomyces cerevisiae*

Lihua Liu [a,b,1], Jin Qi [a,c,1], Zemin Yang [a], Lianghong Peng [b], Chenghua Li [a,*]

[a] Center for Growth, Metabolism and Aging, College of Life Sciences, Sichuan University, Chengdu 610064, China
[b] Department of Ophthalmology, General Hospital of Guangzhou Military Command of Chinese PLA, Guangzhou 510010, China
[c] Department of Endodontics, Affiliated Hospital of Stomatology, Chongqing Medical University, Chongqing 400015, China

ARTICLE INFO

Article history:
Received 5 March 2012
Available online 16 March 2012

Keywords:
Copper homeostasis
Transporter
Yeast
Transcription factor
Mobilization

ABSTRACT

Copper is an indispensable metal for life. For convenience of genetic manipulation and sharing similar metabolic pathway of metals with mammalian cells, the yeast *Saccharomyces cerevisiae* is widely used for metal homeostasis studies. Storage and mobilization of copper ions in yeast vacuoles or mammalian lysosomes are important for cells to avoid their toxicity and elevate their utility. Though regulation of other genes involved in copper homeostasis is well understood, the regulation of gene encoding low-affinity copper transporter Ctr2p, which mediates mobilization of vacuolar or lysosomal stored copper ions, is still unclear. In this study, we found that copper depletion can upregulate yeast *CTR2* gene transcription while copper overload downregulate it. The copper-depletion induced *CTR2* transcription can be abrogated by genetic deletion of copper-sensing transcription factor Mac1p. Though absent of consensus Mac1p binding sequences, *CTR2* promoter region is demonstrated to be occupied by Mac1p, according to our results of chromatin immunoprecipitation (ChIP) assay. Overexpression of Mac1p can upregulate *CTR2* transcription and partially complement the growth defect of copper-deficient yeast strain. Taken together, our results suggest that Mac1p can activate the expression of vacuolar copper transporter Ctr2p in response to copper deficiency, resulting in yeast resistance to copper starvation.

1. Introduction

As prosthetic groups of enzymes such as copper/zinc superoxide dismutase (Cu/Zn SOD or SOD1), cytochrome *c* oxidase (CcO) and ferrous transporter 3 (Fet3p), the transition metal copper ions are indispensable for life [1,2]. Organisms ranging from bacteria and plants to mammals have developed sophisticated mechanisms to control copper homeostasis. For convenience of genetic manipulation and sharing similar metabolic pathway of metals with mammalian cells, the yeast *Saccharomyces cerevisiae* is widely used for metal homeostasis studies [1–3].

Copper uptake into the eukaryotic cell is predominantly accomplished by the high-affinity transporter Ctr1 which is very specific for Cu(I). Ctr1 is an integral membrane protein conserved from yeast to human [2,4]. The low-affinity transporter Fet4p also contributes to copper uptake in yeast [5,6]. Incorporated copper ions are delivered to their destinations under the escorting of metallochaperones including Atx1p, Cox17p and Lys7p, which target copper ions to Golgi body, mitochondria and SOD1, respectively. The concentration of intracellular free copper ions is strictly limited, and excess of them are bond to copper scavengers (such as metallothionein and glutathione) or stored in vacuoles/lysosomes [3,7–9]. When necessary, vacuolar copper can be mobilized by Ctr2p, which is a low-affinity copper transporter located at vacuolar membrane and provides copper for cytosolic metallochaperones from vacuoles [5,6,10]. The yeast strain deleted with *CTR2* (*ctr2*Δ) accumulates excess copper in the vacuole and is resistant to toxic high levels of copper [10,11]. It's recently reported that human Ctr2 is localized in late endosomes and lysosomes and mediates copper mobilization of lysosomal copper stores [12].

Genes involved in metal homeostasis are tightly regulated by the intracellular metal levels. *MAC1* (Metal-binding activator 1) encodes a transcription factor that can be inactivated by copper overload and regulates the expression of genes involved in copper transportation [13]. In response to low copper levels, Mac1p induces expression of the copper transporters Ctr1p and Ctr3p [14–16]. However, the regulation of Ctr2p expression is not clear. According to results of Culotta's group, Ctr2p cannot be suppressed by supplemented coppers in the media, and they failed to identify any consensus sequences [TTTGC(T/G)C(A/G)] for Mac1p binding in the upstream promoter region of *CTR2* [5].

* Corresponding author. Fax: +86 28 85415509.
E-mail address: lichenghua@scu.edu.cn (C. Li).
[1] These authors contribute equally to this work.

0006-291X/$ - see front matter © 2012 Elsevier Inc. All rights reserved.
http://dx.doi.org/10.1016/j.bbrc.2012.03.040

Unlike their data, we previously reported that a copper chelator, clioquinol (CQ), significantly enhances *CTR2* transcription [17], indicating that *CTR2* expression may be regulated by copper level.

In this study, we find that another copper chelator, bathocuproine disulfonate (BCS), can also upregulate *CTR2* expression, while treatment with high concentration of copper downregulates it, confirming that *CTR2* expression is controlled by copper level. Genetic ablation of *MAC1* abrogates the copper-depletion induced *CTR2* transcription, suggesting that copper regulated expression of *CTR2* may be mediated by Mac1p. Though there are no consensus Mac1p binding sequences [TTTGC(T/G)C(A/G)] in the *CTR2* promoter, our results of chromatin immunoprecipitation (ChIP) assay revealed that Mac1p can bind to this region and overexpression of Mac1p upregulates *CTR2* transcription. Ctr2p or Mac1p overexpression can partially complement the growth defect of copper-deficient yeast strains on nonfermentable media. Our results suggest that copper-sensing transcription factor Mac1p can regulate low-affinity copper transporter *CTR2* expression, likely via binding to some unknown novel sequences in *CTR2* promoter region. This regulation may make organisms survive copper starvation.

2. Materials and methods

2.1. Yeast strains and constructs

Wild type BY4742 (genotype: *MATα, his3Δ, leu2Δ, lys2Δ, ura3Δ*), *ace1Δ* (BY4742 background; genotype: *MATα, his3Δ, leu2Δ, lys2Δ, ura3Δ, ace1Δ::KanMX4*) and *ctr1Δ* (BY4742 background; genotype: *MATα, his3Δ, leu2Δ, lys2Δ, ura3Δ, ctr1Δ::KanMX4*) were bought from Invitrogen. *mac1Δ* (BY4742 background; genotype: *MATα, his3Δ, leu2Δ, lys2Δ, ura3Δ, mac1-Δ::URA3*) and *ctr1Δ, ctr2Δ* (BY4742 background; genotype: *MATα, his3Δ, leu2Δ, lys2Δ, ctr1Δ::KanMX4, ctr2Δ::URA3*) were constructed previously and stored in our laboratory [17].

Coding regions of yeast *MAC1* and *CTR2* genes were each cloned into a modified pRS315 vector (Invitrogen), pADH1-Flag/LEU2, in which Mac1p or Ctr2p was tagged with a FLAG epitope at the C terminus and controlled by an ADH1 promoter. All the constructs were verified by sequencing. Plasmids were amplified in *Escherichia coli* DH5α and extracted with Plasmid DNA mini-prep kit (Sangon, Shanghai, China). Mac1 or Ctr2 expression constructs, or their vector control were transformed into yeast of desired background by standard lithium acetate method [18]. Genotypes of resulting overexpression yeast trains were as follows: BY4742/Mac1, *MATα, his3Δ, lys2Δ, ura3Δ*, (*pADH1-Mac1-Flag/LEU2*); BY4742/Vector, *MATα, his3Δ, lys2Δ, ura3Δ*, (*pADH1-Flag/LEU2*); *ctr1*Δ /Ctr2, *MATα, his3Δ, lys2Δ, ctr1*Δ::*KanMX4*, (*pADH1-Ctr2-Flag/LEU2*); *ctr1*Δ /Mac1, *MATα, his3Δ, lys2Δ, ctr1*Δ::*KanMX4*, (*pADH1-Mac1-Flag/LEU2*); *ctr1*Δ *ctr2*Δ/Mac1, *MATα, his3Δ, lys2Δ, ctr1*Δ::*KanMX4, ctr2Δ*::*URA3*, (*pADH1-Mac1-Flag/LEU2*); *ctr1*Δ *ctr2*Δ/Ctr2, *MATα, his3Δ, lys2Δ, ctr1*Δ::*KanMX4, ctr2Δ*::*URA3*, (*pADH1-Ctr2-Flag/LEU2*); *ctr1*Δ *ctr2*Δ/Vector, *MATα, his3Δ, lys2Δ, ctr1*Δ::*KanMX4, ctr2Δ*::*URA3*, (*pADH1-Flag/LEU2*).

2.2. Yeast culture and growth conditions

Standard yeast media and growth conditions were used [19]. Plate assay was carried out as described previously [17]. In brief, 10^5 or 10^4 yeast cells were spotted onto YPD [1% (w/v) yeast extract, 2% (w/v) peptone, 2% (w/v) dextrose, 3% (w/v) agar] or YPG (substituting dextrose with glycerol) plates.

Wild type BY4742, *mac1*Δ, or *ace1*Δ yeast cells grown in liquid YPD [1% (w/v) yeast extract, 2% (w/v) peptone, 2% (w/v) dextrose] to midlog phase was 1:1 inoculated into fresh liquid YPD, and indicated chemicals was supplemented [17]. For strain of wild type BY4742 transformed with Mac1 or its vector control, the medium was substituted with liquid SD-Leu (Genmed, USA). Experiments were performed in triplicates. 5 h later, cells were harvested and subjected to qRT-PCR or ChIP assay.

2.3. Quantitative reverse transcription-polymerase chain reaction (qRT-PCR)

RNAs were extracted with hot phenol method [17] and digested with RNase-free DNaseI to remove genomic DNA contamination. Reverse transcription with Superscript III Reverse Transcriptase (Invitrogen) was performed as described in the instruction. Quantitative PCR experiments were carried out on a 7300 ABI instrument (Invitrogen) using the standard PCR protocol (denaturation at 95 °C and annealing/extension at 60 °C) with the addition of a final dissociation step to ensure amplicon-specific detection by SYBR Green. Samples were prepared by adding cDNA to SYBR Green PCR Master Mix (Applied) using the following primers: GGTGCACACGCGTGGCTTTT and CTGTGGTCGTGGCCCGCATT for *CTR2*; ATTGCTGTTGCCGATACCACTTC and GTCGCGCTCTATGTTTGCTTGAT for *CTR1*; TTTGGTTCCGGTGTTATTGTTGC and CCCCAGTTACCGGTTTGTCCTAC for *ZRT1*. We chose *ACT1* as a reference gene because it has a very low variation coefficient under different conditions. Its primers were as follows: TCCGGTGATGGTGTTACTCA and GGCCAAATCGATTCTCAAAA.

2.4. Chromatin immunoprecipitation (ChIP)

Chromatin Immunoprecipitation was carried out as previously described [20]. Cells were grown to mid log phase in SD-Leu medium and crosslinked with formaldehyde. After cell lysis by vortexing with glass beads and ultrasonication to shear DNA, 20% of cell lysate was directly subjected to DNA extraction and used as input control. The remainder (about 500 μg of protein) was divided into two equal halves for immuno-precipitation with IgG Sepharose beads (GE Healthcare) plus 3 μg of M2 Flag mouse monoclonal antibody (Sigma) or normal mouse IgG (as negative control), respectively. The precipitated and extracted DNA was used for PCR with primers for the *CTR2* promoter region. The primers were as follows: AGACTCTTTCGCTGCCAACTG and ATTCTTCTTCGATTCTCAACA.

2.5. Statistical analysis

Data are shown as means ± standard deviations (SD). *P*-values were calculated using the Student's *t* test.

3. Results

3.1. mRNA level of Ctr2 is regulated by copper level

Ctr2p is a low-affinity copper transporter located at vacuolar membrane. According to other's results, neither 0.15 nor 1 μM copper supplemented into the media could suppress Ctr2p expression in yeast [5]. However, our previous data showed that a lipophilic copper chelator, clioquinol, could significantly upregulate Ctr2p expression [17]. This indicates that, like high-affinity copper transporter Ctr1p, expression of Ctr2p may be induced by copper depletion.

To confirm that expression of Ctr2p can be controlled by copper level, we treated wild type yeast strain, BY4742, with 40 μM BCS (bathocuproine disulfonate), which is a hydrophilic copper chelator, or 100 μM $CuCl_2$. Quantitative reverse transcription-polymerase chain reaction (qRT-PCR) results (Fig. 1) show that, like *CTR1*, *CTR2* is upregulated by BCS and downregulated by copper. As a

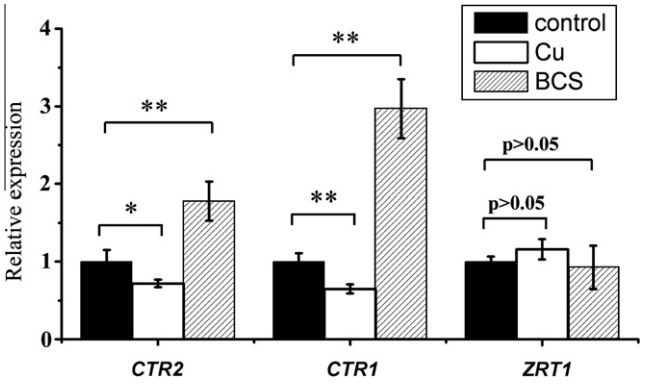

Fig. 1. mRNA level of *CTR2* is regulated by copper level. Wild type BY4742 cells treated with 100 μM CuCl2 or 40 μM BCS were subjected to qRT-PCR for *CTR2*, *CTR1* (copper-responsive control) and *ZRT1* (copper-unresponsive control) genes, using *ACT1* as a reference gene. Relative expression levels of the three genes in untreated controls were respectively set as 1. $^{*}p < 0.05$; $^{**}p < 0.01$; unpaired *t* test, $n = 3$.

copper-unresponsive control, mRNA level of high-affinity transporter *ZRT1* is not significantly changed by either BCS or copper. This reveals that, like *CTR1*, *CTR2* can also be upregulated by copper depletion and downregulated by copper overload.

3.2. Deletion of MAC1 gene abrogates copper-depletion induced CTR2 expression

Two transcription factors, Mac1p and Ace1p (also called Cup2p), are reported to sense the intracellular copper level and regulate transcription of genes involved in copper homeostasis [14–16,21–23]. To identify the factor mediating the regulation of *CTR2*, we used the yeast strains with genetic ablation of these two transcription factors, *mac1*Δ and *ace1*Δ, respectively. qRT-PCR results (Fig. 2) demonstrate that genetic deletion of *MAC1*, but not *ACE1*, abrogates CQ induced upregulation of *CTR2* expression. This suggests that copper-depletion induced *CTR2* expression is mediated by Mac1p.

3.3. Mac1p binds to the upstream promoter region of CTR2 and upregulates its expression

To check if transcription factor Mac1p can directly bind to the upstream promoter region of *CTR2*, we generated a yeast strain

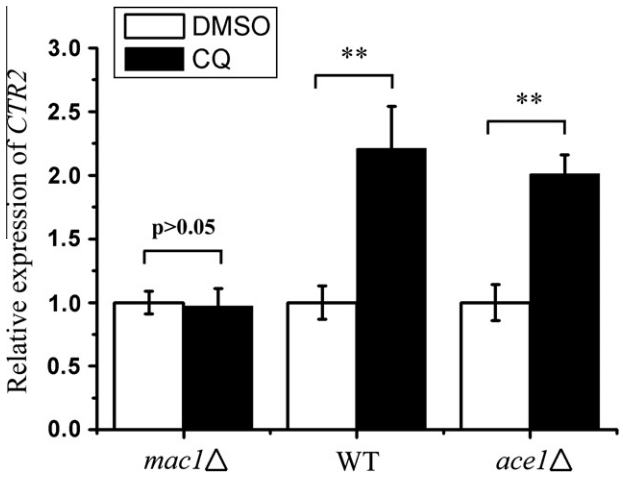

Fig. 2. Deletion of *MAC1* gene abrogates copper-depletion induced *CTR2* expression. BY4742 (WT), *mac1Δ*, and *ace1Δ* cells treated with 80 μM CQ were subjected to qRT-PCR for *CTR2*, using *ACT1* as a reference gene. DMSO treatment was used as vehicle control of CQ. Relative expression level of *CTR2* in vehicle control was set as 1. $^{**}p < 0.01$; unpaired *t* test, $n = 3$.

constitutively overexpressing Mac1-Flag fusion protein, BY4742/Mac1, and subjected it to chromatin immunoprecipitation (ChIP) with Flag antibody. The results (Fig. 3A) demonstrate that DNA fragment of the upstream promoter region of *CTR2* can be detected in products precipitated with Flag antibody, indicating that Mac1p directly binds to the upstream promoter region of *CTR2*. Further study (Fig. 3B) demonstrates that, like *CTR1*, *CTR2* is also upregulated by overexpression of Mac1p. As a negative control, *ZRT1* is not significantly affected by Mac1p overexpression. These results indicate that *CTR2* is a downstream target of transcription factor Mac1p.

3.4. Either Ctr2p or Mac1p partially complements growth defect of copper-deficient yeast strains

Incorporation of copper ions into yeast cells is predominantly accomplished by two high-affinity copper transporters, Ctr1p and Ctr3p. But *CTR3* gene is interrupted by insertion of a Ty2 element in some laboratory strains including BY4742, which is used in this work [1,24]. So *ctr1*Δ under BY4742 background is deficient in mitochondrial respiration resulting from copper deficiency [4,24]. It was reported that Ctr2p can mobilize copper stored in vacuole and enhance yeast growth under copper starvation [10,11]. To test if the regulation of *CTR2* by Mac1p can restore the respiration in copper-deficient yeast cells, yeast strains overexpressing *MAC1* or *CTR2* under background of *ctr1*Δ or *ctr1*Δ *ctr2*Δ were spotted on nonfermentable media YPG. As shown in Fig. 4, *ctr1*Δ and *ctr1*Δ *ctr2*Δ yeast trains cannot grow on YPG due to mitochondrial respiration defects though they grow well on YPD; exogenous overexpression of *CTR2* can partially rescue the growth defect of *ctr1*Δ on YPG media, and *MAC1* can mimic it; however, under *ctr1*Δ *ctr2*Δ background, only exogenous *CTR2*, but not *MAC1*, can restore the growth. This implies that copper sensing transcription factor Mac1p can restore mitochondrial respiration under copper starvation to make yeast cells survive, via enhancing Ctr2p expression and thus mobilizing vacuolar stored copper ions.

4. Discussion

Copper is an essential trace metal involved in many biological processes, especially in mitochondrial respiration. However, high concentration of intracellular free copper ion is toxic. So copper metabolism in the cell is tightly controlled [1]. Constant concentration of cytosolic free copper ions is kept via three ways: (1) Regulation of plasma-membrane transporters. In yeast, two high-affinity transporters, Ctr1p and Ctr3p, are regulated by the intracellular copper status. When the cell is copper deficient, the copper sensing transcription factor Mac1p will be activated to upregulate *CTR1* and *CTR3* [13,25]. There are also reports that Ctr1p is prone to degrade under copper overload condition [26,27]. (2) Scavenging system for excess metal ions. A large part of copper ions incorporated into cells are buffered by metal scavenging system including glutathione and metallothionein to prevent their toxic accumulation [7–9]. Transcription of yeast metallothionein encoding genes, *CUP1* and *CRS5* are specifically induced by the copper-dependent transcription activator Ace1p in response to high levels of copper ions [21–23]. (3) Storage or mobilization of metal. Vacuoles in yeast or lysosomes in mammalian cells play critical roles in metal homeostasis [28]. Excess of copper ions are stored in this compartment to avoid the toxic high level of cytosolic copper ions. These stored copper ions can be mobilized and utilized when necessary. The mobilization of vacuolar copper ions is mediated by low-affinity copper transporter Ctr2p [10,12].

Though it is well understood that genes encoding plasma-membrane copper transport system and scavenging system are tightly

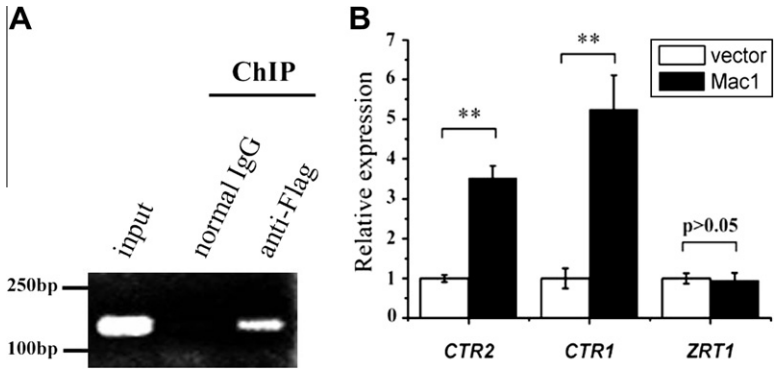

Fig. 3. Mac1p binds to the upstream promoter region of *CTR2* and upregulates its expression. (A) BY4742 overexpressing Mac1-Flag fusion protein (BY4742/Mac1) was subjected to ChIP-PCR. (B) BY4742/Mac1 (Mac1) or BY4742/vector (vector) was subjected to qRT-PCR for *CTR2*, *CTR1* and *ZRT1*, using *ACT1* as a reference gene. Relative expression levels of the three genes in vector controls were respectively set as 1. $^{**}p < 0.01$; unpaired *t* test, $n = 3$.

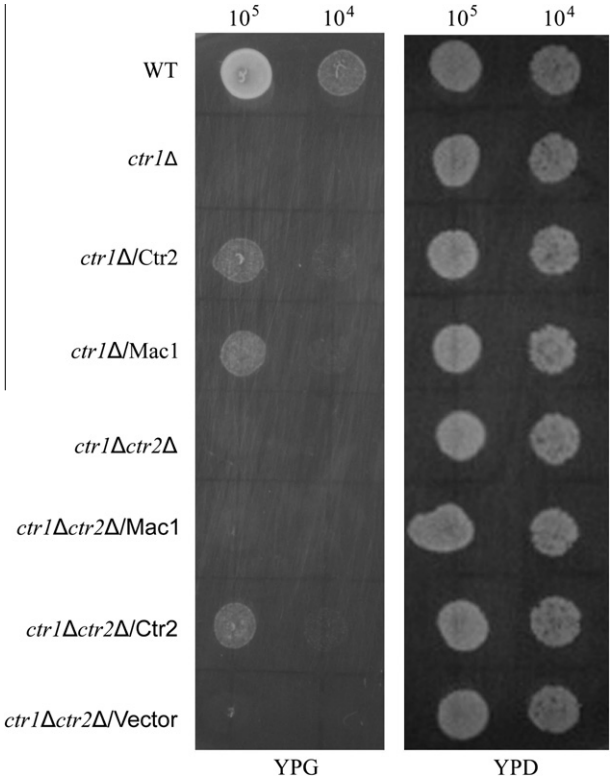

Fig. 4. Exogenous overexpression of either *CTR2* or *MAC1* partially complements growth defect of copper-deficient yeast strains. Wild type (WT), copper-deficient mutant yeast strains (*ctr1Δ*, *ctr1Δctr2Δ*), or mutants overexpressing *CTR2* (*ctr1Δ*/Ctr2, *ctr1Δctr2Δ*/Ctr2) or *MAC1* (*ctr1Δ*/Mac1, *ctr1Δctr2Δ*/Mac1), were grown on YPG or YPD (as growth control) plates. 10^5 or 10^4 cells were spotted.

controlled by copper-dependent transcription factors Mac1p and Ace1p, respectively, according to the intracellular copper level, the regulation of vacuolar copper transporter Ctr2p remains unclear [13,21–23,25]. In our study, copper chelators, either CQ or BCS, can upregulate *CTR2* transcription, while high concentration of added copper ions can downregulate it. Further study demonstrated that genetic deletion of *MAC1*, but not *ACE1*, can abolish the copper depletion induced *CTR2* upregulation. Mac1p has been reported to bind to promoter regions of *CTR1*, *CTR2*, *FRE1* and *FRE7*. The consensus Mac1p binding sequences in these promoters were summarized as TTTGC(T/G)C(A/G). Although absent of these consensus sequences in the *CTR2* promoter, our ChIP results revealed that Mac1p can directly bind to this region, indicating the presence of Mac1p binding sites other than known binding sequences. It might be meaningful to investigate the precise binding sites of Mac1p in *CTR2* promoter region, so as to further understand the regulation of this copper sensing transcription factor. Given that Mac1p regulation is not sensitive to elevated copper level [16], 1 μM supplemented copper ions in the study of Culotta's group might be not sufficient to suppress the expression of *CTR2* [5]. Mac1p upregulated *CTR2* expression under copper deficient condition may be beneficial for the cells to mobilize vacuolar stored copper ions to meet the copper requirement for biological processes, such as mitochondrial respiration.

Acknowledgments

This work was supported by National Natural Science Foundation of China (#31100982), Research Foundation for the Doctoral Program, Ministry of Education of China (#20110181120082), and Priming Scientific Research Foundation for the Junior Teachers in Sichuan University (#2010SCU11068).

References

[1] J. De Freitas, H. Wintz, J.H. Kim, H. Poynton, T. Fox, C. Vulpe, Yeast, a model organism for iron and copper metabolism studies, Biometals 16 (2003) 185–197.
[2] H. Kozlowski, A. Janicka-Klos, J. Brasun, E. Gaggelli, D. Valensin, G. Valensin, Copper, iron, and zinc ions homeostasis and their role in neurodegenerative disorders (metal uptake, transport, distribution and regulation), Coord. Chem. Rev. 253 (2009) 2665–2685.
[3] T.D. Rae, P.J. Schmidt, R.A. Pufahl, V.C. Culotta, T.V. O'Halloran, Undetectable intracellular free copper: the requirement of a copper chaperone for superoxide dismutase, Science 284 (1999) 805–808.
[4] B. Zhou, J. Gitschier, hCTR1: a human gene for copper uptake identified by complementation in yeast, Proc. Natl. Acad. Sci. U. S. A. 94 (1997) 7481–7486.
[5] M.E. Portnoy, P.J. Schmidt, R.S. Rogers, V.C. Culotta, Metal transporters that contribute copper to metallochaperones in *Saccharomyces cerevisiae*, Mol. Genet. Genomics 265 (2001) 873–882.
[6] R. Hassett, D.R. Dix, D.J. Eide, D.J. Kosman, The Fe(II) permease Fet4p functions as a low affinity copper transporter and supports normal copper trafficking in *Saccharomyces cerevisiae*, Biochem. J. 351 (Pt 2) (2000) 477–484.
[7] D.H. Hamer, Metallothionein, Annu. Rev. Biochem. 55 (1986) 913–951.
[8] J.H. Freedman, M.R. Ciriolo, J. Peisach, The role of glutathione in copper metabolism and toxicity, J. Biol. Chem. 264 (1989) 5598–5605.
[9] A.R. White, A.I. Bush, K. Beyreuther, C.L. Masters, R. Cappai, Exacerbation of copper toxicity in primary neuronal cultures depleted of cellular glutathione, J. Neurochem. 72 (1999) 2092–2098.
[10] E.M. Rees, J. Lee, D.J. Thiele, Mobilization of intracellular copper stores by the ctr2 vacuolar copper transporter, J. Biol. Chem. 279 (2004) 54221–54229.
[11] K. Kampfenkel, S. Kushnir, E. Babiychuk, D. Inze, M. Van Montagu, Molecular characterization of a putative Arabidopsis thaliana copper transporter and its yeast homologue, J. Biol. Chem. 270 (1995) 28479–28486.
[12] P.V. van den Berghe, D.E. Folmer, H.E. Malingre, E. van Beurden, A.E. Klomp, B. van de Sluis, M. Merkx, R. Berger, L.W. Klomp, Human copper transporter 2 is localized in late endosomes and lysosomes and facilitates cellular copper uptake, Biochem. J. 407 (2007) 49–59.

[13] J. Jungmann, H.A. Reins, J. Lee, A. Romeo, R. Hassett, D. Kosman, S. Jentsch, MAC1, a nuclear regulatory protein related to Cu-dependent transcription factors is involved in Cu/Fe utilization and stress resistance in yeast, EMBO J. 12 (1993) 5051–5056.
[14] J.A. Graden, D.R. Winge, Copper-mediated repression of the activation domain in the yeast Mac1p transcription factor, Proc. Natl. Acad. Sci. U. S. A. 94 (1997) 5550–5555.
[15] S. Labbe, Z. Zhu, D.J. Thiele, Copper-specific transcriptional repression of yeast genes encoding critical components in the copper transport pathway, J. Biol. Chem. 272 (1997) 15951–15958.
[16] C. Gross, M. Kelleher, V.R. Iyer, P.O. Brown, D.R. Winge, Identification of the copper regulon in *Saccharomyces cerevisiae* by DNA microarrays, J. Biol. Chem. 275 (2000) 32310–32316.
[17] C. Li, J. Wang, B. Zhou, The metal chelating and chaperoning effects of clioquinol: insights from yeast studies, J. Alzheimers Dis. 21 (2010) 1249–1262.
[18] R.D. Gietz, R.H. Schiestl, Applications of high efficiency lithium acetate transformation of intact yeast cells using single-stranded nucleic acids as carrier, Yeast 7 (1991) 253–263.
[19] F. Sherman, Getting started with yeast, Methods Enzymol. 194 (1991) 3–21.
[20] L.K. Wood, D.J. Thiele, Transcriptional activation in yeast in response to copper deficiency involves copper-zinc superoxide dismutase, J. Biol. Chem. 284 (2009) 404–413.
[21] D.J. Thiele, ACE1 regulates expression of the *Saccharomyces cerevisiae* metallothionein gene, Mol. Cell. Biol. 8 (1988) 2745–2752.
[22] C. Buchman, P. Skroch, J. Welch, S. Fogel, M. Karin, The CUP2 gene product, regulator of yeast metallothionein expression, is a copper-activated DNA-binding protein, Mol. Cell. Biol. 9 (1989) 4091–4095.
[23] J. Welch, S. Fogel, C. Buchman, M. Karin, The CUP2 gene product regulates the expression of the CUP1 gene, coding for yeast metallothionein, EMBO J. 8 (1989) 255–260.
[24] S.A. Knight, S. Labbe, L.F. Kwon, D.J. Kosman, D.J. Thiele, A widespread transposable element masks expression of a yeast copper transport gene, Genes Dev. 10 (1996) 1917–1929.
[25] D.R. Winge, L.T. Jensen, C. Srinivasan, Metal-ion regulation of gene expression in yeast, Curr. Opin. Chem. Biol. 2 (1998) 216–221.
[26] C.E. Ooi, E. Rabinovich, A. Dancis, J.S. Bonifacino, R.D. Klausner, Copper-dependent degradation of the *Saccharomyces cerevisiae* plasma membrane copper transporter Ctr1p in the apparent absence of endocytosis, EMBO J. 15 (1996) 3515–3523.
[27] M.M. Pena, S. Puig, D.J. Thiele, Characterization of the *Saccharomyces cerevisiae* high affinity copper transporter Ctr3, J. Biol. Chem. 275 (2000) 33244–33251.
[28] D.J. Klionsky, P.K. Herman, S.D. Emr, The fungal vacuole: composition, function, and biogenesis, Microbiol. Rev. 54 (1990) 266–292.

Biochemical and Biophysical Research Communications 420 (2012) 605–610

Contents lists available at SciVerse ScienceDirect

Biochemical and Biophysical Research Communications

journal homepage: www.elsevier.com/locate/ybbrc

The p53 inhibitor, pifithrin-α, suppresses self-renewal of embryonic stem cells

Essam Mohamed Abdelalim [a,b,*], Ikuo Tooyama [a]

[a] Molecular Neuroscience Research Center, Shiga University of Medical Science, Setatsukinowa-cho, Otsu, Shiga 520-2192, Japan
[b] Department of Cytology and Histology, Faculty of Veterinary Medicine, Suez Canal University, Ismailia 41522, Egypt

ARTICLE INFO

Article history:
Received 3 March 2012
Available online 16 March 2012

Keywords:
ES cells
Tumor suppressor gene
Nanog
Cyclin D1
Proliferation

ABSTRACT

Recent studies have reported the role of p53 in suppressing the pluripotency of embryonic stem (ES) cells after DNA damage and blocking the reprogramming of somatic cells into induced pluripotent stem (iPS) cells. However, to date no evidence has been presented to support the function of p53 in unstressed ES cells. In this study, we investigated the effect of pifithrin (PFT)-α, an inhibitor of p53-dependent transcriptional activation, on self-renewal of ES cells. Our results revealed that treatment of ES cells with PFT-α resulted in the inhibition of ES cell propagation in a dose-dependent manner, as indicated by a marked reduction in the cell number and colony size. Also, PFT-α caused a cell cycle arrest and significant reduction in DNA synthesis. In addition, inhibition of p53 activity reduced the expression levels of cyclin D1 and Nanog. These findings indicate that p53 pathway in ES cells rather than acting as an inactive gene, is required for ES cell proliferation and self-renewal under unstressful conditions.

1. Introduction

Embryonic stem (ES) cells are a unique population of stem cells which are derived from the inner cell mass of the blastocyst [1]. Unlike somatic cells, ES cells are spontaneously immortal and appear able to indefinite self-renewal while retaining their wide range differentiation potential. They exhibit a very unusual cell cycle structure, characterized by a short G1 phase and a high proportion of cells in the S phase [2], which is associated with a unique mechanism of cell cycle regulation.

An emerging role for p53 in regulating differentiation and self-renewal of ES cells [3–6] as well as its role in the reprogramming process of induced pluripotent stem (iPS) cells [7–9] has generated great interest. Conflicting reports of p53 localization and activity has been reported in ES cells in response to DNA damage. Earlier report demonstrated that ES cells express high levels of p53, which is functionally active as determined by its ability to bind DNA specifically and to activate transcription of target genes [10]. In contrast, another study reported that mouse ES cells do not activate p53-dependent DNA damage response and undergo p53-independent apoptosis in response to ionizing radiation [11]. Some reports indicate that murine ES cells express stable p53 protein at high levels under basal conditions, which is localized in the cytoplasm [12,13] even under conditions of DNA damage [12]. Recent studies reported that p53 can successfully translocate to the nucleus after DNA damage [3–5]. These reports indicate that ES cells respond to DNA damage by activation of p53, inducing differentiation of ES cells by directly suppressing Nanog expression in mouse ES cells [3], and human ES cells [4,5]. Surprisingly, a recent report indicates an antidifferentiation function of p53 in murine ES cells through directly regulating the Wnt signaling pathway, which suggest that p53 may regulate both prodifferentiation and antidifferentiation program in murine ES cells [14].

Nanog is required for the self-renewal of ES cells and counteracts removal of LIF [15,16]. Furthermore, reduction of Nanog expression in ES cells leads to spontaneous differentiation of ES cells [16]. However, recent reports have demonstrated that transient down regulation of Nanog predisposes ES cells towards differentiation but does not mark commitment, and *Nanog* null ES cells expand, colonize embryonic germ layers and exhibit multilineage differentiation both in fetal and adult chimeras [17].

It was first proposed that p53 is functional only during DNA damage in ES cells. As no role has been established for p53 in unstressed ES cells, we aimed to inhibit the p53 activity in ES cells using a p53-specific inhibitor pifithrin (PFT)-α and examined its effect on ES cell self-renewal. The data presented here show that p53 is required for ES cell proliferation.

2. Material and methods

2.1. Embryonic stem cell culture

Murine ES cells (E14TG2a) (CRL-1821; American Type Culture Collection, Manassas, VA) were maintained in DMEM/F-12

* Corresponding author at: Department of Cytology and Histology, Faculty of Veterinary Medicine, Suez Canal University, Ismailia 41522, Egypt. Fax: +20 643207052.
E-mail address: essam_abdelalim@yahoo.com (E.M. Abdelalim).

0006-291X/$ - see front matter © 2012 Elsevier Inc. All rights reserved.
http://dx.doi.org/10.1016/j.bbrc.2012.03.041

medium (Sigma) that was supplemented with 1000 U/mL LIF (Chemicon), 11% fetal bovine serum, 2 mM L-glutamine (Nacalai Tesque, Japan), 1 mM sodium pyruvate (Sigma), 1% MEM nonessential amino acids (GIBCO), 0.1 mM 2-mercaptoethanol (Sigma) and 1% penicillin–streptomycin. Murine ES cells were cultured under feeder-free conditions in the presence of LIF. Pifithrin-α (Sigma) was added to the cultured ES cells at 10 μM, and 20 μM, while the control cells received vehicle alone (DMSO).

2.2. Western blotting

Total protein extracts were prepared from ES cells, dissolved in SDS–PAGE buffer, and transferred to nitrocellulose membranes (Amersham Biosciences, Freiburg, Germany). Proteins were detected using antibodies against Oct4 (1:1000, sc-5279; Santa Cruz Biotechnology), Nanog (1:8000, A300-397A; Bethyl Laboratories), cyclin D1 (1:1000, sc-450; Santa Cruz Biotechnology) and β-actin (1:8000, sc-47778; Santa Cruz Biotechnology). The secondary antibodies were peroxidase-conjugated anti-rabbit IgG or peroxidase-conjugated anti-mouse IgG (all 1:10,000; Jackson ImmunoResearch Lab, Inc.). The blots were developed using SuperSignal West Pico Chemiluminescent substrate (Pierce), and visualized using an LAS-3000 FujiFilm Lumino-Image Analyzer (FujiFilm, Tokyo, Japan).

2.3. Alkaline phosphatase (AP) activity assay

To determine the ability of ES cells to retain an undifferentiated phenotype, alkaline phosphatase (AP) activity assays were performed using an AP kit (Chemicon) as previously described [18].

2.4. Cell cycle analysis

The cells were fixed overnight in 70% ethanol at 4 °C. Enzymatic removal of RNA was carried out using 100 μg/mL RNase (Boehringer Mannheim GmbH, Mannheim, Germany) at room temperature for 20 min. The cells were then stained with 5 μg/mL propidium iodide (Sigma) at 4 °C for 40 min. Flow cytometric analysis was carried out on 20,000 gated events. Data acquisition was performed using a FACSCalibur (BD Biosciences) and the cell cycle phase distribution was analyzed using ModFit LT flow cytometry modeling software (Verity Software House, Topsham, ME).

2.5. Bromodeoxyuridine (BrdU) incorporation

The level of BrdU incorporation was measured together with the DNA content as previously described [19]. Briefly, ES cells 24 h after PFT-α treatment were pulsed (45 min) with BrdU (1:100; Invitrogen). ES cells were dispersed into single cells; the cells were fixed overnight in 70% ethanol at 4 °C. DNA denaturation was subsequently performed by incubation in 1 N HCl for 20 min at room temperature. The cells then washed and incubated with 0.1 M sodium tetraborate for 10 min at room temperature. The cells were incubated with Alexa Fluor 488-conjugated mouse anti-BrdU antibody (1:100; Molecular Probes) in 2% BSA-PBS for 2 h at 4 °C. The cells were then incubated with 100 μg/mL RNase (Boehringer Mannheim) for 15 min, followed by 40 min of incubation in freshly prepared PI (5 μg/mL). At least 10,000 cells events were recorded for each sample using a FACSCalibur (BD Biosciences) and analyzed using the CellQuest program. The samples were subjected to two-parameter dot plot histogram analysis (BrdU incorporation *vs*. DNA content).

2.6. Cell proliferation assay

In order to determine the number of cells, the cells were washed with PBS and trypsinized from the culture dishes. The cell suspension was mixed with tryphan blue solution, and the number of live cells was determined using a haemocytometer. Cells failing to exclude the dye were considered nonviable. Adherent ES cell colonies stained with crystal violet.

2.7. Statistical analysis

The results are expressed as mean ± standard deviation, as indicated in the figure legends. Statistical significance was assessed by two-tailed Student's *t*-tests. Values of $P < 0.05$ were considered significant.

3. Results

3.1. PFT-α induces growth arrest of ES cells

It has been reported that murine ES cells express high levels of p53 [10,11,13]. Therefore, in this study, we investigated the function of endogenous p53 in undifferentiated murine ES by inhibiting p53 activity with PFT-α, a selective inhibitor of p53 transcriptional activity [20–22]. To determine the effect of PFT-α on ES cell proliferation and cell cycle progression, ES cells were treated with PFT-α at a concentration of 10 μM and 20 μM. Treatment of ES cells with PFT-α for 24 or 48 h significantly reduced the number and colony size of the ES cells in a dose dependent manner, as compared with the ES cells that were treated with the DMSO (Fig. 1A, B).

To examine the effect of inhibition of p53 activity on self-renewal at the single cell level, ES cells were seeded at low density in the presence of LIF and treated with PFT-α for 5 days to form secondary ES cell colonies. The number of formed colonies of PFT-α-treated ES cells was significantly reduced in comparison to those of DMSO-treated cells (Fig. 1C). We also evaluated colony morphology and AP activity in ES cells cultured in the presence of LIF. The AP-staining, which is indicative of the undifferentiated property of ES cells, was not affected in ES cells treated with PFT-α in comparison to those treated with DMSO (Fig. 1D). These findings suggest that p53 activity in unstressed ES cells is required for their propagation *in vitro*.

To validate further the observed decrease in ES cell proliferation after inhibition of p53 activity, PFT-α and DMSO-treated cells were exposed to bromo-deoxyuridine (BrdU), and its incorporation into ES cells was quantified by flow cytometry. ES cells were examined 24 h after PFT-α treatment and following pulsed incorporation of BrdU (45 min). Flow cytometric analysis of BrdU, which was performed concurrent with the analysis of the cellular DNA content, showed a reduction in BrdU incorporation in ES cells treated with PFT-α in a dose dependent manner in comparison to those of DMSO-treated cells (Fig. 2A, B), suggesting the role of p53 in promoting DNA synthesis in ES cells under normal growth conditions.

3.2. PFT-α leads to cell cycle arrest of ES cells

Next, we examined whether the progression of the ES cell cycle changed in response to PFT-α treatment. Flow cytometric analysis of DNA content showed that the distribution of cells in cell cycle phases changed after PFT-α treatment (Fig. 2C, D). Whereas DMSO-treated cells showed normal cell cycle profile, then after PFT-α treatment we found fewer cells in G2/M phases and increased number of cells in the G1 phase. Higher concentration of PFT-α resulted in a higher number of cells in the G1 phase and fewer cells in the G2/M phases (Fig. 2C, D). Thus, inhibition of p53 activity suppresses ES cell proliferation by blocking cell cycle progression in G1 phase.

To further understand how inhibition of p53 activity could affect on the cell cycle progression, we performed western blot

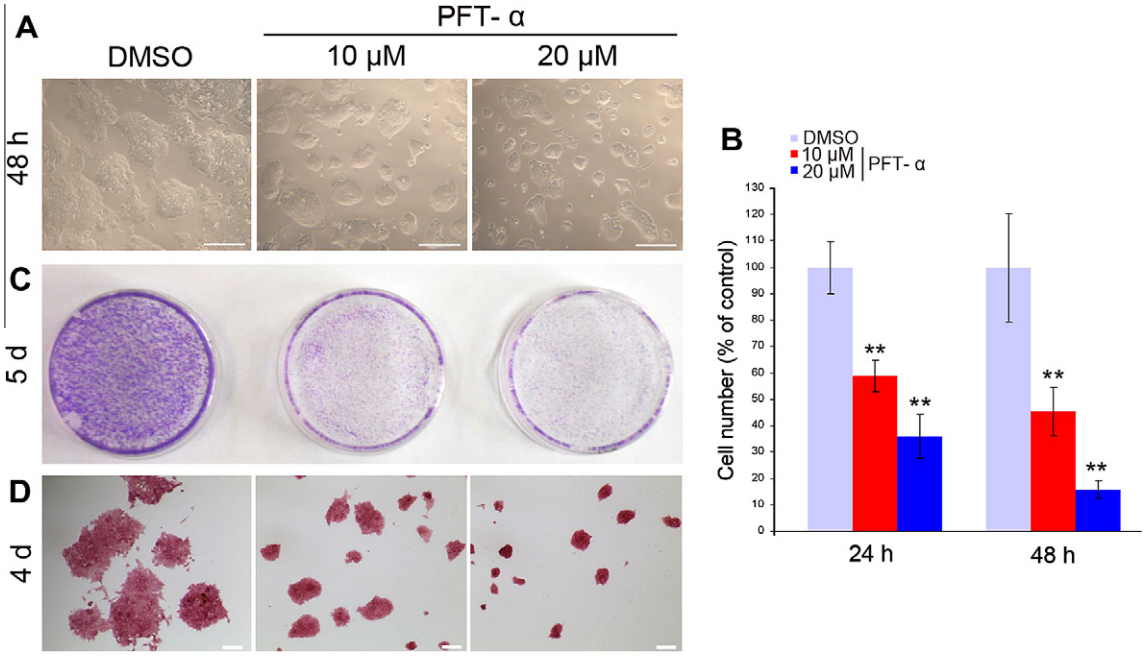

Fig. 1. Inhibition of p53 activity by PFT-α suppresses the self-renewal of murine ES cells. (A) Morphologies of murine ES cells 48 h after treatment with PFT-α (10 μM and 20 μM) or vehicle (DMSO). (B) Quantification of ES cells treated as in A after 24 h and 48 h. (C) Photographs of the formed colonies after 5 days from the treatment of ES cells as in A, stained with crystal violet. (D) Alkaline phosphatase (AP) staining of ES cells 4 days after treatment with PFT-α as in A. Data represent mean ± s.d ($n = 3$); $^{*}P < 0.05$ or $^{**}P < 0.01$ (two-tailed t-test). Scale bar = 100 μM.

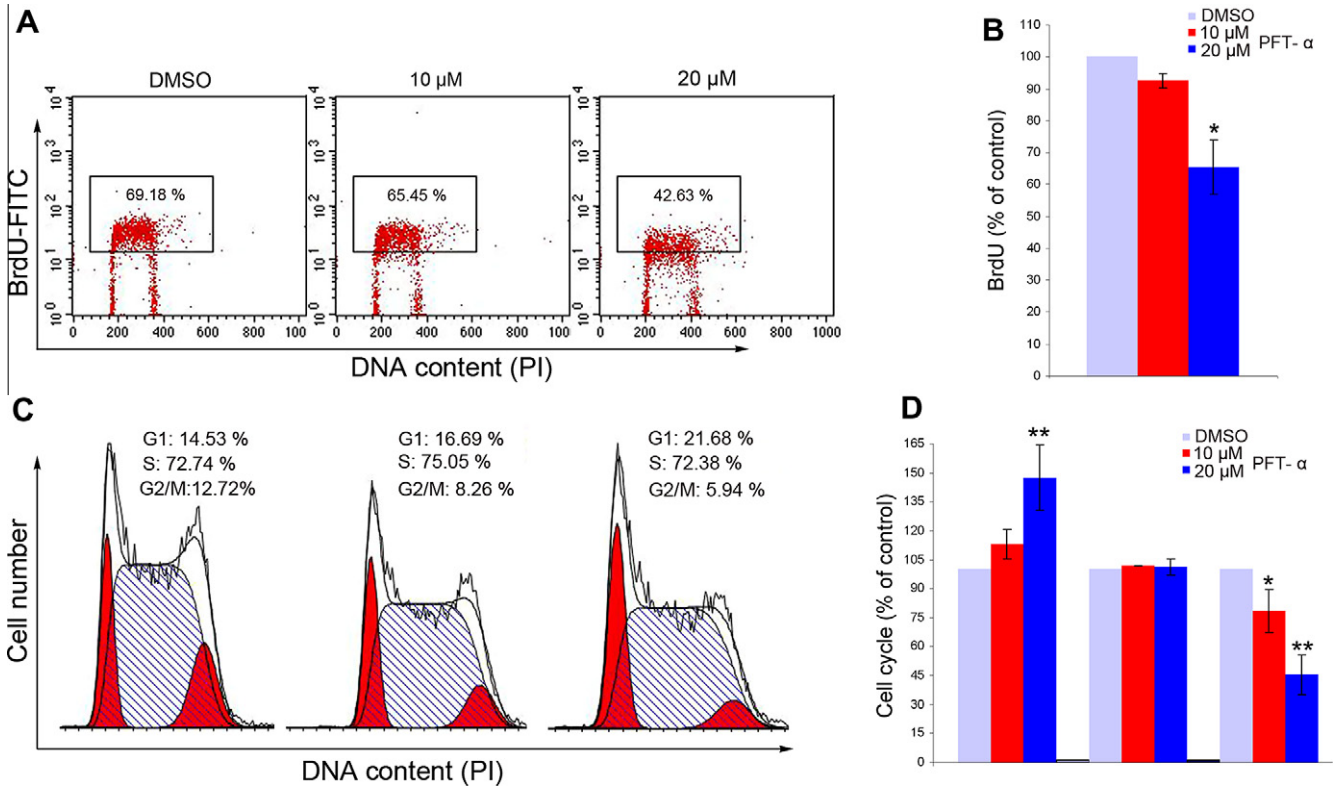

Fig. 2. Effects of PFT-α on DNA synthesis and cell cycle of ES cells. (A) Flow cytometric analysis of BrdU incorporation in ES cells treated with the DMSO or PFT-α (10 μM and 20 μM). x-axis, DNA content, as shown by propidium iodide (PI) binding; y-axis, BrdU uptake after 45 min of exposure. (B) Quantitative analysis of the BrdU incorporation shown in A. (C) Cell cycle distribution of ES cells treated as in A. (D) Percentages of cells in G1, S, and G2/M phases of cell cycle. Data represent mean ± s.d ($n = 3$); $^{*}P < 0.05$ or $^{**}P < 0.01$ (two-tailed t-test).

analysis of cells treated with PFT-α or DMSO for cyclin D1 expression. Consistent with the changes in the cell cycle, PFT-α treatment for 6 h led to downregulation in the expression level of cyclin D1, one of the G1-phase cyclins (Fig. 3A, B). We predicted from these results that p53 may act as a positive regulator of cyclin D1 in ES cells under unstressful culture conditions.

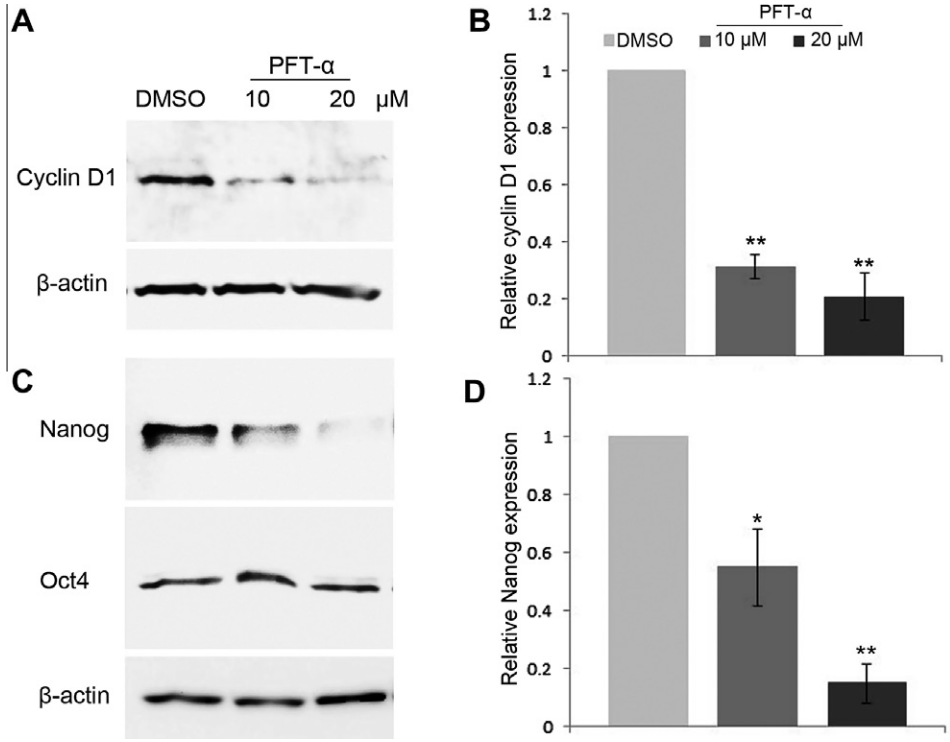

Fig. 3. PFT-α downregulates the expression of cyclin D1 and Nanog. (A) Representative protein blot of cyclin D1 treated with DMSO, or PFT-α for 6 h. (B) Quantitative analysis of the western blots shown in A. (C) Representative protein blot of Nanog and Oct4 proteins in ES cells treated as in A. (D) Quantitative analysis of the western blots shown in C. Data represent mean ± s.d ($n = 3$). $^{*}P < 0.05$ or $^{**}P < 0.01$ (two-tailed t-test).

3.3. PFT-α downregulates Nanog expression

The effect of PFT-α on the pluripotency markers Nanog and Oct4 were examined in ES cells. Treatment of ES cells with PFT-α for 6 h significantly downregulated Nanog protein levels in a dose dependent manner, as compared with the ES cells that were treated with the DMSO (Fig. 3C, D). In contrast, Oct4 protein levels were not affected by the same treatment, suggesting that the reduction of Nanog protein levels is not as a result of the induction of differentiation (Fig. 3C). In these experiments, the level of Oct4 protein was not noticeably affected by PFT-α treatment, suggesting that the pluripotency of the ES cells was not affected by inhibition of p53 activity.

3.4. PFT-α does not affect on the ES cell viability

The apoptosis assay was performed using Annexin V as a marker for apoptotic cells. Flow cytometric analysis showed that the percentage of cells undergoing apoptosis was not affected by PFT-α treatment (Fig. 4A). These data indicate that inhibition of p53 activity has no effect on ES cell viability.

4. Discussion

Here we present evidence demonstrating that p53 is critical for the self-renewal of murine ES cells under unstressful conditions. Our novel findings are summarized as follows: (1) Inhibition of p53 function by a chemical inhibitor (PFT-α) resulted in growth arrest of murine ES cells. (2) PFT-α suppresses cell cycle progression, and downregulates the expression levels of Nanog and cyclin D1. Since murine ES cells have a high level of p53 protein which is mainly localized in the cytoplasm under unstressful conditions [3,6,11,13], these findings strongly support that the cytoplasmic expression of p53 in ES cells is necessary for the ability of ES cells to self-renew and their rapid proliferation. Thus, the dual role played by p53 in murine ES cells, inducing ES cell differentiation upon exposure to DNA damage [3] as well as maintaining the self-renewal of ES cells under unstressful conditions, suggesting its unique role in ES cells. Also, these findings suggest that p53 pathway in ES cells rather than acting as an inactive gene, promotes ES cell proliferation.

Conflicting evidence has been reported as to whether the p53 is functional or unfuntional in ES cells. For example, Aladjem et al. [11] reported that p53 is inactive in murine ES cells and ES cells do not activate p53-dependent DNA damage response. In contrast, Lin et al. [3] reported that p53 is activated in response to DNA damage leading to Nanog suppression. Interestingly, a recent report indicates an antidifferentiation function of p53 in murine ES cells through directly regulating the Wnt signaling pathway, which suggest that p53 can promote cell proliferation and prevent differentiation in undamaged cells [14]. The apparent discrepancies between these conclusions may result from difference in cell types, experimental protocols, or cell growth state. Taken together with our results, p53 appears to display both induced differentiation and promotes self-renewal, depending on the presence or absence of DNA damage.

In this study, we found that treatment of ES cells with PFT-α reduced proliferation and downregulated the expression of cyclin D1, while the ES cells are maintained undifferentiated. Although these findings are disagree with the earlier report showed that $p53^{-/-}$ ES cells proliferate faster than $p53^{+/-}$ ES cells [10], it is consistent with the recent report which noticed that ES cells lacking p53 proliferates slower in comparison with their parental counterpart [13]. However, they could not explain this observation. Also, our findings are supported by a recent report on cancer cells showed that inhibition of p53 reduces proliferation in melanoma cells [23].

Furthermore, our results revealed that treatment of ES cells with PFT-α caused a marked decline in ratio of cells in G2/M phases of the cell cycle and an increase in the ratio of cells in G1

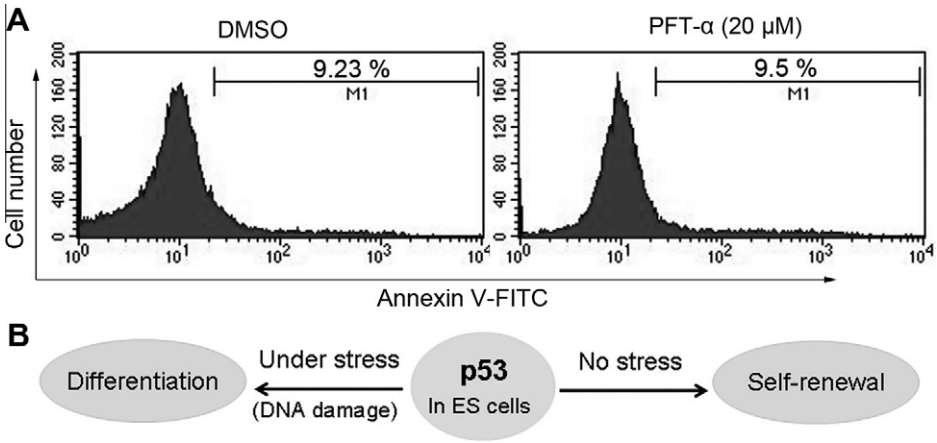

Fig. 4. PFT-α does not affect on the ES viability. (A) Apoptosis assay of ES cells treated with DMSO, or PFT-α for 24 h. The number represents the percentage of Annexin V-positive cells. (B) Model illustrating the roles of p53 in murine ES cells.

phase. Consistent with these findings, p53 inhibition led to down-regulation in the expression of cyclin D1, a well-known positive regulator of ES cell proliferation [24]. Given that cyclin D1 expression is mechanistically coupled to the G1-phase, ES cells may have unique mechanisms controlling cyclin D1 expression in order to coordinate with their unique proliferative properties. Taken together, these findings suggest that p53 is an essential regulator of ES cell cycle by regulating cyclin D1 level. However, the exact mechanism by which p53 influences the expression of cyclin D1 is yet to be identified.

Moreover, the results of BrdU incorporation analysis closely resembled those of cell population growth analysis. Therefore, it would be plausible to propose that p53 inhibition induces cell cycle arrest and subsequently ES cell growth arrest.

Interestingly, inhibition of p53 activity led to a significant suppression of Nanog expression while Oct4 was not affected. In agreement with our results, it has been reported that knockdown of p53 using p53 siRNA leads to suppression of *Nanog* gene [25]. It has been found that Nanog-deficient blastocysts appear to be normal, but the inner cell mass fails to generate epiblast and only produces parietal endoderm-like cells when cultured *in vitro* [16]. However, it has been reported that permanent genetic deletion of *Nanog* does not abolish pluripotency, but rather reduces self-renewal ability by generating a transient state which is reversibly poised to both self-renewal and differentiation commitment [17]. Although ES cells do not require Nanog for maintaining the pluripotency, at least in some contexts [17], the function of Oct4 cannot be replaced by other pluripotency factors [26]. Also, our AP-staining results showed no change after PFT-α treatment. These findings indicate that suppression of Nanog expression in PFT-α-treated ES cells may be compensated by marinating the Oct4 expression to keep the ES cells pluripotent.

Recently, it has been demonstrated that reducing p53 activity enhances iPS cells generation through cell cycle acceleration [7–9]. Utikal et al. [9] demonstrated that transient, rather than permanent, inhibition of p53 promotes reprogramming efficiency. In contrast, Marion et al. [27] showed that iPS cells deficient of p53 exhibit foci of DNA damage and chromosomal aberrations, and loss of their typical round morphology after expansion. Reprogramming of somatic cells is associated with stress inducing p53 accumulation. Therefore, transient inhibition of p53 during the reprogramming process facilitates the reprogramming. Taken together with our results, these suggest that inhibition of p53 during stress may improve self-renewal of the stem cells, but under unstressful conditions p53 is required for maintaining the self-renewal of stem cells.

In conclusion, based on our findings as well as those of others, we propose an expanded model to explain the role of p53 in ES cells (Fig. 4B). In the absence of stress, the majority of p53 is localized in the cytoplasm of ES cells where it plays a role in regulating ES cell self-renewal by marinating the expression levels of Nanog and cyclin D1. After stress, p53 translocated to the nucleus and cause suppression of Nanog expression and subsequently ES cell differentiation. The precise mechanism involved in this effect is not fully understood. Nevertheless, considering the importance of p53 in ES cells and iPS cells biology, our results clearly open new avenues for understanding the molecular mechanisms of p53 functions in stem cells.

References

[1] Y. Suda, M. Suzuki, Y. Ikawa, S. Aizawa, Mouse embryonic stem cells exhibit indefinite proliferative potential, J. Cell Physiol. 133 (1987) 197–201.
[2] T. Burdon, A. Smith, P. Savatier, Signaling, cell cycle and pluripotency in embryonic stem cells, Trends Cell Biol. 12 (2002) 432–438.
[3] T. Lin, C. Chao, S. Saito, S.J. Mazur, M.E. Murphy, E. Appella, Y. Xu, p53 induces differentiation of mouse embryonic stem cells by suppressing Nanog expression, Nat. Cell Biol. 7 (2005) 165–171.
[4] H. Qin, T. Yu, T. Qing, Y. Liu, Y. Zhao, J. Cai, J. Li, Z. Song, X. Qu, P. Zhou, J. Wu, M. Ding, H. Deng, Regulation of apoptosis and differentiation by p53 in human embryonic stem cells, J. Biol. Chem. 282 (2007) 5842–5852.
[5] T. Maimets, I. Neganova, L. Armstrong, M. Lako, Activation of p53 by nultin leads to rapid differentiation of human embryonic stem cells, Oncogene 27 (2008) 5277–5287.
[6] T. Zhao, Y. Xu, p53 and stem cells: new developments and new concerns, Trends Cell Biol. 20 (2010) 170–175.
[7] Y. Zhao, X. Yin, H. Qin, F. Zhu, H. Liu, W. Yang, Q. Zhang, C. Xiang, P. Hou, Z. Song, Y. Liu, J. Yong, P. Zhang, J. Cai, M. Liu, H. Li, Y. Li, X. Qu, K. Cui, W. Zhang, T. Xiang, Y. Wu, Y. Zhao, C. Liu, C. Yu, K. Yuan, J. Lou, H. Ding, H. Deng, Two supporting factors greatly improve the efficiency of human iPSC generation, Cell Stem Cell 3 (2008) 475–479.
[8] T. Kawamura, J. Suzuki, Y.V. Wang, S. Menendez, L.B. Morera, A. Raya, G.M. Wahl, J.C. Belmonte, Linking the p53 tumour suppressor pathway to somatic cell reprogramming, Nature 460 (2009) 1140–1144.
[9] J. Utikal, J.M. Polo, M. Stadtfeld, N. Maherali, W. Kulalert, R.M. Walsh, A. Khalil, J.G. Rheinwald, K. Hochedlinger, Immortalization eliminates a roadblock during cellular reprogramming into iPS cells, Nature 460 (2009) 1145–1148.
[10] K. Sabapathy, M. Klemm, R. Jaenisch, E.F. Wagner, Regulation of ES cell differentiation by functional and conformational modulation of p53, EMBO J. 16 (1997) 6217–6229.
[11] M.I. Aladjem, B.T. Spike, L.W. Rodewald, T.J. Hope, M. Klemm, R. Jaenisch, G.M. Wahl, ES cells do not activate p53-dependent stress responses and undergo p53-independent apoptosis in response to DNA damage, Curr. Biol. 8 (1998) 145–155.
[12] Y. Hong, P.J. Stambrook, Restoration of an absent G1 arrest and protection from apoptosis in embryonic stem cells after ionizing radiation, Proc. Natl. Acad. Sci. USA 101 (2004) 14443–14448.
[13] V. Solozobova, A. Rolletschek, C. Blattner, Nuclear accumulation and activation of p53 in embryonic stem cells after DNA damage, BMC Cell Biol. 10 (2009) 46.
[14] L.H. Lee, M. Li, A.M. Michalowski, X. Zhang, H. Liao, L. Chen, Y. Xu, X. Wu, J. Huang, A genome wide study identifies the Wnt signaling pathway as a major

target of p53 in murine embryonic stem cells, Proc. Natl. Acad. Sci. USA 107 (2010) 69–74.

[15] I. Chambers, D. Colby, M. Robertson, J. Nichols, S. Lee, S. Tweedie, A. Smith, Functional expression cloning of Nanog, a pluripotency sustaining factor in embryonic stem cells, Cell 113 (2003) 643–655.

[16] K. Mitsui, Y. Tokuzawa, H. Itoh, K. Segawa, M. Murakami, K. Takahashi, M. Maruyama, M. Maeda, S. Yamanaka, The homeoprotein Nanog is required for maintenance of pluripotency in mouse epiblast and ES cells, Cell 113 (2003) 631–642.

[17] I. Chambers, J. Silva, D. Colby, J. Nichols, B. Nijmeijer, M. Robertson, J. Vrana, K. Jones, L. Grotewold, A. Smith, Nanog safeguards pluripotency and mediates germline development, Nature 450 (2007) 1230–1234.

[18] E.M. Abdelalim, I. Tooyama, NPR-A regulates self-renewal and pluripotency of embryonic stem cells, Cell Death Dis. 2 (2011) e127.

[19] E.M. Abdelalim, I. Tooyama, BNP signaling is crucial for embryonic stem cell proliferation, PLoS One 4 (2009) e5341.

[20] P.G. Komarov, E.A. Komarova, R.V. Kondratov, K. Christov-Tselkov, J.S. Coon, M.V. Chernov, A.V. Gudkov, A chemical inhibitor of p53 that protects mice from the side effects of cancer therapy, Science 285 (1999) 1733–1737.

[21] J. Nomura, M. Maruyama, M. Katano, H. Kato, J. Zhang, S. Masui, Y. Mizuno, Y. Okazaki, M. Nishimoto, A. Okuda, Differential requirement for nucleostemin in embryonic stem cell and neural stem cell viability, Stem Cells 27 (2009) 1066–1076.

[22] E. M. Abdelalim, I. Tooyama, NPR-C protects embryonic stem cells from apoptosis by regulating p53 levels, Stem Cell Dev., in press.

[23] K.A. Avery-Kiejda, N.A. Bowden, A.J. Croft, L.L. Scurr, C.F. Kairupan, K.A. Ashton, B.A. Talseth-Palmer, H. Rizos, X.D. Zhang, R.J. Scott, P. Hersey, p53 in human melanoma fails to regulate target genes associated with apoptosis and the cell cycle and may contribute to proliferation, BMC Cancer 11 (2011) 203.

[24] L. Jirmanova, M. Afanassieff, S. Gobert-Gosse, S. Markossian, P. Savatier, Differential contributions of ERK and PI3-kinase to the regulation of cyclin D1 expression and to the control of the G1/S transition in mouse embryonic stem cells, Oncogene 21 (2002) 5515–5528.

[25] E. Ungewitter, H. Scrable, Δ40p53 controls the switch from pluripotency to differentiation by regulating IGF signaling in ESCs, Genes Dev. 24 (2010) 2408–2419.

[26] N. Ivanova, R. Dobrin, R. Lu, I. Kotenko, J. Levorse, C. DeCoste, X. Schafer, Y. Lun, I.R. Lemischka, Dissecting self-renewal in stem cells with RNA interference, Nature 442 (2006) 533–538.

[27] R.M. Marion, K. Strati, H. Li, M. Murga, R. Blanco, S. Ortega, O. Fernandez-Capetillo, M. Serrano, M.A. Blasco, A p53-mediated DNA damage response limits reprogramming to ensure iPS cell genomic integrity, Nature 460 (2009) 1149–1153.

Biochemical and Biophysical Research Communications 420 (2012) 611–615

Contents lists available at SciVerse ScienceDirect

Biochemical and Biophysical Research Communications

journal homepage: www.elsevier.com/locate/ybbrc

Thyroglobulin (Tg) activates MAPK pathway to induce thyroid cell growth in the absence of TSH, insulin and serum

Mariko Sue [a], Moyuru Hayashi [a], Akira Kawashima [a], Takeshi Akama [a], Kazunari Tanigawa [a], Aya Yoshihara [a], Takeshi Hara [a], Yuko Ishido [a], Tetsuhide Ito [b], Shin-Ichiro Takahashi [c], Norihisa Ishii [d], Koichi Suzuki [a,*]

[a] Laboratory of Molecular Diagnostics, Department of Mycobacteriology, Leprosy Research Center, National Institute of Infectious Diseases, Higashimurayama, Tokyo 189-0002, Japan
[b] Department of Medicine and Bioregulatory Science, Kyushu University, Fukuoka 812-8582, Japan
[c] Department of Animal Sciences, Graduate School of Agriculture and Life Science, The University of Tokyo, Bunkyo-ku, Tokyo 113-8657, Japan
[d] Leprosy Research Center, National Institute of Infectious Diseases, Higashimurayama, Tokyo 189-0002, Japan

ARTICLE INFO

Article history:
Received 8 March 2012
Available online 16 March 2012

Keywords:
Thyroid gland
Thyroglobulin
Growth
TSH
FRTL-5 cells

ABSTRACT

The growth of thyroid cells is tightly regulated by thyroid stimulating hormone (TSH) through the cyclic adenosine 3′, 5′-monophosphate (cAMP) signaling pathway by potentiating the mitogenic activity of insulin and insulin-like growth factors (IGFs). However, we recently reported that thyroglobulin (Tg), a major product of the thyroid, also induces the growth of thyroid cells cultured in 0.2% serum in the absence of TSH and insulin. In this report, we demonstrate that Tg induced phosphorylation of molecules of the c-Raf/MEK/ERK pathway of the mitogen-activated protein kinase (MAPK). The MEK-1/2 inhibitor PD98059 suppressed Tg-induced phosphorylation of ERK1/2 and reduced bromodeoxyuridine (BrdU) incorporation. Tg also induced expression of the essential transcriptional factors c-Myc, c-Fos and c-Jun and phosphorylation of the retinoblastoma (Rb) protein. The present results, together with the previous report, suggest that Tg utilizes multiple signaling cascades to induce thyroid cell growth independent of TSH/cAMP stimulation.

1. Introduction

Thyroid stimulating hormone (TSH) is the major regulator of thyroid cell growth and endocrine function. The binding of TSH to its receptor (TSHR) promotes Gs protein to couple to adenylate cyclase and produce cyclic adenosine 3′, 5′-monophosphate (cAMP). In turn, cAMP activates protein kinase A (PKA) to induce the expression of various genes necessary for cell proliferation. The mitogenic activity of phosphatidylinositol 3-kinase (PI3K) and mitogen-activated protein kinase (MAPK), induced by insulin-like growth factors (IGFs) and insulin, is also potentiated by TSH as shown in humans, dogs, rodents and FRTL-5 thyroid cells [1–6].

In addition to these essential factors responsible for thyroid cell growth, we reported that thyroglobulin (Tg), a major product of the thyroid gland stored in the thyroid follicle, induces thyroid cell growth independently of TSH, insulin and IGFs stimulation [7]. Thus, physiologic concentrations of follicular Tg stimulated the growth of rat thyroid FRTL-5 cells through the phosphatidylinositol 3′-kinase (PI3K)-Akt pathway in the absence of TSH, insulin and serum that contains IGF-I [7]. Tg induced comparable kinase activity of Akt as stimulation with TSH, insulin and serum with no increase in cellular cAMP levels [7].

Tg is the major synthetic product of the thyroid and is a large glycoprotein that forms a 660 kDa dimer. Dietary iodide is concentrated in the thyroid gland and is attached to tyrosyl residues within the Tg molecule to produce the thyroid hormone precursors diiodotyrosine (DIT) and monoiodotyrosine (MIT) [8]. In addition to this classical role of hormone biosynthesis, Tg also acts as a potent autocrine suppressor of follicular function which is mediated by transcriptional suppression of genes essential for iodide transport and hormone synthesis [9,10]. Follicular Tg suppresses iodide uptake both *in vivo* and *in vitro* and suppresses the mRNA expression of thyroid-specific genes such as thyroperoxidase (*Tpo*), sodium/iodide symporter (*Slc5a5*; NIS), the TSH receptor (*Tshr*) as well as *Tg* itself by suppressing specific transcription factors, such as *Nkx2–1, Foxe1* and *Pax8* [9,10].

Although the Tg-recognition system of the thyroid cells and the underlying molecular mechanism of Tg action remain largely unknown, these effects were shown to be specific to Tg. Thus, strong activities were obtained in the Tg fractions prepared by Sephacryl chromatography and high pressure gel permeation chromatography (HPGPC) [7,11]. An antibody against Tg suppressed its activity

* Corresponding author. Address: Laboratory of Molecular Diagnostics, Department of Mycobacteriology, Leprosy Research Center, National Institute of Infectious Diseases, 4-2-1 Aoba-cho, Higashimurayama, Tokyo 189-0002, Japan. Fax: +81 42 394 9092.
E-mail address: koichis@nih.go.jp (K. Suzuki).

0006-291X/$ - see front matter © 2012 Elsevier Inc. All rights reserved.
http://dx.doi.org/10.1016/j.bbrc.2012.03.046

[7,12]. Interestingly, Tg prepared from iodide-deficient goiters, colloid adenomas or congenital goiters suppressed thyroid-specific gene expression more effectively than Tg prepared from normal tissue [9,13]. The observed activities were not mimicked by factors such as thyroid hormones, iodide, TSH, osmotic pressure, non-specific protein concentrations, or any other known hormones and cytokines [7,9,11,12].

It seems that there are at least two distinct mechanisms of Tg action that have different kinetics. Lower concentrations of Tg induce cell growth and expression of major histocompatibility complex (MHC) class I and Pendred syndrome gene (*Slc26a4*), while all these are suppressed by higher concentrations of Tg. Similarly, suppression of thyroid-specific gene expression is induced by higher concentrations of Tg in a dose-dependent manner [7,9,14]. Therefore, it is possible that different recognition systems rather than the two different domains of Tg protein are responsible for the biphasic action [14–17].

Our previous study revealed that the PI3K/Akt pathway is involved in Tg-induced thyroid cell growth. Thus, Tg significantly increased Akt kinase activity to the same level induced by stimulation with TSH, insulin and serum. However, Tg did not increase cellular cAMP levels and inhibition of the PI3K/Akt pathway did not completely suppress Tg-induced cell growth [7]. The present study was undertaken to explore other potential mechanisms of Tg-induced thyroid cell growth.

2. Materials and methods

2.1. Cell culture and treatment

Rat thyroid FRTL-5 cells were incubated using Coon's modified Ham's F-12 medium supplemented with 5% bovine serum (Invitrogen, Carlsbad, CA) and a six-hormone mixture consisting of bovine TSH, insulin, hydrocortisone, transferrin, glycyl-L-histidyl-L-lysine acetate and somatostatin as described [18,19]. The cells were initially grown in medium for 2 days, and then changed to medium with 0.2% serum but without TSH and insulin for 7 days before experiments. Tg and all other reagents were purchased from Sigma (St. Louis, MO) unless otherwise specified. Tg was dissolved in culture medium at a final concentration of 5 mg/ml. PD98059 at a final concentration of 50 μM from a stock solution dissolved in dimethyl sulfoxide (DMSO) was used 30 min prior to the Tg stimulation.

2.2. Bromodeoxyuridine (BrdU) assay

Cellular DNA synthesis was assessed by BrdU incorporation using 5′-Bromo-2′deoxyuridine Labeling & Detection Kit III (Roche) according to the manufacturer's recommendations as described [18].

2.3. DNA microarray analysis

Rat thyroid FRTL-5 cells maintained in the absence of TSH, insulin and with 0.2% serum were treated with the medium containing 5 mg/ml of Tg for 6 h. Total RNA was isolated using the RNeasy Mini Kit (Qiagen, Valencia, CA) as described [18,19]. Synthesis of cDNA, Cy3 labeling, hybridization with array and detection were performed as described [18].

2.4. Reverse transcription-polymerase chain reaction (RT-PCR)

Total RNA was isolated using the RNeasy Mini Kit (Qiagen) and was reverse transcribed to cDNA using the High-Capacity cDNA Reverse Transcription Kits (Applied Biosystems, Foster City, CA) as previously described [18,19]. PCR was carried out using the following sets of primers: c-*Myc* forward, 5′-CCCATCAAGAGGCCAC AGCAAA-3′; c-*Myc* reverse, 5′-TCAGCTCGTTTCTCCTCTGACG-3′; c-*Fos* forward, 5′-CGTTGCAGACCGAGATTGCC-3′; c-*Fos* reverse, 5′-ACCAGACAGGTCCACATCTG-3′; c-*Jun* forward, 5′-AACTCGGAC CTTCTCACGTCG-3′; c- *Jun* reverse, 5′-TGCTGAGGTTGGCGTAGACC-3′; *Actb* forward; 5′-AGCCATGTACGTAGCCATCC-3′, *Actb* reverse; 5′-TGTGGTGGTGAAGCTGTAGC-3′. The PCR products were analyzed using 2% agarose gel electrophoresis.

2.5. Western blotting analysis

Cellular protein was isolated, electrophoresed and transferred to nitrocellulose membrane as described [18,19]. Membranes were washed with phosphate-buffered saline with 0.1% Tween 20 (PBST) and incubated in blocking buffer (5% skim milk in PBST) for 1 h. Membranes were then incubated with primary antibodies directed against c-Myc, c-Fos, c-Jun, phospho-c-Raf, phospho-MEK1/2 (all from Cell Signaling, Beverly, MA) or phospho-ERK1/2 (Santa Cruz, Santa Cruz, CA) for 1 h at room temperature. Specific proteins were visualized using ECL Plus Reagent (GE Healthcare) as previously described [18,19].

3. Results

3.1. Physiologic concentrations of follicular Tg promotes FRTL-5 cell growth

We first confirmed Tg-induced cell proliferation using rat thyroid FRTL-5 cells and examined the effect of various concentrations of Tg. Cell cycle arrest was induced by culturing cells for 7 days in reduced serum (0.2% instead of 5%) without TSH and insulin [20]. Cells were then stimulated with various concentrations of Tg for 3 days and cell number counted. As shown in Fig. 1A, the number of cells significantly increased by low concentrations of follicular Tg in accordance with a previous report [7]. The Tg-induced increase in cell number was comparable with that induced by TSH plus insulin whilst the same concentration of the control protein BSA had no effect (Fig. 1B). Cellular DNA synthesis was assessed by BrdU incorporation and was maximal 36 h after Tg stimulation (Fig. 1C).

3.2. Tg increases mRNA and protein levels of genes that regulate cell proliferation

As we have confirmed Tg induction of the MAPK/ERK pathway, we further investigated whether the Tg stimulation modulates downstream factors that regulate the cell cycle. The mRNA levels of c-*Myc, c-Fos* and c-*Jun* were increased by Tg stimulation within 1 h and gradually decreased in 12 h (Fig. 2A). In addition, the protein levels of c-Myc, c-Fos and c-Jun were also significantly induced in 1–2 h (Fig. 2B).

Requirements for cell growth include complexes of cyclins and cyclin-dependent kinases (CDK) that phosphorylate retinoblastoma (Rb) protein. The resultant inhibition of Rb activity results in the release of the key transcription factor E2F that allows cells in the G_1 phase of cell cycle to enter the S phase [21]. We therefore investigated whether Tg promotes the levels of cell cycle regulating proteins. Western blot analysis clearly demonstrated that Tg increased the protein level of cyclin D1, cyclin D2, CDK2 and CDK4 and increased Rb phosphorylation in FRTL-5 cells (Fig. 2C) thereby suggesting that these molecules promote Tg-induced thyroid cell growth.

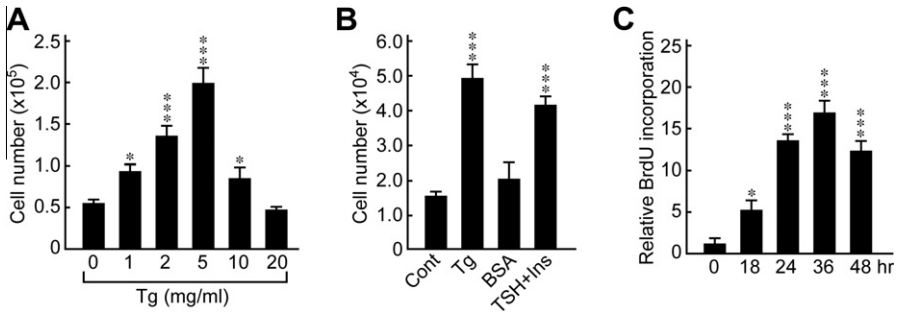

Fig. 1. Tg induces the growth and DNA synthesis of FRTL-5 thyroid cells. FRTL-5 cells were maintained in 0.2% serum in the absence of TSH and insulin. (A) The indicated amount of Tg was added to cells in the 24-well culture plate for 3 days and cell numbers were counted with a hemocytometer. (B) Cells were treated with 1 mg/ml of Tg or BSA, or 5 mU/ml TSH plus 10 μg/ml insulin for 3 days and cell numbers were counted with a hemocytometer. (C) FRTL-5 cells maintained in a 96-well cell culture plate were treated with 5 mg/ml of Tg and cultured for the indicated period of time. BrdU incorporation was determined as described in Section 2. Results were expressed as the mean ± SEM ($n = 4$). $^{*}P < 0.05$; $^{**}P < 0.01$ relative to control by Student's t-test.

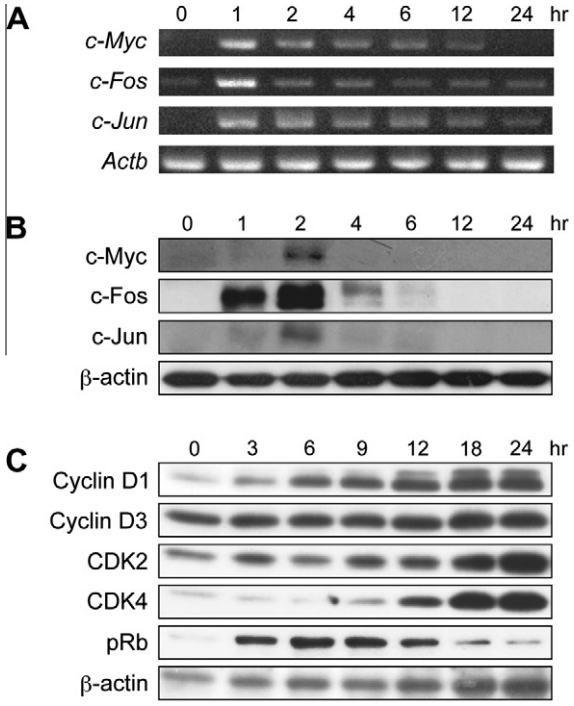

Fig. 2. Tg induces expression of cell cycle related proteins. FRTL-5 cells were maintained in 0.2% serum without TSH or insulin in 6-well cell culture plates. Cells were then treated with 5 mg/ml of Tg for the indicated period of time. Total RNA was extracted and subjected to RT-PCR analysis (A) or cellular protein was extracted and subjected for Western blot analysis (B and C) as described in Section 2. Representative results from at least three independent experiments are shown.

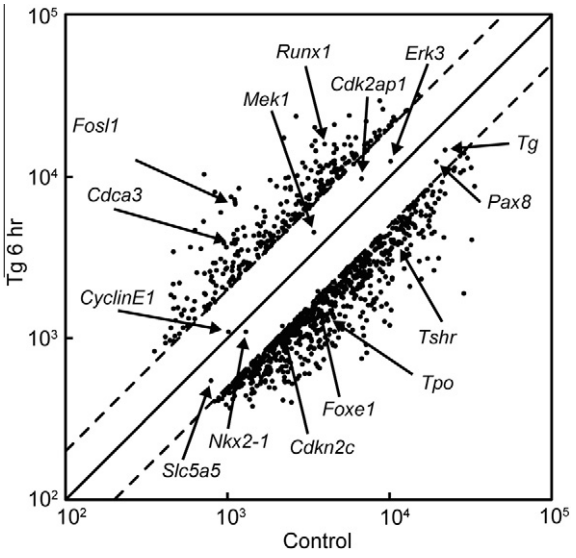

Fig. 3. DNA microarray analysis of genes expressed in Tg-stimulated FRTL-5 thyroid cells cultured in 0.2% serum without TSH or insulin. FRTL-5 cells maintained in 0.2% serum without TSH or insulin were exposed to 5 mg/ml of Tg for 6 h. Total RNA was extracted and subjected to DNA microarray analysis as described in Section 2. Each *dot* corresponds to the fluorescent intensity of each gene on the microarray of control cells (x-axis) and Tg-treated cells (y-axis). 2-Fold, and 0.5-fold changes in expression are indicated as parallel lines. The spots of genes related to cell signaling, cell cycle and thyroid function are indicated.

3.3. Follicular Tg induces gene expression related to cell signaling and proliferation in the absence of TSH, insulin and serum

Although the PI3K/Akt pathway is involved in Tg-mediated thyroid cell growth, there was no activation of cAMP/PKA by Tg despite this being a major pathway of TSH action [7]. To explore which genes may be influenced by Tg to mediate cell growth, FRTL-5 cells stimulated for 6 h with Tg in the absence of TSH, insulin and serum underwent DNA microarray analysis. Tg treatment for 6 h up-regulated 291 genes more than two-fold and down-regulated 709 genes by more than 50% (Fig. 3). The suppressive effect of Tg upon a series of thyroid-specific gene expression and the inducing effect upon *Slc26a4* expression was much weaker in the absence of TSH, insulin and serum [9,10,14,22]. Up-regulated genes after 6 h of Tg stimulation included early growth response 1 (*Egr1*), cell division cycle associated 7 (*Cdca7*), fos-like antigen 1 (*Fosl1*), and runt related transcription factor 1 (*Runx1*), which are involved in cell signaling and cell cycle regulation (Fig. 1 and Table 1). Among these *Egr-1* and *Runx2* are known to be induced by the MAPK/ERK signaling pathway [23,24].

3.4. Tg activates the c-Raf/MEK/ERK pathway of the MAPK in the absence of TSH, insulin and serum

The c-Raf/MEK/ERK pathway is known to be activated downstream of the IGF-1/insulin receptor, which mediates signal transduction in response to extracellular stimuli and affects various cellular functions including proliferation and differentiation [25,26]. Based on the information obtained by DNA microarray analysis, we undertook studies to determine whether Tg simulation alone can activate the c-Raf/MEK/ERK pathway in FRTL-5 thyroid cells in the absence of TSH, insulin and serum. Western blot analysis revealed that Tg strongly phosphorylated c-Raf, MEK1/2 and ERK1/2, which are essential signaling molecules of the c-Raf/

Table 1
Genes whose expression was modulated by Tg treatment.

Gene symbol	Fold change	Description
Up-regulated genes		
Ptges	9.64	Prostaglandin E synthase
Egr1	8.94	Early growth response 1
Fn1	7.81	Fibronectin 1
RGD1562617	7.42	Similar to RAB7-like protein
Fosl1	7.17	Fos-like antigen 1
Serpine1	6.63	Serine (or cysteine) peptidase inhibitor, clade E, member 1
Dhrs9	6.22	Dehydrogenase/reductase (SDR family) member 9
Rgc32	5.21	Response gene to complement 32
Runx1	4.79	Runt related transcription factor 1
Cdca7	4.07	Cell division cycle associated 7
Thyroid-specific genes		
Tg	0.77	Thyroglobulin
Slc26a4	1.40	Solute carrier family 26, member 4 (pendrin)
Slc5a5	0.76	Solute carrier family 5, member 5 (sodium iodide symporter)
Tpo	0.32	Thyroid peroxidase
Nkx2–1	0.73	NK2 homeobox 1 (thyroid transcription factor 1)
Foxe1	0.47	Forkhead box E1 (thyroid transcription factor 2)
Pax8	0.67	Paired box 8
Tshr	0.36	Thyroid stimulating hormone receptor

MEK/ERK pathway (Fig. 4A). In order to confirm the specificity of this activation, we evaluated the effect of PD98059 – a potent inhibitor of MEK1/2. Phosphorylation of ERK1/2 was strongly inhibited by treating FRTL-5 cells with PD98059 at a final concentration of 50 μM 30 min prior to Tg stimulation (Fig. 4B).

We further evaluated if PD98059 suppressed the induction of DNA synthesis by Tg stimulation. FRTL-5 cells were treated with PD985059 30 min prior to stimulation with Tg or TSH. PD98059 significantly suppressed Tg-induced DNA synthesis measured at 48 h, while it did not affect TSH-induced BrdU incorporation (Fig. 4C). These results clearly indicate that Tg stimulation activates the c-Raf/MEK/ERK pathway and increases DNA synthesis of FRTL-5 cells in the absence of TSH and insulin and in the presence of 0.2% serum.

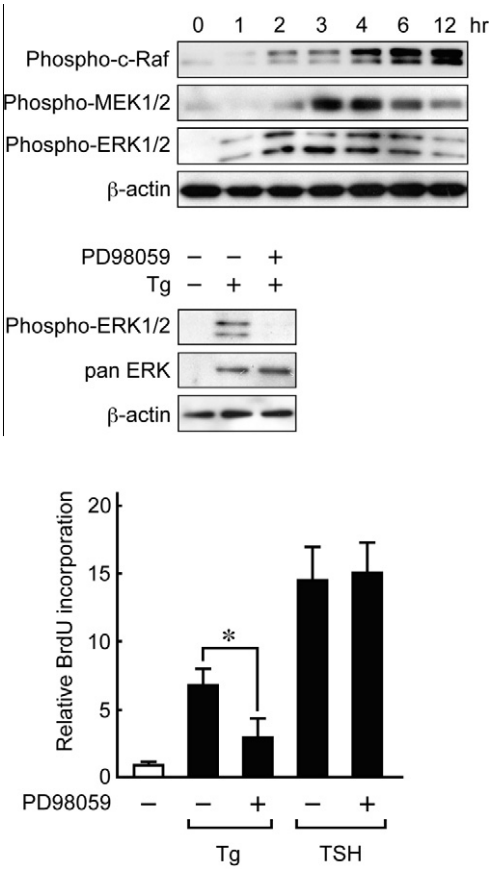

Fig. 4. Tg activates the MAPK/ERK pathway. (A) FRTL-5 cells maintained in 0.2% serum without TSH or insulin were treated with 5 mg/ml of Tg for the indicated period of time. Total protein was extracted and analyzed by Western blot as described in Section 2. (B) FRTL-5 cells maintained in 0.2% serum without TSH or insulin were pre-incubated with 50 μM of PD98059 for 30 min prior to the addition of 5 mg/ml of Tg for 24 h. Total protein was extracted and analyzed by Western blot as described in Section 2. (C) FRTL-5 cells in 0.2% serum without TSH or insulin were pre-incubated with 50 μM of PD98059 for 30 min prior to the addition of Tg (5 mg/ml) or TSH (1 mU/ml) for 24 h. BrdU incorporation was determined as described in the Materials and Methods. Results were expressed as the mean ± SEM ($n = 4$). $^{*}P < 0.01$. Representative results from at least three independent experiments are shown.

4. Discussion

We have previously reported that low concentrations of Tg stimulated rat thyroid FRTL-5 cell growth in the absence of TSH, insulin and serum [7]. Unlike TSH, Tg did not increase cellular cAMP levels, but activated the PI3K/Akt pathway. However, inhibition of the PI3K/Akt pathway did not completely suppress Tg-induced cell growth. Therefore, it was suggested that there were other as yet unknown pathways that might be specific to the action of Tg [7]. In this study, we have additionally shown that Tg activates the c-Raf/MEK/ERK pathway with the subsequent induction of cyclin/CDK and phosphorylation of Rb and the promotion of DNA synthesis in FRTL-5 cells.

Tg protein stored in the thyroid follicle has also been shown to act as a potent suppressor of thyroid follicular function by suppressing iodide uptake and the transcription of essential genes including the *Tg* gene itself [9,10]. Since the functions of thyroid follicles are not synchronized, but rather quite heterogeneous, this is thought to be an autocrine, negative feedback mechanism to suppress the further synthesis of hormone precursors, DIT and MIT, when the follicle has sufficient Tg [13,16,17]. Tg stimulation of thyroid follicular cell growth, which would expand the follicular capacity to store more hormone precursors, is also a plausible mechanism for the physiologic regulation of follicles. However, the underlying mechanisms whereby the huge glycoprotein Tg is recognized by thyroid cells and exerts its regulatory action remain unclear [13,14,16,17]. Similarly, the signaling pathways that are activated downstream of Tg stimulation remained largely unknown. The range of Tg concentrations required to induce thyroid cell growth was 1–5 mg/ml, which is within the range of normal follicular Tg concentrations, 0.1–250 mg/ml, as measured by aspiration biopsy or micropuncture of a single follicle [27–29]. The relatively large range of the estimates of follicular Tg concentration may be the result of significant functional heterogeneity among follicles.

We have previously shown that Tg-induced growth of quiescent FRTL-5 cells grown in 0.2% serum without TSH or insulin is mediated at least in part through the PI3K/Akt pathway [7]. The PI3K/Akt signaling pathway acts as cellular sensor to relay mitogenic signals to internal cellular effectors and regulates fundamental cellular functions such as transcription, translation, growth and survival. The activation of the c-Raf/MEK/ERK pathway demonstrated in the present study provides an additional mechanism of Tg action to induce thyroid cell growth.

Signal transduction pathways that respond to external signals through the MAPK family or protein kinases are involved in diverse responses in eukaryotic cells. There are three main classes of MAPK, *i.e.* ERKs, stress-activated protein kinases that are also

known as c-Jun NH_2-terminal protein kinases (JNKs) and p38-MAPKs [25,30,31]. The c-Raf/MEK/ERK pathway is essential for cell proliferation [32] and our results indicate that Tg increased the phosphorylation of c-Raf, MEK1/2 and ERK1/2 thereby suggesting that Tg utilizes the c-Raf/MEK/ERK pathway to induce thyroid cell proliferation. This was confirmed by the inhibitory effect of the MEK1/2 inhibitor PD98059 that strongly suppressed ERK phosphorylation and Tg-induced BrdU incorporation. The translocation of phosphorylated ERK to the nucleus can activate transcription factors such as *c-Myc, c-Fos and c-Jun* and this was demonstrated in the present study. Thus, our results suggest that the signals initiated from Tg activate the c-Raf/MEK/ERK pathway result in the induction of *c-Myc, c-Fos and c-Jun* and finally promote DNA synthesis through activating cyclins, CDKs and p53.

We have shown in previous and present reports that Tg activates two independent pathways in the absence of TSH, insulin and serum. One pathway is the PI3K/Akt pathway that is common for both Tg and TSH whilst the other is the c-Raf/MEK/ERK pathway that is specific to Tg. The potent stimulation of cell proliferation induced by Tg can be explained by its activation of these two pathways. We have previously shown that Tg prepared from goiters have stronger effects than Tg prepared from normal tissue [9,13], suggesting that poorly iodinated and/or poorly sialylated Tg may induce thyroid cell growth more effectively than fully iodinated and/or sialylated Tg. The etiology of thyroid goiters and neoplasms are largely unknown and, since Tg can strongly promote thyroid cell growth, an abnormality of cell growth mechanisms regulated by Tg might be related to the pathogenesis of such disorders. Future understanding of the cellular recognition system of Tg and detailed signaling cascades will lead to further understanding of the potential pathological consequences as well as thyroid physiology.

Acknowledgments

This work was supported in part by a Grant-in-Aid for Scientific Research from the Japan Society for the Promotion of Science (#15390296 and #23801300 to K.S.).

References

[1] T. Kimura, A. Van Keymeulen, J. Golstein, A. Fusco, J.E. Dumont, P.P. Roger, Regulation of thyroid cell proliferation by TSH and other factors: a critical evaluation of in vitro models, Endocr. Rev. 22 (2001) 631–656.
[2] D. Tramontano, A.C. Moses, B.M. Veneziani, S.H. Ingbar, Adenosine 3′,5′-monophosphate mediates both the mitogenic effect of thyrotropin and its ability to amplify the response to insulin-like growth factor I in FRTL5 cells, Endocrinology 122 (1988) 127–132.
[3] T. Nedachi, M. Akahori, M. Ariga, H. Sakamoto, N. Suzuki, K. Umesaki, F. Hakuno, S.I. Takahashi, Tyrosine kinase and phosphatidylinositol 3-kinase activation are required for cyclic adenosine 3',5'-monophosphate-dependent potentiation of deoxyribonucleic acid synthesis induced by insulin-like growth factor-I in FRTL-5 cells, Endocrinology 141 (2000) 2429–2438.
[4] J.M. Suh, J.H. Song, D.W. Kim, H. Kim, H.K. Chung, J.H. Hwang, J.M. Kim, E.S. Hwang, J. Chung, J.H. Han, B.Y. Cho, H.K. Ro, M. Shong, Regulation of the phosphatidylinositol 3-kinase, Akt/protein kinase B, FRAP/mammalian target of rapamycin, and ribosomal S6 kinase 1 signaling pathways by thyroid-stimulating hormone (TSH) and stimulating type TSH receptor antibodies in the thyroid gland, J. Biol. Chem. 278 (2003) 21960–21971.
[5] S. Takahashi, M. Conti, C. Prokop, J.J. Van Wyk, H.S. Earp, Thyrotropin and insulin-like growth factor I regulation of tyrosine phosphorylation in FRTL-5 cells. Interaction between cAMP-dependent and growth factor-dependent signal transduction, J. Biol. Chem. 266 (1991) 7834–7841.
[6] S. Takahashi, M. Conti, J.J. Van Wyk, Thyrotropin potentiation of insulin-like growth factor-I dependent deoxribonucleic acid synthesis in FRTL-5 cells: mediation by an autocrine amplification factor(s), Endocrinology 126 (1990) 736–745.
[7] Y. Noguchi, N. Harii, C. Giuliani, I. Tatsuno, K. Suzuki, L.D. Kohn, Thyroglobulin (Tg) induces thyroid cell growth in a concentration-specific manner by a mechanism other than thyrotropin/cAMP stimulation, Biochem. Biophys. Res. Commun. 391 (2010) 890–894.
[8] J.T. Dunn, A.D. Dunn, Update on intrathyroidal iodine metabolism, Thyroid 11 (2001) 407–414.
[9] K. Suzuki, S. Lavaroni, A. Mori, M. Ohta, J. Saito, M. Pietrarelli, D.S. Singer, S. Kimura, R. Katoh, A. Kawaoi, L.D. Kohn, Autoregulation of thyroid-specific gene transcription by thyroglobulin, Proc. Natl. Acad. Sci. USA 95 (1998) 8251–8256.
[10] K. Suzuki, A. Mori, J. Saito, E. Moriyama, L. Ullianich, L.D. Kohn, Follicular thyroglobulin suppresses iodide uptake by suppressing expression of the sodium/iodide symporter gene, Endocrinology 140 (1999) 5422–5430.
[11] L. Ulianich, K. Suzuki, A. Mori, M. Nakazato, M. Pietrarelli, P. Goldsmith, F. Pacifico, E. Consiglio, S. Formisano, L.D. Kohn, Follicular thyroglobulin (TG) suppression of thyroid-restricted genes involves the apical membrane asialoglycoprotein receptor and TG phosphorylation, J. Biol. Chem. 274 (1999) 25099–25107.
[12] K. Suzuki, A. Mori, S. Lavaroni, E. Miyagi, L. Ulianich, R. Katoh, A. Kawaoi, L.D. Kohn, In vivo expression of thyroid transcription factor-1 RNA and its relation to thyroid function and follicular heterogeneity: identification of follicular thyroglobulin as a feedback suppressor of thyroid transcription factor-1 RNA levels and thyroglobulin synthesis, Thyroid 9 (1999) 319–331.
[13] K. Suzuki, A. Mori, S. Lavaroni, L. Ulianich, E. Miyagi, J. Saito, M. Nakazato, M. Pietrarelli, N. Shafran, A. Grassadonia, W.B. Kim, E. Consiglio, S. Formisano, L.D. Kohn, Thyroglobulin regulates follicular function and heterogeneity by suppressing thyroid-specific gene expression, Biochimie 81 (1999) 329–340.
[14] K. Suzuki, L.D. Kohn, Differential regulation of apical and basal iodide transporters in the thyroid by thyroglobulin, J. Endocrinol. 189 (2006) 247–255.
[15] L.D. Kohn, K. Suzuki, M. Nakazato, I. Royaux, E.D. Green, Effects of thyroglobulin and pendrin on iodide flux through the thyrocyte, Trends Endocrinol. Metab. 12 (2001) 10–16.
[16] K. Suzuki, A. Kawashima, A. Yoshihara, T. Akama, M. Sue, A. Yoshida, H.J. Kimura, Role of thyroglobulin on negative feedback autoregulation of thyroid follicular function and growth, J. Endocrinol. 209 (2011) 169–174.
[17] K. Suzuki, M. Nakazato, L. Ulianich, A. Mori-Aoki, E. Moriyama, H.K. Chung, M. Pietrarelli, A. Grassadonia, H. Matoba, L.D. Kohn, Thyroglobulin autoregulation of thyroid-specific gene expression and follicular function, Rev. Endocr. Metab. Disord. 1 (2000) 217–224.
[18] T. Akama, M. Sue, A. Kawashima, H. Wu, K. Tanigawa, S. Suzuki, M. Hayashi, A. Yoshihara, Y. Ishido, N. Ishii, K. Suzuki, Identification of microRNAs that mediate thyroid cell growth induced by TSH, Mol. Endocrinol. (2012).
[19] A. Kawashima, K. Tanigawa, T. Akama, H. Wu, M. Sue, A. Yoshihara, Y. Ishido, K. Kobiyama, F. Takeshita, K.J. Ishii, H. Hirano, H. Kimura, T. Sakai, N. Ishii, K. Suzuki, Fragments of genomic DNA released by injured cells activate innate immunity and suppress endocrine function in the thyroid, Endocrinology 152 (2011) 1702–1712.
[20] A. Hirai, S. Nakamura, Y. Noguchi, T. Yasuda, M. Kitagawa, I. Tatsuno, T. Oeda, K. Tahara, T. Terano, S. Narumiya, L.D. Kohn, Y. Saito, Geranylgeranylated rho small GTPase(s) are essential for the degradation of p27Kip1 and facilitate the progression from G1 to S phase in growth-stimulated rat FRTL-5 cells, J. Biol. Chem. 272 (1997) 13–16.
[21] G. Barrera-Hernandez, K.S. Park, A. Dace, Q. Zhan, S.Y. Cheng, Thyroid hormone-induced cell proliferation in GC cells is mediated by changes in G1 cyclin/cyclin-dependent kinase levels and activity, Endocrinology 140 (1999) 5267–5274.
[22] I.E. Royaux, K. Suzuki, A. Mori, R. Katoh, L.A. Everett, L.D. Kohn, E.D. Green, Pendrin, the protein encoded by the Pendred syndrome gene (PDS), is an apical porter of iodide in the thyroid and is regulated by thyroglobulin in FRTL-5 cells, Endocrinology 141 (2000) 839–845.
[23] H.M. Jeong, E.H. Han, Y.H. Jin, Y.P. Hwang, H.G. Kim, B.H. Park, J.Y. Kim, Y.C. Chung, K.Y. Lee, H.G. Jeong, Saponins from the roots of Platycodon grandiflorum stimulate osteoblast differentiation via p38 MAPK- and ERK-dependent RUNX2 activation, Food Chem. Toxicol. 48 (2010) 3362–3368.
[24] H.W. Yu, Q.F. Liu, G.N. Liu, Positive regulation of the Egr-1/osteopontin positive feedback loop in rat vascular smooth muscle cells by TGF-beta, ERK, JNK, and p38 MAPK signaling, Biochem. Biophys. Res. Commun. 396 (2010) 451–456.
[25] C.J. Marshall, MAP kinase kinase kinase, MAP kinase kinase and MAP kinase, Curr. Opin. Genet. Dev. 4 (1994) 82–89.
[26] D.K. Morrison, R.E. Cutler, The complexity of Raf-1 regulation, Curr. Opin. Cell Biol. 9 (1997) 174–179.
[27] L.J. Hayden, J.M. Shagrin, J.A. Young, Micropuncture investigation of the anion content of colloid from single rat thyroid follicles. A micromethod for the simultaneous determination of iodide and chloride in nanomole quantities, Pflugers Arch. 321 (1970) 173–186.
[28] G.B. Salabe, L. Corvo, H. Lotz, Thyroglobulin determined in thyroid fine needle aspiration biopsies by radial immunodiffusion and electroimmunodiffusion, Eur. J. Clin. Chem. Clin. Biochem. 34 (1996) 43–47.
[29] S. Smeds, A microgel electrophoretic analysis of the colloid proteins in single rat thyroid follicles. II. The protein concentration of the colloid single rat thyroid follicles, Endocrinology 91 (1972) 1300–1306.
[30] M. Aouadi, B. Binetruy, L. Caron, Y. Le Marchand-Brustel, F. Bost, Role of MAPKs in development and differentiation: lessons from knockout mice, Biochimie 88 (2006) 1091–1098.
[31] E.K. Kim, E.J. Choi, Pathological roles of MAPK signaling pathways in human diseases, Biochim. Biophys. Acta 2010 (1802) 396–405.
[32] M.M. McKay, D.K. Morrison, Integrating signals from RTKs to ERK/MAPK, Oncogene 26 (2007) 3113–3121.

Biochemical and Biophysical Research Communications 420 (2012) 616–622

Contents lists available at SciVerse ScienceDirect

Biochemical and Biophysical Research Communications

journal homepage: www.elsevier.com/locate/ybbrc

Neuronal glycosylation differentials in normal, injured and chondroitinase-treated environments

Michelle Kilcoyne [a], Shashank Sharma [a], Niamh McDevitt [b], Claire O'Leary [b], Lokesh Joshi [a], Siobhán S. McMahon [b,*]

[a] Glycoscience Group, National Centre for Biomedical Engineering Science, National University of Ireland, Galway, Ireland
[b] Anatomy, School of Medicine, National University of Ireland, Galway, Ireland

ARTICLE INFO

Article history:
Received 23 February 2012
Available online 20 March 2012

Keywords:
Spinal cord injury
Lectins
Glycosylation
Chondroitin sulphate proteoglycans
Neurons
In silico analysis

ABSTRACT

Glycosylation is found ubiquitously throughout the central nervous system (CNS). Chondroitin sulphate proteoglycans (CSPGs) are a group of molecules heavily substituted with glycosaminoglycans (GAGs) and are found in the extracellular matrix (ECM) and cell surfaces. Upon CNS injury, a glial scar is formed, which is inhibitory for axon regeneration. Several CSPGs are up-regulated within the glial scar, including NG2, and these CSPGs are key inhibitory molecules of axonal regeneration. Treatment with chondroitinase ABC (ChABC) can neutralise the inhibitory nature of NG2. A gene expression dataset was mined *in silico* to verify differentially regulated glycosylation-related genes in neurons after spinal cord injury and identify potential targets for further investigation. To establish the glycosylation differential of neurons that grow in a healthy, inhibitory and ChABC-treated environment, we established an indirect co-culture system where PC12 neurons were grown with primary astrocytes, Neu7 astrocytes (which over-express NG2) and Neu7 astrocytes treated with ChABC. After 1, 4 and 8 days culture, lectin cytochemistry of the neurons was performed using five fluorescently-labelled lectins (ECA MAA, PNA, SNA-I and WFA). Usually α-(2,6)-linked sialylation scarcely occurs in the CNS but this motif was observed on the neurons in the injured environment only at day 8. Treatment with ChABC was successful in returning neuronal glycosylation to normal conditions at all timepoints for MAA, PNA and SNA-I staining, and by day 8 in the case of WFA. This study demonstrated neuronal cell surface glycosylation changes in an inhibitory environment and indicated a return to normal glycosylation after treatment with ChABC, which may be promising for identifying potential therapies for neuronal regeneration strategies.

1. Introduction

Complex carbohydrates are found ubiquitously throughout the CNS and are involved in many developmental and functional processes in the nervous system, including cell–cell and cell–ECM interactions, adhesion and axonal guidance and neuronal migration [1,2]. *In vivo*, they interact with lectins, non-enzymatic carbohydrate-binding proteins of non-immune origin that precipitate glycoproteins or polysaccharides and agglutinate cells [3,4]. The expression of carbohydrates and their corresponding lectins is differentially regulated both temporally and spatially in the developing CNS [1,2,5] and cell surface glycosylation is known to be altered during cell differentiation [6] and disease states such as cancer [7].

After CNS injury, a glial scar is formed at the injury site which creates an inhibitory environment for axonal regeneration and remyelination [8]. This scar contains several growth-inhibitory compounds including myelin-associated glycoprotein (MAG, siglec-4), Nogo, semaphorines and CSPGs, of which NG2, neurocan and versican are the major components [9,10]. CSPGs are a group of molecules consisting of a protein core heavily substituted with covalently attached GAGs. CSPGs are normally found in the ECM and on cell surfaces, playing roles in barrier formation and axonal guidance [8].

Potential therapies for repair and regeneration after CNS injury include the manipulation or removal of GAGs from the injury site [8,11] by treatment with ChABC [12]. Numerous studies have demonstrated that ChABC treatment promotes functional recovery and axon regeneration [11–13]. Perineuronal nets (PNNs) are composed of CSPGs and hyaluronic acid and encase neurons in the spinal cord. As ChABC digests GAGs, it has been hypothesised that digestion of the PNNs contributes to the recovery of plasticity, improving functional recovery after peripheral nerve injury [14]. In addition, dermatan sulphate disaccharide, one possible product of ChABC degradation of CS, promoted neurite outgrowth in immortalised rat pheochromocytoma PC12 cells and primary cultures of hippocampal neurons and promoted neuronal survival *ex vivo* and *in vivo* [15].

* Corresponding author. Fax: +353 91 494520.
E-mail address: siobhan.mcmahon@nuigalway.ie (S.S. McMahon).

0006-291X/$ - see front matter © 2012 Elsevier Inc. All rights reserved.
http://dx.doi.org/10.1016/j.bbrc.2012.03.047

Given the importance of glycosylation in the CNS, there has been little attention to glycosylation changes of neurons in the injured environment or to the effect of ChABC treatment upon neuronal glycosylation. A multidisciplinary approach was taken to address these questions. Initially, *in silico* mining of a publicly available gene expression dataset was done to verify that glycosylation-related genes were differentially regulated after spinal cord injury and to identify potential targets for further investigation. An *in vitro* model with PC12 cells was then used to examine glycosylation expression in simulated normal, injured and ChABC-treated environments.

The PC12 cell line differentiates into neuron-like cells upon treatment with neurotrophins [16], and has been extensively used as a model for studying neuronal functions and responses including neurite outgrowth [17,18] and neuro-protective effects [19,20]. PC12 cells were co-cultured with various astrocytes [17,20] (normal primary astrocytes, Neu7 astrocytes and Neu7 astrocytes treated with ChABC) to model the different environments [21]. The Neu7 astrocytic cell line is an inhibitory cell line that has been engineered to overproduce NG2, versican and the CS-56 antigen [22] and is used to mimic the inhibitory environment which occurs following spinal cord injury [21–23]. The glycosylation expression profile of the PC12 cell surface was examined at intervals using lectin cytochemistry. Lectins bind specifically to distinct carbohydrate moieties, but may also contain one or more non-carbohydrate ligand sites [24]. Plant lectins have long been used as an analytical tool in tissue and cell histochemistry and particular carbohydrate motifs have been associated with otherwise indistinguishable cell types and stages of cell differentiation [4,6,25].

We present *in silico* mining and lectin profiling results of a healthy, injured and ChABC-treated model to profile cell surface glycosylation of neurons and attribute any glycosylation changes to the presence and removal of one class of glial scar inhibitory molecule, GAGs on CSPGs.

2. Materials and methods

2.1. Materials

Culture trays, transwells and cell culture plastics were from BD Falcon. Lectins were purchased from EY Labs (CA, USA). ProLong Gold antifade was from Invitrogen (Biosciences, Dublin, Ireland). PC12 cells were from ECACC (Salisbury, UK). All other reagents were from Sigma Aldrich Co. (Dublin, Ireland) unless otherwise indicated, and were of the highest grade available.

2.2. Cell cultures and environmental models

PC12 cells were cultured on poly-L-lysine (PLL; 10 μg/μL for 3 h) coated cover slips in 12-well trays in Dulbecco's modified eagle's medium (D-MEM, high glucose with L-glutamine) supplemented with 10% horse serum, 5% foetal bovine serum (FBS) and 1% penicillin and streptomycin (P/S) at 37 °C in a 5% humidified CO_2 atmosphere. The medium was supplemented with nerve growth factor (50 ng/mL) at intervals of three days for PC12 cell differentiation.

Primary cerebral astrocytes were obtained from P2 Sprague Dawley rat pups, purified and cultured as previously described [21]. Neu7 astrocytes were cultured in D-MEM supplemented with 10% horse serum, 1% L-glutamine and 1% P/S.

For 'normal' condition simulation, PC12 cells were co-cultured with primary astrocytes. PC12 cells were seeded at 5000 cells for 8 days *in vitro* (DIV), 10,000 cells for 4 DIV, and 50,000 cells for 1 DIV per PLL coated transwell in a 12-well tray. Astrocytes were seeded at the same density as above onto sterile cover slips in a 12-well tray. The PC12 cells were grown on the transwell to allow CSPGs secreted from the astrocytes grown in the same well to enter the media and interact with the PC12 cells, but not allow the two cell types to interact. For 'injured' condition, PC12 cells were grown with Neu7 cells. The 'treated' model consisted of PC12 cells grown with Neu7 cells with media treated with 0.1 unit/mL ChABC every 2 days, i.e. treated day 0 and every two days thereafter.

2.3. Lectin cytochemistry

Lectin cytochemistry at room temperature was performed on PC12 cells after growth at 1, 4 and 8 DIV as follows. Cells were fixed with 4% para-formaldehyde for 10 min and washed four times in 10 mM Tris–HCl, 1 mM $CaCl_2$, 1 mM $MgCl_2$, pH 7.4 (TBS). Cells were blocked with 2% periodate-treated [26] bovine serum albumin (BSA) in TBS for 30 min. The cells were washed four times in TBS and then incubated with fluorescein isothiocyanate (FITC)-labelled lectins (Table 1) for 1 h in the dark at the following concentrations: SNA-I, MAA, PNA and ECA at 20 μg/mL and WFA at 10 μg/mL in TBS. Inhibitory controls were also carried out in parallel by preincubation of the lectins with 100 mM concentrations of the appropriate haptenic carbohydrates in TBS for 1 h prior to cell staining as follows: SNA-I, MAA and PNA were prepared in lactose, ECA in galactose (Gal) and WFA in *N*-acetylgalactosamine (GalNAc) and staining was carried out in the presence of the sugar. The cells were washed twice in TBS, counterstained with 1 μg/mL DAPI in TBS for 5 min, washed four times in TBS and mounted on glass slides with a drop of ProLong Gold antifade.

2.4. Image and statistical analysis

Cells were imaged on an Olympus IX81 fluorescent microscope using Perkin-Elmer Volocity® image acquisition software. Observed intensity of staining for PC12 cells were tabulated using a scale of no binding (−), slight binding (+), moderate binding (++), intense binding (+++) and very intense binding (++++).

2.5. In silico data mining

A gene expression dataset of the response of rat motor neurons 0, 2, 7, 21 and 60 days after spinal cord injury (GeneChip rat genome 230 3.0 array, Affymetrix Inc., Santa Clara, CA) was downloaded from the Gene Expression Omnibus (accession number GSE19701, www.ncbi.nlm.nih.gov/geo/) [27]. Gene expression

Table 1
Lectins and their corresponding carbohydrate binding specificity.

Abbreviation	Lectin	Origin	Binding specificity
ECA	*Erythrina cristigalli* agglutinin	*Erythrina cristagalli* (coral tree)	Terminal Gal-β-(1→4)-GlcNAc/Glc (LacNAc/Lac), GalNAc, Gal
PNA	Peanut agglutinin	*Arachis hypogaea* (peanut)	β-Gal, Gal-β-(1→3)-GalNAc, (T-antigen), Lac
WFA	*Wisteria floribunda* agglutinin	*Wisteria floribunda* (Japanese wisteria)	GalNAc, lactose, Gal, chondroitin sulphate
MAA	*Maackia amurensis* agglutinin	*Maackia amurensis*	Neu-α-(2→3)-Gal-β-(1→4)-Glc(NAc), Gal-3-SO_4
SNA-I	*Sambucus nigra* lectin-I	*Sambucus nigra* (elderberry)	Neu-α-(2→6)-Gal(NAc)

analyses were performed using GeneSpring 11.5 (Agilent Technologies, Cork, Ireland) and further detailed in supplementary data.

3. Results

3.1. In silico analysis

In silico mining was done on a study of gene expression response of rat motor neurons following spinal cord injury [27]. After statistical and gene expression analyses, 6790 out of 31,099 probes were identified as having a 1.2-fold change above or below control day 0. From these probes, glycosylation-related genes were extracted and genes associated with the sialic acid pathway, glycosaminoglycans and chondroitin sulphate proteoglycans, galactose and lectins, including galectins, were differentially regulated and their products have been reported to have altered expression after spinal cord injury [9,28–30] (see supplementary data). Neuronally expressed β-galactoside α-2,3-sialyltransferase (ST) genes were both up- and down-regulated after injury, with two of the initially up-regulated post-injury genes down-regulated again at 21 days post-injury. Only one α-2,6- and one α-2,8-ST were extracted and both were down-regulated at all timepoints post-injury (Fig. 1A). *N*-acetylgalactosaminyltransferases (GalNAcTs) and galactosyltransferases (GalTs) were both significantly up- and down-regulated post-injury, with one GalNAcT going from up- to down-regulated at 7 days post-injury and returning to up-regulated by 21 days. One GalT (a β-1,3GalT) went from initial down-regulation at day 2 to subsequent up-regulation at all later timepoints and conversely, the only significant α-1,3GalT (AI178222) went from initial up-regulation to down-regulation from 7 days onwards (Fig. 1B).

C-type lectin family genes were all up-regulated at all timepoints, confirming the presence of carbohydrate recognition domains on cell surface. Galectins are β-galactoside binding lectins [1,31]. The majority of extracted galectin genes were up-regulated at all timepoints following injury except for a soluble galectin-3 (NM_031832), which was down-regulated at day 7 post-injury but up-regulated at all other timepoints, and a galectin-related protein (NM_057187), which was down-regulated at all timepoints but up-regulated at day 7 post-injury (Fig. S1, supplementary).

3.2. In vitro profiling

The cell surface glycosylation changes of differentiated PC12 cells were analysed after 1, 4 and 8 DIV using fluorescently-labelled lectins selected to detect sialic acid-, galactose- and chondroitin sulphate-related motifs. The intensity of staining was recorded and tabulated (Table 2). All lectin cytochemistry was also carried out in parallel in the presence of haptenic sugars. A reduction in binding intensity was noted in these cases (not shown), demonstrating that lectin binding was carbohydrate-mediated [25].

Slight staining of PC12 cells with ECA was observed at 1 and 8 days in the 'healthy' primary astrocyte co-culture (Fig. 2A and G, respectively), but increased staining intensity was observed at

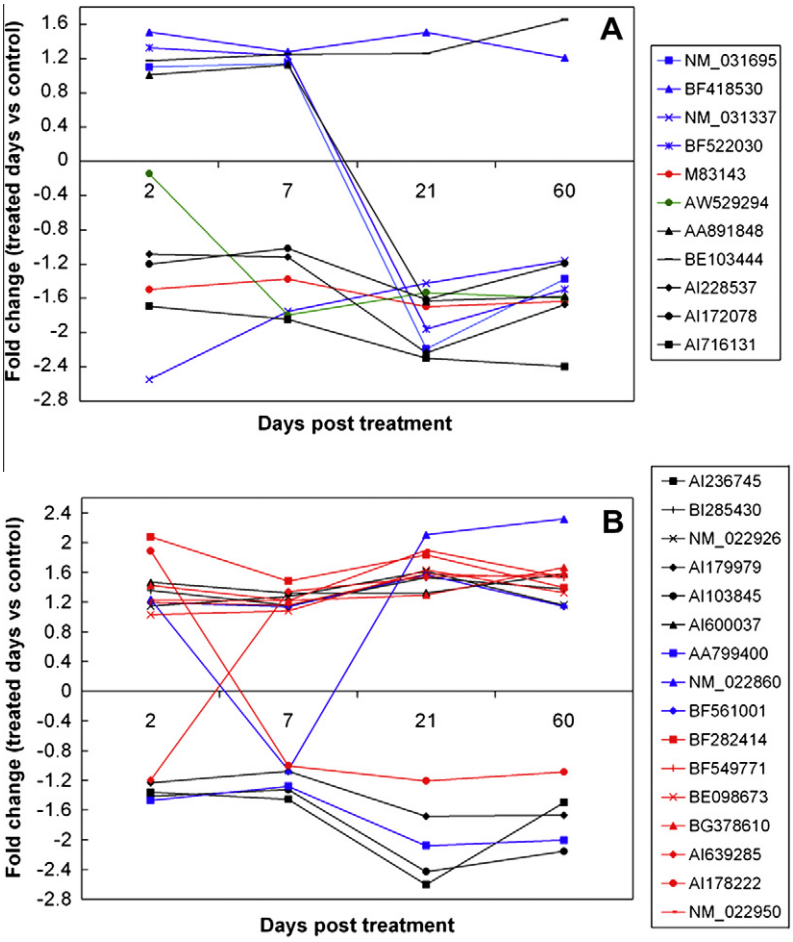

Fig. 1. Up- and down-regulated glycosylation-related genes compared to control day 0. (A) Sialic acid pathway related genes where the accession numbers of β-galactoside α-2,3-STs are blue, α-2,6-ST is red, α-2,8-ST is green and others which include sialic acid transporters are black. (B) Galactose-related genes where the accession numbers of polypeptide GalNAcTs are black, GalNAcTs are blue and GalTs are red. See supplementary data for full assignment of GenBank accession numbers (For interpretation of the references to colour in this figure legend, the reader is referred to the web version of this article).

Table 2
Intensity of lectin binding to PC12 cells. 'Normal' condition was simulated by PC12/primary astrocyte co-culture, 'injured' condition by PC12/Neu7 astrocyte co-culture and 'treated' condition by treatment of media of PC12/Neu7 astrocyte co-culture with ChABC.

Day	Lectin	Normal	Injured	Treated
1	ECA	+	++	++
4		+++	+	++
8		+	+++	+++
1	PNA	+	+	+
4		++++	+	+++
8		++	+++	++
1	WFA	++	±	+
4		+	+	++
8		+++	++	+++
1	MAA	+	+	+
4		+	++	+
8		++++	++	+++
1	SNA-I	–	–	–
4		–	–	–
8		–	++	–

– No binding; + slight binding; ++ moderate binding; +++ intense binding; ++++ very intense binding.

4 days (Fig. 2D and Table 2). Cells grown in the 'inhibitory' environment (Fig. 2B) showed more intense staining than cells growing in a normal astrocyte environment at 1 DIV, and maximum staining intensity was reached at 8 DIV (Fig. 2H), delayed compared to the 'healthy' environment. The ChABC-treated group showed no change in intensity of staining over time. At 1 DIV in the 'treated' environment, the staining intensity was moderate and highest intensity was observed on the cell surface, at 'caps' on the cells (Fig. 2C). At 4 DIV, the intensity remained moderate but was dispersed throughout the cell and was increased by 8 DIV, comparable to 4 DIV in the normal environment (Table 2 and Fig. 2F and I).

PNA staining of PC12 cells was observed under all conditions, at all timepoints, differing in intensity and staining dispersal and was similar to that of ECA for normal condition. Cells grown in 'normal' and 'treated' conditions stained slightly and very slightly, respectively, at 1 DIV. The intensity increased by day 4 and decreased again to moderate binding by day 8. Day 4 of 'normal' co-culture cells appeared to have maximal binding at the cell surface, especially where cells touched one another (Fig.S2 and Table 2). In contrast, cells grown in 'injured' conditions only reached maximal intensity by day 8.

In the 'normal' co-culture group, WFA bound with moderate intensity to PC12 cells at 1 DIV, with greatest intensity observed where cells touched one another. Binding intensity decreased to slight binding at day 4 and increased to very intense at 8 DIV, in common with both injured and treated environments (Fig. S3 and Table 2). The binding intensity variation of the injured and treated environments were similar, with very slight intensity

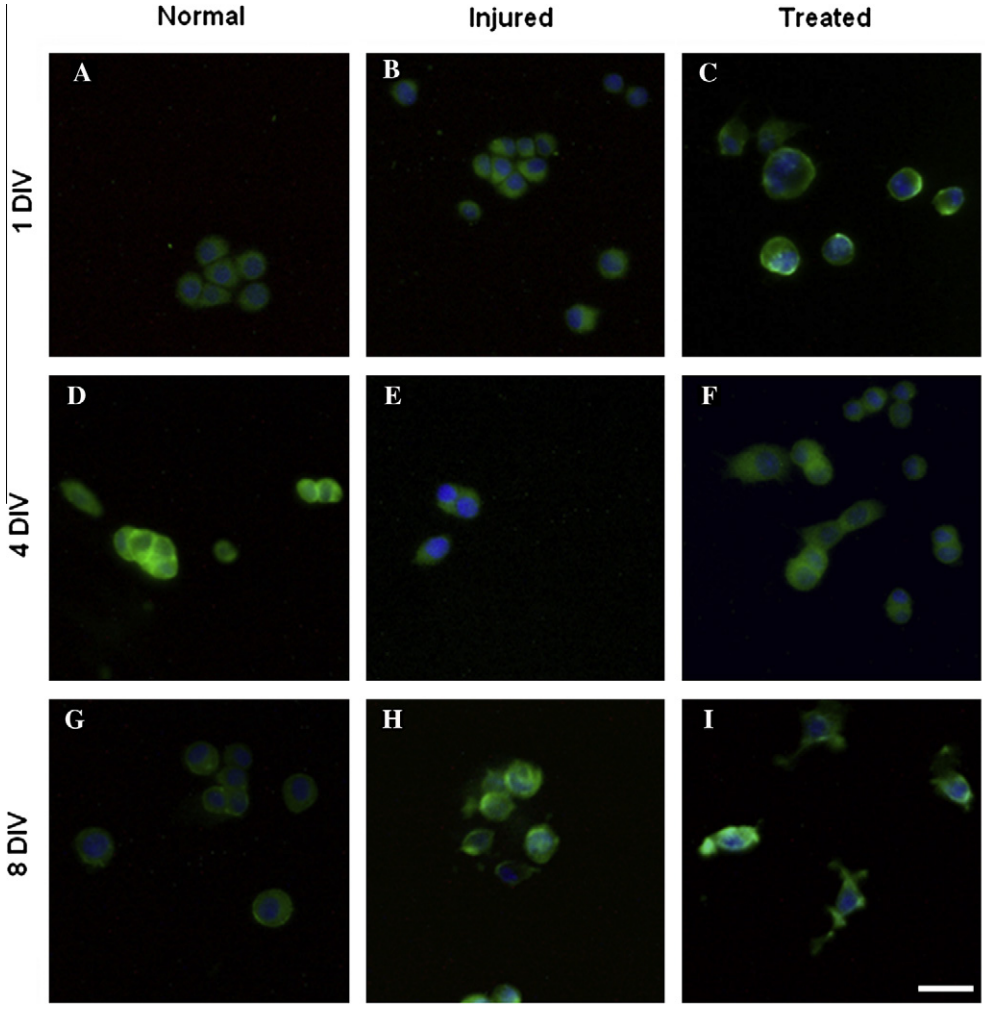

Fig. 2. Photomicrographs of ECA–FITC stained PC12 cells at 1 (A–C), 4 (D–F) and 8 DIV (G–I) co-cultured with primary astrocytes ('normal'), Neu7 cells ('injured') and Neu7 cells treated with ChABC ('treated'), respectively. Scale bar = 30 μm.

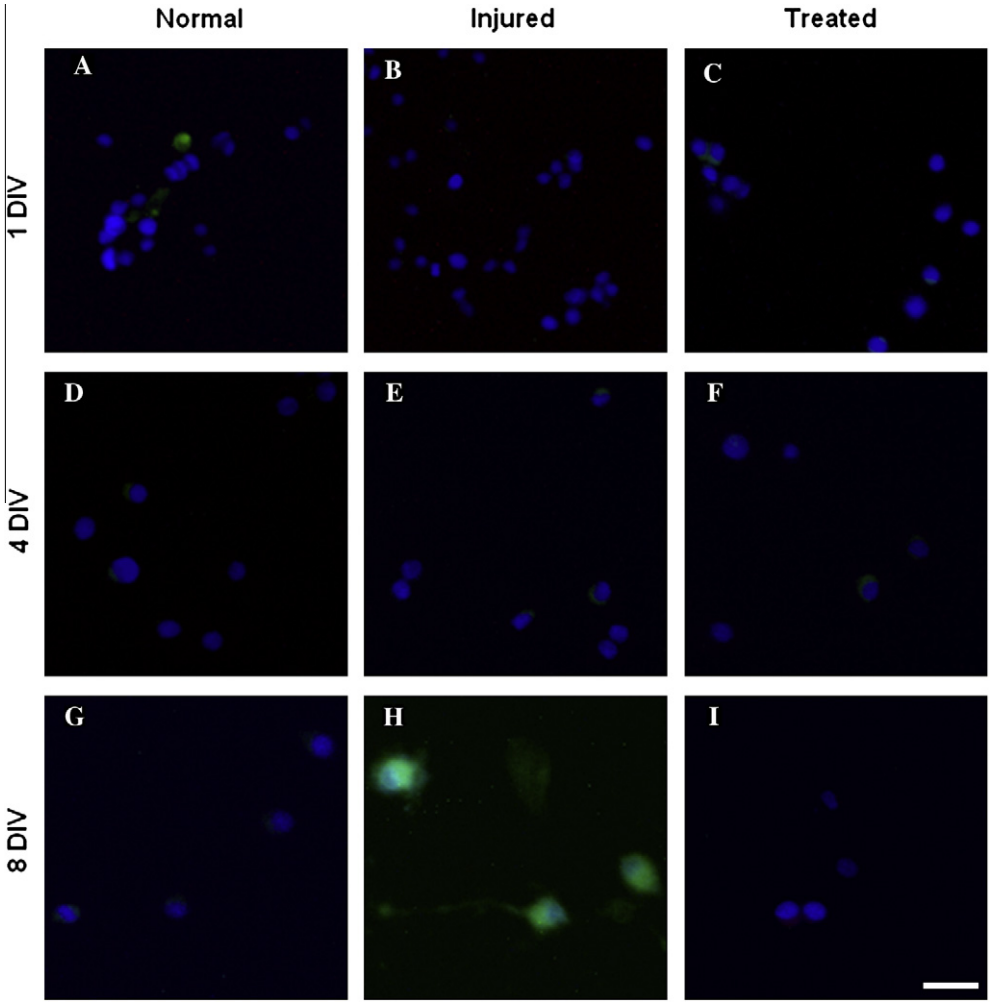

Fig. 3. Photomicrographs of SNA-I-FITC stained PC12 cells at 1 (A–C), 4 (D–F) and 8 DIV (G–I) co-cultured with primary astrocytes ('normal'), Neu7 cells ('injured') and Neu7 cells treated with ChABC ('treated'), respectively. Scale bar = 30 μm.

binding of WFA at 1 DIV, slightly increased binding at day 4 and greater intensity observed where cells touched one another in the 'injured' environment (Fig. S3E), and moderate to intense binding at day 8. The slight binding intensity observed at 4 DIV in the 'injured' co-culture environment was most apparent at the point where the cells touched or at the cell surface.

MAA stained PC12 cells under all conditions at each timepoint, and staining intensity increased over time reaching greatest intensity at 8 DIV for all environments (Fig. S4 and Table 2).

SNA-I did not stain the PC12 cells at any timepoint or condition (Fig. 3A–G and I), except at 8 DIV (Fig. 3H and Table 2) in the 'injured' co-culture group where cell bodies and neurites were moderately stained.

4. Discussion

The retrieved genes from the *in silico* analysis verified that the expression of glycosylation-related genes was altered at various timepoints post-injury and identified STs, GalNAcTs, GalTs and galectins as potential targets for differential expression in injury conditions. The *in vitro* model used to simulate normal, injured and ChABC-treated environments suggested that neuronal glycosylation changes occurred in these conditions.

The lectin ECA binds with greatest affinity to unsialylated terminal *N*-acetyllactosamine (LacNAc) structures, which are a major component of glycoprotein *N*-linked oligosaccharides and glycolipids (Table 1). Zhang, et al. [28] found that ECA binding increased after brain injury in mice, correlating to our observations at 8 DIV in the 'injured' environment. ECA staining where the cells touch may indicate a role for this carbohydrate motif in cell–cell adhesion. Galectins are involved in cell–cell interactions, adhesion, differentiation, apoptosis and axonal guidance [1,31], and bind to motifs elucidated by ECA. The majority of galectins with altered expression post-injury were up-regulated at all timepoints. Expression of the potential galectin receptor evidenced by ECA binding seemed to be time-dependent, and reached a maximum in the 'healthy' culture at day 4, which may in turn reflect temporal expression of galectins in the CNS. However, expression of this receptor appeared to be delayed in the injured environment as maximum expression was at day 8, in common with the treated environment.

In common with ECA, PNA also stained at areas of cell–cell contact and staining intensity was temporally regulated, except for the treated environment which was more similar to the healthy condition rather than the injured (Table 2). In the *in silico* analysis, all significant β-GalTs were up-regulated by day 7 post-injury, which may correlate with the intense PNA and ECA staining of the PC12 cells at 8 DIV.

WFA lectin is commonly used as a marker for PNNs [11,32]. In all three culture conditions maximal WFA intensity was noted at the latest timepoint, and was most intense where the cells

touched, which may indicate a role for the elucidated motif in adhesion. However, by day 7 post-injury, only one β1,4GalNAcT (BF561001) was up-regulated in the *in silico* analysis but the majority of CSPG-related significant genes were up-regulated at all timepoints post-injury (supplementary data).

Sialic acids are the mainly terminal residues of complex *N*- and *O*-linked oligosaccharides of glycoproteins and glycolipids and comprise polysialic acid in an α-(2,8)-linkage on neural cell adhesion molecule (NCAM). Sialylated motifs on the cell surfaces of vertebrates are involved in cell–cell communication, development and adhesion [33], interacting with siglecs and galectins [31]. The lectins MAA and SNA-I have binding specificity for α-(2,3)- and α-(2,6)-linked sialic acid, respectively, and MAA is also known to bind to Gal-3-SO_4 [34] (Table 1). In the brain, the occurrence of α-(2,3)-linked sialic acid is predominant with little to no α-(2,6)-linkage expected [2]. SNA-I binding was observed in the 'inhibitory' environment at 8 DIV, but was not seen in the ChABC-treated condition, where cell glycosylation was comparable to the 'normal' environment. The altered expression of significant α-2,6- and α-2,3-STs post-injury did not correlate with staining intensities, and interestingly, expression of the α-2,8-ST, relevant to PSA synthesis, was down-regulated at all timepoints. Electrical signalling in neurons, skeletal muscle cells and cardiomycetes is modulated by the sialic acid content of particular isoforms of ion channels [35]. Altered or aberrant sialic acid expression could impact neuron polarisation [35], which may be consistent with altered excitability of neurons post-injury [33]. Exposure of α-(2,6)-linked sialic acid and binding to SNA-I has been observed on apoptotic and necrotic cells [36], and α-(2,6)-sialylation has been identified as blocking binding to galectins, hence functioning as a biological 'off switch' [31]. Interestingly, the expression of α-2,6-ST was down-regulated at all timepoints post-injury while galectin-1 expression, which has been associated with pathogenesis in the injured spinal cord [30], was up-regulated.

ChABC treatment promotes functional recovery and reduces the inhibitory effect of CSPGs but anatomical regeneration post-treatment is limited [28]. This may be due in part to the potentially immunogenic carbohydrate 'stub' structures created by ChABC action [13]. The NG2 protein core has also been suggested to have an inhibitory effect on axonal growth [9]. However, in the model system, treatment with ChABC appeared to be successful in returning the neuronal glycosylation to normal conditions at all timepoints in the case of MAA, PNA and SNA-I staining, and by day 8 in the case of WFA.

A multidisciplinary approach allowed the *in silico* verification of differentially regulated glycosylation-related genes in neurons and targeting of altered carbohydrate motifs. The model system demonstrated neuronal cell surface glycosylation changes in an inhibitory environment and may be the first indication of the occurrence of abnormal sialylation in an injured environment. The limited number of cell types in a controlled environment can help attribute any changes to specific molecules and their degradation products alone, and help fit this information into a wider injury picture. In addition, this model indicated a return to normal neuronal glycosylation after treatment with ChABC which may be promising for identifying points of intervention or potential therapies for neuronal regeneration strategies.

Acknowledgments

The authors thank Dr. J.Q. Gerlach (NUI Galway) for helpful discussions, and Dr. J. Rogers and Prof. J. Fawcett (University of Cambridge) for their kind gift of the Neu7 astrocyte cell line. This work was supported by the Health Research Board of Ireland (SMcM), and grants 08/SRC/B1393 from Science Foundation Ireland for Alimentary Glycoscience Research Cluster (SS and LJ) and 260600 from the EU FP7 program for GlycoHIT (MK and LJ).

Appendix A. Supplementary data

Supplementary data associated with this article can be found, in the online version, at doi:10.1016/j.bbrc.2012.03.047.

References

[1] T.M. Jessell, M.A. Hynes, J. Dodd, Carbohydrates and carbohydrate-binding proteins in the nervous system, Annu. Rev. Neurosci. 13 (1990) 227–255.
[2] R. Kleene, M. Schachner, Glycans and neural cell interactions, Nat. Rev. Neurosci. 5 (2004) 195–208.
[3] I.J. Goldstein, R.C. Hughes, M. Monsigny, T. Osawa, N. Sharon, What should be called a lectin? Nature 285 (1980) 66.
[4] N. Sharon, H. Lis, Lectins, Kluwer Academic Publishers, Dordrecht, 2003.
[5] J. Tenne-Brown, A.C. Puche, B. Key, Expression of galectin-1 in the mouse olfactory system, Int. J. Dev. Biol. 42 (1998) 791–799.
[6] M.C. Dodla, A. Young, A. Venable, K. Hasneen, R.R. Rao, D.W. Machacek, S.L. Stice, Differing lectin binding profiles among human embryonic stem cells and derivatives aid in the isolation of neural progenitor cells, PLoS One 6 (2011) e23266.
[7] S.D. Szajda, A. Jankowska, K. Zwierz, Carbohydrate markers in colon carcinoma, Dis. Markers 25 (2008) 233–242.
[8] S.A. Busch, J. Silver, The role of extracellular matrix in CNS regeneration, Curr. Opin. Neurobiol. 17 (2007) 120–127.
[9] A.M. Tan, W. Zhang, J.M. Levine, NG2: a component of the glial scar that inhibits axon growth, J. Anat. 207 (2005) 717–725.
[10] R.A. Asher, D.A. Morgenstern, M.C. Shearer, K.H. Adcock, P. Pesheva, J.W. Fawcett, Versican is upregulated in CNS injury and is a product of oligodendrocyte lineage cells, J. Neurosci. 22 (2002) 2225–2236.
[11] J.M. Massey, C.H. Hubscher, M.R. Wagoner, J.A. Decker, J. Amps, J. Silver, S.M. Onifer, Chondroitinase ABC digestion of the perineuronal net promotes functional collateral sprouting in the cuneate nucleus after cervical spinal cord injury, J. Neurosci. 26 (2006) 4406–4414.
[12] E.J. Bradbury, L.D.F. Moon, R.J. Popat, V.R. King, G.S. Bennett, P.N. Patel, J.W. Fawcett, S.B. McMahon, Chondroitinase ABC promotes functional recovery after spinal cord injury, Nature 416 (2002) 636–640.
[13] D. Crespo, R.A. Asher, R. Lin, K.E. Rhodes, J.W. Fawcett, How does chondroitinase promote functional recovery in the damaged CNS? Exp. Neurol. 206 (2007) 159–171.
[14] C.M. Galtrey, R.A. Asher, F. Nothias, J.W. Fawcett, Promoting plasticity in the spinal cord with chondroitinase improves functional recovery after peripheral nerve repair, Brain 130 (2007) 926–939.
[15] A. Rolls, H. Avidan, L. Cahalon, H. Schori, S. Bakalash, V. Litvak, S. Lev, O. Lider, M. Schwartz, A disaccharide derived from chondroitin sulphate proteoglycan promotes central nervous system repair in rats and mice, Eur. J. Neurosci. 20 (2004) 1973–1983.
[16] L.A. Greene, A.S. Tischler, Establishment of a noradrenergic clonal line of rat adrenal pheochromocytoma cells which respond to nerve growth factor, Proc. Natl. Acad. Sci. U. S. A. 73 (1976) 2424–2428.
[17] J.L. Anderl, S. Redpath, A.J. Ball, A neuronal and astrocyte co-culture assay for high content analysis of neurotoxicity, J. Vis. Exp. 27 (2009).
[18] M.R. Andrews, S. Czvitkovich, E. Dassie, C.F. Vogelaar, A. Faissner, B. Blits, F.H. Gage, C. Ffrench-Constant, J.W. Fawcett, A9 integrin promotes neurite outgrowth on tenascin-C and enhances sensory axon regeneration, J. Neurosci. 29 (2009) 5546–5557.
[19] S. Yu, M. Liu, X. Gu, F. Ding, Neuroprotective effects of salidroside in the PC12 cell model exposed to hypoglycemia and serum limitation, Cell. Mol. Neurobiol. 28 (2008) 1067–1078.
[20] R.B. Tjalkens, X. Liu, B. Mohl, T. Wright, J.A. Moreno, D.L. Carbone, S. Safe, The peroxisome proliferator-activated receptor-γ agonist 1,1-bis(3′-indolyl)-1-(p-trifluoromethylphenyl)methane suppresses manganese-induced production of nitric oxide in astrocytes and inhibits apoptosis in cocultured PC12 cells, J. Neurosci. Res. 86 (2008) 618–629.
[21] E.M. Donnelly, P.M. Strappe, L.M. McGinley, N.N. Madigan, E. Geurts, G.E. Rooney, A.J. Windebank, J. Fraher, P. Dockery, T. O'Brien, S.S. McMahon, Lentiviral vector-mediated knockdown of the neuroglycan 2 proteoglycan or expression of neurotrophin-3 promotes neurite outgrowth in a cell culture model of the glial scar, J. Gene Med. 12 (2010) 863–872.
[22] P.S. Fidler, K. Schuette, R.A. Asher, A. Dobbertin, S.R. Thornton, Y. Calle-Patino, E. Muir, J.M. Levine, H.M. Geller, J.H. Rogers, A. Faissner, J.W. Fawcett, Comparing astrocytic cell lines that are inhibitory or permissive for axon growth: the major axon-inhibitory proteoglycan is NG2, J. Neurosci. 19 (1999) 8778–8788.
[23] W.-L. Kuan, C.B. Hurelbrink, R.A. Barker, Increased capacity for axonal outgrowth using xenogenic tissue in vitro and in a rodent model of Parkinson's disease, Xenotransplantation 13 (2006) 233–247.
[24] S.H. Barondes, Bifunctional properties of lectins: lectins redefined, Trends Biochem. Sci. 13 (1988) 480–482.
[25] J.Q. Gerlach, M. Kilcoyne, S. Eaton, V. Bhavanandan, L. Joshi, Non-carbohydrate-mediated interaction of lectins with plant proteins, in: A.M. Wu (Ed.), The

Molecular Immunology of Complex Carbohydrates-3, Springer, New York, pp. 257–269.
[26] W.F. Glass, R.C. Briggs, L.S. Hnilica, Use of lectins for detection of electrophoretically separated glycoproteins transferred onto nitrocellulose sheets, Anal. Biochem. 115 (1981) 219–224.
[27] J. Ryge, O. Winther, J. Wienecke, A. Sandelin, A.-C. Westerdahl, H. Hultborn, O. Kiehn, Transcriptional regulation of gene expression clusters in motor neurons following spinal cord injury, BMC Genomics 11 (2010) 365.
[28] H. Zhang, T. Muramatsu, A. Murase, S. Yuasa, K. Uchimura, K. Kadomatsu, *N*-Acetylglucosamine 6-*O*-sulfotransferase-1 is required for brain keratan sulfate biosynthesis and glial scar formation after brain injury, Glycobiology 16 (2006) 702–710.
[29] Y. Zhang, M. Ghadiri-Sani, X. Zhang, P.M. Richardson, J. Yeh, X. Bo, Induced expression of polysialic acid in the spinal cord promotes regeneration of sensory axons, Mol. Cell. Neurosci. 35 (2007) 109–119.
[30] D. Kurihara, M. Ueno, T. Tanaka, T. Yamashita, Expression of galectin-1 in immune cells and glial cells after spinal cord injury, Neurosci. Res. 66 (2010) 265–270.
[31] Y. Zhuo, S.L. Bellis, Emerging role of α2,6-sialic acid as a negative regulator of galectin binding and function, J. Biol. Chem. 286 (2011) 5935–5941.
[32] J. Ajmo, A. Eakin, M. Hamel, P. Gottschall, Discordant localization of WFA reactivity and brevican/ADAMTS-derived fragment in rodent brain, BMC Neurosci. 9 (2008) 14.
[33] E. Repnikova, K. Koles, M. Nakamura, J. Pitts, H. Li, A. Ambavane, M.J. Zoran, V.M. Panin, Sialyltransferase regulates nervous system function in *Drosophila*, J. Neurosci. 30 (2010) 6466–6476.
[34] X. Bai, J.R. Brown, A. Varki, J.D. Esko, Enhanced 3-*O*-sulfation of galactose in Asn-linked glycans and *Maackia amurenesis* lectin binding in a new Chinese hamster ovary cell line, Glycobiology 11 (2001) 621–632.
[35] T.A. Schwetz, S.A. Norring, E.S. Bennett, *N*-glycans modulate Kv1.5 gating but have no effect on Kv1.4 gating, Biochim. Biophys. Acta 1798 (2010) 367–375.
[36] N. Malagolini, M. Chiricolo, M. Marini, F. Dall'Olio, Exposure of α2,6-sialylated lactosaminic chains marks apoptotic and necrotic death in different cell types, Glycobiology 19 (2009) 172–181.

Biochemical and Biophysical Research Communications 420 (2012) 623–627

Contents lists available at SciVerse ScienceDirect

Biochemical and Biophysical Research Communications

journal homepage: www.elsevier.com/locate/ybbrc

Real-time monitoring of inflammation status in 3T3-L1 adipocytes possessing a secretory Gaussia luciferase gene under the control of nuclear factor-kappa B response element

Haruka Nagasaki [1], Takeshi Yoshimura [1], Naohito Aoki *

Department of Life Sciences, Graduate School of Bioresources, Mie University, Tsu 514-8507, Japan

ARTICLE INFO

Article history:
Received 11 March 2012
Available online 17 March 2012

Keywords:
Adipocyte
Inflammation
NF-κB

ABSTRACT

We have established 3T3-L1 cells possessing a secretory Gaussia luciferase (GLuc) gene under the control of nuclear factor-kappa B (NF-κB) response element. The 3T3-L1 cells named 3T3-L1-NF-κB-RE-GLuc could differentiate into adipocyte as comparably as parental 3T3-L1 cells. Inflammatory cytokines such as tumor necrosis factor (TNF)-α and interleukin (IL)-1β induced GLuc secretion of 3T3-L1-NF-κB-RE-GLuc adipocytes in a concentration- and time-dependent manner. GLuc secretion of 3T3-L1-NF-κB-RE-GLuc adipocytes was also induced when cultured with RAW264.7 macrophages and was dramatically enhanced by lipopolysaccharide (LPS)-activated macrophages. An NF-κB activation inhibitor BAY-11-7085 and an antioxidant N-acetyl cysteine significantly suppressed GLuc secretion induced by macrophages. Finally, we found that rosemary-derived carnosic acid strongly suppressed GLuc secretion induced by macrophages and on the contrary up-regulated adiponectin secretion. Collectively, by using 3T3-L1-NF-κB-RE-GLuc adipocytes, inflammation status can be monitored in real time and inflammation-attenuating compounds can be screened more conveniently.

1. Introduction

Obesity is highly associated with the increased incidence of various diseases including hypertension, arteriosclerosis, and type 2 diabetes [1]. Recent studies have suggested that low-grade inflammation caused in obese adipose tissue may be a potential mechanism by which obesity leads to insulin resistance [2,3].

It has been demonstrated that obese adipose tissue is characterized by the enhanced infiltration of macrophages [4,5]. Macrophages produce various inflammatory cytokines such as tumor necrosis factor (TNF)-α, interleukin (IL)-1β, and IL-6 and thereby contribute to inflammation in obese adipose tissue [6]. Critical involvement of these cytokines has been evidenced in adipose tissues of various models of mice and human obesity [7–9]. Suganami et al. reported that the paracrine loop involving adipocyte-derived free fatty acid (FFA), MCP-1, and macrophage-derived TNF-α establishes a vicious cycle that aggravates the inflammatory changes and insulin resistance in obese adipose tissue [10].

When inflammatory cytokines act on the adipocytes, nuclear factor-kappa B (NF-κB) pathway is activated [4] leading to inhibition of insulin action, glucose incorporation, and dysregulation of adipocytokine production, which can be evaluated by cumbersome and time-consuming strategies. For instance, insulin action can be evaluated by using phospho-specific antibodies directed against insulin receptor and its downstream molecules such as insulin receptor substrate (IRS)-1/2 and Akt. Glucose incorporation assay is generally required to use radiolabeled 2-deoxyglucose. Expression and secretion of adipocytokines are in most cases examined by using commercial expensive ELISA kits.

In this study, we established 3T3-L1 cells constitutively possessing a secretory Gaussia luciferase (GLuc) gene under the control of NF-κB response element (NF-κB-RE). Upon TNF-α or IL-1β treatment, GLuc activity was easily detected in the conditioned medium (CM) of the established adipocytes in a concentration-dependent manner, and time-dependent response to these cytokines could be examined without cell lysis. Macrophage-induced inflammation could also be monitored in real time by examining GLuc activity in a small volume of the CM. Finally, the established adipocytes were applied to screen natural compounds to attenuate macrophage-induced inflammation.

2. Materials and methods

2.1. Materials

Recombinant mouse TNF-α was purchased from R&D systems (Minneapolis, MN). IL-1β, lipopolysaccharide (LPS), carnosic acid,

* Corresponding author. Address: Department of Life Sciences, Graduate School of Bioresources, Mie University, 1577 Kurimamachiya-cho, Tsu 514-8507, Japan. Fax: +81 59 231 9675.
E-mail address: n-aoki@bio.mie-u.ac.jp (N. Aoki).
[1] These authors contributed equally to this study.

0006-291X/$ - see front matter © 2012 Elsevier Inc. All rights reserved.
http://dx.doi.org/10.1016/j.bbrc.2012.03.049

and ursolic acid were obtained from Sigma–Aldrich (St. Louis, MO). (−)-Epigallocatechin-3-gallate (EGCG) was kindly provided by Mitsui Norin Co., Ltd. (Tokyo, Japan). An antibody to adiponectin was kindly provided by Dr. Kihara (Osaka University).

2.2. Plasmid

pGLuc Mini-TK plasmid vector was purchased from New England BioLabs (Ipswich, MA). Two oligonucleotides corresponding to NF-κB responsive element (NF-κB-RE) such as 5′-AGCTGGGAATTTCC GGGGACTTTCCGGGAATTTCCGGGGACTTTCCGGGAATTTCC-3′ and 5′-GATCGGAAATTCCCGGAAAGTCCCCGGAAATTCCCGGAAAGTCCCC GGAAATTCCC-3′ were synthesized, annealed and inserted into pGLuc Mini-TK vector through the HindIII and BamHI sites, generating pGLuc-NF-κB-RE. Insertion was confirmed by sequencing.

2.3. Cell culture and transfection

3T3-L1 cells were cultured in DMEM (high glucose) supplemented with 10% fetal calf serum (FCS) and transfected with the pGLuc-NF-κB-RE or pGLuc Mini-TK (mock) plasmid by using FuGENE6 (Roche Applied Science, Indianapolis, IN). Following selection with G418 (1 mg/ml) for 2 weeks, survived polyclonal cell populations, named 3T3-L1-NF-κB-RE-GLuc or 3T3-L1-TK-GLuc, were harvested, expanded and directly used for the indicated assays to avoid clonal deviation and loss of adipogenic properties. We have often experienced that 3T3-L1 cells relatively easily lose adipogenic properties following clonal selection. Adipogenic differentiation of the cells was induced as described [11]. Images were taken by microscope (IX71; Olympus, Tokyo, Japan) equipped with cooled CCD camera (DP72; Olympus). RAW264.7 (RAW) macrophages were cultured in DMEM (high glucose) supplemented with 10% FCS.

2.4. Co-culture of adipocytes and macrophages

RAW macrophages (1.7×10^4 cells) were plated onto fully differentiated 3T3-L1-NF-κB-RE-GLuc or 3T3-L1-TK-GLuc adipocytes (Day 8 after differentiation induction) in 500 μL DMEM + 10% FCS/well of 24-well plate and cultured for the indicated periods with or without the indicated compounds. In some cases, RAW macrophages were pretreated with 100 ng/mL LPS for 24 h.

2.5. GLuc activity assay

GLuc activity in the conditioned medium (CM) was examined by using BioLux Gaussia Luciferase Assay Kit (New England BioLabs) according to the manufacturer's instructions. Briefly, 10 μl aliquots of the CM were mixed with 10 μl of 100-fold diluted substrate solution and incubated at 37 °C for 5 min. Luminescence was measured for 30 s by using Luminescencer Octa (ATTO, Tokyo, Japan).

3. Results

3.1. Establishment of 3T3-L1 cells stably expressing GLuc under the control of NF-κB-RE

It is generally believed that transfection into 3T3-L1 cells is relatively harder than that into other cell lines. However, by using FuGENE6 transfection reagent, we could achieve nearly 50% transfection efficiency (data not shown). Following transfection with pGLuc-NF-κB-RE or pGLuc Mini-TK and subsequent G418 selection, survived polyclonal cell populations, named 3T3-L1-NF-κB-RE-GLuc or 3T3-L1-TK-GLuc, were found to be able to fully differentiate into adipocytes comparable to parental 3T3-L1 adipocytes (Fig. 1A). Secretion of adiponectin of the established adipocytes was also comparable to parental 3T3-L1 adipocytes (Fig. 1B). After adipogenic differentiation induction, 3-day CM was sequentially collected and assayed for GLuc activity. As shown in Fig. 1C, the day 2–5 CM of 3T3-L1-NF-κB-RE-GLuc adipocytes exhibited relatively higher GLuc activity. GLuc activity of the day 5–8 CM decreased to nearly 50% and the activity was thereafter constantly detected. Throughout the time course, GLuc activity of 3T3-L1-NF-κB-RE-GLuc adipocytes was always over that of 3T3-L1-TK-GLuc, suggesting that endogenous stimuli could activate NF-κB and such stimuli might be independent of adipogenic maturation. All the properties examined of the established cell populations remained unchanged after repeated subcultures, and the same study was repeated twice generating essentially the same results (data not shown).

3.2. Treatment of 3T3-L1-NF-κB-GLuc adipocytes with TNF-α or IL-1β induced GLuc secretion in a concentration- and time-dependent manner

Inflammatory cytokines such as TNF-α and IL-1β are well known to induce NF-κB activation. When treated with TNF-α or IL-1β, 3T3-L1-NF-κB-GLuc adipocytes secreted GLuc into culture medium in a concentration-dependent manner (Fig. 2A and B), while 3T3-L1-TK-GLuc adipocytes did not respond to TNF-α or IL-1β at all (data not shown). At least 100 pg/ml of TNF-α or IL-1β was required to significantly induce GLuc activity. Time course analyses revealed that significant GLuc activity was first detected 2 h after TNF-α or IL-1β stimulation at the concentration of 10 ng/mL (Fig. 2C and D). In the case of TNF-α, GLuc activity increased up to 48 h and was kept up to 72 h following stimulation. On the other hand, IL-1β stimulation abruptly increased GLuc activity up to 8 h and thereafter the activity was constantly detected. Throughout the time course, TNF-α-induced GLuc activity was higher than IL-1β-induced one although both inflammatory cytokines were added at the same concentration. When treated with TNF-α in the presence of BAY-11-7085, one of the NF-κB activation inhibitors, GLuc activity was significantly decreased to nearly 20% of vehicle (DMSO)-added control, strongly suggesting NF-κB-dependent secretion of GLuc by 3T3-L1-NF-κB-GLuc adipocytes (Fig. 2E).

3.3. Co-culture of 3T3-L1-NF-κB-GLuc adipocytes with RAW264.7 macrophages induced GLuc secretion

Co-culture of 3T3-L1-NF-κB-GLuc adipocytes with RAW macrophages also induced GLuc secretion into CM (Fig. 3A). Significant GLuc activity was detected 4 h after co-culture with RAW macrophages and then reached a plateau at 24 h. When RAW macrophages were pretreated with LPS, much higher GLuc activity was induced and the difference between non-stimulated and LPS-stimulated macrophages was significant ($P < 0.01$) throughout the time course.

In the presence of BAY-11-7085, co-culture induced GLuc activity was significantly suppressed to less than 10% of vehicle (DMSO)-added control (Fig. 3B), suggesting that macrophage-derived inflammatory cytokines induced GLuc secretion through the activation of NF-κB. TNF-α has been known to induce production of reactive oxygen species (ROS) [12] and ROS activates NF-κB [13]. Therefore, an antioxidant compound was next examined to attenuate co-culture induced GLuc secretion. Upon treatment with a typical antioxidant N-acetyl cysteine (NAC), co-culture-induced GLuc activity was also significantly suppressed to nearly 20% of vehicle (PBS)-added control.

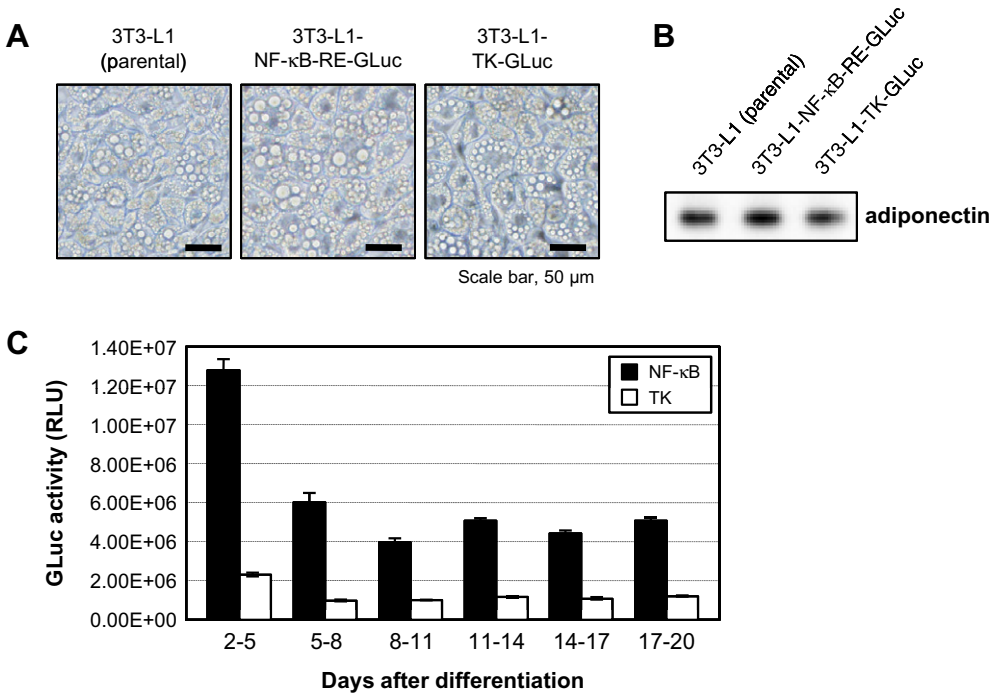

Fig. 1. Establishment of 3T3-L1-NF-κB-RE-GLuc adipocytes. (A) Parental 3T3-L1, 3T3-L1-NF-κB-RE-GLuc or 3T3-L1-TK-GLuc cells were induced to adipogenic differentiation and the pictures were taken at day 8 following differentiation induction. (B) Two-days conditioned medium (day 8–10) of each was collected and an aliquot was assessed by immunoblotting with anti-adiponectin antibody. *C*, Three-days conditioned medium of 3T3-L1-NF-κB-RE-GLuc or 3T3-L1-TK-GLuc adipocytes were sequentially collected and subjected to GLuc assay. Data are expressed as means ± SEM ($n = 3$).

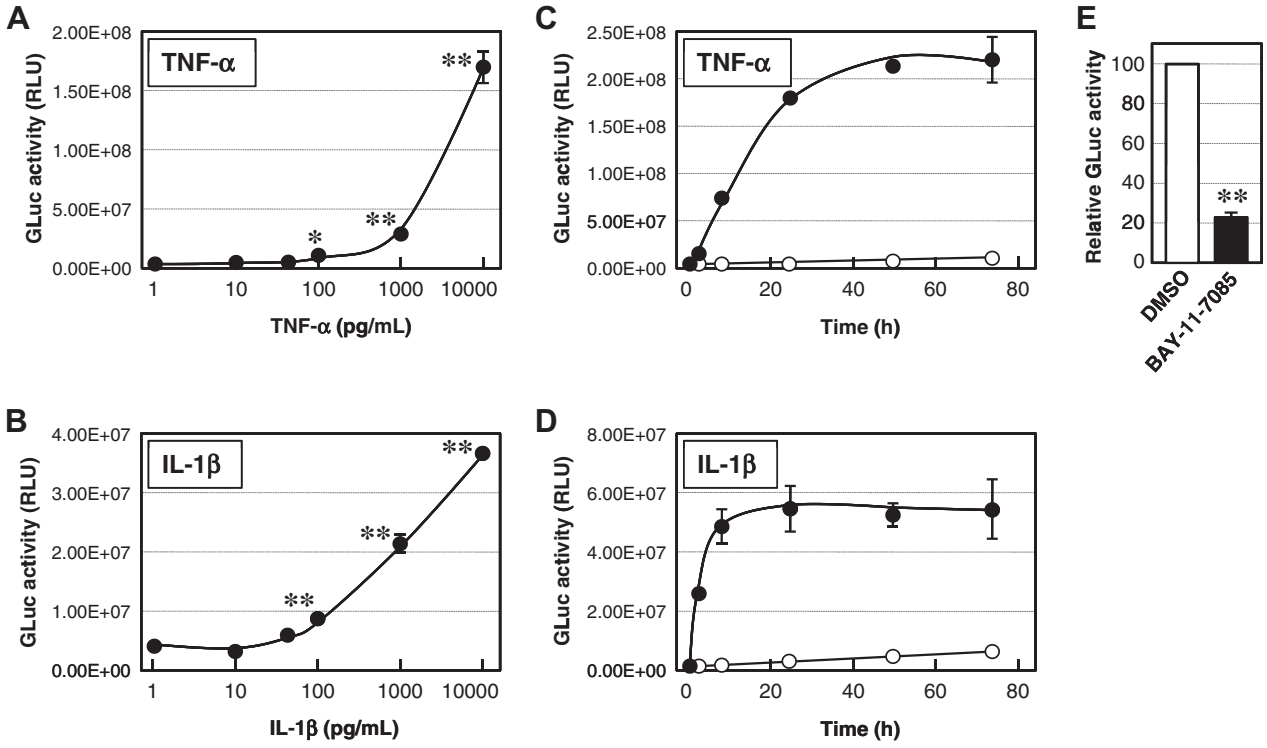

Fig. 2. Induction of GLuc activity in 3T3-L1-NF-κB-RE-GLuc adipocytes by TNF-α and IL-1β treatment (A and B) 3T3-L1-NF-κB-RE-GLuc adipocytes at day 8 were treated with 1, 10, 50, 100, 1000, and 10000 pg/mL TNF-α or IL-1β for 3 days and an aliquot of the conditioned medium was assayed for GLuc activity. PBS was used as vehicle control. Data are expressed as means ± SEM ($n = 3$). $^{*}P < 0.05$; $^{**}P < 0.01$ vs. PBS control. (C and D) 3T3-L1-NF-κB-RE-GLuc adipocytes at day 8 were treated with 10 ng/mL of TNF-α or IL-1β and aliquots (10 μL) of the conditioned medium was collected at 2, 4, 8, 24, 48 and 72 h after stimulation for GLuc activity (closed circles). PBS was used as vehicle control (open circles). Data are expressed as means ± SEM ($n = 3$). In the case of TNF-α, at all the points except for 2 h, GLuc activity upon stimulation was significantly ($P < 0.01$) higher than PBS control. In the case of IL-1β, at all the points, GLuc activity upon stimulation was significantly ($P < 0.01$) higher than PBS control. (E) 3T3-L1-NF-κB-RE-GLuc adipocytes at day 8 were treated with 500 pg/mL of TNF-α in the presence of 10 μM BAY-11-7085 for 24 h and GLuc activity was examined as above.

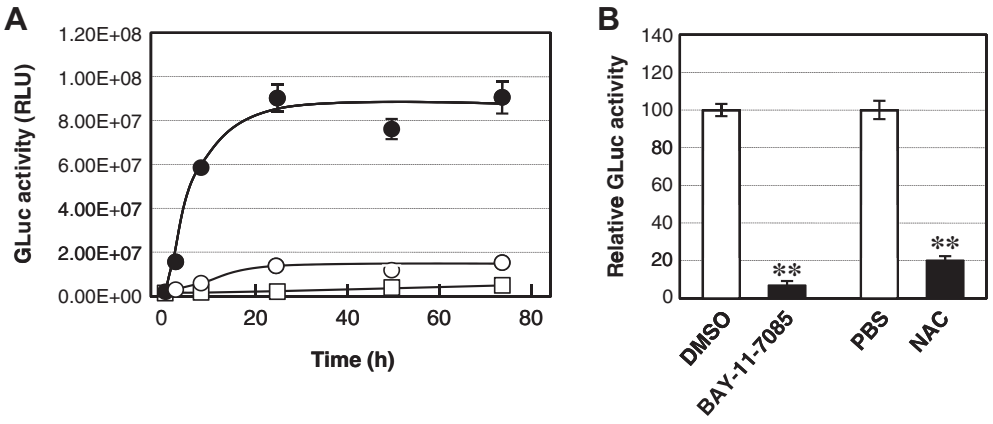

Fig. 3. Induction of GLuc secretion by co-culturing 3T3-L1-NF-κB-RE-GLuc adipocytes with RAW macrophages. (A) 3T3-L1-NF-κB-RE-GLuc adipocytes (day 8) were co-cultured with RAW macrophages which had been untreated (open circles) or pretreated (closed circles) with 100 ng/mL LPS. 3T3-L1-NF-κB-RE-GLuc adipocytes without RAW macrophages were cultured as control (open square). At 2, 4, 8, 24, 48 and 72 h after beginning of co-culture, an aliquot of culture medium was collected and assayed for GLuc activity. Upon co-culture with untreated RAW, GLuc activity was significantly ($P < 0.05$; 24, 72 h, $P < 0.01$; 4, 8, 48 h) higher than that of control culture. Upon co-culture with pretreated RAW, GLuc activity was significantly ($P < 0.01$) higher than that of co-culture with untreated RAW or that of control culture throughout the time course. (B) 3T3-L1-NF-κB-RE-GLuc adipocytes (day 8) were co-cultured in the presence of 10 mM NAC or 10 μM Bay-11-7085 for 24 h with RAW macrophages which had been pretreated with LPS. An aliquot was assayed for GLuc activity.

3.4. Antioxidant natural compounds suppressed GLuc secretion of 3T3-L1-NF-κB-GLuc adipocytes co-cultured with RAW264.7 macrophages

Finally, by using a co-culture system with the 3T3-L1-NF-κB-GLuc adipocytes and RAW macrophages, natural compounds with potential antioxidant activity were examined to suppress GLuc secretion. Natural compounds were dissolved in DMSO, added to the co-culture assay at the final concentration of 10 μM, and incubated for 8 h. As shown in Fig. 4A, rosemary-derived carnosic acid [14] strongly suppressed GLuc secretion to about 25% of vesicle-added control (Fig. 4A). Ursolic acid, which is widely distributed in a large variety of therapeutic herbs [15], also significantly suppressed GLuc secretion, whereas EGCG, which is one of the well-known green tea-derived polyphenols [16], exhibited less effect. Carnosic acid up-regulated adiponectin secretion over vesicle-added control (Fig. 4B), suggesting that carnosic acid attenuate dysfunction of adipocytes induced by macrophages.

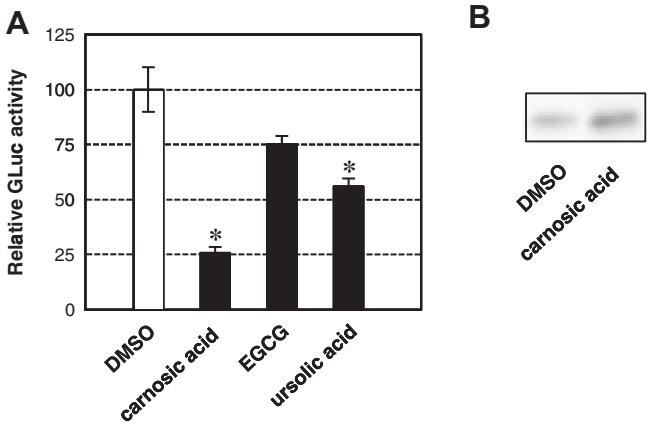

Fig. 4. Carnosic acid suppressed GLuc secretion and up-regulated adiponectin secretion of 3T3-L1-NF-κB-RE-GLuc adipocytes in co-culture with RAW macrophages. 3T3-L1-NF-κB-RE-GLuc adipocytes (day 8) were co-cultured in the presence of 10 μM carnosic acid, EGCG, or ursolic acid for 8 h with RAW macrophages. An aliquot was assayed for GLuc activity (panel A). In the case of carnosic acid treatment, an aliquot was also subjected to immunoblotting for adiponectin (panel B). Data are expressed as means ± SEM ($n = 3$). *$P < 0.05$ vs. DMSO.

4. Discussion

It is widely accepted that NF-κB is a central key transcriptional factor in inflammatory signaling in various cell types including adipocytes [17]. Macrophage-derived TNF-α, one of the most critical inflammatory cytokines, largely contributes to adipose dysfunctions such as induction of insulin resistance and dysregulated adipocytokine production by activating the NF-κB pathway [10]. Thus, it is important and useful to assess NF-κB activity in adipocytes. To evaluate NF-κB status, in this study, we established 3T3-L1 adipocytes by introducing Gaussia luciferase gene as a reporter gene under the control of NF-κB-RE (3T3-L1-NF-κB-RE-GLuc). Gaussia luciferase is a secretory enzyme and relatively stable in a cell culture medium. A freeze–thaw cycle exhibited nearly no effects on the GLuc activity (data not shown). Without cell lysis, by taking just an aliquot of cell culture medium, NF-κB status can be monitored in real time, which is more advantageous than conventional reporter gene assays using e.g., firefly-derived luciferase gene [18].

Both TNF-α and IL-1β induced GLuc secretion of 3T3-L1-NF-κB-RE-GLuc adipocytes in a concentration-dependent manner (Fig. 2A and B). In both cases, minimum concentration of 100 pg/mL was required to significantly induce GLuc secretion. Time course analysis, however, revealed a little difference between the inflammatory cytokines. GLuc activity was gradually induced by TNF-α and reached a plateau 24 to 48 after stimulation, whereas IL-1β drastically induced GLuc activity and maximum activity was detected 8 h after stimulation (Fig. 2C and D). When added at the same concentration, maximum GLuc activity induced by TNF-α was much stronger than induced by IL-1β. Thus it is suggested that intracellular machinery leading to NF-κB activation could be different to each other.

Upon co-culturing with RAW macrophages, real time monitoring of NF-κB-mediated inflammation was also achieved by using the 3T3-L1-NF-κB-RE-GLuc adipocytes. Significant GLuc activity was already detected 4 h after co-culture with untreated RAW macrophages started (Fig. 3A). Upon co-culturing with LPS-activated RAW macrophages, much more GLuc activity was induced at the same time point and reached a plateau at 24 h. This time course of GLuc induction was similar to that of TNF-α treatment (Fig. 2C) and the maximum GLuc activity is equivalent to that of TNF-α treatment at the concentration of 1 to 10 ng/mL (Fig. 2A).

Addition of BAY-11-7085 significantly attenuated GLuc activity (Fig. 3B). It is most likely that BAY-11-7805 acts downstreams of inflammatory cytokine such as TNF-α in the adipocytes. However, we can not exclude the possibility that the inhibitor could also act on RAW macrophages, because the effect of BAY-11-7805 on the GLuc activity in the co-culture system (Fig. 3B) was more obvious than that in the TNF-α-treated adipocytes (Fig. 2E) under similar experimental conditions.

It has been reported ROS production increases during differentiation of 3T3-L1 cells into adipocytes and that such oxidative stress decreases adiponectin production [19]. In 3T3-L1-NF-κB-RE-GLuc cells, significant up-regulation of GLuc activity was not observed during the course of adipogenic differentiation process until 20 days following differentiation induction (Fig. 1C). These results suggest that lipid-accumulation induced ROS production is independent of NF-κB activation in fully differentiated adipocytes, while ROS is involved in macrophage-induced NF-κB activation (Fig. 3B).

By using a co-culture system, carnosic acid was found to strongly suppress macrophage-induced NF-κB activation (Fig. 4A) and conversely up-regulated adiponectin secretion (Fig. 4B). It has recently been reported that carnosic acid inhibits adipogenic differentiation of 3T3-L1 cells through induction of phase2 enzymes and activation of glutathione metabolism at the concentration of 10 μM [20]. Carnosic acid, therefore, might be a strong candidate for treatment of obesity-induced inflammation and insulin resistance.

In summary, we have established a useful adipocyte cell line possessing secretory luciferase gene under the control of NF-κB. By using this cell line, inflammation status in adipocytes can be monitored in real time and inflammation-attenuating compounds can be screened more conveniently.

References

[1] P.J. Miranda, R.A. DeFronzo, R.M. Califf, J.R. Guyton, Metabolic syndrome: definition, pathophysiology, and mechanisms, Am. Heart J. 149 (2005) 33–45.

[2] J.M. Fernandez-Real, W. Ricart, Insulin resistance and chronic cardiovascular inflammatory syndrome, Endocr. Rev. 24 (2003) 278–301.

[3] P. Dandona, A. Aljada, A. Bandyopadhyay, Inflammation: the link between insulin resistance, obesity and diabetes, Trends Immunol. 25 (2004) 4–7.

[4] S.P. Weisberg, D. McCann, M. Desai, M. Rosenbaum, R.L. Leibel, A.W. Ferrante Jr., Obesity is associated with macrophage accumulation in adipose tissue, J. Clin. Invest. 112 (2003) 1796–1808.

[5] H. Xu, G.T. Barnes, Q. Yang, G. Tan, D. Yang, C.J. Chou, J. Sole, A. Nichols, J.S. Ross, L.A. Tartaglia, H. Chen, Chronic inflammation in fat plays a crucial role in the development of obesity-related insulin resistance, J. Clin. Invest. 112 (2003) 1821–1830.

[6] H. Hauner, The new concept of adipose tissue function, Physiol. Behav. 83 (2004) 653–658.

[7] K.T. Uysal, S.M. Wiesbrock, M.W. Marino, G.S. Hotamisligil, Protection from obesity-induced insulin resistance in mice lacking TNF-alpha function, Nature 389 (1997) 610–614.

[8] M. Bluher, M. Fasshauer, A. Tonjes, J. Kratzsch, M.R. Schon, R. Paschke, Association of interleukin-6, C-reactive protein, interleukin-10 and adiponectin plasma concentrations with measures of obesity, insulin sensitivity and glucose metabolism, Exp. Clin. Endocrinol. Diabetes 113 (2005) 534–537.

[9] P. Trayhurn, I.S. Wood, Signalling role of adipose tissue: adipokines and inflammation in obesity, Biochem. Soc. Trans. 33 (2005) 1078–1081.

[10] T. Suganami, J. Nishida, Y. Ogawa, A paracrine loop between adipocytes and macrophages aggravates inflammatory changes: role of free fatty acids and tumor necrosis factor alpha, Arterioscler. Thromb. Vasc. Biol. 25 (2005) 2062–2068.

[11] R. Ogawa, C. Tanaka, M. Sato, H. Nagasaki, K. Sugimura, K. Okumura, Y. Nakagawa, N. Aoki, Adipocyte-derived microvesicles contain RNA that is transported into macrophages and might be secreted into blood circulation, Biochem. Biophys. Res. Commun. 398 (2010) 723–729.

[12] G.C. Yen, Y.C. Chen, W.T. Chang, C.L. Hsu, Effects of polyphenolic compounds on tumor necrosis factor-alpha (TNF-alpha)-induced changes of adipokines and oxidative stress in 3T3-L1 adipocytes, J. Agric. Food Chem. 59 (2011) 546–551.

[13] C.K. Sen, L. Packer, Antioxidant and redox regulation of gene transcription, FASEB J. 10 (1996) 709–720.

[14] O.I. Aruoma, B. Halliwell, R. Aeschbach, J. Loligers, Antioxidant and pro-oxidant properties of active rosemary constituents: carnosol and carnosic acid, Xenobiotica 22 (1992) 257–268.

[15] J. Liu, Pharmacology of oleanolic acid and ursolic acid, J. Ethnopharmacol. 49 (1995) 57–68.

[16] H.N. Graham, Green tea composition, consumption, and polyphenol chemistry, Prev. Med. 21 (1992) 334–350.

[17] P.J. Barnes, M. Karin, Nuclear factor-kappaB: a pivotal transcription factor in chronic inflammatory diseases, N. Engl. J. Med. 336 (1997) 1066–1071.

[18] H. Fushiki, Y. Hayakawa, A. Gomori, T. Seo, S. Tewari, S. Ozaki, R. Yoshimoto, In vivo imaging of obesity-induced inflammation in adipose tissue, Biochem. Biophys. Res. Commun. 391 (2010) 674–678.

[19] S. Furukawa, T. Fujita, M. Shimabukuro, M. Iwaki, Y. Yamada, Y. Nakajima, O. Nakayama, M. Makishima, M. Matsuda, I. Shimomura, Increased oxidative stress in obesity and its impact on metabolic syndrome, J. Clin. Invest. 114 (2004) 1752–1761.

[20] T. Takahashi, T. Tabuchi, Y. Tamaki, K. Kosaka, Y. Takikawa, T. Satoh, Carnosic acid and carnosol inhibit adipocyte differentiation in mouse 3T3-L1 cells through induction of phase2 enzymes and activation of glutathione metabolism, Biochem. Biophys. Res. Commun. 382 (2009) 549–554.

Biochemical and Biophysical Research Communications 420 (2012) 628–634

Contents lists available at SciVerse ScienceDirect

Biochemical and Biophysical Research Communications

journal homepage: www.elsevier.com/locate/ybbrc

Apurinic/apyrimidinic endonuclease1/redox factor-1 (Ape1/Ref-1) is essential for IL-21-induced signal transduction through ERK1/2 pathway

Farha M. Juliana [a], Hidetoshi Nara [a], Tadashi Onoda [a,b], Mizanur Rahman [a], Akemi Araki [a], Lianjin Jin [a], Hodaka Fujii [c], Nobuyuki Tanaka [d,e], Tomoaki Hoshino [f], Hironobu Asao [a,*]

[a] Department of Immunology, Yamagata University Faculty of Medicine, Yamagata, Japan
[b] Department of Pediatrics, Yamagata University Faculty of Medicine, Yamagata, Japan
[c] Combined Program on Microbiology and Immunology, Research Institute for Microbial Diseases, Osaka University, Suita, Japan
[d] Division of Immunology, Miyagi Cancer Center Research Institute, Natori, Japan
[e] Department of Cancer Medical Science, Tohoku University Graduate School of Medicine, Sendai, Japan
[f] Department of Internal Medicine 1, Kurume University School of Medicine, Kurume, Japan

ARTICLE INFO

Article history:
Received 9 March 2012
Available online 17 March 2012

Keywords:
IL-21
ERK1/2
Apurinic/apyrimidinic endonuclease1/redox factor-1
Signal transduction

ABSTRACT

IL-21 is a pleiotropic cytokine that regulates T-cell and B-cell differentiation, NK-cell activation, and dendritic cell functions. IL-21 activates the JAK-STAT, ERK, and PI3K pathways. We report here that Ape1/Ref-1 has an essential role in IL-21-induced cell growth signal transduction. Overexpression of Ape1/Ref-1 enhances IL-21-induced cell proliferation, but it is suppressed by overexpressing an N-terminal deletion mutant of Ape1/Ref-1 that lacks the redox domain. Furthermore, knockdown of the Ape1/Ref-1 mRNA dramatically compromises IL-21-induced ERK1/2 activation and cell proliferation with increasing cell death. These impaired activities are recovered by the re-expression of Ape1/Ref-1 in the knockdown cells. Our findings are the first demonstration that Ape1/Ref-1 is an indispensable molecule for the IL-21-mediated signal transduction through ERK1/2 activation.

1. Introduction

IL-21 is a pleiotropic cytokine that was originally identified in activated $CD4^+$ T cells [1]. It was later found to be expressed in many types of lymphocytes, including Th17 cells, natural killer T cells, and follicular helper T cells [2–6]. IL-21 binds to a heterodimeric receptor complex composed of a cognate receptor, IL-21 receptor (IL-21R), and the common cytokine receptor γ chain [7,8]. This receptor is widely expressed on cells in the lymphocytic and myelocytic lineages, and IL-21 elicits many effects in these cells [9]. Notably, IL-21 plays an important role in the differentiation of human and mouse Th17 cells [2]. Therefore, IL-21 is involved in the pathogenesis of many inflammatory diseases including allergy and autoimmune disease. IL-21 also has potent anti-tumor activity for many cancers [10,11].

We and other groups previously reported that IL-21 activates the JAK-STAT, MAP kinase, and PI3 kinase pathways [7,12,13]; however, the complete details of its signaling cascades still need to be investigated. Our overarching goal is to elucidate the details of the IL-21-induced signal-transduction mechanism, which is necessary for understanding and controlling cytokine signaling and the immune response.

Cytokine binding to cell-surface receptors activates pathways that regulate nuclear events affecting cell proliferation, differentiation, and function. For signals to be propagated from the cytoplasm to the nucleus, signaling molecules must cross the nuclear envelope. Using the inducible translocation trap, a reporter gene-based system for detecting the induced nuclear translocation of proteins [14,15], we sought to identify novel molecules that enter the nucleus from the cytoplasm upon IL-21 stimulation. Among the several candidates we identified, we focused on Ape1/Ref-1.

Ape1/Ref-1, the mammalian ortholog of Escherichia coli Xth, possesses DNA-repair activity [16,17] and plays a central role in the base excision repair of DNA damaged by exposure to reactive oxygen species (ROS), alkylating drugs, and other insults [18]. Independent of its DNA-repair activity, Ape1/Ref-1 acts as a redox factor (Ref) that is a reductive activator of activation protein-1 (AP-1) [19]. It also participates in important cellular functions, including the response to oxidative stress, regulation of transcription factors, control of cell cycling, and apoptosis [20]. Transcription factors that are activated by Ape1/Ref-1 include p53, NF-κB, and HIF1-α [21], which are involved in cancer promotion and progression. Indeed, Ape1/Ref-1 is highly expressed in many tumor

Abbreviations: Ape1/Ref-1, apurinic/apyrimidinic endonuclease 1/redox effector factor-1; ROS, reactive oxygen species; Dox, doxycycline.

* Corresponding author. Address: Department of Immunology, Yamagata University Faculty of Medicine, 2-2-2 Iida-Nishi, Yamagata 990-9585, Japan. Fax: +81 23 628 5267.
E-mail address: asao-h@med.id.yamagata-u.ac.jp (H. Asao).

0006-291X/$ - see front matter © 2012 Elsevier Inc. All rights reserved.
http://dx.doi.org/10.1016/j.bbrc.2012.03.051

cells [18]. Furthermore, it is reported to activate a multi-drug-resistance gene (*MDR1*) [22]. Together, these properties indicate that, Ape1/Ref-1 is a strong candidate for a chemotherapeutic target in cancer treatment [23].

In the immune system, the redox activity of Ape1/Ref-1 is reported to be involved in CD40-mediated B cell activation [24,25]. Ape1/Ref-1 is also cleaved and inactivated during granzyme A- and/or granzyme K-mediated cell killing by cytotoxic lymphocytes [26,27]. Despite this accumulating information, Ape1/Ref-1's function in cytokine signaling is still poorly understood. Here we examined the function of Ape1/Ref-1 in response to IL-21 signaling in a mouse B-cell line. We found that Ape1/Ref-1 has an indispensable role in IL-21-induced cell proliferation and survival.

2. Materials and methods

2.1. Cells and cell culture

Ba/F3 is an IL-3-dependent murine pro-B cell line [28]. Its sublines, BAF21RWT-1 and BAFmyc21R, which express human IL-21R and myc-tagged human IL-21R, respectively, and BLG-139–3 were described previously [29,30,14]. Ba/F3 and all its sublines, including BAF21RWT-1, BAFmyc21R-To, BAFmyc21R-To-Ape, BAFmyc21R-To-ApedN, B21RApeKD, B21RKDC, B21RApeKDR, BLG-139–3, and BLG-139–3-21RWT-1, were maintained in RPMI1640 medium supplemented with 10% heat-inactivated FBS, 50 μM 2-mercaptoethanol, 15% conditioned medium from WEHI3 cells as a source of IL-3, penicillin, and streptomycin. PLAT-E, a potent retrovirus packaging cell line, and human NK cell line, NK0 cells were maintained, as described previously [31,32]. All the cells were cultured at 37 °C in a humidified incubator with 5% CO_2.

2.2. Cytokines and antibodies

Human recombinant IL-21 and IL-2 were purchased from PeproTech EC. We used 1 nM IL-21 to stimulate cells. Antibodies we used in this study are as follows, anti-Ape1/Ref-1 Ab (Novus Biologicals), anti-STAT3 Ab (Santa Cruz Biotechnology), anti-α-tubulin mAb (B5–1-2) and anti-Flag mAb (M2) (Sigma Aldrich), anti-phospho-STAT3 (Y705) Ab, anti-phospho-ERK1/2 (T202/Y204) Ab, HRP-labeled anti-mouse IgG Ab, and HRP-labeled anti-rabbit IgG Ab (Cell Signaling Technology), and anti-acetyl histon H3 Ab (gift from Drs. K. Tachibana and C. Kitanaka).

2.3. Preparation of cDNA library

Poly (A)+ RNA was prepared from BLG-139–3 cells. A unidirectional cDNA library was constructed using the SuperScript plasmid system (Invitrogen). First-strand cDNA was synthesized with a *Not*I-oligo dT primer. After second-strand synthesis, a *Sal*I linker was ligated to the end of the cDNA. The *Sal*I linker-ligated cDNAs were digested with *Not*I.

The *Sal*I site of pLG was removed by blunting after *Sal*I digestion [14,15]. 5′-AATTGGTCGACC-3′ oligonucleotides were annealed to each other to prepare the *EcoR*I-*Sal*I linker, and ligated to the *EcoR*I site of pLG without *Sal*I site. We named this construct as pLG2. The cDNAs were then ligated to the *Sal*I-*Not*I sites of the pLG2. The cDNA library plasmid vectors were transfected into PLAT-E cells to prepare the retrovirus particles [31].

2.4. Inducible translocation trap

BLG-139–3 is a Ba/F3-derived cell line containing the LexA-d1EGFP reporter gene [14,15]. A human IL-21R expression plasmid, pEFneohIL-21R, was transfected into BLG-139–3 by electroporation to establish BLG-139–3-21RWT-1.

We infected BLG-139–3-21RWT-1 with retrovirus containing the cDNA library, prepared as described above. Two days after infection, cells were starved of IL-3 for 12 h, and stimulated with IL-21 for another 12 h. GFP-positive cells were sorted out by FACSAria.

To analyze the cDNA inserts in the GFP-positive clones, genomic PCR was performed using the primer set 5′-CAATGGATGATGTATAT AACTATCTATTCGAT-3′ and 5′-TCCCCCCTTTTTCTGGAGACTAAAT AAAAT-3′.

2.5. Immunoblot analysis

Preparation of whole-cell extracts and immunoblot analysis were performed as described previously [33]. We used ProteoExtract Subcellular Proteome Extraction Kit (Calbiochem) to prepare cytosolic and nuclear cell fractions.

2.6. RT-PCR analysis

The total RNA preparation and Real-time quantitative PCR amplification were performed, as described previously [29]. The Ape1/Ref-1 mRNA expression level was normalized to the amount of β-actin mRNA. The primer sets used for the amplification of Ape1/Ref-1 and β-actin cDNA were 5′-GCAAAGAAAACCGAGAAG-GAG-3′ and 5′-GGGGTGTATCGTGTTCTCC-3′, and 5′-TGACAGGATG CAGAAGGAGA-3′ and 5′-GCTGGAAGGTGGACAGTGAG-3′, respectively.

2.7. Tet-on inducible gene expression system

We constructed pRetroX-Tight-Pur-Ape1/Ref-1 and pRetroX-Tight-Pur-Flag-dN-Ape1/Ref-1 retroviral vectors to express wild type and Flag-tagged N-terminal redox domain-deletion mutant form of Ape1/Ref-1, respectively with Tet-on Advanced Inducible Gene Expression System (Clontech). The cDNAs of these form of Ape1/Ref-1 were prepared by PCR using the primer sets 5′-TTGGATCCTTCGTCACAGCGATGCCAAA-3′ and 5′-TTGAATTCTCTCC CAGGCAGGAAGCTAC-3′, and 5′-AAGGATCCACCATGGACTACAAA-GACGATGACGACAAGTACTGGTCAGCTCCGTCA-3′ and 5′-TTGAATTC TCTCCCAGGCAGGAAGCTAC-3′, respectively. The PCR products were digested with *BamH*I and *EcoR*I, and the DNA fragments were cloned into the pRetroX-Tight-Pur. To produce retrovirus particles, we used PLAT-E packaging cells. BAFmyc21R-To cells, which express the reverse tetracycline transactivator, were infected with the retroviruses and cultured with 1 μg/ml puromycin [30]. The BAFmyc21R-To-Ape and BAFmyc21R-To-ApedN clones, which inducibly expressed wild-type Ape1/Ref-1 or its N-terminal deletion mutant, were established, respectively, upon doxycycline (Dox) (Calbiochem) treatment.

2.8. Knockdown of Ape1/Ref-1 using shRNA and establishment of Ape1/Ref-1 revertant clones

An Ape1/Ref-1-shRNA-containing plasmid, pLKO.1-puro-Ape1/Ref-1 shRNA (NM_009687.1-1033s1c1), was purchased from Sigma–Aldrich. Its target sequence, 5′-GTAGCTTCCTGCCTGGGAGAT-3′, is in the 3′-non-coding region of mouse Ape1/Ref-1. *Sca*I linearized-pLKO.1-puro-Ape1/Ref-1 shRNA plasmid was transfected into BAF21RWT-1 cells by electroporation. Twenty-four hours later, 1 μg/ml puromycin was added to the cultures to select for resistant clones (B21RApeKD clones). To establish control cells (B21RKDC clones), pLKO.1-puro-Ape1/Ref-1 shRNA digested with *Nde*I and *EcoR*I to remove the short hairpin sequence was used. To establish Ape1/Ref-1 revertant clones (B21RApeKDR clones), we prepared Ape1/Ref-1 expression plasmid excluding the shRNA target sequence. The cDNA of Ape1/Ref-1 was prepared by PCR using the primer set 5′-TTGGATCCTTCGTCACAGCGATGCCAAA-3′ and 5′-

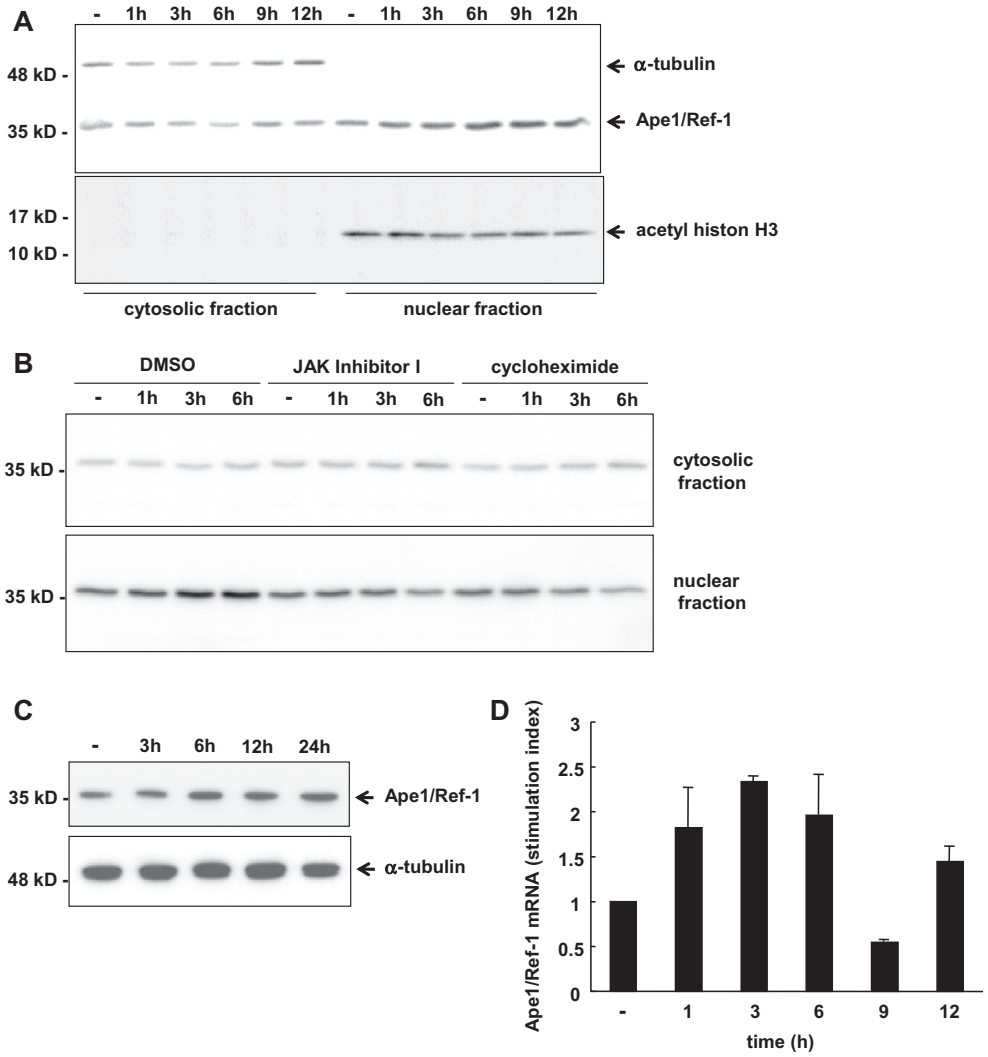

Fig. 1. IL-21-induced nuclear accumulation of the Ape1/Ref-1 protein. (A and B) The Ape1/Ref-1 protein expression in BAF21RWT-1 cells was analyzed by an immunoblot assay. Cells were starved of IL-3 for 8 h (−), and stimulated with IL-21 (A) or pretreated with JAK inhibitor I or cycloheximide for 30 min and then stimulated with IL-21 in the presence of these inhibitors (B). Ape1/Ref-1 was detected with an anti-Ape1/Ref-1 Ab (A, upper panel and B). α-tubulin and acetyl histon H3 were detected as controls (A). (C) The Ape1/Ref-1 protein expression in NK0 cells was analyzed. Cells were starved of IL-2 for 72 h (−), and stimulated with IL-21. Whole cell protein was analyzed with an anti-Ape1/Ref-1 Ab (upper panel) then the filter was re-probed with an anti-α-tubulin Ab (lower panel). (D) BAF21RWT-1 cells were starved of IL-3 for 8 h (−), then stimulated with IL-21. The Ape1/Ref-1 mRNA expression was analyzed by quantitative real-time RT-PCR. The results are expressed as a stimulation index (mRNA of stimulated cells/mRNA of IL-21-unstimulated cells). These experiments were repeated three times, and representative results are shown.

AAGAATTCAGGAGGGTATCACAGTGCTAGGT-3′. The PCR product was cloned into pKU2-Hyg expression vector. The resulting plasmid, pKUH-ApeΔ3′ was transfected into the Ape1-knockdown cell line, B21RApeKD-12. Twenty-four hours later, 2 mg/ml hygromycin was added to the cultures to select for resistant clones.

2.9. Statistical analysis

The results of the thymidine incorporation assay and cell count assay are presented as means ± S.E.M., and statistical significances were determined using Student's *t*-test.

3. Results and discussion

3.1. Identification of Ape1/Ref-1 as an IL-21-induced nuclear accumulated molecule

To find new components involved in the IL-21-mediated signaling pathway, we examined molecules that were translocated from the cytoplasm to the nucleus upon IL-21 treatment. Using the inducible translocation trap system, we isolated several candidate cell clones as described in Materials and methods, and sequenced the cDNA insert in these cells. One of these sequences matched Ape1/Ref-1, and we focused on this molecule for further analysis.

To test the nuclear localization of the endogenous Ape1/Ref-1 protein, we treated BAF21RWT-1 cells with IL-21 and cellular protein was fractionated and then Ape1/Ref-1 was detected by immunoblotting experiment. Under IL-3-starved condition, Ape1/Ref-1 was detected in both cytoplasm and nucleus (Fig. 1A). After IL-21 stimulation, we could detect very little change of cytosolic Ape1/Ref-1 protein, in contrast, nuclear Ape1/Ref-1 was marginally increased within 1 h and gradually increased up to 6 h. The purity and specificity of the cytosolic and nuclear fraction were monitored by the expression of α-tubulin (cytosolic protein) and histon (nuclear protein). Then we examined whether the Ape1/Ref-1 nuclear accumulation is dependent on IL-21-induced JAK activation or not, and required *de novo* protein synthesis or not. In the presence of JAK inhibitor I (Calbiochem) or cycloheximide (Sigma),

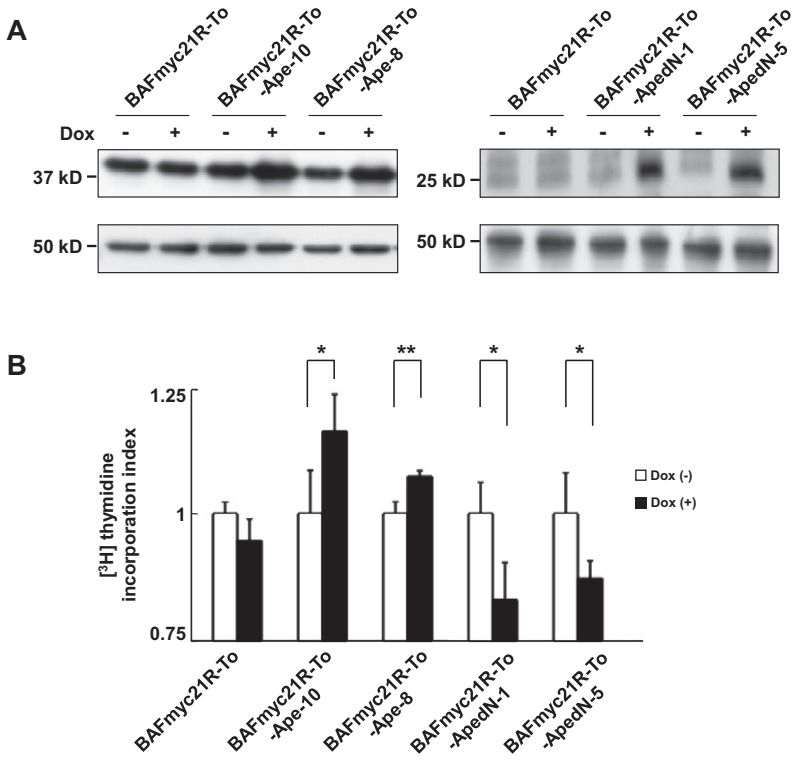

Fig. 2. Ape1/Ref-1 controls IL-21-induced cell proliferation. (A) Immunoblot analysis of wild type or mutant Ape1/Ref-1 expression in Tet-on inducible cell clones. Cells were stimulated with 0.3 μg/ml Dox for 24 h (+) or not (−). Whole-cell extracts were prepared and the wild type or mutant Ape1/Ref-1 was detected with an anti-Ape1/Ref-1 Ab (left upper panel) or an anti-FLAG Ab (right upper panel), respectively. The filters were then re-probed with an anti-α-tubulin Ab (lower panels). (B) Cells were starved of IL-3 for 12 h in the presence (solid bars) or absence (open bars) of 0.3 μg/ml Dox, then stimulated with IL-21 for 60 h. Thymidine incorporation assay was performed as described previously [33]. The data are presented as the thymidine incorporation index (Dox^+/Dox^-) in each cell line. $^*P < 0.05$, $^{**}P < 0.01$. Each experiment was repeated at least twice, and representative results are shown.

IL-21 could not accumulate Ape1/Ref-1 into the nucleus (Fig. 1B). These results suggest that IL-21 induces nuclear accumulation of Ape1/Ref-1 mainly via IL-21-induced JAK activation signal and then with protein synthesis, but not by nuclear translocation from the stored cytosolic protein. We confirmed the IL-21-induced Ape1/Ref-1 protein synthesis in another type of cell, NK0 (Fig. 1C).

Real-time quantitative RT-PCR demonstrated a marked up-regulation of the Ape1/Ref-1 mRNA up to 6 h after IL-21 stimulation, which then transiently decreased (Fig. 1D). This mRNA expression pattern was reproducible and agrees with previous reports that Ape1/Ref-1 inhibits its own expression by binding to nCa-RE sequences within the Ape1/Ref-1 distal promoter, thus constituting an autoregulatory functional loop [18,20]. On the other hand, constitutively active form of STAT3 up-regulates the Ape1/Ref-1 expression in mouse primary hepatocytes [34]. So it is possible that IL-21-activated STAT3 induces *Ape1/Ref-1* gene expression. We thus need to analyze the *Ape1/Ref-1* gene carefully to determine how IL-21 regulates Ape1/Ref-1 expression.

3.2. Ape1/Ref-1 may enhance IL-21-induced cell proliferation through N-terminal redox domain

We next examined the function of Ape1/Ref-1 in IL-21-induced cell proliferation using the Tet-on inducible system. We established several BAFmyc21R-To-Ape clones, which inducibly expressed a wild-type Ape1/Ref-1 and BAFmyc21R-To-ApedN clones, which inducibly expressed a mutant Ape1/Ref-1, Ape1/Ref-1dN116 that lacked the N-terminal 116 amino acids, including the entire redox domain. Dox treatment increased the Ape1/Ref-1 proteins in BAFmyc21R-To-Ape-10 and -8, and BAFmyc21R-To-ApedN-1 and -5, but not in the parent BAFmyc21R-To cells (Fig. 2A). Thymidine incorporation assay was then performed in these cells. Dox enhanced the thymidine incorporation in the wild type Ape1/Ref-1-overexpressing clones, whereas Dox decreased that of the mutant Ape1/Ref-1-expressing clones compared to that of parent cells (Fig. 2B). These results suggest that Ape1/Ref-1 enhances the IL-21-induced cell proliferation, in contrast the N-terminal deletion mutant functions as a dominant-negative form. The redox domain is thought to be important not only for its redox regulation, but also for its enhancing activity on many transcription factors. Therefore, the redox domain of Ape1/Ref-1 must be essential for the IL-21-induced cell-proliferation signal. We could not show such big differences with or without DOX treatment of these cells. It may be due to the presence of relatively high amount of endogenous Ape1/Ref-1. So next we employed Ape1/Ref-1 knock down method.

3.3. Ape1/Ref-1-knockdown cells show compromised cell proliferation and survival response to IL-21

To confirm the function of Ape1/Ref-1, we prepared Ape1/Ref-1-knockdown cells, B21RApeKD-11 and -12, using the shRNA system. Ape1/Ref-1 protein expression in these cells was obviously decreased, whereas it was not decreased in B21RKDC-1 and -3 control cells (Fig. 3A). Compared to the parent cells, IL-21 could not support the long-term cell proliferation of these knockdown cells (Fig. 3B). Whereas, B21RKDC-1 and -3 control cells proliferated similarly to the BAF21RWT-1 parent cells.

We examined whether Ape1/Ref-1 knockdown diminished cell division rate or enhanced cell death. CFSE (Molecular Probes) labeling experiment showed that cell division of B21RApeKD-12 was a little bit slower than that of parent cells (Fig. 3C, left pan-

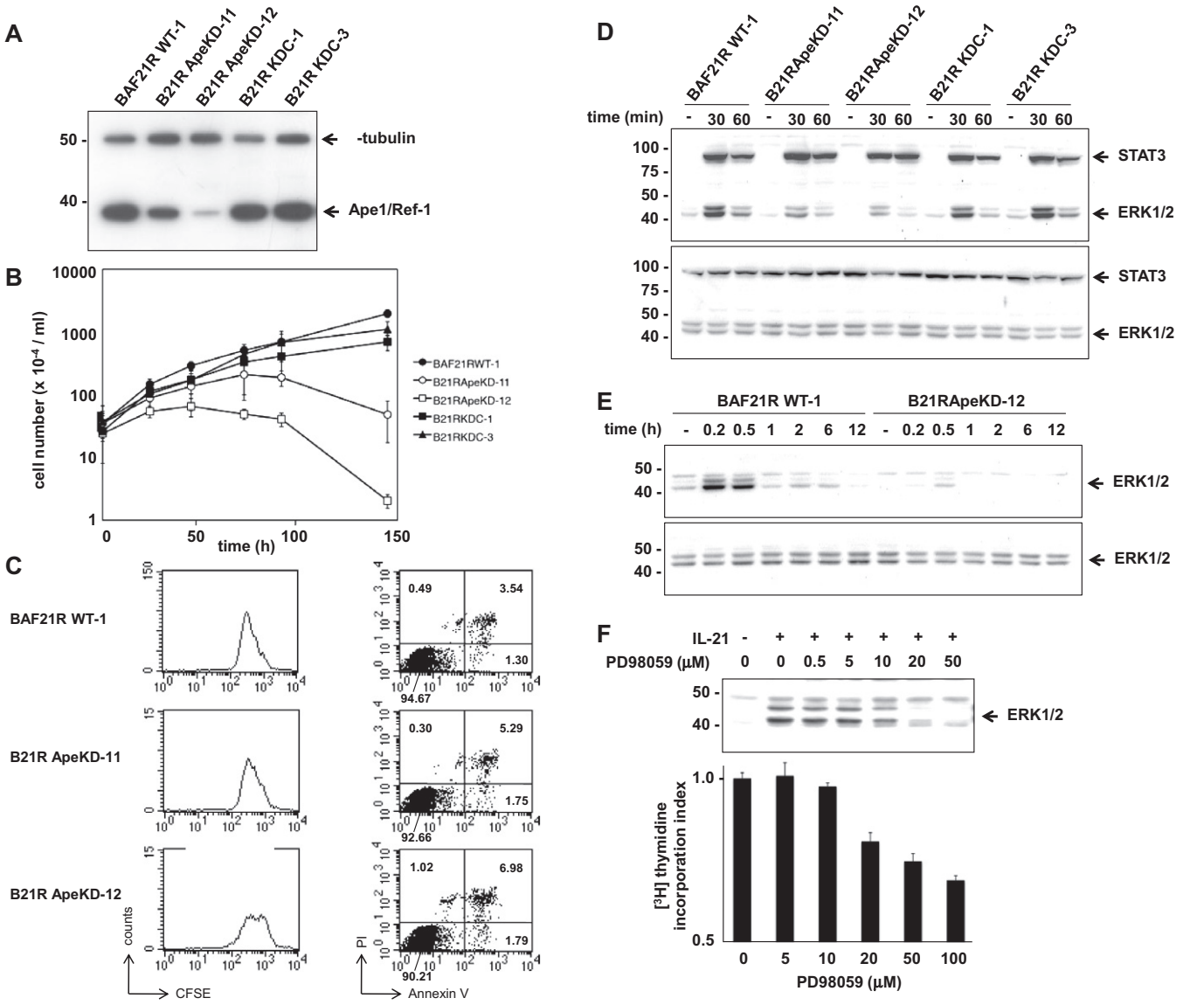

Fig. 3. Ape1/Ref-1 knockdown cells show compromised cell proliferation, survival and ERK activation with IL-21 treatment. (A) Ape1/Ref-1 expression in Ape1/Ref-1-knockdown clones. Whole-cell extracts of BAF21RWT-1, Ape1/Ref-1 knockdown cell clones (B21RApeKDs) and Ape1/Ref-1 knockdown control cell clones (B21RKDCs) were analyzed by immunoblot assay with an anti-Ape1/Ref-1 and an anti-α-tubulin Abs. (B) Cells were cultured in the presence of IL-21 without IL-3. Living cells were assessed by the trypan blue exclusion assay. Each experiment was repeated three times, and representative result is shown. (C) Cells were cultured for 6 days in culture media containing 1nM IL-21, and then labeled with CFSE. Labeled cells were cultured for another 3 days in the presence of 1nM IL-21. CFSE intensity was determined by flow cytometry (left panels). Cells were cultured for 60 h in the presence of 1nM IL-21 and then stained with FITC-Annexin V and PI. Numbers in each quadrant indicate the percentage of the shown cells (right panels). (D and E) Cells were starved of IL-3 for 10 h (−) then stimulated with IL-21. Whole-cell extracts were analyzed by immunoblot assay with an anti-phospho-STAT3 (D) and an anti-phospho-ERK1/2 Abs (D and E) (upper panels). The filters were re-probed with an anti-STAT3 (D) and an anti-ERK1/2 Abs (D and E) (lower panels). (F) BAF21RWT-1 cells were pretreated with a MEK1 inhibitor (PD98059) at the indicated concentrations for 1 h, then stimulated with IL-21 for 30 min. Whole-cell extracts were analyzed by immunoblot assay with an anti-phospho-ERK1/2 Ab (upper panel). BAF21RWT-1 cells were starved of IL-3 for 8 h, and then stimulated with IL-21 in the presence of MEK1 inhibitor at the indicated concentrations for 36 h. Thymidine incorporation assay was performed (lower panel). The data are presented as the thymidine incorporation index ($PD98059^{+}/PD98059^{-}$). Each experiment was repeated three times, and representative results are shown.

els). In case of B21RApeKD-11, the difference compare to the parent cells was small, if any. Next cells were cultured in the presence IL-21 for 5 days then stained with Annexin V (Biolegend) and PI (Sigma). Percentage of Annexin V positive cell fraction were increased in B21RApeKD-12 (8.77%) and in B21RApeKD-11 (7.04%) compared to the parent cells (4.84%) (Fig. 3C, right panels). These results suggest that Ape1/Ref-1 has indispensable roles in both IL-21-induced cell division and also cell survival. In these assays we could see a small difference between parent and B21RApeKD-11 cells. It may be due to the relative high amount of Ape1/Ref-1 expression in B21RApeKD-11 compared to B21RApeKD-12.

3.4. Ape1/Ref-1 regulates the ERK1/2 signaling pathway

Next question is how Ape1/Ref-1 regulates IL-21-induced cell proliferation and survival signals. We examined the activation of STAT3 and ERK1/2 in our knockdown cells (Fig. 3D). STAT3 phosphorylation level in the Ape1/Ref-1-knockdown cells was comparable to that in the parent cells. In contrast, IL-21-induced ERK1/2 phosphorylation was markedly reduced in the knockdown cells. Kinetics experiment up to 12 h stimulation confirmed the down regulation of ERK1/2 phosphorylation in B21RApeKD-12 (Fig. 3E). Then we examined the role of MEK-ERK pathway in the IL-21-induced cell proliferation signal. The MEK1 inhibitor PD98059 (Cell

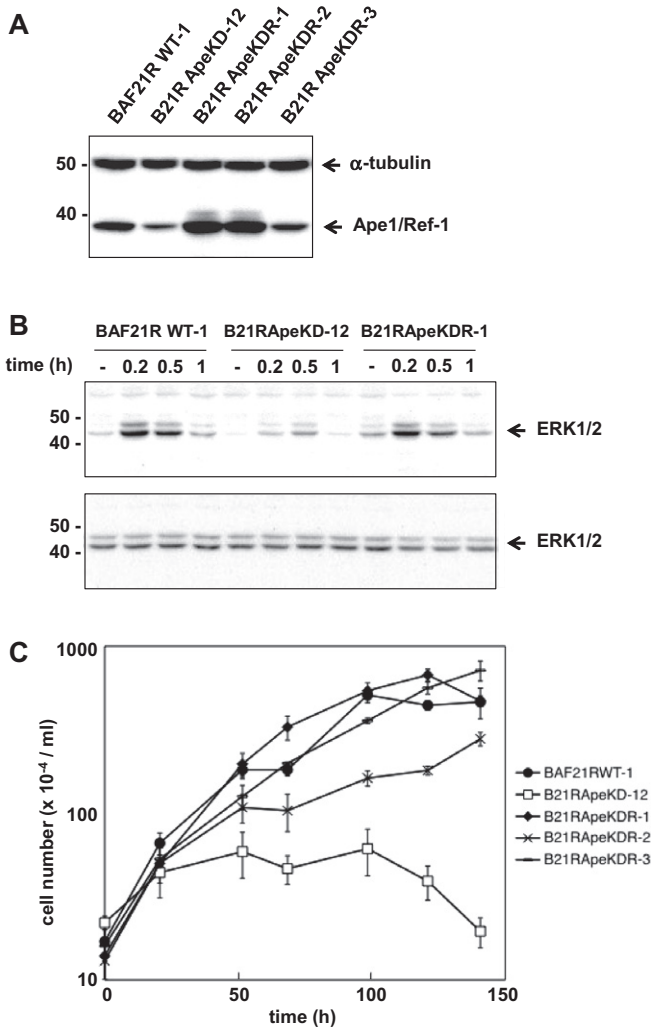

Fig. 4. Ape1/Ref-1 re-expression in the Ape1/Ref-1 knockdown cell rescues the ERK1/2 phosphorylation and cell-proliferation activities. (A) Ape1/Ref-1 expression in Ape1/Ref-1-revertant clones. Whole-cell extracts of BAF21RWT-1, Ape1/Ref-1 knockdown cell clone (B21RApeKD-12) and Ape1/Ref-1 revertant clones (B21RApeKDRs) were analyzed by immunoblot assay with an anti-Ape1/Ref-1 Abs. (B) Cells were starved of IL-3 for 10 h (−) then stimulated with IL-21. Whole-cell extracts were analyzed by immunoblot assay with an anti-phospho-ERK1/2 Ab (upper panel). The filter was re-probed with an anti-ERK1/2 Ab (lower panel). (C) Cells were cultured in the presence of IL-21 without IL-3. Living cells were assessed by the trypan blue exclusion assay. Each experiment was repeated three times, and representative result is shown.

Signaling Technology) clearly inhibited the IL-21-induced ERK1/2 phosphorylation and cell proliferation, indicating that the MEK-ERK signaling pathway is crucial for this cell proliferation (Fig. 3F).

3.5. Ape1/Ref-1 re-expression rescues the ERK1/2 and cell-proliferation activity

To further confirm the function of Ape1/Ref-1 in ERK activation, we re-expressed wild type Ape1/Ref-1 in the Ape1/Ref-1 knockdown cell, B21RApeKD-12. The expression levels of Ape1/Ref-1 protein in these revertant clones (B21RApeKDRs) are shown (Fig. 4A). In the revertant clone B21RApeKDR-1, the IL-21-induced ERK1/2 phosphorylation was similar to that of the parent cells (Fig. 4B). The IL-21-dependent cell proliferation of these revertant clones also recovered (Fig. 4C). Taken together, ore results indicate that Ape1/Ref-1 is indispensable for the IL-21-induced cell proliferation and cell survival signals through the ERK pathway. Since Ape1/Ref-1 is multifunctional protein, other signaling molecules may be affected in the Ape1/Ref-1 knockdown cells. For example NF-κB is a target of Ape1/Ref-1, however, even in the parent cells NF-κB was not activated by IL-21 stimulation (data not shown). Further study is needed for this point. Previous reports that showed MEK-ERK activity prevented IL-3 deprivation-induced cell death in BaF3 cells are consistent with our results [35,36].

MEK-ERK pathway plays pivotal roles in the development of various organs and in cell proliferation and survival. Therefore, regulation of the MEK-ERK pathway may be one mechanism by which Ape1/Ref-1 controls cellular responses and carcinogenesis. To understand how Ape1/Ref-1 regulates ERK activity, we tried to detect the interaction between Ape1/Ref-1 and ERK1/2. However, we could not detect any interactions so far. Controlling cytokine signaling is promising strategy for immune disease treatment. Further studies are required to unravel the mechanism by which IL-21 and Ape1/Ref-1 regulates ERK activity.

Acknowledgment

We thank Dr. Toshio Kitamura (The University of Tokyo) for providing the PLAT-E and Ba/F3 cells, and Dr. Kazuo Sugamura (Miyagi Cancer Center Research Institute) and Dr. Naoto Ishii (Tohoku University) for generously providing us with critical reagents. This work was supported in part by Grant-in-Aid for Scientific Research (C), 22590432, and Grant-in-Aid for Global Center of Excellence (G-COE) Program of the Japan Society for the Promotion of Science.

References

[1] J. Parrish-Novak, S.R. Dillon, A. Nelson, et al., Interleukin 21 and its receptor are involved in NK cell expansion and regulation of lymphocyte function, Nature 408 (2000) 57–63.
[2] E.K. Deenick, S.G. Tangye, Autoimmunity: IL-21: a new player in Th17-cell differentiation, Immunol. Cell Biol. 85 (2007) 503–505.
[3] T. Onoda, M. Rahman, H. Nara, et al., Human CD4+ central and effector memory T cells produce IL-21: effect on cytokine-driven proliferation of CD4+ T cell subsets, Int. Immunol. 19 (2007) 1191–1199.
[4] M. Harada, K. Magara-Koyanagi, H. Watarai, et al., IL-21-induced Bepsilon cell apoptosis mediated by natural killer T cells suppresses IgE responses, J. Exp. Med. 203 (2006) 2929–2937.
[5] J.M. Coquet, K. Kyparissoudis, D.G. Pellicci, et al., IL-21 is produced by NKT cells and modulates NKT cell activation and cytokine production, J. Immunol. 178 (2007) 2827–2834.
[6] T. Chtanova, S.G. Tangye, R. Newton, et al., T follicular helper cells express a distinctive transcriptional profile, reflecting their role as non-Th1/Th2 effector cells that provide help for B cells, J. Immunol. 173 (2004) 68–78.
[7] H. Asao, C. Okuyama, S. Kumaki, et al., Cutting edge, the common gamma-chain is an indispensable subunit of the IL-21 receptor complex, J. Immunol. 167 (2001) 1–5.
[8] T. Habib, S. Senadheera, K. Weinberg, et al., The common γ chain (γc) is a required signaling component of the IL-21 receptor and supports IL-21-induced cell proliferation via JAK3, Biochemistry 41 (2002) 8725–8731.
[9] W.J. Leonard, R. Spolski, Interleukin-21: a modulator of lymphoid proliferation, apoptosis and differentiation, Nat. Rev. Immunol. 5 (2005) 688–698.
[10] I.D. Davis, K. Skak, M.J. Smyth, et al., Interleukin-21 signaling: functions in cancer and autoimmunity, Clin. Cancer Res. 13 (2007) 6926–6932.
[11] R. Spolski, W.J. Leonard, The Yin and Yang of interleukin-21 in allergy, autoimmunity and cancer, Curr. Opin. Immunol. 20 (2008) 295–301.
[12] K. Ozaki, K. Kikly, D. Michalovich, et al., Cloning of a type I cytokine receptor most related to the IL-2 receptor β chain, Proc. Natl. Acad. Sci. USA 97 (2000) 11439–11444.
[13] R. Zeng, R. Spolski, E. Casas, et al., The molecular basis of IL-21-mediated proliferation, Blood 109 (2007) 4135–4142.
[14] A. Hoshino, S. Matsumura, K. Kondo, et al., Inducible translocation trap: a system for detecting inducible nuclear translocation, Mol. Cell 15 (2004) 153–159.
[15] S. Saint Fleur, H. Fujii, Cytokine-induced nuclear translocation of signaling proteins and their analysis using the inducible translocation trap system, Cytokine 41 (2008) 187–197.
[16] C.N. Robson, I.D. Hickson, Isolation of cDNA clones encoding a human apurinic/apyrimidinic endonuclease that corrects DNA repair and mutagenesis defects in E. coli xth (exonuclease III) mutants, Nucleic Acids Res. 19 (1991) 5519–5523.

[17] B. Demple, T. Herman, D.S. Chen, Cloning and expression of APE, the cDNA encoding the major human apurinic endonuclease: definition of a family of DNA repair enzymes, Proc. Natl. Acad. Sci. USA. 88 (1991) 11450–11454.
[18] A.R. Evans, M. Limp-Foster, M.R. Kelley, Going APE over ref-1, Mutat. Res. 461 (2000) 83–108.
[19] S. Xanthoudakis, T. Curran, Identification and characterization of Ref-1, a nuclear protein that facilitates AP-1 DNA-binding activity, EMBO J. 11 (1992) 653–665.
[20] G. Tell, F. Quadrifoglio, C. Tiribelli, et al., The many functions of APE1/Ref-1: not only a DNA repair enzyme, Antioxid. Redox Signal. 11 (2009) 1–19.
[21] K.K. Bhakat, A.K. Mantha, S. Mitra, Transcriptional regulatory functions of mammalian AP-endonuclease (APE1/Ref-1), an essential multifunctional protein, Antioxid. Redox Signal. 11 (2009) 621–638.
[22] R. Chattopadhyay, S. Das, A.K. Maiti, et al., Regulatory role of human AP-endonuclease (APE1/Ref-1) in YB-1-mediated activation of the multidrug resistance gene MDR1, Mol. Cell Biol. 28 (2008) 7066–7080.
[23] M.L. Fishel, M.R. Kelley, The DNA base excision repair protein Ape1/Ref-1 as a therapeutic and chemopreventive target, Mol. Aspects Med. 28 (2007) 375–395.
[24] S. Merluzzi, M. Moretti, S. Altamura, et al., CD40 stimulation induces Pax5/BSAP and EBF activation through a APE/Ref-1-dependent redox mechanism, J. Biol. Chem. 279 (2004) 1777–1786.
[25] S. Merluzzi, G. Gri, V. Gattei, et al., APE/Ref-1 makes fine-tuning of CD40-induced B cell proliferation, Mol. Immunol. 45 (2008) 3731–3739.
[26] Z. Fan, P.J. Beresford, D. Zhang, et al., Cleaving the oxidative repair protein Ape1 enhances cell death mediated by granzyme A, Nat. Immunol. 4 (2003) 145–153.
[27] Y. Guo, J. Chen, T. Zhao, et al., Granzyme K degrades the redox/DNA repair enzyme Ape1 to trigger oxidative stress of target cells leading to cytotoxicity, Mol. Immunol. 45 (2008) 2225–2235.
[28] R. Palacios, M. Steinmetz, Il-3-dependent mouse clones that express B-220 surface antigen, contain Ig genes in germ-line configuration, and generate B lymphocytes in vivo, Cell 41 (1985) 727–734.
[29] M. Rahman, H. Nara, T. Onoda, et al., Cloning and characterization of an isoform of interleukin-21, FEBS Letter. 581 (2007) 4001–4009.
[30] H. Nara, T. Onoda, M. Rahman, et al., Regulation of interleukin-21 receptor expression and its signal transduction by WSB-2, Biochem. Biophys. Res. Commun. 392 (2010) 171–177.
[31] S. Morita, T. Kojima, T. Kitamura, Plat-E: an efficient and stable system for transient packaging of retroviruses, Gene Ther. 7 (2007) 1063–1066.
[32] S.J. Lee, Y.S. Cho, M.C. Cho, et al., Both E6 and E7 oncoproteins of human papillomavirus 16 Inhibit IL-18-induced IFN-γ production in human peripheral blood mononuclear and NK cells, J. Immunol. 167 (2001) 497–504.
[33] H. Asao, X.Y. Fu, Interferon-gamma has dual potentials in inhibiting or promoting cell proliferation, J. Biol. Chem. 275 (2000) 867–874.
[34] S. Haga, K. Terui, Q. Zhang, et al., Stat3 protects against Fas-induced liver injury by redox-dependent and -independent mechanisms, J. Clin. Invest. 112 (2003) 989–998.
[35] K. Terada, Y. Kaziro, T. Satoh, Analysis of Ras-dependent signals that prevent caspase-3 activation and apoptosis induced by cytokine deprivation in hematopoietic cells, Biochem Biophys Res Commun. 267 (2000) 449–455.
[36] A. von Gise, P. Lorenz, C. Wellbrock, et al., Apoptosis suppression by Raf-1 and MEK1 requires MEK- and phosphatidylinositol 3-kinase-dependent signals, Mol. Cell Biol. 21 (2001) 2324–2336.

Biochemical and Biophysical Research Communications 420 (2012) 635–638

Contents lists available at SciVerse ScienceDirect

Biochemical and Biophysical Research Communications

journal homepage: www.elsevier.com/locate/ybbrc

Probing the stability and mechanism for folding of the GrpE1-112 tetrameric deletion mutant of the GrpE protein from *E. coli*

Andrew F. Mehl *, Kelby Okada, Shirley M. Dehn, Sarah Kurian

Department of Chemistry and The Program in Biochemistry, Knox College, 2 East South St., Galesburg, IL 61401, USA

ARTICLE INFO

Article history:
Received 10 February 2012
Available online 17 March 2012

Keywords:
Protein stability
Protein folding
Oligomeric
Tetrameric
Four-helix bundle

ABSTRACT

Insight into the stability and folding of oligomeric proteins is essential to the understanding of protein folding, especially since the majority of proteins found in nature are oligomeric. A deletion mutant of the GrpE protein from *Escherichia coli*, that contains the first 112 residues (GrpE1-112) of 197 total, is an oligomeric protein forming a tetrameric structure. A four-helix bundle structure is formed via the interaction of an α-helix (22 amino acids in length) from each monomer. Using both thermal and chemical (urea) denaturation studies, the GrpE1-112 protein has rather low stability with a T_m of unfolding of 37 °C, a C_m (urea) of 1.3 M, and a $\Delta G_{unfolding}$ of 8.4 kJ mol^{-1}. Investigation into the folding pathway using circular dichroism (CD) stopped-flow revealed a two step process with a fast first phase ($k_{refolding} = 8.0 \times 10^6$ s^{-1} M^{-1}) forming a multimeric intermediate that possesses significant α-helical content followed by a slow, first order, step forming the folded tetramer.

1. Introduction

How a protein folds into its final shape and what forces are at work in providing stability to the native structure are questions that have intrigued many protein biochemists during the past 30–40 years. Major advances in the area of protein stability and folding have been accomplished, especially concerning relatively small monomeric globular proteins [1]; however, research concerning the stability and folding/unfolding pathways for oligomeric proteins, mainly dimers and tetramers, has not been as extensive as with the monomeric counterparts [2]. Additionally, formulations relating oligomeric folding to an energy landscape model are just beginning to be worked out [3]. With oligomeric proteins there are additional modes of stabilization at the quaternary level.

The majorities of proteins in nature are not monomeric, but rather exist in higher order "multiple subunit"-type structures [4]. Additionally, the formation of the stable oligomeric structure via a protein–protein interaction is a phenomenon found throughout biology with respect to the transient protein–protein interactions that play fundamental roles initiating many biological processes.

This work describes the investigation into the stability and folding pathway for a tetrameric protein containing the common four-helix bundle fold. Specifically, the model protein is a deletion mutant of the GrpE protein from *Escherichia coli* (GrpE1-112) retaining the first 112 residues of 197 total found in the full length protein. This mutant was created in a prior study of GrpE to investigate the requirements for dimerization [5]. Full length GrpE is a dimer where each monomer contributes a long α-helix (residues 35–88) that pair together and form a "tail" section in the dimer; additionally, each monomer contributes two short α-helical regions (residues 89–109 and 117–137) that form the four-helix bundle motif in the dimer structure. Finally, each monomer contains a β-sheet region (residues 139–197) which is not part of the dimer interface. One interesting result from the prior work [5] revealed that GrpE1-112 did not form a dimer but instead formed a tetramer. Thus having one α-helical region of 24 residues (88–112) enabled a hydrophilic core to be formed. The working model (see Fig. 1) for the structure of this tetramer involves the formation of a four-helix bundle where each monomer contributes an α-helix in an anti-parallel topology [5]. Evidence in support of this structure has recently been observed with the creation of a designed protein based on this four-helix bundle interaction motif as the basis for a new hydrogel biopolymer formation (unpublished results).

The results presented here suggest overall low protein stability for GrpE1-112 protein and the folding pathway of this tetramer proceeds via a two step mechanism involving a relatively fast phase forming a multimeric intermediate followed by a slow step to the final folded tetramer.

2. Materials and methods

2.1. Materials

The GrpE1-112 deletion mutant protein was prepared as previously described [5]. All chemicals were purchased from

* Corresponding author. Fax: +1 309 341 7083.
E-mail address: amehl@knox.edu (A.F. Mehl).

0006-291X/$ - see front matter © 2012 Elsevier Inc. All rights reserved.
http://dx.doi.org/10.1016/j.bbrc.2012.03.052

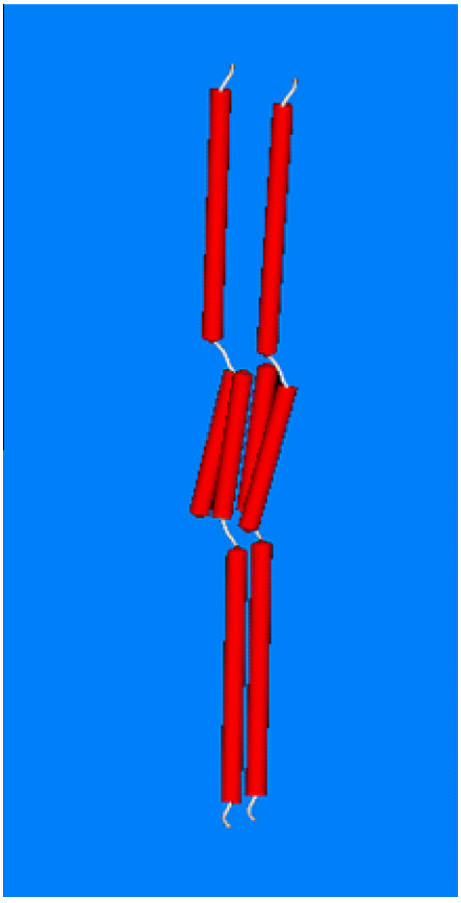

Fig. 1. A schematic representation for the proposed model for the GrpE1-112 deletion mutant protein that is forming a homotetramer utilizing a four-helix bundle within the structure. This figure was created using Weblab ViewerPro Version 3.7.

Sigma–Aldrich Company. Unless indicated otherwise, all experiments were carried out in potassium phosphate buffer (25.0 mM, pH 7.20 plus 5.0% glycerol).

2.2. Determination of protein concentration

The concentration of the purified GrpE1-112 protein was determined by the method of Bradford [6], using Bovine γ-globulin as a standard. Unless stated otherwise, all molar concentrations are given based on the monomeric molecular mass for GrpE1-112 (12,614 g/mol).

2.3. Equilibrium studies

Circular dichroism (CD) spectra were recorded using an OLIS (Online Instruments Inc., Bogart, GA, USA) RSM 1000 spectrometer configured with a CD module for dual beam CD. Initial spectra were obtained used the following conditions: T, 20 °C; pathlength, 0.1 cm; protein concentrations, 0.5–0.7 mg/ml; scanned from 260 to 190 nm (2 nm step size) with a rate dependent on the amount of signal produced at each wavelength. Temperature was controlled using a Peltier-type temperature control system (OLIS and Quantum Northwest, Spokane, WA, USA). Thermal unfolding studies were carried out using the same conditions described above. A full scan was taken at each temperature from 6 to 94 °C (every 2 °C) with an equilibration time of 2 min at each temperature. Protein refolding/unfolding was monitored by following the change in ellipticity at 222 nm as a function of urea concentration in phosphate buffer. Urea solutions were prepared and utilized within 10 h. Samples were incubated with the chemical denaturant for a minimum of 2 h to ensure complete equilibration.

Thermal and chemical denaturation data were analyzed for thermodynamic parameters according to the method by Pace et al. [7]. Briefly, for the equilibrium studies the K_{eq} (unfolded/folded) can be calculated from the fraction of unfolded protein at each temperature (or at each urea concentration) near the transition point using a two-state model and by knowing the ellipticity for the fully folded and fully unfolded species. Knowing the K_{eq}, the standard Gibbs free energy (ΔG°) for unfolding at each temperature or urea concentration is calculated using,

$$\Delta G^{\circ} = -RT \ln K_{eq}$$

where R is the ideal gas constant and T is the specific temperature. The Gibbs free energy is then plotted versus temperature or urea concentration to determine the T_m and ΔH of unfolding in the thermal study or determination of C_m (concentration of urea at the midpoint), m (the slope which reflects the sensitivity of the transition to the concentration of denaturant), and $\Delta G_{unfolding}$ in the urea concentration study. With the T_m, ΔH and an estimated value of the ΔC_p [7], the Gibbs–Helmholtz equation:

$$\Delta G(T) = \Delta H_m(1 - T/T_m) + \Delta C_p[T - T_m - T\ln(T/T_m)]$$

was utilized to calculate the value of ΔG at any temperature (T).

2.4. Stopped-flow kinetic studies

Refolding and unfolding experiments were carried out using an OLIS stop-flow module configured to the previously described OLIS CD instrument (see above). The stop-flow module has a pathlength of 2.0 mm and dead time between 3 and 5 ms. All experiments used a 10–1 mixing ratio and, in general, for each experimental condition a minimum of eight shots were averaged to improve the signal-to-noise ratio. Data were fit to either a single exponential growth (for unfolding) or a double exponential decay (for refolding) function. The values of the rate constants reported in Table 1 were obtained by extrapolation to 0 M urea using the concentration dependence on the rate constant plots (see inset graphs in Figs. 3 and 5).

3. Results and discussion

3.1. Equilibrium studies

The thermal and chemical denaturation transitions of GrpE1-112 protein proceeding from the folded state to an unfolded state were examined by monitoring the loss of α-helical structure via CD spectroscopy. Fig. 2 shows the results for both the thermal (Fig. 2A) and chemical (urea) (Fig. 2B) equilibrium studies. Both studies reveal a simple two-state process with the absence of multiple points

Table 1
Equilibrium and kinetic parameters for GrpE1-112.

T_m (°C)	C_m (M)	m-Value (kJ mol^{-1} K^{-1})	$\Delta G_{unfolding}$ (kJ mol^{-1})[a]
I Equilibrium parameters			
37.4	1.3	6.3	8.38 (Urea) 8.46 (Thermal)
$k_{refolding}$ (Fast) (s^{-1} M^{-1})		$k_{refolding}$ (Slow) (s^{-1})	$k_{unfolding}$ (s^{-1})
II Kinetic parameters			
8.0×10^6		1.2×10^1	5.2×10^{-1}

[a] For comparison purposes both $\Delta G_{unfolding}$ values were determined at 20 °C.

of inflection which would be indicative of any potential unfolding intermediates. Additionally, equilibrium type gel filtration studies using both urea and guanidine hydrochloride as denaturants also did not give any indication of long-lived stable intermediates (data not shown). In contrast, equilibrium studies of the tetrameric Bovine liver catalase have shown that intermediate dimers are stable and possess enzymatic activity [8]. The stability of the tetrameric GrpE1-112 is quite low with a transition temperature (T_m) of only 37.4 °C and a ΔG of unfolding of 8.4 kJ mol^{-1} (see Table 1). A very similar protein to GrpE1-112 is the mutant RM6 of the ROP protein, this protein is tetrameric with four monomers having all α-helical structures with a length of 29 residues and a heptad repeat throughout. The stability of this mutant is very high (T_m = 101 °C, ΔG of unfolding of 195 kJ mol^{-1}) due to the increased hydrophobic core and the additional feature of having a coiled-coil structure [9]. The GrpE1-112 mutant does not have a heptad repeat and thus one would not expect any supercoiling within the four-helix bundle.

Another similar oligomeric proteins is the small tetrameric protein domain from tumor suppressor p53, where each monomer contains an α-helical region of 20 residues, and a β-strand region containing 8 residues; this protein has an intermediate stability (T_m = 75.3 °C) [10] between that of GrpE1-112 and the mutant RM6 of ROP. The structure of small tetrameric domain of p53 involves the interactions of the α-helices from each monomer through a hydrophobic core involving mostly Leu residues in an anti-parallel arrangement to create a dimer and then two dimers interact orthogonally generating the tetramer, although not in a four-helix bundle fold.

Structurally speaking, the wild-type ROP protein that contains a dimer where each monomer contributes two α-helices (each 29 residues in length) joined by a loop region to create a four-helix bundle fold is very similar to the proposed structure of the GrpE1-112 mutant. Interestingly, a natural homolog to ROP from *Proteus vulgaris* has comparable thermodynamic parameters to GrpE1-112 with a T_m of 55 °C, a C_m = 1.4 M, and *m*-value of 13 kJ mol^{-1} K^{-1}[11].

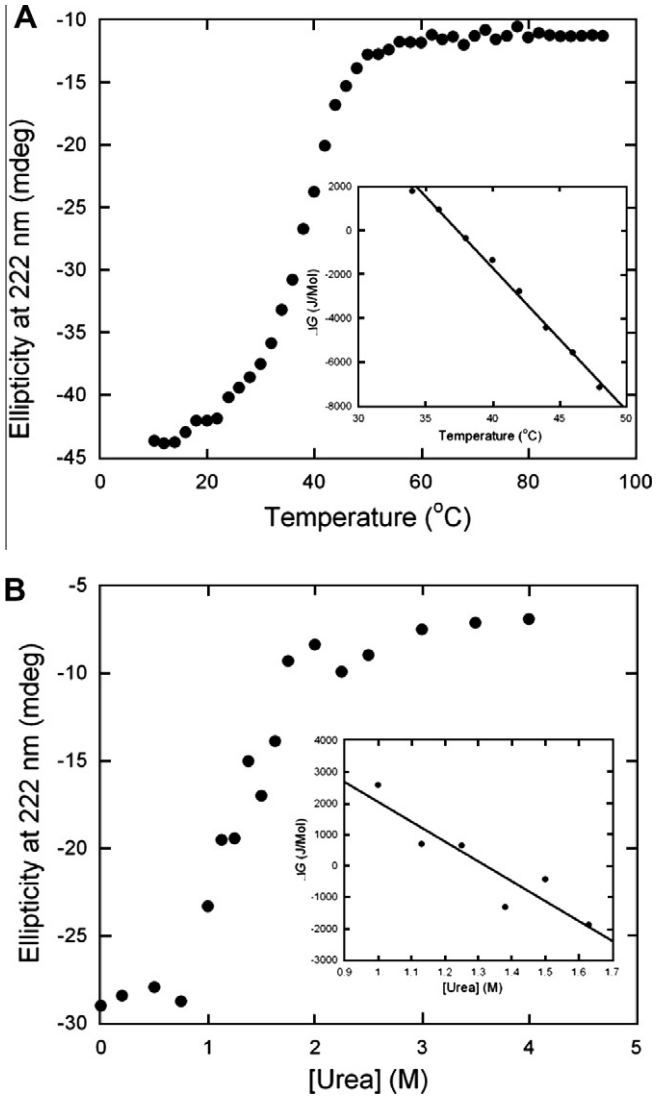

Fig. 2. (A) Thermal denaturation curve for the GrpE1-112 protein determined at pH 7.2 in 25.0 mM phosphate buffer as described in materials and methods. Inset shows the $\Delta G_{unfolding}$ as a function of temperature in the transition region. (B) Urea denaturation curve for the GrpE1-112 protein determined at pH 7.2 and 25 mM phosphate buffer as described in materials and methods. Inset shows the $\Delta G_{unfolding}$ as a function of urea molarity in the transition region.

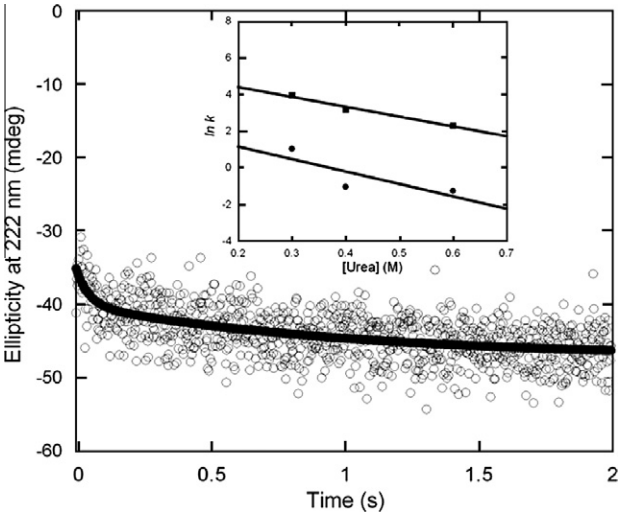

Fig. 3. A representative kinetic trace of the GrpE1-112 protein refolding monitored by stopped-flow CD spectroscopy when refolding to 0.40 M urea. The solid line shows the fitting result to a two step, three species model. Inset shows the ln*k* versus urea concentration for both the fast phase (■) and slow phase (●) of folding, respectively.

3.2. Refolding of GrpE1-112

We investigated the refolding of GrpE1-112 by stopped-flow CD spectroscopy. GrpE1-112 follows a biphasic refolding kinetics with the majority of secondary structure forming in the first 100 ms during the fast initial step (see Fig. 3). The refolding data was fit to a two step sequential mechanism with one intermediate. To test whether each step in the refolding process is unimolecular or multimolecular, we studied the dependence of the refolding rates for GrpE1-112 on protein concentration. Fig. 4 shows the plot of protein concentration versus the rate constant, *k*, for both steps. The results indicate that the fast phase has a significant dependence on protein concentration, whereas the slow phase shows no dependence on protein concentration. Thus the first step involves a multimeric species and the second utilizes a single species. The rate for the fast phase (see Table 1) is comparable to other similar tetrameric proteins such as the tumor suppressor p53 protein with an initial fast step rate of 3.1×10^5 s^{-1}M^{-1} forming a dimeric intermediate.

The GrpE1-112 deletion mutant protein has 4 proline residues in the unstructured region (residues 1–34) and thus these prolines would not influence the refolding rate being monitored at 222 nm

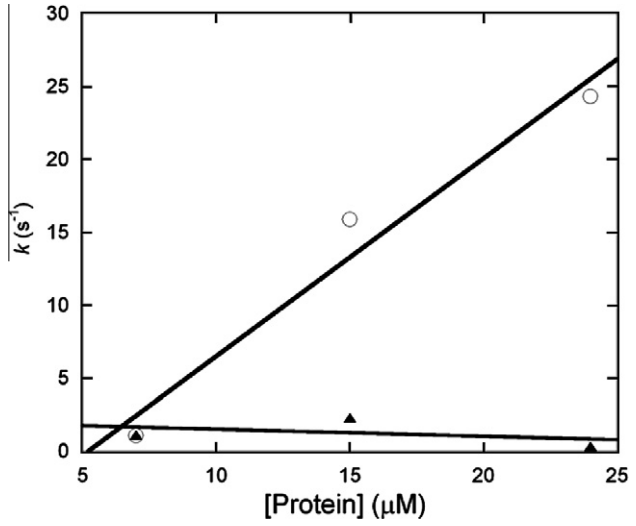

Fig. 4. The dependence of refolding rates of GrpE1-112 on protein concentration. Refolding was monitored by CD stopped-flow spectroscopy to a final concentration of 0.40 M urea. The fast phase is shown by (○) and the slow phase is shown by (▲).

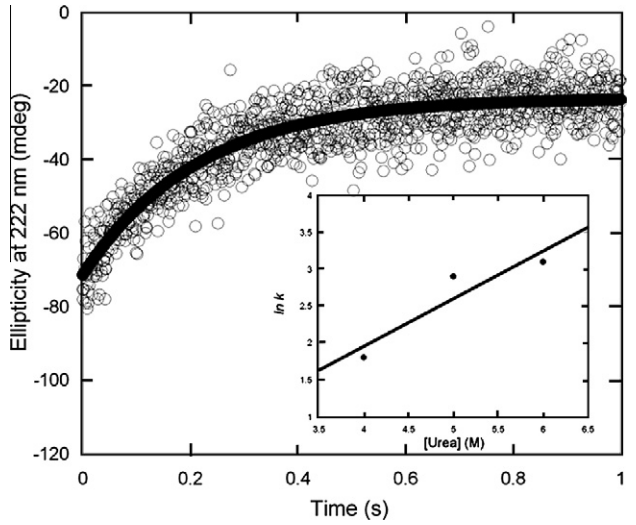

Fig. 5. A representative kinetic trace of the GrpE1-112 protein unfolding monitored by stopped-flow CD spectroscopy when unfolding to a final concentration of 4.0 M urea. The solid line shows the fitting result of a single exponential. Inset shows the ln*k* versus final urea concentration.

via stopped-flow CD spectroscopy. However, there is one additional proline reside at position 97 found within the α-helix forming region and it could have an effect of the rate of refolding. The slower second step could be limited by the proline residue having to adopt the correction conformation to be found in an α-helix.

3.3. Unfolding of GrpE1-112

The results of the unfolding kinetics for GrpE1-112 are shown in Fig. 5. The data fit best to a single slow step of protein unfolding at all urea concentrations studied. The unfolding rate of $5.2 \times 10^{-1}\ s^{-1}$ (see Table 1) is significantly faster than that of other similar proteins; the tetrameric p53 has a rate of $3.7 \times 10^{-3}\ s^{-1}$, and the dimeric ROP has a rate of $6 \times 10^{-7}\ s^{-1}$. Since the overall stability of GrpE1-112 is lower than both the p53 and ROP proteins this is in agreement with the faster rate for unfolding.

4. Summary

The simplest pathway for the folding of GrpE1-112 that is consistent with all of the above data is as follows:

$$4M_u \overset{Fast}{\rightarrow} 2D_I(\text{or } T_I) \overset{Slow}{\rightarrow} T_f$$

where M_u is unfolding monomer, D_I is a dimeric intermediate, T_I is a tetrameric intermediate and T_f is the folded tetramer. The exact identity of the transient intermediate can't be deduced fully, only to note that since the first fast step showed dependence on protein concentration there must be a minimum of two species interacting to form the intermediate product; thus either two dimers interacting or four monomers interacting forming the intermediate species. Earlier crosslinking studies [5] did show a dimeric entity being formed, however the experiment was carried out as a time course, and the possibility exists that even though a dimer was trapped it could have originated from being a tetramer and only with more time would the crosslinking sufficiently trap the tetramer. A similar two-step mechanism is proposed for the tumor suppressor p53 protein, with the major difference being the direct evidence for a dimeric intermediate through studies with stable dimeric mutants [12]. Additionally, the folding mechanism for the $(H3–H4)_2$ histone tetramer also involves a dimeric intermediate [3].

Acknowledgments

This research was supported in part by Grant #0961739 from the NSF to A.F.M. Additional support was provided by an Undergraduate Science Education Grant from the Howard Hughes Medical Institute (#52005130), the Knox College Ford Fellowship Program, the Knox College Ronald E. McNair Post-baccalaureate Achievement Program funded through a Grant from the Department of Education and Paul K. Richter and Evalyn E. Cook Richter Memorial Trusts.

References

[1] K.W. Plaxco, K.T. Simons, I. Ruczinski, D. Baker, Topology, stability, sequence, and length: defining the determinants of two-state protein folding kinetics, Biochemistry 39 (2000) 11177–11183.
[2] R. Jaenicke, H. Lilie, Folding and association of oligomeric and multimeric proteins, Advances in Protein Chemistry 53 (2000) 329–401.
[3] D.D. Banks, L.M. Gloss, Folding mechanism of the $(H3–H4)_2$ histone tetramer of the core nucleosome, Protein Science 13 (2004) 1304–1316.
[4] M.J. Bennett, M.P. Schlunegger, D. Eisenberg, 3D domain swapping: a mechanism for oligomer assembly, Protein Science 4 (1995) 2455–2468.
[5] A.F. Mehl, L.D. Heskett, S.S. Jain, B. Demeler, Insights into dimerization and four-helix bundle formation found by dissection of the dimer interface of the GrpE protein from *Escherichia coli*, Protein Science 12 (2003) 1205–1215.
[6] M.M. Bradford, A rapid and sensitive method for the quantitation of microgram quantities of protein utilizing the principle of protein-dye binding, Analytical Biochemistry 72 (1976) 248–254.
[7] C.N. Pace, B.A. Shirley, J.A. Thomson, Measuring the conformational stability of a protein, in: T.E. Creighton (Ed.), Protein Structure a Practical Approach, Oxford University Press, Oxford, 1990, pp. 311–330.
[8] K. Prakash, S. Prajapati, A. Ahmad, S.K. Jain, V. Bhakuni, Unique oligomeric intermediates of bovine liver catalase, Protein Science 11 (2002) 46–57.
[9] N.M. Glykos, Y. Papanikolau, M. Vlassi, D. Kotsifaki, G. Cesareni, M. Kokkinidis, Loopless Rop: structure and dynamics of an engineered homotetrameric variant of the repressor of primer protein, Biochemistry 45 (2006) 10905–10919.
[10] C.R. Johnson, P.E. Morin, C.H. Arrowsmith, E. Freire, Thermodynamic analysis of the structural stability of the tetrameric oligomerization domain of p53 tumor suppressor, Biochemistry 34 (1995) 5309–5316.
[11] S. Dalal, D. Canet, S.E. Kaiser, C.M. Dobson, L. Regan, Conservation of mechanism, variation of rate: folding kinetics of three homologous four-helix bundle proteins, Protein Eng. Des. Sel. 21 (2008) 197–206.
[12] M.G. Mateu, M.M. Sánchez Del Pino, A.R. Fersht, Mechanism of folding and assembly of a small tetrameric protein domain from tumor suppressor p53, Natural Structural Biology 6 (1999) 191–198.

Biochemical and Biophysical Research Communications 420 (2012) 639–643

Contents lists available at SciVerse ScienceDirect

Biochemical and Biophysical Research Communications

journal homepage: www.elsevier.com/locate/ybbrc

A model for heterooligomer formation in the heat shock response of *Escherichia coli*

Eamonn F. Healy *

Department of Chemistry, St. Edward's University, Austin, TX 78704, USA

ARTICLE INFO

Article history:
Received 5 March 2012
Available online 17 March 2012

Keywords:
Escherichia coli
IbpA
IbpB
Heat shock proteins
sHSP
α-Crystallin
Molecular Dynamics
Dehydron

ABSTRACT

Small heat shock proteins (sHsp) are widely distributed molecular chaperones that bind to misfolded proteins to prevent irreversible aggregation and aid in refolding to a competent state. The sHsps characterized thus far all contain a conserved α-crystallin, and variable N- and C-termini critical for chaperone activity and oligomerization. The *Escherichia coli* sHsps IbpA and IbpB share 48% sequence homology, are induced by heat shock and oxidative stress, and each requires the presence of the other to effect protein protection. Molecular Dynamics (MD) simulations of homology-modeled monomers and heterooligomers of these sHsps identify a possible mechanism for cooperation between IbpA and IbpB.

1. Introduction

The chaperone activity of the small heat shock protein (sHsp) dimer of various α-crystallins has been postulated to coincide with the exposure of hydrophobic interface sites after a temperature-regulated subunit exchange or dissociation of the oligomer [1,2]. This results in the sequestration of the target protein in a high mass complex, thereby preventing formation of an amorphous protein aggregate [3]. The oligomeric structures of these α-crystallins consistently show the C-terminus of one subunit, containing the conserved IXI sequence, extending into the hydrophobic groove formed by the β_4 and β_8 strands of the neighbouring subunit, in what is described as a "patching" motif [4]. This structure is consistent with a model of sHsp function in which the larger assembly acts as a reservoir from which the chaperone-active dimer is released to interact with protein targets [3]. Thermodynamic profiles of sHsp chaperone capacity have identified this dimer–dimer interface as a vital element in conferring the oligomer with a plasticity necessary for the detection of non-native proteins [5].

Solvent-exposed intramolecular backbone hydrogen bonds, or dehydrons, have been previously identified as vulnerabilities or structural defects in the packing of a wide array of proteins [6,7]. Exposure of such dehydrons to an aqueous environment has previously been shown to weaken protein secondary structures [8,9]. In turn excluding solvent from protein regions containing exposed hydrogen bonds has been implicated as a determinant factor in ligand–protein [10] and protein–protein [11] interactions. Indeed a screening protocol that identifies such structural vulnerabilities, or dehydrons, has been developed [12], and used to guide the rational development of more selective inhibitors [13]. Since dehydron distributions have been shown to correlate with protein subunit assembly [11] as well as playing potentially determinant roles in protein binding, it must be considered highly possible, if not probable, that protection of exposed backbone hydrogen bonds by solvent exclusion plays a role in the chaperone activity of small heat shock proteins containg the α-cystallin domain.

The Ig-like β fold structure of the α-crystallin domain provides an ideal topology for the presentation of solvent-exposed backbone hydrogen bonds. Dehydron analysis, Fig. 1 and [14], identifies two such solvent-accessible backbone hydrogen bonds that are conserved across many different α-crystallin domains. Previous MD equilibrations performed on solvated α-crystallin oligomers confirmed these β_8–β_9 inter-strand hydrogen bonds as vulnerable to solvent exposure. Trajectory analyses indicated that solvent exposure triggers a small but important dislocation of the β_8 strand relative to the β_9 strand, initiated by the migration of solvent molecules towards these underwrapped, and thus exposed, backbone hydrogen bonds. This dislocation is sufficient in scope to disrupt key β_8–β_9 inter-strand stabilizing forces.

These MD simulations, in conjunction with a structural analysis of the alignment sequences, combined to provide a mechanistic picture whereby release of the chaperone-active dimer of *Mycobacterium tuberculosis* α-crystallin1 exposes the β_4–β_8 hydrophobic groove, thus inducing the attachment of a target peptide loop so as to exclude water and maintain the integrity of the sHSP Ig β-fold [14].

* Fax: +1 512 448 8492.
E-mail address: healy@stedwards.edu

0006-291X/$ - see front matter © 2012 Elsevier Inc. All rights reserved.
http://dx.doi.org/10.1016/j.bbrc.2012.03.054

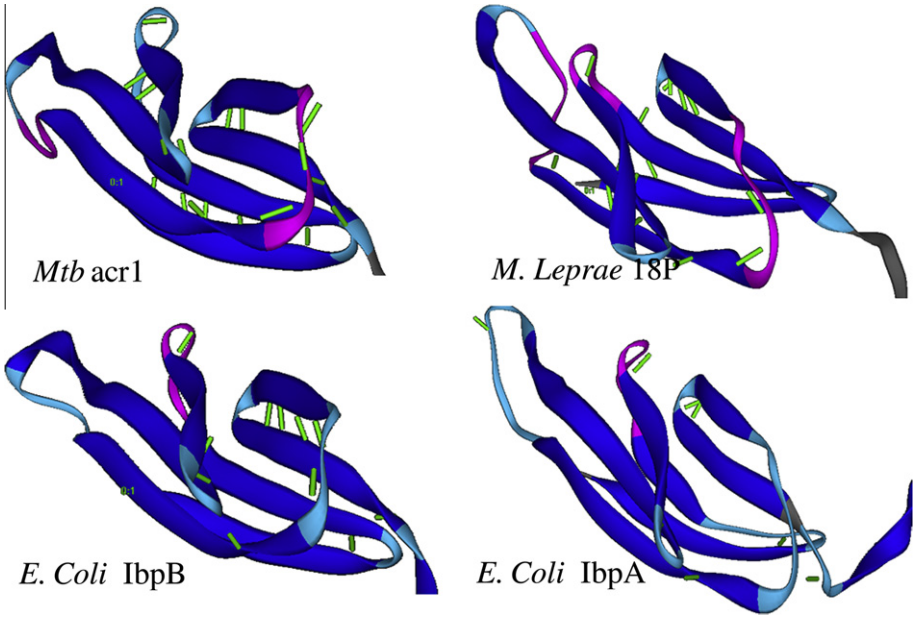

Fig. 1. The α-crystallin domains of four sHSPs with the solvent exposed backbone hydrogen bonds, or dehydrons, identified as green segments connecting the C_α of the linked residues [images generated with YAPView, available from http://sourceforge.net/projects/protlib/files/yapview/]. (For interpretation of reference to color in this figure legend, the reader is referred to the web version of this article.)

While the *Escherichia coli* sHSPs IbpA and IbpB show distinct activities, cooperation between them is crucial for the prevention of protein aggregation. Studies have revealed that while homooligomers of IbpA or IbpB exhibit only weak chaperone activities at relatively low temperatures, the simultaneous presence of IbpA and IbpB leads to very efficient stabilization of protein aggregates in a refolded state at higher temperatures [15]. Since no ternary complex containing both sHSPs and the substrate were detected *in vitro* it was postulated that IbpA or IbpB acted at high temperature to facilitate the conversion of the other to its active state [15]. Further, it has also been demonstrated that the chaperone activities of heterooligomeric bacterial sHSPs was indistinguishable from the activity of comparable homooligomers, even when the constituent proteins originate from different species [16]. Despite the nomenclature the *E. coli* sHSPs IbpA and IbpB are both Class A (prokaryote) proteins, an important common feature given that heterooligomer formation is restricted to members of the same sHSP class [16]. A functional analysis of N- and C-termini truncated IbpA mutants has revealed that while deletion of either the N- or C-terminus of IbpA compromises the ability of the sHSP to complex with the substrate during denaturation, such mutants interact with IbpB in a manner similar to full length IbpA [17]. Finally these sHSPs exhibit a somewhat unique temperature profile. The IbpA/IbpB function depends on elevated temperature, with protein reactivation and protection from degradation found at higher temperatures, while no protection from degradation by IbpA/IbpB observed at 15 °C [18]. Additionally whereas IbpA/IbpB production is observed to be strongly induced immediately after a temperature upshift, their ability to effect disaggregation is not observed when *E. coli* is exposed to these elevated temperatures for just a brief time (15 min at 45 °C) [19]. Thus these *E. coli* sHSPs are critical under conditions of extreme long-term heat shock, but show little activity under physiological conditions.

This paper seeks to explore the possibility that the dehydron hypothesis can provide a structure-based mechanism for the heat activation of IbpB by IbpA. Specifically MD simulations were performed to look at the role that solvent exclusion by the C-terminal extension of the IbpB sHSP from the region adjacent to the β_8–β_9 fold of an IbpA monomer might play in the formation of an IbpA–IbpB heterooligomer.

2. Methods

The dodecameric structure resulting from the docking of the α-crystallin domain from *T. aestivium* (wheat) into the density map of *Mtb* Acr is available from the RCSB (www.rcsb.org) as Protein Data Bank (pdb) code entry 2BYU. Homology models for the alpha-crystallin domains of *Mtb* acr1, *Mycobacterium Leprae* 18P and the *E. coli* heat shock proteins IbpA and IbpB were generated from sequence alignments (UniProt P0A5B7, P12809, P0C054 and P0C058, respectively) with the 2BYU homolog, using the MODELER protocol as implemented in the Discovery Studio program suite from Accelrys Inc. All proteins were subjected to a short energy minimization using the CHARMM force field [20], followed by successive steepest descent and conjugate gradient minimizations. The extent of hydrogen bond desolvation is quantified as the number of non-bonded, carbonaceous groups, ρ, contained within a domain centered on the residues linked by the interaction [11]. This desolvation domain is defined as two intersecting spheres of fixed radius centered on the C_α atoms of the linked residues. Dehydrons are then identified as those backbone hydrogen bonds that are underwrapped by non-polar groups, and defined as those interactions with ρ values at or below the average minus one root mean squared deviation. In this work the default values for domain radius, 6.2 Å, and dehydron cutoff, $\rho \leqslant 19$, were used as per [10]. These dehydrons for the α-crystallin domains of the four heat shock proteins are shown as green connectors in Fig. 1.

The fitted structure 2BYU includes the conserved IXI motif of the C-terminal extension but lacks the remainder of the C-terminal tail. The missing residues at positions 138–146 were added from the wheat structure (available as pdb code 1GME) after superposition of the backbones of residues 133–138 and 147–151. After adding hydrogens the inserted loop residues and the hydrogen positions were subjected to a short energy minimization using the CHARMM force field [20]. Homology

models of IbpA–IbpA and IbpA–IbpB complexes were assembled as interacting monomers by fitting the subunits onto the oligomeric structure of 2BYU. These oligomeric models were then were subjected to a short energy minimization followed by successive steepest descent and conjugate gradient minimizations.

Molecular Dynamics (MD) calculations were performed on the IbpA monomer and the IbpA–IbpB heterooligomer by first solvating both model structures with TIP3P explicit water molecules, occupying a sphere of radius 20 Å from the C_α carbon of the key Tyr_{118} residue of IbpA, and employing an explicit spherical boundary with harmonic restraint. The system was minimized by steepest descent and conjugate gradient. A harmonic restraint was then applied to the subunit containing the C-terminal extension, though the loop itself was left unrestrained and therefore free to move. The complexes were then heated to 350 K, and equilibrated at 350 K for 2 ns. The SHAKE algorithm was employed to keep bonds involving hydrogen atoms at their equilibrium length, allowing the use of a 2 fs time step.

3. Results and discussion

Dehydron analysis of a series of homology-modeled α-crystallin domains, Fig. 1, reveals two solvent-exposed backbone hydrogen bonds common to three of the four sequences studied. A similar pattern was observed in our earlier study of Mtb α-crystallin1 oligomer dynamics where all of the modeled systems contained these same underwrapped hydrogen bonds [14]. The only exception in either study is IbpA where the corresponding hydrogen-bonding pair of Asn_{111} in the β_8 strand and Tyr_{118} in the β_9 strand are well protected with ρ values of 26, compared to a $\langle\rho\rangle$ of 28. The reason for this exception can be seen in Fig. 2A where the Tyr_{118} side chain and the methylene groups of the Asn_{111} residue are positioned so as to exclude solvent from the β_8–β_9 surface. By contrast the dehydron pattern computed for IbpB is comparable to that found in both *Mtb* and *M. leprae*, with all of these sHSPs exhibiting exposed hydrogen-bonds between key residues (Thr_{109} and His_{116} in IbpB) responsible for stabilizing the β_8–β_9 fold. This means that whereas exposure of the β_4–β_8 hydrophobic groove to water for IbpB would be expected to induce attachment of a target peptide loop, so as to exclude water and maintain the integrity of the sHSP Ig β-fold, for IbpA no such activity should be observed. This is consistent with the observation that IbpA offers little protection to proteins under physiological conditions.

To investigate how IbpA/IbpB activity might be induced after a temperature upshift MD simulations of the solvated IbpA monomer were performed at 350 K. Fig. 2C highlights the dramatic tilt of the β_8 strand relative to the β_9 strand observed in the IbpA α-crystallin domain after a 2 ns equilibriation at 350 K. This dislocation is caused by a loss of the (Asn_{111})NH–OC(Tyr_{118}) hydrogen bond due to a severe contraction of the NHO angle to less than 90°. Coupled with a similar deformation of the (Val_{113})CO–HN(Leu_{116}) hydrogen bond in the β_8–β_9 turn (NHO angle of 106°) this results in a loss of the β_8–β_9 fold. Analysis of the vicinity of the fold identifies a well defined solvent shell of water molecules surrounding $Asn_{111,}$ with a persistent hydrogen bond clearly evident between one water oxygen and the amide hydrogen of $Asn_{111.}$ This exposure is also facilitated by the movement of the Tyr_{118} ring proximate to the (Val_{113})NH–OC(Leu_{116}) hydrogen

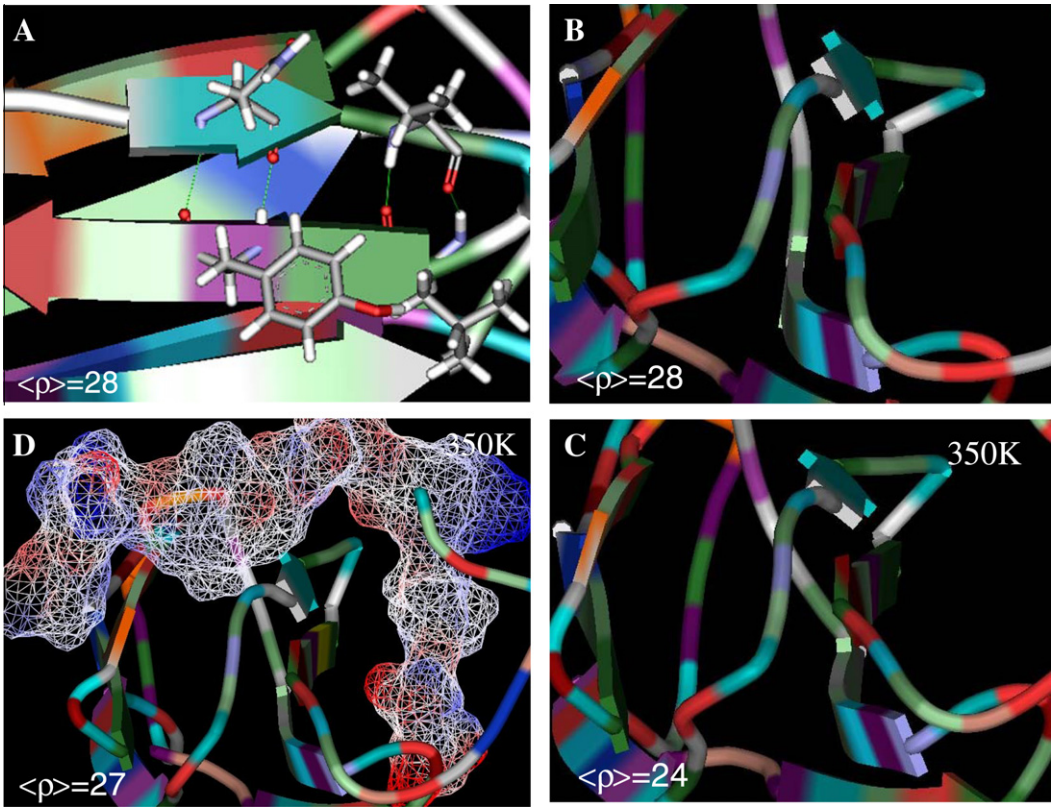

Fig. 2. (A) The β_8–β_9 fold in the homology-modeled IbpA α-crystallin monomer highlighting, from left to right the key (Asn_{111})NH–OC(Tyr_{118}) and (Asn_{111})CO–HN(Tyr_{118}) hydrogen bonds stabilizing the fold, and the (Val_{113})NH–OC(Leu_{116}) and (Val_{113})CO–HN(Leu_{116}) in the turn; (B) The view from the N- to the C-terminus of the β_8–β_9 fold in the IbpA α-crystallin monomer; (C) The view from the N- to the C-terminus of the β_8–β_9 fold in the IbpA α-crystallin monomer after a 2 ns equilibriation at 350 K, highlighting the dramatic tilt of the β_8 strand relative to the β_9 strand; (D) The view from the N- to the C-terminus of the β_8–β_9 fold in the IbpA–IbpB heterooligomer after a 2 ns equilibriation at 350 K, with the solvent accessible surface for C-terminus "patch" from the IbpB subunit shown in wire mesh.

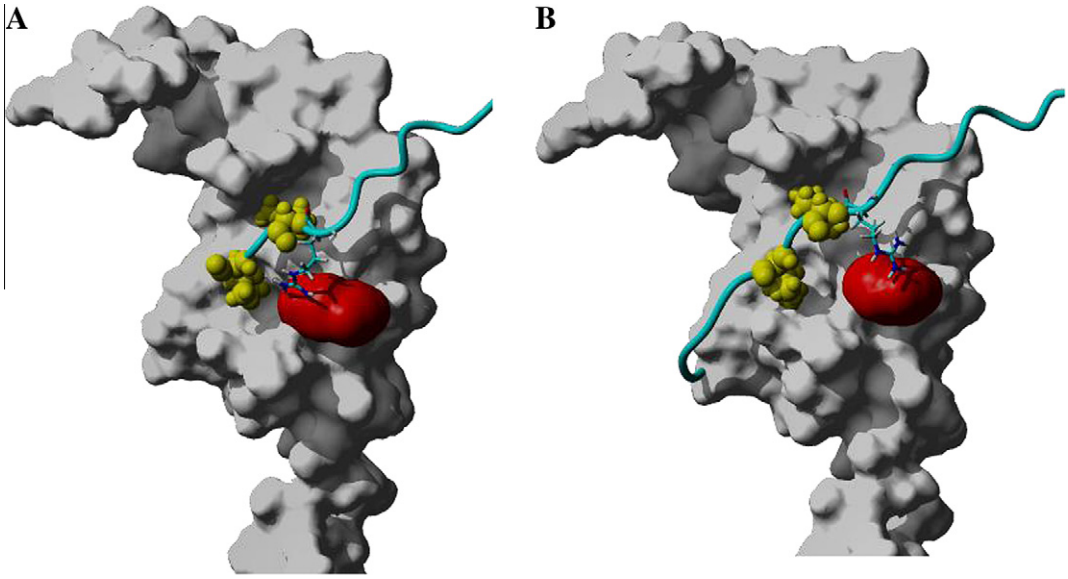

Fig. 3. Diagram of the (A) IbpA homooligomer and (B) IbpAIbpB heterooligomer highlighting: the IbpA subunit (gray surface); The C-terminal extension of the adjacent subunit (ribbon); the conserved Ile residues of the IXI motif (yellow ball); The Arg residue conserved as RIXI in both IbpA and IbpB (stick) that has been shown to be important for chaperone activity and higher order structure [17], possibly through the formation of a salt bridge with a conserved Glu (Glu_{62} in IbpA, shown as a red surface). (For interpretation of reference to color in this figure legend, the reader is referred to the web version of this article.)

bond, an underwrapped dehydron as identified in Fig. 1. Based on our dehydron-based mechanism therefore heating of IbpA, by exposing a solvent-exposed weakness between the Asn_{111} and Tyr_{118} residues, would induce attachment of a target peptide loop to the β_4–β_8 hydrophobic groove so as to exclude water and maintain the integrity of the sHSP Ig β_8–β_9 fold at this elevated temperature.

Fig. 3 highlights the inter-subunit contact observed in our IbpA–IbpA and IbpA–IbpB oligomeric models. The longer C-terminal chain found in IbpB clearly allows for more extensive "patching" of the hydrophobic groove of the adjacent IbpA monomer in the IbpA–IbpB heterooligomer (Fig. 3B), relative to that found in the IbpA homooligomer (Fig. 3A). Given that our analysis shows no vulnerabilities, and thus no need for an extensive peptide "cover", in the β_8–β_9 fold of IbpA comparable to those found in other α-crystallins, this less extensive patching in the homoligomer is not surprising. The advantage of a more extensive patch, or cover, only becomes apparent at an elevated temperature, given that our simulations indicate a newly exposed vulnerability between the Asn_{111} and Tyr_{118} residues of IbpA at 350 K. Thus our model would suggest that MD simulation of the IbpAIbpB heterooligomer at 350 K should illustrate the benefit of solvent exclusion by the IbpB C-terminal extension by showing no disruption of the β_8–β_9 fold. As can be seen from Fig. 2D equilibrating a solvated and pre-heated IbpA–IbpB dimer at 350 K for 2 ns yields a β_8–β_9 topology identical to that found in the unheated IbpA monomer. Analysis identifies a hydrogen bonding pattern similar to that observed for the IbpA monomer, Fig. 2A, with the critical (Asn_{111})NH–OC(Tyr_{118}) hydrogen bond intact.

These results lead to a mechanism for the heat activation of the *E. coli* sHSPs that involves, as is indicated by the results highlighted in [15,16,17,18,19], the formation of an IbpA–IbpB heterooligomer. Specifically it is proposed that exposure to an elevated temperature destabilizes the β_8–β_9 fold found in the IbpA α-crystallin domain, thereby inducing de-oligomerization of the IbpA homooligomer. Exposure of the β_4–β_8 hydrophobic groove of IbpA now induces de-oligomerization of the IbpB homooligomer, to facilitate the patching of the groove by the C-terminus of IbpB through the formation of a heterooligomer. By thus releasing the chaperone-active IbpB dimer, protein protection and reactivation would be facilitated.

Acknowledgements

The author wishes to thank the Welch Foundation (Grant# BH-0018) for its continuing support of the Chemistry Department at St. Edward's University.

References

[1] D.P. Claxton, P. Zou, H.S. Mchaourab, Structure and orientation of T4 lysozyme bound to the small heat shock protein alpha-crystallin, J. Mol. Biol. 375 (2008) 1026–1039.
[2] E. Basha, K.L. Friedrich, E. Vierling, The N-terminal arm of small heat shock proteins is important for both chaperone activity and substrate specificity, J. Biol. Chem. 281 (2008) 39943–39952.
[3] R. Stamler, G. Kappé, W. Boelens, C. Slingsby, Wrapping the alpha-crystallin domain fold in a chaperone assembly, J. Mol. Biol. 353 (2005) 68–79.
[4] H.S. McHaourab, J.A. Godar, P.L. Stewart, Structure and mechanism of protein stability sensors: chaperone activity of small heat shock proteins, Biochemistry 48 (2009) 3828–3837.
[5] L. Gu, A. Abulimiti, W. Li, Z. Chang, Monodisperse Hsp16.3 nonamer exhibits dynamic dissociation and reassociation, with the nonamer dissociation prerequisit for chaperone-like activity, J. Mol. Biol. 319 (2002) 517–526.
[6] A. Fernández, H. Scheraga, Insufficiently dehydrated hydrogen bonds as determinants of protein interactions, Proc. Natl. Acad. Sci. USA 100 (2003) 113–118.
[7] E.F. Healy, S. Johnson, C. Hauser, P. King, Tyrosine kinase inhibition: ligand binding and conformational change in c-Kit and c-Abl, FEBS Lett. 583 (2009) 2899–2906.
[8] E.F. Healy, The effect of desolvation on nucleophilic halogenase activity, Comput. Theoret. Chem. 964 (2011) 91–93.
[9] E.F. Healy, P. Romano, M. Mejia, G. Lindfors III, Acetylenic inhibitors of ADAM10 and ADAM17: in silico analysis of potency and selectivity, J. Mol. Graph. Model 29 (2010) 436–442.
[10] A. Fernández, S. Ridgway, Dehydron: a structure-encoded signal for protein interactions, Biophysical J. 85 (2003) 1914–1928.
[11] S. Maddipati, A. Fernández, Feature-similarity protein classifier as a ligand engineering tool, Biomol. Eng. 23 (2006) 307–315.
[12] A. Fernández, R.S. Berry, Extent of hydrogen-bond protection in folded proteins: a constraint on packing architectures, Biophys. J. 83 (2002) 2474–2481.
[13] A. Fernández, A. Sanguino, Z. Peng, A. Crespo, E. Ozturk, X. Zhang, S. Wang, W. Bornmann, G. Lopez-Berestein, Rational drug redesign to overcome drug resistance in cancer therapy: imatinib moving target, Cancer Res. 67 (2007) 4028–4033.

[14] E.F. Healy, P.J. King, A Mechanism of Action for Small Heat Shock Proteins, Biochem. Biophys. Res. Commun. 417 (2012) 268–273.

[15] E. Matuszewska, J. Kwiatkowska, E. Ratajczak, D. Kuczynska-Wisnik, E. Laskowska, Role of *Escherichia coli* heat shock proteins IbpA and IbpB in protection of alcohol dehydrogenase AdhE against heat inactivation in the presence of oxygen, Acta Biochim. Pol. 56 (2009) 55–61.

[16] S. Studer, F. Narberhaus, Chaperone activity and homo- and hetero-oligomer formation of bacterial small heat shock proteins, J. Mol. Biol. 275 (2000) 37212–37218.

[17] J. Strozecka, E. Chrusciel, E. Gorna, A. Szymanska, S. Zietkiewicz, K. Liberek, Importance of the N- and C-terminal regions of IbpA, the *Escherichia coli* small heat shock protein, for chaperone function and oligomerization, J. Biol. Chem. 287 (2012) 2843–2853.

[18] H. LeThanh, P. Neubauer, F. Hoffmann, The small heat-shock proteins IbpA and IbpB reduce the stress load of recombinant *Escherichia coli* and delay degradation of inclusion bodies, Microb. Cell Factories 4 (2005) 6.

[19] D. Kuczyńska-Wiśnik, S. Kedzierska, E. Matuszewska, P. Lund, A. Taylor, B. Lipińska, E. Laskowska, The *Escherichia coli* small heat-shock proteins IbpA and IbpB prevent the aggregation of endogenous proteins denatured in vivo during extreme heat shock, Microbiology 148 (2002) 1757–1765.

[20] B.R. Brooks, R.E. Bruccoleri, B.D. Olafson, D.J. States, S. Swaminathan, M. Karplus, CHARMM: A program for macromolecular energy, minimization, and dynamics calculations, J. Comput. Chem. 4 (1983) 187–217.

Biochemical and Biophysical Research Communications 420 (2012) 644–650

Contents lists available at SciVerse ScienceDirect

Biochemical and Biophysical Research Communications

journal homepage: www.elsevier.com/locate/ybbrc

Differentiation induction enhances bortezomib efficacy and overcomes drug resistance in multiple myeloma

Jing-li Gu, Juan Li *, Zheng-hai Zhou, Jun-ru Liu, Bei-hui Huang, Dong Zheng, Chang Su

Department of Hematology, The First Affiliated Hospital, Sun Yat-sen University, Guangzhou 510080, China

ARTICLE INFO

Article history:
Received 7 March 2012
Available online 17 March 2012

Keywords:
Multiple myeloma
Bortezomib
Differentiation
Drug resistance

ABSTRACT

Aim: It is of clinical importance to find methods to overcome bortezomib resistance. In the current study, we clarified the relationship between resistance to bortezomib and the differentiation status of myeloma cells, and explored the feasibility of induction of differentiation in overcoming bortezomib resistance in myeloma.

Methods: Cell morphology, immunoglobulin light-chain protein secretion levels, and XBP-1 expression were used to evaluate the differentiation status of myeloma cells. Low dose 2-ME2 alone or in combination with ATRA was used to induce differentiation in myeloma cells.

Results: The differentiation status of myeloma cells was related to myeloma sensitivity to bortezomib. After successful induction of differentiation, the myeloma cells were more sensitive to bortezomib with decreased growth and an increased rate of apoptosis. Induction of differentiation increased the proteasome workload in myeloma cells by increasing immunoglobulin secretion, while reducing proteasome capacity by decreasing proteasome activity. The imbalance between increased proteasome workload and decreased proteasome capacity is a possible mechanism by which induction of differentiation overcomes myeloma resistance to bortezomib.

Conclusion: The current study demonstrated, for the first time, that myeloma differentiation status is associated with myeloma sensitivity to bortezomib and that induction of differentiation can overcome myeloma resistance to bortezomib.

1. Introduction

Multiple myeloma (MM) is a malignant plasma cell neoplasm which is characterized by an abundant secretion of monoclonal immunoglobulin, destruction of bone, and aberrant plasma cell infiltration in the bone marrow [1]. Despite advances in immunomodulatory therapies and hematopoietic stem cell transplantation, MM remains incurable, largely due to drug resistance. Bortezomib, a novel therapeutic agent targeting the ubiquitin–proteasome system, has resulted in a breakthrough in the therapy of MM. The 5-year survival has increased from 33% before 2000 to >50% after bortezomib use in anti-myeloma regimens [2]; however, approximately one-third of MM patients are primarily resistant to bortezomib. Hence, it is of clinical importance to find new methods to overcome bortezomib resistance.

Bortezomib is a potent inhibitor of the proteasome by selectively combining to the β5 subunit of the 26S proteasome [3–5]. Previous experiments have shown that the level of immunoglobulin secretion is associated with myeloma sensitivity to bortezomib [6,7]. MM is essentially characterized by secreting large quantities of monoclonal immunoglobulins, which depends on the proteasome from protein synthesis to protein folding, protein quality control, and protein transportations [8–11]. Thus, a higher level of immunoglobulin secretion is inevitably associated with a higher workload on proteasome capacity. The induction of a higher level of immunoglobulin production might increase myeloma sensitivity to bortezomib.

A possible method by which to increase the production of immunoglobulins in MM is to induce differentiation of tumor cells. According to previous reports, 2-methoxyestrodiol (2-ME2) or all-trans-retinoicacid (ATRA) induce differentiation in myeloma cells [12,13] and the level of immunoglobulin secretion is associated with the level of differentiation in MM [14]. Thus, we hypothesized that induction of differentiation might overcome myeloma resistance to bortezomib by increasing the level of immunoglobulin secretion.

In this study, we focused on two aims: (1) to clarify the relationship of myeloma resistance to bortezomib and the differentiation status of myeloma cells; and (2) to observe the change in myeloma sensitivity to bortezomib after induction of differentiation and to further explore the underlying mechanisms.

* Corresponding author. Fax: +86 20 87333455.
E-mail address: luliyuan@tom.com (J. Li).

0006-291X/$ - see front matter © 2012 Elsevier Inc. All rights reserved.
http://dx.doi.org/10.1016/j.bbrc.2012.03.056

2. Materials and methods

2.1. Isolation of primary myeloma cells

Bone marrow mononuclear cells (BMMNCs) were freshly isolated from 26 patients with MM by Ficoll-Hypaque density gradient centrifugation. Informed consent was obtained from all patients in accordance with the Helsinki protocol. A smear of the BMMNCs was stained and the percentage of myeloma cells was determined by differentiating the myeloma cells in 100 BMMNCs under microscopy. The total number of myeloma cells harvested was calculated by multiplying the total number of harvested BMMNCs and the percentage of myeloma cells [15]. Further purification of myeloma cells by CD138-positive magnet selection was performed if the estimated number of total myeloma cells was $>2 \times 10^6$. The purity of myeloma cells were then tested by the percentage of CD 138-positive cells in FACS after the purification.

2.2. Cell lines and reagents

The human myeloma cell lines, KM3 and MM1.S, were kindly provided by Professor Jian-Hou (The Changzhen Hospital, Shanghai, China) and Professor Nancy Furey (Northwestern University, Chicago, IL, USA), respectively. U266 was purchased from the American Type Culture Collection (Manassas, VA, USA). All cell lines were cultured in RPMI-1640 supplemented with 10% fetal bovine serum, 1% L-glutamine, and 1% penicillin/streptomycin. 2-ME2 and ATRA were purchased from Sigma–Aldrich Company (St. Louis, MO, USA). 2-ME2 and ATRA were dissolved in DMSO at stock concentrations of 1 mM and 1 M, respectively, then stored at −20 °C. The proteasome inhibitor, bortezomib (PS-341, Velcade), was purchased from Millennium Predictive Medicine, Inc. (Cambridge, MA, USA) and was dissolved in 0.9% NaCl at a stock concentration of 2 mM.

2.3. Growth inhibition assays

A 100-ul suspension of 5×10^5 cells was added to each well of a 96-well flat-bottomed plate. Various concentrations of bortezomib were added to the wells. After a 48-h incubation, growth inhibition was assessed using the MTT assay (Sigma–Aldrich). The plates were then centrifuged horizontally and the supernatants were aspirated before 100 μl of DMSO was added to each well. Absorbance values measured at 490 nm and the IC_{50} values were calculated using CalcuSyn software.

2.4. Apoptosis assays

Flow cytometry analysis of Annexin V-FITC- and PI-stained cells was performed using an apoptosis detection kit (Biovison, Milpitas CA, USA) according to the manufacturer's instructions. Briefly, cells (5×10^5) treated were washed with 50 mM cold phosphate buffer (pH 7.6) and centrifuged at 12,000g for 5 min. The cells were suspended in 100 ul of binding buffer. A mixture of 5 ul of fluorescence-conjugated Annexin V and 2 ul of PI was added to the cell suspension, and incubated for 15 min at room temperature. The samples were analyzed for Annexin V binding after 1 h by flow cytometry (Beckman Coulter, Brea, CA USA). Data were collected and analyzed by WINMDI software.

2.5. Morphologic evaluation of myeloma cells

After exposure to 0.5 uM 2-ME2 with or without 1 uM ATRA for 48 h, the myeloma cells were sampled and analyzed morphologically. Cells were processed with cytospin, followed by Wright-Giemsa staining and examination under 1000× microscopy. Photographs were obtained with JVC tk-C1381 imaging system.

2.6. Enzyme-linked immunosorbent assay

The human lambda and kappa (bound and free) ELISA Quantification Kit (Bethy Laboratories, Montgomery, TX, USA) was used to detect the secreted light chain protein, according to the manufacturer's instructions. All supernatants were collected and stored at −20 °C until thawed and measured at the same time. For myeloma cell lines, cells in log growth phase were washed twice in PBS, counted, and resuspended in culture media at a concentration of 5×10^5 viable cells/ml, as determined by trypan blue exclusion. Following 4 h of culture at 37 °C, cells were pelleted, and the supernatant collected for analysis. After exposure to 0.5 uM 2-ME2 with or without 1 uM ATRA for 48 h, myeloma cells were treated the same way as described above. For primary myeloma cells, the supernatants were collected when 5×10^5 isolated BMMNCs were cultured for 24 h. At the same time, a smear from the same BMMNC sample was stained using the Wright-Giemsa method and the percentage of myeloma cells was determined by differentiating the myeloma cells in 100 MNCs under microscopy. The level of secretion of light chain protein was then calculated as the supernatant light chain protein level with ELISA/total myeloma cells (pg/cell) [15].

2.7. Proteasome activity assay

Proteasome activity was assessed in myeloma cell extracts using fluorogenic peptides as described previously [6]. Briefly, cells were sonicated in ice cold lysis buffer, and extracts were prepared by centrifugation for 15 min at 13,000g. Chymotrypsin-like proteasome activity was assayed by monitoring the production of 7-amino-4-methylocoumarin (AMC) from 100 uM Suc-LLVY-AMC in assay buffer. Reactions were started by adding an aliquot of cellular extract (40 ug of total protein), and the fluorescence of released AMC (excitation, 380 nm; emission, 460 nm) was monitored continuously at 37 °C with a Carry Eclipse spectrofluorometer (Varian, Palo Alto, CA, USA). Assays were calibrated using standard solutions of free AMC, and the activities at the end of a 2-h continuous scan was measured and recorded as the final proteasome activity. Substrate consumption at the end of incubation never exceeded 5%.

2.8. Reverse transcriptase-polymerase chain reaction

Total cell RNA was extracted with Trizol, then reverse-transcribed into cDNA according to the manual of the RT-PCR kit (Formentas, Glen Burnie, MD, USA). Resultant cDNA was normalized for expression of the constitutively-expressed housekeeping gene, beta-actin (F:ACCAACTGGGACGATATGGAGAAGA; R:TACGACCAGA GGCATACAGGGACAA). The spliced form of XBP-1 mRNA was analyzed by PCR, as described previously [16], with primers flanking the 26b intron (F: GGAGTTAAGACAGCGCTTGG; R: ACTGGGTCCAA GTTGTCCAG). PCR products, including the spliced and unspliced XBP-1 mRNAs, were resolved by electrophoresis on a 2.5% agarose gel and visualized with ethidium bromide.

2.9. Immunoblotting

Whole cell lysates from 1.0×10^6 cells were prepared in RIPA buffer (Biyuntian Company, Shanghai, China). Total protein (20 ug) was resolved on 10–15% SDS–polyacrylamide gels and transferred to PVDF membranes. The following antibodies were used: anti- XBP-1 polyclonal antibody (1:200; Santa Cruz Biotechnology, Inc., Santa Cruz, CA, USA), anti-actin monoclonal

antibody (1:1000; Cell Signaling, Danvers, MA, USA), and anti-ubiquitin monoclonal antibody (1:1000; Santa Cruz Biotechnology, Inc.). Secondary antibodies were obtained from Santa Cruz Biotechnology Inc. Blots were developed using enhanced chemiluminescence (Pierce, Rockford, IL, USA).

2.10. Statistical analysis

All continuous variable comparisons between two groups were analyzed using a *t*-test and one-way ANOVA was used to compare continuous variables among more than two groups.

3. Results

3.1. Myeloma sensitivity to bortezomib is associated with differentiation status in myeloma cell lines

Three myeloma cell lines with different sensitivities to bortezomib were used in the current study. Each cell line was treated for 48 h with increasing concentrations of bortezomib. MM1.S cells were most sensitive to bortezomib, U266 cells were intermediately sensitive to bortezomib, and KM3 cells were least sensitive to bortezomib with an IC_{50} of 6.4 ± 2.2, 22.0 ± 4.7, and 52.8 ± 6.8 nM, respectively.

Based on previous reports [12,13], we chose a morphology study, light chain secretion levels, and XBP-1s expression to evaluate the differentiation status of myeloma cell lines. Our analysis showed that KM3 cells were the least mature cells, whereas MM1.s cells were the most mature cells.

KM3 cells showed morphologic features of blast cells with a high N:C ratio, fine chromatin, scant cytoplasm, and no hof (the clear area just outside the nucleus which represents the Golgi apparatus). U266 cells were relatively mature with partially condensed chromatin, more abundant cytoplasm, and hof, whereas MM1.S cells were most mature morphologically with a highly condensed nucleus and abundant cytoplasm [Fig. 1(A)].

Light chain protein was selected to represent the secretion of immunoglobulin. The level of light chain secretion was significantly different among cell lines ($p < 0.05$). The highest level of secretion occurred in the most mature MM1.S cells (3.55 ± 0.25 pg/cell), an intermediate level of secretion occurred in the U266 cells (2.18 ± 0.26 pg/cell), and the lowest level of secretion occurred in the least mature KM3 cells (0.53 ± 0.09 ng/ug).

X box binding protein-1 (XBP-1), a transcription factor in the CREB/ATF family, is required for plasma cell differentiation [16] and might play an important role in the induction of differentiation in myeloma cells [12]. we next evaluated the expression of XBP-1 protein in myeloma cell lines. XBP-1 mRNA is activated by splicing out of a 26-bp fragment containing a stop code. Hence, the XBP-1 protein has two subtypes (XBP-1u [unspliced form] and XBP-1s [spliced form]). XBP-1s, the activated form, is larger than XBP-1u because the translation of XBP-1u is stopped by an earlier stop code [17]. As shown by immunoblotting and RT-PCR analysis, the level of expression of XBP-1s was lowest in immature KM3, and higher in U266 and MM1.S cells. [Fig. 1(B and C)].

3.2. Myeloma sensitivity to bortezomib is associated with higher differentiation status in primary myeloma cells

We further investigated the relationship between sensitivity to bortezomib and the differentiation status of primary myeloma cells. The sensitivity of primary myeloma cells to bortezomib was evaluated *in vivo* according to the efficacy of clinical therapy. Patients achieving ⩾partial response (PR) were sensitive, while those achieving <PR were resistant to bortezomib. The level of light chain secretion was higher in the sensitive group (2.8 ± 1.8 pg/cell; range, 1.1–4.1 pg/cell) than the resistant group (1.7 ± 0.7 pg/cell; range, 0.4–3.2 pg/cell; $p < 0.01$). Although the level of expression of XBP-1u was similar in the sensitive and resistant groups, the sensitive group had a higher level of expression of XBP-1s than the resistant group [Fig. 2(A and B)], suggesting that the sensitivity of primary myeloma cells to bortezomib is related to a higher differentiation status of the myeloma cells.

3.3. 2-ME2 alone or in combination with ATRA induces myeloma differentiation

To further evaluate the induction of differentiation in increasing myeloma cell sensitivity to bortezomib, we used a low dose of 2-ME2 [12] with or without ATRA [13] to induce myeloma differentiation.

After treatment with 0.5 uM 2-ME2 for 48 h, the U266 and KM3 cells exhibited more mature morphologic features with a lower N:C ratio and eccentric nuclei. ATRA (1 uM) alone did not induce morphologic changes in myeloma cells (data not shown); however, the combination of 1 uM ATRA and 0.5 uM 2-ME2 induced the most mature morphologic changes [Fig. 3(A)].

We next compared the level of light chain protein secretion and level of expression of XBP-1 protein before and after treatment with 0.5 uM 2-ME2 alone or with 1 uM ATRA. With 0.5 uM 2-ME2 treatment alone, KM3 and U266 cells had higher levels of light chain protein (0.97 ± 0.17 pg/cell and 4.42 ± 0.31 pg/cell vs. 0.53 ± 0.09 pg/cell and 2.17 ± 0.26 pg/cell, respectively, for the control group, $p < 0.05$) and XBP-1s expression [Fig. 3(B and C)]. The addition of 1 uM ATRA to 2-ME2 enhanced these effects with higher levels of light chain protein (1.36 ± 0.17 pg/cell and 5.59 ± 0.29 pg/cell vs. 0.53 ± 0.09 pg/cell and 2.17 ± 0.26 pg/cell, respectively, for the control group, $p < 0.05$) and XBP-1s expression [Fig. 3(B and C)], suggesting that a low dose 2-ME2 with or without ATRA induced myeloma differentiation.

3.4. Induction of differentiation overcomes myeloma resistance to bortezomib

We then compared myeloma sensitivity to bortezomib before and after the induction of differentiation to determine whether or not induction of differentiation could overcome myeloma resistance to bortezomib.

The IC_{50} of the KM3 and U266 cell lines was decreased after treatment with 0.5 uM 2-ME (35.6 ± 4.8 and 15.4 ± 2.7 nM vs. 52.8 ± 5.1 and 23.7 ± 3.2 nM for the control group, $p < 0.05$) and further after treatment with 0.5 uM 2-ME plus 1 uM ATRA (25.4 ± 3.3 and 10.3 ± 2.5 nM vs. 52.8 ± 5.1 and 23.7 ± 3.2 nM for the control group, $p < 0.05$).

The induction of apoptosis to bortezomib was also enhanced after induction of differentiation. The apoptosis rates of KM3 and U266 cell lines to 20 nM bortezomib were increased significantly from 12.7 ± 1.8% and 20.7 ± 2.1% before induction of differentiation to 17.6 ± 3.4% and 31.5 ± 4.8% after 2-ME2 induction, and further to 24.5 ± 3.7% and 34.5 ± 5.2% after treatment with 2-ME2 plus ATRA, respectively [Fig. 4(A)].

3.5. Induction of differentiation changes the balance between proteasome workload and capacity

The imbalance between proteasome workload and capacity has been reported to determine the sensitivity of myeloma cells to bortezomib [6]. As we showed above, the induction of differentiation increased immunoglobulin secretion, possibly leading to an increased burden of degradation for the proteasome system. However, whether or not the induction of differentiation could decrease

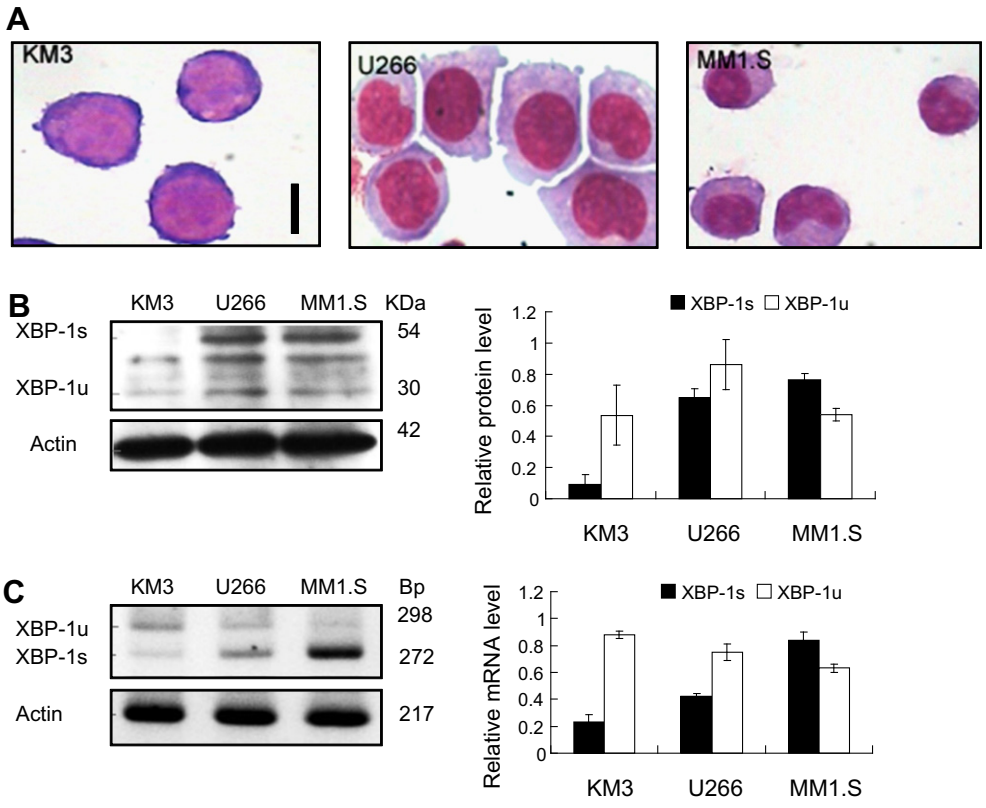

Fig. 1. Three myeloma cell lines show different differentiation statuses. (A) Wright-Giemsa stain of KM3, U266, and MM1.s cells (original magnification, ×1000). KM3 demonstrated a blast-like morphology, while U266 and MM1.s were more mature. Size bar equals 10 μm. (B) Western blot analysis of XBP-1 protein expression among myeloma cell lines. (C) XBP-1 mRNA profiling among myeloma cell lines.

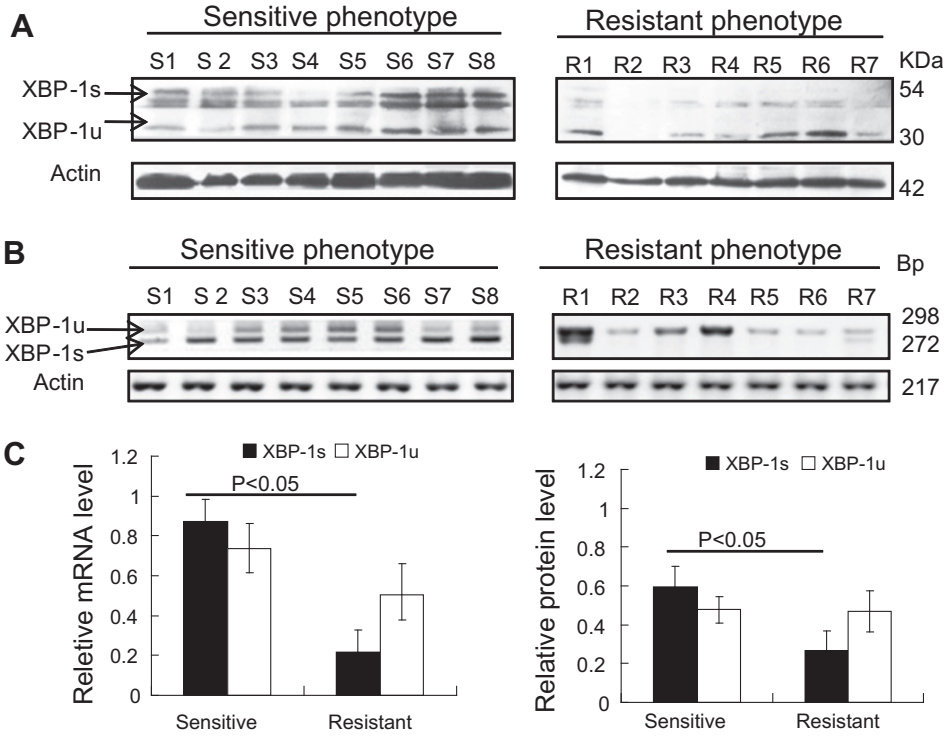

Fig. 2. Sensitivity of primary myeloma cells to bortezomib is associated with the cell differentiation status. (A) XBP-1s protein expression comparison between sensitive and resistant primary myeloma cells. (B) Comparison of XBP-1s mRNA expression between sensitive and resistant primary myeloma cells. (C) The quantification of XBP-1 expression between sensitive and resistant primary myeloma cells.

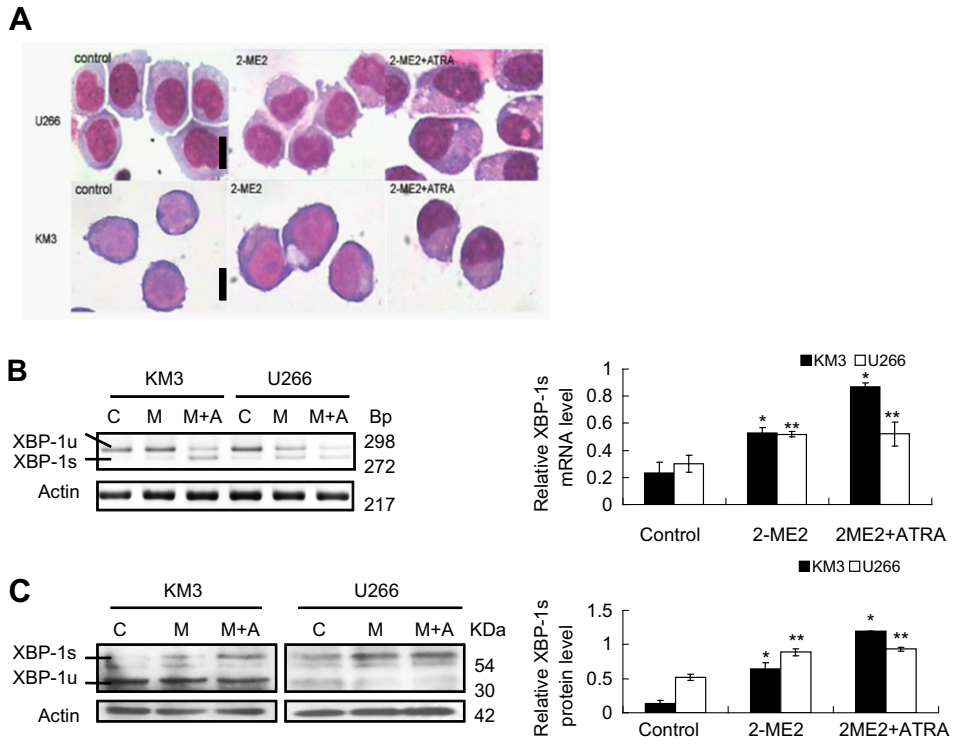

Fig. 3. 2-ME2 alone or in combination with ATRA induced differentiation in myeloma cell lines. KM3 and U266 were incubated with 2-ME2 (0.5 uM) alone or plus ATRA (1 uM) for 48 h to induce differentiation. (A) Cells demonstrated more mature morphology after single or combined induction of differentiation. Size bar equals 10 μm. (B) XBP-1s mRNA expression increased after induction of differentiation. (C) XBP-1s protein expression raised after induction of differentiation.

the proteasome capacity is unknown. Hence, we monitored the proteasome activity to measure the capacity of the proteasome.

The results showed that the proteasome activity of KM3 and U266 cells was decreased after the induction of differentiation by 2-ME2 alone (374 ± 48 and 236 ± 39 AU vs. 451 ± 45 and 387 ± 45 AU, respectively, for the control group, $p < 0.05$) or combined with ATRA (298 ± 48 and 183 ± 19 AU vs. 451 ± 45 and 387 ± 45 AU, respectively, for the control group, $p < 0.05$).

After induction of differentiation, myeloma cells had higher levels of ubiquitin-conjugated proteins and lower levels of free ubiquitin levels [Fig. 4(B)], suggesting that differentiated myeloma cells are under proteasome stress as the result of an imbalance between a heavier workload and a lower capacity of the proteasome.

4. Discussion

The induction of differentiation has achieved great success in patients with acute promyelocytic leukemia and opened a new era in the paradigm for cancer therapy [18]. A variety of differentiation status also exist in MM. Furthermore, mature myeloma cells have been reported to be an indicator of better prognosis, while plasmablastic morphology is associated with poor prognosis in MM [19]. Hence, the induction of differentiation might improve the outcome of MM. Differentiation has been successfully induced in several classic myeloma lines and even in primary myeloma cells [12,13]. Therefore, induction of differentiation might be a promising therapy for MM.

Bortezomib, a new and effective anti-myeloma drug [20], targets the proteasome and disrupts the protein degradation system in myeloma cells. Previous studies have indicated that myeloma could be sensitized to bortezomib by up-regulating immunoglobulin production [6,7]. It is well-accepted that the level of immunoglobulin secretion increases with the differentiation of plasma cells. Even in myeloma cells, the counterpart tumor of plasma cells, immunoglobulin secretion is also associated with differentiation status [12–14]. Hence, we suggest that induction of differentiation might enhance myeloma sensitivity to bortezomib.

In the current study, the differentiation status of myeloma cell lines and primary myeloma cells was associated with the myeloma sensitivity to bortezomib. With the increasing maturation of myeloma cells after induction of differentiation, myeloma cells were more sensitive to bortezomib with increasing growth inhibition and apoptosis to bortezomib. These promising results indicated that *in vitro* induction of differentiation of myeloma cells overcame myeloma resistance to bortezomib in some myeloma cell lines. Although still in need of confirmation in animal models, differentiation is an attractive alternative for overcoming myeloma drug resistance to bortezomib.

In the plasma cell differentiation process, proteasome activity decreases gradually, although the level of immunoglobulin secretion increases dramatically [21]. Such a high secretion-low degradation capacity imbalance leads to accumulation of toxic protein products in cells, consequently resulting in cell apoptosis. This imbalance is important in preventing antibody overproduction to maintain an appropriate antibody-mediated immune response. This imbalance could also explain the exquisite sensitivity of antibody secretors to proteasome inhibitors [22,23].

In the myeloma cell differentiation process induced in the current study, the proteasome activity decreased significantly, although the proteasome workload increased with a higher level of immunoglobulin secretion and XBP-1 expression. The sensitivity of MM cells to bortezomib has been reported to be determined by the capacity of the proteasome and the workload of protein degradation [6]. This might explain why induction of differentiation could increase myeloma sensitivity to bortezomib. Proteasomes not only degrade damaged or inappropriately folded proteins, but also participate in cell cycle control, cell differentiation, cell signal-

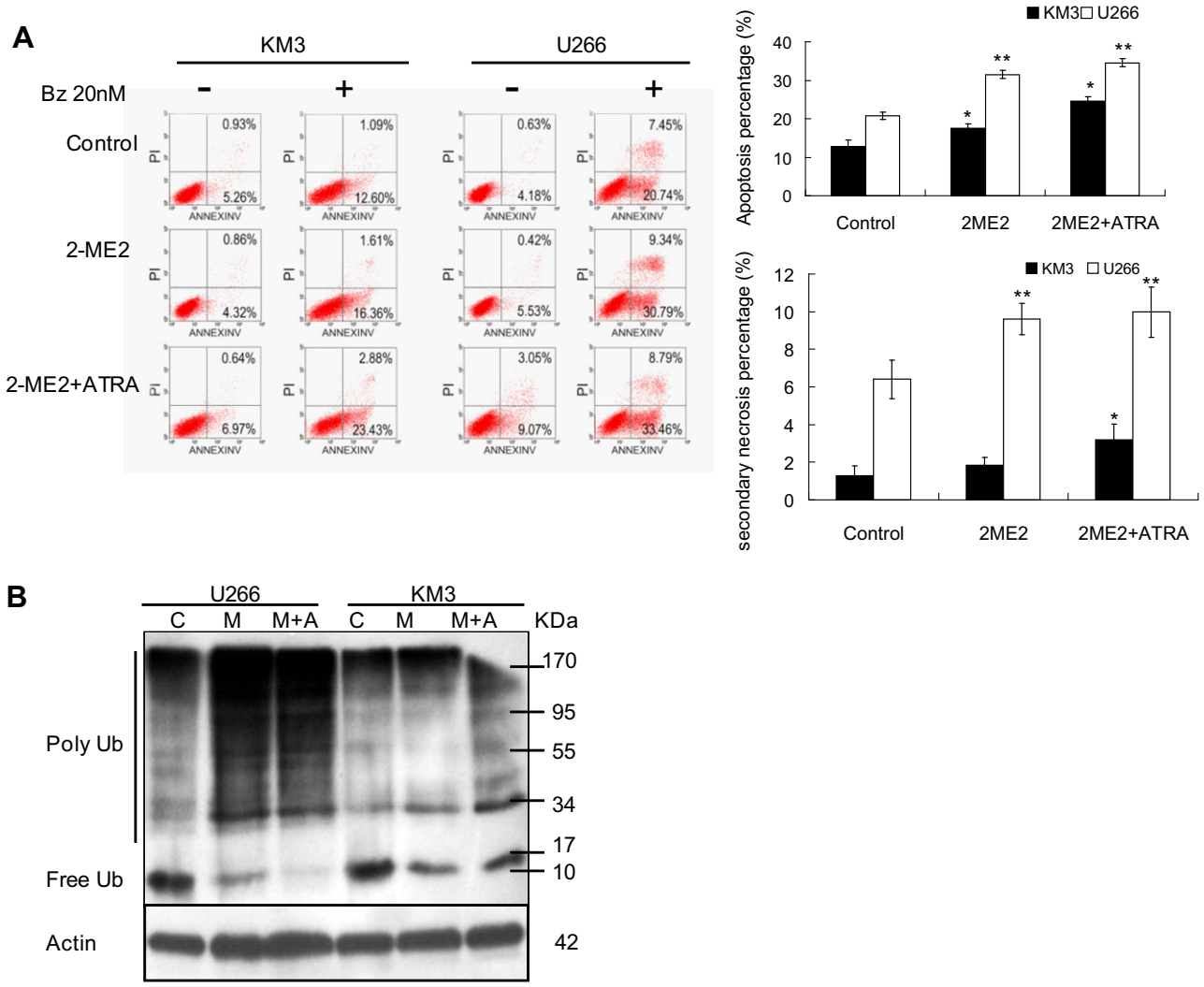

Fig. 4. Induction of differentiation enhanced apoptosis of myeloma cells to bortezomib and cause proteasome stress in myeloma cells. (A) The flow cytometry dot plots and quantitative analysis of apoptosis evaluated by Annexin V staining. Cells were incubated with 2-ME2 (0.5 uM) alone or plus ATRA (1 uM) for 48 h. In the dot plots of one representative experiment, the LR and the UR quadrant indicate the percentage of apoptotic and secondary necrosis cells respectively. Data in the histograms are expressed as the mean ± SD from three individual experiments ($^{*}P < 0.05$ compared to the control group in the KM3 cell line, $^{**}P < 0.05$ compared to the control group in the U266 cell line). (B) Representative picture of Western blotting of ubiquitin-conjugated protein and free ubiquitin after induction of differentiation.

ing, cell stress responses, and cell apoptosis [24]. Hence, proteasomes protect cells from apoptosis [25,26]. Tumors with higher proteasome activity are more resistant to proteasomes [27–30]. In a study comparing proteasome activity among myeloma cell lines, the higher the proteasome activity of the myeloma cell lines, the more resistant the cell line to bortezomib [6]. This evidence supports the notion that lower proteasome capacity is associated with higher sensitivity to proteasome inhibitors in myeloma cells. It is believed that lower proteasome capacity in myeloma cells results in accumulation of toxic degraded protein and deactivation of important biological proteins, finally leading to myeloma cell apoptosis [6].

In conclusion, our *in vitro* study demonstrated that induction of differentiation can enhance bortezomib efficacy and overcome drug resistance in MM. Based on the findings herein, we propose a new strategy to improve outcomes in patients with MM.

5. Funding

This work was supported by the Natural Science Foundation of Guangdong Province, China (No. 2008-8151008901000064) and the Science and Technology Planning Project of Guangdong Province, China (No. 2010B060900022).

References

[1] R.A. Kyle, S.V. Rajkumar, Multiple myeloma, N. Engl. J. Med. 351 (2004) 1860–1873.
[2] A. Jemal, R. Siegel, E. Ward, et al., Cancer statistics, CA Cancer J. Clin. 57 (2007) (2007) 43–66.
[3] M. Boccadoro, G. Morgan, J. Cavenagh, Preclinical evaluation of the proteasome inhibitor bortezomib in cancer therapy, Cancer Cell Int. 5 (2005) 18.
[4] H. Rumpold, C. Salvador, A.M. Wolf, et al., Knockdown of PgP resensitizes leukemic cells to proteasome inhibitors, Biochem. Biophys. Res. Commun. 361 (2007) 549–554.
[5] X. Wu, Y. Shao, Y. Tao, et al., Proteasome inhibitor lactacystin augments natural killer cell cytotoxicity of myeloma via downregulation of HLA class I, Biochem. Biophys. Res. Commun. 415 (2011) 187–192.
[6] G. Bianchi, L. Oliva, P. Cascio, et al., The proteasome load versus capacity balance determines apoptotic sensitivity of multiple myeloma cells to proteasome inhibition, Blood 113 (2009) 3040–3049.
[7] S. Meister, U. Schubert, K. Neubert, et al., Extensive immunoglobulin production sensitizes myeloma cells for proteasome inhibition, Cancer Res. 67 (2007) 1783–1792.
[8] U. Schubert, L.C. Anton, J. Gibbs, et al., Rapid degradation of a large fraction of newly synthesized proteins by proteasomes, Nature 404 (2000) 770–774.

[9] A.L. Goldberg, Protein degradation and protection against misfolded or damaged proteins, Nature 426 (2003) 895–899.
[10] S. Wuilleme-Toumi, V. Trichet, P. Gomez-Bougie, et al., Reciprocal protection of Mcl-1 and Bim from ubiquitin–proteasome degradation, Biochem. Biophys. Res. Commun. 361 (2007) 865–869.
[11] Y. Zhou, J.M. Goodenbour, L.A. Godley, et al., High levels of tRNA abundance and alteration of tRNA charging by bortezomib in multiple myeloma, Biochem. Biophys. Res. Commun. 385 (2009) 160–164.
[12] J. Hou, H. Xiong, W. Gao, et al., 2-Methoxyestradiol at low dose induces differentiation of myeloma cells, Leuk. Res. 29 (2005) 1059–1067.
[13] H. Huang, D. Wu, J. Fu, et al., All-trans retinoic acid can intensify the growth inhibition and differentiation induction effect of rosiglitazone on multiple myeloma cells, Eur. J. Haematol. 83 (2009) 191–202.
[14] V.I. Turilova, T.D. Smirnova, M.P. Samoilovich, et al., Functional morphology of nucleolus organizer regions of chromosomes and nucleoli in human multiple myeloma cell lines. I. Variation of the morphology and silver staining of nucleolus organizer regions of chromosomes in RMPI 8226 and U 266 cell lines with different level of differentiation of during 7 days after cell passage], Tsitologiia 40 (1998) 536–548.
[15] S.E. Salmon, Immunoglobulin synthesis and tumor kinetics of multiple myeloma, Semin. Hematol. 10 (1973) 135–144.
[16] A.M. Reimold, N.N. Iwakoshi, J. Manis, et al., Plasma cell differentiation requires the transcription factor XBP-1, Nature 412 (2001) 300–307.
[17] M. Nakamura, T. Gotoh, Y. Okuno, et al., Activation of the endoplasmic reticulum stress pathway is associated with survival of myeloma cells, Leuk. Lymphoma 47 (2006) 531–539.
[18] F. Grignani, M. Fagioli, M. Alcalay, et al., Acute promyelocytic leukemia: from genetics to treatment, Blood 83 (1994) 10–25.
[19] P.R. Greipp, N.M. Raymond, R.A. Kyle, et al., Multiple myeloma: significance of plasmablastic subtype in morphological classification, Blood 65 (1985) 305–310.
[20] P.G. Richardson, P. Sonneveld, M.W. Schuster, et al., Bortezomib or high-dose dexamethasone for relapsed multiple myeloma, N. Engl. J. Med. 352 (2005) 2487–2498.
[21] S. Cenci, A. Mezghrani, P. Cascio, et al., Progressively impaired proteasomal capacity during terminal plasma cell differentiation, EMBO J. 25 (2006) 1104–1113.
[22] P. Cascio, L. Oliva, F. Cerruti, et al., Dampening Ab responses using proteasome inhibitors following in vivo B cell activation, Eur. J. Immunol. 38 (2008) 658–667.
[23] K. Neubert, S. Meister, K. Moser, et al., The proteasome inhibitor bortezomib depletes plasma cells and protects mice with lupus-like disease from nephritis, Nat. Med. 14 (2008) 748–755.
[24] L. Huang, C.H. Chen, Proteasome regulators: activators and inhibitors, Curr. Med. Chem. 16 (2009) 931–939.
[25] Y. Liu, X. Liu, T. Zhang, et al., Cytoprotective effects of proteasome beta5 subunit overexpression in lens epithelial cells, Mol. Vis. 13 (2007) 31–38.
[26] M.K. Kwak, B. Huang, H. Chang, et al., Tissue specific increase of the catalytic subunits of the 26S proteasome by indirect antioxidant dithiolethione in mice: enhanced activity for degradation of abnormal protein, Life Sci. 80 (2007) 2411–2420.
[27] Z.X. Du, X. Meng, H.Y. Zhang, et al., Caspase-dependent cleavage of BAG3 in proteasome inhibitors-induced apoptosis in thyroid cancer cells, Biochem. Biophys. Res. Commun. 369 (2008) 894–898.
[28] L. Magill, J. Lynas, T.C. Morris, et al., Proteasome proteolytic activity in hematopoietic cells from patients with chronic myeloid leukemia and multiple myeloma, Haematologica 89 (2004) 1428–1433.
[29] C. Aghajanian, S. Soignet, D.S. Dizon, et al., A phase I trial of the novel proteasome inhibitor PS341 in advanced solid tumor malignancies, Clin. Cancer Res. 8 (2002) 2505–2511.
[30] J. Cortes, D. Thomas, C. Koller, et al., Phase I study of bortezomib in refractory or relapsed acute leukemias, Clin. Cancer Res. 10 (2004) 3371–3376.

Biochemical and Biophysical Research Communications 420 (2012) 651–655

Contents lists available at SciVerse ScienceDirect

Biochemical and Biophysical Research Communications

journal homepage: www.elsevier.com/locate/ybbrc

SKP1-CULLIN1-F-box (SCF)-mediated DRG2 degradation facilitated chemotherapeutic drugs induced apoptosis in hepatocellular carcinoma cells

Chen jie, Shen bai-yong, Deng xia-xing, Zhan qian, Peng cheng-hong *

Department of General Surgery, Ruijin Hospital, Shanghai Jiao Tong University School of Medicine, Shanghai, China

ARTICLE INFO

Article history:
Received 6 March 2012
Available online 17 March 2012

Keywords:
DRG2
SKP1-CULLIN1-F-box
Chemotherapeutic drugs
Hepatocellular carcinoma cells

ABSTRACT

Developmentally regulated GTP-binding protein 2 (DRG2), an evolutionarily conserved member of the DRG subfamily in the GTP-binding protein, is thought to play an essential role in the control of cell growth and differentiation. However, the role of DRG2 in hepatocellular carcinoma cells is largely unknown. Here, we show that DRG2 is down-regulated during chemotherapeutic drug induced apoptosis in four hepatocellular carcinoma cell lines. We further provided evidence that DRG2 was a substrate of a SKP1-CULLIN1-F-box E3 ligase complex and inhibition the function of Cullin1 prevented the degradation of DRG2 during apoptosis. Moreover, over-expression of DRG2 inhibited doxorubicin induced apoptosis in hepatocellular carcinoma cells. Taken together, these results demonstrate that regulated degradation of DRG2 has a role in chemotherapeutic drug induced hepatocellular carcinoma cells apoptosis.

1. Introduction

Hepatocellular carcinoma is the fifth most common cancer and the fourth leading cause of cancer-related mortality worldwide [1]. Although surgical management has been wildly used to against hepatocellular carcinoma, the incidence of this disease continues to rise year by year [2]. Apoptosis is an important physiological process of cell death and occurs during tissue remodeling, immune regulation, and tumor regression. Most of the chemotherapeutic drugs cause cancer cells death by inducing apoptotic death pathways [3]. Apoptosis is a highly regulated cell suicide process that is mediated through two central pathways: the extrinsic pathway involving death receptors and the intrinsic pathway involving the mitochondria/endoplasmic reticulum [4]. When stimulated, these two pathways lead to the release of cytochrome c from the mitochondria and to the activation of caspase 3 and cell death [4].

Fundamental cellular functions such as cell growth, differentiation and apoptosis are accomplished by large, multi-protein and highly precisely regulated molecular machines. Numerous reports have clearly shown that E3 ubiquitin ligases have essential roles in cell death controls by targeting key apoptosis-regulated proteins for destruction [5–9]. E3 ubiquitin ligases have been classified into three groups: the single-subunit RING-FINGER type, the multisubunit RING-finger type and the HECT-domain type. Most of the multi-subunit RING-finger type of E3 ligases contains a Cullin protein including Cul1, Cul2, Cul3, Cul4, Cul5 and Cul7 [10]. Many structural and functional details have been described for the most well-characterized mammalian Cullin-dependent ligase—the SKP1-CULLIN1-F-box (SCF) ligase [11–13]. In this ligase, Cul1 functions as a molecular scaffold that simultaneously interacts at the amino terminus with the crucial adaptor subunit Skp1 which recruits one of many F-box proteins and at the carboxyl terminus with a RING-finger protein Rbx1 and a specific E2 enzyme such as Ubc3, Ubc4 or Ubc5. Each F-box protein appears to be matched with a discrete number of specific substrates through a protein–protein interaction domain [14].

Developmentally regulated GTP-binding proteins (DRG) are an evolutionally conserved novel GTP binding protein. These proteins harbor the five characteristic motifs, G1–G5, that are believed to interact with GTP [15]. Apart from these motifs, they do not display significant similarity with the well-characterized G-proteins and therefore, they constitute a new subfamily within the superfamily of GTP-binding proteins [16]. There are at least two distinct members, DRG1 and DRG2, and they are widely expressed in human and mouse tissues and show a very similar distribution pattern [15], which suggests the similar functions of these two DRGs. Mouse DRG1 expression was highly regulated during embryonic development and over-expression of mouse DRG1 together with c-myc and ras was found to stimulate cell transformation in fibroblast [17]. Fish DRG2 was increased by rhabdovirus infection and human DRG2 was down-regulated in fibroblasts transformed by SV40 [18]. Over-expression of DRG2 increased G2/M phase cells and decreased sensitivity to nocodazole-induced apoptosis in human T cells [19]. However, whether DRG2 plays a role in hepatocellular carcinoma is completely unknown.

Here, we show that DRG2 was ubiquitinated and degradated by a SCF complex during apoptosis in hepatocellular carcinoma cell

* Corresponding author. Fax: +86 021 64370045 680503.
E-mail address: chhpeng_submit@126.com (P. cheng-hong).

0006-291X/$ - see front matter © 2012 Elsevier Inc. All rights reserved.
http://dx.doi.org/10.1016/j.bbrc.2012.03.058

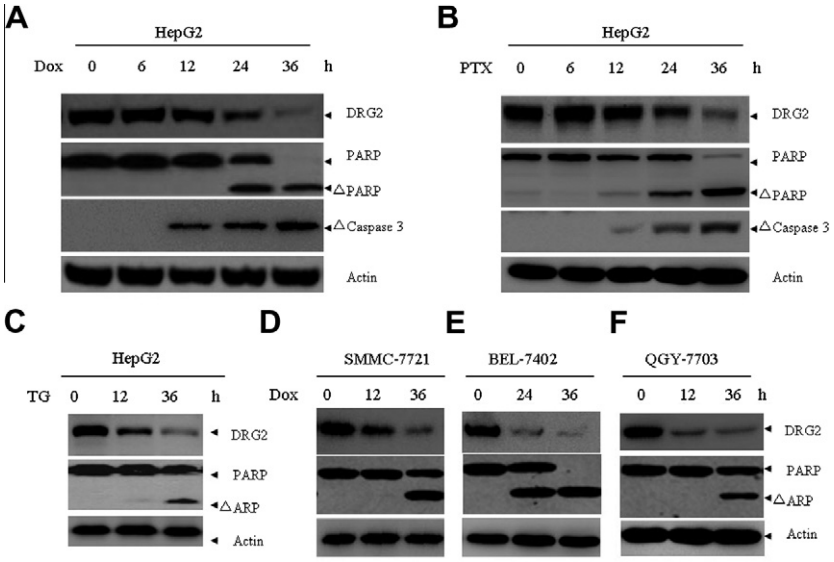

Fig. 1. DRG2 was down-regulated during apoptosis in hepatocellular carcinoma cell lines. (A) HepG2 cells were treated with Dox (1 μg/ml) for indicated times and the indicated proteins were detected by western blot. (B and C) HepG2 cells were treated with PTX (1 μM) (B) or TG (1 mM) (C) for indicated times and the indicated proteins were detected by western blot. (D–F) SMMC-7721 (D), BEL-7402 (E) and QGY-7703 (F) cells were treated with Dox for indicated times and the indicated proteins were detected by western blot.

lines. Inhibition of SCF by dominant Cullin1 prevented the degradation of DRG2 during apoptosis. Over-expressing of DRG2 in hepatocellular carcinoma cells inhibited doxorubicin induced apoptosis. Our data might shed new insight on the role of DRG2 in hepatocellular carcinoma cells apoptosis and the post-translational regulation of DRG2.

2. Materials and methods

2.1. Cell culture and drugs

293T cells were cultured in Dulbecco's modified Eagle's medium (Invitrogen) supplemented with 10% fetal calf serum (Gibco BRL, Gaithersburg, MD). Hepatocellular carcinoma cell lines including HepG2, SMMC-7721, BEL-7402, and QGY-7703 (from Cell Bank of Shanghai Institutes of Biological Sciences, Shanghai, China) were cultured in RPMI-1640 medium (Sigma, St Louis, MI) supplemented with 10% fetal calf serum. All these cells were cultured in a 5% CO_2/95% air at 37 °C. DMSO and drugs in this work were purchased from sigma.

2.2. Antibodies

Antibodies were obtained from the following sources: anti-DRG2 (BD Biosciences, USA), anti-cleaved caspase-3 (Cell Signaling, USA), anti-poly-ADP ribose polymerase (PARP), anti-Flag M2 (Sigma, USA), anti-HA, Cul1, Skp1 (Santa Cruz Biotech, USA) and anti-actin (Calbiochem, Germany),

2.3. Plasmids and transfection

All the plasmids of this work are purchased from Addgene. All the transient transfections were conducted using Lipofectamine 2000 (Invitrogen) according to the manufacturer's instructions.

2.4. RNA isolation and real-time PCR analysis

Total RNA was isolated from tissues or cells using TRIzol (Invitrogen) according to the manufacturer's instructions. In order to quantify the transcripts of the interest genes, real-time PCR was performed using a SYBR Green Premix Ex Taq (Takara, Japan) on LightCycler 480 (Roche, Switzerland). The primers used were available upon request.

2.5. Western blotting

Protein extracts were equally loaded on 10% SDS–PAGE, electrophoresed, and transferred to nitrocellulose membrane (Amersham Bioscience, Buckinghamshire, UK). After blocking with 5% nonfat milk in PBS, the membranes were incubated with the indicated primary antibodies and followed by horseradish peroxidase (HRP)-linked secondary antibodies (Cell signaling). The signals were detected by chemiluminescence phototope-HRP kit (Pierce Biotechnology, Rockford, USA) according to manufacturer's instructions.

2.6. Immunoprecipitation

Cells were lysed in 6 ml of lysis buffer (50 mM Tris-HCl pH 7.5, 250 mM NaCl, 0.5% Nonidet P40, Roche complete EDTA-free protease inhibitor cocktail) for 20 min with gentle rocking at 4 °C. Lysates were cleared using centrifugation (13,000 rpm, 10 min), the supernatant was subjected to immunoprecipitation (IP) with 20 μl of anti-DRG2 antibody for 4 h at 4 °C and 50 μl protein A/G beads (Santa Cruz Biotech, USA) were added and incubated overnight at 4 °C with gentle inversion. Beads containing immune complexes were washed with 1 ml ice cold lysis buffer four times followed by three 1 ml Tris Buffered Saline (TBS) washes. Precipitates were denatured in Laemmli (gel loading) buffer at 95 °C for 5 min.

2.7. Cycloheximide inhibition test

HepG2 cells were treated with Dox in the presence or absence of 10 μg/ml cycloheximide (CHX, Sigma–Aldrich) for the indicated time points. The expression of DRG2 protein was measured by western blots with b-actin as loading control.

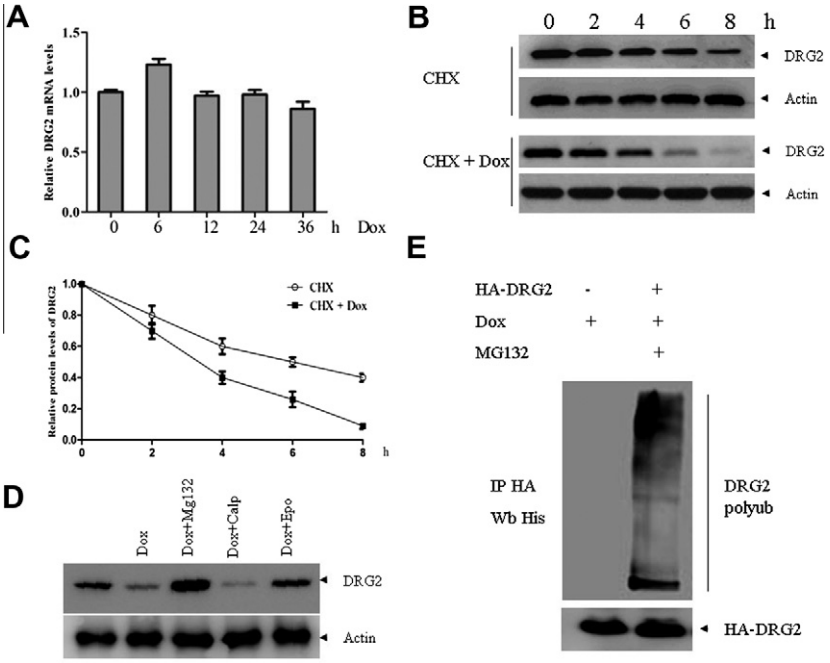

Fig. 2. The ubiquitin–proteasome system mediated the down-regulation of DRG2 protein during apoptosis. (A) HepG2 cells were treated with Dox (1 μg/ml) for the indicated times and the mRNA level of DRG2 was measured by real-time RT-PCR. (B–C) HepG2 cells were treated with Dox (1 μg/ml) in the presence or absence of CHX (20 μg/ml) for the indicated times and the protein level of DRG2 was examined by western blot with actin as loading control. (C) Folds of decrease of DRG2 protein/actin ratios against untreated cells are shown as means ± SD of three independent experiments. (D) HepG2 cells were treated with Dox (1 μg/ml) in the presence or absence of MG132 (20 μM), epoxomicin (10 μM), or calpeptin (50 μM) for 6 h, and then the indicated proteins were examined by western blot.

2.8. Apoptosis assay

To assess the distribution of nuclear DNA content, cells were collected, rinsed and fixed overnight in 70% cold ethanol at −20 °C. Then, cells were treated with Tris-HCl buffer (pH 7.4) supplemented with 1% RNaseA and stained with 25 mg/ml propidium iodide (PI, Sigma). The samples were read on a Coulter Elite Flow Cytometer using Elite software program 4.0 for two-color detector (Beckman Coulter). The percentage of cells in the apoptotic sub-G1 phage was calculated using multicycle software (Phoenix Flow Systems).

3. Results

3.1. DRG2 was down-regulated during apoptosis in hepatocellular carcinoma cell lines

To investigate the function of DRG2 in hepatocellular carcinoma cells, we first checked the endogenous protein level of DRG2 during apoptosis. Hepatocellular carcinoma cell line HepG2 cells were treated with Doxorubincin (Dox), which induced the appearance of the active fragment of caspase 3, followed by the cleavage of PARP (Fig. 1A). Interestingly, DRG2 was significantly decreased by Dox in a dose dependent manner (Fig. 1A). To examine whether this effect is Dox-specific, HepG2 cells were treated with the paclitaxel (PTX), thapsigargin (TG) and etoposide (VP-16), respectively. All of these treatments led to down-regulation of DRG2 (Fig. 1B and C). In order to rule out cell type-specific effect, several other hepatocellular carcinoma cell lines including SMMC-7721, BEL-7402, and QGY-7703 were treated with Dox for different time points. Consistent with the phenomenon observed in HepG2 cells, Dox treatment led to the reduction of DRG2 in all these hepatocellular carcinoma cells we tested (Fig. 1D–F). Together, these data indicated that the down-regulation of DRG2 protein is a common event during apoptosis induction of hepatocellular carcinoma cell lines.

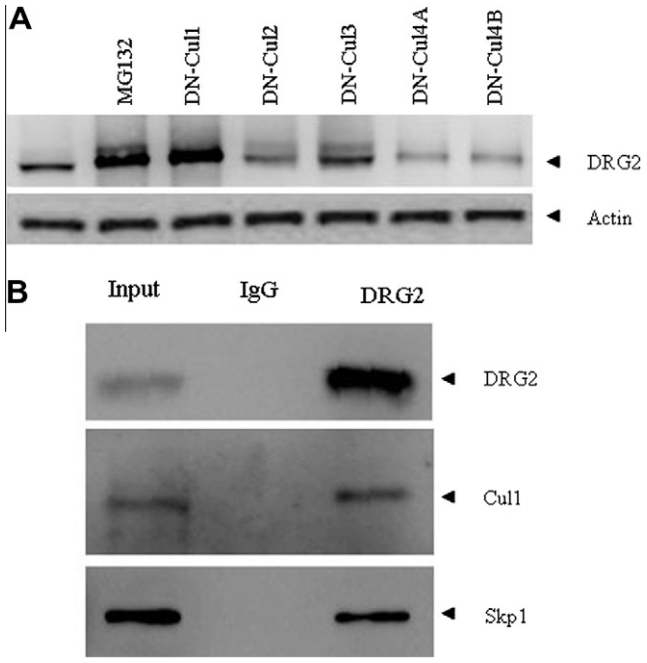

Fig. 3. Cullin1 was required for the efficient degradation of DRG2 during apoptosis. (A) Dominant Cullins plasmids were transfected into HepG2 cells. 24 h later after transfection, Dox was added to trigger apoptosis and the protein level of DRG2 was examined by western blot with actin as loading control. (B) Lysates of HepG2 cells were subjected to immunoprecipitation (IP) with Mouse IgG or DRG2 antibody followed by western blot with indicated antibodies.

3.2. The ubiquitin–proteasome system mediated the down-regulation of DRG2 protein during apoptosis

To investigate how DRG2 was down-regulated during apoptosis, we checked the mRNA level of DRG2 during Dox induced apop-

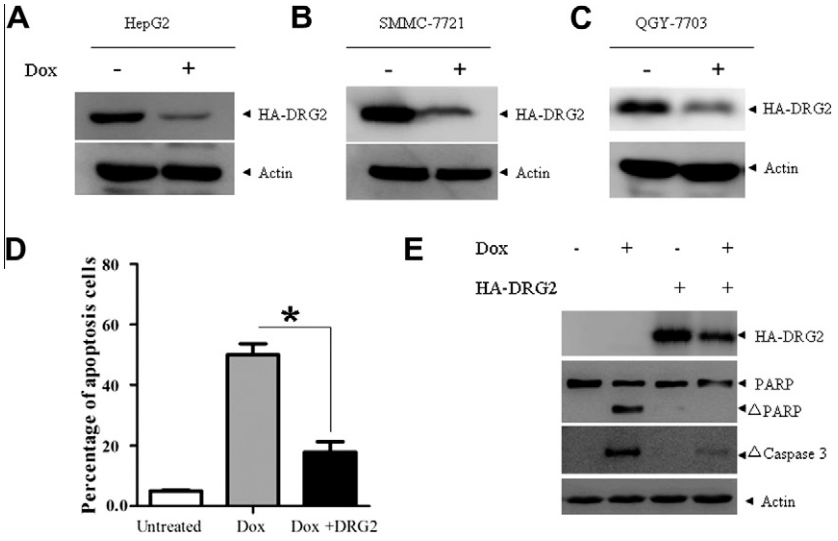

Fig. 4. Over-expression of DRG2 prevented Dox-induced apoptosis in hepatocellular carcinoma cells. (A–C) HepG2 (A), SMMC-7721 (B) and QGY-7703 (C) cells were transfected with HA-DRG2 and treated with or without Dox for 24 h, the protein level of DRG2 was examined by western blot with actin as loading control. (D) HepG2 cells transfected with or without HA-DRG2 were either untreated or treated with Dox (1 μg/ml) for 36 h. Apoptotic cells were analyzed by a sub-G1 DNA content assay. $^{*}p < 0.01$ versus mock transfected cells treated with Dox. (E) HepG2 cells transfected with or without HA-DRG2 were either untreated or treated with Dox (1 μg/ml) for 36 h, and then the indicated proteins were examined by western blot.

tosis of HepG2 cells. However, DRG2 mRNA level remained unchanged in Dox-treated HepG2 cells (Fig. 2A). We then tested whether DRG2 is regulated at the post-transcriptional level. To test this purpose, HepG2 cells were treated by 20 μg/ml protein synthesis inhibitor cycloheximide (CHX) with or without Dox for different time points. As shown in Fig. 2B and C, the half-life of DRG2 protein was significantly decreased in Dox-treated cells than untreated HepG2 cells, indicating that the stability of DRG2 was lowered upon Dox treatment. To identify which pathway is responsible for DRG2 protein degradation, HepG2 cells were treated with Dox in the presence of MG132 or epoxomicin a more specific proteasome inhibitor [20], or calpeptin, a calpain-specific inhibitor [21]. Our results showed that MG-132 and epoxomicin but not calpeptin could significantly block Dox-induced DRG2 degradation (Fig. 2D). Moreover, in the presence of MG132, Dox treatment rapidly increased the ubiquitinated DRG2 protein (Fig. 2E). All these data indicated that proteasome, but not calpain, mediated Dox -induced degradation of DRG2.

3.3. Cullin1 was required for the efficient degradation of DRG2 during apoptosis

Because the Cullin-based ubiquitin ligases are involved in the degradation of many key proteins during DNA damage and apoptosis, we now tested whether a Cullin-based ubiquitin ligase is required for the degradation of DRG2. We first tested which Cullin is required for the degradation of DRG2. We expressed one of five dominant negative (DN) Cullin members, including DN-Cullin1, DN-Cullin2, DN-Cullin3, DN-Cullin4A and DN-Cullin4B, into HepG2 cells. Then Dox was added to trigger apoptosis. Interestingly, only DN-Cullin1 could significantly prevent the degradation of DRG2 (Fig. 3A), which indicated DRG2 maybe a substrate of an SCF complex. To further prove this possibility, we then tested whether DRG2 interacts with components of the SCF complex. Endogenous DRG2 was immunoprecipitated by DRG2 antibody from HepG2 cell lysate, both CUL1 and SKP1 were detected in the precipitated DRG2 complex (Fig. 3B). These results suggest that DRG2 associates with the SCF E3 complex in vivo.

3.4. Over-expression of DRG2 prevented Dox-induced apoptosis in hepatocellular carcinoma cells

To investigate the biological function of DRG2, we over-expressed HA-DRG2 in a serial of hepatocellular carcinoma cells including HepG2, SMMC-7721 and QGY-7703. These cells were then treated with 1um Dox. The results showed that Dox treatment also reduced the ectopically expressed DRG2 protein levels (Fig. 4A–C), which further support that DRG2 is regulated at the post-transcriptional level during apoptosis induction. Then, we tested whether DRG2 contributes to apoptosis resistance. Upon Dox treatment, significant decrease of apoptosis was observed in DRG2 over-expressed HepG2 cells compared with that in empty vector transfection cells (Fig. 4D). In line with this, decreased levels of the cleaved caspase 3 and PARP were observed (Fig. 4E). These data indicated that DRG2 can inhibit Dox-induced hepatocellular carcinoma cells apoptosis.

4. Discussion

Although well-studied in embryonic development and cell transformation, the role of DRG2 in apoptosis and its regulation remain largely unknown. Here we demonstrated that in response to chemotherapeutic stimuli, the DRG2 protein was rapidly degraded by the proteasome system and over-expression of DRG2 prevents Dox-induced hepatocellular carcinoma apoptosis.

In the present study, we firstly showed that DRG2 is down-regulated during apoptosis in hepatocellular carcinoma cell lines. Then we found that the ubiquitin–proteasome system mediated the down-regulation of DRG2 protein during apoptosis. We also provided evidence that DRG2 was a direct target of SCF complex. Indeed, DRG2 interacted with both Cullin1 and Skp1. Inhibition the function of endogenous Cullin1 prevented the degradation of DRG2. However, SCF complex targets substrates for destruction required one F-box protein which belongs to a super-family containing at least 70 members [22]. Usually, F-box proteins recognized phosphorylated substrates for ubiquitination [23,24]. Both the F-box protein and kinase for the destruction of DRG2 remain un-

known. Thus, the mechanisms underlying the degradation of DRG2 warrant further investigation.

It has been reported that over-expression of DRG2 increases G2/M phase cells and decreases sensitivity to nocodazole-induced apoptosis in human T cells [19]. In line with this, over-expression of DRG2 prevented Dox-induced apoptosis in hepatocellular carcinoma cells by decreasing the levels of the cleaved caspase 3. Our data suggest that DRG2 could be a promising target for future cancer therapy strategies. Further exploration of the mechanisms underlying DRG2 degradation may lead to the identification of new ways to against hepatocellular carcinoma.

References

[1] H.B. El-Serag, K.L. Rudolph, Hepatocellular carcinoma: epidemiology and molecular carcinogenesis, Gastroenterology 132 (2007) 2557–2576.
[2] J.M. Llovet, Updated treatment approach to hepatocellular carcinoma, J. Gastroenterol. 40 (2005) 225–235.
[3] I.M. Ghobrial, T.E. Witzig, A.A. Adjei, Targeting apoptosis pathways in cancer therapy, CA Cancer J. Clin. 55 (2005) 178–194.
[4] G. Kroemer, L. Galluzzi, C. Brenner, Mitochondrial membrane permeabilization in cell death, Physiol. Rev. 87 (2007) 99–163.
[5] X. Zhao, J.I. Heng, D. Guardavaccaro, R. Jiang, M. Pagano, F. Guillemot, A. Iavarone, A. Lasorella, The HECT-domain ubiquitin ligase Huwe1 controls neural differentiation and proliferation by destabilizing the N-Myc oncoprotein, Nat. Cell Biol. 10 (2008) 643–653.
[6] D. Guardavaccaro, M. Pagano, Oncogenic aberrations of Cullin-dependent ubiquitin ligases, Oncogene 23 (2004) 2037–2049.
[7] N.V. Dorrello, A. Peschiaroli, D. Guardavaccaro, N.H. Colburn, N.E. Sherman, M. Pagano, S6K1- and betaTRCP-mediated degradation of PDCD4 promotes protein translation and cell growth, Science 314 (2006) 467–471.
[8] E. Dehan, F. Bassermann, D. Guardavaccaro, G. Vasiliver-Shamis, M. Cohen, K.N. Lowes, M. Dustin, D.C. Huang, J. Taunton, M. Pagano, BetaTrCP- and Rsk1/2-mediated degradation of BimEL inhibits apoptosis, Mol. Cell 33 (2009) 109–116.
[9] D. Frescas, M. Pagano, Deregulated proteolysis by the F-box proteins SKP2 and beta-TrCP: tipping the scales of cancer, Nat. Rev. Cancer 8 (2008) 438–449.
[10] T. Cardozo, M. Pagano, The SCF ubiquitin ligase: insights into a molecular machine, Nat. Rev. Mol. Cell Biol. 5 (2004) 739–751.
[11] N. Zheng, B.A. Schulman, L. Song, J.J. Miller, P.D. Jeffrey, P. Wang, C. Chu, D.M. Koepp, S.J. Elledge, M. Pagano, R.C. Conaway, J.W. Conaway, J.W. Harper, N.P. Pavletich, Structure of the Cul1-Rbx1-Skp1-F boxSkp2 SCF ubiquitin ligase complex, Nature 416 (2002) 703–709.
[12] B.A. Schulman, A.C. Carrano, P.D. Jeffrey, Z. Bowen, E.R. Kinnucan, M.S. Finnin, S.J. Elledge, J.W. Harper, M. Pagano, N.P. Pavletich, Insights into SCF ubiquitin ligases from the structure of the Skp1-Skp2 complex, Nature 408 (2000) 381–386.
[13] B. Hao, N. Zheng, B.A. Schulman, G. Wu, J.J. Miller, M. Pagano, N.P. Pavletich, Structural basis of the Cks1-dependent recognition of p27(Kip1) by the SCF(Skp2) ubiquitin ligase, Mol. Cell 20 (2005) 9–19.
[14] J.R. Skaar, V. D'Angiolella, J.K. Pagan, M. Pagano, SnapShot: F Box Proteins II, Cell 137 (2009) 1358. 1358 e1351.
[15] B. Li, B. Trueb, DRG represents a family of two closely related GTP-binding proteins, Biochim. Biophys. Acta 1491 (2000) 196–204.
[16] T. Schenker, C. Lach, B. Kessler, S. Calderara, B. Trueb, A novel GTP-binding protein which is selectively repressed in SV40 transformed fibroblasts, J. Biol. Chem. 269 (1994) 25447–25453.
[17] M.A. Mahajan, S.T. Park, X.H. Sun, Association of a novel GTP binding protein, DRG, with TAL oncogenic proteins, Oncogene 12 (1996) 2343–2350.
[18] D. Wei, J. Yao, X. Yang, L. Cheng, D. Lu, J. Xue, Molecular cloning and expression of two closely related GTP-binding proteins from zebrafish, DNA Seq. 15 (2004) 246–250.
[19] H. Song, S.I. Kim, M.S. Ko, H.J. Kim, J.C. Heo, H.J. Lee, H.S. Lee, I.S. Han, K. Kwack, J.W. Park, Overexpression of DRG2 increases G2/M phase cells and decreases sensitivity to nocodazole-induced apoptosis, J. Biochem. 135 (2004) 331–335.
[20] L. Meng, R. Mohan, B.H. Kwok, M. Elofsson, N. Sin, C.M. Crews, Epoxomicin, a potent and selective proteasome inhibitor, exhibits in vivo antiinflammatory activity, Proc. Natl. Acad. Sci. USA 96 (1999) 10403–10408.
[21] A.M. Gwozdz, R. Leung, H. Wang, K.W. Bang, M.A. Packham, J. Freedman, M.L. Rand, Calpain inhibition by calpeptin does not prevent APLT activity reduction in PS-exposing platelets, but calpeptin has independent pro-apoptotic effects, Thromb. Haemost. 103 (2010) 1218–1227.
[22] J. Jin, T. Cardozo, R.C. Lovering, S.J. Elledge, M. Pagano, J.W. Harper, Systematic analysis and nomenclature of mammalian F-box proteins, Genes. Dev. 18 (2004) 2573–2580.
[23] D.I. Lin, O. Barbash, K.G. Kumar, J.D. Weber, J.W. Harper, A.J. Klein-Szanto, A. Rustgi, S.Y. Fuchs, J.A. Diehl, Phosphorylation-dependent ubiquitination of cyclin D1 by the SCF(FBX4-alphaB crystallin) complex, Mol. Cell 24 (2006) 355–366.
[24] H. Inuzuka, A. Tseng, D. Gao, B. Zhai, Q. Zhang, S. Shaik, L. Wan, X.L. Ang, C. Mock, H. Yin, J.M. Stommel, S. Gygi, G. Lahav, J. Asara, Z.X. Xiao, W.G. Kaelin Jr., J.W. Harper, W. Wei, Phosphorylation by casein kinase I promotes the turnover of the Mdm2 oncoprotein via the SCF(beta-TRCP) ubiquitin ligase, Cancer Cell 18 (2010) 147–159.

Biochemical and Biophysical Research Communications 420 (2012) 656–661

Contents lists available at SciVerse ScienceDirect

Biochemical and Biophysical Research Communications

journal homepage: www.elsevier.com/locate/ybbrc

Conformation and dynamics of nucleotides in bulges and symmetric internal loops in duplex DNA studied by EPR and fluorescence spectroscopies

Pavol Cekan, Snorri Th. Sigurdsson *

University of Iceland, Science Institute, Dunhaga 3, 107 Reykjavik, Iceland

ARTICLE INFO

Article history:
Received 5 March 2012
Available online 17 March 2012

Keywords:
ESR
Site-directed spin-labeling
SDSL
Nitroxide
Aminoxyl radical

ABSTRACT

The dynamics and conformation of base bulges and internal loops in duplex DNA were studied using the bifunctional spectroscopic probe **Ç**, which becomes fluorescent (**Ç^{f}**) upon reduction of the nitroxide functional group, along with EPR and fluorescence spectroscopies. A one-base bulge was in a conformational equilibrium between looped-out and stacked states, the former favored at higher temperature and the latter at lower temperature. Stacking of bulge bases was favored in two- and three-base bulges, independent of temperature, resulting in DNA bending as evidenced by increased fluorescence of **Ç^{f}**. EPR spectra of **Ç**-labeled three-, four- and five-base symmetrical interior DNA bulges at 20 °C showed low mobility, indicating that the spin-label was stacked within the loop. The spin-label mobility at 37 °C increased as the loops became larger. A considerable variation in fluorescence between different loops was observed, as well as a temperature-dependence within constructs. Fluorescence unexpectedly increased as the size of the loop decreased at 2 °C. Fluorescence of the smallest loops, where a single T·T mismatch was located between the stem region and the probe, was even larger than for the single strand, indicating a considerable local structural deformation of these loops from regular B-DNA. These results show the value of combining EPR and fluorescence spectroscopy to study non-helical regions of nucleic acids.

1. Introduction

Nucleic acids fold into different secondary and tertiary structures to enable various biological functions, with bulges and loops being abundant. Bulges are formed when one strand within a duplex is longer than the other strand, i.e. when there are nucleotides in a duplex region that are not involved in canonical base-pairing. Loops can be at the end of a duplex region (hairpin loops) or within duplexes containing consecutive mismatches (e.g. T·T, U·U or G·A, internal or interior loops). Internal loops can be either symmetric (both strands in the loop are of the same length) or asymmetric.

Bulges and loops can have different effects on DNA structure. They can distort the stacking of bases in the duplex [1,2], induce a bend in the nucleic acid [3,4], reduce the stability of the helix [5], and/or increase the major groove accessibility at base-pairs flanking the bulge [6]. Bulges are often intermediates for errors in DNA replication, targets for repair enzymes in imperfect homologous recombination [7], and are believed to play a significant role in many diseases, including muscular dystrophy and Alzheimer's disease [8]. Single nucleotide polymorphisms that account for ~90% of mutations in an individual's DNA also include some forms of single-base bulges [9]. RNA contains an abundance of internal loops that are important for their function and often targets for drugs, for example the bacterial ribosome [10] and the viral TAR-RNA [11]. Understanding the structure and stability of bulges, loops and mismatches is also essential for prediction of mishybridization events in all nucleic acid hybridization assays such as northern blots, RT-PCR and *in situ* hybridization assays.

Bulged nucleic acids have been studied by different biophysical techniques. NMR studies of single nucleotide bulges have shown that bulged purines prefer to stack within the helix while pyrimidines either loop out or stack, depending on the identity of the base, flanking sequence and temperature [1,12,13]. Fluorescence spectroscopy, utilizing fluorescent nucleoside analogs to elucidate structural perturbations within nucleic acids [14], has been used to study the structure and dynamics of bulges [15,16], hairpins [17,18] and loops [15,19]. Furthermore, gel electrophoretic mobility, FRET measurements and electron microscopy have showed that bulges introduce kinks into DNA helices [20].

X-ray crystallography has infrequently been used to study DNA bulges or loops. In one example, crystallographic analysis showed a looped-out structure of a single-nucleotide adenine (A) bulge, while an NMR study of the same sequence showed that the A stacked into the helix [21]. These apparently conflicting results show the importance of using more than one technique for studying conformations of non-duplex nucleic acid structures. Furthermore, it is important to obtain information about conformational dynamics.

Electron paramagnetic resonance (EPR) spectroscopy is a useful technique for studying both structure and dynamics, but has not

* Corresponding author. Fax: +354 552 8911.
E-mail address: snorrisi@hi.is (S.T. Sigurdsson).

0006-291X/$ - see front matter © 2012 Elsevier Inc. All rights reserved.
http://dx.doi.org/10.1016/j.bbrc.2012.03.059

been frequently applied to bulges and loops. EPR studies of nucleic acids require site-directed spin-labeling [22]. We have used EPR to study the mobility of the bulge in the TAR-RNA after incorporation of a probe into the 2′-position of selected nucleotides [23]. Information about TAR-dynamics gave insight into structural changes upon binding to a variety of different ligands, such as metal ions [24], small organic molecules [25] and peptides [26].

The rigid nitroxide nucleoside **Ç** [27], which forms a stable base-pair with guanine (Fig. 1) [28], reports directly on the motion of the base to which the nitroxide is fused, unlike most other labels that are connected with a flexible tether. **Ç** has been used to investigate the dynamics of DNA hairpin loops [29], bulges [30], folding of the DNA cocaine aptamer [31] and measure long-range distances and orientations [32,33]. It has also enabled the study of internal motions of DNA duplexes by EPR using either continuous wave- [34] or pulsed-EPR spectroscopy [35]. The nitroxide functional group can be reduced to the corresponding amine, which is strongly fluorescent [36]. Thus, the two almost identical labels, **Ç** and **Ç^f** (Fig. 1), can be used to study the same sample with two spectroscopic techniques. In a previous study of conformation and dynamics of nucleotides in hairpin loops, we found the fluorescence data to be fully consistent with the EPR results, where higher quantum yield corresponded to higher mobility of the labeled nucleotide [29]. However, there have also been cases where fluorescence data from **Ç^f** have complemented the EPR results, by giving additional insights into conformational equilibria. For example, unusually large changes in fluorescence of a base-paired nucleotide at a helical junction, which had limited mobility as shown by EPR, indicated a helical tilt during folding of the cocaine aptamer [31].

We have previously used EPR spectroscopy to study the conformational dynamics of bulges in duplex DNA, including a single-bulged nucleotide that was able to participate in base-pair exchange with nucleotides in an adjacent mismatch [30]. In this paper, we extend the study of simple one- to three-base bulges to include fluorescence spectroscopy. Both the EPR and fluorescence data indicated that the single-base bulge was in a temperature-dependent equilibrium between a stacked and a looped-out conformation while bases in two- and three-base bulges were stacked into the helix. The EPR studies of less studied symmetrical internal loops demonstrated direct correlation between size of the loops and their mobility at 37 °C. Unexpectedly high fluorescence of the smallest and most immobile loops indicated local structural perturbations.

2. Materials and methods

2.1. General

Water was purified on a MILLI-Q water purification system. DNA oligomers were synthesized on an ASM 800 DNA synthesizer from Biosset (Russia). All commercial phosphoramidites and columns were purchased from ChemGenes. Solvents and reagents were purchased from ChemGenes, Sigma–Aldrich and Applied Biosystems. Molecular weight (MW) of DNA was determined by MALDI-Tof analysis and mass spectra recorded on a Bruker Autoflex III. UV–vis spectra were recorded on a PerkinElmer Lambda 25 UV–vis spectrometer. Continuous wave (CW) EPR spectra were recorded on a MiniScope MS200 (Magnettech, Germany) X-band spectrometer. Steady-state fluorescence measurements were carried out in a macro fluorescence cell (Spectrocell, USA) with a path length of 0.5 cm on a SPEX FluoroMax spectrometer.

2.2. DNA synthesis and purification

The probe was site-specifically incorporated into DNA by manual coupling, purified and quantified as described before [29]. Spin-labeled DNA was reduced with Na_2S, purified by gel electrophoresis [36] and characterized by MALDI-Tof [29].

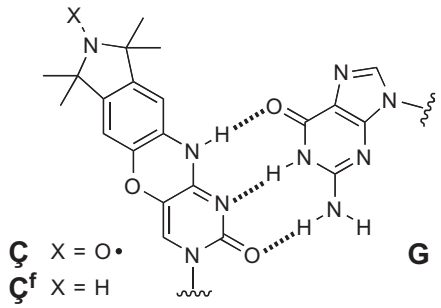

Fig. 1. Rigid spin-label **Ç** and reduced spin-label **Ç^f** base-paired to guanine.

2.3. Spectroscopic measurements

EPR spectra of spin-labeled DNA duplexes (final conc. 200 μM of duplex) were prepared in PNE buffer (10 mM Na_2HPO_4, 100 mM NaCl, 0.1 mM Na_2EDTA, pH 7.0; 10 μL), the samples were placed in a quartz capillary and EPR spectra collected as previously described [29]. All fluorescent DNA samples were measured at 12.5 μM in 400 μL of PNE buffer using an excitation wavelength of 365.5 nm [36]. Fluorescence spectra were averaged over five scans. Quantum yields were determined as previously described [36].

3. Results and discussion

3.1. Bulges containing one- to three-bases

For preparation of DNA duplexes containing bulged nucleotides, the spin-labeled DNA 14-mer (**x**) (Fig. 2) was synthesized and annealed to shorter complementary strands to form one- (**X2**), two- (**X3**) or three-base (**X4**) bulges, respectively (Fig. 2). The X-band CW EPR data was subsequently collected at 2 and 20 °C (Fig. 2).

The EPR spectrum of the one-base bulge (**X2**) at 20 °C contains a fast-motion component that has similar mobility as the single-stranded DNA (**x**). Thus, the EPR spectrum reflects a mixture of single-stranded-like spectrum and a duplex-like spectrum, indicating that the bulged **Ç** can be present in either a looped-out or a stacked conformation [30], consistent with early optical and photochemical experiments on synthetic RNAs showing that extra pyrimidines can loop out [37,38]. Furthermore, NMR analysis of a 13-mer DNA containing a thymidine (T) in a one-base bulge has previously shown that the extra T is in a conformational equilibrium between looped-out and stacked states [1]. However, when the temperature of **X2** was lowered to 2 °C, the EPR spectrum became similar to all others (Fig. 2), indicating that stacking of **Ç** is favored at low temperatures.

The EPR spectra of the two- (**X3**), and three-base (**X4**) bulges at both temperatures are similar to the EPR spectrum of the fully base-paired duplex (**X1**) (Fig. 2). The reduced mobility relative to the one-base bulge is consistent with stacking. NMR studies have shown that As in one-, two-, or three-nucleotide bulges stack into the duplex [3], and generate a local bend [4], or a kink in the duplex DNA [20]. Purines, in general, prefer to stack in multi-nucleotide bulges [39,40] and in contrast to pyrimidines [2,37], prefer to stack within the duplex in one-base bulges [12,13].

The bulges were also studied by fluorescence spectroscopy, which is a useful technique to probe the solvent exposure of chromophores [14,41]. The fluoroside **Ç^f** (Fig. 1) has already shown its usefulness in studying nucleotide conformations in hairpin loops [29]. A potential pitfall is flanking-sequence dependence on the

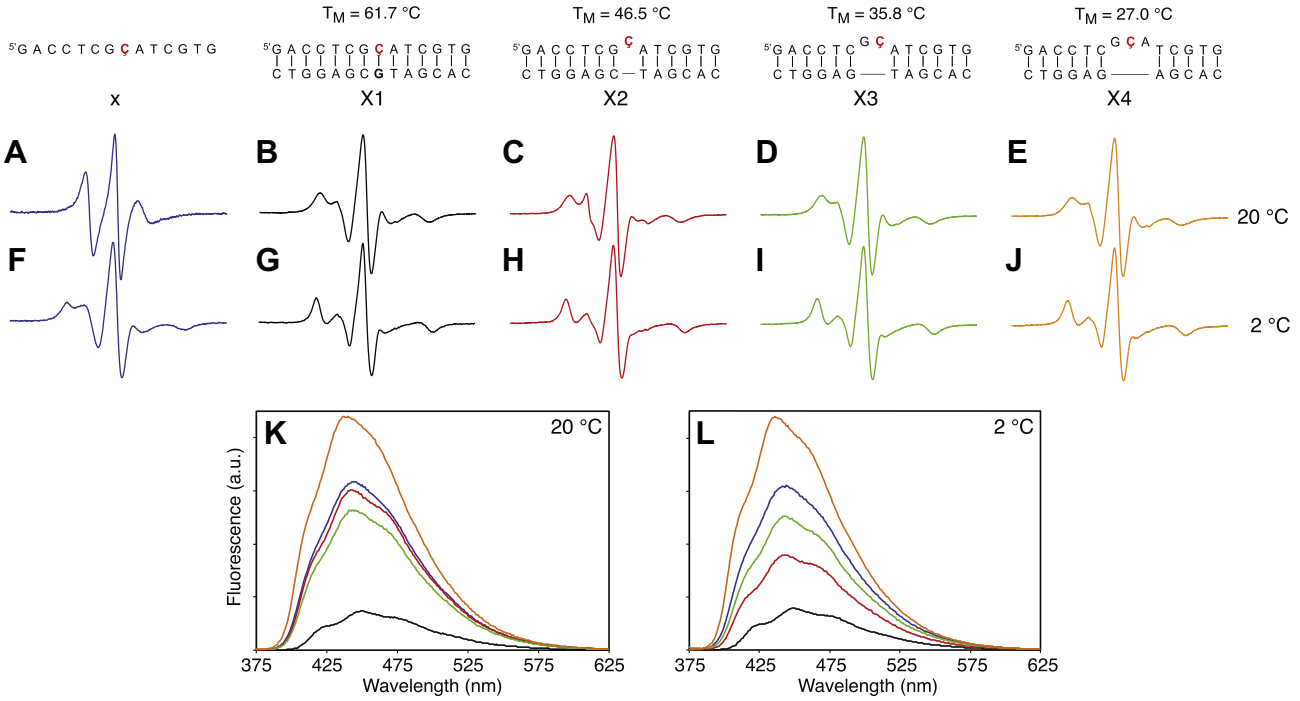

Fig. 2. EPR spectra of single-stranded oligomer **x** (A, F, blue), fully base-paired duplex **X1** (B, G, black), one-base bulge **X2** (C, H, red), two-base bulge **X3** (D, I, green) and three-base bulge **X4** (E, J, orange) were collected at 20 and 2 °C. Fluorescence spectra (K, L) of **x** and **X1**–**X4**, which are shown using the same color-code as for EPR spectra, were collected at the same temperatures. T_M data of duplexes **X1**–**X4** are shown above the sequences. (For interpretation of the references to color in this figure legend, the reader is referred to the web version of this article.)

fluorescence signal, which has been observed with **Ç**$^{\mathbf{f}}$ [42]. However, the flanking sequence is the same in all the bulges and the fluoroside should, therefore, report on the solvent exposure of **Ç**$^{\mathbf{f}}$.

As expected, the fluorescence intensity of all three bulges at 2 and 20 °C was considerably higher than of the fully base-paired duplex, because a nucleotide in a DNA bulge is more exposed to the solvent than one that is placed in a duplex region (Fig. 2). Fluorescence of the bulges not only increases with size, but the fluorescence of the three-base bulge is also much higher than of the single strand. This indicates that the kink in the duplex makes **Ç**$^{\mathbf{f}}$ more solvent-exposed than when placed in the single strand, where it may be partially stacked. This is corroborated by NMR studies of the bulge sequences AAA [3], ATA [4], AAAAA [39] and AATAA [40], all of which have the nucleotides of the bulges localized at intrahelical positions within the double helices. This induces a local bend in the bulged DNA and exposes the bulged nucleotides to the solvent.

When lowering the temperature to 2 °C, the fluorescence of the one-base bulge dropped substantially, while the fluorescence of the other sequences remained unchanged. Thus, both the fluorescence and EPR data showed that the equilibrium between a stacked and a looped-out nucleotide is temperature-dependent and that stacking of **Ç**/**Ç**$^{\mathbf{f}}$ is favored at low temperature. In contrast, a cytidine one-base bulge, flanked by two Gs has shown the inverse trend and was predominantly looped-out at 0 °C [43]. NMR studies have also shown that flanking sequences have an effect on temperature-dependent equilibria of some one-base bulges [1]. Not all one-base bulges have temperature-dependent transitions, for example C was found to be looped-out at different temperatures when flanked by two As, presumably because of the propensity of the As to stack together [2].

3.2. Symmetrical internal loops

Having established that **Ç** and **Ç**$^{\mathbf{f}}$ were useful probes to investigate conformation and dynamics of nucleotides in bulges, we extended this study to the more flexible internal loops. Although the thermodynamic stability of small internal loops has been studied [44], little is known about their conformational dynamics. To systematically study internal loops, a family of duplexes (**Y1**–**Y9**) was prepared (Fig. 3). All the duplexes contained the central sequence 5′-d(CT**Ç**TC); the loop structure was changed by incorporating Gs (Fig. 3, bold) into the pyrimidine-rich opposing strand. As expected, thermodynamic stability of the duplexes increases as the size of the loops decreases (Fig. 3). Although internal loops are considerably less stable than duplex regions (for example, five-base loop **Y2** is ca. 28 °C less stable than duplex **Y1**) they are significantly more stable than asymmetric internal loops of the same length [44].

The EPR spectra of duplexes **Y1**–**Y9** and single-stranded DNA (**y**) were collected at 20 and 37 °C. Of all the EPR spectra collected at 20 °C, only the EPR spectrum of the five-base bulge **Y2** is slightly different, showing a more pronounced fast-motion component than the other spin-labeled oligomers (Fig. 3). However, the EPR spectrum of **Y2** is more similar to the spectrum of the fully base-paired duplex **Y1** than to the single strand (**y**) or even the one-base bulge **X2** (Fig. 2C). Thus, the mobility of **Ç** is severely restricted in the bulge, presumably due to stacking of the probe within the loop. The EPR spectra of all the other bulges (**Y3–Y9**) are identical to those of the fully base-paired duplex (**Y1**), showing that these loops are not very flexible at 20 °C and indicative of stacking within the internal loop.

In contrast to the EPR data at 20 °C, the EPR spectra of the duplexes at 37 °C reflect a greater variation in spin-label mobility (Fig. 3 and Fig. 4A). As a more quantitative measure of the mobility of **Ç** in different loops (**Y2**–**Y9**), we plotted the ratio of the height of the center peak of EPR spectrum (h_c) and the low-field peak (h_l) for all the spectra, except for the single strand (**y**) (Fig. 4A) [31]. Because h_l corresponds to the fast-motion component, a high h_l/h_c ratio reflects high spin-label mobility. This analysis revealed that oligomers **Y1–Y9** fall into three mobility categories. Duplex **Y2**, which contains the largest internal loop shows the most mobility

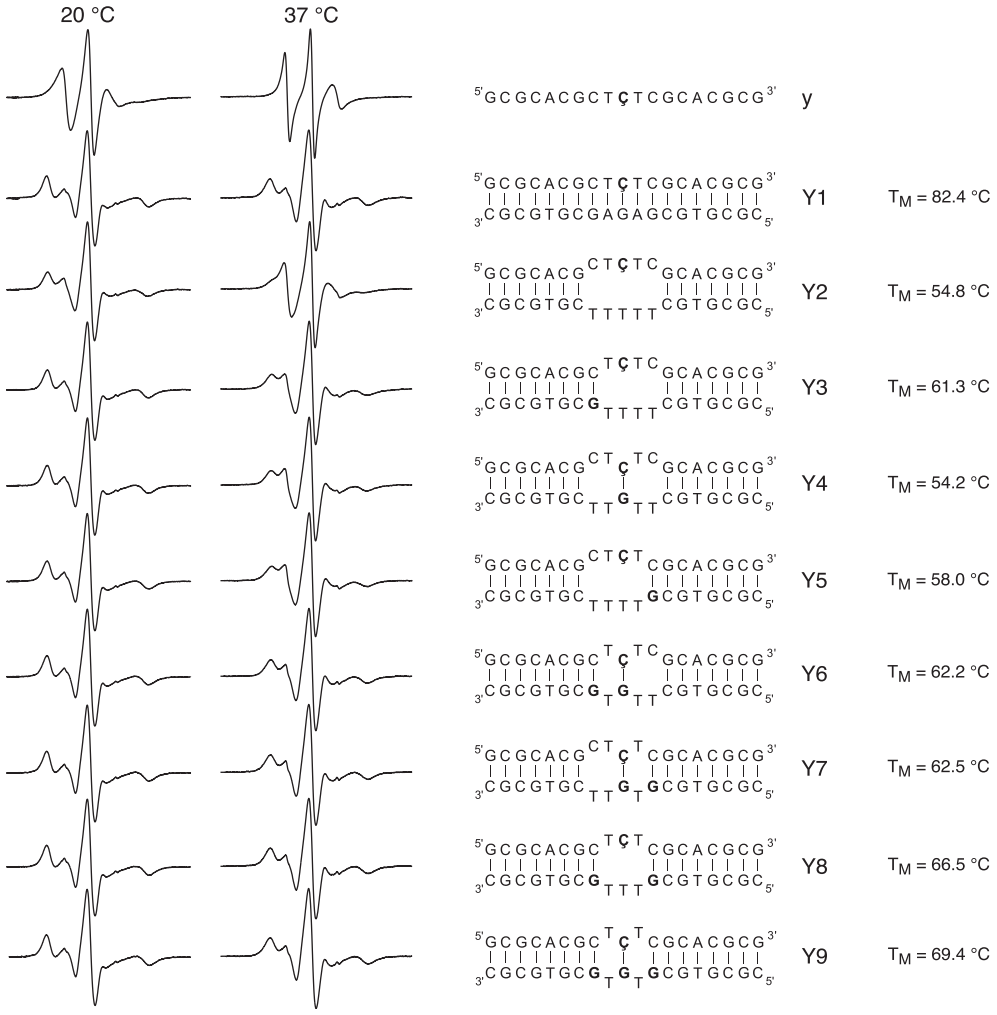

Fig. 3. EPR (left) and T_M data (right) of internal loops **Y2**–**Y9**. EPR spectra of single strand **x**, fully base-paired duplex **Y1** and internal loops **Y2**–**Y9** in aqueous solution at 20 and 37 °C. The size of the loop was systematically varied by introducing Gs (shown bold) into the loop.

and is in a category by itself, displays spin-label mobility similar to the single strand (**y**). The second category contains duplexes **Y3**–**Y5**, all of which contain four mismatched pairs in the loop. The position of the additional base-pair, compared to **Y2**, does not appreciably affect the spin-label mobility. Duplexes **Y6**–**Y9** belongs to the third category, containing three or fewer bases in the loop. This category of loops, with the lowest h_l/h_c ratio, shows the most extensive immobilization of **Ç** and has mobility similar to that of the duplex (**Y1**). Thus, EPR data of duplexes **Y1**–**Y9** at 37 °C shows a clear correlation between the h_l/h_c ratio and a number of bases that are unpaired in the internal loop; the fewer unpaired bases in the loop, the lower the mobility of the probe.

The fluorescence quantum yields were also determined for duplexes **Y1**–**Y9** after reduction of **Ç** to **Ç^f**. The results for each construct at 2 and 37 °C are shown in Fig. 4B. For 37 °C, there is no obvious trend visible, in contrast to the EPR data. However, the fluorescence of the fully base-paired duplex **Y1** is considerably lower than for all other constructs, showing that fluorescence increases dramatically when **Ç^f** is placed in the loops. It is also noteworthy that loop **Y2**, which has the highest mobility among the internal loops as judged by EPR (Fig. 4A), has a substantially lower fluorescence at 2 °C than at 37 °C, indicating that base-stacking is favored in large internal loops at lower temperatures.

A clear trend was observed for the internal loops in duplexes **Y2**–**Y9** at 2 °C, where the fluorescence increased as the size of the loop decreased. Since the EPR data showed that the label was fully stacked within the duplex at 20 and 0 °C (data not shown), the fluorescence most likely reflects changes in the structure/dynamics of the loop. However, it is surprising that the fluorescence increased with decreased size of the loop. One might have expected the fluorescence to decrease with decreasing loop size, since the fluorescence of the fully base-paired duplex (**Y1**) is by far the lowest.

It is particularly striking that **Y8** and **Y9** show higher fluorescence than the single strand (**y**), which was also observed for the three-base bulge (**X4**). This data indicates a considerable local structural deformation of these loops from regular B-DNA that increases the exposure of the label to the solvent. NMR studies of single-base mismatches have shown that a single T·T mismatch is present as a wobble pair in duplex DNA; two hydrogen bonds are formed between carbonyls and imino protons, which causes only a minor distortion of the duplex structure [45]. Thus, it is unlikely Ts are looping out, although it cannot be ruled out, since the NMR studies were performed using a high salt concentration to stabilize the duplex structure. If a T·T mismatch that is positioned between a duplex stem and **Ç^f** is a dynamic equilibrium between stacked and looped-out conformation, it could lead to conformations where it is exposed to the solvent and lead to increased fluorescence. Our data show that duplexes **Y6** and **Y7**, both of which can form one T·T mismatch that is positioned between a duplex

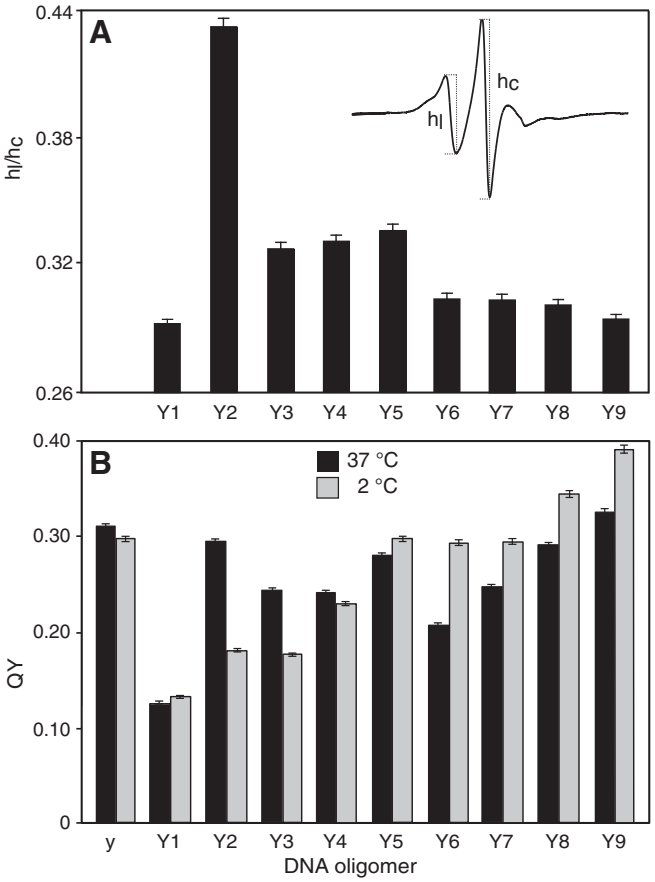

Fig. 4. (A) Mobility of **Ç** in **Y1**–**Y9** at 37 °C quantified as the h_l/h_c ratio. Determination the h_l/h_c ratio from the EPR spectrum; h_l is the height of the low-field peak, h_c is the height of the center peak. (B) Fluorescence quantum yield of single-stranded 19-mer **y**, fully base-paired duplex **Y1** and internal loops **Y2**–**Y9** at 37 °C (black) and 2 °C (gray).

stem and the label, have fluorescence similar to that of a single strand while **Y9** has two such T·T mismatches and has ca. 30% higher fluorescence than the single strand.

In conclusion, conformational dynamics of bulges and internal loops in duplex DNA were studied using the complementary techniques of EPR and fluorescence spectroscopy. The EPR and fluorescence data of the bulged DNAs show that stacking of the nucleotides is highly favored in all three bulges at both temperatures, except for the one-base bulge, which is present in temperature-dependent conformational equilibrium between looped-out and stacked states. The fluorescence of the larger bulges increased with increased size of the bulge, consistent with bending of the duplex and greater exposure of the fluorescent nucleoside to the solvent. EPR results of the symmetric internal loops did not show evidence of a looped-out conformation for the spin-labeled nucleotide at 20 °C, but the mobility of the nucleotides in the loop increased as the loop became larger at 37 °C. Fluorescence was unexpectedly highest for the smallest internal loops that had the lowest mobility by EPR, indicating local structural perturbation from B-form DNA. Thus, the complementary methods of EPR and fluorescence spectroscopies yield more information than either individual technique alone.

Acknowledgments

This work was supported by The Icelandic Research Fund (06002821) and by a doctoral fellowship to P. Cekan from the Eimskip Fund of the University of Iceland.

References

[1] M.W. Kalnik, D.G. Norman, B.F. Li, et al., Conformational transitions in thymidine bulge-containing deoxytridecanucleotide duplexes: role of flanking sequence and temperature in modulating the equilibrium between looped-out and stacked thymidine bulge states, J. Biol. Chem. 265 (1990) 636–647.
[2] K.M. Morden, Y.G. Chu, F.H. Martin, et al., Unpaired cytosine in the deoxyoligonucleotide duplex dCAAACAAAG.dCTTTTTTG is outside of the helix, Biochemistry 22 (1983) 5557–5563.
[3] M.A. Rosen, D. Live, D.J. Patel, Comparative NMR study of an bulge loops in DNA duplexes - intrahelical stacking of A, A–A, and A–A–A bulge loops, Biochemistry 31 (1992) 4004–4014.
[4] M.A. Rosen, L. Shapiro, D.J. Patel, Solution structure of a trinucleotide A–T–A-bulge loop within a DNA duplex, Biochemistry 31 (1992) 4015–4026.
[5] A. Bhattacharyya, D.M. Lilley, The contrasting structures of mismatched DNA sequences containing looped-out bases (bulges) and multiple mismatches (bubbles), Nucleic Acids Res. 17 (1989) 6821–6840.
[6] K.M. Weeks, C. Ampe, S.C. Schultz, et al., Fragments of the HIV-1 Tat protein specifically bind TAR RNA, Science 249 (1990) 1281–1285.
[7] A. Stassinopoulos, J. Ji, X.L. Gao, et al., Solution structure of a two-base DNA bulge complexed with an enediyne cleaving analog, Science 272 (1996) 1943–1946.
[8] E.M. McNally, D. Duggan, J.R. Gorospe, et al., Mutations that disrupt the carboxyl-terminus of gamma-sarcoglycan cause muscular dystrophy, Hum. Mol. Genet. 5 (1996) 1841–1847.
[9] F.S. Collins, L.D. Brooks, A. Chakravarti, A DNA polymorphism discovery resource for research on human genetic variation, Genome Res. 8 (1998) 1229–1231.
[10] J. Poehlsgaard, S. Douthwaite, The bacterial ribosome as a target for antibiotics, Nat. Rev. Microbiol. 3 (2005) 870–881.
[11] A.I. Murchie, B. Davis, C. Isel, et al., Structure-based drug design targeting an inactive RNA conformation: exploiting the flexibility of HIV-1 TAR RNA, J. Mol. Biol. 336 (2004) 625–638.
[12] M.W. Kalnik, D.G. Norman, P.F. Swann, et al., Conformation of adenosine bulge-containing deoxytridecanucleotide duplexes in solution: extra adenosine stacks into duplex independent of flanking sequence and temperature, J. Biol. Chem. 264 (1989) 3702–3712.
[13] E. Nikonowicz, V. Roongta, C.R. Jones, et al., Two-dimensional ^{1}H- and ^{31}P-NMR spectra and restrained molecular dynamics structure of an extrahelical adenosine tridecamer oligodeoxyribonucleotide duplex, Biochemistry 28 (1989) 8714–8725.
[14] R.W. Sinkeldam, N.J. Greco, Y. Tor, Fluorescent analogs of biomolecular building blocks: design, properties, and applications, Chem. Rev. 110 (2010) 2579–2619.
[15] H.S. Jeong, S. Kang, J.Y. Lee, et al., Probing specific RNA bulge conformations by modified fluorescent nucleosides, Org. Biomol. Chem. 7 (2009) 921–925.
[16] D.P. Millar, Fluorescence studies of DNA and RNA structure and dynamics, Curr. Opin. Struct. Biol. 6 (1996) 322–326.
[17] J.D. Ballin, S. Bharill, E.J. Fialcowitz-White, et al., Site-specific variations in RNA folding thermodynamics visualized by 2-aminopurine fluorescence, Biochemistry 46 (2007) 13948–13960.
[18] B.J. Lee, M. Barch, E.W. Castner Jr, et al., Structure and dynamics in DNA looped domains: CAG triplet repeat sequence dynamics probed by 2-aminopurine fluorescence, Biochemistry 46 (2007) 10756–10766.
[19] K.B. Hall, 2-aminopurine as a probe of RNA conformational transitions, Methods Enzymol. 469 (2009) 269–285.
[20] D.M.J. Lilley, Kinking of DNA and RNA by base bulges, Proc. Natl. Acad. Sci. U. S. A. 92 (1995) 7140–7142.
[21] L. Joshua-Tor, D. Rabinovich, H. Hope, et al., The three-dimensional structure of a DNA duplex containing looped-out bases, Nature 334 (1988) 82–84.
[22] S.A. Shelke, S.T. Sigurdsson, Site-directed spin labelling of nucleic acids, Eur. J. Org. Chem. (2012), http://dx.doi.org/10.1002/ejoc.201101434.
[23] T.E. Edwards, T.M. Okonogi, B.H. Robinson, et al., Site-specific incorporation of nitroxide spin labels into internal sites of the TAR RNA: structure-dependent dynamics of RNA by EPR spectroscopy, J. Am. Chem. Soc. 123 (2001) 1527–1528.
[24] T.E. Edwards, T.M. Okonogi, S.T. Sigurdsson, Investigation of RNA-protein and RNA-metal ion interactions by electron paramagnetic resonance spectroscopy. The HIV TAR-Tat motif, Chem. Biol. 9 (2002) 699–706.
[25] T.E. Edwards, S.T. Sigurdsson, Electron paramagnetic resonance dynamic signatures of TAR RNA - small molecule complexes provide insight into RNA structure and recognition, Biochemistry 41 (2002) 14843–14847.
[26] T.E. Edwards, B.H. Robinson, S.T. Sigurdsson, Identification of amino acids that promote specific and rigid TAR RNA-tat protein complex formation, Chem. Biol. 12 (2005) 329–337.
[27] N. Barhate, P. Cekan, A.P. Massey, et al., A nucleoside that contains a rigid nitroxide spin label: a fluorophore in disguise, Angew. Chem., Int. Ed. 46 (2007) 2655–2658.
[28] T.E. Edwards, P. Cekan, G.W. Reginsson, et al., Crystal structure of a DNA containing the planar, phenoxazine-derived bi-functional spectroscopic probe Ç, Nucleic Acids Res. 39 (2011) 4419–4426.
[29] P. Cekan, A.L. Smith, N. Barhate, et al., Rigid spin-labeled nucleoside Ç: a nonperturbing EPR probe of nucleic acid conformation, Nucleic Acids Res. 36 (2008) 5946–5954.

[30] A.L. Smith, P. Cekan, G.P. Brewood, et al., Conformational equilibria of bulged sites in duplex DNA studied by EPR spectroscopy, J. Phys. Chem. B 113 (2009) 2664–2675.

[31] P. Cekan, E.O. Jonsson, S.T. Sigurdsson, Cocaine aptamer folding studied by EPR and fluorescence spectroscopies, Nucleic Acids Res. (2009) 3990–3995.

[32] A. Marko, D. Margraf, P. Cekan, et al., Analytical method to determine the orientation of rigid spin labels in DNA, Phys. Rev. E: Stat., Nonlinear, Soft Matter Phys. 81 (2010) 21911–21919.

[33] O. Schiemann, P. Cekan, D. Margraf, et al., Relative orientation of rigid nitroxides by PELDOR: beyond distance measurements in nucleic acids, Angew. Chem., Int. Ed. 48 (2009) 3292–3295.

[34] A.L. Smith, P. Cekan, D.P. Rangel, et al., Theory for spin-lattice relaxation of spin probes on weakly deformable DNA, J. Phys. Chem. B 112 (2008) 9219–9236.

[35] A. Marko, V. Denysenkov, D. Margraf, et al., Conformational flexibility of DNA, J. Am. Chem. Soc. 133 (2011) 13375–13379.

[36] P. Cekan, S.T. Sigurdsson, Single base interrogation by a fluorescent nucleotide: each of the four DNA bases identified by fluorescence spectroscopy, Chem. Commun. (2008) 3393–3395.

[37] D.H. Evans, A.R. Morgan, Extrahelical bases in duplex DNA, J. Mol. Biol. 160 (1982) 117–122.

[38] A.J. Lomant, J.R. Fresco, Polynucleotides. XIV. Photochemical evidence for an extrahelical, solvent-accessible environment of non-complementary residues in polynucleotide helices, J. Mol. Biol. 77 (1973) 345–354.

[39] U. Dornberger, A. Hillisch, F.A. Gollmick, et al., Solution structure of a five-adenine bulge loop within a DNA duplex, Biochemistry 38 (1999) 12860–12868.

[40] F.A. Gollmick, M. Lorenz, U. Dornberger, et al., Solution structure of dAATAA and dAAUAA DNA bulges, Nucleic Acids Res. 30 (2002) 2669–2677.

[41] J.N. Wilson, E.T. Kool, Fluorescent DNA base replacements: reporters and sensors for biological systems, Org. Biomol. Chem. 4 (2006) 4265–4274.

[42] H. Gardarsson, S.T. Sigurdsson, Large flanking sequence effects in single nucleotide mismatch detection using fluorescent nucleoside ζ^{f}, Bioorg. Med. Chem. 18 (2010) 6121–6126.

[43] M.W. Kalnik, D.G. Norman, M.G. Zagorski, et al., Conformational transitions in cytidine bulge-containing deoxytridecanucleotide duplexes: extra cytidine equilibrates between looped out (low temperature) and stacked (elevated temperature) conformations in solution, Biochemistry 28 (1989) 294–303.

[44] J. SantaLucia Jr., D. Hicks, The thermodynamics of DNA structural motifs, Annu. Rev. Biophys. Biomol. Struct. 33 (2004) 415–440.

[45] V. Gervais, J.A. Cognet, M. Le Bret, et al., Solution structure of two mismatches A.A and T.T in the K-ras gene context by nuclear magnetic resonance and molecular dynamics, Eur. J. Biochem. 228 (1995) 279–290.

Biochemical and Biophysical Research Communications 420 (2012) 662–665

Contents lists available at SciVerse ScienceDirect

Biochemical and Biophysical Research Communications

journal homepage: www.elsevier.com/locate/ybbrc

Formation of nanofilms on cell surfaces to improve the insertion efficiency of a nanoneedle into cells

Yosuke Amemiya [a], Keiko Kawano [b], Michiya Matsusaki [c], Mitsuru Akashi [c], Noriyuki Nakamura [b], Chikashi Nakamura [a,b,*]

[a] Biomedical Research Institute, National Institute of Advanced Industrial Science and Technology (AIST), Central 4, 1-1-1 Higashi, Tsukuba, Ibaraki 305-8562, Japan
[b] Department of Biotechnology and Life Science, Tokyo University of Agriculture and Technology, 2-24-26 Naka-cho, Koganei, Tokyo 184-8588, Japan
[c] Department of Applied Chemistry, Graduate School of Engineering Science, Osaka University, 2-1 Yamada-oka, Suita, Osaka 565-0871, Japan

ARTICLE INFO

Article history:
Received 2 March 2012
Available online 17 March 2012

Keywords:
Atomic force microscopy
Nanoneedle
Insertion efficiency
Nanofilm
Fibronectin
Layer by layer formation

ABSTRACT

A nanoneedle, an atomic force microscope (AFM) tip etched to 200 nm in diameter and 10 μm in length, can be inserted into cells with the aid of an AFM and has been used to introduce functional molecules into cells and to analyze intracellular information with minimal cell damage. However, some cell lines have shown low insertion efficiency of the nanoneedle. Improvement in the insertion efficiency of a nanoneedle into such cells is a significant issue for nanoneedle-based cell manipulation and analysis. Here, we have formed nanofilms composed of extracellular matrix molecules on cell surfaces and found that the formation of the nanofilms improved insertion efficiency of a nanoneedle into fibroblast and neural cells. The nanofilms were shown to improve insertion efficiency even in cells in which the formation of actin stress fibers was inhibited by the ROCK inhibitor Y27632, suggesting that the nanofilms with the mesh structure directly contributed to the improved insertion efficiency of a nanoneedle.

1. Introduction

Analyzing intracellular information *in vivo* is a prominent way of understanding the cellular function and the techniques employed are significant for development of novel biomedical applications. The recent progress of nanotechnology has promoted the development of the needle-shaped devices for molecular delivery into cells and analysis of intracellular information with minimum cell damage. Carbon or boron nitride nanotube tips were used for the introduction of quantum dots into a single cell and motion analysis of the quantum dots in the intracellular environments was performed [1,2]. The use of arrays of the vertically aligned carbon or silicon nanowires, carbon nanofibers and carbon nanosyringes enabled the simultaneous introduction of functional molecules into multiple cells [3–6]. Electrophysiological analysis in the intracellular environment can be performed with needle-shaped nanoelectrodes partially coated with insulating materials [7–9]. Recently, the endoscopic approaches using the needle-shaped devices have been proposed. A multiwalled carbon nanotube tip coated with gold particles was used as a probe in surface-enhanced Raman spectroscopy [10] and an SnO_2 nanowire was used as an optical waveguide to illuminate the excitation light at a high spatial resolution in the cells [11].

We have been developing techniques for cell manipulation and analysis using an atomic force microscope (AFM) with a silicon "nanoneedle", which is a silicon AFM tip etched to a cylindrical shape with a 200 nm diameter and a 10 μm length using a focused ion beam. The nanoneedle can be efficiently inserted into cells [12,13] and the use of a functionalized nanoneedle allows highly efficient DNA transfection [14] and detection of intracellular mRNA [15] and cytoskeletal proteins [16]. The use of AFM for inserting nanoneedle into cells has the advantage that the insertion events can be confirmed by analyzing the force response during the insertion process [13]. Techniques for the validation of the insertion events are essential for surveying intracellular information without artifacts derived from the false insertion. It is reported that the nanosized electrodes with a 150 nm diameter and a 1.5 μm length cannot penetrate the cell membrane of HL-1 cells (a mouse cardiac muscle cell line), which had been seeded on a nanosized electrode array, without applying external voltage [9]. Similarly, we found that some cell lines showed low insertion efficiency of the nanoneedle using our manipulation apparatus. We reported that the insertion efficiency of the nanoneedle varies depending on the cell species and that stress fibers and actin meshwork comprising the plasmalemmal undercoat is essential for the nano-

* Corresponding author at: Biomedical Research Institute, National Institute of Advanced Industrial Science and Technology (AIST), Central 4, 1-1-1 Higashi, Tsukuba, Ibaraki 305-8562, Japan. Fax: +81 29 861 3048.
E-mail address: chikashi-nakamura@aist.go.jp (C. Nakamura).

0006-291X/$ - see front matter © 2012 Elsevier Inc. All rights reserved.
http://dx.doi.org/10.1016/j.bbrc.2012.03.062

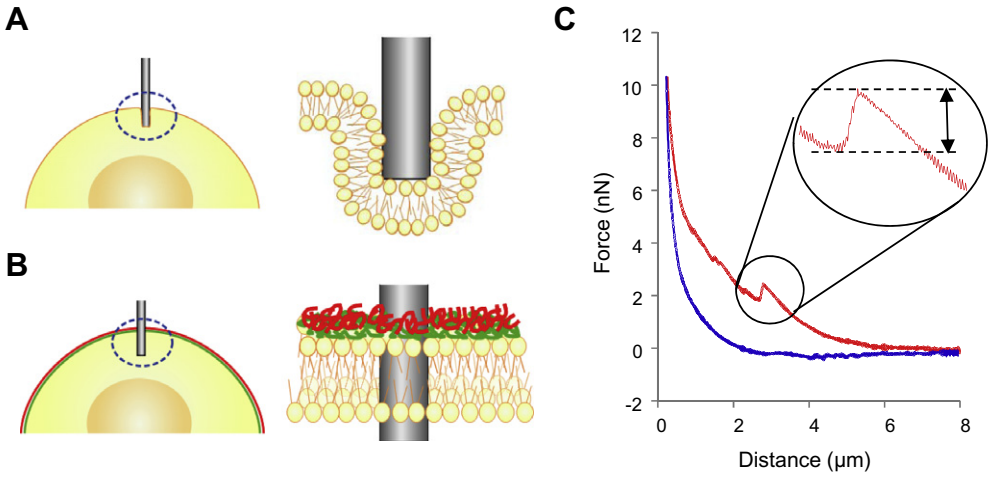

Fig. 1. Schematic illustrations of the nanoneedle insertion into cells, without (A) and with (B) the FN-G or FN-DS nanofilms on cell surfaces. Green lines indicate fibronectin and red lines indicate gelatin or dextran sulfate. The force drop event shown in the force curve was obtained as a nanoneedle was extended to and then retracted from cells (C).

needle insertion [17]. This finding led us to conceive the idea that mesh structures formed on a cell surface would improve the insertion efficiency of the nanoneedle (Fig. 1A and B). The nano-sized mesh-like morphology of the thin films, which consist of extracellular matrix molecules, can be form on the cell surface using a layer-by-layer technique [18,19]. The cytotoxicity of the nanofilms is low and therefore the nanofilms are good candidates as nanostructures formed on the cell surface for the improvement in the insertion efficiency of the nanoneedle. Here, we investigated the effect of the nanofilms formed on cell surfaces on the insertion efficiency of the nanoneedle.

2. Methods

2.1. Cell culture

1×10^5 cells of mouse embryonic fibroblast cell line, Balb3T3 (RIKEN Cell Bank, Tsukuba, Japan) were seeded on collagen-coated 35 mm glass-bottom culture dishes (φ 27 mm, Asahi Glass, Tokyo, Japan) and cultivated in Dulbecco's Modified Eagle's Medium (DMEM) (Invitrogen, Carlsbad, CA, USA) containing 10% fetal bovine serum (FBS) (Gibco, Grand Island, NY, USA), overnight. The collagen-coated glass-bottom culture dishes were prepared by putting the 0.05 mg/mL collagen (Collagen Type I from calf skin, Sigma–Aldrich, St. Louis, MO, USA) solution on the glass surface and then incubating for 1 h at room temperature, followed by washing with PBS. 1×10^5 cells of mouse P19 embryonic carcinoma cells (Dainippon Sumitomo Pharma, Osaka, Japan) were cultivated in polystyrene Petri dishes (φ 90 mm, As one, Tokyo, Japan) with α-MEM (Invitrogen) containing 10% FBS, 2 mM GlutaMAX (Gibco), Gentamicin–Amphotericin B (10 and 0.25 μg/mL, Cascade Biologics, Portland, OR, USA) for 4 days in the presence of 1 μM all-trans retinoic acid (RA) (Sigma–Aldrich). The resulting cell aggregates were treated with 0.025% trypsin and 0.01% EDTA solution for 10 min at room temperature and then centrifuged to form a pellet. The cell pellet was dispersed in the culture media and the cells were seeded onto the plastic slips (Cell Desk, Sumitomo Bakelite, Tokyo, Japan) coated with polyethyleneimine (Sigma–Aldrich). The polyethyleneimine-coated plastic slips were prepared by incubating coverslips in 0.02% polyethyleneimine solution for 1 h, followed by washing with PBS. The cells were cultivated on the plastic slip for 2–6 days. All cells were cultured at 37 °C under 5% CO_2.

2.2. Formation of nanofilms on cell surfaces

The nanofilms composed of fibronectin (fibronectin from Bovine Plasma, Wako, Osaka, Japan) and gelatin (Wako) (FN-G nanofilm) and fibronectin and dextran sulfate (Wako) (FN-DS nanofilm) were formed on cell surfaces using a layer by layer technique, as described previously [18]. Briefly, the cultured Balb3T3 or differentiation-induced P19 cells were incubated in PBS containing 0.2 mg/mL fibronectin for 1 min at room temperature and then washed with PBS. The cells were incubated in PBS containing 0.2 mg/mL gelatin or sodium dextran sulfate for 1 min at room temperature and then washed with PBS. The consecutive treatments with fibronectin and gelatin were conducted 1, 3, 5 and 10 times to form FN-G nanofilms (FN-G1, FN-G3, FN-G5, and FN-G10) on cell surfaces. The consecutive treatments with fibronectin and dextran sulfate were conducted once to form FN-DS nanofilms (FN-DS1). The cells coated with the nanofilms were cultivated for 24 h and used for the following experiments.

2.3. Treatment of cells with Y27632

The Balb3T3 cells coated with FN-G3 were incubated in the culture media containing 100 μM Y27632 (Calbiochem, Darmstadt, Germany) for 1 h at 37 °C, followed by washing with PBS.

2.4. Immunostaining

P19 cells treated with RA were fixed with 4% formaldehyde (Wako) for 15 min, washed with PBS and treated with 0.1% Triton X-100 (Nacalai Tesque, Kyoto, Japan) in PBS for 3 min. The cells were then washed with PBS 3 times and treated with 4% BLOCK ACE (Dainippon Sumitomo Pharma, Osaka, Japan) for 1 h at room temperature. The cells were incubated with PBS containing 15 nM anti-Neurofilament-L antibody (Neurofilament-L (C28E10) Rabbit mAb, Cell Signaling Technology, Danvers, MA, USA) for 1 h at room temperature and then washed with PBS. The cells were incubated with PBS containing 15 nM Alexa Fluor 568-labeled goat anti-rabbit IgG (Invitrogen) for 1 h at room temperature and then washed with PBS. Consecutively, the cells were incubated with PBS containing 15 nM anti-βIII tubulin antibody (Neuronal Class III β-Tubulin (TUJ1) Mouse Monoclonal Antibody, Covance, Berkeley, CA, USA) for 1 h at room temperature. The cells were washed with PBS and then incubated with PBS containing 15 nM Alexa

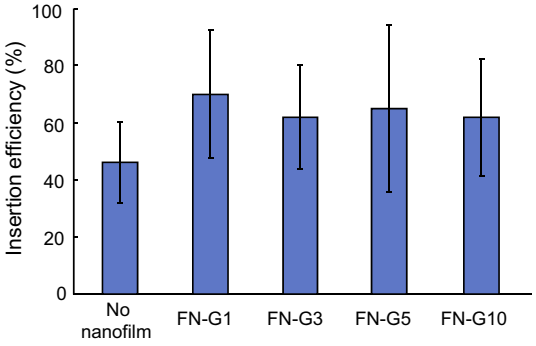

Fig. 2. Insertion efficiency of a nanoneedle into Balb3T3 cells where FN-G nanofilms were formed with different numbers of deposition processes.

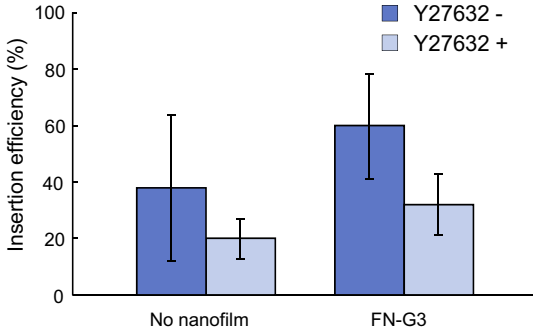

Fig. 3. Insertion efficiency of nanoneedle into Balb3T3 cells treated with Y27632. The cells coated with and without FN-G3 were used.

Fluor 488-labeled goat anti-mouse IgG (Invitrogen) for 1 h at room temperature. The cells were washed with PBS and then observed on a fluorescence microscope equipped with a cooled CCD camera system (DP 30/IX71, Olympus, Tokyo, Japan).

2.5. Insertion of a nanoneedle into cells and force measurements

The silicon nanoneedle with a cylindrical tip with a 200 nm diameter and a 10 μm length was prepared as described previously [13], except for selecting a cantilever with a spring constant of 0.03 to 0.2 N/m (ATEC-CONT, Nanosensors, Neuchatel, Switzerland). Insertions of the nanoneedle into cells were conducted with AFM, model NanowizardII BioAFM (JPK Instruments, Berlin, Germany). The force exerted on the nanoneedle during the insertion and retraction process was monitored using a force spectroscopy mode. Insertion of a nanoneedle was performed 10 times per cell at different positions on the cell with a tip velocity of 10 μm/s. The insertion efficiency was calculated by measuring the appearance frequency of force drop events, which indicated the penetration of cell membrane by the nanoneedle (Fig. 1C) [12], against 10 cells at each condition. A force drop of over 300 pN was judged as a successful insertion of the nanoneedle into cells.

3. Results and discussion

3.1. Insertion of a nanoneedle into Balb3T3 cells coated with FN-G nanofilms

Formation of FN-G nanofilms on Balb3T3 cells increased the insertion efficiency of a nanoneedle into the cells (Fig. 2). While the average insertion efficiency of the nanoneedle into Balb3T3 cells without the nanofilms was 46%, the average efficiency obtained with FN-G nanofilms was 65%. It is strongly suggested that this increase of the insertion efficiency is due to the formation of FN-G nanofilms with the mesh-like structure on the cell surface, as has been observed in another study [19]. Repetition of the deposition processes of forming the FN-G nanofilms did not increase the insertion efficiency (Fig. 2), suggesting the uniform formation of the nanofilms on the cell surfaces in a single deposition process. Phase contrast microscopy did not show any significant morphological changes of the cells caused by forming the nanofilms on the cell surfaces (Supplementary Fig. 1), indicating the low cytotoxicity of the FN-G nanofilms [19].

3.2. Effect of Y27632 treatment to Balb3T3 cells coated with FN-G nanofilms on insertion efficiency of a nanoneedle

Reorganization of stress fibers in cells is deeply involved with fibronectin–integrin interactions [20]. Therefore, the increased insertion efficiency of the nanoneedle by forming FN-G nanofilms on the cell surfaces may not be due to the direct effect of the mesh nanostructures formed on the cell surfaces, but the indirect effect of reorganized stress fibers induced by fibronectin–integrin interactions. To exclude the effect of stress fibers on the insertion efficiency of the nanoneedle into cells, we diminished stress fibers in Balb3T3 cells coated with FN-G3 by treating the cells with a ROCK inhibitor Y27632 (Supplementary Fig. 2) [21]. The insertion efficiency of the nanoneedle into the cells treated with Y27632 is shown in Fig. 3. The cells coated with FN-G3 showed an increased insertion efficiency compared to those without the nanofilms even after treatment with Y27632, suggesting that the nanofilms formed on the cell surface were directly involved with the increased insertion efficiency of the nanoneedle.

3.3. Insertion of a nanoneedle into P19 cells differentiation-induced into neural cells coated with FN-G or FN-DS nanofilms.

The nanoneedle was inserted into RA-treated P19 cells, both without and with FN-G1 or FN-DS1. Differentiation induction of P19 cells into neural cells was confirmed by immunostaining of neurofilament and βIII tubulin after the insertion experiments. Not all cells showed the both neurofilament and βIII tubulin positive (Supplementary Fig. 3). We thus calculated the insertion efficiency of the nanoneedle in the double positive cells. The insertion efficiency of the nanoneedle into the neural cells was extremely low (~20%) (Fig. 4). Interestingly, formation of FN-G1 on the neural cells did not increase the insertion efficiency of nanoneedle, unlike the Balb3T3 cells (Figs. 2 and 4). Then we formed FN-DS nanofilms, which are thicker than FN-G nanofilms [19], on the neural cells and measured the insertion efficiency of the nanoneedle. The formation of FN-DS1 on the Day 3 neural cells

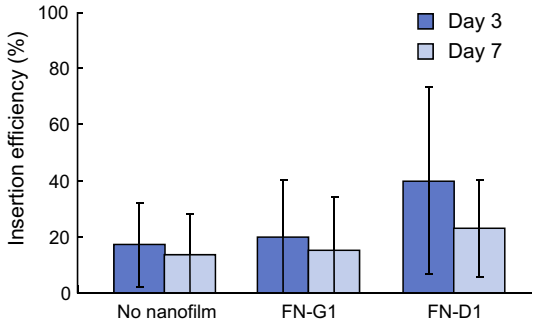

Fig. 4. Insertion efficiency of nanoneedle into neural cells induced from P19 cells. The induced cells were cultivated for 2 or 6 days after RA treatment and then FN-G1 or FN-DS1 was formed on the cell surfaces.

increased the insertion efficiency up to around 40% (Fig. 4). This may be because the FN-DS1is more stable on neural cells than FN-G1. However, formation of the FN-DS1 on the Day 7 neural cells increased the insertion efficiency only up to around 25% (Fig. 4). This suggests that the FN-DS1 formed on the Day 7 neural cells was unstable compared to those on Day 3 neural cells. In cortical progenitor cells, expression of α5β1 integrin decreases during neuronal differentiation [22]. All nanofilms used here are based on fiblonectin and therefore, the nanofilms do not adhere strongly to the cells with a low expression level of integrin. In this study, the Day 7 neural cells were detached more frequently from the dish surface than the Day 3 neural cells, indicating that the Day 7 neural cells have weak adhesion to the dish surface. This may be a result from reorganization of stress fiber caused by the decreased expression of integrin in the cells and lead to the low insertion efficiency observed in the Day 7 neural cells coated with nanofilms.

In the present study, we utilized extracellular matrix nanofilms formed on cell surfaces to improve insertion efficiency of the nanoneedle. Increased insertion efficiency was exhibited in Balb3T3 fibroblasts and neural cells differentiation-induced from P19 cells where the nanofilms with nanosized mesh-like morphology were formed. No obvious cytotoxicity was seen after forming the nanofilms on the cell surfaces. Therefore, this technique is considered to be useful for the nanoneedle-based cell manipulation and intracellular analysis.

Acknowledgments

This research was partially supported by the Japan Society for the Promotion of Science (JSPS) through the "Funding Program for Next Generation World-Leading Researchers (NEXT Program)", initiated by the Council for Science and Technology Policy (CSTP).

Appendix A. Supplementary data

Supplementary data associated with this article can be found, in the online version, at http://dx.doi.org/10.1016/j.bbrc.2012.03.062.

References

[1] X. Chen, A. Kis, A. Zettl, et al., A cell nanoinjector based on carbon nanotubes, Proc. Natl. Acad. Sci. USA 104 (2007) 8218–8222.
[2] K. Yum, S. Na, Y. Xiang, et al., Mechanochemical delivery and dynamic tracking of fluorescent quantum dots in the cytoplasm and nucleus of living cells, Nano. Lett. 9 (2009) 2193–2198.
[3] W. Kim, J.K. Ng, M.E. Kunitake, et al., Interfacing silicon nanowires with mammalian cells, J. Am. Chem. Soc. 129 (2007) 7228–7229.
[4] D.G. Mann, T.E. McKnight, J.T. McPherson, et al., Inducible RNA interference-mediated gene silencing using nanostructured gene delivery arrays, ACS Nano 2 (2008) 69–76.
[5] S. Park, Y.S. Kim, W.B. Kim, et al., Carbon nanosyringe array as a platform for intracellular delivery, Nano. Lett. 9 (2009) 1325–1329.
[6] A.K. Shalek, J.T. Robinson, E.S. Karp, et al., Vertical silicon nanowires as a universal platform for delivering biomolecules into living cells, Proc. Natl. Acad. Sci. USA 107 (2010) 1870–1875.
[7] P. Sun, F.O. Laforge, T.P. Abeyweera, et al., Nanoelectrochemistry of mammalian cells, Proc. Natl. Acad. Sci. USA 105 (2008) 443–448.
[8] X. Duan, R. Gao, P. Xie, et al., Intracellular recordings of action potentials by an extracellular nanoscale field-effect transistor, Nat. Nanotechnol. 7 (2012) 174–179.
[9] C. Xie, Z. Lin, L. Hanson, et al., Intracellular recording of action potentials by nanopillar electroporation, Nat. Nanotechnol. 7 (2012) 185–190.
[10] R. Singhal, Z. Orynbayeva, R.V. Kalyana Sundaram, et al., Multifunctional carbon-nanotube cellular endoscopes, Nat. Nanotechnol. 6 (2011) 57–64.
[11] R. Yan, J.H. Park, Y. Choi, et al., Nanowire-based single-cell endoscopy, Nat. Nanotechnol. 7 (2012) 191–196.
[12] I. Obataya, C. Nakamura, S. Han, et al., Nanoscale operation of a living cell using an atomic force microscope with a nanoneedle, Nano. Lett. 5 (2005) 27–30.
[13] I. Obataya, C. Nakamura, S. Han, et al., Mechanical sensing of the penetration of various nanoneedles into a living cell using atomic force microscopy, Biosens. Bioelectron. 20 (2005) 1652–1655.
[14] S. Han, C. Nakamura, N. Kotobuki, et al., High-efficiency DNA injection into a single human mesenchymal stem cell using a nanoneedle and atomic force microscopy, Nanomedicine 4 (2008) 215–225.
[15] T. Kihara, N. Yoshida, T. Kitagawa, et al., Development of a novel method to detect intrinsic mRNA in a living cell by using a molecular beacon-immobilized nanoneedle, Biosens. Bioelectron. 26 (2010) 1449–1454.
[16] S. Mieda, Y. Amemiya, T. Kihara, et al., Mechanical force-based probing of intracellular proteins from living cells using antibody-immobilized nanoneedles, Biosens. Bioelectron. 31 (2012) 323–329.
[17] H. Kagiwada, C. Nakamura, T. Kihara, et al., The mechanical properties of a cell, as determined by its actin cytoskeleton, are important for nanoneedle insertion into a living cell, Cytoskeleton 67 (2010) 496–503.
[18] M. Matsusaki, K. Kadowaki, Y. Nakahara, et al., Fabrication of cellular multilayers with nanometer-sized extracellular matrix films, Angew. Chem. Int. Ed. Engl. 46 (2007) 4689–4692.
[19] K. Kadowaki, M. Matsusaki, M. Akashi, Control of cell surface and functions by layer-by-layer nanofilms, Langmuir 26 (2010) 5670–5678.
[20] I. Wierzbicka-Patynowski, J.E. Schwarzbauer, The ins and outs of fibronectin matrix assembly, J. Cell Sci. 116 (2003) 3269–3276.
[21] M. Uehata, T. Ishizaki, H. Satoh, et al., Calcium sensitization of smooth muscle mediated by a Rho-associated protein kinase in hypertension, Nature 389 (1997) 990–994.
[22] N. Yoshida, S. Hishiyama, M. Yamaguchi, et al., Decrease in expression of alpha 5 beta 1 integrin during neuronal differentiation of cortical progenitor cells, Exp. Cell Res. 287 (2003) 262–271.

Biochemical and Biophysical Research Communications 420 (2012) 666–670

Contents lists available at SciVerse ScienceDirect

Biochemical and Biophysical Research Communications

journal homepage: www.elsevier.com/locate/ybbrc

Maternally-derived antibody to fibroblast growth factor-23 reduced dietary phosphate requirements in growing chicks

Elizabeth A. Bobeck, Kimberly S. Burgess, Taylor R. James, Michelle L. Piccione, Mark E. Cook *

Animal Sciences Department, 1675 Observatory Drive, University of Wisconsin-Madison, Madison, WI 53706, USA

ARTICLE INFO

Article history:
Received 2 March 2012
Available online 17 March 2012

Keywords:
FGF-23
Anti-FGF-23 antibody
Phosphate requirement
Chicken
Dietary phosphate
Plasma phosphate

ABSTRACT

Phosphate in manure of monogastric animals pollutes the environment if improperly applied to soil. Strategies that reduce phosphate inputs into animal production systems reduce environmental pollution. Using a novel vaccine to fibroblast growth factor-23 (FGF-23), we induced neutralizing antibodies that reduced the phosphate requirement of growing chickens. Breeding hens were injected with a FGF-23 peptide (AFLPGMNP) conjugate. Antibody was passively transferred from hen to chick and chick response to deficient dietary phosphate intake was determined. Chicks without passive anti-FGF-23 antibody had a 43% and 21% reduction in blood phosphate and bone ash, respectively, when fed a phosphate deficient diet and compared to chicks fed a phosphate replete diet ($P < 0.05$). Chicks with circulating anti-FGF-23 antibodies fed the phosphate deficient diet had plasma phosphate and bone ash that did not differ from chicks fed the phosphate replete diet ($P > 0.05$). Neutralization of FGF-23 offers a new approach to reduce phosphate requirements of farmed animals and may provide a new means to reduce phosphate pollution related to animal farming.

1. Introduction

Fibroblast growth factor-23 (FGF-23) is a hormone that inhibits renal tubular phosphate resorption. FGF-23 reduces synthesis and increases degradation of active vitamin D_3, a renal activated vitamin necessary for maintenance of intestinal phosphate absorption [1]. Levels of circulating FGF-23 increase in healthy humans and animals to homeostatically regulate serum phosphate levels that transiently increase in response to diet [2,3]. In modern animal agriculture (e.g., swine and poultry), dietary phosphate is tightly controlled in an attempt to minimize excreted phosphate and to control feed cost [4]. While FGF-23's regulation of plasma phosphate is biologically relevant when dietary phosphate levels vary greatly (such as wildlife), FGF-23's response to farmed animal diets could be counterproductive since dietary phosphate levels rarely exceed animal needs.

Phosphate levels in monogastric animal excreta limits the quantity of manure that can be applied to soils for crop production. Manure application rates necessary to meet crop nitrogen requirements results in excess phosphate levels and potential environmental pollution, hence manure is applied based upon soil phosphate concentration and crop phosphate requirements [5]. Manure applied to meet crop phosphate needs requires a second application of inorganic nitrogen fertilizer to the soils (a significant cost to the crop producer, also increasing soil compaction). Ideally, excreta is most valuable if the N:P ratio equals plant needs. Current methods to reduce dietary phosphate inputs into monogastric diets involve the use of phytase that improves the bioavailability of plant phytate phosphate present in animal feeds; however, simply improving phosphate bioavailability will not improve absorption of phosphate particularly if phosphate absorption is under regulation of FGF-23. We hypothesized that neutralization of circulating FGF-23 would significantly reduce the dietary requirement for phosphate and thereby reduce the total phosphate input needed for animal agriculture.

Indeed, FGF-23 knockout mice fed the recommended NRC dietary level of phosphate develop hyperphosphatemia [6]. This finding suggests that neutralization of FGF-23 alters an animal's response to dietary phosphate. To test this hypothesis, we used a chick model with maternally-derived passive antibody to FGF-23 to determine if antibody neutralization of FGF-23 early in life would decrease the phosphate requirement of growing chicks. We identified a specific FGF-23 peptide that when used as a maternal vaccine, reduced the progeny dietary phosphate requirement.

2. Methods

2.1. Peptide selection

Universal Protein Resource Knowledgebase (Uniprot KB) was used to access the sequence of human fibroblast growth factor

* Corresponding author. Fax: +1 608 262 5157.
E-mail address: mcook@wisc.edu (M.E. Cook).

0006-291X/$ - see front matter © 2012 Elsevier Inc. All rights reserved.
http://dx.doi.org/10.1016/j.bbrc.2012.03.063

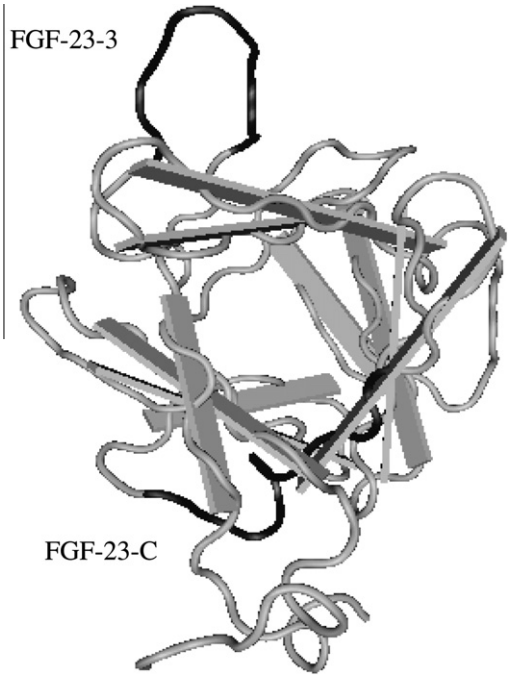

Fig. 1. Human FGF-23 (PDB ID: 2P39; Uniprot ID: Q9GZV9) with FGF-23-3 (AFLPGMNP) and FGF-23-C (QTIYSALMI) peptide sequences. Black highlighting on the FGF-23 molecule denotes peptide region used to make a peptide conjugate for stimulation of antibody production in the laying hen.

23 (FGF-23) (Uniprot ID: Q9GZV9). The sequence was directly copied into BepiPred 1.0 server to identify antigenic regions. Due to the high sequence homology of human FGF-23 and chick putative FGF-23 (Uniprot ID: F1P5Y6), the human 3-dimensional structure (PDB ID: 2P39) was used to identify antigenic peptide regions (9 and 8 amino acids in length, respectively) that were found on the surface of the molecule. Two regions on opposing sides of the FGF-23 molecule were selected to produce peptides for antibody synthesis, internally coded as FGF-23-C (QTIYSALMI) and FGF-23-3 (AFLPGMNP) (Fig. 1). Peptide sequences chosen were synthesized in 5-milligram quantities by Genscript (Piscataway, NJ).

2.2. Peptide antibody production: conjugation and injection

Each of the peptides (FGF-23-C and FGF-23-3) were individually conjugated to bovine gamma globulin (BgG, Sigma, St. Louis, MO) using glutaraldehyde conjugation. Briefly, 2 mg of the carrier protein BgG was dissolved in 0.1 molar acetate buffer. 2 mg of each peptide was then added to the buffer (1:1 peptide to carrier protein ratio), followed by 0.23 mL of 2 M glutaraldehyde and allowed to conjugate for 3 h at room temperature. The reaction was stopped with 10 mg glycine for 1 h. Dialysis occurred overnight in 1L PBS at room temperature using 6000-8000 molecular weight dialysis tubing. Three hens per peptide were injected using 0.33 mg/hen/injection using methods previously described [7]and yolks were freeze-dried for subsequent antibody analyses.

2.3. Enzyme-linked immunosorbent assay (ELISA)

ELISA was utilized to demonstrate the presence of the anti-FGF-23 peptide antibodies in the yolks of eggs laid by vaccinated hens. Indirect ELISA methods were as previously described [7] except the antigen coated was 100 μg/ plate of ovalbumin (OVA) or peptide-specific (3 or C) OVA conjugate, and blocking was accomplished using a non-protein blocking buffer (175 μl/well, Pierce Scientific, Rockford, IL). A second ELISA was run as described above, except native FGF-23 (human recombinant, Adipogen, San Diego, CA) or ovalbumin (OVA, Pierce Scientific) was used to coat the plate overnight (0.5 mg/mL) instead of an OVA-peptide conjugate. After blocking, antibodies to FGF-23-3, FGF-23-C, or FCA were incubated overnight at 1:1000 dilution and secondary antibody, substrate, and stop solution were all applied as described above. Primary antibodies applied to OVA were used as blanks (negative control; indicator of non specific binding).

Table 1
Experimental diet and base mix composition*.

Ingredient	Deficient Pi (%)	Adequate Pi (%)
Base Mix*	96.60	96.60
$CaCO_3$	–	0.96
KH_2PO_4	–	1.20
Sand	3.40	1.24
Base Mix*		g/100 g
Corn		51.93
Soy 48		40.50
Corn Oil		5.10
$CaCO_3$		1.35
Salt		0.41
DL-Methionine		0.20
Vit-Min Mix		0.51

* A corn and soy-based base mix was formulated according to chick requirements, less added inorganic phosphate [8,9]. The base mix contained (by analysis) 0.4% total phosphate, with 0.13% calculated to be inorganic phosphate and 0.27% calculated as unavailable phytate phosphate. The base mix vitamin/ mineral mix in a corn starch carrier supplied/ kg diet 70 mg Mn; 71.4 mg Zn; 5 mg Cu; 4550 IU vitamin A; 600 IU vitamin D_3; 182 IU vitamin E; 1 mg vitamin K; 20 ug B12; 49.5 mg niacin; 43 mg pantothenate; 4.95 mg riboflavin; and 2001 mg choline chloride. The final two diets were prepared by adding the supplements shown to the base mix. For the adequate phosphate diet, phosphate was added for a final diet composition of 0.62% total phosphate where 0.36% was inorganic phosphate and 0.26% was phytate phosphate. The normal diet was supplemented with calcium carbonate in a manner to maintain a total phosphate: calcium ratio of 1:2. Abbreviations; Pi = inorganic phosphate, VitMin = Vitamin/Mineral Premix.

2.4. Experimental animal population

All experimental procedures were approved by the University of Wisconsin College of Agricultural and Life Sciences Animal Care and Use Committee. Single Comb White Leghorn laying hens injected with the above mentioned FGF-23 peptide conjugates or FCA control were artificially inseminated once a week for two consecutive weeks with pooled New Hampshire rooster semen after 21 days following the primary injection or within 2 months of any booster injection used. Fertile eggs were incubated for 21 days, hatched, divided into groups based on the hens' peptide injection treatment, and assigned to one of two diets (Table 1): Diet 1) Basal: no added dietary phosphate (phosphate deficient with 0.13% available inorganic phosphorus and 0.27% unavailable phytate phosphorus, where the chick requirement = 0.40% available phosphorus) [8], Diet 2) Basal+calcium and phosphorus in a balance ratio of 2:1 to meet dietary requirements. Chicks per treatment varied due to number of fertile eggs laid, set, and hatched per hen within each treatment group (see results for n/group). On day 14 on the experimental diets, chicks were weighed, bled for the determination of plasma phosphate, and the tibiotarsi were collected from euthanized chicks for bone ash determination as previously described [9]. Day 14 was used as the termination date to prevent severe phosphate deficient rickets and to assure continued presence of maternal antibody.

2.5. Data analysis

Data were analyzed by using two-way ANOVA as a 2×3 factorial (two diets and three antibody treatments) with SAS (SAS Institute Inc., Cary, NC). Data were analyzed for main effects of diet,

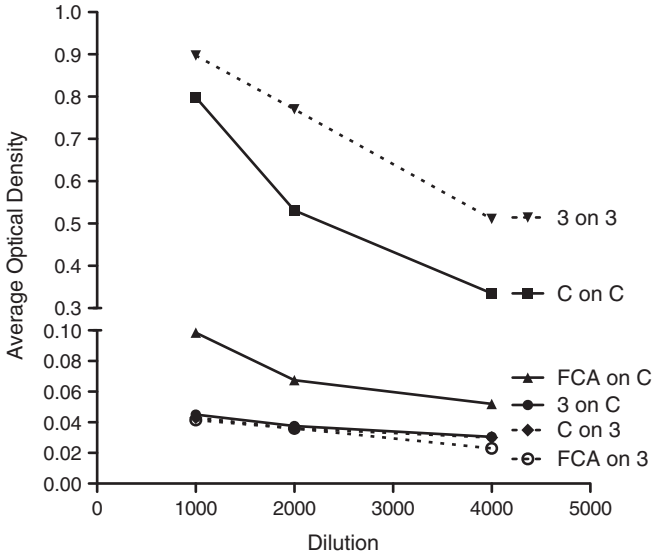

Fig. 2A. Specificity of antibodies to their respective peptides. Antibodies were collected from egg yolks of hens injected with control (FCA; adjuvant only), FGF-23 peptide 3, or FGF-23 peptide C and were conjugated to bovine gamma globulin. Each extracted antibody (see materials and methods) was diluted 1:1000, 1:2000, or 1:4000 for determination of reactivity against peptide 3 or C conjugated to ovalbumin (OVA) using enzyme-linked immunosorbent assay (ELISA). In the graph legend, (X on Y, where X = antibody and Y = OVA-conjugate, e.g., anti-FGF-23 antibody tested on ova-peptide C conjugate), only background optical density values were observed when antibody and conjugate was dissimilar.

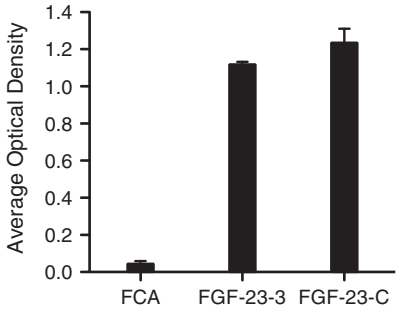

Fig. 2B. Specificity of antibodies to respective regions on the native human recombinant FGF-23 protein molecule. Antibodies were collected from egg yolks of hens injected with control (FCA; adjuvant only), and FGF-23 peptide 3, or FGF-23 peptide C conjugated to bovine gamma globulin. Each extracted antibody (see materials and methods) was diluted 1:1000 for determination of reactivity against the native FGF-23 protein. Results above show both FGF-23-3 and FGF-23-C peptide antibodies specifically recognize native FGF-23, whereas FCA antibodies do not.

antibody and the diet X antibody interactions. Post-ANOVA analyses of mean treatment differences were conducted if the diet X antibody interaction was significant ($P < 0.05$) using least squared differences (plasma phosphate and bone ash percentage). Data are shown as mean ± standard error of the mean.

3. Results

Eggs collected from hens injected with control or their respective peptide conjugate were used in an ELISA assay to determine the transfer of peptide specific antibody to the egg yolk. Egg yolk antibody diluted as little as 1:1000 showed peptide specific binding when compared to control antibody or nonspecific peptide conjugate antibody (i.e., FGF-23-C antibody on FGF-23-3 peptide or vice versa, Fig. 2A). When FGF-23 or FCA control antibodies were co-incubated with native FGF-23, both FGF-23 antibodies bound equally to native FGF-23, whereas control antibody did not (Fig. 2B).

Following the artificial insemination procedures, eggs were collected from the control and FGF-23 vaccinated hens. A total of 30, 41, and 39 eggs were collected from the hens injected with the control, FGF-23-C, and FGF-23-3, respectively. No differences in the percent egg fertility and hatch of fertile eggs was observed as a result of vaccine treatment. All chicks within a vaccine treatment group were divided equally and assigned to either the low or adequate phosphate diet: FCA control, 10 chicks each for low and adequate phosphate diets; FGF-23-C, 12 and 11 chicks for low and adequate phosphate diet; and FGF-23-3, 18 chicks each for the low and adequate phosphate diet. After 2 weeks on the dietary treatments, chicks fed the adequate phosphate diet across all vaccine treatment groups had similar levels of plasma phosphate; whereas those fed the low phosphate diet had dissimilar plasma phosphate (diet X vaccine interaction $P < 0.027$, Fig. 3A).

Control chicks on a low phosphate diet had 43% less plasma phosphate as compared to control chicks fed adequate phosphate ($P = 0.0032$), anti-FGF-23-C chicks fed a low phosphate diet had a 50% reduction in plasma phosphate compared to anti-FGF-23-C chicks fed adequate phosphate ($P < 0.0001$), whereas anti-FGF-23-3 chicks fed a low phosphate diet showed no significant decrease in plasma phosphate relative to anti-FGF-23-3 chicks fed adequate phosphate ($P = 0.19$). Chicks with circulating anti-FGF-23-3 maternal antibodies and fed the low phosphate diet, had plasma phosphate that was increased 31% and 33% above chicks fed the same diet but with circulating levels of control or anti-FGF-23-C antibodies, respectively ($P < 0.05$). Hens producing control, anti-FGF-23-C and anti-FGF-23-3 antibodies had similar plasma phosphate levels (control = 4.8 mg/dL ± 0.95; anti-FGF-23-C = 4.4 mg/dL ± 0.98; anti-FGF-23-3 = 5.3 mg/dL ± 0.40).

Percent bone ash was similar between vaccine treatment groups fed the phosphate adequate diet; however, a significant interaction between diet and maternal vaccination was observed ($P > 0.05$, Fig. 3B). Control antibody and anti-FGF-23-C antibody chicks fed the phosphate deficient diet had a 21% ($P = 0.014$) and 29% ($P < 0.001$), respectively, reduction in bone ash percent when compared to relevant chicks fed adequate levels of phosphate. However, chicks with maternal anti-FGF23-3 antibody did not have a significantly reduced percent bone ash when fed a low phosphate diet and compared to anti-FGF-23-3 chicks fed adequate phosphate ($P = 0.44$). Chicks with anti-FGF-23-3 maternal antibody and fed a low phosphate diet had an 11% ($P = 0.19$) and 20% ($P = 0.01$) increase in bone ash percent when compared to control and FGF-23-C chicks, respectively, fed the low phosphate diet.

While chicks fed low phosphate had decreased weight gain regardless of maternal antibody type (main effect of diet, $P = 0.0006$), there was no protection against decreased weight gain due to maternal antibody source (interaction of diet X maternal antibody, $P = 0.65$, Fig. 3C).

4. Discussion

The use of therapeutic antibodies to host targets is well described in the literature. Humanized monoclonal antibodies for the treatment of inflammatory disease are routine [10]. Recently, researchers have shown that the injection of neutralizing antibodies to FGF-23 was effective at improving phosphate status of the *Hyp* mouse; a line of mice that have hypophosphatemia due to elevated circulatory levels of FGF-23 [11,12]. Here we demonstrate that neutralizing antibodies to FGF-23 were effective at reducing the phosphate requirement of healthy chicks, an approach not previously studied. In retrospect, the results of our study were not surprising since it was also well established that deletion of gene for FGF-23 induced hyperphosphatemia [13], a finding which

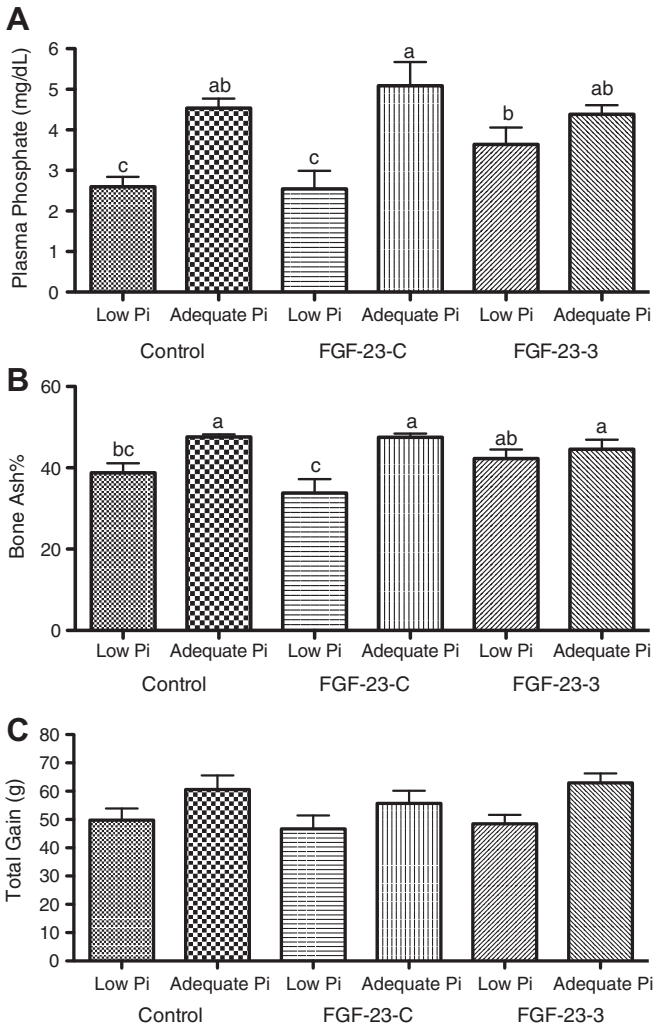

Fig. 3. (A) Plasma phosphate (mg/dL); (B), bone ash percentage; and (C), total gain (grams) of chicks from hens vaccinated to induce the passive transfer of anti-FGF-23 antibodies to the chicks. Low Pi and adequate Pi contained 0.13% and 0.36% available phosphate, respectively, and were the diet chicks were fed the first 14 days post hatch. Control, FGF-23-C and FGF-23-3 are indicative of the vaccines used in the maternal vaccination to stimulate antibody to FGF-23. Hens injected with control received on the adjuvant, and hens injected with FGF peptides conjugated to bovine gamma globulin. ^{abc}Indicates significant difference between groups, $P < 0.05$. Abbreviations: Pi = inorganic phosphate. Total gain has no superscript since antibody * diet interaction was non-significant and hence post-ANOVA analyses were not conducted.

suggested the key role of FGF-23 in limiting dietary phosphate assimilation and increased renal excretion of phosphate. Producers of farm animals seek to maximize the intestinal absorption and retention of phosphate both for cost implications (dietary phosphate is an expensive feed ingredient) and for environmental reasons (phosphate excretion is an environmental concern in animal production systems). Hence, the finding that neutralization of FGF-23 decreases chick phosphate requirement has potential use in modern agricultural systems.

The model used in these experiments, where maternal neutralizing antibody is passed to the newly hatch chick, is essentially equivalent to the direct injection of neutralizing antibody. The maternal antibody transfer model was used in these initial studies to eliminate potential confounding effects of other direct immune responses (e.g., cellular immunity) since cellular immune elements are not passively transferred to the chick. Maternal antibody in the chick is well documented to circulate for up to 3 weeks post-hatch [14,15], and has been used as a means of delivering antibodies to alter biological function in the progeny [16,17]. While it is not shown here, a direct vaccination of an animal to induce auto-neutralizing antibodies to FGF-23 may also be an effective means of reducing the phosphate requirement of an animal.

Chicks with circulatory anti-FGF-23-3 antibody and fed adequate levels of phosphate did not have increased blood phosphate levels when compared to control fed chicks. In addition, hens that were injected with FGF-23-3 (the peptide associated with reduced phosphate requirements in the progeny) appeared to have normal plasma phosphate levels and health was not compromised as a result of the vaccine. Sitara et al. (2008) reported that FGF-23 double knockout mice had severe hyperphosphatemia at 3–6 weeks of age (2-fold increase in serum phosphate as compared to controls) [6]. Nakatani et al. (2009) also reported hyperphosphatemia by 3–6 weeks of age in knockout FGF-23 mice [13]. Findings of hyperphosphatemia in FGF-23 knockout mice compared to the results reported here (no abnormal increase in plasma phosphate) could have been a function of dietary phosphate used relative to the animals' requirement. In the chick study, the dietary level of non-phyate phosphate used was 0.36% compared to the minimal chick requirement of 0.4%, a diet slightly less than the minimal requirement of the chick. In the study by Nakatani et al., the levels of dietary non-phytate phosphate (0.37%) was 23% greater than the minimal level of dietary non-phytate phosphate known to prevent deficiency in mice [18]. Other possible reasons could be related to the mechanism by which FGF-23 levels were controlled. In knockout models, no FGF-23 is produced, whereas in the neutralization models, FGF-23 production continues, but the neutralization may be incomplete or limited to microenvironments within the animal.

While antibody to FGF-23 peptide 3 appeared to prevent a decrease in plasma phosphate and bone ash percent in chicks fed a low phosphate diet, chick growth was depressed due to the reduction in dietary non-phytate phosphate. The highest priority for the use of phosphate in the chick is maintaining skeletal development, followed by blood phosphate, then growth rate, hence, the first clinical sign of phosphate deficiency in young growing chicks is a decline in growth rate, and the last clinical sign of phosphate deficiency restored to normalcy is also growth rate [19]. The inability to completely prevent the decline in growth rate may suggest that the level of phosphate used in the low phosphate diet was not sufficient even when FGF-23 was neutralized. Another possibility is that the neutralization antibody was limited in its ability to neutralize FGF-23 and that better peptides could be constructed for vaccine development. Future studies should investigate both the use of new FGF-23 peptides for vaccine use as well as a dietary phosphate dose dependent study to determine the specific phosphate requirement in the presence of neutralizing antibodies to FGF-23.

In this study, measures of phosphate deficiency were the primary focus. Others have shown that neutralization of FGF-23, whether by the use of antibody [11,12] or by the use of FGF-23 gene deletion [20] results in elevated plasma 1α 25, dihydroxycholecalciferol (1α, 25 $(OH)_2D_3$) in mice fed adequate levels of dietary phosphate. Increased plasma 1α, 25 $(OH)_2D_3$ has been shown to increase the intestinal phosphate absorption (both the non-phytate and phytate forms) by action of intestinal alkaline phosphatase [21] and increased sodium phosphate codependent phosphate transporter expression levels in the intestinal mucosa [22]. Additional studies should explore whether increased efficiency in intestinal phosphate absorption can be achieved due to neutralization of FGF-23. In other words, the decreased phosphate requirement due to FGF-23 neutralization may be more complex than simply increased retention of phosphate by reduced renal excretion. Studies should also examine if the neutralization of FGF-23 increases the level of dietary phosphate needed to induce toxicity.

For reasons stated above, as the requirement for dietary phosphate decreases with the neutralization of FGF-23, the level of phosphate needed to induce toxicity should also decrease due to reduced capacity to excrete phosphate.

When this study was initiated, the human FGF-23 amino acid sequence was available but the amino acid sequence of chicken FGF-23 had not been reported. In 2011, subsequent to the start of the experiments reported, an algorithmic prediction of the chicken amino acid sequence of FGF-23 was published as preliminary data. An alignment of the human and predicted chicken sequence showed that FGF-23-C was identical in human and chicken, while FGF-23-3 had two non-matching amino acids between human and chicken, where one of these was a conservative substitution (groups based on acidity, charge, hydrophobicity, etc.) and the other amino acid was non-conservative. Overall, the human sequence (251 amino acids) and chick predicted sequence (253 amino acids) had 128 identical positions, 72 similar positions, and 49.6% identity. Analysis of the antibodies clearly showed that the antibodies were specific to their respective peptides. Both anti-FGF-23-C and anti-FGF-23-3 also effectively bound recombinant human FGF-23; however, only anti-FGF-23-3 was found to be effective at reducing the phosphate requirement of the chick. The reason why anti-FGF-23-C was ineffective at preventing low dietary phosphate-induced decreases in plasma phosphate and bone ash percent when compared to anti-FGF-23-3 is not clear. Perhaps there is less homology between human and chicken FGF-23-C than the algorithm predicted and therefore the antibody to the human peptide-C did not cross-react with the chicken homolog. Also possible is that the peptide-C region in the chicken is located within circulating FGF-23 such that the peptide region is inaccessible to the antibody. For example, when the location of the two peptides within the crystalline structure of human FGF-23 was examined, peptide-3 (outer loop of FGF-23) appeared to be more readily accessible to an antibody than an antibody to peptide-C (internal beta sheet of the FGF-23 structure, Fig. 1). In addition, the topology of FGF-23 shows that FGF-23 peptide-C is located in a barrel feature associated with a beta sheet. Changes in the tertiary structure of chicken FGF-23 in the peptide-C region could influence antibody binding. It has been well documented that the tertiary structure of antigens can influence the specificity of an antibody [23].

While the findings of this study clearly show that antibodies to a specific peptide sequence found in FGF-23 (FGF-23-3) was effective at preventing the clinical signs of phosphate deficiency, many questions remain unanswered. Experiments that show that an FGF-23 vaccine can reduce excreta phosphate would have considerable value for improving the sustainable use of agricultural manure on farmlands. Use of the vaccine approach to altering phosphate requirements should also be studied with other phosphate management tools such as phytases. While our findings may be preliminary, the data support that a vaccine approach to control FGF-23 function may provide a new means to help manage phosphate in commercial animal agricultural facilities. Our finding also describes the first use of a vaccine to reduce a nutrient requirement of an animal.

Disclosure

Research was supported through royalties received from the Wisconsin Alumni Research Foundation (WARF). WARF has filed a patent application on technology described in this paper. All the authors declare no financial conflict of interest.

Acknowledgments

The authors thank Jeff Bishop and Debra Schneider for aiding in sample collection and analysis, as well as the UW Animal Care Staff (Dawn Irish, George Bradley, Angel Gutierrez-Velin) for animal care.

References

[1] K. Nakai, H. Komaba, M. Fukagawa, New insights into the role of fibroblast growth factor 23 in chronic kidney disease, J. Nephrol. 23 (2010) 619–625.
[2] S.L. Ferrari, J.P. Bonjour, R. Rizzoli, Fibroblast growth factor-23 relationship to dietary phosphate and renal phosphate handling in healthy young men, J. Clin. Endocrinol. Metab. 90 (2005) 1519–1524.
[3] F. Perwad, N. Azam, M.Y. Zhang, T. Yamashita, H.S. Tenenhouse, A.A. Portale, Dietary and serum phosphorus regulate fibroblast growth factor 23 expression and 1,25-dihydroxyvitamin D metabolism in mice, Endocrinology 146 (2005) 5358–5364.
[4] K.A. Ward, Phosphorus-friendly transgenics, Nat. Biotechnol. 19 (2001) 415–416.
[5] R.D. Harmel, B. Harmel, M.C. Patterson, On-farm agro-economic effects of fertilizing cropland with poultry litter, J. Appl. Poult. Res. 17 (2008) 545–555.
[6] D. Sitara, S. Kim, M.S. Razzaque, C. Bergwitz, T. Taguchi, C. Schuler, R.G. Erben, B. Lanske, Genetic evidence of serum phosphate-independent functions of FGF-23 on bone, PLoS Genet. 4 (2008) e1000154.
[7] D.L. Trott, M. Yang, J. Gonzalez, A.E. Larson, W.H. Tepp, E.A. Johnson, M.E. Cook, Egg yolk antibodies for detection and neutralization of *Clostridium botulinum* type A neurotoxin, J. Food Prot. 72 (2009) 1005–1011.
[8] National Research Council (US). Subcommittee on Poultry Nutrition, Nutrient requirements of poultry, ninth rev. ed., National Academy Press, Washington, DC, 1994.
[9] E.A. Bobeck, K.M. Meyer, C. Helvig, M. Petkovich, M.E. Cook, Sevelamer hydrochloride binds phosphate released from phytate in chicks fed 1α-hydroxy cholecalciferol, Journal of Renal Nutrition, in press, http://dx.doi.org/10/1053/j.jrn.2011.12.005. [Epub ahead of print].
[10] L. Broderick, L.M. Tourangeau, A. Kavanaugh, S.I. Wasserman, Biologic modulators in allergic and autoinflammatory diseases, Curr. Opin. Allergy Clin. Immunol. 11 (2011) 355–360.
[11] Y. Aono, H. Hasegawa, Y. Yamazaki, T. Shimada, T. Fujita, T. Yamashita, S. Fukumoto, Anti-FGF-23 neutralizing antibodies ameliorate muscle weakness and decreased spontaneous movement of Hyp mice, J. Bone Miner. Res. 26 (2011) 803–810.
[12] Y. Aono, Y. Yamazaki, J. Yasutake, T. Kawata, H. Hasegawa, I. Urakawa, T. Fujita, M. Wada, T. Yamashita, S. Fukumoto, T. Shimada, Therapeutic effects of anti-FGF23 antibodies in hypophosphatemic rickets/osteomalacia, J. Bone Miner. Res. 24 (2009) 1879–1888.
[13] T. Nakatani, B. Sarraj, M. Ohnishi, M.J. Densmore, T. Taguchi, R. Goetz, M. Mohammadi, B. Lanske, M.S. Razzaque, In vivo genetic evidence for klotho-dependent, fibroblast growth factor 23 (Fgf23) -mediated regulation of systemic phosphate homeostasis, FASEB J. 23 (2009) 433–441.
[14] M.E. Rose, E. Orlans, Immunoglobulins in the egg, embryo and young chick, Dev. Comp. Immunol. 5 (1981) 15–20.
[15] J. Brierley, W.A. Hemming, The selective transport of antibodies from the yolk sac to the circulation of the chick, J. Embryol. Exp. Morphol. 4 (1956) 34–41.
[16] J.L. Pimentel, M.E. Cook, J.M. Jonsson, Research note: increased growth of chicks and poults obtained from hens injected with jackbean urease, Poult. Sci. 70 (1991) 1842–1844.
[17] J.L. Pimentel, M.E. Cook, Improved growth in the progeny of hens immunized with jackbean urease, Poult. Sci. 67 (1988) 434–439.
[18] National Research Council (US). Subcommittee on Laboratory Animal Nutrition, Nutrient requirements of laboratory animals, fourth rev. ed., National Academy of Sciences, Washington, DC, 1995.
[19] B.A. Sommerville, J. Blahos, S. Harvey, A. Chadwick, G.S. Spencer, The time sequence of adaptive changes to dietary phosphorus deficiency in the chick, Horm. Metab. Res. 17 (1985) 247–250.
[20] T. Shimada, M. Kakitani, Y. Yamazaki, H. Hasegawa, Y. Takeuchi, T. Fujita, S. Fukumoto, K. Tomizuka, T. Yamashita, Targeted ablation of Fgf23 demonstrates an essential physiological role of FGF23 in phosphate and vitamin D metabolism, J. Clin. Invest. 113 (2004) 561–568.
[21] S.J. Birge, R.C. Avioli, Intestinal phosphate transport and alkaline phosphatase activity in the chick, Am. J. Physiol. 240 (1981) E384–390.
[22] T. Berndt, R. Kumar, Novel mechanisms in the regulation of phosphorus homeostasis, Physiology 24 (2008) 17–25.
[23] D. Mirano-Bascos, N.K. Steede, J.E. Robinson, S.J. Landry, Influence of disulfide-stabilized structure on the specificity of helper T-cell and antibody responses to HIV envelope glycoprotein gp120, J. Virol. 84 (2010) 3303–3311.

Biochemical and Biophysical Research Communications 420 (2012) 671–675

Contents lists available at SciVerse ScienceDirect

Biochemical and Biophysical Research Communications

journal homepage: www.elsevier.com/locate/ybbrc

Increased transcript level of poly(ADP-ribose) polymerase (PARP-1) in human tricuspid compared with bicuspid aortic valves correlates with the stenosis severity

Edit Nagy [a,c,*], Kenneth Caidahl [b,e], Anders Franco-Cereceda [b,d], Magnus Bäck [a,c]

[a] Department of Medicine, Karolinska Institutet, Stockholm, Sweden
[b] Department of Molecular Medicine and Surgery, Karolinska Institutet, Stockholm, Sweden
[c] Department of Cardiology, Karolinska University Hospital, Stockholm, Sweden
[d] Department of Throracic Surgery, Karolinska University Hospital, Stockholm, Sweden
[e] Department of Clinical Physiology, Karolinska University Hospital, Stockholm, Sweden

ARTICLE INFO

Article history:
Received 1 March 2012
Available online 17 March 2012

Keywords:
Aortic valve stenosis
Inflammation
Cytokines
Valvular interstitial cells
Echocardiography

ABSTRACT

Oxidative stress may contribute to the hemodynamic progression of aortic valve stenosis, and is associated with activation of the nuclear enzyme poly(ADP-ribose) polymerase (PARP) 1. The aim of the present study was to assess the transcriptional profile and the topological distribution of PARP-1 in human aortic valves, and its relation to the stenosis severity. Human stenotic aortic valves were obtained from 46 patients undergoing aortic valve replacement surgery and used for mRNA extraction followed by quantitative real-time PCR to correlate the PARP-1 expression levels with the non invasive hemodynamic parameters quantifying the stenosis severity. Primary isolated valvular interstitial cells (VICs) were used to explore the effects of cytokines and leukotriene C_4 (LTC_4) on valvular PARP-1 expression. The thickened areas of stenotic valves with tricuspid morphology expressed significantly higher levels of PARP-1 mRNA compared with the corresponding part of bicuspid valves (0.501 vs 0.243, $P = 0.01$). Furthermore, the quantitative gene expression levels of PARP-1 were inversely correlated with the aortic valve area (AVA) ($r = -0.46$, $P = 0.0469$) and AVA indexed for body surface area (BSA) ($r = -0.498$; $P = 0.0298$) only in tricuspid aortic valves. LTC_4 (1 nM) significantly elevated the mRNA levels of PARP-1 by 2.38-fold in VICs. Taken together, these data suggest that valvular DNA-damage pathways may be associated with inflammation and the stenosis severity in tricuspid aortic valves.

1. Introduction

Calcified aortic valve stenosis is a progressive disorder regardless of the original valve anatomy containing the entire disease spectrum from early signs to most pronounced morphological changes of the valve [1]. However, some substantial differences exist between valvular stenosis with an underlying bicuspid (BAV) and tricuspid (TAV) aortic valve anatomy. For example, TAV is characterized by significantly more infiltrating inflammatory cells (CD 68, CD 8) compared with BAV [2]. Moreover, the rate of the hemodynamic progression is faster in patients with BAV compared with TAV, suggested to be due to geometric differences and different commissural orientation resulting in abnormal systolic flow distribution in BAV [3]. In contrast, epidemiological studies have associated TAV with established cardiovascular risk factors and age [4]. In addition, oxidative stress may contribute to calcification both in tricuspid [5,6] and bicuspid [7] valves. However, no previous study compared the extent of oxidative/nitrosative stress between BAV and TAV or assessed its relation to stenosis progression.

Previous findings provided evidence for increased levels of superoxide and H_2O_2 in the calcified regions of stenotic aortic valves, which was not counterbalanced by antioxidant enzymes, indicating dysfunctional protection [6]. Nitric oxide acts under physiological conditions as a potent anti-inflammatory [8], anti-apoptotic [9], vasodilatator agent [10] and may protect against valvular calcification. In contrast, oxidative stress causing altered intracellular signaling, gene expression and rise in intracellular [Ca^{2+}], may lead to DNA-injury with subsequent activation of the nuclear enzyme poly(ADP-ribose) polymerase (PARP) [11]. DNA strand breakage through hydroxyl radical, nitroxyl anion and peroxy-nitrite (reactive oxidant formed from the reaction of nitric oxide and superoxide) is the obligatory trigger of PARP activation. PARP consists of a family of enzymes which catalyzes poly(ADP-ribosyl)ation of DNA-binding proteins. Seven isoforms have been identified. PARP-1 is the best characterized member, and works as

Abbreviations: PARP-1, poly(ADP-ribose) polymerase; VIC, valvular interstitial cell; AVA, aortic valve area; AVA/BSA, aortic valve area indexed for the body surface area; BAV, bicuspid aortic valve; TAV, tricuspid aortic valve.

* Corresponding author at: Center for Molecular Medicine, CMM L8:03, Karolinska University Hospital, 171 76 Stockholm, Sweden.
E-mail address: edit.nagy@karolinska.se (E. Nagy).

0006-291X/$ - see front matter © 2012 Elsevier Inc. All rights reserved.
http://dx.doi.org/10.1016/j.bbrc.2012.03.064

a DNA-damage nick sensor protein using beta-NAD(+) to form polymers of ADP-ribose [12]. Previous studies showed increased oxidative and nitrosative stress in response to myocardial infarction i.e. increased nitrotyrosine staining, oxidative stress, antioxidant depletion, increase in oxidative markers, increase in circulating nitrite/nitrate formation (breakdown products of nitric oxide), and has been demonstrated in the late stage of reperfusion [13]. Overactivation of PARP in oxidatively stressed cells can lead to suppression of cellular metabolic function with subsequent depletion of cellular NAD+ and ATP content, mitochondrial dysfunction and ultimately necrotic cell death and organ dysfunction [14], representing a final common pathway involved in the pathophysiology of many cardiovascular diseases. However, the PARP-1 pathway has not previously been explored in the context of aortic valve stenosis.

We have recently demonstrated that a rise in intracellular [Ca^{2+}] in valvular interstitial cells (VICs), increased reactive oxygen species (ROS) production, reduced mitochondrial membrane potential and increased intracellular vacuole formation in response to the inflammatory mediator leukotriene C_4 (LTC_4) [2]. Since our previous study suggested a series of events leading to activation of the cell death pathways, the aim of the present study was to investigate the transcription profile of PARP-1 in stenotic aortic valves and its relation to the hemodynamic progression in different valve anatomies.

2. Materials and methods

2.1. Patients

The study consisted of 46 surgically explanted stenotic aortic valves with either bicuspid or tricuspid anatomy derived from patients without concomitant significant obstructive coronary artery disease and no history of rheumatic heart disease. The study was approved by the local ethics committee (Ref. 2008/630-32), and all patients gave informed consent. An extensive description of patient population and study design has been presented elsewhere [2]. Moreover, additional valves derived from 6 patients were used for cell culture experiment.

2.2. Echocardiography

All patients underwent two-dimensional transthoracic Doppler echocardiography using a Philips IE33 system (Philips Medical Systems, Andover, MA). The severity of aortic valve stenosis was based on (1) the aortic valve area (AVA, cm^2) calculated using the continuity equation, (2) AVA indexed for body surface area (AVA/BSA, cm^2/m^2), (3) the ratio of the systolic time velocity integral (VTI) in the left ventricle outflow tract to the VTI in the aortic valve, and (4) the mean transvalvular pressure gradient according to the current guidelines [15,16]. The left ventricular geometry and function, and aortic root dimensions were measured according to the recommendations of the American Society of Echocardiography [17]. The echocardiographic assessment of the aortic valve anatomy as bicuspid or tricuspid was confirmed intraoperatively.

Based on the echocardiographic assessment, the study population was categorized into 2 groups: isolated, severe aortic stenosis with either a (1) bicuspid, $n = 23$ or a (2) tricuspid, $n = 23$ valve anatomy.

2.3. Sample preparation and macroscopic dissection

Immediately after surgical removal, valves were immersed in RNA Later (Qiagen) and stored at 4 °C until transport to the laboratory. By macroscopic dissection each individual cusp was subsequently divided in the RNA Later solution into: (1) normal areas defined as non-calcified, smooth, pliable, and opalescent; (2) thickened areas; and (3) calcified areas. From each class, 1 sample from each cusp was frozen at −80 °C until RNA extraction. The macroscopic definitions were verified by histology in a subset of preparations ($n = 89$) using eosin and hematoxylin, Masson trichrome and Alizarin red, as previously described [2].

2.4. RNA extraction and quality assessment

Total RNA was isolated from 190 preparations from 46 patients, representing the various portions (normal, thickened, and calcified) from each aortic valve cusp, using the RNeasy Lipid Tissue Mini kit (Qiagen). RNA concentrations were measured spectrophotometrically at 260 nm (A260/280 nm, Agilent Technologies, Palo Alto, CA). Then, the quality of the RNA was analyzed on a 2100 Bioanalyzer (Agilent, Palo Alto, CA, USA) using RNA 6000 NANO chips to assess the RNA Integrity Number (RIN), as described [18].

On average, 4 preparations were examined for each aortic valve. In subsequent analyses, a mean value of each tissue category (i.e. normal, thickened, and calcified, respectively) was calculated for each individual.

2.5. TaqMan real-time PCR

First-strand cDNA was synthesized from 0.5 μg RNA (Superscript II, Invitrogen, Carlsbad, CA) with random hexamers according to the manufacturer's instructions. Quantitative TaqMan PCR was performed on a 7900HT Fast real-time PCR system (Applied Biosystems) with primer/probe pairs that were obtained using Assay-on-demand™ from Applied Biosystems (Cyclophilin A = PPIA: Hs99999904_m1; poly(ADP-ribose) polymerase 1 = PARP-1: Hs00911369_g1); the reactions contained 5 μl cDNA that was diluted to 1.5 ng/μl and 5 μl TaqMan™ Fast Universal PCR Master Mix (Applied Biosystems, Foster City, USA).

2.6. Immunohistochemistry

Transversal cryosections (10 μm thick) were cut, oriented from the cusp base to the free edge, and fixed in acetone. Double immunofluorescence stainings were performed using polyclonal rabbit anti-human PARP-1 (Abcam) and monoclonal mouse anti-human vimentin (Dako) as primary antibodies. Isotype-specific either DyLight 594 or DyLight 488-conjugated secondary antibodies (Vector) were used and the nuclei were counterstained with 4′,6-diamino-2-phenylindol (DAPI, Vector). Images were captured with confocal microscope Leica DMI.

2.7. Isolation of valvular interstitial cells

Aortic valve samples from 6 patients were transported immediately in cell culture medium to the laboratory, where the valves were dissected under sterile conditions. Valvular endothelial cells were gently removed using a scalpel and further digested from the leaflets with collagenase type I A at 37 °C in a shaking water bath for 120 min. Then, the valvular pieces were rinsed in Dulbecco's modified Eagle's medium and centrifuged for 5 min at 1500 rpm. After removing the supernatants the cells were covered with Dulbecco's modified Eagle's medium supplemented with 10% heat-inactivated fetal bovine serum, 100 IU/ml streptomycin, 50 IU/ml penicillin, and 2.5 μg/ml Fungizone and placed in an incubator at 37 °C and 5% CO_2.

The culture medium was changed 3 times per week, and the confluence of VICs was evaluated. On average, 2–3 weeks of incubation was needed to obtain confluent outgrowth of the VIC. At this point, the cells were detached and reseeded onto culture dishes. Cells were used for experiments between passages 2 and 4.

2.8. Transcriptional changes in valvular interstitial cells

To evaluate transcriptional changes induced by various cytokines and LTC_4, VICs were seeded in six-well plates (10^5 cells per well). After 24 h serum-starvation, VICs were incubated in the absence or presence of TGF-β1 (10 ng/ml), IL-1β (10 ng/ml) and LTC_4 (1 nM) for 24 h and collected for RNA extraction with subsequent analysis of transcription profile of PARP-1 using TaqMan real time PCR. The concentrations of LTC_4, TGF-β1 and IL-1β were comparable to previous reports [2,19,20].

2.9. Data analysis

Clinical parameters and gene expression data are expressed as median and ranges. After normality test (Shapiro–Wilk) and equality variance test, single comparisons were analyzed by *t*-test. Correlations between quantitative gene expression data and echocardiographic parameters were established by Spearman correlation. In the cell culture experiment for single comparisons Mann–Whitney Rank Sum test was used. Separate multiple regression analysis was performed to evaluate the best predictor among the independent variables including echocardiographic and clinical parameters predicting the depending variable: the expression level of PARP-1. A P value <0.05 was considered significant. Analyses were performed using SigmaPlot version 11 (Systat Software, Inc.)

3. Results

3.1. Gene expression analysis in BAV and TAV

The patient characteristics are shown in Table 1 according to diagnosis groups demonstrating significant difference between the ages of BAV- and TAV-patients. Neither the non invasive hemodynamic parameters assessing the stenosis severity nor the clinical parameters showed any differences between BAV and TAV.

The gene expression for PARP-1 in the normal and calcified area of the valve did not differ significantly between BAV and TAV (Fig. 1A, C). In contrast, the thickened areas of stenotic valves exhibited significantly higher levels of PARP-1 mRNA ($P = 0.01$) in TAV compared with the corresponding part of BAV (Fig. 1B).

3.2. Correlation of the quantitative gene expression data to the severity of stenosis and to the clinical parameters

The gene expression level for PARP-1 demonstrated significant correlations with age ($r = 0.374$, $P = 0.0322$) and with the number of the cusps ($r = 0.457$, $P = 0.00772$). Subsequent correlations to the aortic stenosis severity were therefore performed separately for valves with underlying bicuspid and tricuspid anatomy. In the thickened areas, the transcript levels of PARP-1 exhibited inverse correlation to AVA, and to AVA/BSA (Table 2). There were no significant correlations between the qPCR data for PARP-1 and the parameters quantifying the stenosis severity in the corresponding valvular tissue of BAV (Table 2). Univariate correlation analyses between transcript levels for PARP-1 and the other clinical parameters listed in the Table 1 did not reveal any significant associations in either TAV or BAV (Table 2). Multiple regression analysis with backward stepwise selection demonstrated a linear combination of independent variables: AVA/BSA ($P = 0.009$), high sensitive (hs) CRP ($P = 0.043$), serum creatinine ($P = 0.03$) and HBA1cA ($P = 0.01$) which remained significantly correlated with the dependent variable: the transcript levels of PARP-1 in the thickened part of TAV.

3.3. Immunohistochemical analysis

Double immunofluorescence staining in TAV revealed nuclear localization of PARP-1 in vimentin-positive valvular interstitial cells (Fig. 1D).

3.4. The transcription profile of PARP-1 in valvular interstitial cells treated by different stimuli

Primary cultures of VICs exhibited significantly increased PARP-1 mRNA levels after stimulation with LTC_4 (1 nM; 2.38-fold increase; $P = 0.006$; Fig. 2). Addition of either TGF-β1 (10 ng/ml) or IL-1β (10 ng/ml) the transcript levels of PARP-1 were not significantly altered compared with untreated.

4. Discussion

The results of the present study point to dominating expression levels of PARP-1 in TAV compared with BAV. In addition, PARP-1

Table 1
Patient characteristics.

	Aortic valve stenosis		Overall *P*-value
	Bicuspid aortic valve	Tricuspid aortic valve	
No. of patients	23	23	
Male, n (%)	16 (35%)	13 (28%)	
Age, y	64.4 (28.5–82.4)	76.2 (57.9–87.1)*	<0.001
BMI, kg/m^2	26.9 (19.2–34.7)	26.3 (21.6–37.4)	0.682
AVA, cm^2	0.76 (0.47–1.2)	0.72 (0.45–1)	0.134
AVA/BSA, cm^2/m^2	0.4 (0.3–0.6)	0.38 (0.25–0.58)	0.255
VTI-ratio	0.2 (0.16–0.28)	0.2 (0.14–0.37)	0.613
Aorta Vmax, m/s	4.5 (3.4–5.7)	4.5 (4–5.8)	0.255
P-mean, mm Hg	51 (27–85)	49 (37–93)	0.403
Left ventricular EF, %	61% (44–78)	64%(42–75)	0.55
LVEDD, mm	49 (36–63)	47 (37–57)	0.234
Hs CRP	1 (0.2–18)	1.5 (0.35–14.6)	0.59
Creatinine	76 (47–134)	79 (60–156)	0.235
HbA1c	4.5 (3.9–6.3)	4.5 (3–6.3)	0.659
t-cholesterol (mmol/l)	5 (2.7–6.7)	4.7 (3.3–6.1)	0.094
LDL-C (mmol/l)	3.05 (1.3–4.4)	1.8 (1.4–4.2)	0.26
HDL-C (mmol/l)	1.4 (0.5–2.9)	1.4 (0.6–2.5)	0.785
Triglyceride (mmol/l)	0.91 (0.42–13.8)	1.1 (0.38–3.7)	0.775

BMI: body mass index; AVA: aortic valve area; AVA/BSA: aortic valve area, indexed for body surface area; VTI-ratio: velocity time integral ratio; Aorta Vmax: antegrade velocity across the narrowed aortic valve; *P*-mean: mean transvalvular pressure; Left ventricle EF: left ventricle ejection fraction; LVEDD: left ventricle end diastolic diameter; Hs CRP: high sensitive CRP; HbA1c: Hemoglobin A1c; LDL-C: LDL-cholesterol; HDL-C: HDL-cholesterol. Values are medians and ranges unless otherwise stated.
* $P < 0.05$ compared with BAV.

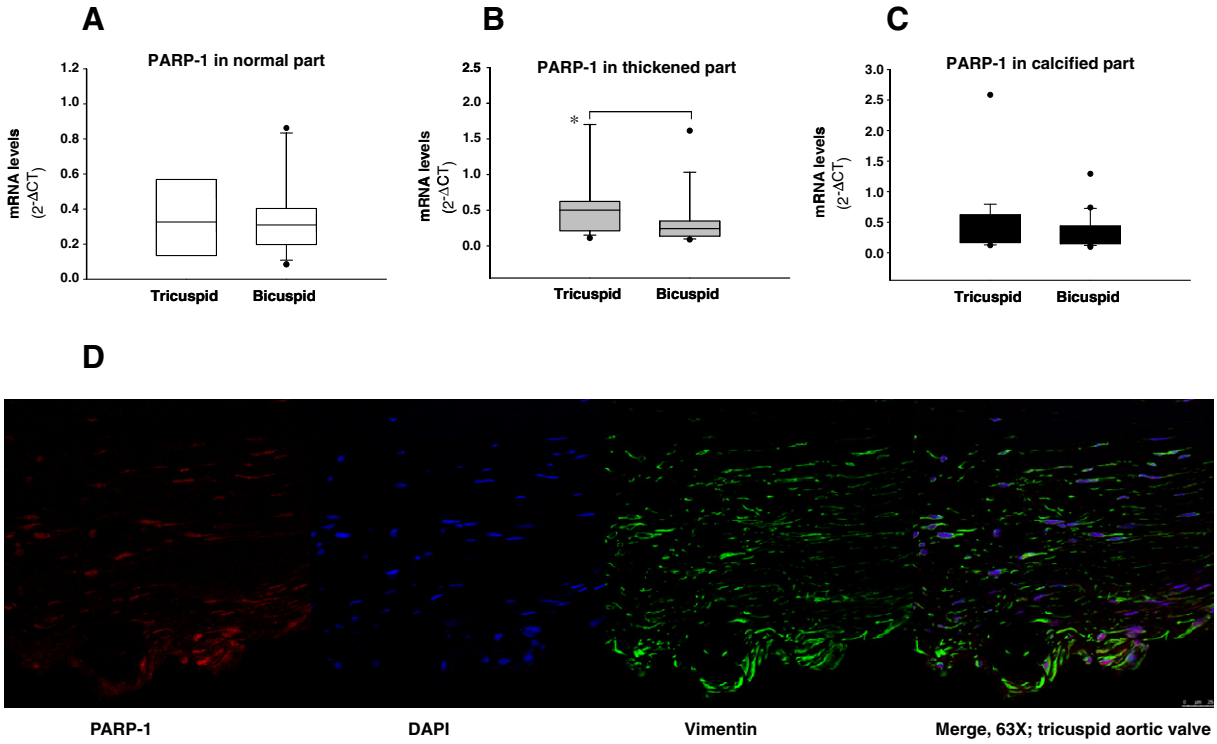

Fig. 1. (A) The transcript levels of PARP-1 in the normal part of the valvular tissue in different valve anatomies. (B) The transcript levels of PARP-1 in the thickened part of valvular tissue exhibiting significant increased expression levels in TAV compared with BAV ($P = 0.01$). (C) The transcript levels of PARP-1 in the calcified part of the valvular tissue in different valve anatomies. (D) Immunofluorescence staining of human stenotic aortic valves demonstrates nuclear localization of PARP-1 in vimentine-positive VICs.

Table 2
Correlations between echocardiographic and clinical parameters and gene expression levels for PARP-1 in thickened areas of stenotic aortic valves.

		PARP-1 in TAV	PARP-1 in BAV
AVA, cm^2	Correlation coeff.	−0.46	0.174
	P-value	0.0469	0.542
AVA/BSA, cm^2/m^2	Correlation coeff.	−0.498	−0.0462
	P-value	0.0296	0.868
Age	Correlation coeff.	0.246	−0.130
	P-value	0.305	0.648
High sensitive CRP	Correlation coeff.	0.267	−0.0837
	P-value	0.264	0.762
Creatinine	Correlation coeff.	−0.224	0.207
	P-value	0.349	0.463
HbA1c	Correlation coeff.	0.192	−0.0490
	P-value	0.422	0.856
t-cholesterol (mmol/l)	Correlation coeff.	0.157	0.121
	P-value	0.512	0.67
LDL-C (mmol/l)	Correlation coeff.	0.0827	0.111
	P-value	0.732	0.693
HDL-C (mmol/l)	Correlation coeff.	−0.0511	−0.266
	P-value	0.832	0.348
Triglyceride (mmol/l)	Correlation coeff.	0.0816	−0.00220
	P-value	0.732	0.988

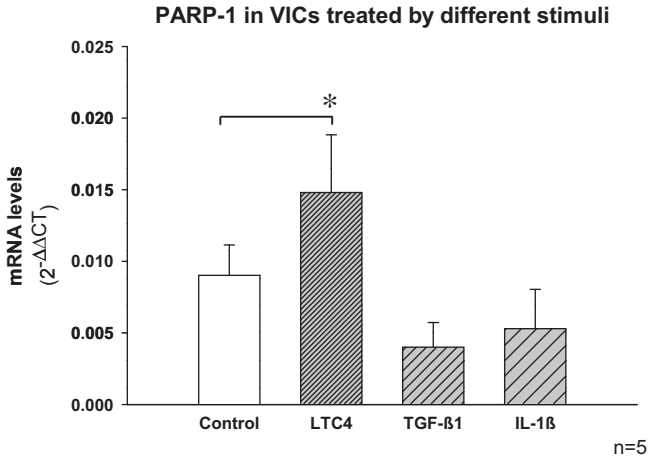

Fig. 2. In vitro cell culture experiment on VICs using LTC_4, TGF-β1, and IL-1β. Bars represent mean ± SEM. The transcript level of PARP-1 exhibited significant increase at 1 nM LTC_4 ($P = 0.006$).

expression correlated with the severity of stenosis in TAV but not in BAV, and was induced in vitro by the inflammatory mediator LTC_4. Taken together, these findings implicate differential distribution of DNA-damage pathways in aortic stenosis with bi- and tricuspid valves, and an association of PARP-1 with stenosis severity and with inflammation in TAV.

We recently demonstrated that macroscopic dissection of human stenotic valves allows detecting differential gene expression pattern at different stages of the valvular disease [2]. In particular, the thickened part of diseased valves stands for an intermediate stage of aortic stenosis, which potentially could represent a vulnerable and modifiable stage of disease. It is therefore interesting that the thickened part exhibited significantly increased PARP-1 expression in TAV compared with BAV. These results suggest that TAV, which demonstrates a slower disease progression compared with BAV, is associated with increased expression of PARP-1. These findings provide a first suggestion of potential differences in DNA damage pathways between bi- and tricuspid valves.

Furthermore, the expression level for PARP-1 in TAV was associated with the aortic stenosis severity (measured as AVA and AVA/BSA), whereas PARP-1 expression in BAV was unrelated to stenosis severity. These findings further support that a potential link between the PARP-1 pathway and aortic valve stenosis severity may be limited to tricuspid valves. Our multivariate analysis in addition demonstrated that PARP-1 expression could be

independently predicted by a combination of AVA/BSA, CRP, creatinine and HBA1c-levels in TAV when taking into account other clinical and echocardiographic parameters.

Inflammation is a key step promoting the pathological process with superimposed calcification in aortic stenosis [1,21,22]. Our previous findings assessing the proinflammatory roles of leukotrienes in human aortic valve stenosis showed that LTC_4 increased intracellular [Ca^{2+}], ROS production and also induced a dissipation of the mitochondrial membrane potential in human VICs, a series of events ultimately leading to activation of cell death pathways [2]. Double immunofluorescence staining revealed colocalisation of PARP-1 with vimentin, indicating that VICs are the source of PARP-1 in tricuspid aortic valves. Based on these observations, we therefore next evaluated the effect of LTC_4 on PARP-1 expression in valvular interstitial cells. Earlier investigations demonstrated TGF-β1 as an inducer of apoptosis and of pro-osteogenic signaling in human VICs in vitro [23,24]. However, in the present study, no significant alterations of PARP-1 expression were induced by either TGF-β or IL-1β. In contrast, LTC_4 stimulation resulted in a significant, approximately 2-fold increase in the transcript level of PARP-1. These effects were observed at low concentrations of LTC_4, which is in line with our previous study, indicating LTC_4 as a potent inducer of PARP-1 in VICs. Along with our previously demonstrated deleterious effects of LTC_4 on VICs [2], the induction of PARP-1 may enhance the hemodynamic progression linking inflammation and cuspal calcification together in TAV. The role of inflammation in PARP-1 induction was also supported by a significant association of PARP-1 expression with CRP in TAV in the multivariate analysis.

Some limitations of the present study must be acknowledged. Although the correlation between PARP-1 expression with stenosis severity in TAV provides a first indication for hemodynamic implications of this pathway, it cannot be excluded that the findings are dependent on unknown covariates. In studies comparing BAV and TAV, an age difference between the groups is commonly encountered, which applies also to this study. Nevertheless, it is unlikely that age could explain the observed differences, since a combination of several independent variables was a significant predictor of PARP-1 expression in the multivariate analysis. Furthermore, the lack of correlation between PARP-1 expression the stenosis severity in BAV argues against that stenosis severity *per se* induced PARP-1 expression. Further mechanistic studies are needed to establish the causal relationship between the PARP-1 pathway, tissue damage and local calcification in the affected aortic valves.

In summary, the present study highlights the extent and topology of PARP-1 and its relation to stenosis in TAV and identifies the proinflammatory mediator LTC_4 as a potent inducer of PARP-1. Increased transcriptional profile of PARP-1, revealing increased susceptibility to nitrosative stress in TAV may hence be associated with aortic valve stenosis progression. In conclusion, these results suggest PARP-1 as potential therapeutic target in aortic stenosis.

Acknowledgements

The authors thank Professor Göran K Hansson for helpful advice on the study. The study was supported by the Swedish Heart and Lung Foundation, and the Swedish Medical Research Council. AFC was supported by a donation from Fredrik Lundberg.

References

[1] C.M. Otto, J. Kuusisto, D.D. Reichenbach, A.M. Gown, K.D. O'Brien, Characterization of the early lesion of 'degenerative' valvular aortic stenosis. Histological and immunohistochemical studies, Circulation 90 (1994) 844–853.
[2] E. Nagy, D.C. Andersson, K. Caidahl, M.J. Eriksson, P. Eriksson, A. Franco-Cereceda, G.K. Hansson, M. Bäck, Upregulation of the 5-lipoxygenase pathway in human aortic valves correlates with severity of stenosis and leads to leukotriene-induced effects on valvular myofibroblasts, Circulation 123 (2011) 1316–1325.
[3] S. Beppu, S. Suzuki, H. Matsuda, F. Ohmori, S. Nagata, K. Miyatake, Rapidity of progression of aortic stenosis in patients with congenital bicuspid aortic valves, Am. J. Cardiol. 71 (1993) 322–327.
[4] R.V. Freeman, C.M. Otto, Spectrum of calcific aortic valve disease: pathogenesis, disease progression, and treatment strategies, Circulation 111 (2005) 3316–3326.
[5] M. Liberman, E. Bassi, M.K. Martinatti, F.C. Lario, J. Wosniak Jr., P.M. Pomerantzeff, F.R. Laurindo, Oxidant generation predominates around calcifying foci and enhances progression of aortic valve calcification, Arterioscler. Thromb. Vasc. Biol. 28 (2008) 463–470.
[6] J.D. Miller, Y. Chu, R.M. Brooks, W.E. Richenbacher, R. Pena-Silva, D.D. Heistad, Dysregulation of antioxidant mechanisms contributes to increased oxidative stress in calcific aortic valvular stenosis in humans, J. Am. Coll. Cardiol. 52 (2008) 843–850.
[7] N.M. Rajamannan, Bicuspid aortic valve disease: the role of oxidative stress in Lrp5 bone formation, Cardiovasc. Pathol. 20 (2011) 168–176.
[8] A.K. Larsson, M. Bäck, J. Hjoberg, S.E. Dahlen, Inhibition of nitric-oxide synthase enhances antigen-induced contractions and increases release of cysteinyl-leukotrienes in guinea pig lung parenchyma: nitric oxide as a protective factor, J. Pharmacol. Exp. Ther. 315 (2005) 458–465.
[9] X. Nie, S. Song, L. Zhang, Z. Qiu, S. Shi, Y. Liu, L. Yao, D. Zhu, 15-Hydroxyeicosatetraenoic acid (15-HETE) protects pulmonary artery smooth muscle cells from apoptosis via inducible nitric oxide synthase (iNOS) pathway, Prostaglandins Other Lipid Mediat. 97 (2012) 50–59.
[10] M. Bäck, L. Walch, X. Norel, J.P. Gascard, G. Mazmanian, C. Brink, Modulation of vascular tone and reactivity by nitric oxide in porcine pulmonary arteries and veins, Acta Physiol. Scand. 174 (2002) 9–15.
[11] I. Geistrikh, L. Visochek, R. Klein, L. Miller, L. Mittelman, A. Shainberg, M. Cohen-Armon, Ca^{2+} induced PARP-1 activation and ANF expression are coupled events in cardiomyocytes, Biochem. J. 438 (2011) 337–347.
[12] P. Pacher, C. Szabo, Role of the peroxynitrite-poly(ADP-ribose) polymerase pathway in human disease, Am. J. Pathol. 173 (2008) 2–13.
[13] E. Toth-Zsamboki, E. Horvath, K. Vargova, E. Pankotai, K. Murthy, Z. Zsengeller, T. Barany, T. Pek, K. Fekete, R.G. Kiss, I. Preda, Z. Lacza, D. Gero, C. Szabo, Activation of poly(ADP-ribose) polymerase by myocardial ischemia and coronary reperfusion in human circulating leukocytes, Mol. Med. 12 (2006) 221–228.
[14] L. Virag, E. Szabo, E. Bakondi, P. Bai, P. Gergely, J. Hunyadi, C. Szabo, Nitric oxide-peroxynitrite-poly(ADP-ribose) polymerase pathway in the skin, Exp. Dermatol. 11 (2002) 189–202.
[15] A. Vahanian, H. Baumgartner, J. Bax, E. Butchart, R. Dion, G. Filippatos, F. Flachskampf, R. Hall, B. Iung, J. Kasprzak, P. Nataf, P. Tornos, L. Torracca, A. Wenink, Guidelines on the management of valvular heart disease: the task force on the management of valvular heart disease of the European Society of Cardiology, Eur. Heart J. 28 (2007) 230–268.
[16] H. Baumgartner, J. Hung, J. Bermejo, J.B. Chambers, A. Evangelista, B.P. Griffin, B. Iung, C.M. Otto, P.A. Pellikka, M. Quinones, Echocardiographic assessment of valve stenosis: EAE/ASE recommendations for clinical practice, Eur. J Echocardiogr. 10 (2009) 1–25.
[17] R.M. Lang, M. Bierig, R.B. Devereux, F.A. Flachskampf, E. Foster, P.A. Pellikka, M.H. Picard, M.J. Roman, J. Seward, J.S. Shanewise, S.D. Solomon, K.T. Spencer, M.S. Sutton, W.J. Stewart, Recommendations for chamber quantification: a report from the American Society of Echocardiography's Guidelines and Standards Committee and the Chamber Quantification Writing Group, developed in conjunction with the European Association of Echocardiography, a branch of the European Society of Cardiology, J. Am. Soc. Echocardiogr. 18 (2005) 1440–1463.
[18] A. Schroeder, O. Mueller, S. Stocker, R. Salowsky, M. Leiber, M. Gassmann, S. Lightfoot, W. Menzel, M. Granzow, T. Ragg, The RIN: an RNA integrity number for assigning integrity values to RNA measurements, BMC Mol. Biol. 7 (2006) 3.
[19] B. Jian, N. Narula, Q.Y. Li, E.R. Mohler 3rd, R.J. Levy, Progression of aortic valve stenosis: TGF-beta1 is present in calcified aortic valve cusps and promotes aortic valve interstitial cell calcification via apoptosis, Ann. Thorac. Surg. 75 (2003) 457–465 [discussion 65–6.].
[20] J.J. Kaden, C.E. Dempfle, R. Grobholz, H.T. Tran, R. Kilic, A. Sarikoc, M. Brueckmann, C. Vahl, S. Hagl, K.K. Haase, M. Borggrefe, Interleukin-1 beta promotes matrix metalloproteinase expression and cell proliferation in calcific aortic valve stenosis, Atherosclerosis 170 (2003) 205–211.
[21] N.M. Rajamannan, B. Gersh, R.O. Bonow, Calcific aortic stenosis: from bench to the bedside–emerging clinical and cellular concepts, Heart 89 (2003) 801–805.
[22] S. Helske, M. Kupari, K.A. Lindstedt, P.T. Kovanen, Aortic valve stenosis: an active atheroinflammatory process, Curr. Opin. Lipidol. 18 (2007) 483–491.
[23] I. Cucoranu, R. Clempus, A. Dikalova, P.J. Phelan, S. Ariyan, S. Dikalov, D. Sorescu, NAD(P)H oxidase 4 mediates transforming growth factor-beta1-induced differentiation of cardiac fibroblasts into myofibroblasts, Circ. Res. 97 (2005) 900–907.
[24] J.N. Clark-Greuel, J.M. Connolly, E. Sorichillo, N.R. Narula, H.S. Rapoport, E.R. Mohler 3rd, J.H. Gorman 3rd, R.C. Gorman, R.J. Levy, Transforming growth factor-beta1 mechanisms in aortic valve calcification: increased alkaline phosphatase and related events, Ann. Thorac. Surg. 83 (2007) 946–953.

Biochemical and Biophysical Research Communications 420 (2012) 676–679

Contents lists available at SciVerse ScienceDirect

Biochemical and Biophysical Research Communications

journal homepage: www.elsevier.com/locate/ybbrc

Antimicrobial properties of analgesic kyotorphin peptides unraveled through atomic force microscopy

Marta M.B. Ribeiro [a], Henri G. Franquelim [a], Inês M. Torcato [a], Vasanthakumar G. Ramu [b], Montserrat Heras [b], Eduard R. Bardaji [b], Miguel A.R.B. Castanho [a,*]

[a] Instituto de Medicina Molecular, Faculdade de Medicina de Lisboa, Av. Professor Egas Moniz, 1649-028 Lisboa, Portugal
[b] Laboratori d'Innovació en Processos i Productes de Síntesi Orgànica (LIPPSO), Departament de Química, Universitat de Girona, Campus Montilivi, 17071 Girona, Spain

ARTICLE INFO

Article history:
Received 21 February 2012
Available online 17 March 2012

Keywords:
Kyotorphin derivatives
Analgesic
Atomic force microscopy
Antimicrobial
Peptide
Hemolytic

ABSTRACT

Antimicrobial peptides (AMPs) are promising candidates as alternatives to conventional antibiotics for the treatment of resistant pathogens. In the last decades, new AMPs have been found from the cleavage of intact proteins with no antibacterial activity themselves. Bovine hemoglobin hydrolysis, for instance, results in AMPs and the minimal antimicrobial peptide sequence was defined as Tyr-Arg plus a positively charged amino acid residue. The Tyr-Arg dipeptide alone, known as kyotorphin (KTP), is an endogenous analgesic neuropeptide but has no antimicrobial activity itself. In previous studies new KTP derivatives combining C-terminal amidation and Ibuprofen (Ib) – KTP–NH_2, IbKTP, IbKTP–NH_2 – were designed in order to improve KTP brain targeting. Those modifications succeeded in enhancing peptide-cell membrane affinity towards fluid anionic lipids and higher analgesic activity after systemic injection resulted therefrom. Here, we investigated if this affinity for anionic lipid membranes also translates into antimicrobial activity because bacteria have anionic membranes. Atomic force microscopy revealed that KTP derivatives perturbed *Staphylococcus aureus* membrane structure by inducing membrane blebbing, disruption and lysis. In addition, these peptides bind to red blood cells but are non-hemolytic. From the KTP derivatives tested, amidated KTP proves to be the most active antibacterial agent. The combination of analgesia and antibacterial activities with absence of toxicity is highly appealing from the clinical point of view and broadens the therapeutic potential and application of kyotorphin peptides.

1. Introduction

The rapid rise in the emergence of bacterial strains resistant to multiple classes of antimicrobial agents created an urgent need to develop novel antimicrobial therapies to fight these pathogens. Antimicrobial peptides are promising drug candidates because target bacteria do not seem to develop resistance. As part of the innate immune system, AMPs are widely distributed in different species, usually with a broad killing spectrum for pathogens such as both Gram-negative and Gram-positive bacteria [1]. AMPs are short amphiphilic and generally cationic sequences with high affinity for bacterial-like membranes: they bind preferably to negatively charged membranes and liquid disordered domains [2]. In fact and despite the ubiquity of different mechanisms possible for AMP mode of action, the bacteria membrane appears to be their primary target.

Besides being present in organisms external surfaces like skin [3], several AMPs were found to be released by cleavage of intact proteins with no or limited antibacterial activity themselves. These include milk lactoferrin [4], human lactoferrin [4], hen egg white lysozyme [5] and bovine hemoglobin [6]. In the case of mammalian hemoglobin, the peptides resulting from its hydrolysis revealed to be a source of biologically active compounds with opioid, analgesic and bacterial growth-stimulating activities, in addition to antimicrobial function [7]. Guillochon and colleagues have extensively studied bovine hemoglobin peptides obtained at low hydrolysis degrees. They reported that both α- and β-chain of hemoglobin comprise peptides with antimicrobial activity and that the shortest the peptide, the highest the activity [7–12]. Accordingly, they defined that the minimal sequence required for antimicrobial activity is the dipeptide Tyr-Arg associated with one positively charged amino acid residue, Lys and His for α- and β-chain, respectively [11,12].

Abbreviations: AMPs, antimicrobial peptides; KTP, kyotorphin; KTP–NH_2, kyotorphin amide; IbKTP, kyotorphin linked to ibuprofen; IbKTP–NH_2, kyotorphin amide linked to ibuprofen; AFM, atomic force microscopy; RBCs, red blood cells; MHB, Mueller Hinton Broth; MHA, Mueller Hinton agar; IPS, Instituto Português do Sangue.

* Corresponding author. Fax: +351 217999477.
E-mail address: macastanho@fm.ul.pt (M.A.R.B. Castanho).
URL: http://www.imm.fm.ul.pt/web/imm/physicalbiochemistry (M.A.R.B. Castanho).

0006-291X/$ - see front matter © 2012 Elsevier Inc. All rights reserved.
http://dx.doi.org/10.1016/j.bbrc.2012.03.065

The Tyr-Arg dipeptide has been previously found in mammalian brain and named kyotorphin due to its opioid like analgesic activity following peptide central delivery [13]. To increase brain targeting, we recently designed new KTP derivatives combining C-terminal amidation and Ibuprofen (Ib) – KTP–NH_2, IbKTP, IbKTP–NH_2. The strategy was to enhance peptide-cell membrane affinity, which facilitates the translocation of epithelial barriers, such as the blood–brain barrier. The end result was that the analgesic activity was increased after systemic injection. Amidation endowed one additional positive charge to the peptide and Ibuprofen increased its lipophilicity. This may explain why, unlike original kyotorphin, KTP–NH_2, IbKTP and IbKTP–NH_2 displayed an increased interaction for vesicles, with a preference for anionic liquid disordered membranes [14].

In the present study, we investigated if the cationic charge and selectivity for interacting with anionic membranes of these novel KTP derivatives translate into antimicrobial activity against *Escherichia coli* (*E. coli*, gram-negative) and *Staphylococcus aureus* (*S. aureus*, gram-positive) bacteria. Following antimicrobial and hemolytic assays, atomic force microscopy (AFM) was used to image the effect of each KTP derivative on the bacterial envelope morphology as well as possible alterations in the red blood cells (RBCs) membranes.

2. Materials and methods

2.1. Peptide synthesis

KTP and KTP derivatives – KTP–NH_2, IbKTP and IbKTP–NH_2 – were synthesized as previously described [14,15].

2.2. Preparation of bacterial cells

E. coli from American Type Culture Collection (ATCC 25922) and *S. aureus* (ATCC 25923) were chosen as models of Gram-negative and Gram-positive bacteria, respectively. For *S. aureus* a bacterial concentration of 2.78×10^8 colony forming units/ml (cfu/ml) was found to correspond to Optical Density (OD) at 600 nm, $OD_{600} = 0.319$ for Mueller Hinton Broth media (MHB, Oxoid). Regarding *E. coli*, values previously reported were used [16]. *E. coli* and *S. aureus* from stock cultures were allowed to grow between 18 h and 24 h at 37 °C on Mueller Hinton agar (MHA). 3 to 5 isolated colonies were then resuspended in 5 mL of MHB and incubated until reaching required OD_{600}. Bacterial suspensions were diluted using fresh media to 2×10^5 cfu/ml for antimicrobial activity assays and 2×10^7 cfu/ml for atomic force microscopy imaging experiments.

2.3. Antibacterial assays

Antimicrobial activities of KTP, KTP–NH_2, IbKTP and IbKTP–NH_2 against *E. coli* and *S. aureus* were monitored using a slightly modified microtiter broth dilution method [16]. Briefly, KTP derivatives were incubated for 18 h at 37 °C with bacterial suspensions in polypropylene microtiter plates (Costar 3879). Peptide concentrations up to 100 μM were tested in triplicate. Sterilized Milli-Q water was used as positive control and as negative controls the antibiotics Tetracycline (Sigma–Aldrich) and Kanamycin (Sigma–Aldrich) were used for *E. coli* and *S. aureus* at 10 μg/ml (22.5 and 18.9 μM, respectively). Antibacterial activities were measured through OD_{600} in polystyrene plates (TPP 92096).

2.4. Blood

Human blood samples were obtained from healthy volunteer donors at the public blood bank Instituto Português do Sangue (IPS, Lisbon, Portugal), with their informed written consent, under an institutional agreement between IPS and Instituto de Bioquímica from Faculdade de Medicina da Universidade de Lisboa. This study was approved by the Ethics Committee of Faculdade de Medicina da Universidade de Lisboa.

2.5. Atomic force microscopy

The effect of KTP derivatives on *S. aureus* and RBC membranes was followed by AFM imaging. KTP, KTP–NH_2, IbKTP and IbKTP–NH_2 at 10 μM were incubated for 2 h at 37 °C with *S. aureus* and samples prepared according to Reference [16]. KTP derivatives effect in RBC membranes was also evaluated as previously established [17], following incubation for 2 h at room temperature with 10 or 100 μM of each KTP derivative. The two hours incubation time has been formerly optimized: it allows peptides to interact with the cell while the untreated bacteria/RBCs preserve the normal morphology [16,17]. A JPK NanoWizard II equipment (JPK Instruments, Berlin, Germany) mounted on an Axiovert 200 inverted microscope (Carl Zeiss, Jena, Germany) in intermittent contact mode using oxidized sharpened silicon cantilevers (ACL from Applied Nanostructures with an average tip radius of 6 nm, a resonance frequency of 190 kHz and spring constant of 45 N/m) was used. Images were acquired with a typical resolution of 512×512 pixels for *S. aureus* and 256×256 pixels for RBCs. Height, error and phase-shift signals were collected and images were line-fitted as required. Tip artifacts were ruled out by image processing. Data were analyzed using JPK image processing software Version 4.0.13 and Gwyddion Version 2.19.

2.6. Hemolytic studies

Human red blood cells were isolated from total blood. All peptide solutions were assayed in triplicate, prepared in phosphate buffered saline (PBS, pH 7.4) buffer and tested up to 100 μM: 0.049, 0.098, 0.195, 0.391, 0.781, 1.563, 3.125, 6.250, 12.5, 25, 50 and 100 μM. Melittin (Sigma, USA) was used as a positive control and PBS buffer as negative control. Experiment and analysis were conducted as described elsewhere [18].

3. Results

The antimicrobial activities of KTP derivatives against *E. coli* and *S. aureus* were determined using a modified microtiter broth dilution method. All peptides were found to be inactive against the Gram-negative bacterium *E. coli* at concentrations up to 100 μM. As to *S. aureus*, KTP did not induce any effect on bacterial growth. The *S. aureus* survival rate at 12.5 μM for KTP–NH_2 is 49%. On the other hand, Ibuprofen containing peptides IbKTP–NH_2 and IbKTP, showed at the same concentration a bacterial survival rate of 65% and 85% that did not decrease for higher peptide concentrations.

Further information on the effects induced by KTP derivatives in *S. aureus* cells was obtained by AFM. This technique has provided detailed images of the bacteria undergoing various stages of antimicrobial peptide actions on a nanometer scale [16,17]. A typical image of untreated *S. aureus* bacteria dried in air is presented in Fig. 1A. cells are spherical-like shaped with a smooth surface with no visible pores or ruptures. Colonies of *S. aureus* usually appear in pairs, chains, or clusters, as seen in Fig. 1. *S. aureus* bacteria treated with 10 μM of KTP or IbKTP resembled the control experiments (Fig. 1B and D). In contrast, at 10 μM, amidated derivatives KTP–NH_2 and IbKTP–NH_2 induced shape alterations. Membrane blebbing and disruption were observed, especially for KTP–NH_2 (see highlighted regions in Fig. 1C and E). From all the KTP-derivatives,

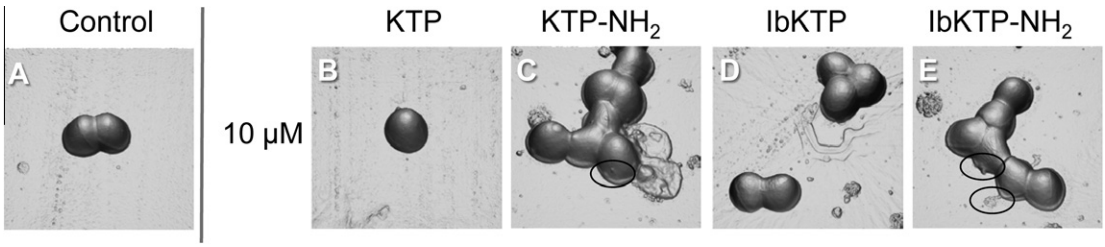

Fig. 1. The effect of KTP derivatives on the shape and surface structure of *S. aureus* followed by atomic force microscopy. *S. aureus* were incubated for 2 h with PBS (control) or KTP, KTP–NH_2, IbKTP and IbKTP–NH_2 at 10 μM. AFM height images are displayed in 3D orthogonal projection. Total scanning area for each image: 4 × 4 μm^2. Highlighted areas are described in the text.

KTP–NH_2 showed to induce the strongest perturbation with a pronounced collapse of the bacterial cells (Fig. 1C).

The toxicity of KTP derivatives for eukaryotic cells was evaluated through hemolytic assays in human RBCs with peptide concentrations up to 100 μM (Fig. 2). All KTP peptides showed virtually no hemolytic effects. Ibuprofen containing peptides are slightly hemolytic only at the highest tested concentration (16%), which is probably due to the effect of the Ibuprofen residue. Melittin is an AMP with a potent antimicrobial activity but also with high lytic activity in RBCs and is therefore taken as a positive control [19]. When compared to melittin, the hemolytic profile of KTP peptides is non-significant.

AFM imaging was used to evaluate if KTP peptides induce any perturbation on RBCs membrane structure (Fig. 3). PBS treated RBCs have disk shapes with uniform borders and a flat surface (Fig. 3A). Although this is not the "iconic" concave shape, swollen RBCs are usually present in normal blood, constituting the thermodynamically more favorable shape and therefore are not indicative of cell damaging [20]. RBCs with concave shape are shown in all the remaining panels of Fig. 3(B–I). Incubation of KTP peptides with RBCs led to membrane structure alterations in some of the imaged cells: they appear spinulated, with spiky boundaries, a shape known as echinocyte Fig. 3(B–I) [21]. A concentration effect is apparent, with an increased number of echinocyte and/or spikes more pronounced for the highest concentration tested. There are no clear differences between the peptides, except for KTP–NH_2 that showed to have less effect on the RBCs membrane.

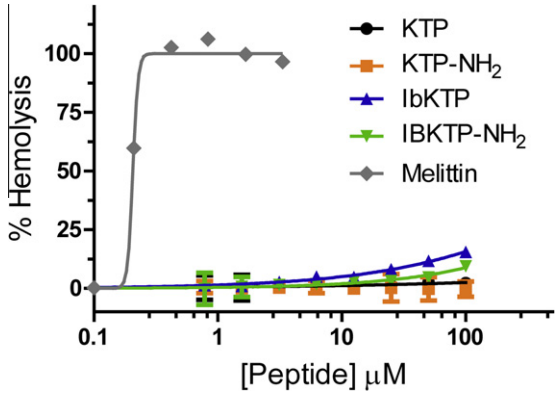

Fig. 2. Quantification of the hemolytic activity of KTP derivatives. Percentage of hemolysis for KTP, KTP–NH_2, IbKTP, IbKTP–NH_2 and Melittin (positive control), as determined by absorbance at 415 nm. Error bars represent SD.

4. Discussion

The mode of action of analgesic kyotorphin peptides at the molecular level has been previously explored with biophysical studies. In this work, we evaluated if the preferential interaction of KTP derivatives with anionic model membranes could imply antimicrobial activity. Unlike unmodified KTP, the KTP derivatives affected the *S. aureus* cell structure. Detailed information on the membranolytic properties of these peptides against *S. aureus* was achieved with AFM imaging. The observed membrane disturbing effect of amidated peptides and especially for KTP–NH_2 can be explained by the peptide charge at physiologic pH, which is +2 for KTP–NH_2, +1 for IBKTP–NH_2 and null for IbKTP. A positive net charge is a common characteristic of most AMPs and the interaction with the negatively charged membrane of bacteria is dominated by electrostatic forces. The results presented in Fig. 1 show that the primary bactericidal effect is exerted at the membrane level. Alterations to bacteria membrane morphology were noticeable although distinct from the severe effects observed with other AMPs [16].

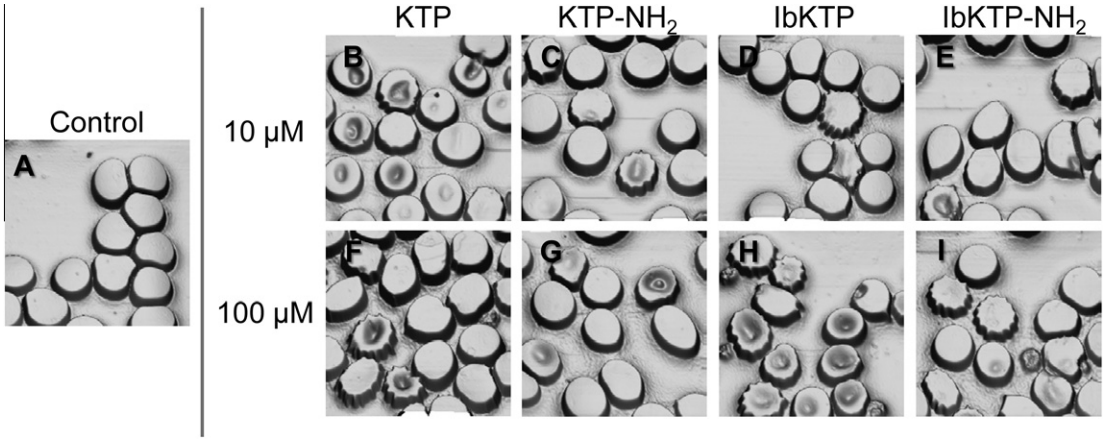

Fig. 3. AFM height images of the effect of KTP derivatives on the shape and surface structure of RBCs shapes. RBCs were incubated for 2 h with PBS (control) or KTP, KTP–NH_2, IbKTP and IbKTP–NH_2 at 10 μM and 100 μM. AFM height images are displayed in 3D orthogonal projection. Total scanning area for each image: 40 × 40 μm^2.

While for mammalian cells the Ibuprofen residue in the peptide revealed to be central to its interaction with membranes and subsequent analgesic activity, the same was not observed for the lytic action on bacteria.

A common drawback of AMPs is their nonspecific cytotoxicity. For this reason, we studied the effect of KTP derivatives on human red blood cells, which are models of eukaryotic cells. Hemolytic assays showed that all KTPs are virtually non-hemolytic, but we went further and performed AFM imaging to gain high-resolution knowledge on the possible effect of KTP derivatives in RBCs membrane. According to the bilayer couple hypothesis [21,22], the insertion of foreign compounds in the outer membrane monolayer of RBC induces echinocytes formation. This can explain the effect of KTP peptides on the shape alterations of some RBCs. These results imply that KTP peptides are binding the outer monolayer, which corroborates the biophysical studies in model membranes where KTP derivatives showed to be located mainly at the membrane surface [14]. Similar results were obtained by Manrique-Moreno et al. for Ibuprofen treated RBC using scanning electron microscopy [23]. It should be stressed that this shape alteration is reversible and demonstrates that KTP peptides are interacting with RBCs membrane but are not prone to destroy the cells and are therefore non-toxic. Comprehensive studies of KTP derivatives for analgesic potency were performed using animal models with no harm effects detected [14,15]. The results reported here increase the therapeutic potential of amidated KTP derivatives. In addition to analgesic, these peptides are also antibacterial, which is a very appealing combination from the clinical point of view.

Catiau et al. [12] have previously defined that one needs Tyr-Arg plus a positively charged aminoacid residue (Lys or His) to have a peptide with antibacterial activity. In this work, we showed that the minimal peptidic sequence is indeed Tyr-Arg, if amidated, a transformation that grants the needed extra net positive charge to the molecule.

Acknowledgments

Unidade de Microbiologia Molecular e Infecção from Instituto de Medicina Molecular are acknowledged for the kind gift of *E. coli* and *S. aureus* strains. Dr. Sónia T. Henriques is acknowledged for helpful discussions. Fundação para a Ciência e Tecnologia (Portugal) is acknowledged for funding (SFRH/BD/42158/2007 fellowship to M.M.B.R. and SFRH/BD/39039/2007 fellowship to H.G.F.). Marie Curie Industry-Academia Partnerships and Pathways (European Commission) is also acknowledged for funding and fellowship to V. G. R. (FP7-PEOPLE-2007-3-1-IAPP, Project 230654).

References

[1] M.N. Melo, R. Ferre, M.A. Castanho, Antimicrobial peptides: linking partition, activity and high membrane-bound concentrations, Nat. Rev. Microbiol. 7 (2009) 245–250.
[2] S.T. Henriques, M.N. Melo, M.A. Castanho, Cell-penetrating peptides and antimicrobial peptides: how different are they?, Biochem J 399 (2006) 1–7.
[3] R.M. Epand, H.J. Vogel, Diversity of antimicrobial peptides and their mechanisms of action, Biochim. Biophys. Acta 1462 (1999) 11–28.
[4] W. Bellamy, M. Takase, K. Yamauchi, H. Wakabayashi, K. Kawase, M. Tomita, Identification of the bactericidal domain of lactoferrin, Biochim. Biophys. Acta 1121 (1992) 130–136.
[5] Y. Mine, F. Ma, S. Lauriau, Antimicrobial peptides released by enzymatic hydrolysis of hen egg white lysozyme, J. Agric. Food Chem. 52 (2004) 1088–1094.
[6] R. Froidevaux, F. Krier, N. Nedjar-Arroume, D. Vercaigne-Marko, E. Kosciarz, C. Ruckebusch, P. Dhulster, D. Guillochon, Antibacterial activity of a pepsin-derived bovine hemoglobin fragment, FEBS Lett. 491 (2001) 159–163.
[7] N. Nedjar-Arroume, V. Dubois-Delval, K. Miloudi, R. Daoud, F. Krier, M. Kouach, G. Briand, D. Guillochon, Isolation and characterization of four antibacterial peptides from bovine hemoglobin, Peptides 27 (2006) 2082–2089.
[8] R. Daoud, V. Dubois, L. Bors-Dodita, N. Nedjar-Arroume, F. Krier, N.E. Chihib, P. Mary, M. Kouach, G. Briand, D. Guillochon, New antibacterial peptide derived from bovine hemoglobin, Peptides 26 (2005) 713–719.
[9] N. Nedjar-Arroume, V. Dubois-Delval, E.Y. Adje, J. Traisnel, F. Krier, P. Mary, M. Kouach, G. Briand, D. Guillochon, Bovine hemoglobin: an attractive source of antibacterial peptides, Peptides 29 (2008) 969–977.
[10] E.Y. Adje, R. Balti, M. Kouach, P. Dhulster, D. Guillochon, N. Nedjar-Arroume, Obtaining antimicrobial peptides by controlled peptic hydrolysis of bovine hemoglobin, Int. J. Biol. Macromol. 49 (2011) 143–153.
[11] L. Catiau, J. Traisnel, N.E. Chihib, G. Le Flem, A. Blanpain, O. Melnyk, D. Guillochon, N. Nedjar-Arroume, RYH: a minimal peptidic sequence obtained from beta-chain hemoglobin exhibiting an antimicrobial activity, Peptides 32 (2011) 1463–1468.
[12] L. Catiau, J. Traisnel, V. Delval-Dubois, N.E. Chihib, D. Guillochon, N. Nedjar-Arroume, Minimal antimicrobial peptidic sequence from hemoglobin alpha-cha: KYR, Peptides 32 (2011) 633–638.
[13] H. Takagi, H. Shiomi, H. Ueda, H. Amano, Morphine-like analgesia by a new dipeptide, L-tyrosyl–L-arginine (kyotorphin) and its analogue, Eur. J. Pharmacol. 55 (1979) 109–111.
[14] M.M. Ribeiro, A.R. Pinto, M.M. Domingues, I. Serrano, M. Heras, E.R. Bardaji, I. Tavares, M.A. Castanho, Chemical conjugation of the neuropeptide kyotorphin and ibuprofen enhances brain targeting and analgesia, Mol. Pharm. 8 (2011) 1929–1940.
[15] M.M. Ribeiro, A. Pinto, M. Pinto, M. Heras, I. Martins, A. Correia, E. Bardaji, I. Tavares, M. Castanho, Inhibition of nociceptive responses after systemic administration of amidated kyotorphin, Br. J. Pharmacol. 163 (2011) 964–973.
[16] C.S. Alves, M.N. Melo, H.G. Franquelim, R. Ferre, M. Planas, L. Feliu, E. Bardaji, W. Kowalczyk, D. Andreu, N.C. Santos, M.X. Fernandes, M.A. Castanho, *Escherichia coli* cell surface perturbation and disruption induced by antimicrobial peptides BP100 and pepR, J. Biol. Chem. 285 (2010) 27536–27544.
[17] S.T. Henriques, Y.H. Huang, K.J. Rosengren, H.G. Franquelim, F.A. Carvalho, A. Johnson, S. Sonza, G. Tachedjian, M.A. Castanho, N.L. Daly, D.J. Craik, Decoding the membrane activity of the cyclotide kalata B1: the importance of phosphatidylethanolamine phospholipids and lipid organization on hemolytic and anti-HIV activities, J. Biol. Chem. 286 (2011) 24231–24241.
[18] Y.H. Huang, M.L. Colgrave, R.J. Clark, A.C. Kotze, D.J. Craik, Lysine-scanning mutagenesis reveals an amendable face of the cyclotide kalata B1 for the optimization of nematocidal activity, J. Biol. Chem. 285 (2010) 10797–10805.
[19] M.T. Tosteson, S.J. Holmes, M. Razin, D.C. Tosteson, Melittin lysis of red cells, J. Membr. Biol. 87 (1985) 35–44.
[20] R. Nowakowski, P. Luckham, P. Winlove, Imaging erythrocytes under physiological conditions by atomic force microscopy, Biochim. Biophys. Acta 1514 (2002) 170–176.
[21] A. Zachowski, Phospholipids in animal eukaryotic membranes: transverse asymmetry and movement, Biochem J. 294 (Pt 1) (1993) 1–14.
[22] A. Iglic, V. Kralj-Iglic, H. Hagerstrand, Amphiphile induced echinocyte-spheroechinocyte transformation of red blood cell shape, Eur. Biophys. J. 27 (1998) 335–339.
[23] M. Manrique-Moreno, F. Villena, C.P. Sotomayor, A.M. Edwards, M.A. Munoz, P. Garidel, M. Suwalsky, Human cells and cell membrane molecular models are affected in vitro by the nonsteroidal anti-inflammatory drug ibuprofen, Biochim. Biophys. Acta 1808 (2011) 2656–2664.

Biochemical and Biophysical Research Communications 420 (2012) 680–684

Contents lists available at SciVerse ScienceDirect

Biochemical and Biophysical Research Communications

journal homepage: www.elsevier.com/locate/ybbrc

Down-regulated expression of the protein-tyrosine phosphatase 1B (PTP1B) is associated with aggressive clinicopathologic features and poor prognosis in hepatocellular carcinoma

Long-Yi Zheng [a,1], Dong-Xun Zhou [b,1], Jin Lu [a], Wen-Jun Zhang [c], Da-Jin Zou [a,*]

[a] Department of Endocrinology, Changhai Hospital, 168 Changhai Road, Shanghai 200433, China
[b] Department of Comprehensive Treatment II, Eastern Hepatobiliary Surgery Hospital, 225 Changhai Road, Shanghai 200438, China
[c] Department of Emergency, Changhai Hospital, 168 Changhai Road, Shanghai 200433, China

ARTICLE INFO

Article history:
Received 20 February 2012
Available online 17 March 2012

Keywords:
PTP1B
Hepatocellular carcinoma
Prognosis
Tumor-initiating cells
β-Catenin

ABSTRACT

The protein-tyrosine phosphatase 1B (PTP1B) is a classical non-transmembrane protein tyrosine phosphatase that plays a key role in metabolic signaling and can exert both tumor suppressing and tumor promoting effects in different cancers depending on the substrate involved and the cellular context. However, the expression level and function of PTP1B in hepatocellular carcinoma (HCC) remain unclear. In this study, PTP1B expression was detected by immunohistochemistry in normal liver tissue ($n = 16$) and hepatocellular carcinoma ($n = 169$). The correlations between PTP1B expression level and clinicopathologic features and patient survival were also analyzed. One hundred and eleven of 169 HCC patients (65.7%) had negative or low PTP1B expression in tumorous tissues, whereas normal tissues always expressed strong PTP1B. Decreased PTP1B expression was significantly associated with aggressive clinicopathologic features and poor prognosis. Immunohistochemistry also showed that low PTP1B expression level was correlated with high percentage of $OV6^+$ tumor-initiating cells (T-ICs) and high frequency of nuclear β-Catenin expression in HCC specimens. Our findings demonstrate for the first time that the loss of inhibitory effect of PTP1B may contribute to progression and invasion of HCC through activation of Wnt/β-Catenin signaling and expansion of liver T-ICs. PTP1B may serve as a valuable prognostic biomarker and potential therapeutic target in HCC.

1. Introduction

Hepatocellular carcinoma (HCC) is one of the most common malignant solid tumors in the world [1]. Although the short-term prognosis of HCC has been improved due to recent advances in the early diagnosis and treatment, the long-term prognosis of HCC remains dismal even after radical excision. Vascular invasion, metastasis, and recurrence are major causes of treatment failure [2]. Understanding the molecular mechanisms underlying HCC progression and invasion is therefore critical for improving the accuracy of prognostic outcome prediction.

Tyrosine phosphorylation, which is controlled by protein-tyrosine kinases (PTKs) and protein-tyrosine phosphatases (PTPs), is an essential primary step in signal transduction cascades that regulate proliferation, survival, differentiation, migration and apoptosis of normal cells. Abnormal control of tyrosyl phosphorylation may result in various human diseases, including cancer [3]. It is now well established that the protein-tyrosine phosphatase 1B (PTP1B) has emerged as a critical regulator of multiple signaling networks involved in human disorders such as diabetes, obesity, and cancer [4,5]. Liver-specific $PTP1B^{-/-}$ mice have increased hepatic insulin signaling and enhanced glucose tolerance [6]. Levels of PTB1B were also found to modulate the apoptotic pathways triggered by trophic factors withdrawal in hepatocytes [7]. However, its involvement in human HCC progression and invasion remains unclear.

In this study, we evaluated the expression of PTP1B in 169 HCC cases by immunohistochemistry and correlated the immunostaining scores with clinicopathologic features and patient prognosis. We also explored the relationship between the PTP1B expression and expansion of $OV6^+$ tumor-initiating cells.

2. Materials and methods

2.1. Patients

One hundred and sixty-nine HCC specimens were randomly collected from HCC patients who underwent curative resection in Eastern Hepatobiliary Surgery Hospital (Shanghai, China).

Abbreviations: HCC, hepatocellular carcinoma; PTPs, protein-tyrosine phosphatases; T-ICs, tumor-initiating cells.

* Corresponding author. Fax: +86 21 53961632.
E-mail address: dajinzou@hotmail.com (D.-J. Zou).

[1] These two authors contributed equally to this work.

0006-291X/$ - see front matter © 2012 Elsevier Inc. All rights reserved.
http://dx.doi.org/10.1016/j.bbrc.2012.03.066

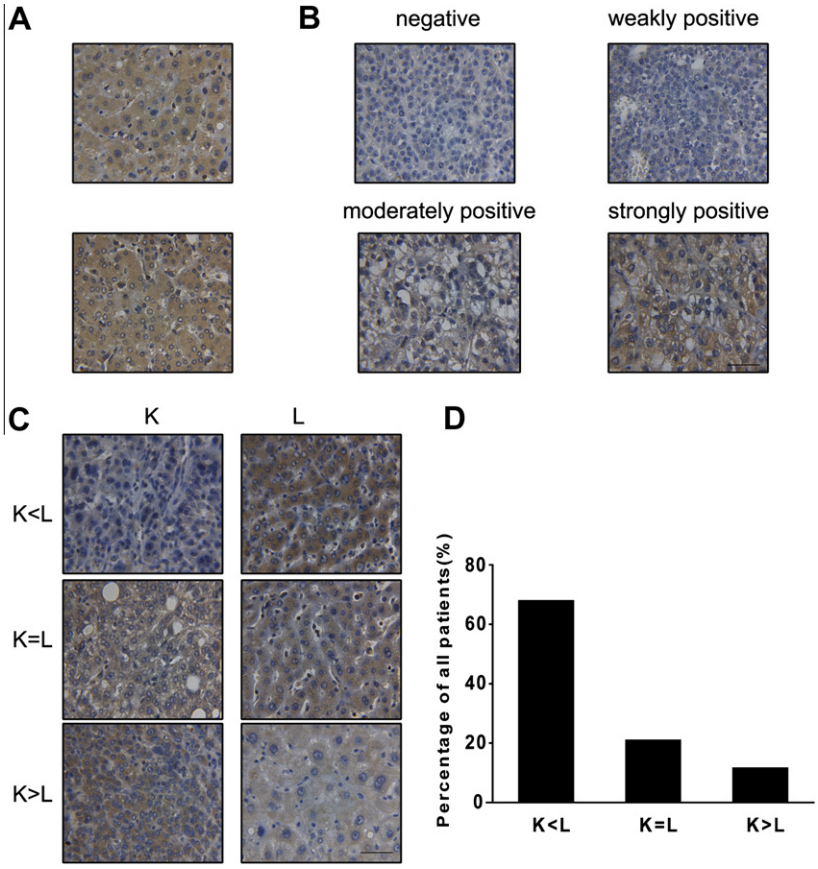

Fig. 1. PTP1B protein showed decreased expression in HCC tissues. (A) Immunohistochemical analysis of PTP1B expression in normal livers. (B) Representative immunohistochemical staining of PTP1B in HCC specimens. (C) Representative immunohistochemical staining of PTP1B in tumors and paired non-tumorous livers. K: hepatocellular carcinoma; L: paired nontumorous liver parenchyma (scale bar = 50 μm). (D) 149 HCC patients were categorized into three groups according to the different PTP1B expression between tumors and paired non-tumorous livers. K: hepatocellular carcinoma; L: paired nontumorous liver parenchyma.

Human normal liver tissues were obtained from distal normal liver tissue of liver hemangioma patients. Informed consent was obtained in all cases before surgery. The diagnosis of HCC was confirmed by pathological results. Sixty patients were followed up until December 2010. Overall survival (OS) was defined as the interval between the dates of surgery and death. Disease-free survival (DFS) was defined as the interval between the dates of surgery and first recurrence of disease. First recurrence was classified as recurrence, distant recurrence, or a combination of both.

2.2. Immunohistochemistry

Liver tissue was divided and fixed in phosphate-buffered neutral formalin, embedded in paraffin, and cut into 5-μm-thick sections. The following primary antibodies were used: rabbit anti-PTP1B, mouse anti-β-Catenin (Santa Cruz Biotech), mouse anti-OV6 (R&D). Vector ABC kit (Vector Laboratories) and DAB reagent (Dako Comp) were employed in the detection procedure. All the slides were observed and photographed with an Olympus microscope (OLYMPUS, Tokyo, Japan).

2.3. Evaluation of PTP1B, OV6 and β-Catenin staining

Staining of the whole tissue sections were examined and scored by two independently observers who were blind to the clinicopathological data of the tumors. Based on the intensity of the stained tumor cells, PTP1B immunostaining was scored as 0, negative; 1+, weakly positive; 2+, moderately positive; or 3+, strongly positive. High expression of PTP1B in tumor cells was defined as score $\geqslant$2+. If there was positive staining in more than 30% of the cancer cells, the tumors were recorded as having high percentage of $OV6^{+}$ cells. Tumors with more than 10% of cancer cells positive for nuclear staining of β-Catenin were regarded as positive samples.

2.4. Statistical analysis

Analysis was performed with SAS 9.1.3 software (SAS Institute Inc., Cary, NC). The χ^2 test was used to compare qualitative variables. Kaplan–Meier analysis was used to determine the survival. Log-rank test was used to compare patients' survival between subgroups.

3. Results

3.1. PTP1B down-regulation is a common event in HCC tissues

To explore the role of PTP1B in HCC, we first evaluated the expression of PTP1B in normal human liver and HCC specimens using immunohistochemical staining. As shown in Fig. 1A, normal liver tissues showed strong PTP1B expression in the cytoplasm of liver cells (n = 16). Although the expression patterns varied significantly among the HCC samples (Fig. 1B), PTP1B was undetected or weakly stained in 111 of 169 (65.7%) HCC tissues. Among the 149 HCC patients with paired tumorous and non-tumorous samples for

Table 1
Correlation between PTP1B expression and clinicopathological characteristics in human HCC specimens.

	High PTP1B expression (No. of cases)	Low PTP1B expression (No. of cases)	*P*
Age			
<50 years	22	59	<0.01
⩾50 years	36	52	
Gender			
Male	52	98	
Female	6	13	
HBV infection			
Absent	6	8	
Present	52	103	
AFP			
<200 ng/ml	38	51	<0.05
⩾200 ng/ml	20	60	
Liver cirrhosis			
Absent	20	33	
Present	38	78	
Tumor multiplicity			
Single	39	78	
Multiple	19	33	
Maximal tumor size			
<5 cm	18	38	
⩾5 cm	40	73	
Tumor encapsulation			
Absent	24	69	<0.01
Present	34	42	
Portal vein thrombosis (Gross)			
Absence	50	82	
Present	8	29	
Microscopic portal vein invasion			
Absence	37	45	<0.01
Present	21	66	

evaluation, PTP1B-expression was decreased in HCC relative to paired non-tumorous tissues in 101 (67.79%) patients (Fig. 1C and D). These data suggested that PTP1B down-regulation was a common event in HCC tissues.

3.2. Low PTP1B expression predicts poor prognosis of HCC

Based on the results from immunohistochemistry, all 169 HCC patients were divided into two groups: high PTP1B expression group ($n = 58$) and low PTP1B expression group ($n = 111$). As shown in Table 1, patients in low expression group were significantly associated with aggressive clinicopathologic features (HCC onset in patients <50 years, high serum alpha-fetoprotein level, absence of tumor encapsulation, and microscopic portal venous invasion). To further confirm that down-regulation of PTP1B correlates with HCC prognosis, expression of PTP1B was examined by IHC in sections from 60 HCC specimens with disease-free survival (DFS) and overall survival (OS) time. Kaplan–Meier survival analysis revealed that patients in low PTP1B expression group ($n = 37$) had either shorter DFS or worse OS (Fig. 2) than the high PTP1B expression group ($n = 23$). These data suggested that low PTP1B expression could serve as a valuable predicting factor for recurrence and poor survival of HCC patients.

3.3. Low PTP1B expression is correlated with high percentage of $OV6^+$ T-ICs in HCC specimens

Increasing evidence has shown that liver tumor-initiating cells (T-ICs) or cancer stem cells (CSC) may be associated with HCC initiation and progression [8]. $OV6^+$ cells have been reported to exhibit stronger T-ICs or CSC characteristics than the corresponding $OV6^-$ cells in HCC cell lines and HCC specimens [9]. To evaluate the correlation between PTP1B expression and expansion of $OV6^+$ tumor cells, we examined OV6 expression in 158 previously used HCC tissue samples. The pattern of OV6 staining was variable, some samples were scored semi-quantitatively as low as 0% to <30% positive, others as high as ⩾30% in HCC cells. The representative positive immunostaining of HCC specimens were shown in Fig. 3A. As shown in Fig. 3C, patients with low PTP1B expression had much more $OV6^+$ cells in their tumor tissues, suggesting that decreased expression of PTP1B may promote expansion of tumorigenic cells, and thus contribute to the development and progression of HCC.

3.4. Low PTP1B expression is associated with high frequency of nuclear β-Catenin expression

Wnt/β-Catenin signaling pathway is known to be responsible for activation and expansion of cancer stem cells in human HCC [9]. To identify if β-Catenin is involved in expansion of $OV6^+$ T-ICs in HCC specimens, we examined β-Catenin expression in these HCC specimens. Consistent with previous report, nuclear accumulation of β-Catenin, a marker of Wnt/β-Catenin signaling activation, was observed in 39.24% of HCC specimens (Fig. 3B). Intriguingly, low PTP1B expression was associated with high frequency of tumor cells with nuclear β-Catenin expression (Fig. 3C), indicating

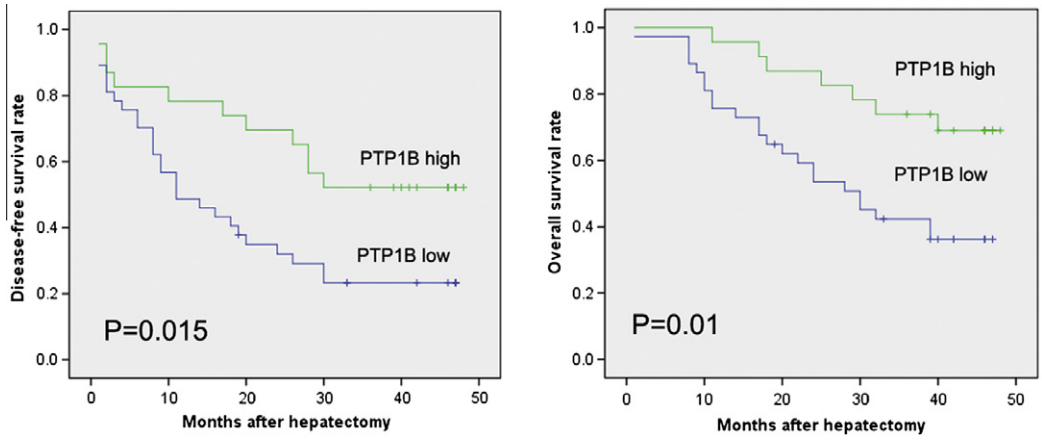

Fig. 2. Low PTP1B expression predicts poor prognosis of HCC. The disease-free survival (DFS) and overall survival (OS) rates of 60 patients with HCC were compared between two groups.

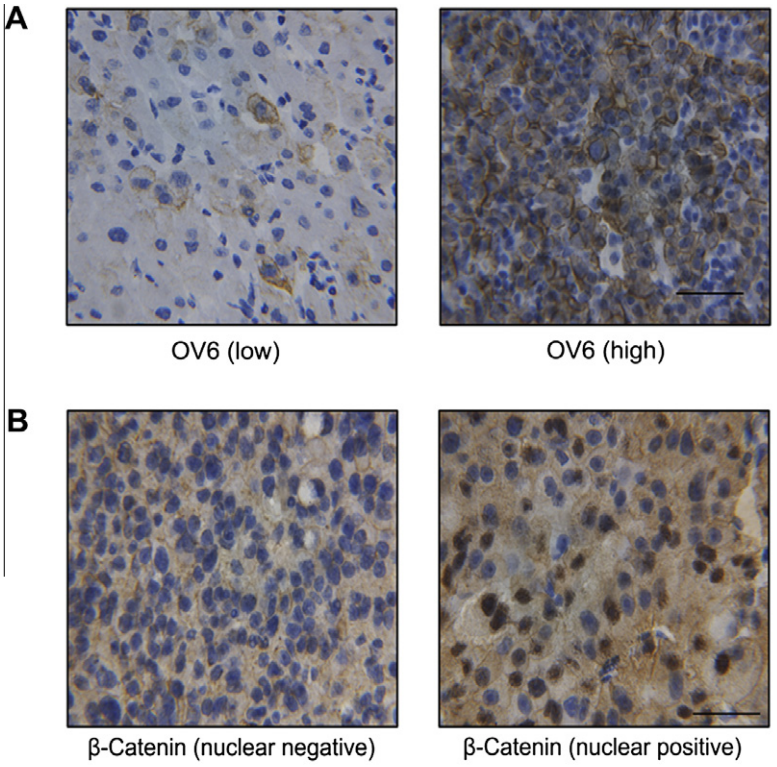

C

	Low PTP1B (No. of Cases)	High PTP1B (No. of Cases)	P value
Percentage of OV6+ tumor cells			
<30%	37	31	<0.05
≥30%	64	26	
Nuclear β-catenin positive tumor cells			
<10%	54	42	<0.05
≥10%	47	15	

Fig. 3. Low PTP1B expression was correlated with expansion of $OV6^+$ tumor-initiating cells and activation of Wnt/β-Catenin signaling. (A) Representative OV6 staining patterns of HCC specimens. (B) Representative nuclear β-Catenin staining patterns of HCC specimens (scale bar = 50 μm). (C) Summary of the expression of PTP1B, OV6, and β-Catenin in human HCC specimens.

that decreased expression of PTP1B may promote $OV6^+$ T-ICs expansion through activation of Wnt/β-Catenin signaling pathway.

4. Discussion

As the first PTP that has been purified, PTP1B is a central player in negatively regulating insulin and leptin signaling in mice [10–12] and has attracted much attention as a potential drug target for obesity and type 2 diabetes. Nevertheless, the function of PTP1B is not restricted to metabolic regulation, and numerous groups focused on the possible role for PTP1B in oncogenesis in the last few decades [5]. PTP1B may also directly dephosphorylate a number of oncogenic receptor tyrosine kinases, and inhibit signaling from other RTKs, such as the platelet-derived growth factor and hepatocyte growth factor receptors [13,14]. When overexpressed, PTP1B can inhibit transformation by oncogenes that increase tyrosine phosphorylation, including ErbB2, Src, Ras [15–17]. However, recent findings have also suggested that PTP1B was overexpressed in erbB2-transformed breast cancer cell lines, and deficiency or inhibition of PTP1B delayed ErbB2-induced mammary tumorigenesis and prevented lung metastasis [18].

HCC was the fifth most common solid cancer and the third leading cause of cancer-related mortality worldwide, caused approximately 600,000 deaths yearly [1]. Thus, it is crucial to evaluate the expression level and function of PTP1B in HCC. Here we demonstrated for the first time that expression of PTP1B was down-regulated in the majority of the HCC patients. More importantly, we also revealed that patients with low PTP1B expression were significantly associated with aggressive clinicopathologic features and poor prognosis. These findings suggested that PTP1B may play an important role in suppressing hepatocarcinogenesis.

The balance of proper protein tyrosine phosphorylation levels is also critical for stem cells maintenance and function. Shp2, a tyrosine phosphatase with 2 Src-homology 2 (SH2) domains, plays a critical role in maintenance of a functional HSC pool in adult mammals [19]. The T cell protein tyrosine phosphatase (TC-PTP) has also been shown to play an important role in hematopoiesis [20]. Recent advances in the fields of cancer biology and stem cells have demonstrated that tumor-initiating cells (T-ICs) [21] exist in leuke-

mia and a variety of solid tumors (including breast, brain, prostate, and HCC). T-ICs had a pivotal role in tumorigenesis, tumor progression, and metastasis. However, the relationship between tyrosine phosphatase and expansion of stem cells, especially T-ICs or CSCs, remains unclear. OV6, previously used as marker of hepatic progenitor cells, was recently identified as a novel T-ICs marker. The subpopulation of $OV6^+$ HCC cells possessed a greater tumor initiating ability *in vivo* and showed a substantial resistance to standard chemotherapy [9]. To our note, this is the first report to investigate the relationship between PTP1B and liver T-ICs. We showed here that, in low PTP1B expression HCCs, percentage of patients with high OV6 staining was 63.4%, higher than that of high PTP1B expression group. Thus our results shed new light on the role of PTP1B in regulating expansion of liver T-ICs.

β-Catenin is an essential component of both intercellular junctions and the canonical Wnt signaling pathway, which plays important roles in regulation of cell proliferation, differentiation, self-renewal and movement [22]. Aberrant activation of Wnt/β-Catenin is primarily involved in the pathogenesis of hepatic tumors, especially HCC [23]. Activation of β-Catenin can also promote the proliferation of hepatic progenitor cells in rodent models and expansion of cancer stem cells in HCC [9,24,25]. Phosphorylation-dependent release of β-Catenin from the cadherin complex not only affected the integrity and function of the adhesion complex, but may also be an alternative mechanism for activating β-Catenin signaling [26]. PTP1B has been reported to associate with the cytoplasmic domain of N-cadherin and regulate cadherin function through dephosphorylation of β-Catenin [27]. So it was not surprising that low PTP1B expression level was correlated with high frequency of nuclear β-Catenin expression in HCC specimens. These results suggested that the loss of inhibitory effect of PTP1B may contribute to progression and invasion of HCC through activation of Wnt/β-Catenin signaling and expansion of liver T-ICs.

In this study, we demonstrated for the first time that PTP1B down-regulation was a common event in HCC patients and low expression of PTP1B in HCC predicted poor prognosis. Our results provide novel evidence for the inhibitory effect of PTP1B in hepatocarcinogenesis and highlight that PTP1B may serve as a valuable prognostic biomarker and potential therapeutic target in HCC.

Acknowledgment

Research was supported by the project from National Natural Science Foundation of China (81170738 and 81070619).

References

[1] A. Jemal, R. Siegel, J. Xu, E. Ward, Cancer statistics 2010, CA Cancer J. Clin. 60 (2010) 277–300.
[2] R. Tung-Ping Poon, S.T. Fan, J. Wong, Risk factors, prevention, and management of postoperative recurrence after resection of hepatocellular carcinoma, Ann. Surg. 232 (2000) 10–24.
[3] P. Blume-Jensen, T. Hunter, Oncogenic kinase signalling, Nature 411 (2001) 355–365.
[4] S.C. Yip, S. Saha, J. Chernoff, PTP1B: a double agent in metabolism and oncogenesis, Trends Biochem. Sci. 35 (2010) 442–449.
[5] L. Lessard, M. Stuible, M.L. Tremblay, The two faces of PTP1B in cancer, Biochim. Biophys. Acta 2010 (1804) 613–619.
[6] M. Delibegovic, D. Zimmer, C. Kauffman, K. Rak, E.G. Hong, Y.R. Cho, J.K. Kim, B.B. Kahn, B.G. Neel, K.K. Bence, Liver-specific deletion of protein-tyrosine phosphatase 1B (PTP1B) improves metabolic syndrome and attenuates diet-induced endoplasmic reticulum stress, Diabetes 58 (2009) 590–599.
[7] A. Gonzalez-Rodriguez, O. Escribano, J. Alba, C.M. Rondinone, M. Benito, A.M. Valverde, Levels of protein tyrosine phosphatase 1B determine susceptibility to apoptosis in serum-deprived hepatocytes, J. Cell. Physiol. 212 (2007) 76–88.
[8] J.E. Visvader, Cells of origin in cancer, Nature 469 (2011) 314–322.
[9] W. Yang, H.X. Yan, L. Chen, Q. Liu, Y.Q. He, L.X. Yu, S.H. Zhang, D.D. Huang, L. Tang, X.N. Kong, C. Chen, S.Q. Liu, M.C. Wu, H.Y. Wang, Wnt/beta-catenin signaling contributes to activation of normal and tumorigenic liver progenitor cells, Cancer Res. 68 (2008) 4287–4295.
[10] M. Elchebly, P. Payette, E. Michaliszyn, W. Cromlish, S. Collins, A.L. Loy, D. Normandin, A. Cheng, J. Himms-Hagen, C.C. Chan, C. Ramachandran, M.J. Gresser, M.L. Tremblay, B.P. Kennedy, Increased insulin sensitivity and obesity resistance in mice lacking the protein tyrosine phosphatase-1B gene, Science 283 (1999) 1544–1548.
[11] A. Cheng, N. Uetani, P.D. Simoncic, V.P. Chaubey, A. Lee-Loy, C.J. McGlade, B.P. Kennedy, M.L. Tremblay, Attenuation of leptin action and regulation of obesity by protein tyrosine phosphatase 1B, Dev. Cell 2 (2002) 497–503.
[12] J.M. Zabolotny, K.K. Bence-Hanulec, A. Stricker-Krongrad, F. Haj, Y. Wang, Y. Minokoshi, Y.B. Kim, J.K. Elmquist, L.A. Tartaglia, B.B. Kahn, B.G. Neel, PTP1B regulates leptin signal transduction in vivo, Dev. Cell 2 (2002) 489–495.
[13] F.G. Haj, B. Markova, L.D. Klaman, F.D. Bohmer, B.G. Neel, Regulation of receptor tyrosine kinase signaling by protein tyrosine phosphatase-1B, J. Biol. Chem. 278 (2003) 739–744.
[14] A. Kakazu, G. Sharma, H.E. Bazan, Association of protein tyrosine phosphatases (PTPs)-1B with c-Met receptor and modulation of corneal epithelial wound healing, Invest. Ophthalmol. Vis. Sci. 49 (2008) 2927–2935.
[15] T.A. Woodford-Thomas, J.D. Rhodes, J.E. Dixon, Expression of a protein tyrosine phosphatase in normal and v-src-transformed mouse 3T3 fibroblasts, J. Cell Biol. 117 (1992) 401–414.
[16] N. Dube, A. Cheng, M.L. Tremblay, The role of protein tyrosine phosphatase 1B in Ras signaling, Proc. Natl. Acad. Sci. USA 101 (2004) 1834–1839.
[17] K.R. LaMontagne Jr., G. Hannon, N.K. Tonks, Protein tyrosine phosphatase PTP1B suppresses p210 bcr-abl-induced transformation of rat-1 fibroblasts and promotes differentiation of K562 cells, Proc. Natl. Acad. Sci. USA 95 (1998) 14094–14099.
[18] S.G. Julien, N. Dube, M. Read, J. Penney, M. Paquet, Y. Han, B.P. Kennedy, W.J. Muller, M.L. Tremblay, Protein tyrosine phosphatase 1B deficiency or inhibition delays ErbB2-induced mammary tumorigenesis and protects from lung metastasis, Nat. Genet. 39 (2007) 338–346.
[19] H.H. Zhu, K. Ji, N. Alderson, Z. He, S. Li, W. Liu, D.E. Zhang, L. Li, G.S. Feng, Kit-Shp2-Kit signaling acts to maintain a functional hematopoietic stem and progenitor cell pool, Blood 117 (2011) 5350–5361.
[20] K.E. You-Ten, E.S. Muise, A. Itie, E. Michaliszyn, J. Wagner, S. Jothy, W.S. Lapp, M.L. Tremblay, Impaired bone marrow microenvironment and immune function in T cell protein tyrosine phosphatase-deficient mice, J. Exp. Med. 186 (1997) 683–693.
[21] J.E. Visvader, G.J. Lindeman, Cancer stem cells in solid tumours: accumulating evidence and unresolved questions, Nat. Rev. Cancer 8 (2008) 755–768.
[22] R. Fodde, T. Brabletz, Wnt/beta-catenin signaling in cancer stemness and malignant behavior, Curr. Opin. Cell Biol. 19 (2007) 150–158.
[23] M.D. Thompson, S.P. Monga, Wnt/beta-catenin signaling in liver health and disease, Hepatology 45 (2007) 1298–1305.
[24] M. Hu, M. Kurobe, Y.J. Jeong, C. Fuerer, S. Ghole, R. Nusse, K.G. Sylvester, Wnt/beta-catenin signaling in murine hepatic transit amplifying progenitor cells, Gastroenterology 133 (2007) 1579–1591.
[25] U. Apte, M.D. Thompson, S. Cui, B. Liu, B. Cieply, S.P. Monga, Wnt/beta-catenin signaling mediates oval cell response in rodents, Hepatology 47 (2008) 288–295.
[26] W.J. Nelson, R. Nusse, Convergence of Wnt, beta-catenin, and cadherin pathways, Science 303 (2004) 1483–1487.
[27] G. Xu, C. Arregui, J. Lilien, J. Balsamo, PTP1B modulates the association of beta-catenin with N-cadherin through binding to an adjacent and partially overlapping target site, J. Biol. Chem. 277 (2002) 49989–49997.

Biochemical and Biophysical Research Communications 420 (2012) 685–691

Contents lists available at SciVerse ScienceDirect

Biochemical and Biophysical Research Communications

journal homepage: www.elsevier.com/locate/ybbrc

Hypoxia attenuates inflammatory mediators production induced by *Acanthamoeba via* Toll-like receptor 4 signaling in human corneal epithelial cells

Hong Pan [a,b], Xinyi Wu [a,*]

[a] *Department of Ophthalmology, Qilu Hospital, Shandong University, 107#, Wenhua Xi Road, Jinan 250012, PR China*
[b] *The Key Laboratory of Cardiovascular Remodeling and Function Research, Chinese Ministry of Education and Chinese Ministry of Public Health, Qilu Hospital, Shandong University, 107#, Wenhua Xi Road, Jinan 250012, PR China*

ARTICLE INFO

Article history:
Received 6 March 2012
Available online 17 March 2012

Keywords:
Acanthamoeba keratitis
Corneal susceptibility
Hypoxia
Inflammatory cytokine
TLR4

ABSTRACT

Acanthamoeba keratitis (AK) is a vision-threatening corneal infection that is intimately associated with contact lens use which leads to hypoxic conditions on the corneal surface. However, the effect of hypoxia on the *Acanthamoeba*-induced host inflammatory response of corneal epithelial cells has not been studied. In the present study, we investigated the effect of hypoxia on the *Acanthamoeba*-induced production of inflammatory mediators interleukin-8 (IL-8) and interferon-β (IFN-β) in human corneal epithelial cells and then evaluated its effects on the Toll-like receptor 4 (TLR4) signaling, including TLR4 and myeloid differentiation primary response gene (88) (MyD88) expression as well as the activation of nuclear factor kappa-light-chain-enhancer of activated B cells (NF-κB) and extracellular signal-regulated kinases 1/2 (ERK1/2). We then studied the effect of hypoxia on a TLR4-specific inflammatory response triggered by the TLR4 ligand lipopolysaccharide (LPS). Our data showed that hypoxia significantly decreased the production of IL-8 and IFN-β. Furthermore, hypoxia attenuated *Acanthamoeba*-triggered TLR4 expression as well as the activation of NF-κB and ERK1/2, indicating that hypoxia abated *Acanthamoeba*-induced inflammatory responses by affecting TLR4 signaling. Hypoxia also inhibited LPS-induced IL-6 and IL-8 secretion, myeloid differentiation primary response gene (88) MyD88 expression and NF-κB activation, confirming that hypoxia suppressed the LPS-induced inflammatory response by affecting TLR4 signaling. In conclusion, our results demonstrated that hypoxia attenuated the host immune and inflammatory response against *Acanthamoeba* infection by suppressing TLR4 signaling, indicating that hypoxia might impair the host cell's ability to eliminate the *Acanthamoeba* invasion and that hypoxia could enhance cell susceptibility to *Acanthamoeba* infection. These results may explain why contact lens use is one of the most prominent risk factors for AK.

1. Introduction

Acanthamoeba keratitis (AK) is a vision-threatening disease caused by a free-living, pathogenic *Acanthamoeba*, the incidence of which was recently increased substantially. Contact lens use has been regarded as one of the most significant risk factors for AK [1]. The incidence of AK was found to be 17.53–21.14 per million contact lens users in the United Kingdom [2] and 1.65–2.01 per million contact lens users in the United States [3]. AK is still a challenging disease to treat because the mechanisms of *Acanthamoeba*-induced corneal pathogenesis and the host inflammatory response are not yet fully understood. An improved understanding of the effects of contact lens use on the corneal innate immune and inflammatory response to *Acanthamoeba* infection is urgently required to identify potential preventative and therapeutic strategies.

Contact lenses hinder the natural absorption of oxygen into the cornea, and its epithelial cells, leading to an unhealthy condition known as hypoxia [4]. Hypoxia has been assumed to be a prominent mechanism driving contact lens-associated keratitis [5,6]. Hypoxia negatively affects corneal epithelial cell biology [6] and enhances the binding of infectious agents to these cells [7,8]. Human corneal epithelia cells (HCECs) serve as the first-line defensive barrier of the innate immune system and participate in the host inflammatory response to invasive pathogens through specific recognition of pathogens. This recognition triggers the production of inflammatory cytokines and chemokines, ultimately resulting in the clearance of invading pathogens [9]. Therefore, further studies are needed to identify the effects of hypoxia on the *Acanthamoeba*-induced host immune and inflammatory response in HCECs.

Abbreviations: HCEC, human corneal epithelial cell; AK, *Acanthamoeba keratitis*; LPS, lipopolysaccharide; TLR, Toll-like receptor; PAMP, pathogen-associated molecular pattern; NF-κB, nuclear factor kappa-light-chain-enhancer of activated B cells; ERK1/2, extracellular signal-regulated kinases 1/2; MyD88, myeloid differentiation primary response gene (88); IL-6, interleukin-6; IL-8, interleukin-8; IFN-β, interferon-β.

* Corresponding author. Fax: +86 531 8216 9206.
E-mail address: xywu8868@163.com (X. Wu).

0006-291X/$ - see front matter © 2012 Elsevier Inc. All rights reserved.
http://dx.doi.org/10.1016/j.bbrc.2012.03.069

Toll-like receptors (TLRs) are important receptors in innate immunity, playing crucial roles in the recognition of pathogen-associated molecular patterns (PAMPs) found in invading pathogens and the subsequent activation of the innate immune and inflammatory response [10]. Recognition of distinct patterns by TLRs induces cell signaling cascades that regulate the production of cytokines, chemokines and other innate defense molecules that form an effective host immune response. Our previous studies demonstrated that TLR1–TLR9 were expressed in HCECs [11] and that, through different TLRs, HCECs recognized various pathogens, including *Pseudomonas aeruginosa* [12], *Fusarium solu* [13], *Aspergillus fumigates* [9] and *Acanthamoeba* [14]. This recognition activated complex signaling cascades to release inflammatory cytokines and chemokines, such as interleukin-1β (IL-1β), interleukin-6 (IL-6), IL-8, interferon-β (IFN-β) and TNF-α. These findings indicate that TLRs in HCECs possess multiple ligand specificity and that they are able to trigger the host immune and inflammatory response to prevent invasion by pathogens.

We previously showed that TLR4 expression was highly elevated in HCECs after *Acanthamoeba* challenge, that it initiated the activation of NF-κB and ERK1/2 and promoted the secretion of IL-8, TNF-α and IFN-β [14]. In the present study, we investigated the effects of hypoxia on the production of inflammatory cytokines induced by *Acanthamoeba* in HCECs. We also evaluated the effects of hypoxia on the expression of TLR4 and molecules downstream of *Acanthamoeba*-triggered TLR4 signaling to determine whether these factors were involved in the hypoxia-mediated modulation of the inflammatory response in *Acanthamoeba*-challenged HCECs.

2. Materials and methods

2.1. Cell culture

Human telomerase-immortalized corneal epithelial cells [15] were kindly provided by Professor Fu-Shin X. Yu. HCECs were cultured in Dulbecco's modified Eagle's medium (DMEM)/F12 (Invitrogen–Gibco) supplemented with 50% defined keratinocyte serum free medium (Invitrogen–Gibco) at 37 °C in a humidified 5% CO_2 incubator. To generate hypoxic stress conditions, cells were incubated at 1% O_2 with 5% CO_2 and 94% N_2 in a humidified incubator (HERA Cell 150, Heraeus, Osterode, Germany) for varying time periods.

2.2. Flow cytometry assay

Flow cytometry assay was performed using the Annexin V–PE/7–AAD Apoptosis Detection Kit I (B&D Systems) according to the manufacturer's protocol. HCECs were collected after treatment, washed twice with cold PBS and resuspended in 1X Binding Buffer at a concentration of 1×10^6 cells ml^{-1}. Then, 100 μl of the solution (1×10^5 cells) was transferred to a 5 ml culture tube. We then added 5 μl of Annexin V–PE and 5 μl of 7–AAD to the cells and incubated the cells for 15 min at room temperature in the dark. Finally, 400 μl of 1X Binding Buffer was added to each tube, and flow cytometry analysis was performed within 1 h.

2.3. Acanthamoeba challenge

Acanthamoeba was kindly provided by the Beijing Eye Institute, clinically isolated and identified as genotype T4 based on 18S rRNA gene sequences [16]. The *Acanthamoeba* were grown in 5 ml of peptone–yeast–glucose medium at 28 °C. After 95% trophozoites were observed, *Acanthamoeba* were centrifuged at 500g for 7 min. The precipitate was washed with PBS and resuspended in DMEM/F12 to adjust the concentration to 1×10^6 cells ml^{-1}. After exposure to normoxia or hypoxia for 24 h, HCECs were challenged with *Acanthamoeba* resuspension for 30 min under normoxic condition followed by incubation with culture medium for an additional 6 h under normoxia or hypoxia, depending on the exposure condition.

2.4. LPS challenge

HCECs were seeded into six-well plates at a density of 2×10^5 cells per well. When the cells achieved 80% confluence, they were exposed to normoxia or hypoxia for 24 h. Cells were then challenged with the TLR4 ligand LPS (1 μg ml^{-1}) derived from *Escherichia coli* (Sigma–Aldrich, St Louis, Mo). The cells and culture supernatants were then collected for further examination.

2.5. Real-time reverse transcription-polymerase chain reaction (real-time RT-PCR) analysis

Total RNA was extracted with Trizol (Invitrogen) and 1 μg of total RNA was reverse transcribed using the PrimeScript ® RT reagent Kit (TaKaRa Biotechnology,) according to the manufacturer's protocols. Primer pairs (Table 1) used for real-time RT-PCR were designed using Primer Express 3.0 software (Applied Biosystems). Real-time RT-PCR was performed with the SYBR® Premix Ex Taq™ kit (TaKaRa Biotechnology) using a LightCycler instrument (Roche Applied Science). The mRNA expression level of each gene was calculated relative to the amount of β-Actin in the same sample.

2.6. Western blot analysis

Cells were lysed with radioimmunoprecipitation (RIPA) buffer (Beyotime) containing protease inhibitors. Protein concentration was then quantified by BCA protein assay (Beyotime). Equal amounts of protein were boiled for 10 min in sodium dodecyl sulfate (SDS) lysis buffer, loaded on a 10% SDS–polyacrylamide gel and transferred onto a polyvinylidene difluoride (PVDF) membrane (Millipore). The membrane was blocked with 5% nonfat dry milk in Tris-buffered saline containing 0.1% Tween 20 (TBST) for 1 h and incubated with primary antibodies at 4 °C overnight. The primary antibodies that were used were as follows: TLR4 from Abcam; β-Actin from Santa Cruz Biotechnology; and p-IκB-α, IκB-α, and p-ERK1/2 from Cell Signaling Technology. Membranes were washed with TBST and then incubated with the corresponding secondary antibody for 1 h. Washing was repeated, and proteins were visualized by chemiluminescence using an Immobilon Western Chemiluminescent HRP Substrate kit (Millipore).

2.7. Enzyme-linked immunosorbent assays (ELISA)

The protein levels of IL-8, IFN-β and IL-6 in cell culture supernatants were determined using enzyme-linked immunosorbent assay kits (B&D Systems) according to the manufacturer's protocols.

2.8. Statistical analysis

All data were expressed as the mean ± SEM from at least three independent experiments. Statistical comparisons between the groups were performed by a one-way ANOVA with Dunnett's multiple comparisons using SPSS (version 16.0). $P < 0.05$ was considered to be statistically significant.

3. Results

3.1. Hypoxia diminished Acanthamoeba-induced IL-8 and IFN-β production

To determine the effect of hypoxia and *Acanthamoeba* challenge on cell viability, cell apoptosis and necrosis were examined by flow

Table 1
Primers used for real time RT-PCR in this experiment.

Gene	Primer sequences (5′ to 3′)	GenBank Accession No.	Product size (bp)
TLR4	Forward: GATTGCTCAGACCTGGCAGTT Reverse: TGTCCTCCCACTCCAGGTAAGT	NM_138554.4	143
IL-8	Forward: TGAGAGTGATTGAGAGTGGACCA Reverse: TCAGCCCTCTTCAAAAACTTCTCC	NM_000584.3	136
IFN-β	Forward: CATTACCTGAAGGCCAAGGA Reverse: CAGCATCTGCTGGTTGAAGA	NM_002176.2	167
MyD88	Forward: GCTGAGAAGCCTTTACAGGTG Reverse: CTGGGGCAATAGCAGATGAAG	NM_002468.4	137
β-Actin	Forward: CTACAATGAGCTGCGTGTG Reverse: TGGGGTGTTGAAGGTCTC	NM_001101.3	121

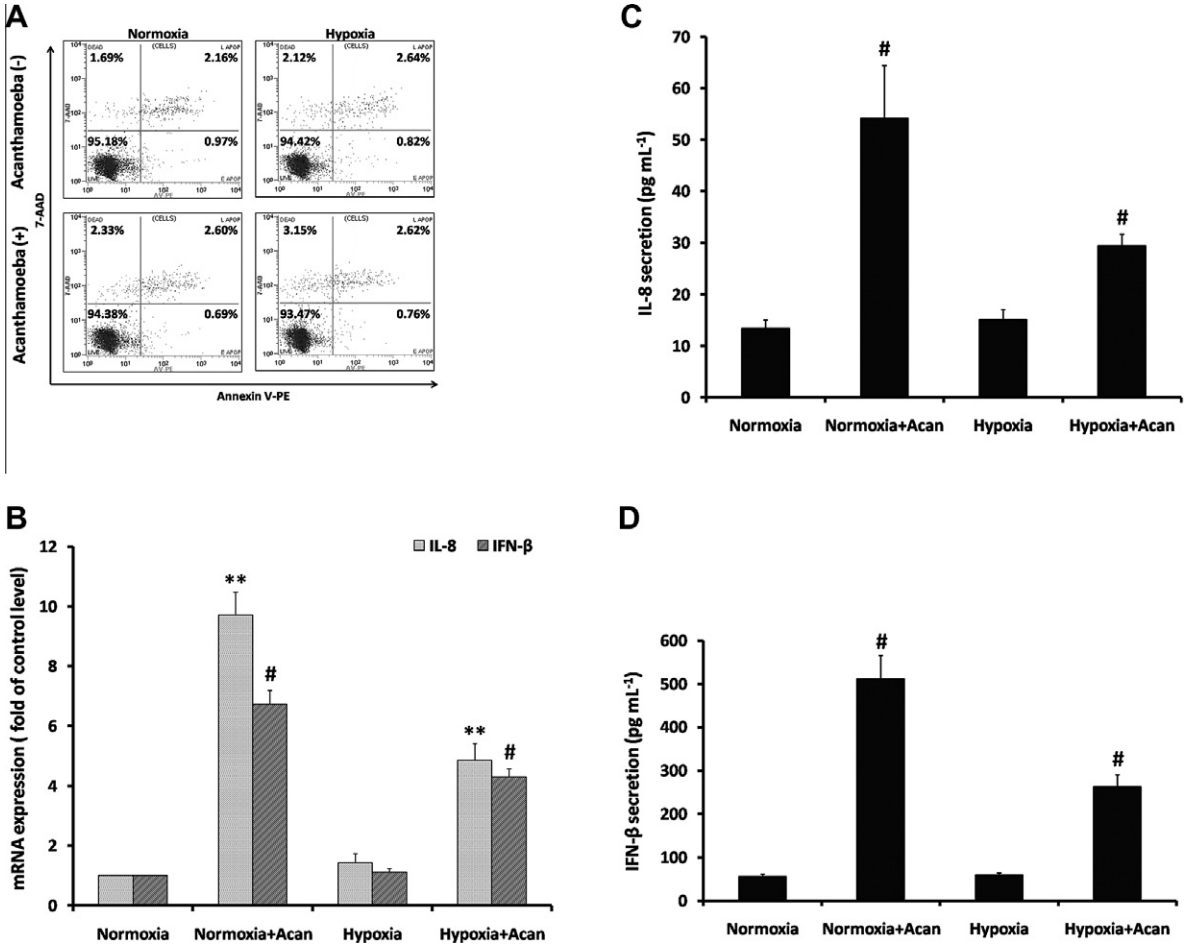

Fig. 1. Effects of hypoxia on *Acanthamoeba*-induced IL-8 and IFN-β production in HCECs. (A) Apoptotic and necrotic effects were evaluated by flow cytometry using Annexin V–PE/7–AAD staining. (B) mRNA expression levels of IL-8 and IFN-β in *Acanthamoeba*-challenged HCECs were determined by RT-PCR and normalized to β-Actin. (C and D) The secretion of IL-8 and IFN-β was analyzed by ELISA. Data shown are from three independent experiments. #, $P < 0.05$; ∗∗, $P < 0.01$, Acan stands for *Acanthamoeba*.

cytometry. The data showed that there was no significant change in the percentage of cells undergoing apoptosis and necrosis when the cells were exposed to hypoxia, *Acanthamoeba* challenge or both compared with the untreated control (Fig. 1A), indicating that the viability of HCECs was maintained under hypoxia and *Acanthamoeba* challenge. Our previous observations indicated that *Acanthamoeba* stimulated HCECs to initiate an inflammatory response, leading to the production of IL-8 and IFN-β [14]. To determine the effect of hypoxia on IL-8 and IFN-β production, the mRNA and protein levels of both cytokines were measured by RT-PCR and ELISA. The expression levels of IL-8 and IFN-β mRNA under hypoxia were significantly decreased to ∼50% and ∼64% of the control level, respectively (Fig. 1B). Similar to the down-regulation in mRNA expression, the protein levels of IL-8 and IFN-β under hypoxia were also reduced to ∼65% and ∼72% of the control level, respectively (Fig. 1C and D). However, hypoxia without challenge did not alter IL-8 and IFN-β production compared with normoxia.

3.2. Hypoxia down-regulated TLR4 expression

To determine whether hypoxia decreased the *Acanthamoeba*-induced production of inflammatory mediators through TLR4, we determined the effect of hypoxia on TLR4 expression. HCECs were incubated under normoxia and hypoxia for 6 h, 12 h, 24 h and 48 h.

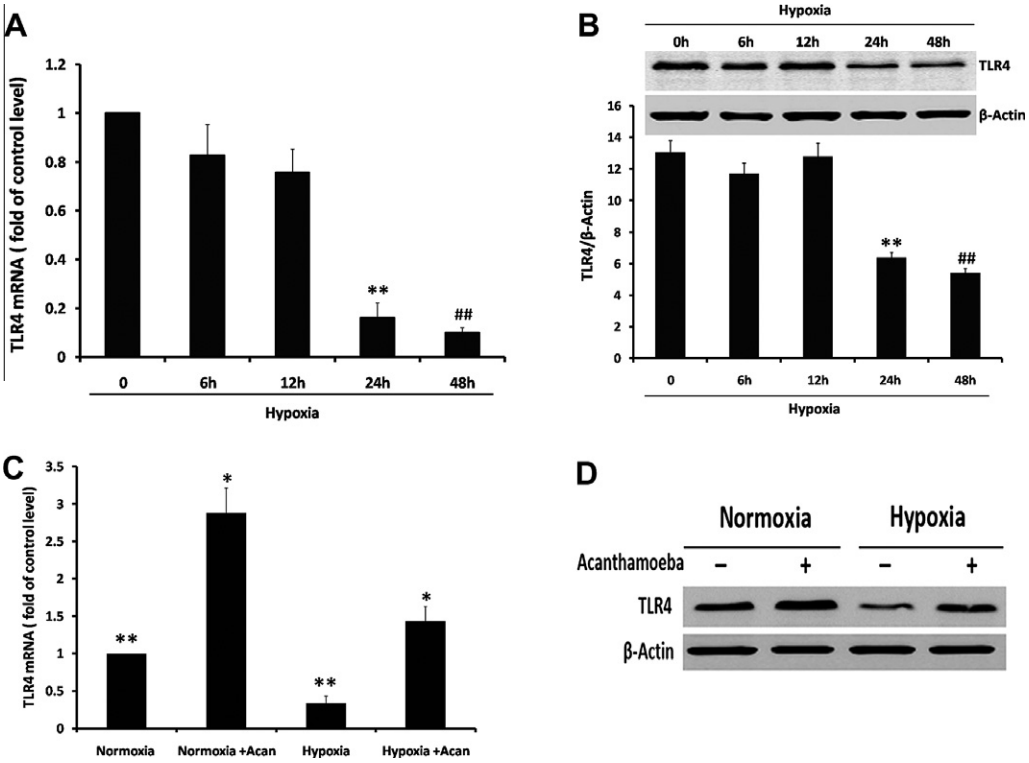

Fig. 2. Effects of hypoxia on TLR4 mRNA and protein expression in HCECs. (A) The mRNA level of TLR4 in HCECs was measured at different time points by real-time RT-PCR. (B) The protein level of TLR4 in HCECs was determined by Western blot analysis. (C-D) The mRNA and protein levels of TLR4 in HCECs under the exposure to *Acanthamoeba* and hypoxia were examined. Data shown are means ± SEM from three independent experiments. β-Actin was used as an internal loading control. ∗, $P < 0.05$; ∗∗ and ##, $P < 0.01$, indicating significant differences from control.

mRNA and protein levels of TLR4 were measured by real-time RT-PCR and western blot analysis. Real-time RT-PCR results showed that TLR4 mRNA expression significantly decreased to ~16% and ~10% of the control level at 24 h and 48 h after hypoxic exposure, respectively; down-regulation was not apparent after 6 h and 12 h of hypoxia (Fig. 2A). Moreover, the decrease of TLR4 mRNA level occurred in a time-dependent manner (Fig. 2A). Western blot analysis for TLR4 protein expression demonstrated that TLR4 protein levels were significantly diminished to ~65% and ~45% of the control level after 24 h and 48 h of hypoxic exposure (Fig. 2B). Furthermore, the effect of hypoxia on *Acanthamoeba*-induced the expression of TLR4 was also investigated. Real-time RT-PCR results showed that *Acanthamoeba*-induced TLR4 mRNA expression in HCECs under hypoxia was remarkably decreased to ~53% of normoxia control (Fig. 2C), while TLR4 protein expression was also significantly reduced to ~64% of normoxia control (Fig. 2D).

3.3. Hypoxia inhibited Acanthamoeba-induced the expression of MyD88 and the activation of NF-κB and ERK1/2

To investigate whether hypoxia regulates *Acanthamoeba*-induced the activation of NF-κB and ERK1/2 in HCECs, we used Western blot analysis and assessed NF-κB activation by detecting the phosphorylation and degradation of IκB-α and assessed ERK1/2 activation by detecting ERK1/2 phosphorylation. The data showed that under hypoxia, IκB-α phosphorylation was attenuated, its degradation was enhanced and ERK1/2 phosphorylation was decreased compared with the normoxia group (Fig. 3A and B). We also detected MyD88 mRNA level by real-time RT-PCR analysis and found that *Acanthamoeba*-induced MyD88 expression was significantly reduced to ~59% of normoxia control under hypoxia (Fig. 3C).

3.4. Hypoxia attenuated LPS-induced IL-6 and IL-8 production, MyD88 expression and NF-κB activation

Considering the data showing that hypoxia decreased the *Acanthamoeba*-induced production of inflammatory mediators by affecting the TLR4 signaling, we were interested in determining whether hypoxia could also attenuate the production of inflammatory mediators in response to LPS, a TLR4–specific ligand. First, the effect of LPS and hypoxia exposure on cell viability was determined as described above; the results showed that there was no loss of cell viability when compared with the control (data not shown). In this study, the effects of hypoxia on LPS-induced mRNA expression and secretion of IL-6 and IL-8 were analyzed by RT-PCR and ELISA. The data showed that hypoxia reduced the mRNA expression of IL-6 and IL-8 to 9% and 8% of the control level, respectively (Fig. 4A). The secretion of IL-6 and IL-8 was also decreased under hypoxia when compared with LPS exposure alone (~62% and ~52% of control level, respectively) (Fig. 4B and C). However, the secretion of IL-6 and IL-8 was not significantly changed by hypoxia compared with normoxia. These results demonstrate that LPS-induced secretion of inflammatory cytokines was reduced in HCECs under hypoxia.

Since LPS triggers TLR4 signaling through the adaptor molecule MyD88 to induce NF-κB activation and subsequent production of inflammatory mediators, we were also interested in determining whether MyD88 expression and NF-κB activity could account for the hypoxia-mediated effects on the LPS-induced inflammatory response. The effects of hypoxia on LPS-induced MyD88 expression and NF-κB activity were examined in HCECs by RT-PCR and Western blot analysis. The mRNA level of MyD88 under hypoxia was decreased to ~41% of the control level in LPS-treated HCECs (Fig. 4D). For NF-κB activity, the data showed that IκB-α phosphor-

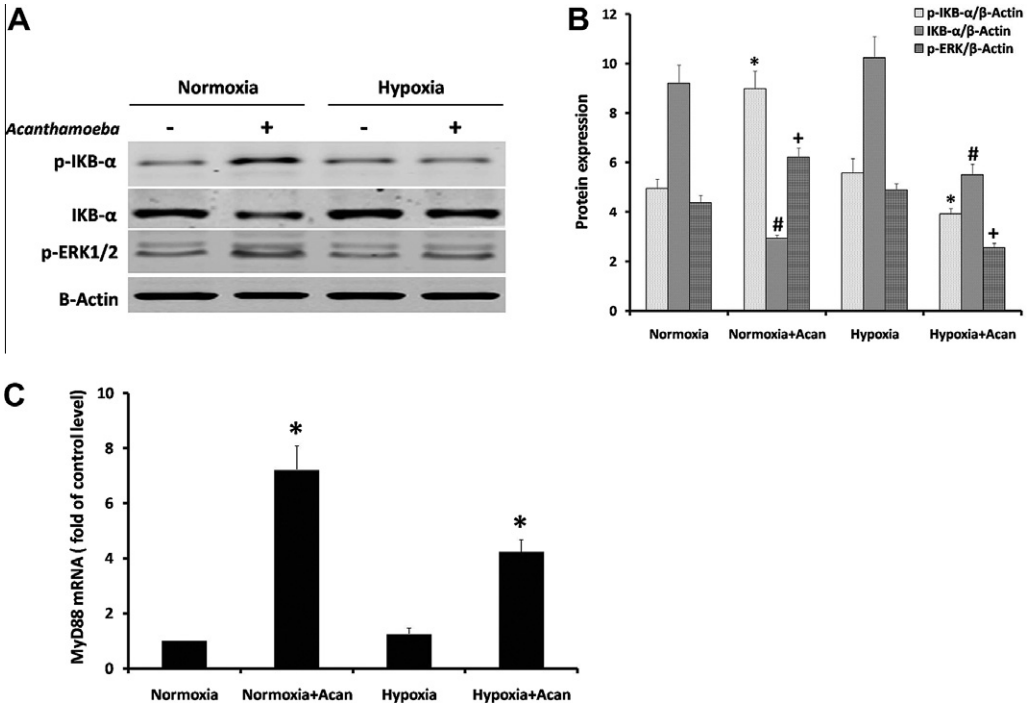

Fig. 3. Effects of hypoxia on *Acanthamoeba*-induced NF-κB and ERK1/2 activation, and MyD88 expression in HCECs. (A-B) The protein levels of phospho-IκB-α (p-IκB-α), total IκB-α and phospho-ERK1/2 (p-ERK1/2) were measured by western blot analysis and β-Actin was used as an internal control. (C) The mRNA level of MyD88 was measured by real-time RT-PCR and normalized to β-Actin. The data shown are from three independent experiments.∗, # and +, $P < 0.05$, indicate significant differences from control. Acan stands for *Acanthamoeba*.

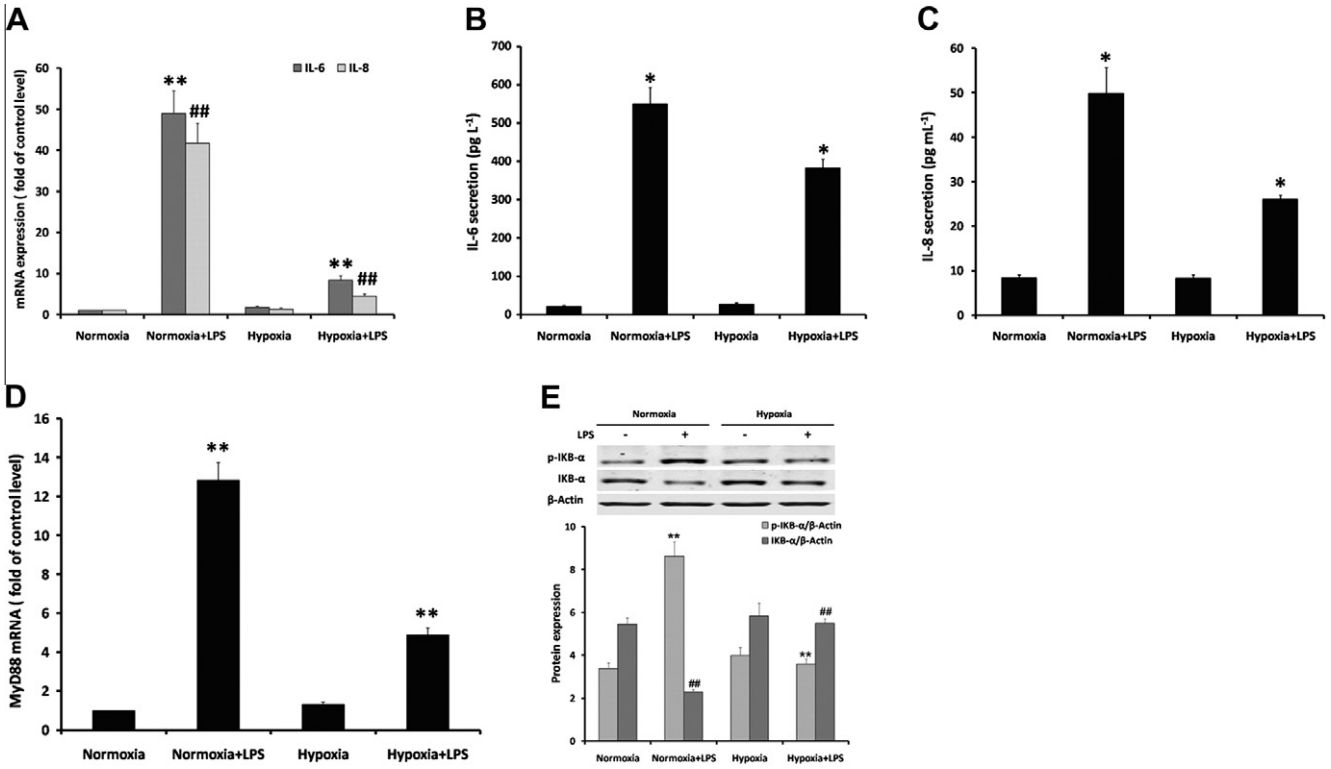

Fig. 4. Effects of hypoxia on LPS-induced IL-6 and IL-8 production in HCECs. (A) The mRNA levels of IL-6 and IL-8 were measured by real-time RT-PCR and normalized by β-Actin mRNA level. (B and C) The protein levels of IL-6 and IL-8 were evaluated by ELISA. (D) The mRNA level of MyD88 was examined by RT-PCR and normalized to β-Actin. (E) The protein levels of p-IκB-α and IκB-α were determined by Western blot analysis. β-Actin was used as an internal loading control. All these data shown are means ± SEM from three independent experiments. ∗, $P < 0.05$; ∗∗ and ##, $P < 0.01$, indicate significant differences from LPS exposure under normoxia.

ylation was remarkably attenuated and that IκB-α degradation was enhanced under hypoxia compared with the normoxia group (Fig. 4E).

4. Discussion

Contact lens use is considered one of the most significant risk factors for AK. A better understanding of the mechanisms involved in contact lens use and corneal susceptibility to AK is important for us to defend against *Acanthamoeba* infection and to prevent disease outbreaks. Since corneal hypoxia is the most common implication of contact lens use, the effect of hypoxia on corneal susceptibility to *Acanthamoeba* required further investigation. However, the effect of hypoxia on this disease and the essential mechanisms involved remain unexplored. In the present study, we addressed this knowledge gap and demonstrated that hypoxia attenuated the *Acanthamoeba*-induced production of inflammatory mediators in HCECs. Hypoxia inhibited multiple downstream molecules in *Acanthamoeba*-triggered TLR4 signaling including TLR4 and MyD88 expression, NF-κB and ERK1/2 activation, which might account for the attenuated inflammatory response.

Our previous study revealed that *Acanthamoeba* induced the production of inflammatory mediators in HCECs including IL-8, TNF-α and IFN-β [14]. IL-8 is a pro-inflammatory chemokine secreted from macrophages, epithelial cells and other cell types. The primary function of IL-8 is to recruit neutrophils to phagocytose the antigen. IFN-β is a pro-inflammatory cytokine that is released from most immune cells, including macrophages and natural killer cells, in response to challenges from viruses, parasites and tumor cells. IFN-β possesses the ability to interfere with viral replication, activate immune cells and up-regulate antigen presentation to T lymphocytes. For the first time, we demonstrate that hypoxia attenuated the production of IL-8 and IFN-β, suggesting that hypoxia impairs the cell's immune and inflammatory ability to eliminate *Acanthamoeba* invasion and enhances cell susceptibility to *Acanthamoeba* infection.

Since TLR4 bridges *Acanthamoeba* challenge and the production of IL-8 and IFN-β in HCECs, the effects of hypoxia might be associated with TLR4 expression. Our data showed that hypoxia inhibited Acanthamoeba-induced TLR4 expression. We also found that hypoxia down-regulated TLR4 mRNA and protein expression in HCECs without Acanthamoeba stimulation which indicated that this down-regulation might be not dependent on the source of stimulation. Consistent with our results, other investigators have reported that hypoxia also diminished TLR4 expression in SV40–HCECs at 48 h exposure [17] and in human umbilical vein endothelial cells for 48–72 h exposure [18]. In contrast, other findings have demonstrated that hypoxia increased TLR4 expression in mouse microglia cells after 8 h exposure [19] and in mouse macrophage cells for 2–4 h exposure [20]. These studies indicate that different cell types and hypoxic exposure durations lead to different cellular responses of TLR4 expression. However, the mechanism of hypoxia-mediated TLR4 dysregulation remains controversial. Ishida et al. [18] reported that hypoxia-mediated TLR4 down-regulation might be due to the mitochondrial reactive oxygen species (ROS)-mediated attenuation of AP–1 transcriptional activity in endothelial cells. Kim et al. [20] found that hypoxia increased TLR4 expression in mouse macrophages because hypoxia inducible factor-1α (HIF-1α) directly bound to TLR4 promoter region and increased its promoter activity. In addition to these mechanisms, other regulators may be involved in TLR4 dysregulation under hypoxia, such as microRNAs (miRNAs). miRNAs are a class of endogenous 20–24 nucleotides non-coding RNAs that regulate gene expression at the post-transcriptional level by targeting the 3′ untranslated region (3′UTR) and mediating translational suppression or/and mRNA degradation [21]. Many hypoxia-regulated miRNAs are known to be involved in post-transcriptional gene regulation under low oxygen [22], so it is of great interest to further study miRNA-mediated hypoxic responses in HCECs to identify the post-transcriptional regulatory mechanisms of hypoxia-induced TLR4 down-regulation.

Our present results revealed the important function of TLR4 signaling, specifically NF-κB and ERK1/2 activation as well as MyD88 expression, in the hypoxia-mediated decline of inflammatory cytokine production in HCECs. These results indicate that hypoxia might attenuate both the TLR4–NF-κB and TLR4–MAPK signaling pathways. To further investigate this hypothesis, we studied the effects of hypoxia on LPS-induced production of inflammatory mediators and possible changes in TLR4 signaling. TLR4 is the main mediator of responses to LPS. LPS stimulation results in NF-κB activation and ultimately leads to the release of many pro-inflammatory mediators, such as IL-1, IL-6, IL-8 and TNF-α. Our previous study found that LPS stimulation induced the secretion of these inflammatory mediators in HCECs [9]. In this study, we found that hypoxia diminished the production of IL-6 and IL-8 in LPS-treated HCECs. Additionally, we demonstrated that hypoxia inhibited mRNA levels of MyD88 and the activation of NF-κB. Consistent with our data, several *in vitro* studies reported that hypoxia inhibited LPS-induced NF-κB activity in mouse microglia cells [19], human SV40–HCECs [17] and rat alveolar macrophages [23]. Several reports have also demonstrated that hypoxia activates the NF-κB pathway and leads to expression of pro-inflammatory genes through HIF-1α and ROS [18,24,25]. Hypoxia has also been connected to the activation of MAPK pathways, including ERK1/2, JNK and P38, by calcium-dependent mechanisms [26,27]. However, it still remains unclear how hypoxia suppressed *Acanthamoeba* and LPS-induced activation of NF-κB and ERK1/2. An important point for consideration is that hypoxia could differentially regulate the activity of NF-κB and ERK1/2 under various stimulation conditions; other unknown functional factors must also exist in the regulation of NF-κB and ERK1/2 pathway under hypoxia, such as transcription factors and miRNAs [28].

Another important point raised from our study was that hypoxia might enhance cellular susceptibility to microbial infection by attenuating *Acanthamoeba* and LPS-induced TLR4 signaling. Many *in vivo* studies have also supported our findings. Poltorak et al. [29] found that TLR4–mutated C57BL/10ScCr mice lost their ability to respond to LPS and subsequently developed gram-negative infection. Netea et al. [30] also reported that TLR4-defective mice had an increased susceptibility to *C. albicans* infection. Recently, a study showed that in severe COPD patients the expression of TLR4 in respiratory epithelium was reduced, resulting in increased susceptibility to gram-negative pathogens [31]. These findings indicate that insufficient activation of TLR4 triggers an ineffective defense against invasive pathogens. Our results suggest that hypoxia-induced TLR4 down-regulation might also impair the inflammatory response against *Acanthamoeba* as well as increase corneal susceptibility to *Acanthamoeba* infection. Therefore, TLR4 expression in HCECs might represent a useful biomarker of corneal susceptibility to *Acanthamoeba* and gram-negative bacteria infection.

In conclusion, we evaluated the role of hypoxia in the production of inflammatory mediators and TLR4 signaling triggered by *Acanthamoeba* challenge in HCECs. Our results demonstrate that hypoxia attenuated the production of IL-8 and IFN-β, the expression of TLR4 and MyD88 and as well as the activation of NF-κB and ERK1/2 induced by *Acanthamoeba* challenge. Hypoxia-mediated inflammatory cytokine production might be reduced by affecting the TLR4 signaling, but the precise mechanism of TLR4 down-regulation by hypoxia requires further investigation. Our findings suggest that hypoxia possibly abates the host's defensive response against invasive pathogens in HCECs and that hypoxia might enhance cell susceptibility to microbial infection, which explains why contact lens use is one of the prominent risk factors for AK.

Acknowledgments

This work was supported by the Natural Science Foundation of Shandong Province (grant number Y2008C21) and the Graduate Independent Innovation Foundation of Shandong University (grant number 21300070613239). We would like to thank Professor X. Qu (Institute of Basic Medical Sciences, Qilu Hospital, Shandong University) for invaluable suggestions and Dr. X.P. Wang (The Key Laboratory of Cardiovascular Remodeling and Function Research, Chinese Ministry of Education and Chinese Ministry of Public Health, Qilu Hospital, Shandong University) for excellent technical help.

References

[1] A. Patel, K. Hammersmith, Contact lens-related microbial keratitis: recent outbreaks, Curr. Opin. Ophthalmol. 19 (2008) 302–306.
[2] C.F. Radford, D.C. Minassian, J.K. Dart, Acanthamoeba keratitis in England and Wales: incidence, outcome, and risk factors, Br. J. Ophthalmol. 86 (2002) 536–542.
[3] D.A. Schaumberg, K.K. Snow, M.R. Dana, The epidemic of Acanthamoeba keratitis: where do we stand?, Cornea 17 (1998) 3–10
[4] H. Ichijima, T. Hayashi, S. Mitsunaga, et al., Determination of oxygen tension on rabbit corneas under contact lenses, CLAO. J. 24 (1998) 220–226.
[5] T. Zaidi, M. Mowrey-McKee, G.B. Pier, Hypoxia increases corneal cell expression of CFTR leading to increased*Pseudomonas aeruginosa* binding, internalization, and initiation of inflammation, Invest. Ophthalmol. Vis. Sci. 45 (2004) 4066–4074.
[6] N. Yamamoto, N. Yamamoto, J.V. Jester, et al., Prolonged hypoxia induces lipid raft formation and increases Pseudomonas internalization *in vivo* after contact lens wear and lid closure, Eye. Contact. Lens. 32 (2006) 114–120.
[7] P.M. Ladage, K. Yamamoto, D.H. Ren, et al., Proliferation rate of rabbit corneal epithelium during overnight rigid contact lens wear, Invest. Ophthalmol. Vis. Sci. 42 (2001) 2804–2812.
[8] M.C. Lin, K.A. Polse, Hypoxia, overnight wear, and tear stagnation effects on the corneal epithelium: data and proposed model, Eye. Contact. Lens. 33 (2007) 378–381.
[9] H. Guo, X. Wu, Innate responses of corneal epithelial cells against*Aspergillus fumigatus* challenge, FEMS. Immunol. Med. Microbiol. 56 (2009) 88–93.
[10] S. Akira, K. Takeda, Toll-like receptor signaling, Nat. Rev. Immunol. 4 (2004) 499–511.
[11] X.Y. Wu, J.L. Gao, M.Y. Ren, Expression profiles and function of Toll-like receptors in human corneal epithelia, Chinese. Medical. Jounal. 120 (2007) 893–897.
[12] J. Zhang, X.Y. Wu, F.S. Yu, Inflammatory responses of corneal epithelial cells to*Pseudomonas aeruginosa* infection, Curr. Eye. Res. 30 (2005) 527–534.
[13] H. Guo, X. Wu, F.S. Yu, J. Zhao, Toll-like receptor 2 mediates the induction of IL-10 in corneal fibroblasts in response to*Fusarium solu*, Immunol. Cell. Biol. 86 (2008) 271–276.
[14] M. Ren, L. Gao, X. Wu, TLR4: the receptor bridging*Acanthamoeba* challenge and intracellular inflammatory responses in human corneal cell lines, Immunol. Cell. Biol. 88 (2010) 529–536.
[15] I.K. Gipson, S. Spurr-Michaud, P. Argüeso, et al., Mucin gene expression in immortalized human corneal-limbal and conjunctival epithelial cell lines, Invest. Ophthalmol. Vis. Sci. 44 (2003) 2496–2506.
[16] Y. Zhang, X.G. Sun, S.J. Deng, et al., Molecular characteristics of*Acanthamoeba* strains from keratitis patients, Zhonghua. Yan. Ke. Za. Zhi. 40 (2004) 389–394.
[17] Y. Hara, A. Shiraishi, Y. Ohashi, Hypoxia-altered signaling pathways of toll-like receptor 4 (TLR4) in human corneal epithelial cells, Mol. Vis. 15 (2009) 2515–2520.
[18] I. Ishida, H. Kubo, S. Suzuki, et al., Hypoxia diminishes toll-like receptor 4 expression through reactive oxygen species generated by mitochondria in endothelial cells, J. Immunol. 169 (2002) 2069–2075.
[19] J. Ock, J. Jeong, W.S. Choi, et al., Regulation of Toll-like receptor 4 expression and its signaling by hypoxia in cultured microglia, J. Neurosci. Res. 85 (2007) 1989–1995.
[20] S.Y. Kim, Y.J. Choi, S.M. Joung, et al., Hypoxic stress up-regulates the expression of Toll-like receptor 4 in macrophages *via* hypoxia-inducible factor, Immunology 129 (2010) 516–524.
[21] D. Yan, W.L. Ng, X. Zhang, et al., Targeting DNA-PKcs and ATM with miR-101 sensitizes tumors to radiation, PLoS One. 5 (2010) e11397.
[22] M. Gorospe, K. Tominaga, X. Wu, et al., Post-transcriptional control of the hypoxic response by RNA-binding proteins and microRNAs, Front. Mol. Neurosci. 4 (2011) 7.
[23] G.M. Matuschak, R. Nayak, T.M. Doyle, et al., Acute hypoxia decreases E. coli LPS-induced cytokine production and NF-kappaB activation in alveolar macrophages, Respir. Physiol. Neurobiol. 172 (2010) 63–71.
[24] C.T. Taylor, E.P. Cummins, The role of NF-kappaB in hypoxia-induced gene expression, Ann. N. Y. Acad. Sci. 1177 (2009) 178–184.
[25] C. Culver, A. Sundqvist, S. Mudie, et al., Mechanism of hypoxia-induced NF-kappaB, Mol. Cell. Biol. 30 (2010) 4901–4921.
[26] C. Osorio-Fuentealba, J.A. Valdés, D. Riquelme, et al., Hypoxia stimulates *via* separate pathways ERK phosphorylation and NF-kappaB activation in skeletal muscle cells in primary culture, J. Appl. Phy-siol. 106 (2009) 1301–1310.
[27] S.B. Mkaddem, M. Bens, A. Vandewalle, Differential activation of Toll-like receptor-mediated apoptosis induced by hypoxia, Oncotarget. 1 (2010) 741–750.
[28] F. Licausi, D.A. Weits, B.D. Pant, et al., Hypoxia responsive gene expression is mediated by various subsets of transcription factors and miRNAs that are determined by the actual oxygen availability, New. Phytol. 190 (2011) 442–456.
[29] A. Poltorak, X. He, I. Smirnova, et al., Defective LPS signaling in C3H/HeJ and C57BL/10ScCr mice: mutations in Tlr4 gene, Science 282 (1998) 2085–2088.
[30] M.G. Netea, C.A. Van Der Graaf, A.G. Vonk, et al., The role of toll-like receptor (TLR) 2 and TLR4 in the host defense against disseminated candidiasis, J. Infect. Dis. 185 (2002) 1483–1489.
[31] R.E. MacRedmond, C.M. Greene, D.R. Dorscheid, et al., Epithelial expression of TLR4 is modulated in COPD and by steroids, salmeterol and cigarette smoke, Respir. Res. 8 (2007) 84.

Biochemical and Biophysical Research Communications 420 (2012) 692–697

Contents lists available at SciVerse ScienceDirect

Biochemical and Biophysical Research Communications

journal homepage: www.elsevier.com/locate/ybbrc

The structure of putative *N*-acetyl glutamate kinase from *Thermus thermophilus* reveals an intermediate active site conformation of the enzyme

Ramya Sundaresan [a], Preethi Ragunathan [a], Seiki Kuramitsu [b,c], Shigeyuki Yokoyama [d,e], Thirumananseri Kumarevel [b,*], Karthe Ponnuraj [a,*]

[a] Centre of Advanced Study in Crystallography and Biophysics, University of Madras, Guindy Campus, Chennai 600 025, India
[b] RIKEN SPring-8 Center, Harima Institute, 1-1-1 Kouto, Sayo, Hyogo 679-5148, Japan
[c] Department of Biological Sciences, Graduate School of Science, Osaka University, Toyonaka, Osaka 560-0043, Japan
[d] RIKEN Systems and Structural Biology Center, Yokohama Institute, RIKEN, 1-7-22 Suehiro-cho, Tsurumi, Yokohama 230-0045, Japan
[e] Department of Biophysics and Biochemistry, Graduate School of Science, The University of Tokyo, Tokyo 113-0033, Japan

ARTICLE INFO

Article history:
Received 8 March 2012
Available online 20 March 2012

Keywords:
N-acetyl-L-glutamate kinase
Arginine biosynthesis
Crystal structure
Intermediate conformation
Catalytic cycle

ABSTRACT

The de novo biosynthesis of arginine in microorganisms and plants is accomplished via several enzymatic steps. The enzyme *N*-acetyl glutamate kinase (NAGK) catalyzes the phosphorylation of the γ-COO^- group of *N*-acetyl-L-glutamate (NAG) by adenosine triphosphate (ATP) which is the second rate limiting step in arginine biosynthesis pathway. Here we report the crystal structure of putative *N*-acetyl glutamate kinase (NAGK) from *Thermus thermophilus HB8* (TtNAGK) determined at 1.92 Å resolution. The structural analysis of TtNAGK suggests that the dimeric quaternary state of the enzyme and arginine insensitive nature are similar to mesophilic *Escherichia coli* NAGK. These features are significantly different from its thermophilic homolog *Thermatoga maritima* NAGK which is hexameric and arginine-sensitive. TtNAGK is devoid of its substrates but contains two sulfates at the active site. Very interestingly the active site of the enzyme adopts a conformation which is not completely open or closed and likely represents an intermediate stage in the catalytic cycle unlike its structural homologs, which all exist either in the open or closed conformation. Engineering arginine biosynthesis pathway enzymes for the production of L-arginine is an important industrial application. The structural comparison of TtNAGK with EcNAGK revealed the structural basis of thermostability of TtNAGK and this information could be very useful to generate mutants of NAGK with increased overall stability.

1. Introduction

Arginine biosynthesis in microorganisms, plants (also unicellular algae) and fungi is normally carried out from L-glutamate to arginine via *n*-acetylated intermediates in eight enzymatic steps (Supplementary Fig. S1) [1–5]. Microorganisms follow either a linear [1] or cyclic pathway [1,4–5] based on the formation of the intermediate product L-ornithine catalyzed by acetyl ornithinase (AO) or ornithine acetyl transferase (OAT), respectively [5]. Ornithine is later converted to arginine via citrulline and argininosuccinate [5,6]. Microorganisms like *Escherichia coli* and *Sulfolobus solfotaricus* follow a linear pathway while *Thermatoga maritima* and *Thermus aquaticus* follow a more evolved cyclic pathway. *Thermus thermophilus*, an extreme thermophile is believed to take the cyclic route for ornithine production like *T. maritima* [7].

N-acetyl glutamate kinase (NAGK), a key player in second step of arginine biosynthesis catalyzes the phosphorylation of the γ-COO^- group of *N*-acetyl-L-glutamate (NAG) by adenosine triphosphate (ATP) and an ideal candidate for feedback inhibition by arginine in the cyclic pathway. Two classes of NAGKs have evolved based on their sensitivity to arginine namely, arginine-sensitive and arginine-insensitive forms [2,4]. Some of arginine-sensitive NAGKs structurally well characterized till date are from *Pseudomonas aeruginosa* (PaNAGK) [8], *T. maritima* (TmNAGK) [8], *Arabidopsis thaliana* (AtNAGK) [7] and *Synecococcus elongatus* (SeNAGK) [9], while the only arginine insensitive NAGK crystallized and analyzed till date is from *E. coli* (EcNAGK) [2]. EcNAGK is a homodimer while arginine-sensitive forms are hexamers. Here we report the crystal structure of NAGK from *T. thermophilus* (TtNAGK) at a resolution of 1.92 Å. TtNAGK is a dimer unlike its thermophilic homolog (TmNAGK), making it the first NAGK of thermophilic origin possessing dimeric structure.

The absence of NAGK in mammals [10,11] which do not take up this acetylated route for arginine synthesis makes it an attractive target for the development of new antimicrobials for inhibiting

* Corresponding authors. Fax: +91 44 2220 0122 (K. Ponnuraj), fax: +81 791 58 2917 (T. Kumarevel).
E-mail addresses: tskvel@spring8.or.jp (T. Kumarevel), karthe@unom.ac.in, pkarthe@hotmail.com (K. Ponnuraj).

0006-291X/$ - see front matter © 2012 Elsevier Inc. All rights reserved.
http://dx.doi.org/10.1016/j.bbrc.2012.03.072

microbial growth. Despite *T. thermophilus* not being a pathogenic organism, the structural information of TtNAGK could be used for the development of selective inhibitors of NAGKs of pathogenic bacteria.

2. Materials and methods

2.1. Cloning, expression, and purification of TtNAGK

The details of cloning, expression and purification of TtNAGK is given in the supplementary data. Briefly, to overexpress the selenomethionine substituted protein the plasmid harboring the TtNAGK (*ttha1903*) gene was transformed into *E. coli* B834 (DE3) (Stratagene), a Met auxotroph strain. The cells were induced at the mid-log phase by adding 1 mM IPTG and harvested by centrifugation. The cell pellet was resuspended in lysis buffer (20 mM Tris–HCl pH 8.0, 500 mM NaCl, 5 mM 2-mercaptoethanol, 1 mM phenylmethylsulfonylfluoride), sonicated, heat-treated to denature non-thermophilic contaminant proteins and centrifuged. The protein was purified using HisTrap HP5, Superdex 200 and hydroxylapatite (CHT5) columns as described in the supplementary data. The final purified protein was concentrated to 15.8 mg ml^{-1} for crystallization studies.

2.2. Crystallization, data collection and structure determination

Crystals of selenomethionine substituted TtNAGK were produced at 20 °C by the sitting drop vapor diffusion method, by adding 1 μl of protein solution to 1 μl of well solution, containing 0.5 M ammonium sulfate, 0.1 M trisodium citrate dehydrate (pH 5.6), and 1.0 M lithium sulfate. Diffraction quality crystals grew within a week. Crystals were flash-cooled in a nitrogen-gas stream at 100 K and a complete single anomalous dispersion (SAD) data set was obtained on the RIKEN structural genomics beamline I (BL26B2) at SPring-8, Hyogo, Japan. The data set was processed up to 1.92 Å using the HKL 2000 suite [12].

The TtNAGK structure was determined by SAD method using the programs SOLVE [13] and RESOLVE [14]. Improvement of the partial model derived from RESOLVE was performed with the program ARP/wARP [15]. Subsequently the model was subjected to simulated annealing and iterative cycles of positional and temperature factor refinement (20–1.92 Å) followed by manual fitting and rebuilding. Atomic refinement of the model was performed using the program CNS [16] and the program Coot [17] was used for model building. The data collection and refinement statistics are given in Supplementary Table 1. Figures were prepared using the program Pymol (http://www.pymol.org).

3. Results and discussion

3.1. Overall fold and description of structure

TtNAGK is a homodimer comprising of 269 amino acids in each monomer. The monomer has two domains, namely N-domain (1–183) and C-domain (184–269) (Fig. 1A) which are highly identical and superpose with a root-mean-square (r.m.s) deviation of 0.94 Å for 246 aligned Cα atoms. Nevertheless slight structural variations were observed in the C-domain of the molecule. Each monomer contains two sulfate molecules, one located in each domain. Both the domains exhibit an α/β fold formed mainly by parallel β-sheet flanked by helices on either side. The overall structure is alleged to have an α3β8α4 architecture as observed in other NAGK structures. Here we provide limited description of the structure since the structural features of NAGKs have been described in detail previously [8,18].

3.2. Oligomeric state of TtNAGK

The oligomeric state of NAGK is a key element that determines its function and inhibition by arginine [4]. TtNAGK is the first reported dimer of thermophilic origin in contrast to mesophilic EcNAGK dimer (2). The dimer of TtNAGK resembles EcNAGK dimer [18] with the two molecules associating through their N-domain region and oriented such that their corresponding αC helices are almost perpendicular to each other (Fig. 1A & Supplementary Fig. S2). Structural superposition of dimers of TtNAGK and EcNAGK (1gs5) gave an r.m.s. deviation of 2.06 Å for 363 aligned Cα atoms. Superposition of TtNAGK dimer with one of the three dimers of hexameric PaNAGK and TmNAGK resulted in an r.m.s. deviation of 2.41 Å (for 418 aligned Cα atoms) and 2.72 Å (for 423 aligned Cα atoms), respectively suggesting that all the NAGKs have a similar dimeric assembly (Supplementary Fig. S2).

3.3. Sequence and structure comparison

The sequence homologs of TtNAGK were identified using BLASTp search against non-redundant database from NCBI [19]. The top 10 homologs were found to be *N*-acetyl glutamate kinases (NAGKs), however, none of them have structural information. Further details are given in the supplementary data.

A DALI [20] search was performed to identify the structural homologs of TtNAGK. The *Z* scores for top 10 matches, which includes AtNAGK (2rd5), PaNAGK (2buf), TmNAGK (2bty) and EcNAGK (1gs5), with TtNAGK monomer (chain B) varies from 31.7 to 26.9 and r.m.s. deviation in the range of 2.1–2.5 Å for 252–241 aligned Cα atoms. The closest match was found to be AtNAGK complexed with PII signaling protein (2rd5) whereas the least match was found to be NAGS from *Neisseria gonorrhoeae* complexed with coenzyme A and NAG (3b8 g).

Despite the lack of sequence homology (Supplementary Fig. S3) of TtNAGK (AtNAGK – 36%, PaNAGK – 30%, TmNAGK – 32% and EcNAGK – 27%), the overall structure is conserved in all NAGKs (Fig. 1B). The structural superposition also revealed that the N-domain of all these molecules superposed well in comparison with their C-domains. Notable structural variations at the N-domain include (1) the N-terminal helix, which is absent in TtNAGK and EcNAGK (Fig. 1B & Supplementary Fig. S3) (2) the flap like lid region formed by residues G49–D67 connecting the helices αB (38–48) and αC (67–93) covers the putative NAG binding site (Fig. 1B). This lid region in TtNAGK is longer (consists of 17 residues) and forms a short antiparallel β-sheet unlike all other homologs namely AtNAGK (88–100, 12 residues), TmNAGK (74–86, 12 residues), PaNAGK (80–92, 12 residues) and EcNAGK (57–68, 11 residues) in which the lid is formed by a loop (Fig. 1B & Supplementary Fig. S3). (3) the connecting segment (103–138) between β5 and αD. This region is positioned close to the flap-like lid region and is very long both in TtNAGK and PaNAGK structures (approximately 35 residues) in comparison to a shorter segment of approximately 26 residues in TmNAGK, EcNAGK and AtNAGK structures (Supplementary Fig. S3).

At the C-domain, the orientation of helices αF and αG in TtNAGK are significantly different from the corresponding helices in other NAGK structures (Fig. 1B) in addition to the structural variations at many loop regions.

3.4. NAG binding site

TtNAGK is devoid of the substrate NAG which is known to bind in the N-domain of the molecule. To analyze its putative binding site, NAG was docked with TtNAGK using the program Autodock [21]. The lowest energy structure obtained from Autodock showed that NAG was bound in a pocket situated above the helix αE. The

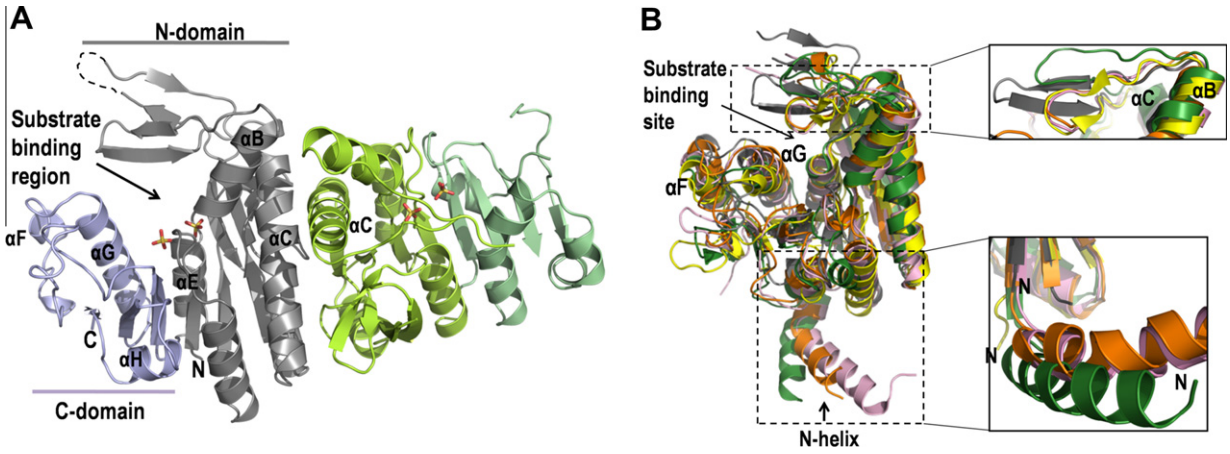

Fig. 1. Structure of TtNAGK and comparison with its homologs. (A) Ribbon representation of TtNAGK dimer [Molecule A – N-domain (gray) and C-domain (light blue); Molecule B – N-domain (lemon green) and C-domain (light green)]. Bound sulfates are shown in stick. (B) Superposition of TtNAGK monomer with the monomers (open conformation) of EcNAGK (yellow, 2x2w), TmNAGK (green, 2bty), PaNAGK (light pink, 2buf) and AtNAGK (orange, 2rd5). The boxed region at the top and bottom are magnified, showing the structural variation at the flap-like lid region and the N-terminal region in various NAGKs respectively. (For interpretation of the references to color in this figure legend, the reader is referred to the web version of this article.)

structural features of this pocket were highly homologous to the NAG binding site of EcNAGK (Fig. 2A).

In the TtNAGK–NAG complex, NAG makes hydrogen bonds with residues G37, S38, R64, Y78 and N168. In EcNAGK complex (2x2w), NAGP interacts with G44, G45, R66, N158 and A161. The positions of these residues are homologous to one another. Also these residues are conserved in other NAGKs, indicating an identical mode of binding of NAG in all homologs.

TtNAGK monomer contains two sulfate molecules, namely SO_4(I) and SO_4(II) at the active site. These sulfates probably come from the crystallization solution which contains 0.5 M ammonium sulfate. SO_4(I) is at the NAG binding pocket whereas SO_4(II) is bound at the ATP binding site and is about 5.5 Å away from the first sulfate (Fig. 2B). On comparing TtNAGK with that of EcNAGK complexes namely EcNAGK–NAGP (2x2w) and EcNAGK–MgAMPPNP–NAG (1gs5), it is evident that SO_4(I) of TtNAGK is located very close

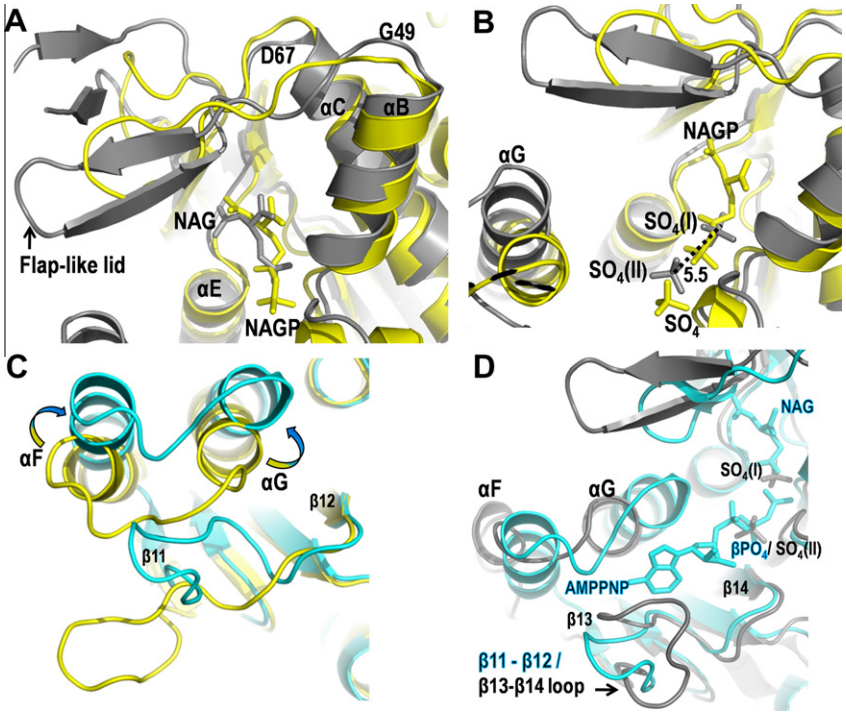

Fig. 2. Comparison of substrate binding site of TtNAGK (gray) and EcNAGK (yellow & cyan). (A) NAG docked at the active center of TtNAGK superimposed with the corresponding region of EcNAGK–NAGP complex structure (2x2w). The mode of binding of NAG in TtNAGK is highly similar to that of EcNAGK complex. (B) Comparison of NAG binding site of TtNAGK and EcNAGK–NAGP complex (2x2w). The SO_4(I) of TtNAGK is located at the same position where the carboxylate oxygen of NAGP is positioned. The distance between SO_4(I) and SO_4(II) is 5.5 Å. (C) Comparison of ATP binding site of apo-EcNAGK (open, 2wxb) with the corresponding region of EcNAGK–AMPPNP–NAG complex (closed, 1gs5). The arrow indicates the movement of αF and αG helices from open conformation to closed conformation. (D) Comparison of ATP binding site of EcNAGK–AMPPNP–NAG complex (1gs5) with the corresponding region of TtNAGK. The SO_4(II) of TtNAGK is positioned very close to β-phosphate of AMPPNP. (For interpretation of the references to color in this figure legend, the reader is referred to the web version of this article.)

to carboxylate oxygen atoms of NAGP and NLG, respectively and makes hydrogen bonds with K5, G37, S38 and Y78. TtNAGK was also compared with EcNAGK–ADP–SO_4 complex (1ohb) [22] which has its SO_4 at the NAG binding site and its position is similar to that of SO_4 (I) of TtNAGK.

3.5. ATP binding site

TtNAGK lacks its other substrate, the ATP, at its active site. Our attempts to dock ATP to TtNAGK failed as ATP could not be fit into the active site. A close inspection of the ATP binding region of apo-EcNAGK (2x2w) and EcNAGK–MgAMPPNP complex (1gs5) revealed that the orientation of αF, αG helices and a long loop that connects β11 and β12 had undergone a substantial structural rearrangement from apo to complex structure and that had created a cavity to accommodate the ATP molecule (Fig. 2C). Despite the overall structure of ATP binding site in TtNAGK being similar to the corresponding region of EcNAGK–MgAMPPNP complex, the orientation of αF, αG helices and the β13–β14 loop (analogous to β11–β12 loop of ECNAGK) are significantly different (Fig. 2D) from that seen in EcNAGK complex and these structural features hinder ATP binding by creating short contacts at the active site.

To gain further insights in the ATP binding site of TtNAGK, this region was compared with the corresponding region of ADP complexes of EcNAGK (1ohb) and AtNAGK (2rd5). Interestingly, the second sulfate SO_4(II) observed in our structure is close to the β-phosphate of ADP (Fig. 2D) and makes hydrogen bonds with residues G8, A9 and S191.

3.6. Arginine sensitivity

Feedback inhibition of NAGK by arginine is a vital aspect of the cyclic pathway of arginine biosynthesis and previous studies have revealed that arginine-sensitive NAGKs are hexameric [9], whereas the arginine-insensitive NAGK is a dimer [5,8,18,22]. Another structural feature exclusively associated with arginine sensitivity is the presence of a kinked N-terminal α-helix, the functional importance of which was demonstrated earlier by mutational studies in PaNAGK [2,5,8]. Absence of these features in TtNAGK is suggestive of the arginine insensitive nature of the enzyme and this is in sharp contrast to its thermophilic homolog TmNAGK. To further prove the arginine insensitivity of TtNAGK, its arginine binding region was compared with the corresponding region of TmNAGK and PaNAGK.

In TmNAGK, at the C-domain, the arginine is positioned in a crevice formed by the C-terminal end of N-helix, one end of the central β-sheet and the αH–β16 loop. At this site the residues K196, S214, E266, I267, S269 and G274 of TmNAGK make hydrogen bonding interaction with arginine. Residues K196, S214 and E266 interact with arginine through their side chain atoms while I267, S269 and G274 interact through their backbone carbonyl oxygen or nitrogen atom [8]. The residues corresponding to K196, S214 and E266 in TtNAGK are A186, R208 and A260, respectively, indicating the different environment of TtNAGK which might not be suitable for inhibitor binding (Fig. 3).

Furthermore, in TmNAGK the αH–β16 loop is three residues longer (in comparison to the corresponding loop of TtNAGK) providing not only a deeper cavity for arginine binding but helps in making hydrogen bonds with arginine through I267 and S269 of the loop. Lack of three residues in αH–β16 loop of TtNAGK makes that region very shallow with the absence of hydrogen bonds and hence this region might not be suitable for arginine binding (Fig. 3 & Supplementary Fig. S3). This was further evaluated by a structure based sequence alignment by comparing TtNAGK with other arginine-sensitive structures. Five crystal structures and five homology modeled structures all characterized as arginine sensitive NAGKs were used for structural alignment. The analysis clearly shows that in all arginine sensitive NAGKs the αH–β16 loop contains three additional residues indicating the presence of a deeper cavity for arginine binding which is missing in TtNAGK (see Supplementary Fig. S4). This feature, noticed for the first time, could be considered as a signature motif for differentiating the arginine sensitive NAGKs from insensitive ones in addition to the well characterized signature motif the N-terminal helix.

3.7. Conformational state of the enzyme

The previously solved NAGK structures reveal two conformational states namely open (TmNAGK, 2bty, [8]) and closed (EcNAGK, 1gs5, [18]). The closed conformation refers to N- and C-domain coming close to one another leading to a compact structure. Subsequently, the loop region (αB–αC loop) which is positioned on top of the substrate binding cleft moves in and completely closes the cleft with drastic changes in the orientation of the helices αF and αG of C-domain (Fig. 4A). Alternatively, in the open conformation, the molecule is more relaxed, where the N- and C-domain regions slightly move away from one another with subsequent movement of αB–αC loop thus exposing the substrate binding region (Fig. 4A). The αB–αC loop therefore acts as a lid by opening and closing the substrate binding region on different conformational states of the molecule.

In the closed lid position, the tip of the lid makes hydrogen bonds and van der Waals interactions with the N-terminal end of helix G and these interactions are broken in the open lid position. A detailed analysis of intramolecular interactions ($\leqslant$4.5 Å) between the flap like-lid and the N-terminal of helix G in the open and closed NAGK molecules is given in Supplementary Table 2 and Fig. S5. This analysis clearly shows that TtNAGK exhibits intramolecular interactions suggesting its closed lid conformation. However, the orientation of αF and αG helices of TtNAGK are significantly different from the orientation of corresponding helices in the closed as well as open active site structures (Fig. 4A).

Further it is observed that in closed lid conformation of EcNAGK (1gs5), the three residues important for catalysis namely, K8, D162 and K217 make an ion-pair network (Fig. 4A) [4,8,9]. This ion-pair network is broken in the open state (2x2w) mainly due to the drastic change in the orientation of helix αG of the C-domain that comprises the residue K217 [9] while the positions of residues K8 and D162 from β1 and αE, respectively of N-domain are retained. In TtNAGK the network is broken as observed in the open form of EcNAGK although the lid that covers substrate binding cleft adopts a closed conformation (Fig. 4A).

Another key difference between the open and the closed forms is the distance between the β-phosphate of ADP and carboxylate oxygen of NAG. This measures 5.5 Å in the closed conformation while it is nearly 7.0 Å in the open state as seen in the structure of AtNAGK complex (2rd5) [7]. In TtNAGK, the two sulfates are placed at a distance of 5.5 Å with SO_4(I) and SO_4(II) located very close to that of carboxylate oxygen of NAG and β-phosphate of ADP respectively (Fig. 4B). This suggests the possibility of a closed conformation of the enzyme. Hence, we hypothesize that the two sulfates of TtNAGK found in N-domain [SO_4(I)] and ATP binding region [SO_4(II)] are reminiscent of phosphorylated product (NAGP) and ADP, respectively.

In conclusion, the presence of intramolecular interactions between the flap like-lid and the N-terminal of helix G and the closer distance between the reacting groups (here mimicked by two sulfates) signifies the closed nature of the active site of TtNAGK. However, the broken ion-pair network, orientation of αF and αG helices and the inability of ATP to accommodate in its binding site is contradictory to its closed active site conformation of the molecule. The above mentioned structural features of TtNAGK suggests that

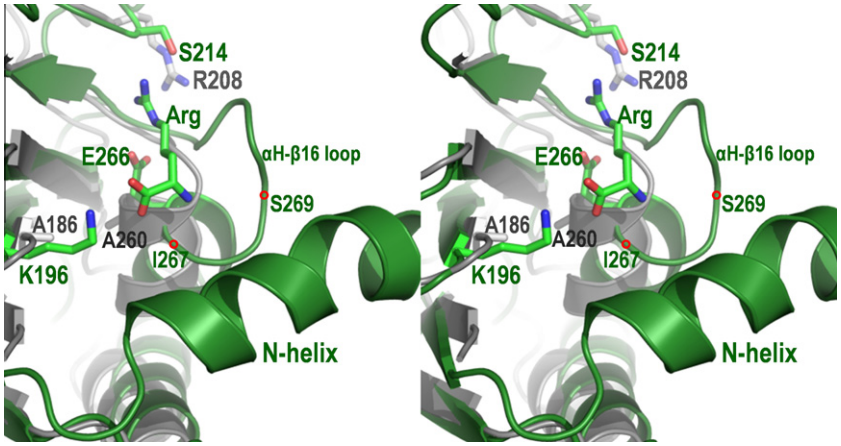

Fig. 3. Comparison of arginine binding site of TmNAGK (green) and TtNAGK (gray). In TmNAGK, the arginine is positioned in a crevice whereas the corresponding region in TtNAGK is very shallow indicating not suitable for arginine binding. (For interpretation of the references to color in this figure legend, the reader is referred to the web version of this article.)

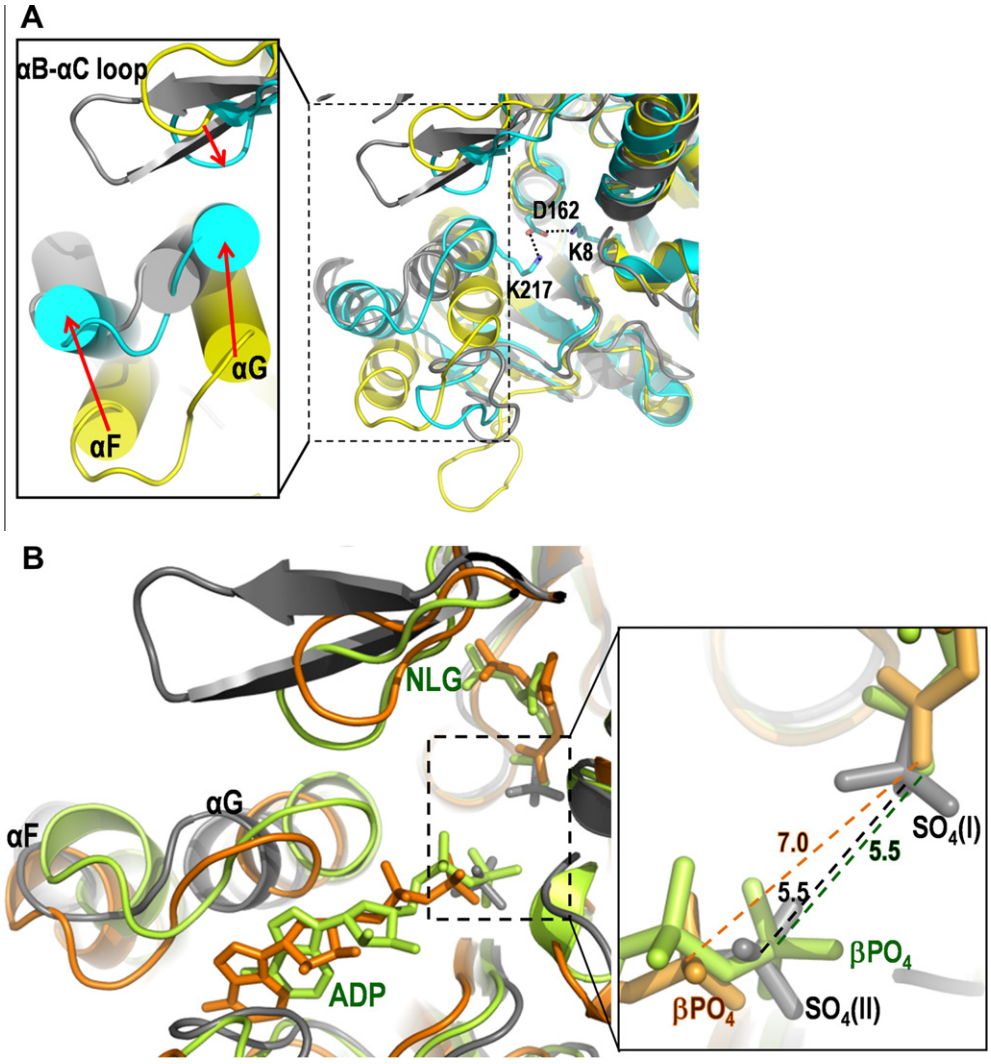

Fig. 4. Structural comparison of TtNAGK with open and closed conformations of EcNAGK and AtNAGK. (A) Superimposition of TtNAGK (gray) with open conformation of EcNAGK–NAGP (yellow, 2x2w) and closed conformation of EcNAGK–AMPPNP–NAG (cyan, 1gs5). In the inset, the direction of movement of helices αF, αG and that of the flap-like lid region from open to closed conformation are indicated in red arrows. The ion-pair network (K8-D162-K217) observed in the closed conformation structure of EcNAGK (1gs5) is shown. (B) Superimposition of TtNAGK with open (orange) and closed (green) conformations of AtNAGK (2rd5) shows the position of sulfates in TtNAGK and that of the reacting groups in AtNAGK structures, highlighted in the box region. The inset in stick representation displays the distances between the βPO_4 of ADP and COO^- group of NAG of open (orange) and closed (green) AtNAGKs, respectively and that between the two sulfates (gray) of TtNAGK suggesting that TtNAGK is similar to the closed AtNAGK. (For interpretation of the references to color in this figure legend, the reader is referred to the web version of this article.)

the active site of the molecule is neither in closed nor in open conformation and probably exists in the intermediate stage of catalysis. It has previously been hypothesized that the NAGK enzymes cycle between an open and closed conformation during catalysis [23]. The intermediate conformation of TtNAGK presents an experimental proof for the previous hypothesis, although its biological significance is yet to be identified.

3.8. Structural basis of the thermostability of TtNAGK

The structure of TtNAGK provides an impetus for a comparison with its mesophilic homolog EcNAGK to understand the structural basis of the thermostability of TtNAGK. Several sequence and structural factors have shown to enhance the stability of thermophilic proteins such as salt bridges, side chain–side chain hydrogen bonds, lesser overall flexibility, increased polar surface area, fewer numbers of Cys and Ser, high occurrence of Arg and Tyr, large number of residues in alpha helical conformation and very few Pro in the helices [24,25]. TtNAGK and EcNAGK are both dimeric and show similar structural compactness. This indicates other structural parameters probably play a major role in the thermostability of TtNAGK.

Detailed structural analysis shows that TtNAGK possesses significantly higher number of ion-pairs, hydrogen bonds and charged residues in comparison with EcNAGK (data not shown). It also contains 18 Arg and 10 Tyr residues, the residues enhance structural stability, in contrast to 9 Arg and 2 Tyr in EcNAGK.

Several strategies have been employed to increase the industrial production of arginine [26,27]. For example, very recently it has been shown that site-directed mutagenesis of the arginine binding residues of NAGK of *Corynebacterium crenatum* abolishes arginine inhibition and increased the arginine production without any perturbation of its activity [28]. Moreover it is well known that mutagenesis of even a single residue can enhance or decrease the thermostability of a protein. In this context, the structural knowledge of the intra and inter molecular interactions as obtained from this work would be useful for engineering NAGKs to enhance their overall stability for industrial use.

Acknowledgments

The authors thank C. Kuroishi for cloning of the *TTHA1903* gene. This work was supported by the RIKEN Structural Genomic/Proteomics Initiative (RSGI), the National Project on Protein Structural and Functional Analyses, Ministry of Education, Culture, Sports, Science and Technology of Japan. R.S. thanks University Grants Commission (UGC), Government of India for providing fellowship.

Appendix A. Supplementary data

Supplementary data associated with this article can be found, in the online version, at http://dx.doi.org/10.1016/j.bbrc.2012.03.072.

References

[1] R. Cunin, N. Glansdorff, A. Pierard, V. Stalon, Bio-synthesis and metabolism of arginine in bacteria, Microbiol. Rev. 50 (1986) 314–352.
[2] M.L. Fernández-Murga, V. Rubio, Basis of arginine sensitivity of microbial *N*-acetyl-L-glutamate kinases: mutagenesis and protein engineering study with the *Pseudomonas aeruginosa* and *Escherichia coli* enzymes, J. Bacteriol. 90 (2008) 3018–3025.
[3] D. Haas, T. Leisinger, *N*-Acetylglutamate 5-phosphotransferase of *Pseudomonas aeruginosa*. Purification and ligand-directed association–dissociation, Eur. J. Biochem. 52 (1975) 365–375.
[4] M.L. Fernández-Murga, F. Gil-Ortiz, J.L. Llácer, V. Rubio, Arginine biosynthesis in *Thermotoga maritima*: characterization of the arginine-sensitive *N*-acetyl-L-glutamate kinase, J. Bacteriol. 186 (2004) 6142–6149.
[5] R.D. Slocum, Genes, enzymes and regulation of arginine biosynthesis in plants, Plant Physiol. Biochem. 43 (2005) 729–745.
[6] Y. Xu, B. Labedan, N. Glansdorff, Surprising arginine biosynthesis: a reappraisal of the enzymology and evolution of the pathway in microorganisms, Microbiol. Mol. Biol. Rev. 71 (2007) 36–47.
[7] Y. Mizuno, G.B. Moorhead, K.S. Ng Kenneth, Structural basis for the regulation of *N*-acetylglutamate kinase by PII in *Arabidopsis thaliana*, J. Biol. Chem. 282 (2007) 35733–35740.
[8] S. Ramón-Maiques, M.L. Fernández-Murga, F. Gil-Ortiz, A. Vagin, I. Fita, V. Rubio, Structural bases of feed-back control of arginine biosynthesis, revealed by the structures of two hexameric *N*-acetylglutamate kinases, from *Thermotoga maritima* and *Pseudomonas aeruginosa*, J. Mol. Biol. 356 (2006) 695–713.
[9] J.L. Llácer, A. Contreras, K. Forchhammer, C. Marco-Marín, F. Gil-Ortiz, R. Maldonado, I. Fita, V. Rubio, The crystal structure of the complex of PII and acetylglutamate kinase reveals how PII controls the storage of nitrogen as arginine, Proc. Natl. Acad. Sci. USA 104 (2007) 17644–17649.
[10] E. Alonso, V. Rubio, Participation of ornithine aminotransferase in the synthesis and catabolism of ornithine in mice. Studies using gabaculine and arginine deprivation, Biochem. J. 259 (1979) 131–138.
[11] M.E. Jones, Catalysts of the urea cycle, Trans. N. Y. Acad. Sci. 41 (1983) 77–82.
[12] Z. Otwinowski, W. Minor, Processing of Xray diffraction data collected in oscillation model, Methods Enzymol. 276 (1997) 307–326.
[13] T.C. Terwilliger, J. Berendzen, Automated MAD and MIR structure solution, Acta. Crystallogr., Sect D: Biol. Crystallogr. D55 (1999) 849–861.
[14] T.C. Terwilliger, Maximum likelihood density modification, Acta Crystallogr., Sect D: Biol. Crystallogr. D56 (2000) 965–972.
[15] A. Perrakis, R. Morris, V.S. Lamzin, Automated protein model building combined with iterative structure refinement, Nat. Struct. Biol. 6 (1999) 458–463.
[16] A.T. Brunger, P.D. Adams, G.M. Clore, P. Gros, R.W. Grosse-Kunstleve, J.-S. Jiang, J. Kuszewski, N. Nilges, N.S. Pannu, R.J. Read, L.M. Rice, T. Simonson, G.L. Warren, Crystallography & NMR System (CNS). A new software suite for macromolecular structure determination, Acta Crystallogr., Sect D: Biol. Crystallogr. D54 (1998) 905–921.
[17] B. Lohkamp, P. Emsley, K. Cowtan, Coot News, CCP4 Newsletter, 42 (2005) Contribution 7.
[18] S. Ramón-Maiques, A. Marina, F. Gil-Ortiz, I. Fita, V. Rubio, Structure of acetylglutamate kinase, a key enzyme for arginine biosynthesis and a prototype for the amino acid kinase enzyme family, during catalysis, Structure 10 (2002) 329–342.
[19] S.F. Altschul, W. Gish, W. Miller, E.W. Myers, D.J. Lipman, Basic local alignment search tool, J. Mol. Biol. 215 (1990) 403–410.
[20] L. Holm, P. Rosenström, Dali server: conservation mapping in 3D, Nucleic Acids Res. 38 (2010) W545–W549.
[21] G.M. Morris, D.S. Goodsell, R.S. Halliday, R. Huey, W.E. Hart, R.K. Belew, A.J. Olson, Automated docking using a lamarckian genetic algorithm and empirical binding free energy function, J. Comput. Chem. 19 (1998) 1639–1662.
[22] F. Gil-Ortiz, S. Ramón-Maiques, I. Fita, V. Rubio, The course of phosphorus in the reaction of *N*-acetyl-L-glutamate kinase, determined from the structures of crystalline complexes, including a complex with an $AlF4^-$ transition state mimic, J. Mol. Biol. 331 (2003) 231–244.
[23] F. Gil-Ortiz, S. Ramón-Maiques, M.L. Fernández-Murga, I. Fita, V. Rubio, Two crystal structures of *Escherichia coli N*-acetyl-L-glutamate kinase demonstrate the cycling between open and closed conformations, J. Mol. Biol. 399 (2010) 476–490.
[24] S. Kumar, C.-J. Tsai, R. Nussinov, Factors enhancing protein thermostability, Protein Eng. 13 (2000) 179–191.
[25] A. Szilagyi, P. Zavodszky, Structural differences between mesophilic, moderately thermophilic and extremely thermophilic protein subunits: results of a comprehensive survey, Structure 8 (2000) 493–504.
[26] B.S. Rajagopal, J. DePonte, M. Tuchman, M.H. Malamy, Use of inducible feedback-resistant *N*-acetylglutamate synthetase (arga) genes for enhanced arginine biosynthesis by genetically engineered *Escherichia coli* K-12 strains, Appl. Environ. Microbiol. 64 (1998) 1805–1811.
[27] M. Xu, Z. Rao, W. Dou, J. Yang, J. Jin, Z. Xu, Site-directed mutagenesis and feedback-resistant *N*-acetyl-L-glutamate kinase (NAGK) increase *Corynebacterium crenatum* L-arginine production, Amino Acids (2011), http://dx.doi.org/10.1007/s00726-011-1069-x.
[28] Y. Xu, B. Labedan, N. Glansdorff, Surprising arginine biosynthesis: a reappraisal of the enzymology and evolution of the pathway in microorganisms, Microbiol. Mol. Biol. Rev. 71 (2007) 36–47.

Biochemical and Biophysical Research Communications 420 (2012) 698

Contents lists available at SciVerse ScienceDirect

Biochemical and Biophysical Research Communications

journal homepage: www.elsevier.com/locate/ybbrc

Letter to the Editor

mtDNA variations other than point mutations may also have a role in carcinogenesis of lung cancer

To the editor,

We read the article by Choi et al. entitled "Mutational hotspots in the mitochondrial genome of lung cancer" [1] with great interest. In this article, aim of authors is detection of mutational hotspots in the mitochondrial genomes in smokers' lung cancer. With this aim, they collected samples from 70 lung cancer patients. Thirty of those patients are smoker, 31 are nonsmoker and 9 are undeclared. Mitochondrial DNA isolation and then whole mtDNA sequencing was made by Affymetrix gene chip human mitochondrial DNA resequencing array 2.0. Five hundred and thirty two somatic mutations were found in a total of 499 positions. Their data suggested that mitochondrial mutations were most frequently mutated in the non-coding D-loop region, and the non-synonymous mutations causing amino acid substitution were concentrated in specific positions in respiratory chain complex 1 at 8701 and 10,398. At this point, we share the authors' scientific view, and think that this study is well constructed and highly scientific.

However, we would like to express some constructive criticism as follows: As known, there are three major alterations of mtDNA: (i) point mutations, (ii) large scale deletions and (iii) mtDNA depletions [2]. Anyone of these alterations can be the cause of severe mitochondrial dysfunction, production of reactive oxygen species, which are known to contribute in cancer development, and may injure DNA further. For example, mitochondrial encephalomyopathy, lactic acidosis and stroke like syndrome (MELAS) occurs with a point mutation. On the other hand, Kearn–Sayre syndrome is caused by large scale deletions. mtDNA depletion may express as Alpers' syndrome. We understand that the authors have considered just point mutations in mtDNA. There are some studies in the literature investigating mtDNA copy number and deletions in lung cancer [3] and in which it has been shown that changes in mtDNA copy number and small or large scale deletions occur in lung cancer. We wanted to add to this well written article that the mtDNA variations other than point mutations may also have a role in carcinogenesis of lung cancer.

References

[1] S.J. Choi, S.H. Kim, H.Y. Kang, et al, Mutational hotspots in the mitochondrial genome of lung cancer, Biochem. Biophys. Res. Commun. 407 (1) (2011) 23–27.
[2] S. DiMauro, E. Bonilla, Mitochondrial encephalomyopathies, in: A.G. Engel, C. Franzini-Armstrong (Eds.), Myology, vol. II, McGrav Hill, Philadelphia, 2004, pp. 1623–1676.
[3] H.D. Hosgood, C.S. Liu, N. Rothman, et al, Mitochondrial DNA copy number and lung cancer risk in a prospective cohort study, Carcinogenesis 31 (5) (2010) 847–849.

Yasemin Gulcan Kurt
Tuncer Cayci
Emin Ozgur Akgul
Department of Biochemistry,
Gulhane Military Medical Academy and Medical School,
Turkey

Bulent Kurt
Department of Pathology,
Gulhane Military Medical Academy and Medical School,
GATA, Patoloji Anabilim Dalı, 06018 Etlik,
Ankara, Turkey
E-mail address: bkurt@gata.edu.tr

Available online 26 March 2012

http://dx.doi.org/10.1016/j.bbrc.2012.03.115

Biochemical and Biophysical Research Communications

Correspondence regarding production may be sent to:

Biochemical and Biophysical Research Communications, Elsevier Inc.

525 B Street, Suite 1800, San Diego, California 92101-4495, USA
Telephone +1 (619) 699-6857, Fax +1 (619) 699-6859, E-mail bbrc@elsevier.com

0006-291X(20120413)420:3;1-V

Cover photo. The cover photo graphic is taken from figure 1A of the paper 'Susceptibility of Antiviral Drugs Against 2009 Influenza A (H1N1) Virus' published in the journal (BBRC Volume 385, pages 390–394). It is reproduced by kind permission of the authors – Supot Hannongbua, et al.